

KONA Powder and Particle Journal

No.34 (2017)



Hosokawa Powder Technology Foundation

available online-www.kona.or.jp

About this Journal

KONA Powder and Particle Journal is a refereed scientific journal that publishes articles on powder and particle science and technology. This journal has been published annually since 1983 and is distributed free of charge to researchers, members of the scientific communities, universities and research libraries throughout the world, by Hosokawa Powder Technology Foundation (<http://www.kona.or.jp/>) established by Mr. Masuo Hosokawa in 1991.

The Chinese character “粉” in the cover is pronounced “KONA” in Japanese, and means “Powder”. The hand written “粉” is after the late Mr. Eiichi Hosokawa, founder of the Hosokawa Micron Corporation (<http://www.hosokawa-micron.co.jp>).

About the Cover

Preventing transfer of pathogens from touch surfaces has been an extremely important topic of research in reducing hospital acquired infections. With increasing challenges of antimicrobial resistance, there is need for new and advanced materials systems that can disinfect pathogens for long periods of time, without inducing concerns of antimicrobial resistance. TiO_2 based photocatalytic system has been used to address this need for inactivation of pathogens via visible light photocatalysis. The proposed mechanism of the self cleaning surface includes contaminant mediated activation of the photocatalytic surface. The presence of visible light absorbing contaminant (microbe) triggers a chain of photocatalytic reactions leading to complete oxidation, degradation and inactivation of the microbe. Please read the paper on pp.234–240.



Headquarters of Hosokawa Micron Corporation

Editorial Board

Editor-in-Chief

J. Hidaka (Doshisha Univ., Japan)

Asian / Oceanian Editorial Board

S. Biggs (Univ. of Queensland, Australia)
 X.S. Cai (Univ. of Shanghai for Sci. & Tech., China)
 T. Charinpanitkul (Chulalongkorn Univ., Thailand)
 Y. Fukumori (Kobe Gakuin Univ., Japan)
 K. Higashitani (Kyoto Univ., Japan)
 H. Kage (Kyushu Institute of Technology, Japan)
 Y. Kang (Chungnam National Univ., Korea)
 D.J. Lee (National Taiwan Univ., Taiwan)
 J.H. Li (Chinese Academy of Science, China)
 H. Makino (CRIEPI, Japan)
 S. Matsusaka (Kyoto Univ., Japan)
 M. Naito (Osaka Univ., Japan)
 K. Nogi (Osaka Univ., Japan)
 K. Okuyama (Hiroshima Univ., Japan)
 Pradip (TRDDC, India)
 M. Rhodes (Monash Univ., Australia)
 M. Takahashi (Nagoya Institute of Technology, Japan)
 H. Takeuchi (Gifu Pharmaceutical Univ., Japan)
 W. Tanthapanichakoon (Chulalongkorn Univ., Thailand)
 Y. Tsuji (Osaka Univ., Japan)
 C.H. Wang (National University of Singapore)
 S. Watano (Osaka Pref. Univ., Japan)

Secretariat

T. Yokoyama (Hosokawa Powder Tech. Foundation, Japan)
 L. Cui (Hosokawa Micron Corp., Japan)

European / African Editorial Board

Chairman

G.M.H. Meesters (Delft Univ. of Technology, Netherlands)
 B. Biscans (Univ. de Toulouse, France)
 M.-O. Coppens (Univ. College London, UK)
 L. Gradon (Warsaw Univ. of Technology, Poland)
 A. Kwade (TU Braunschweig, Germany)
 P. Milani (Univ. of Milan, Italy)
 J.M. Valverde (Univ. of Seville, Spain)

Secretariat

S. Sander (Hosokawa Alpine AG, Germany)
 L. Kneisl (Hosokawa Alpine AG, Germany)

American Editorial Board

Chairman

B.M. Moudgil (Univ. of Florida, USA)
 A.J. Hickey (Univ. of North Carolina, USA)
 V. M. Puri (Pennsylvania State Univ., USA)
 R.K. Rajamani (Univ. of Utah, USA)
 A.D. Rosato (New Jersey Institute of Technology, USA)
 L.M. Tavares (UFRJ, Brazil)

Secretariat

C.C. Huang (Hosokawa Micron Intl. Inc., USA)

Publication Office

Hosokawa Powder Technology Foundation (<http://www.kona.or.jp>)
 (in the headquarters building of Hosokawa Micron Corporation)
 1-9, Shodaitajika, Hirakata-shi, Osaka 573-1132, Japan
 E-mail: contact_zainq@hmc.hosokawa.com

Printing Office: Nakanishi Printing Co., Ltd., Japan

Publication Date: 10 January 2017

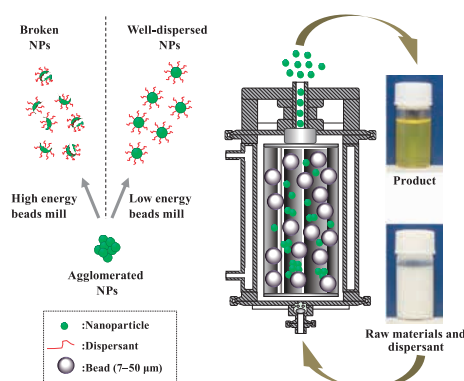
<Editorial>

1 Editor's Preface

<Review Papers>

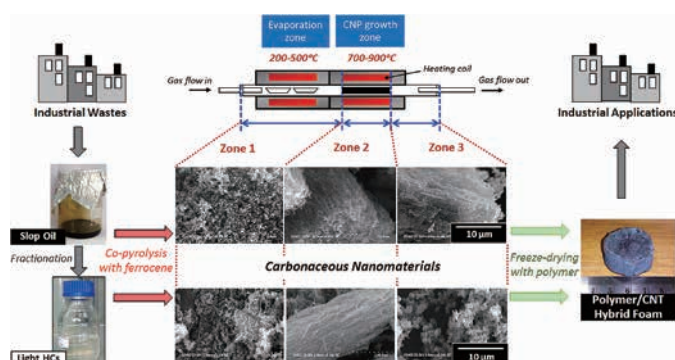
3 Recent Progress in Nanoparticle Dispersion Using Bead Mill

Takashi Ogi, Rizka Zulhijah, Toru Iwaki and Kikuo Okuyama



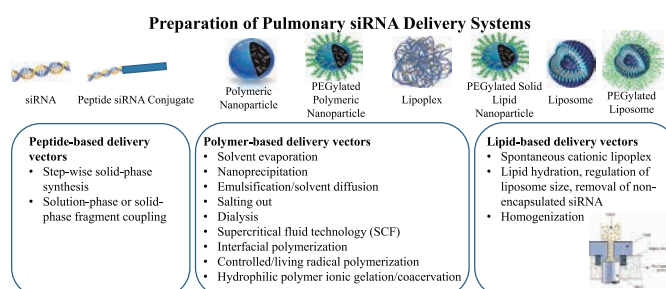
24 Present Advancement in Production of Carbon Nanotubes and Their Derivatives from Industrial Waste with Promising Applications

Konrat Kerdnawee, Chompoopitch Termvidchakorn, Pacharaporn Yaisanga, Jirapat Pakchamsai, Cheewapon Chookiat, Apiluck Eiad-ua, Winadda Wongwiriyan, Weerawut Chaiwat, Sakhon Ratchahat, Kajornsak Faungnawakij, Komkrit Suttiponparnit and Tawatchai Charinpanitkul



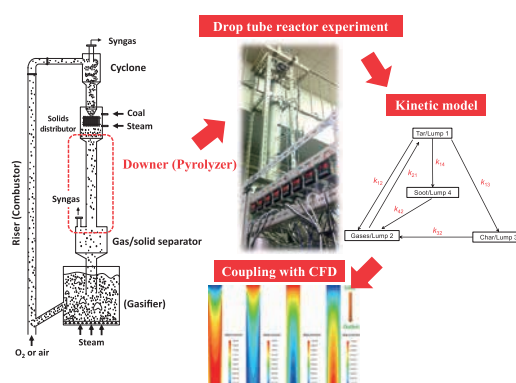
44 Aerosol Delivery of siRNA to the Lungs. Part 2: Nanocarrier-based Delivery Systems

Susanne R. Youngren-Ortiz, Nishant S. Gandhi, Laura España-Serrano and Mahavir B. Chougule

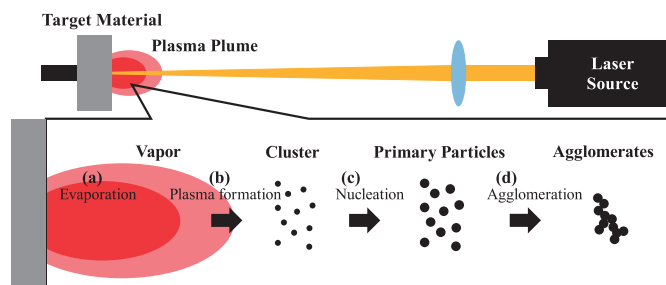


70 Toward Low-Temperature Coal Gasification: Experimental and Numerical Studies of Thermochemical Coal Conversion Considering the Interactions between Volatiles and Char Particles

Cheng-Yi Li, Li-Xin Zhang, Shinji Kudo, Jun-ichiro Hayashi and Koyo Norinaga



80 Synthesis of Nanoparticles by Laser Ablation: A Review



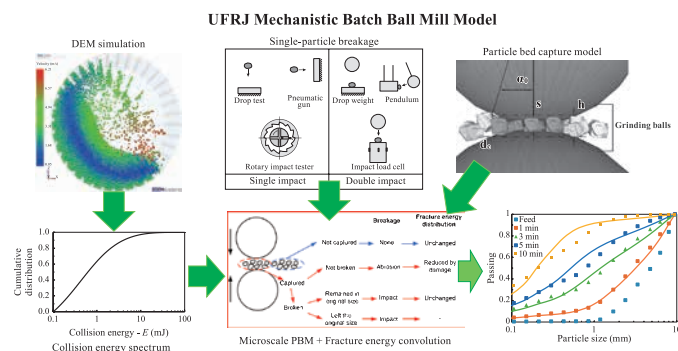
Myungjoon Kim, Saho Osone, Taesung Kim,
Hidenori Higashi and Takafumi Seto

91 Deficiencies in Traditional Oral Dosage Forms and the Emergence of Controlled- Release Powder Manufacturing



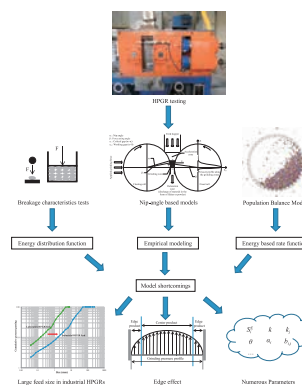
Martin G. Teresk, Cory J. Berkland and Nathan
H. Dormer

106 A Review of Advanced Ball Mill Modelling



Luís Marcelo Tavares

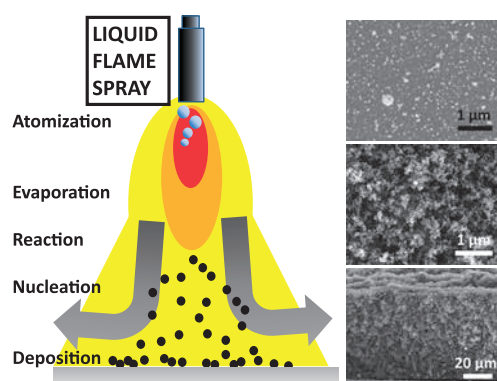
125 A Review of the Modeling of High Pressure Grinding Rolls



Samira Rashidi, Raj K. Rajamani and Douglas
W. Fuerstenau

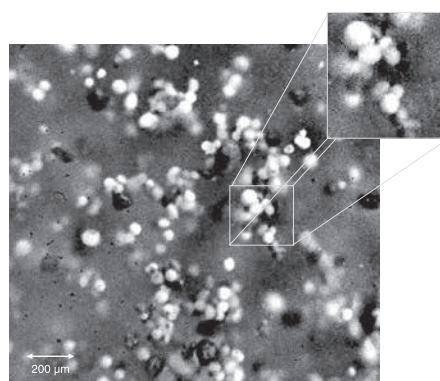
141 Liquid Flame Spray—A Hydrogen-Oxygen Flame Based Method for Nanoparticle Synthesis and Functional Nanocoatings

Jyrki M. Mäkelä, Janne Haapanen, Juha Harra, Paxton Juuti and Sonja Kujanpää



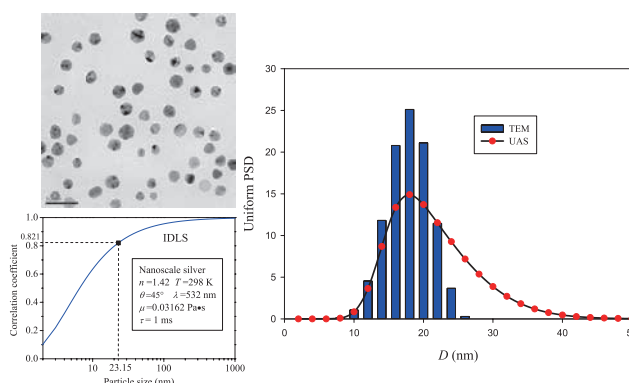
155 Small-Scale Particle Interactions Are Having Significant Effects on Global Fluidized Bed Behavior

Ray Cocco, Allan Issangya, S.B. Reddy Karri, Tim Freeman, Heinrich M. Jaeger and Ted M. Knowlton



168 Advances in Nanoparticle Sizing in Suspensions: Dynamic Light Scattering and Ultrasonic Attenuation Spectroscopy

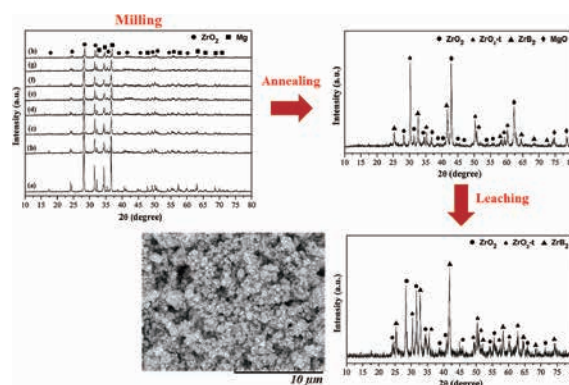
Wu Zhou, Mingxu Su and Xiaoshu Cai



<Original Research Papers>

183 Microstructural Evaluation of $\text{ZrB}_2/\text{ZrO}_2$ Ceramic Powders Prepared by Milling-Assisted Magnesiothermic Reduction of Oxide Raw Materials

Duygu Ağaoğulları, Özge Balcı, M. Lütfi Öveçoğlu and İsmail Duman



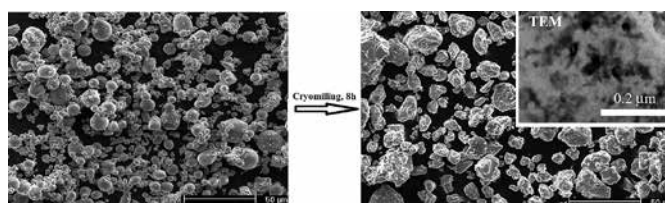
197 Comparison of Compression and Material Properties of Differently Shaped and Sized Paracetamols

Michal Šimek, Veronika Grünwaldová and
Bohumil Kratochvíl



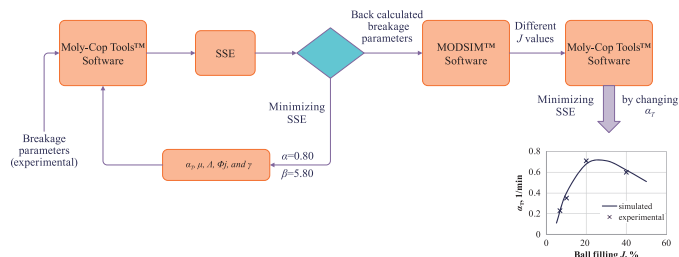
207 Nanocrystallization of Al Powder by Cryomilling Process

Mohammad Hossein Enayati



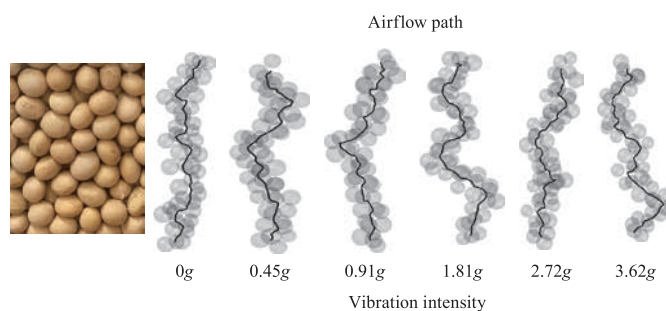
213 Identification of Optimal Mill Operating Parameters during Grinding of Quartz with the Use of Population Balance Modeling

Evangelos Petrakis, Elias Stamboliadis and
Konstantinos Komnitsas



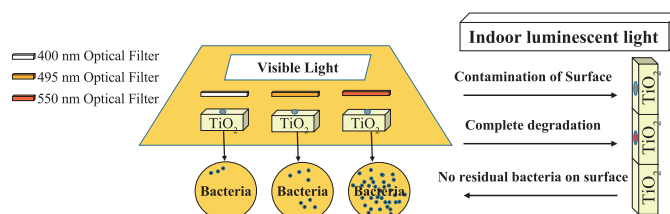
224 Changes in Pore Structures of Porous Beds When Subjected to Vertical Vibration

Rong Yue and Qiang Zhang



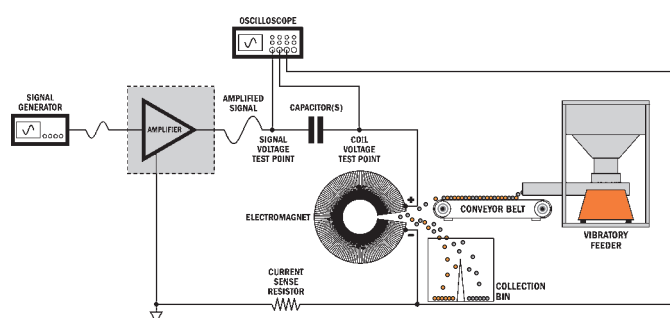
234 Visible Light Photocatalytic Bacterial Inactivation on Titanium Dioxide Coatings

Vignesh Nandakumar, Zhao Han, Zachary Fritz, Vijay Krishna, Ben Koopman and Brij Moudgil



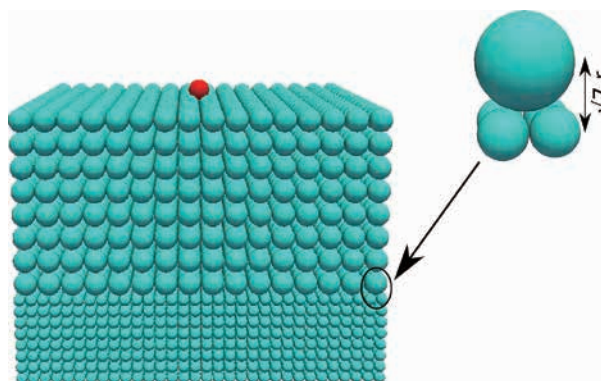
241 Eddy Current Separation of Nonferrous Metals Using a Variable-Frequency Electromagnet

Nakul Dholu, James R. Nagel, Dave Cohrs and Raj K. Rajamani



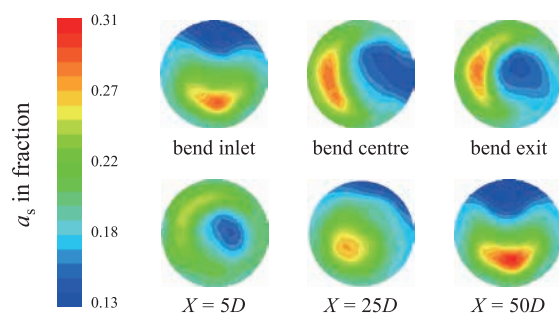
248 Impact Dispersion Using 2D and 3D Composite Granular Packing

Surajit Sen, T. R. Krishna Mohan and Mukesh Tiwari



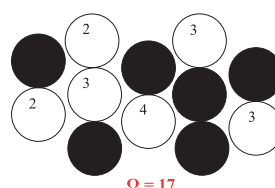
258 Flow of Bi-modal Slurry through Horizontal Bend

Deo Raj Kaushal, Arvind Kumar, Yuji Tomita, Shigeru Kuchii and Hiroshi Tsukamoto



Concentration distributions at $V_m = 3.56$ m/s and $C_{vf} = 16.28\%$

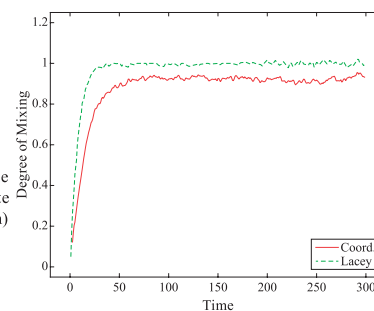
275 A Study of the Mixing Index in Solid Particles



Ω denote the coordinate number of the system, and Ω_{ran} denote the coordinate number of the well-mixed (most random) system

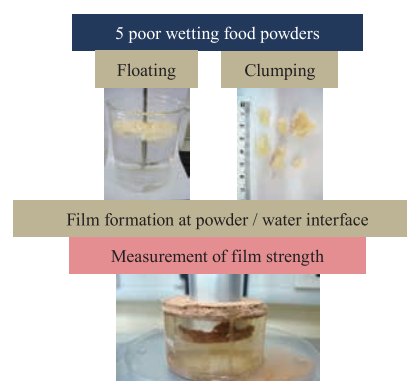
$$\Omega_{ran} = (a-1)bc + (b-1)ca + (c-1)ab$$

$$Coord. = \frac{\Omega}{\Omega_{ran}}$$



Shih-Hao Chou, Yue-Lou Song and Shu-San Hsiau

282 Characterisation of the Wetting Behaviour of Poor Wetting Food Powders and the Influence of Temperature and Film Formation



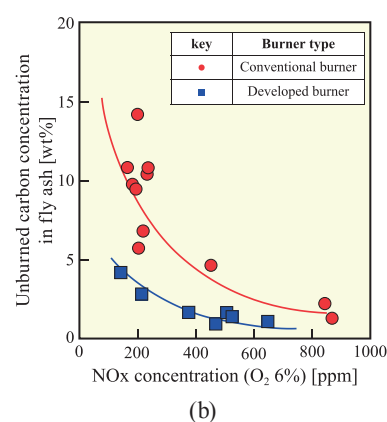
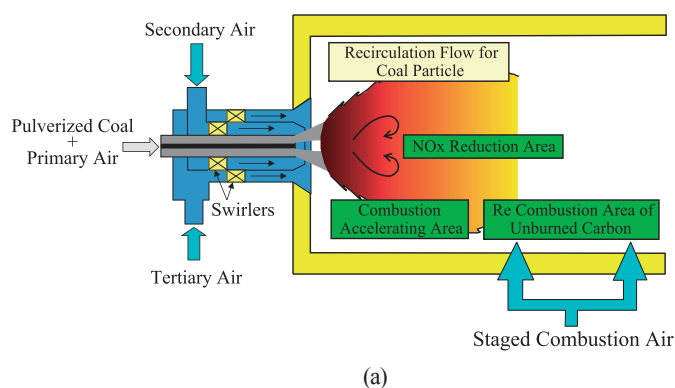
John J. Fitzpatrick, Justine Salmon, Junfu Ji and Song Miao

<Information Articles>

290 The 50th Symposium on Powder Technology

292 The 23rd KONA Award (Awardee: Dr. Hisao MAKINO)

293 General Information



Some achievements of the research for the 23rd KONA Award: (a) Concept of ultra-low NO_x combustion technology and burner. (b) Comparison of unburned fraction against NO_x concentration between developed and conventional burners.(p.292)

Editor's Preface

Jusuke Hidaka, Editor-in-Chief

Doshisha University, Japan



I have the pleasure of sending you the KONA No.34 Journal which had many interesting review papers and original research reports. Two years ago, this annually published KONA Journal was opened to the J-STAGE (Japan Science and Technology Information Aggregator, Electronic), which is an international online archive to support the transmission function of the information of science and technology organized by Japan Science and Technology Agency belonging to Ministry of Education, Culture, Sports, Science and Technology. It introduced the Open Access policy this year to enable free browsing and reuse by the readers all over the world. As a result, the KONA Journal has approximately 300 viewers per day and the latest Impact Factor of this journal is 1.67 and is increasing every year.

The KONA Editorial Committee consists of three editorial boards located in Europe, America and Asia/Oceania, as shown on the opposite side of the front cover of the Journal. The Committee receives papers submitted by authors throughout the year. The papers will then be published worldwide after the submission to the Advance Publication on the J-STAGE passing through the strict reviewing procedures. Among the 22 papers published in No.34, 18 papers have been submitted as Advance Publication and accessed by readers worldwide before the publication of the printed version. We are looking forward to receiving articles from you for the KONA Journal.

Presently our society is continually seeking a higher quality, where people can live healthy and safely with material wealth and spiritual prosperity. In order to achieve this, there is a strong desire to create (/produce) powder materials with a higher quality to solve current problems of our present society with energy, medicine, food etc. and to develop fine particles with advanced functions. In response to these requirements, powder science and technology are advancing remarkably, entering the region of “Product Design”.

Powder technology started from the design of processing system to produce powder materials. It was the engineering for designing the unit operations for powder processing like grinding, classification and the like as well as powder processing systems combining the unit operations. It was thought that the production processes of powder materials would consist of powder unit operations and be constructed just by the combination or connection of generally developed powder machines and equipment. It has worked that way in the age of mass production of general products. However, in the present age, confronting the production of high functional materials, it is required to design microstructure of materials most suitable to achieve the desired functions and the powder processes to realize it precisely. It is also characterized that the powder processes to produce the advanced functional materials need the processing of each specified material and that their individualization and complexity are advancing rapidly.

The KONA Journal is published once a year and the publication frequency is too low to have the research report published. I would like to publish the review papers with high quality concerning the rapidly advancing powder science and technology to contribute for further advancement of powder science and technology in the world. I intend to make every effort to publish the KONA Journal under this editing policy and would like to ask for your cooperation and contributions.

Reviewer Appreciation

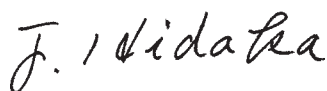
I express our gratitude to the reviewers for the publication of this KONA Powder and Particle Journal. Thanks to the generous contributions of the volunteer reviewers as well as the interest of researchers in our journal, the number of submission to this journal is increasing after the registration on the major international journal platforms and its level is further improving. Because of the limited space of this annual journal, the number of papers published there is regrettably rather restricted. Therefore the papers of good quality need to be selected for the journal and further improved and refined by the reviewing.

The editorial team of KONA Journal would like to take this opportunity to gratefully acknowledge the reviewers here and deeply appreciate their valuable time and professional contributions to this number of KONA Journal. We apologize to any reviewer who may have inadvertently been omitted from this list. We are sincerely grateful to all who have been of any assistance to the publication of this journal.

ADACHI, Motoaki
COPPENS, Marc-Olivier
FUKUMORI, Yoshinobu
HICKEY, Anthony
HUANG, Ching-Chung
KANO, Junya
KIMATA, Mitsumasa
MEESTERS, Gabriel
MILANI, Paolo
MIYAHARA, Minoru

MORI, Yasushige
MOUDGIL, Brij
OKUYAMA, Kikuo
PEUKERT, Wolfgang
PURI, Virendra
RAJAMANI, Raj
SAITO, Fumio
SATO, Munetaka
SUZUKI, Hiroshi
TAKARADA, Takayuki

TAKEDA, Shin-ichi
TANAKA, Hidekazu
TAVARES, Luis Marcelo
TOZUKA, Yuichi
TSUJI, Yutaka
TSUJI, Takuya
WINDOWS-YULE, Kit
YOKOYAMA, Toyokazu
YOSHIDA, Hideto



Jusuke Hidaka
Editor-in-Chief
Prof. emeritus, Doshisha University
October 2016

Recent Progress in Nanoparticle Dispersion Using Bead Mill[†]

Takashi Ogi*, Rizka Zulhijah, Toru Iwaki and Kikuo Okuyama

¹ Department of Chemical Engineering, Hiroshima University, Japan

Abstract

There is great demand for nanoparticles (NPs) dispersed in liquid phases for practical applications of functional NP materials. However, it is difficult to produce NP dispersions with specific particle sizes, concentrations, viscosities, and purities on an industrial scale (large mass production rate and low energy consumption). In this review, we highlight recent developments in NP dispersion using low-energy bead mill. Such processes enable the use of small beads (7–50 μm). Smaller beads reduce the collision and shear energies of NPs during agitation. This minimizes NP breakage/damage, and retains the shape and crystallinity of the NPs, which determine the inherent NP functions. This review starts with a brief explanation of the theory and current status of NP dispersion and describes the mechanism and experimental results for low-energy bead mill processes, i.e., using uniaxial, dual-axial, and all-separator bead mills, and selection of dispersing agent. Applications of NP dispersions, including nanocomposite materials, and methods for dealing with NP dispersion coloration are also discussed, along with future research directions.

Keywords: nanoparticle, dispersion, bead mill, dispersant, nanocomposite material

1. Introduction

1.1 Importance of NP dispersion

This century, research on the synthesis of nanoparticles (NPs) has attracted much attention because of their advantages compared with bulk materials. When the particle size of a material is reduced to the nanoscale range, quantum size effect and size effect become more important than they are for submicron particles. The former effect shows the specific energy band gap differ from bulk solid one, and the latter effect produces high surface areas, single-domain sizes, and high surface activities. These characteristic properties of NPs are important in industrial applications such as catalysts, magnetic storage, optical devices, and ultrafine wiring.

NPs have large surface areas and excess surface energy, and therefore they tend to agglomerate to minimize the energy, which is larger than the kinetic energy caused by Brownian motion. Cohesion and adhesion forces easily arise between NPs because of intermolecular forces such as van der Waals forces, electric dipole interactions, and chemical bonding (hydrogen bonding), which lead to par-

ticle agglomeration and aggregation.

NPs agglomerate and aggregate during synthesis. Agglomerates are loosely attached particles (the so-called primary particles) by van der Waals, capillary, electrostatic or other physical forces. While, primary particles held together by chemical/sinter forces (metallic, ionic or covalent bonds) are termed aggregates. In liquid-phase processes, e.g., precipitation methods, primary particles easily interact each other and agglomerate. Although pH control or surfactant addition is usually used to obtain stable and dispersed NPs (Hwang et al., 2008; Lan et al., 2007), such methods also involve drying at high temperature, which usually causes agglomeration. In gas-phase processes, NP agglomerates and aggregates are easily formed because the high temperature causes sintering. Agglomerations also occurs during condensation and particle collection in NP powder handling.

Control of the repulsive forces between NPs is therefore necessary in NP dispersion. Dispersion control in aqueous or organic solutions is based on the Derjaguin–Landau–Verwey–Overbeek (DLVO) theory or excluded volume effect, respectively.

1.1.1 DLVO theory of dispersion

DLVO theory is based on the van der Waals interaction force (V_A) and electrostatic double layer repulsive force (V_R), which is generated by the surface charge of the particles. NP agglomeration and dispersion are explained using DLVO theory as follows.

[†] Received 30 September 2015; Accepted 24 November 2015
J-STAGE Advance published online 30 January 2016

¹ 1-4-1 Kagamiyama, Higashi-Hiroshima 739-8527, Japan

* Corresponding author: Takashi Ogi;

E-mail : ogit@hiroshima-u.ac.jp

TEL : +81-82-424-3765 FAX: +81-82-424-7850

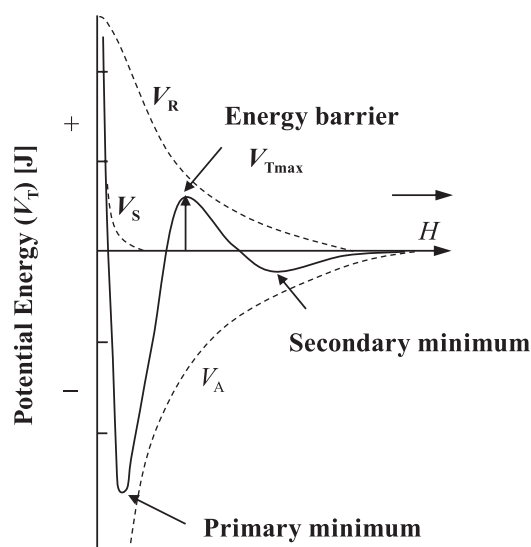


Fig. 1 Cohesion of pair of NPs and potential energy of dispersion. V_A : van der Waals interaction force; V_R : electrostatic double layer repulsive force; V_S : Born repulsive force; H : particle distance.

Fig. 1 shows the potential energy between particles (V_T) as a function of particle distance (H). When the distance between the particles is small, there is a potential energy minimum in the V_T curve (primary minimum). This distance is approximately 4 Å and it indicates an agglomerated state, which depends on the strength of the interparticle bonding, e.g., van der Waals interactions, electrostatic hydrogen bonding, and sintering. A secondary minimum potential also occurs when the distance between the particles is large (secondary minimum), indicating stable particle dispersion. When the potential barrier (V_{Tmax}) between these two minimum potentials is 10–20 times larger than the kinetic energy (kT), the dispersed NPs will be stably suspended in the secondary minimum state. When V_{Tmax} is lower than the kinetic energy, e.g., the zeta potential of the particles is low, the dispersed particles easily revert to the primary minimum state.

When the particle size is in the nanoscale range, the V_A and V_R values become smaller than those of submicron particles. For example, when the particle size is one-tenth that of the submicron range, the potential becomes one-tenth that of the submicron particles. The energy required to disperse agglomerated NPs is lower than that required for submicron particles.

1.1.2 Excluded volume effect for dispersion

The dispersion of particles in an organic solvent is controlled by the dispersant and polymers, and dispersion control is explained based on the excluded volume effect theory. This theory refers to the phenomenon whereby two neighboring particles cannot occupy the same space

in the surrounding dispersant because of steric hindrance or an impediment. In the case of spherical NPs, the closest distance to which two NPs can approach each other is equal to the sum of their radii. Dispersion and agglomeration can therefore be controlled by excluding this volume using dispersants. In the case of nanoscale particles, the energy required to approach the dispersed state from the agglomerated one, in which the NPs are surrounded by dispersant, is also lower than that usually observed for submicron particles.

1.2 Current status of NP dispersion

As explained above, agglomeration and aggregation are inevitable in NP synthesis. However, only well-dispersed NPs can be used for further applications as functional materials such as nanostructured particles and nanocomposite polymer materials (Ogi et al., 2014). Innovative techniques for liquid-phase production of well-dispersed NPs with specific concentrations, viscosities, and purities are therefore needed for practical applications.

The energy needed to disperse agglomerated particles to isolated ones consists of physical (mechanical) and chemical (surface modification) energies. The dispersion process also involves complete wetting of particles, and breakup of agglomerated/aggregated particles into primary particles, followed by particle stabilization. In principle, agglomerates can be broken up by applying compression or shear stress forces, and particle stabilization depends on the electrostatic repulsive force between the particles, or the excluded volume effect, influenced by stabilizing additives.

Table 1 shows widely used methods for NP dispersion. Agglomerated NPs are broken up using various machines by applying compression or shear stresses. Each type of

Table 1 Various dispersion machines used on industrial scale

Dispersion machines	Particle size
Three-roller mill	600 nm–1 μm
Media method	
-Roller mill	600 nm–1 μm
-Ball mill	600 nm–1 μm
-Usual bead mill	100 nm–100 μm
-Low-energy bead mill	5 nm–1 μm
Media-less method	
-Wet jet mill	50 nm–10 μm
-Sonication	50 nm–5 μm
-Cavitation	50 nm–5 μm
-Ultra-thin high shear dispersion	50 nm–5 μm

machine, e.g., three-roller mill, media-less and media dispersion machines, has their own dispersing characteristics. In practice, they are often used in combination, and stress forces can be created by fluid and solid surfaces, as in media dispersion methods.

1.2.1 Three-roller mill

Particles are stressed by a shear gradient arising from the different speeds of the rollers. For high concentrations and large agglomerates, the particles are not only stressed by the shear gradient but also by shear stress in the narrow gap between two rollers. In this condition, the stress force from one roller to the other roller is transferred through the particles. The stress intensity increases with decreasing particles size. (Schilde et al., 2010, 2011).

1.2.2 Media-less dispersion

Particle dispersion is performed using an agitated liquid flow such as sonication, cavitation, or ultrathin high shear dispersion. Such methods are called media-less dispersion. In the case of wet-jet milling, mixing and dispersion are carried out only by mutual collision of particles. Particles flowing in a slurry in an oblique direction at high pressure burst and collide. Dispersion by sonication causes cavitation effects. When a liquid sonicated at high intensities creates vacuum bubbles, which collapse violently, agglomerated particles are separated. Another dispersion technique that involves cavitation force is the use of high-pressure nozzle systems. Collapse of a cavitation bubble can create very high local pressure and release energy, which can break agglomerated particles. Another media-less method is ultrathin-film high-shear dispersion. An ultrathin film is formed along the walls of the vessel, where significant energy from centrifugal force is applied to break up agglomerated NPs.

This media-less dispersion system is appropriate for electronic materials such as battery slurries because it is a contamination-free method. However, in the case of NPs, this method does not give good dispersion because the differences between NP movements in liquid and fluid systems are small because of the low masses of the NPs. In other words, the force applied to the particles will be too small to break up agglomerated NPs. Another dispersion technique such as media dispersion is necessary to provide adequate force to the agglomerated NPs.

1.2.3 Media dispersion

In media dispersion, agglomerated NPs are broken up with the aid of a medium, which is classified as balls or beads, based on sizes of 0.1–40 mm and 0.015–0.5 mm, respectively. A ball mill machine is usually used for crushing large block particles to produce smaller particles for dispersion in a liquid. Bead mill are usually used for dispersion of agglomerated NPs (several micrometers)

that are much smaller than the bead size. Collisions and shear stress between the moving beads during agitation cause separation of agglomerated NPs to their primary particles, as explained in detail in the next section.

Among dispersion machines, media dispersion is most widely used and effectively disperses many types of NPs, depending on the agglomerated state. According to the DLVO theory, a low potential energy is usually needed to separate two particles. If the energy is too high, the NPs will be damaged during dispersion. In media dispersion methods, control of the shear stress and collisions is therefore important to provide appropriate energy for dispersion. Bead mill machines usually use a mesh or slit method for separation of dispersed NPs from the beads, and therefore the bead size limit is above 0.1 mm, which is too large with respect to the NP size. This condition results in supply of too much energy to the dispersion system.

Our groups have therefore developed low-energy bead mill methods. Unlike the usual machines, a centri-separator is used for bead separation, and therefore very small beads (7–50 μm) can be used for NP dispersion. The energy that the NPs receive from collisions and shear of beads can be reduced, and therefore particle breakage/damage can be minimized. Only small beads can produce a low dispersion energy. In the following sections, three types of low-energy bead mill processes are explained in detail. The effects of the experimental conditions, i.e., particle shape (spherical, rod, core-shell), rotation speed, and dispersion time, are also discussed, as well as accompanying phenomena such as dispersion coloring.

2. Low-energy bead mill dispersion

Low-energy bead mill dispersion can be understood using the simple model shown in **Fig. 2**. This model is only applicable when the primary NP size is smaller than 100 nm and the bead size is smaller than 50 μm . Step (i) shows the initial condition of the beads before NP dispersion. The beads move and rotate during agitation. Step (ii) involves collisions between the beads and NPs and application of stress to the agglomerated NPs. After breakup of the aggregated NPs, the surfaces of the isolated NPs become active (formation of activated sites). Step (iii) involves stabilization of the isolated NPs by creating a repulsive force, for example, using a dispersant or zeta potential, to the active sites. The active surface is inhibited by the dispersing agent or zeta potential in the suspension and stable dispersion is achieved. In multicollision phenomena, bead milling affords highly dispersed NPs. This condition can be achieved only when the collision force and shear stress are not too strong. Control of the bead size and rotation speed (very small size and ~ 3 –8 m/s, respectively) is important. Outside these ranges, the energy pro-

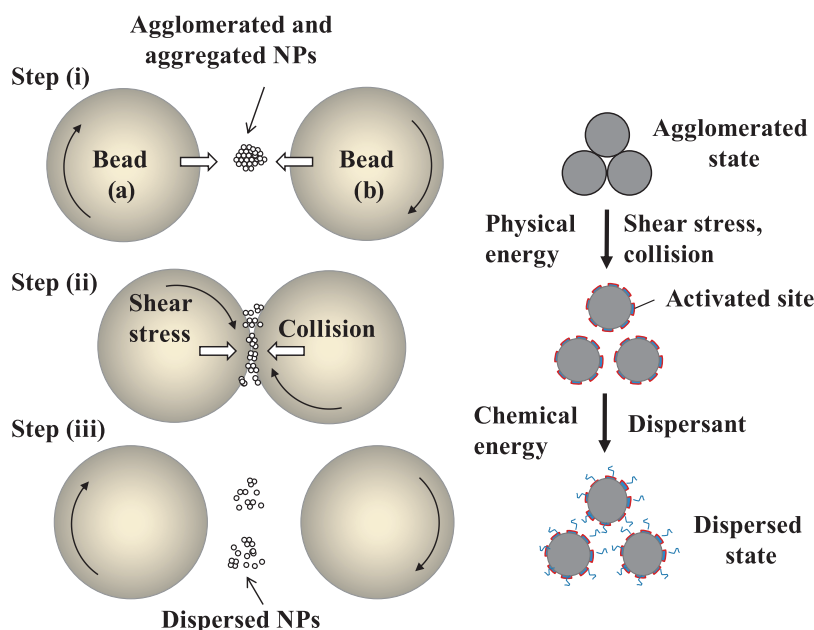


Fig. 2 NP dispersion mechanism during low-energy bead mill process.

vided to the NPs is too high, which results in NP breakage and reagglomeration. Our group has developed three types of bead mill methods, classified based on the provided dispersion energy level, namely, uniaxial, dual-axial, and all-separator bead mills. These are described in the following sections.

2.1 Uniaxial bead mill

The first low-energy bead mill to be developed was a uniaxial bead mill (UAM) (Inkyo et al., 2006). A schematic diagram of a UAM is shown in Fig. 3. The apparatus consists of a 0.15 L vessel, a pump for supplying a slurry, and a slurry tank. The vessel contains a rotor pin and separator, which are set in the lower and upper portions of the vessel, respectively. The vessel is enclosed in a cooling jacket to prevent temperature increases in the system, and is completely sealed from the outside environment. ZrO_2 beads of size 7, 15, 30, and 50 μm are used as the medium (Fig. 4). The ZrO_2 beads occupy 65 % of the vessel volume. The dispersion process is explained as follows.

A slurry containing agglomerated NPs is pumped into the bead mill vessel and through to the lower part. In this part, agglomerated NPs interact with the agitated beads, and the agglomerated NPs are dispersed by collisions and shear stress between the beads. Gradually, the slurry reaches the upper part of the vessel. In this region, separation is performed using a centri-separator, in which the dispersed NPs are separated from the beads by centrifugal force. The beads remain inside the mill, and the NP slurry is pumped out of the vessel. The product particles are collected in the slurry tank and the dispersion process is repeated.

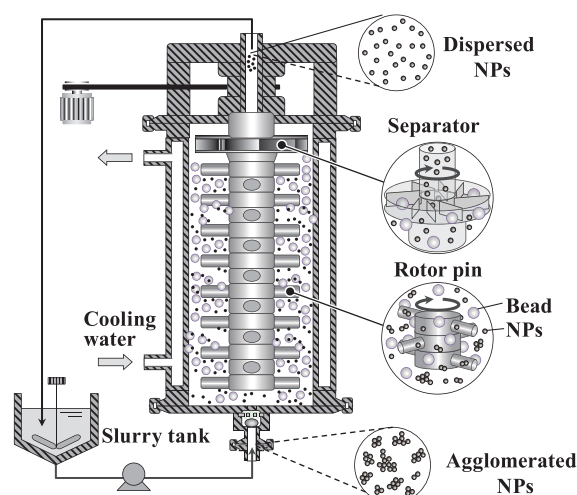


Fig. 3 Schematic diagram of UAM.

2.1.1 Dispersion behavior of TiO_2 NPs using UAM

This UAM was used for the dispersion of needle-type TiO_2 NPs in water (Inkyo et al., 2006). The effects of bead size, dispersion time, and rotation speed on particle breakage and the particle size distribution were investigated; the results are shown in Fig. 5(a). For all the tested beads except those of size 15 μm , the particle size distribution shifted to smaller sizes, and then gradually shifted back to larger sizes, indicating that the agglomerated NPs were dispersed, followed by reagglomeration of the dispersed NPs. Reagglomeration may be caused by activation of the particle surfaces newly generated by the milling process, followed by interactions among broken particles. Breakup of the agglomerated NPs significantly increases the particle concentration in the slurry, which in

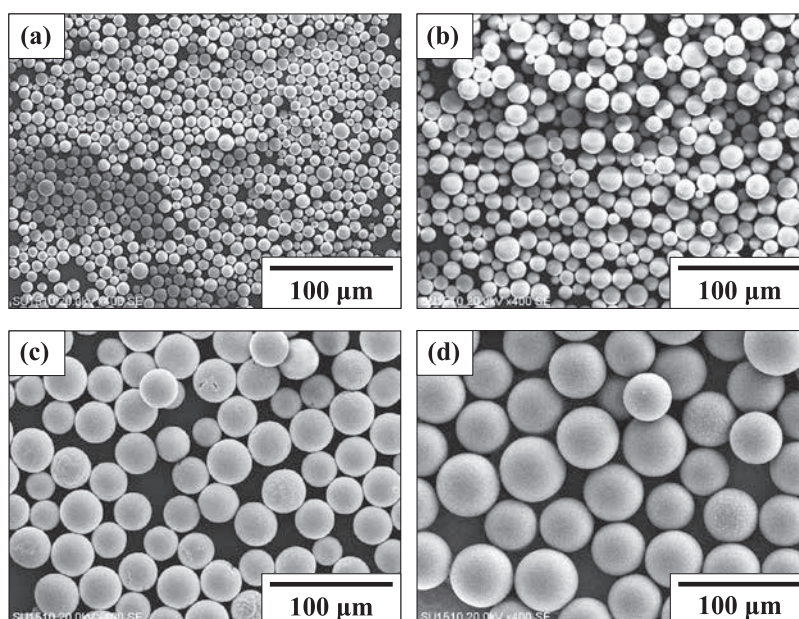


Fig. 4 SEM images of beads of various sizes: (a) 7, (b) 15, (c) 30, and (d) 50 μm .

turn significantly reduces the characteristic coagulation time for particles.

When 100 and 50 μm beads were used, no particles were dispersed to primary particles, showing that the collision force from large beads is too high and damages the particles, followed by reagglomeration of broken particles. The particle size distribution shifted from a unimodal distribution to a bimodal distribution for processing times longer than 240 min. This sudden change in the size distribution cannot be explained by any traditional particle agglomeration mechanism. A possible reason for the shift from a unimodal to a bimodal size distribution is that the broken NPs are deposited on the beads and then grow increasingly large as collisions continue to occur. Once the deposits of broken NPs achieve sufficient size, further collisions may cause these NP deposits to break away from the beads, and the broken NPs agglomerate. These results show that the breakup of agglomerated NPs is eventually followed by reagglomeration. There is therefore an optimum milling time for each dispersion with each bead size before reagglomeration occurs, as indicated by the particle size distribution shifting to larger size. In the cases of 30 and 15 μm beads, the agglomerated NPs were completely dispersed and a sharp peak at 15 nm appeared as the minimum particle size distribution.

The changes in particle size as a function of dispersion time for various bead sizes are shown in **Fig. 5(b)**. In this experiment, spherical TiO_2 NPs were also dispersed for comparison. In general, both needle and spherical TiO_2 NPs have the same dispersion behavior.

The particle size gradually decreased as the dispersion time increased, and reached the primary particle size, indicating that the agglomerated NPs were dispersed to pri-

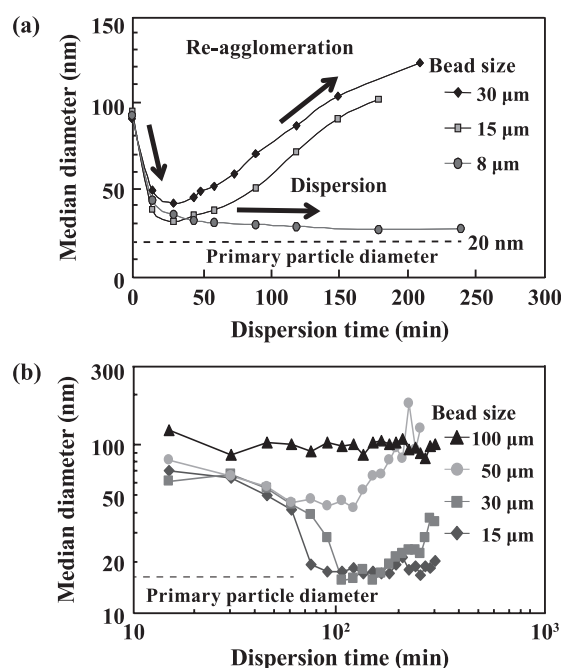


Fig. 5 Effects of bead size and dispersion time on dispersion of TiO_2 NPs: (a) needle TiO_2 NPs; and (b) spherical TiO_2 NPs. **Fig. 5(a):** Reprinted with permission from Inkyo et al., 2006. Copyright: (2006) Elsevier B.V.

mary particles. When excessive energy was provided to the dispersed NPs, the particle size gradually increased, indicating that the primary particles were damaged and broken, resulting in reagglomeration of broken particles. The spherical TiO_2 NPs were easier to disperse than the needle ones. For 8 μm beads only, the agglomerated spherical TiO_2 NPs were dispersed to their primary particles without reagglomeration.

These results are confirmed by transmission electron microscopy (TEM) analysis of the NPs before and after dispersion (**Fig. 6**). Before dispersion, the TiO₂ NP agglomerates were of size 200–300 nm and rod-shaped, like the primary particles. After dispersion with 15 and 30 μm beads, well-dispersed rod-shaped TiO₂ NPs were obtained. Beads of size 50 and 100 μm had little effect on the size of the NP agglomerates. Furthermore, the particle morphology changed from rod-shaped to spherical when 100 μm beads were used.

The detailed effects of rotation speed, bead size, and dispersion time on the dispersibility of rod-type TiO₂ NPs were reported by Tahara et al. (2014). In this study, two rotation speeds (10 and 8 m/s) and various bead sizes (15–50 μm) were used for TiO₂ NP dispersion. At the same rotation speeds, the size of the dispersed particles decreased with increasing dispersion time. The size of the agglomerated NPs decreased rapidly in the initial stage (30 min) and then the particle size changed gradually during dispersion.

At the same rotation speed, larger beads promoted the formation of smaller particles. For the samples dispersed at a rotation speed of 10 m/s and a bead size of 50 μm , the

particle size decreased until 330 min and then gradually increased with milling time. This is possibly because of reagglomeration of broken NPs during milling.

The morphologies of the particles after dispersion using various bead sizes and rotation speeds are shown in **Fig. 7**. Various morphologies are observed, depending on the rotation speed and bead size. At rotation speeds (m/s)/bead sizes (μm) of 8/15 and 8/30, the TiO₂ particles retain their rod shape after bead milling. However, under other conditions, the morphology of the TiO₂ NPs changed from rod shaped to ellipsoidal, and the particle size decreased. For the conditions 8/15 and 8/30, TEM images showed no change in the crystallinity of the particles after dispersion; this was confirmed by X-ray diffraction (XRD) analysis. These results show that the conditions 8/15 and 8/30 effectively provide low energy for dispersion, producing dispersed agglomerated NPs without changing the particle crystallinity. NP dispersion in an organic solvent has also been reported (Joni et al., 2009). **Fig. 8** shows scanning electron microscopy (SEM) images of TiO₂ NPs dispersed in diethylene glycol dimethyl ether (diglyme).

Fig. 9 shows a diagram of the morphological and struc-

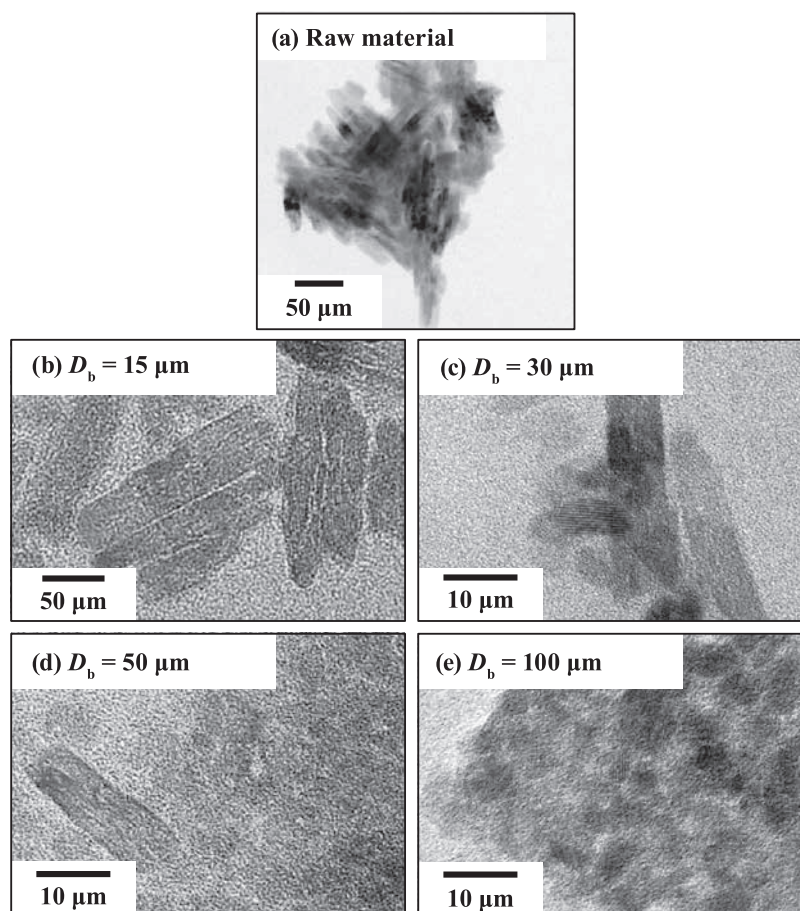


Fig. 6 TEM images of TiO₂ NPs (a) before and (b–e) after dispersion using various bead sizes: (b) 15, (c) 30, (d) 50, and (e) 100 μm . Reprinted with permission from Inkyo et al., 2006. Copyright: (2006) Elsevier B.V.

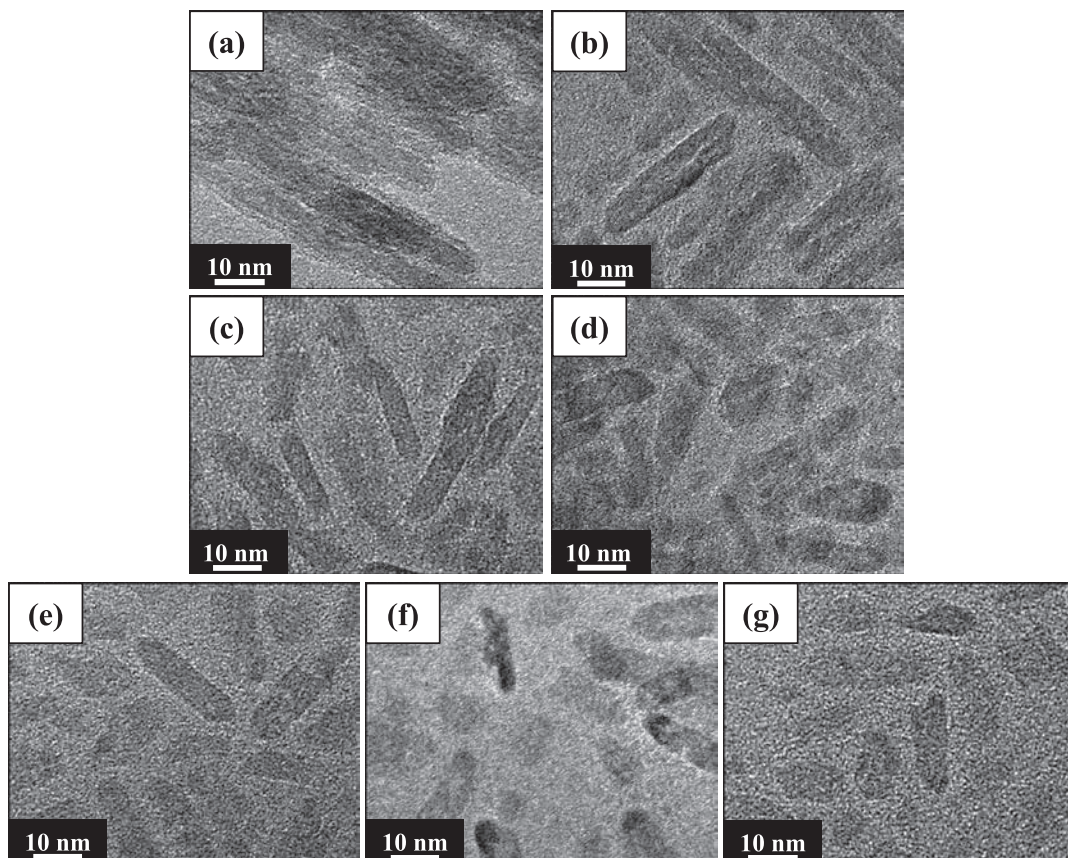


Fig. 7 TEM images of TiO₂ NPs (a) before and (b–g) after bead milling; rotor speed (m/s)/bead size (μm) (b) 8/15, (c) 8/30, (d) 8/50, (e) 10/15, (f) 10/30, and (g) 10/50. Reprinted with permission from Tahara et al., 2014. Copyright: (2014) Elsevier B.V.

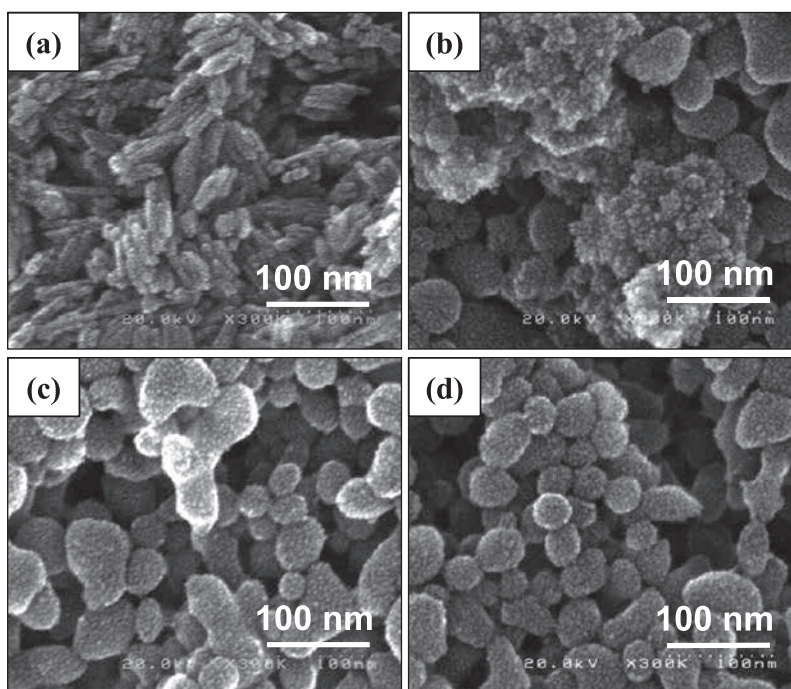


Fig. 8 SEM images of TiO₂ NPs (a) before and (b–d) after bead milling in organic solvent as a function of milling time: (b) 60, (c) 90, and (d) 120 min. Reprinted with permission from Joni et al., 2009. Copyright: (2009) American Chemical Society.

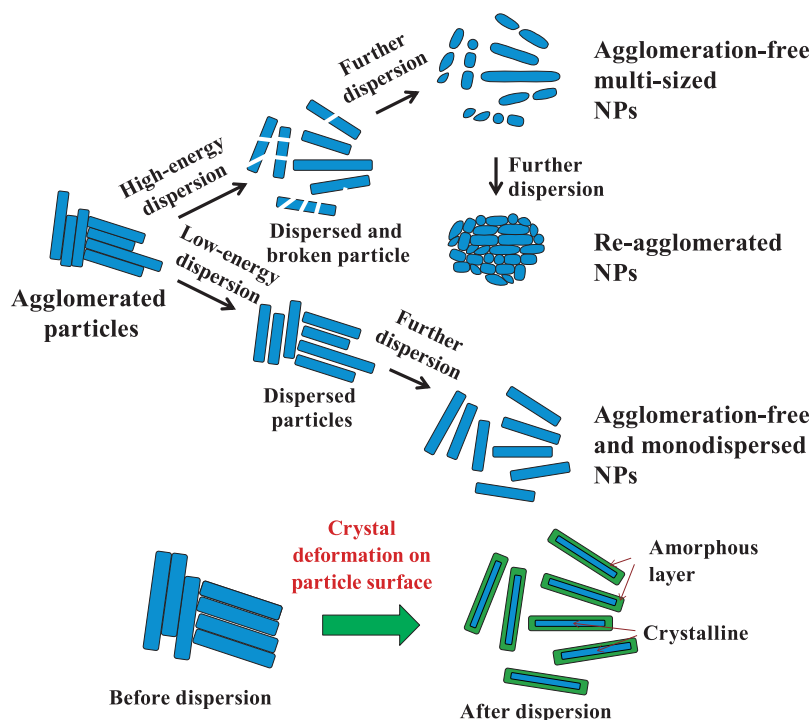


Fig. 9 Diagram of morphological and structural changes in NPs during bead milling depending on supplied energy. Reprinted with permission from Tahara et al., 2014. Copyright: (2014) Elsevier B.V.

tural changes in NPs during bead milling depending on supplied energy (high energy or low energy). Low-energy dispersion defines the condition for bead milling that provide the breakup of agglomerated NPs (not grinding/crushing). High-energy dispersion defines the condition that damages the NP structure and changes the inherent properties of the NPs. Although high-energy dispersion enables rapid breakup of agglomerated NPs, the main body (the material itself) is damaged and broken (destruction of crystal). As a result, the dispersed solution contains multi-sized particles. Because of the high energy, this condition cannot be used for fragile materials such as metal, hollow, and core-shell structured particles. The milling time is also important. A milling time that is too long leads to reagglomeration. NPs are typically softly agglomerated, and therefore the optimum conditions that enable breakup of agglomerated NPs at the agglomerating position only are crucial. In low-energy dispersion processes, the slurry contains single-sized NPs with the inherent material properties.

During bead mill dispersion, the physicochemical properties of the particles may change. These changes are caused by decreases in the particle crystallinity during bead mill dispersion. During bead mill dispersion, collisions between beads and agglomerated TiO_2 particles provide energy that can break the main body of the crystal, resulting in production of smaller particles and an amorphous phase on the crystal surface, and this changes the properties of the dispersed particles (bottom image in

Fig. 9).

Based on the above results, several operating parameters should be considered for providing low-energy dispersion in bead mill processes, including milling time, temperature, bead and particle sizes, rotation speed, physicochemical properties, and composition of dispersed media and agglomerated particles. Low energy can be obtained when the milling process is conducted at less than $0.50 \mu\text{W}/\text{bead}$. This condition can be achieved when the process is conducted below a rotational speed and bead size of 10 m/s and $30 \mu\text{m}$, respectively. Deviation from these conditions results in reagglomeration, production of broken particles, and impairment of the crystallinity and physicochemical properties of the NPs.

2.1.2 Dispersion of boron nitride NPs using UAM

Hexagonal boron nitride (hBN) NPs are an indispensable material for many industrial applications because of their properties such as high thermal conductivity, low thermal expansion, good thermal shock resistance, high electrical resistance, low dielectric constant and loss tangent, and microwave transparency. When inorganic hBN NPs are used as inclusion particles for reinforcement, dispersion is very important. Poorly dispersed hBN NPs in suspension will not give nanostructured materials with excellent properties.

Our group successfully dispersed hBN NPs of primary particle size 35 nm using a UAM, as shown in **Fig. 10**. Two silane coupling agents, i.e., (3-acryloxypropyl)tri-

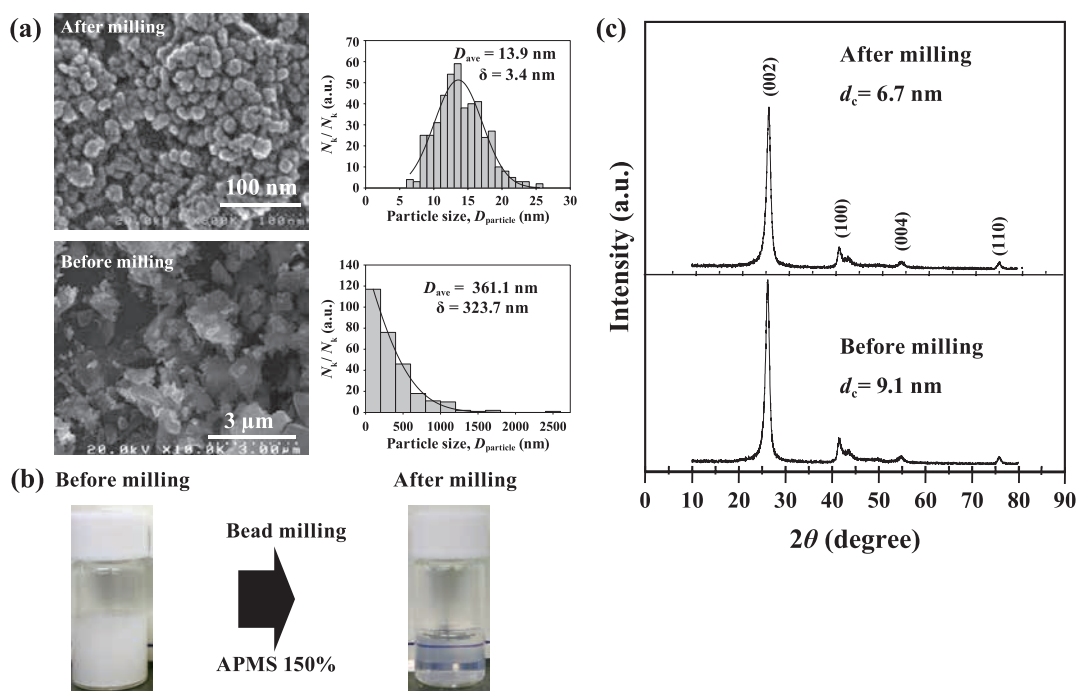


Fig. 10 Dispersion of hBN NPs by UAM. (a), (b), and (c) are SEM images, slurry photographs, and XRD patterns of hBN before and after dispersion. Reprinted with permission from Joni et al., 2011. Copyright: (2011) Elsevier B.V.

thoxysilane (APMS) and trimethoxy(propyl)silane, were used for surface modification to enhance the dispersion stability (Joni et al., 2011). Optimization of the rotation speed, slurry flow rate, and dosage of dispersing agent gave agglomerated hBN NPs that were well dispersed to primary particles. A highly dispersed hBN suspension, with a zeta potential below $\sim +40$ mV, was prepared using APMS as the dispersing agent. The bead mill process did not significantly change the crystallinity and chemical composition of the hBN NPs, but enhanced the dispersion stability (Joni et al., 2011).

2.2 Dual-axial bead mill

Because of the limited bead sizes available with UAM, dual-axial bead mills (DAM) were developed. A schematic diagram of a DAM is shown in Fig. 11. Unlike the case for a UAM, the separator and rotor pin are separated, and therefore they can run independently. Details of this bead mill were reported by Tahara et al. (2011). Use of a DAM enables the rotation speed to be controlled to be lower than the separator speed, allowing the use of smaller beads to provide a lower dispersion energy.

A DAM was used for the dispersion of rod-shaped TiO_2 NPs. Fig. 12 shows the effect of the rotor pin rotation speed in the range from 12 to 3 m/s on dispersion using beads of size 50 μm and separator speed 12 m/s. At a low rotation speed (3 or 6 m/s), the particle size was reduced to 30 nm, indicating that the agglomerated NPs were dis-

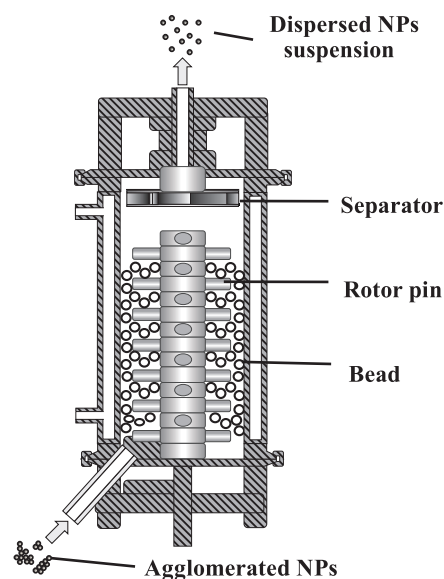


Fig. 11 Schematic diagram of DAM. Reprinted with permission from Tahara et al., 2011. Copyright: (2011) Journal of the Society of Powder Technology, Japan.

persed to the primary particle size without reagglomeration. At a rotation speed higher than 6 m/s, rod-shaped TiO_2 NPs were broken into ellipsoidal shapes and the particle size increased as dispersion continued. Under these conditions, the TiO_2 NPs were damaged and then reagglomeration occurred because of the strong interactions among active broken surfaces.

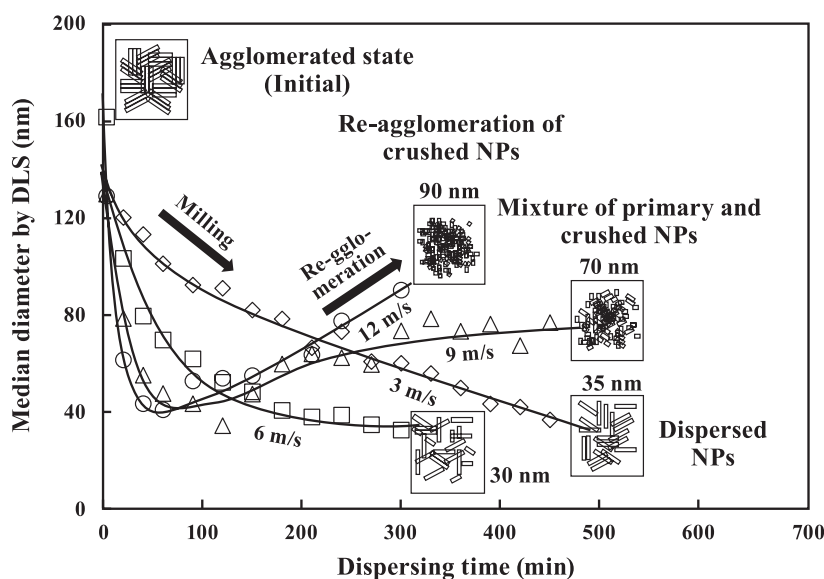


Fig. 12 Effect of rotation speed on dispersion of TiO_2 NPs using DAM. Reprinted with permission from Tahara et al., 2011. Copyright: (2011) Journal of the Society of Powder Technology, Japan.

2.3 All-separator bead mill

Even a DAM has limitations in the dispersion of more fragile NPs such as core-shell NPs. In the cases of a UAM and DAM, well-dispersed NPs are crushed in the separator, in which high energy is needed to separate small beads from dispersed NPs.

Another type of low-energy bead mill apparatus was therefore developed, i.e., an all-separator bead mill (ASM). An ASM consists of only a separator, which is aligned from the bottom to the upper part, without a rotor pin, in the vessel. This new apparatus enables lower-energy dispersion at lower rotation speeds with smaller beads.

A schematic diagram of an ASM is shown in **Fig. 13**. Our group used an ASM to disperse agglomerated core-shell $\alpha\text{-Fe}/\text{Al}_2\text{O}_3$ and $\alpha''\text{-Fe}_{16}\text{N}_2/\text{Al}_2\text{O}_3$ magnetic NPs (Zulhijah et al., 2015). Core-shell $\alpha''\text{-Fe}_{16}\text{N}_2/\text{Al}_2\text{O}_3$ magnetic NPs, the magnetic material with the highest reported saturation magnetization, have good potential for the construction of high-magnetic-moment rare-earth-free magnetic materials. However, $\alpha''\text{-Fe}_{16}\text{N}_2$ magnetic NPs have strong magnetic lateral interactions between NPs; this enables easy NP agglomeration, and decreases their magnetic performance after structuring. The dispersion process is therefore the key to preparing dispersed single-domain magnetic NPs.

Fig. 14(a) shows TEM images of $\alpha''\text{-Fe}_{16}\text{N}_2$ NPs before and after dispersion using different bead sizes and rotation speeds. When the energy supplied was insufficient to break up the agglomerated particles, the particle size was almost the same as the initial one. When sufficient energy was supplied to the agglomerated NPs, the agglomerates were broken up into primary particles without destroying

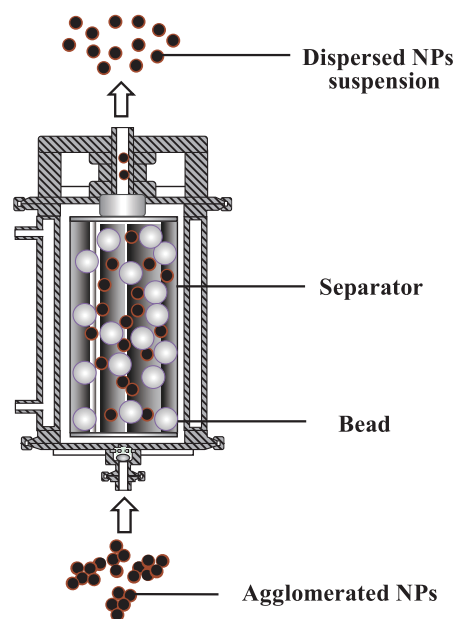


Fig. 13 Schematic diagram of ASM. Reprinted with permission from Zulhijah et al., 2015. Copyright: (2015) American Chemical Society.

the core-shell structure. The crystal structure of the core-shell particle after dispersion was the same as that of the original NPs, as shown in **Fig. 14(b)**. When the applied dispersion energy was too high, rapid breakup of the agglomerated particles on either the agglomeration boundary or main body of the particles occurred, resulting in particle destruction.

The magnetic properties of core-shell $\alpha''\text{-Fe}_{16}\text{N}_2/\text{Al}_2\text{O}_3$ NPs before and after dispersion were also evaluated (**Fig. 14c**). The saturation magnetization of the particles after

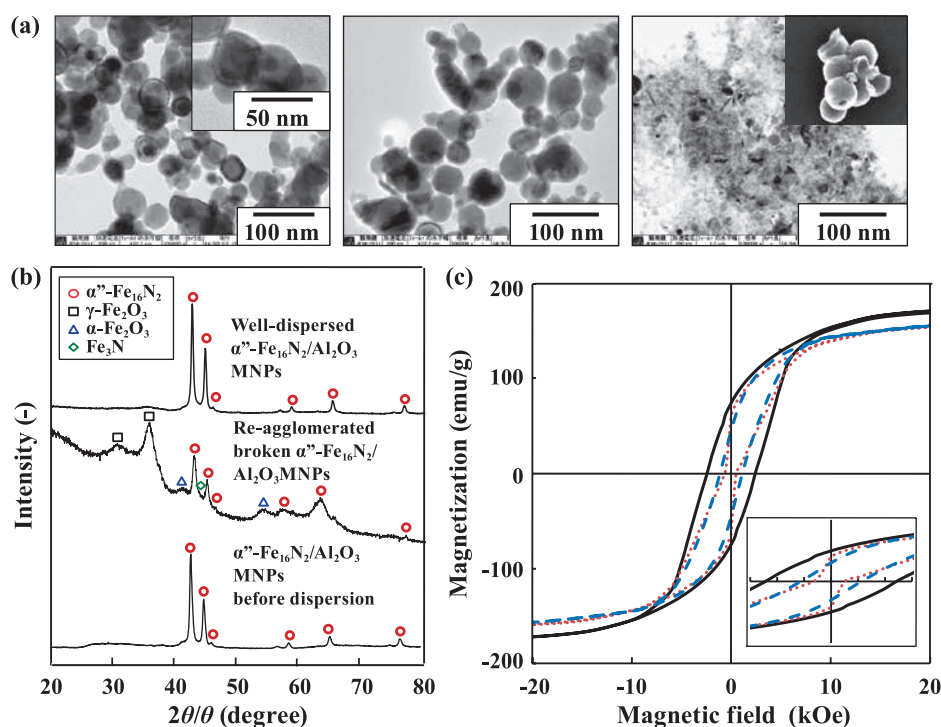


Fig. 14 Dispersion of core-shell α'' -Fe₁₆N₂ NPs using ASM. (a) TEM images (from left to right) of core-shell α'' -Fe₁₆N₂/Al₂O₃ before dispersion, and well-dispersed and reagglomerated broken α'' -Fe₁₆N₂/Al₂O₃; (b) XRD patterns; and (c) magnetic evaluation of particles after dispersion. Black, dotted-red, and dashed-blue hysteresis curves correspond to α'' -Fe₁₆N₂/Al₂O₃ before dispersion, and well-dispersed and aggregated dispersed α'' -Fe₁₆N₂/Al₂O₃ NPs, respectively. Reprinted with permission from Zuhijah et al., 2015. Copyright: (2015) American Chemical Society.

dispersion was similar to that of the particles before dispersion. Different hysteresis was found for the well-dispersed NPs when magnetization relaxation occurred abruptly near zero applied field. This indicates spin coupling of the neighboring magnetic NPs by release of the magnetically decoupled restriction of the high magnetic field, which can be caused by movement of the particles and magnetic moment during measurement (Zuhijah et al., 2015). The morphological changes in the agglomerated core-shell α'' -Fe₁₆N₂/Al₂O₃ NPs are shown in Fig. 15.

A summary of the characteristics, i.e., mean particle diameter, concentration, and viscosity, of NP dispersions prepared by bead milling is shown in Fig. 16.

3. Selection of dispersant

As mentioned above, dispersion in organic solvents is also controlled by the excluded volume effect. The presence of a dispersant that interacts with the particle surface controls the excluded volume and prevents interaction between particles. Selection of an appropriate dispersant is therefore crucial for obtaining stable NP dispersions. However, there is a lack of systematic information on dispersant selection, and selection is based on experience and experimental results.

During dispersion, agglomerated NPs are broken up and then the particle surfaces become active sites. An appropriate surfactant will have good attractive forces with the active sites of the particles and solvent. All of the active sites on the particle surface will then bond with the surfactant, resulting in repulsive forces between the particles, and these prevent reagglomeration. Fig. 17 shows a diagram of dispersant selection for NP dispersion.

Dispersants can be divided into two classes according to their chemical structures: polymeric dispersants and surfactants. The primary differences between polymeric dispersants and surfactants are their molecular weights, stabilization mechanisms, and stabilities. Polymeric dispersants stabilize systems sterically. They have a two-component structure, which must meet the following requirements. (1) They can strongly adsorb on particle surfaces and have specific anchoring groups. (2) They contain polymeric chains that sterically stabilize the solvent or solution system.

In contrast, the stabilization mechanism of surfactants is electrostatic: the polar group forms an electrostatic double layer and produces a coating around the particles. Because of the electrostatic stabilization mechanism and chemical structure of surfactants, the final coating tends to be water sensitive.

The effectiveness of a polymeric dispersant is deter-

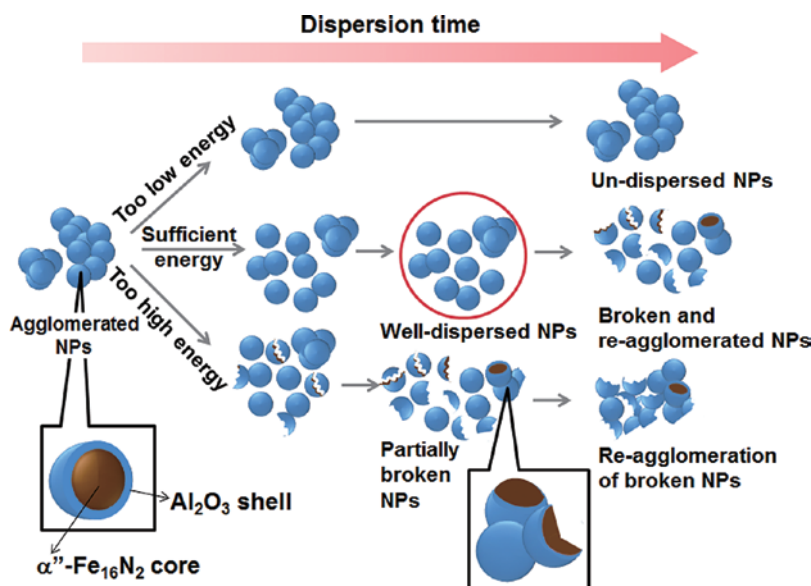


Fig. 15 Illustration of morphological changes of in agglomerated core-shell α'' -Fe₁₆N₂/Al₂O₃ NPs by low-energy bead mill dispersion under various dispersion conditions. Reprinted with permission from Zulhijah et al., 2015. Copyright: (2015) American Chemical Society.

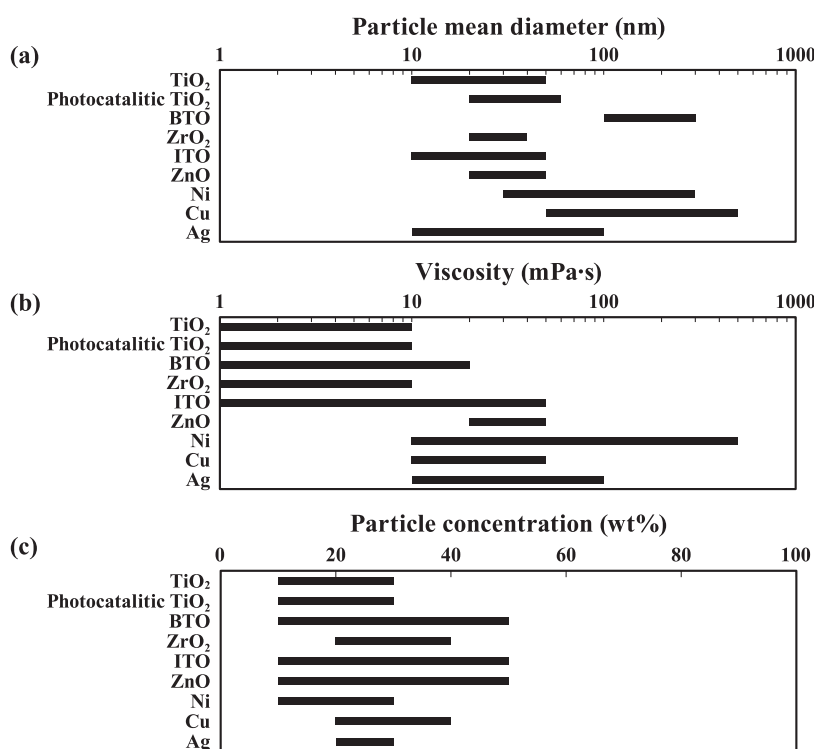


Fig. 16 Summary of NP dispersion characteristics. (a) particle mean diameter, (b) viscosity, and (c) particle concentration

mined by the anchoring groups on the surface. The anchoring groups can be an amine, carboxylic, sulfonic, or phosphoric acid, or their salts. The crucial requirement is that the chains are successfully anchored to the particle surfaces, and particle surfaces are covered with sufficiently dense chains. The chains must have attractive forces with

both the particle surfaces and the solvent, in the presence or absence of a polymer (Takeda et al., 2009).

In general, surfactants are selected based on their polarity and molecular weight, as shown in **Fig. 17**. The characteristics of a surfactant depend on its polarity and molecular weight. An appropriate surfactant for a system

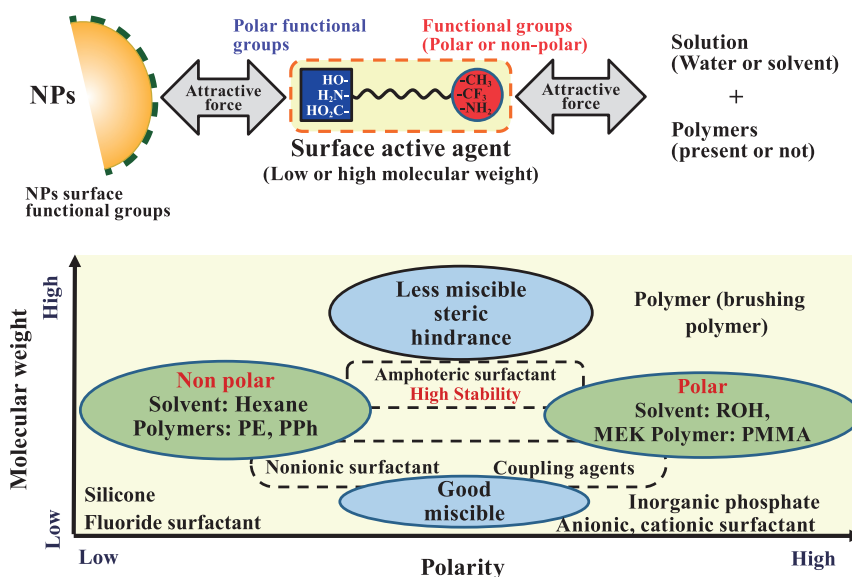


Fig. 17 Selection of dispersant for NP dispersion.

can therefore be identified. The various types of surfactant and their applications in NP dispersion are listed in **Table 2**.

A summary of the use of bead mills and the dispersant types used in dispersion of various NPs is shown in **Table 3**.

4. Optical properties of NP dispersions

4.1 Coloring of NP dispersion

One of the problems with NP dispersions is that their suspensions are colored (**Fig. 18**). For example, well-dispersed TiO₂ NPs in an organic solvent, i.e., diethylene glycol dimethyl ether, are yellow. This suspension is not suitable as an alternative material to glass, because such materials must be colorless and transparent. NP dispersions may be colored because of their complex physicochemical properties (refractive index, bandgap, chemical functions), the dispersing agent, and the solvent.

Fig. 19 shows possible reasons for coloring of NP dispersions. First, Rayleigh scattering of NPs is strongly related to the color of the NP suspension. Rayleigh scattering involves the predominantly elastic scattering of light or other electromagnetic radiation by particles much smaller than the radiation wavelength. The intensity I of light scattered by a small sphere of diameter d and refractive index n from a beam of unpolarized light of wavelength λ and intensity I_0 is given by

$$I = I_0 \frac{1 + \cos^2 \theta}{2R^2} \left(\frac{2\pi}{\lambda} \right)^4 \left(\frac{n^2 - 1}{n^2 + 2} \right)^2 \left(\frac{d}{2} \right)^6 \quad (1)$$

where R is the distance to the particle and θ is the scattering angle. In the case of a spherical particle, the scattering intensity increases in direct proportion to the sixth power of the particle size and in inverse proportion to the fourth power of the light wavelength. A shorter wavelength (blue) is easier to scatter than a longer wavelength (red). Undispersed TiO₂ NPs are white as a result of scattering of all visible wavelengths (sun or room light). In the case of a highly dispersed NP suspension, the transparency is increased because light is not scattered. However, if agglomerated NPs are present in the suspension, only blue light is scattered and yellow light is transmitted as a complementary color. The optical transparency loss of a suspension therefore depends on the average particle size and the presence of aggregates.

The second possible reason is the inherent properties of NP materials. The bandgap of rutile TiO₂ is 3.0 eV and it has an absorption edge at around 413 nm (from purple to blue). If the material has lattice defects and impurities in the crystal structure, impurity levels are formed in the bandgap, and the material absorbs light of wavelength longer than 413 nm. This is why blue light is absorbed by TiO₂ NPs and yellow light is transmitted as a complementary color (**Fig. 19b**). High crystallinity and doping of TiO₂ NPs effectively changes their bandgap (absorption edge).

The third reason is attributed to the structure and functions of the dispersing agent. In our experiment, KBM 5103(3-Acryloxypropyl-trimethoxysilane) was used for TiO₂ NP dispersion. The double bond in KBM 5103 can react with oxygen radicals to form carbon–oxygen radical bonds, as shown in **Fig. 19(c)**. These bonds can cause chemical coloring of the NP dispersion. Selection of an

Table 2 Various types of dispersant for NP dispersion

Surfactant	Nanoparticles	References
Anionic surfactant	CaCO ₃	(Du L. et al., 2013; Hait S. and Chen Y., 2014)
Carbonate (Na stearate)	FeO, Ag, Cu,	(Saterlie M.S. et al., 2012; Wang W. et al., 2014; Zong B.-Y. et al., 2014)
Phosphate salt	CNC, CoFe ₂ O ₄ , γ -Fe ₂ O ₃	(Kovalenko A. et al., 2014; Salajková M. et al., 2012; Tang B.Z. et al., 1999)
Sulfonate salt (SD)	Ag	(Sondi I. et al., 2003)
Cationic surfactant		
Aliphatic amine & Quaternary amine	Laponite,	(Li W. et al., 2012)
Aromatic Quaternary amine salt	Ag	(Sondi I. et al., 2003)
Nonionic surfactants		
Ester type (span)	ZnS	(Naskar M.K. et al., 2006)
Ester-ether type (tween)	Fe ₂ O ₃ , acrylamide	(Guha S. and Mandal B.M., 2004; Guskos N. et al., 2005)
Ether type (PEG dodecylether)	Pt, Ag	(Ingelsten H.H. et al., 2001; Sondi I. et al., 2003)
Polymer (brushing polymer)		
Polyacrylate salt	SiO ₂ , Ag, Fe ₃ O ₄ , BaTiO ₃	(Hajdú A. et al., 2012; Pu Z. et al., 1997; Shen Z.-G. et al., 2004; Zhang Z. et al., 2000)
Polyurethane, polyester type	Fe ₃ O ₄	(Ashjari M. et al., 2010)
Poly(N-isopropyl acrylamide)	Ag	(Dong Y. et al., 2007)
Fluoride surfactant		
Perfluorooctanoic acid	TiO ₂	(Yang J. et al., 2011)
Perfluorooctanoate (K, NH ₄)	Ag, polyampholyte	(Fan X. et al., 2006; Thünemann A.F. et al., 2002)
Silicone (silylating agent)	TiO ₂	(Ouyang G. et al., 2012)
Propyltrimethoxysilane (TMS)	ZrO ₂ , SiO ₂ , BTO	(Luo K. et al., 2008; Nomoto H. et al., 2014; Yang X. and Liu Z.-H., 2010)
Coupling agent		
Silane type		
Methacryloyloxypropyl trimethyl methoxysilane (MTMS)	Fe ₃ O ₄ , Au, Ag, Ni	(Harish S. et al., 2011; Martínez S. et al., 2006; Zhang Y. et al., 2002)
Aluminum type		
Acetoalkoxy Al diisopropylate	ZrO ₂ , Al ₂ O ₃	(Takahashi M. et al., 1992)
Inorganic phosphate		
Hexametaphosphate	TiO ₂ , Fe ₂ O ₃ , ZnS	(Warad H. et al., 2005; Zhang Y. et al., 2008)

appropriate dispersing agent, i.e., without double bonds, is key to avoiding coloration. The use of polymerization inhibitors, which are also considered to cause coloration, should also be avoided.

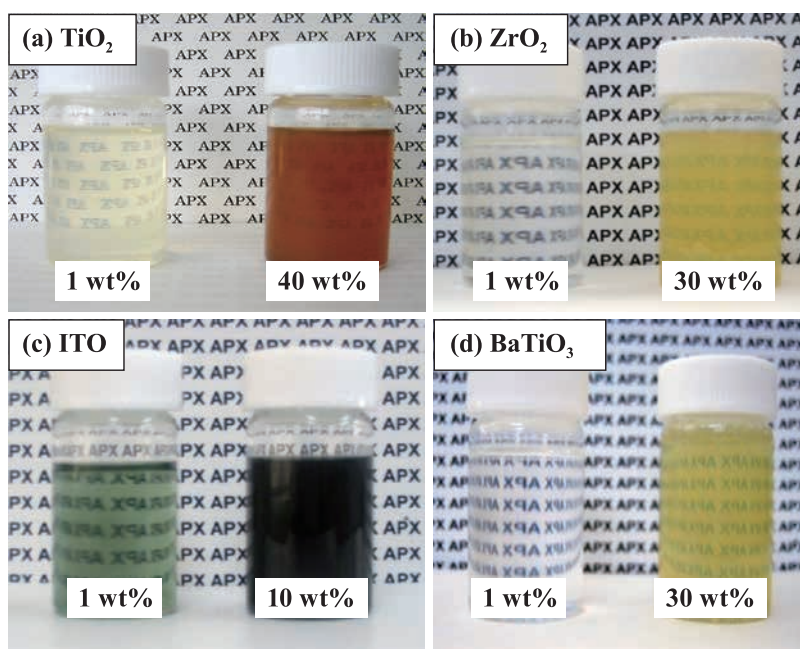
4.2 Decoloring of NP dispersions via UV irradiation

Joni et al. (2012b) reported a method for decoloring a yellow suspension of rutile needle TiO₂ NPs in an organic

solvent (diethylene glycol dimethyl ether). Well-dispersed rod-type TiO₂ NPs of diameter and length 15.5 and 109 nm, respectively, were successfully prepared using a UAM. Although the bead-milled TiO₂ NPs were well dispersed in the organic solvent, the solution was yellow. The color was removed by UV irradiation. After dispersion, the suspension was illuminated under UV irradiation ($\lambda = 254$ nm) for 5 h. **Fig. 20(a)** shows the transmittance properties of the dispersed TiO₂ NPs before and after UV irradiation. UV irradiation changed the surfaces of the

Table 3 Examples of bead mill dispersion of NPs

Material	Solvent	Dispersant	Conc. (wt%)	Particle size (before bead mill)	Particle size (after bead mill)
TiO ₂	Water	—	10	140	25
TiO ₂	Diglyme	Trimethoxypropyl silane	1.0–10	1000	15
TiO ₂	MMA/Toluene	3-Acryloxypropyl trimethoxysilane	1.0–15	> 100000	90–150
TiO ₂	Neo pentyl glycol dimethacrylate	Butyl acetate	10	85	50
BaTiO ₂	Neo pentyl glycol dimethacrylate	Polymeric dispersant solspense	10–20	90	40
BN	Water	3-Acryloxypropyl trimethoxysilane	0.5	1000–3000	46
Al(OH) ₃	MMA	3-Acryloxypropyl trimethoxysilane	1.0–10	750	210
SiO ₂	Methanol	3-Acryloxypropyl trimethoxysilane	4	1000–10000	12
ZnO	Toluene	—	1.0	1000–10000	10
ITO	Toluene	—	1.0	1000–10000	20
ZrO ₂	Toluene	—	1.0	1000–10000	20


Fig. 18 Coloring of highly dispersed NP slurries: (a) TiO₂ (15 nm); (b) ZrO₂ (20 nm); (c) indium-tin oxide (ITO) (20 nm); and (d) BaTiO₃ (20 nm).

dispersed TiO₂ NPs (1 wt%), indicated by a change in the solution color from yellow to colorless and transparent (Joni et al., 2012b).

Optical scattering loss is avoided if the particle mean diameter is less than one-tenth the length of the visible-light wavelength (200–800 nm), typically < 25 nm. In

these experiments, the particle size in the dispersed suspension was 25 nm, and therefore the contribution of the particle size to optical transparency loss can be neglected. The main factors responsible for the strong light scattering loss of the suspension are therefore the refractive indices of the particles and the matrix. Surfactant desorption

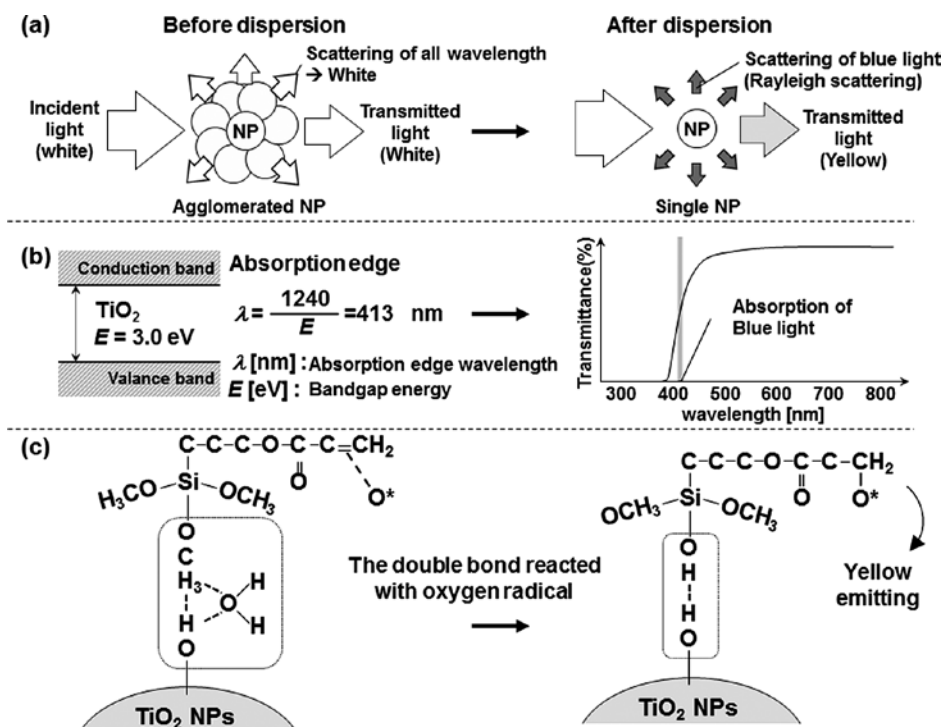


Fig. 19 Possible reasons for coloring of NP dispersion.

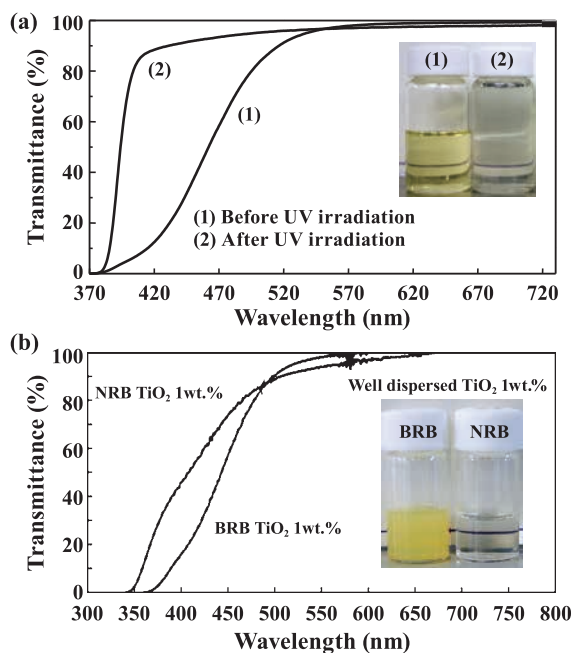


Fig. 20 Comparison of photographs and UV-vis transmissions: (a) before and after UV irradiation and (b) bare (BRB) and nitrogen-doped (NRB) rutile TiO_2 NP suspensions (1 wt%). Reprinted with permission from Joni et al., 2012b, copyright: (2012) Elsevier. B.V.; Joni et al., 2012a, copyright: (2012) American Chemical Society.

was suggested to be the main cause of changes in the refractive index of the matrix, caused by excess surfactant

in the organic solvent. UV irradiation of the suspension resulted in matching of the refractive indices of the particles and the organic solvent. Optical scattering loss was therefore avoided, and the prepared suspension was colorless and transparent.

4.3 Decoloring of NP dispersions via nitrogen doping

Another method for preparing colorless suspensions of TiO_2 NPs in organic solvents is nitrogen doping. Joni et al. reported a study of the synthesis of nitrogen-doped TiO_2 NPs and their dispersion in an organic solvent (diethylene glycol dimethyl ether), with 3-(acryloyloxy)propyltrimethoxysilane as the dispersing agent, using bead milling (Joni et al., 2012a). Yellow nitrogen-doped TiO_2 NP powders were prepared by combustion of a mixture of rutile TiO_2 NPs and urea at 800°C , and then dispersing the NPs using a UAM.

Fig. 20(b) shows photographs and the UV-vis transmissions of dispersed solutions of nitrogen-doped and bare rutile TiO_2 NPs. The bare rutile TiO_2 NP suspensions were yellow. When the materials were doped with nitrogen, the resulting TiO_2 suspensions were colorless (Joni et al., 2012a). This change in color and transparency as a result of nitrogen doping of TiO_2 NPs can be explained by Rayleigh scattering, as follows. According to the Rayleigh law, if the volume fractions are assumed to be the same, the particle sizes and refractive indices of the particles

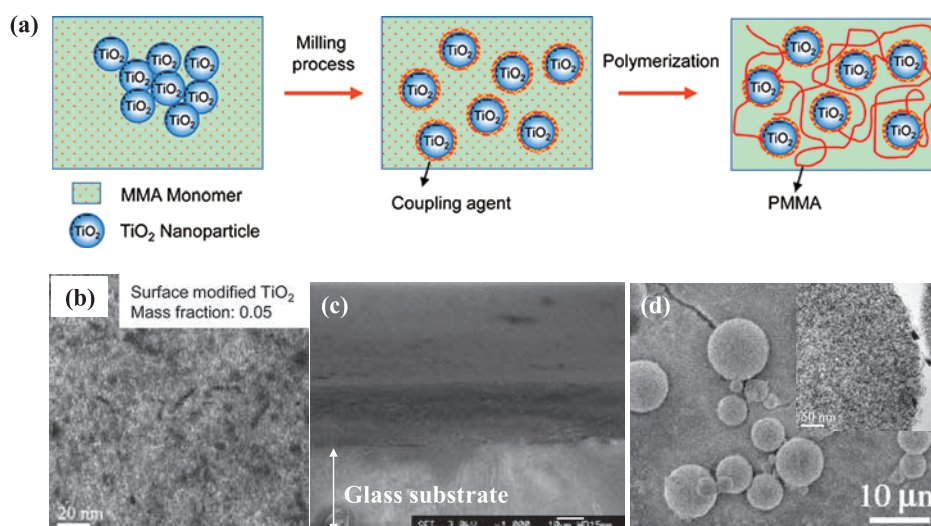


Fig. 21 Applications of dispersed TiO_2 NPs. (a) Representation of milling–polymerization process. (b, c, d) SEM images of TiO_2 particles in PMMA– TiO_2 nanocomposites after polymerization, cross-sectional TiO_2 -dispersed polymer films, and composite polymer microspheres containing dispersed TiO_2 NPs, respectively. Reprinted with permission from Inkyo et al., 2008, copyright: (2008) American Chemical Society; Takeda et al., 2008, copyright: (2008) The Society of Polymer Science, Japan; and Takeda et al., 2009, copyright: (2009) Chemical Society of Japan.

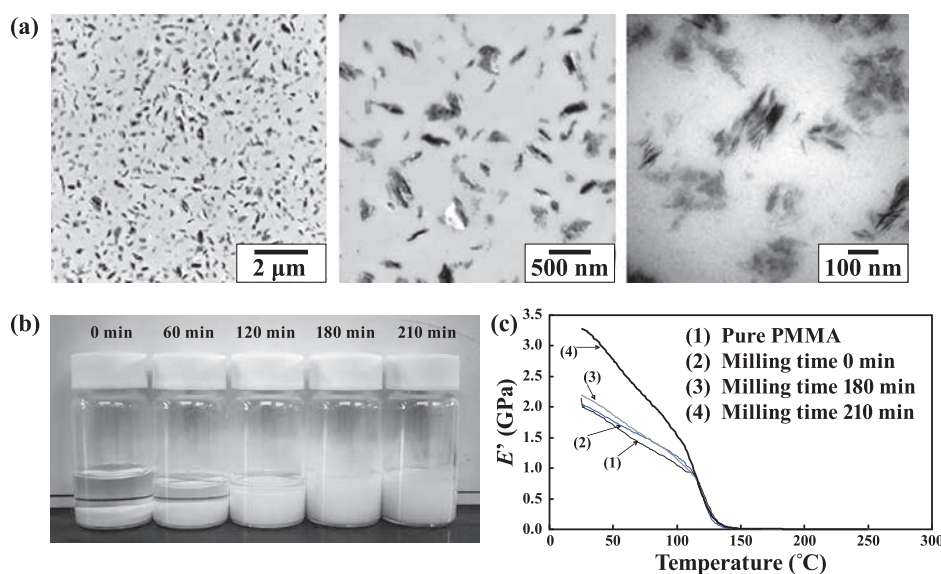


Fig. 22 Applications of dispersed ATH: (a) SEM images of ATH filler dispersed in PMMA–ATH composites at different magnifications; (b) photographs of slurry at various milling times; and (c) storage moduli of PMMA–ATH composites and pure PMMA. Reprinted with permission from Joni et al., 2010. Copyright: (2010) Elsevier B.V.

and monomer (solvent) can be used to reduce the scattering loss and improve the transparency. The refractive indices can be controlled by choosing appropriate fillers and solvents, and through design of the interface. The particle size has to be considerably less than the wavelength of the visible light. As explained above, optical scattering loss can be avoided if the particle domain size (typically < 25 nm) is less than one-tenth of the visible-light wavelength. Ideally, TiO_2 should therefore have a diameter

< 10 nm to avoid coloring issues.

The suspension of bare TiO_2 particles in diethylene glycol dimethyl ether was not transparent, and was yellow because of the presence of some large aggregates of TiO_2 NPs (> 100 nm). These aggregates led to strong light scattering in the visible region. In contrast, in the case of a nitrogen-doped TiO_2 NP dispersion, the particles were smaller and monodispersed, which considerably improved the transparency, and reduced the color, of the suspension.

However, a small percentage of nitrogen-doped TiO_2 was present as aggregates (> 100 nm), indicating that the transparency was not only dependent on the particle size but was also affected by the interfacial properties. These results suggest that nitrogen atoms on the TiO_2 surface also contributed to the lack of color and transparency of the suspension.

5. Applications of NP dispersions

Many reports have shown that composite formation with NPs can alter the thermomechanical properties of polymers, such as the elastic modulus, viscosity, and glass-transition temperature, and the optical properties. NP–polymer composites can be synthesized by dispersing NPs in the monomer and polymerizing in the presence of the NPs.

5.1 Poly(methyl methacrylate)- TiO_2 nanocomposites

Inkyo et al. (2008) studied the synthesis of poly(methyl methacrylate) (PMMA)– TiO_2 NP composites. TiO_2 NPs were dispersed in MMA monomer using a bead mill, followed by polymerization to form PMMA– TiO_2 nanocomposites, as shown in **Fig. 21(a)**. The TiO_2 NPs were well dispersed in the MMA monomer, and therefore transparent composites were formed. In contrast, PMMA– TiO_2 nanocomposites synthesized from undispersed TiO_2 NP suspensions were opaque.

SEM confirmed that the TiO_2 NPs were evenly distributed in the composite, as shown in **Fig. 21(b)**, unlike the case for a composite comprising undispersed TiO_2 NPs. Well-dispersed TiO_2 NPs enhanced the UV-absorbing properties of MMA and increased its thermal stability. Because these PMMA– TiO_2 nanocomposites are transparent and have high refractive indices, they have good potential optical applications.

Our group has also developed TiO_2 -dispersed nanocomposite polymer films with a high concentration of TiO_2 (65 wt%), as shown in **Fig. 21(c)** (Takeda et al., 2009). Bead mill dispersion was used to prepare finely dispersed TiO_2 NPs in the polymer; two monomers (neopentyl glycol dimethacrylate or divinylbenzene) and an organic solvent (butyl acetate) were used as the dispersing medium. The prepared films (thickness: 5 μm) were transparent (81.5 %) and had a high refractive index (1.85). These films had smoother surfaces than films prepared by direct dispersion without bead milling.

Takeda et al. successfully prepared TiO_2 nanocomposite microspheres of high concentration (40 wt%) with acrylic monomer, as shown in **Fig. 21(d)**. These TiO_2 NPs were dispersed in butyl acetate by bead milling. The TiO_2

nanocomposites were prepared by replacement of butyl acetate with the monomer used as the medium. The TiO_2 NPs were close packed and well distributed, without any vacancies in the microspheres (Takeda et al., 2008).

5.2 PMMA–aluminum trihydroxide nanocomposites

Aluminum trihydroxide (ATH) is an attractive alternative to halogen-based flame retardants, which give off heavy smoke and hazardous gases during combustion. The use of these NPs as a filler in polymers such as PMMA, which is widely used as a shatterproof replacement for glass and in surface coatings, improves the thermal stability and mechanical properties of the polymer. The size and dispersibility of the filler (NPs) in the polymer are important in obtaining high-performance materials.

Our group used bead mill dispersion to control the size distribution of an ATH NP filler in MMA. A dispersed solution was obtained by surface modification of ATH NPs using a silane-based dispersing agent, (3-acryloxypropyl) trimethoxysilane (APTMS). In the final product, the ATH NPs were well dispersed in the PMMA, as confirmed by TEM and digital photographs (**Fig. 22a, b**). The mechanical properties and thermal stability of the PMMA–ATH nanocomposite were also investigated (**Fig. 22c**). The storage modulus of the PMMA–ATH nanocomposite in the glassy state was larger than that of pure PMMA. In the composite reported by Joni et al. (2010), the storage modulus increased with increasing amount of ATH NP filler.

6. Conclusion

NP dispersion is an important technique in the synthesis of functional NP materials for practical applications. NP dispersion is also essential for NP assembly and structuring. In this paper, recent progress in the development of bead mill processes for NP dispersion was reviewed. The bead mill machines described here enable the use of smaller beads (5–50 μm) than those normally used. These small beads have a lower dispersion energy and minimize damage to the shape and crystal structure of the NPs. This is a significant advantage and enables NPs to show their inherent superior material properties. Because of their capacity of large-scale operating capacities (10–30 L), these low-energy dispersion machines are now used in many industries. However, the following problems have become apparent: 1) how to find appropriate dispersants efficiently; 2) how to control coloring phenomena of NP dispersions; and 3) how to disperse fragile NPs (metal NPs and hollow NPs) without breaking their structures. NP dispersion using lower dispersion energies should help

to overcome these problems; this would broaden the range of industrial applications of NPs.

Acknowledgments

This work was supported by JSPS KAKENHI Grant Numbers 26709061 and 25620164. We also gratefully acknowledge provision of a scholarship (R.Z.) by the Ministry of Education, Culture, Sports, Science and Technology (MEXT) of Japan.

References

- Ashjari M., Mahdavian A.R., Ebrahimi N.G., Mosleh Y., Efficient dispersion of magnetite nanoparticles in the polyurethane matrix through solution mixing and investigation of the nanocomposite properties, *Journal of Inorganic and Organometallic Polymers and Materials*, 20 (2010) 213–219.
- Dong Y., Ma Y., Zhai T., Shen F., Zeng Y., Fu H., Yao J., Silver nanoparticles stabilized by thermoresponsive microgel particles: Synthesis and evidence of an electron donor-acceptor effect, *Macromolecular Rapid Communications*, 28 (2007) 2339–2345.
- Du L., Wang Y., Luo G., In situ preparation of hydrophobic CaCO_3 nanoparticles in a gas–liquid microdispersion process, *Particuology*, 11 (2013) 421–427.
- Fan X., Mcleod M.C., Enick R.M., Roberts C.B., Preparation of silver nanoparticles via reduction of a highly CO_2 -soluble hydrocarbon-based metal precursor, *Industrial & Engineering Chemistry Research*, 45 (2006) 3343–3347.
- Guha S., Mandal B.M., Dispersion polymerization of acrylamide: iii. Partial isopropyl ester of poly (vinyl methyl ether-alt-maleic anhydride) as a stabilizer, *Journal of Colloid and Interface Science*, 271 (2004) 55–59.
- Guskos N., Typek J., Maryniak M., Roslaniec Z., Petridis D., Kwiatkowska M., FMR study of $\gamma\text{-Fe}_2\text{O}_3$ magnetic nanoparticles in a multiblock poly (ether-ester) copolymer matrix, *Materials Science-Wroclaw*, 23 (2005) 971–976.
- Hait S., Chen Y., Optimization of milling parameters on the synthesis of stearic acid coated CaCO_3 nanoparticles, *Journal of Coatings Technology and Research*, 11 (2014) 273–282.
- Hajdú A., Szekeres M., Tóth I.Y., Bauer R.A., Mihály J., Zupkó I., Tombácz E., Enhanced stability of polyacrylate-coated magnetite nanoparticles in biorelevant media, *Colloids and Surfaces B: Biointerfaces*, 94 (2012) 242–249.
- Harish S., Sabarinathan R., Joseph J., Phani K., Role of pH in the synthesis of 3-aminopropyl trimethoxysilane stabilized colloidal gold/silver and their alloy sols and their application to catalysis, *Materials Chemistry and Physics*, 127 (2011) 203–207.
- Hwang Y., Lee J.-K., Lee J.-K., Jeong Y.-M., Cheong S.-I., Ahn Y.-C., Kim S.H., Production and dispersion stability of nanoparticles in nanofluids, *Powder Technology*, 186 (2008) 145–153.
- Ingelsten H.H., Bagwe R., Palmqvist A., Skoglundh M., Svanberg C., Holmberg K., Shah D.O., Kinetics of the formation of nano-sized platinum particles in water-in-oil microemulsions, *Journal of Colloid and Interface science*, 241 (2001) 104–111.
- Inkyo M., Tahara T., Iwaki T., Iskandar F., Hogan C.J., Okuyama K., Experimental investigation of nanoparticle dispersion by beads milling with centrifugal bead separation, *Journal of Colloid and Interface Science*, 304 (2006) 535–540.
- Inkyo M., Tokunaga Y., Tahara T., Iwaki T., Iskandar F., Hogan C.J., Okuyama K., Beads mill-assisted synthesis of poly methyl methacrylate (PMMA)- TiO_2 nanoparticle composites, *Industrial & Engineering Chemistry Research*, 47 (2008) 2597–2604.
- Joni I.M., Balgis R., Ogi T., Iwaki T., Okuyama K., Surface functionalization for dispersing and stabilizing hexagonal boron nitride nanoparticle by bead milling, *Colloids and Surfaces A: Physicochemical and Engineering Aspects*, 388 (2011) 49–58.
- Joni I.M., Nishiwaki T., Okuyama K., Isoi S., Kuribayashi R., Enhancement of the thermal stability and mechanical properties of a PMMA/aluminum trihydroxide composite synthesized via bead milling, *Powder Technology*, 204 (2010) 145–153.
- Joni I.M., Ogi T., Iwaki T., Okuyama K., Synthesis of a colorless suspension of TiO_2 nanoparticles by nitrogen doping and the bead-mill dispersion process, *Industrial & Engineering Chemistry Research*, 52 (2012a) 547–555.
- Joni I.M., Ogi T., Purwanto A., Okuyama K., Saitoh T., Takeuchi K., Decolorization of beads-milled TiO_2 nanoparticles suspension in an organic solvent, *Advanced Powder Technology*, 23 (2012b) 55–63.
- Joni I.M., Purwanto A., Iskandar F., Okuyama K., Dispersion stability enhancement of titania nanoparticles in organic solvent using a bead mill process, *Industrial & Engineering Chemistry Research*, 48 (2009) 6916–6922.
- Kovalenko A., Jouhannaud J., Polavarapu P., Krafft M.P., Waton G., Pourroy G., Hollow magnetic microspheres obtained by nanoparticle adsorption on surfactant stabilized microbubbles, *Soft Matter*, 10 (2014) 5147–5156.
- Lan Q., Yang F., Zhang S., Liu S., Xu J., Sun D., Synergistic effect of silica nanoparticle and cetyltrimethyl ammonium bromide on the stabilization of o/w emulsions, *Colloids and Surfaces A: Physicochemical and Engineering Aspects*, 302 (2007) 126–135.
- Li W., Yu L., Liu G., Tan J., Liu S., Sun D., Oil-in-water emulsions stabilized by laponite particles modified with short-chain aliphatic amines, *Colloids and Surfaces A: Physicochemical and Engineering Aspects*, 400 (2012) 44–51.
- Luo K., Zhou S., Wu L., Gu G., Dispersion and functionalization of nonaqueous synthesized zirconia nanocrystals via attachment of silane coupling agents, *Langmuir*, 24 (2008) 11497–11505.
- Martínez S., Moreno-Mañas M., Vallribera A., Schubert U., Roig A., Molins E., Highly dispersed nickel and palladium nanoparticle silica aerogels: Sol–gel processing of tethered metal complexes and application as catalysts in the mizo-

- roki–heck reaction, *New Journal of Chemistry*, 30 (2006) 1093–1097.
- Naskar M.K., Patra A., Chatterjee M., Understanding the role of surfactants on the preparation of ZNS nanocrystals, *Journal of Colloid and Interface science*, 297 (2006) 271–275.
- Nomoto H., Mori Y., Matsuo H., Barium titanate dispersion obtained by a high pressure methods and light resistant composites containing the nanoparticles, *Journal of the Ceramic Society of Japan*, 122 (2014) 129–133.
- Ogi T., Nandiyanto A.B.D., Okuyama K., Nanostructuring strategies in functional fine-particle synthesis towards resource and energy saving applications, *Advanced Powder Technology*, 25 (2014) 3–17.
- Ouyang G., Wang K., Chen X., TiO₂ nanoparticles modified polydimethylsiloxane with fast response time and increased dielectric constant, *Journal of Micromechanics and Micro-engineering*, 22 (2012) 074002.
- Pu Z., Mark J.E., Jethmalani J.M., Ford W.T., Effects of dispersion and aggregation of silica in the reinforcement of poly (methyl acrylate) elastomers, *Chemistry of Materials*, 9 (1997) 2442–2447.
- Salajková M., Berglund L.A., Zhou Q., Hydrophobic cellulose nanocrystals modified with quaternary ammonium salts, *Journal of Materials Chemistry*, 22 (2012) 19798–19805.
- Saterlie M.S., Sahin H., Kavlicoglu B., Liu Y., Graeve O.A., Surfactant effects on dispersion characteristics of copper-based nanofluids: A dynamic light scattering study, *Chemistry of Materials*, 24 (2012) 3299–3306.
- Schilde C., Kampen I., Kwade A., Dispersion kinetics of nano-sized particles for different dispersing machines, *Chemical Engineering Science*, 65 (2010) 3518–3527.
- Schilde C., Mages-Sauter C., Kwade A., Schuchmann H., Efficiency of different dispersing devices for dispersing nano-sized silica and alumina, *Powder Technology*, 207 (2011) 353–361.
- Shen Z.-G., Chen J.-F., Zou H.-K., Yun J., Dispersion of nano-sized aqueous suspensions of barium titanate with ammonium polyacrylate, *Journal of Colloid and Interface Science*, 275 (2004) 158–164.
- Sondi I., Goia D.V., Matijević E., Preparation of highly concentrated stable dispersions of uniform silver nanoparticles, *Journal of Colloid and Interface Science*, 260 (2003) 75–81.
- Tahara T., Imajyo Y., Nandiyanto A.B.D., Ogi T., Iwaki T., Okuyama K., Low-energy bead-milling dispersions of rod-type titania nanoparticles and their optical properties, *Advanced Powder Technology*, 25 (2014) 1492–1499.
- Tahara T., Inkyo M., Imajyo Y., Okuyama K., Low energy dispersion of titania nanoparticles by dual axes beads mill *Journal of the Society of Powder Technology, Japan*, 48 (2011) 198–205.
- Takahashi M., Hayashi J., Suzuki S., Ishigure Y., Improvement of the rheological properties of the zirconia/polypropylene system for ceramic injection moulding using coupling agents, *Journal of Materials Science*, 27 (1992) 5297–5302.
- Takeda M., Tanabe E., Iwaki T., Yabuki A., Okuyama K., High-concentration transparent TiO₂ nanocomposite films prepared from TiO₂ nanoslurry dispersed by using bead mill, *Polymer Journal*, 40 (2008) 694–699.
- Takeda M., Tanabe E., Iwaki T., Yabuki A., Okuyama K., Preparation of nanocomposite microspheres containing high concentration of TiO₂ nanoparticles via bead mill dispersion in organic solvent, *Chemistry Letters*, 38 (2009) 448–449.
- Tang B.Z., Geng Y., Lam J.W.Y., Li B., Jing X., Wang X., Wang F., Pakhomov A., Zhang X., Processible nanostructured materials with electrical conductivity and magnetic susceptibility: Preparation and properties of maghemite/polyaniline nanocomposite films, *Chemistry of Materials*, 11 (1999) 1581–1589.
- Thünemann A.F., Wendler U., Jaeger W., Schnablegger H., Nanoparticles of polyampholyte-surfactant complexes with perfluorododecanoic acid, *Langmuir*, 18 (2002) 4500–4504.
- Wang W., Song Y., Liu Q., Yang K., Facile synthesis and catalytic properties of silver colloidal nanoparticles stabilized by SDBS, *Bulletin of Materials Science*, 37 (2014) 797–803.
- Warad H., Ghosh S., Hemtanon B., Thanachayanont C., Dutta J., Luminescent nanoparticles of Mn doped ZnS passivated with sodium hexametaphosphate, *Science and Technology of Advanced Materials*, 6 (2005) 296–301.
- Yang X., Liu Z.-H., A kind of nanofluid consisting of surface-functionalized nanoparticles, *Nanoscale Research Letters*, 5 (2010) 1324–1328.
- Yang J., Zhang Z.-Z., Men X.-H., Xu X.-H., Superoleophobicity of a material made from fluorinated titania nanoparticles, *Journal of Dispersion Science and Technology*, 32 (2011) 485–489.
- Zhang Y., Chen Y., Westerhoff P., Hristovski K., Crittenden J.C., Stability of commercial metal oxide nanoparticles in water, *Water research*, 42 (2008) 2204–2212.
- Zhang Y., Kohler N., Zhang M., Surface modification of superparamagnetic magnetite nanoparticles and their intracellular uptake, *Biomaterials*, 23 (2002) 1553–1561.
- Zhang Z., Patel R.C., Kothari R., Johnson C.P., Friberg S.E., Aikens P.A., Stable silver clusters and nanoparticles prepared in polyacrylate and inverse micellar solutions, *The Journal of Physical Chemistry B*, 104 (2000) 1176–1182.
- Zong B.-Y., Ho P., Zhang Z.-G., Ng G.-M., Yao K., Guo Z.-B., Polypyrrole: FeOx-ZnO nanoparticle solar cells with breakthrough open-circuit voltage prepared from relatively stable liquid dispersions, *RSC Advances*, 4 (2014) 58608–58614.
- Zulhijah R., Suhendi A., Yoshimi K., Kartikowati C.W., Ogi T., Iwaki T., Okuyama K., Low-energy bead-mill dispersion of agglomerated core-shell α -Fe/Al₂O₃ and α ''-Fe₁₆N₂/Al₂O₃ ferromagnetic nanoparticles in toluene, *Langmuir*, 31 (2015) 6011–6019.

Author's short biography



Takashi Ogi

Takashi Ogi is an associate professor in Chemical Engineering at Hiroshima University. He received his PhD degree in Chemical Engineering in 2008 from Hiroshima University. He was a JSPS researcher from 2006 to 2008 and an assistant professor at Osaka Prefecture University from 2008–2010. His current research interests include synthesis of nanostructured particles materials via liquid phase and spray method and recovery of rear metal using biosorption. Especially, he focuses on the development of rare earth free/less nanomaterials, and recovery of rare metal.



Rizka Zulhijah

Rizka Zulhijah is a doctor student at Hiroshima University supervised by Prof. Kikuo Okuyama. She received her BS and MS in Institut Teknologi Sepuluh Nopember Surabaya. Her research focus is magnetic nanoparticles. During her doctoral degree she received research support grant from Hosokawa micron foundation.



Toru Iwaki

Toru Iwaki is a researcher engaged in NEDO project on new magnet development from magnetic nanoparticles at graduate School of Engineering of Hiroshima University. He received Dr. Sci. at Hiroshima University in 1973. He was a chemical assistant at the University before working at Hiroshima R&D Center of Mitsubishi Heavy Industries 1984, Toda Kogyo 1998 and Kotobuki Kogyo 2006. His research area is covering surface and colloid science for nanomaterial applications.



Kikuo Okuyama

Kikuo Okuyama is a Professor of Chemical Engineering at Hiroshima University. He received his doctoral degree in 1978 in chemical engineering at Osaka Prefecture University. His research has touched many aspects of aerosol science and technology, from fundamental investigations on aerosol dynamic behavior to the development of aerosol measurement equipments with a recent focus on nanomaterial synthesis. Prof. Okuyama has received numerous honors and awards, including the Fuchs Memorial Award in 2002, and KONA Award in 2007. He has coauthored more than 450 scientific papers, 120 review papers, 50 books/chapters, and 70 patents.

Present Advancement in Production of Carbon Nanotubes and Their Derivatives from Industrial Waste with Promising Applications[†]

Konrat Kerdnawee¹, Chompoopitch Termvidchakorn¹, Pacharaporn Yaisanga¹, Jirapat Pakchamsai¹, Cheewapon Chookiat¹, Apiluck Eiad-ua², Winadda Wongwiriyan², Weerawut Chaiwat³, Sakhon Ratchahat⁴, Kajornsak Faungnawakij⁵, Komkrit Suttiponparnit⁶ and Tawatchai Charinpanitkul^{1*}

¹ Department of Chemical Engineering, Faculty of Engineering, Chulalongkorn University, Thailand

² College of Nanotechnology, King Mongkut's Institute of Technology Ladkrabang, Thailand

³ Environmental Engineering and Disaster Management Program, Mahidol University, Thailand

⁴ Department of Chemical Engineering, Graduate School of Science and Engineering, Tokyo Institute of Technology, Japan

⁵ National Nanotechnology Center (NANOTEC), National Science and Technology Development Agency, Thailand

⁶ Environmental Research and Management Department, PTT Research and Technology Institute, Thailand

Abstract

An increase in global consumption has led to an exponential increase in industrial production activities which inevitably results in overwhelming remain of industrial waste. Consequently it has driven increasing attentions of research and development teams in various countries to propose and investigate novel methodologies to utilize such industrial waste. Instead of using as alternative energy sources, usage of industrial waste for production of carbonaceous nanomaterials has been examined via various routes, such as catalytic pyrolysis, hydrothermal treatment and so on. Meanwhile, for sustainable and secure continuity of the carbonaceous nanomaterial production, broad spectra of promising applications have also been examined. Among those emerging applications, utilization of carbonaceous nanomaterials in pollution control and prevention has been focused worldwide. Therefore, in this review, relevant research works focusing on catalytic pyrolysis of carbonaceous industrial waste for carbonaceous nanomaterial production were comprehensively analyzed and summarized. In addition, promising applications involving with antibiotic removal, spilled oil handling and pollutant gas detection were also reviewed.

Keywords: carbon, nanomaterial, industrial waste, synthesis, applications

1. Introduction

An increase in global consumption has led to an exponential increase in industrial production activities which has inevitably resulted in overwhelming remain of industrial waste. Such industrial waste management is the major consideration, especially plastics waste like poly-

ethylene, polypropylene, and so on. Consequently it has driven increasing attentions of research and development teams in various countries to propose and investigate novel methodologies to utilize such industrial waste. Instead of using as alternative energy sources to reduce environmental problems from such industrial waste, their usage for production of carbonaceous nanomaterials has been examined via various routes, such as catalytic pyrolysis, hydrothermal treatment and so on (Afre et al., 2006; Liu et al., 2006; Vijayaraghavan and Stevenson, 2007; Zhang et al., 2008; Charinpanitkul et al., 2009a; Zhuo et al., 2010; Alves et al., 2011; Li et al., 2012; Mishra et al., 2012; Sano et al., 2012; Yang et al., 2012; Bajad et al., 2015).

Since the significant findings of new forms of carbonaceous nanomaterials, including buckminsterfullerene (C₆₀) discovered by Kroto et al. in 1985 and carbon nanotubes (CNTs) reported by Iijima in 1991, considerable re-

[†] Received 1 October 2015; Accepted 4 November 2015
J-STAGE Advance published online 30 January 2016

¹ Payathai Rd., Patumwan, Bangkok 10330, Thailand

² Chalongsong Rd., Ladkrabang, Bangkok 10520, Thailand

³ Kanchanaburi Campus, Saiyok, Kanchanaburi 71150, Thailand

⁴ 2-12-1 Ookayama, Meguro-ku, Tokyo 152-8550, Japan

⁵ 111 Thailand Science Park, Paholyothin Rd., Klong Nueng, Klong Luang Pathumthani 12120, Thailand

⁶ 71 Moo 2, Paholyothin Rd., Km.78, Sanubtueb, Wangnoi, Ayutthaya Province 13170, Thailand

* Corresponding author: Tawatchai Charinpanitkul;

E-mail : ctawat@chula.ac.th

TEL: +66-2-218-6894

search and development (R&D) efforts have been made toward the synthesis and applications of functional carbonaceous nanomaterials with diverse structures and morphologies, such as nanotubes, nanohorns, nanocapsules, nano-onions, nanofibers, coin-like hollow carbon, and graphenes (Kroto et al., 1985; Iijima, 1991; Bandow et al., 2000; Thostenson et al., 2001; Andrew et al., 2002; Dai, 2002; Sano et al., 2003; Li et al., 2003; Jang and Bae, 2004; Sano et al., 2004; Sun and Li, 2004; Xiao et al., 2006; Yao et al., 2007; Yuan et al., 2007; de Volder et al., 2013). Such carbonaceous nanomaterial has become of interest for many researchers because of its unique and outstanding properties. **Table 1** would give an outlook of appropriate method which could provide some specific carbonaceous nanomaterials (Dai 2002; Popov 2004; Bazargan and McKay 2012; Iijima, 2012). Each synthesizing technique would provide a variety of carbonaceous nanomaterials with different advantages and disadvantages with respect to production yield, purity, and handling. For instance, arc discharge method with or without usage of catalyst would be appropriate for production of SWCNTs, MWCNTs and fullerenes but scale-up would be a drawback of this method. Meanwhile, chemical vapor deposition (CVD) technique would be very flexible for producing various carbonaceous nanomaterials except carbon nanohorns (CNHs). In term of synthesized products, besides SWCNTs and MWCNTs, graphene and carbon nanohorns (CNHs) have recently become research topics which also draw attention from many research teams. Anyway, a large variety of products at different synthesizing parameters implies that the so-called self-assembly reactions are complicated. The detailed mechanism has not been fully understood at the present time. Therefore, many of recent research and development efforts have been paid for elucidating the formation mechanism of such carbonaceous nanomaterial with respect to each category because such knowledge could be useful for regulating the production cost and their key characteristics.

Unless their actually economic production processes are realized, commercial applications of carbonaceous nanomaterial would not reach their full potential (Thostenson et al., 2001; Dai, 2002; Zhang et al., 2003; Parkansky et al., 2004; Montoro et al., 2005; Kusaba and Tsunawaki, 2006; Guo et al., 2007; Tsai et al., 2009; Lebel et al., 2010; de Volder et al., 2013; Gong et al., 2014). Therefore, there is still much requirement for development of such carbonaceous nanomaterial production from cheaper and stable raw materials of various kinds.

Nevertheless, among those nanomaterials, carbon nanotubes (CNTs) have attracted widespread interest, owing to their unique structures and extraordinary properties in electrical, optical and mechanical properties, which could lead to many highly promising applications including adsorbents, atomic force microscopy (AFM) tips, catalyst or catalyst supports, electrodes for fuel cell and dye-sensitized photovoltaic cells, field emission displays (FED), hydrogen storage, nano-electronic devices, strength reinforcing fillers in polymers (Colomer et al., 2000; Barreiro et al., 2006; Paradise and Goswami, 2007; Arora and Sharma, 2014). In addition, some of their derivatives, such as metal-hybridizing carbon nanotubes are also recognized as novel nanomaterials with some promising applications, such as magnetic recording, medical diagnosis, selective adsorbents and supercapacitors (de Volder et al., 2013). As a result sizable production of CNTs and their derivatives have been continuously proposed and examined for more than two decades. As mentioned above various methods for CNT production would include laser ablation, arc discharge, chemical vapor deposition (CVD), electrolysis, and hydrothermal treatment. A remarkable amount of research attempts have been made toward comparison in various aspects, such as production yield, purity, operating cost, and scalability (Auer et al., 1998; Bandow et al., 2000; Colomer et al., 2000; Serp et al., 2001; Andrew et al., 2002; Sano et al., 2003; Popov, 2004; Barreiro et al., 2006; Xiao et al., 2006; Zeng et al., 2006;

Table 1 Comparison of typical synthesizing techniques and carbonaceous nanomaterials

Technique \ Structure	SWCNT	MWCNT	Fullerene	CNH	Graphene
Arc discharge	x	o	o	o	x
Arc discharge with catalyst	o	o	o	x	x
Laser deposition	x	x	o	o	x
Laser deposition with catalyst	o	o	o	x	x
CVD (Pyrolysis)	o	o	x	x	x
CVD with catalyst	o	o	x	x	o
CVD (Plasma with catalyst)	o	o	o	x	o

Note: o represents “applicable”

x represents “not applicable”

Grobert, 2007; Charinpanitkul et al., 2009b; Puengjinda et al., 2009; Quan et al., 2010; Charinpanitkul et al., 2011). Generally, all of such CNT production methods would require some similar handling process conditions, such as high temperature condition for preparing carbon precursors from decomposition of carbon sources following by the self-assembly processes which could be regulated by various operating parameters. With different controlling parameters, different types of CNTs, which are mainly categorized into single-walled carbon nanotubes (SWCNTs) and multi-walled carbon nanotubes (MWCNTs), could be produced (Kim et al., 2003; Qiu et al., 2010; Altalhi et al., 2013).

Among various synthesizing methodologies, as compared in Table 1 chemical vapor deposition (CVD) or thermal pyrolysis is recognized as an efficient mean because of its advantages in large-scale production with relatively low operating costs and excellent controllability in orientation, alignment, length, diameter, purity and density of resultant CNTs. Many technical reports have indicated that the thermal pyrolysis of organometallic compounds, such as ferrocene, iron phthalocyanine, and nickel phthalocyanine can be employed as either reactants or catalysts for production of carbon nanotubes and nanocapsules (Afre et al., 2006; Liu et al., 2006; Vijayaraghavan and Stevenson, 2007; Charinpanitkul et al., 2009a; Zhuo et al., 2010; Sano et al., 2012; Li et al., 2012; Yang et al., 2012). With the thermal pyrolysis, some metal species, such as Fe, Ni or Co, in those compounds are well recognized to play an important role as catalyst for CNP growth (Auer et al., 1998; Li et al., 2003; Zeng, et al., 2006; Yuan et al., 2007; Morales et al., 2013; Nahil et al., 2015). Many novel methods to incorporate necessary catalyst with carbon sources are also the on-going research issues which have been reported by various research teams around the world. Investigation on tuning of synthesizing parameters for optimized productions of carbonaceous nanomaterials has been one of the most concentrating topics for research teams in many countries.

Meanwhile, it has been well accepted that utilization of alternative carbon sources available in gas, liquid, or solid phase by introducing over catalytic substrates or pre-mixing with catalyst supply would possibly increase production yield, improve CNT quality, or minimize the amount of expensive catalyst usage (Liu et al., 2006; Vijayaraghavan and Stevenson, 2007; Yuan et al., 2007; Zhang et al., 2008; Zhang et al., 2008; Quan et al., 2010; Zhuo et al., 2010; Alves et al., 2011; Sano et al., 2012; Li et al., 2012; Mishra et al., 2012; Yang et al., 2012; Sawant et al., 2013; Bajad et al., 2015). High purity carbon sources (> 99.9 %), such as CO, CO₂, alcohols, and various hydrocarbons (methane, ethylene, acetylene, n-butane, hexane, benzene, toluene, xylene) have been extensively utilized for synthesizing CNTs with specific know-how relevant to synthesizing

and purifying parameters which are synthesizing temperature and pressure, residence time in reactors, ratio of carbon source to catalyst and so on. However, such carbon sources are still expensive and present in limited supply, resulting in elevating attentions to search for alternative carbon sources, which include industrial wastes, municipal wastes (i.e. plastics wastes), food wastes, and low value-added industrial by-products (red oil, glycerol, slop oil). Instead of using as alternative energy sources, such industrial wastes or by-products could be considered as one of good alternatives for production of carbonaceous nanomaterials (Liu et al., 2006; Vijayaraghavan and Stevenson, 2007; Yuan et al., 2007; Zhang et al., 2008; Quan et al., 2010; Zhuo et al., 2010; Alves et al., 2011; Li et al., 2012; Yang et al., 2012; Altalhi et al., 2013; Acomb et al., 2014; Gong et al., 2014; Bajad et al., 2015). **Table 2** summarizes some previous works which have made use of industrial waste as raw material for production of carbon nanotubes (CNTs) and derivatives. It could be clearly observed that some specific catalysts would be essentially required for production of CNTs with different characteristics. Among operating conditions, synthesizing temperature would also be a key parameter for converting raw materials into reactive carbon clusters which would undergo the self-assembly process to generate carbon nanotubes (Lee et al., 2003; Parkansky et al., 2004). Without catalysts, there is high possibility that the resultant products would be carbon black or amorphous carbon nanoparticles (Liu et al., 2006; Zhuo et al., 2010; Li et al., 2012). In addition, because of uncertain compositions, different physical and chemical properties, such industrial wastes or by-products contain some unknown impurities, such as sulfur which is expected to severely affect the synthesizing process, poisoning of catalyst, corrosion of reactor wall and so on. Some counter-measures have been proposed and examined for improving the productivity of carbonaceous nanomaterials from those industrial wastes.

Therefore, in this review, relevant research works focusing on catalytic pyrolysis or chemical vapor deposition of carbonaceous industrial waste for carbon nanomaterial production were comprehensively analyzed and summarized. Synthesizing parameters, such as molar ratio of organometallic catalyst to carbon source, types of catalysts and carbon sources, reaction temperature, were comprehensively examined for improving the synthesis efficiency. Furthermore, some promising applications involving with antibiotic removal, spilled oil handling and pollutant gas detection were also taken into account.

Table 2 Some referable works involving with synthesis of CNTs using industrial wastes

	Synthesizing parameters							Characteristics	
	Source	Feed	Catalyst	Reactor Type	Temperature (°C)	Carrier Gas	Reaction Time	Length	Diameter
Afre et al., 2006	Chemical process waste	Turpentine Oil	Co and Fe	Quartz Tube	500–900	N ₂		NR	2.5 nm
Liu et al., 2006	Petroleum refining process waste	Deoiled Asphalt	Ferrocene	Quartz Tube	700–1200	Ar	20–50 min	NR	180 nm
Bajad et al., 2015	Plastic waste	Polypropylene	Ni/Mo/MgO	Muffle Furnace	700–900		10 min	NR	2–25 nm
Charinpanitkul et al., 2009	Chemical process waste	Naphthalene	Ferrocene	Quartz Tube	600–1000	N ₂	15 min	Several Microns	> 100 nm
Zhuo et al., 2010	Plastic waste	HDPE	304 Stainless steel with Co, Ni or No	Quartz Tube	800		1 min	1–5 µm	15–84 nm
Sano et al., 2012	Petroleum refining process waste	Ethylene	316 Stainless Steel	Quartz Tube	700	H ₂	30 min	5–80 µm	3–10 nm
Li et al., 2012	Petroleum refining process waste	Heavy Oil Residue	Fe, Co, Ni, Au and Pt	Quartz Tube	900	H ₂	20 min	NR	0.89–1.19 nm
Yang et al., 2012	Automobile waste	Scrap Tyre Rubber	Co, Mg, Mn, Al	Quartz Tube	650	H ₂	60 min	NR	30–50 nm
Morales et al., 2013	Petroleum refining process waste	Acetylene	FeAl ₂ O ₄	Quartz Tube	730	H ₂ /N ₂	60 min	NR	2–45 nm

Note: NR represents “not reported”

2. Present advancement of carbonaceous nanomaterial production from industrial waste

A comprehensive search of international journal publications was carried out using keywords of carbonaceous nanomaterial, industrial waste, and applications through the SCOPUS database. It should be noted that most of motivations for industrial waste utilization in those previous works are focused on requirement of reducing greenhouse gases (GHGs) in the atmosphere for mitigation of the global warming effect. It is commonly accepted that the combustion of fossil fuels is responsible for 73 % of CO₂ emission thereby partial replacement of fossil fuels by bioethanol would enable a reduction in the levels of CO₂ emissions. According to the Renewable Fuels Association (RFA), the world bioethanol production in 2008 was approximately 65.6 billion liters (17.3 billion gallons), representing a 24 % increase in the production than the previous year (Yuan et al., 2007; Alves et al., 2011).

Among various environmental concerns, management of plastic waste has posed a serious challenging issue for our society because they make up a significant proportion

of municipal waste, typically around 10 wt% (Altalhi et al., 2013). Even though recycling rates for waste plastics have recently increased there is still a large remaining amount which ends up by being unsustainably disposed in landfill sites (Zhang et al., 2008; Mishra et al., 2012; Bajad et al., 2015; Nahil et al., 2015). In almost every country, the governmental sector has enforced more serious criteria for such industrial waste handling, such as limitation or avoidance of landfilling while encouraging promotion of waste management techniques are provided. In order to develop a more economically competitive usage, it is necessary to develop new methods to use industrial waste as replaced resources. Therefore, one of promising alternatives is to utilize such industrial waste containing carbonaceous content as feed stock for CNT production. If a feasible process could be developed for transforming those available carbon-rich wastes into high value-added products like CNTs, economic benefits could be made through simultaneously solving the plastic wastes and CNT production shortcomings. It seems that the amount of published studies attempting to synthesize CNTs from such industrial wastes were scattered and limited because most of them were exclusive projects or

announced in limited venues. So far serious issues including the variety and fluctuation of chemical compositions within such waste have been explored. It seems that the broad spectra of carbon-containing compounds, such as CH_4 , C_2H_6 , C_2H_4 , C_2H_2 , CO , CH_3OH , and so on, would involve as carbon sources for productions of CNPs (Bai et al., 2003; Lee et al., 2003; Chaisitsak et al., 2007; Zhang et al., 2008; Gong et al., 2014; Bajad et al., 2015). Furthermore, regarding to a common issue on using specific reactor system which would be promising for scalable production, some typical reports available in the public domain could be summarized in Table 2. It should be noted that various types of raw materials existing in gas, liquid and solid phases could be utilized for CNT synthesis with the assistance of various kinds of catalysts, such as ferrocene, nickel, cobalt and iron (Afre et al., 2006; Liu et al., 2006; Vijayaraghavan and Stevenson, 2007; Charinpanitkul et al., 2009b; Zhuo et al., 2010; Sano et al., 2012; Li et al., 2012; Yang et al., 2012; Morales et al., 2013). Those information would be good evidences that utilizing chemical vapor deposition or catalytic pyrolysis is a promising method because of its advantages on practical scalability and handling (Colomer et al., 2000; Grobert, 2007; Bazaegan and McKay, 2012; Mishra et al., 2012). In addition, it has been recognized that the industrial CNT manufacturing processes become sustainable and inherently safe though it would be sensible to use readily-available alternative fuels, such as existing waste streams. At the moment, since the production of CNTs has been successfully transferred from laboratory-scale to industrial-scale, their worldwide market is expected to grow from \$215 million in 2009 to over \$9 billion by 2020 (Iijima, 2012; Li et al., 2012; Nahil et al., 2015).

2.1 Gaseous carbon source

Hydrocarbons, such as methane, acetylene, ethylene, ethane, propane and some of gaseous hydrocarbons have been experimentally confirmed as carbon sources for CNT synthesis (Satishkumar, et al., 1999; Endo, et al., 2001; Bai, et al., 2003; Emmenegger, et al., 2003; Lee, et al., 2003; Liu, et al., 2003; Kim, et al., 2003; Lu et al., 2005a; Paradise and Goswami, 2007; Morales, et al., 2013). As a category of CVD synthesis, combusting or pyrolytic synthesis has the advantage of being an exothermic process which such carbon source can be utilized for in situ synthesis by means of decomposition and catalytic growth of CNTs. The composition of hydrocarbon gasses from those industrial processes would be varied from process to process. For example, in petrochemical downstream processing, the hydrocarbon gasses from the methane reformer would contain high content of CH_4 , CO and CO_2 , while those from refining units would consist of large compositions of BTX, propane and ethylene. The

current strategy for using these hydrocarbon gases is to install the carbon-material production unit on-board where the hydrocarbon sources are produced (Alves et al., 2011; Bazargan and McKay, 2012; Mankhand et al., 2012; Yang et al., 2012; Acomb et al., 2014). The use of suitable combustion equipment and catalyst as well as implementation of appropriate operating conditions, such as carbon source, flow of inert gas, and operating pressure, could realize controllable synthesis of CNTs with specifiable characteristics, such as diameter, length and purity (Liu, et al., 2003; Paradise and Goswami, 2007; Prasek, et al., 2011; Morales, et al., 2013).

Satishkumar et al. (1999) proposed to synthesize MWCNT bundles using pyrolysis of methane, acetylene or butane with the presence of ferrocene as catalyst precursor. The MWCNT bundles associated with nominal diameter in a range 2–13 nm contain iron nanoparticles inside their walls. As a result, such MWCNTs exhibit ferromagnetic behavior showing low saturation magnetization when compared to bulk iron. Meanwhile, Emmenegger et al. (2003) have synthesized MWCNTs from decomposition of C_2H_2 over a thin catalytic film of iron-oxide substrate. C_2H_2 concentration, time of deposition, temperature and ratio of C_2H_2 to N_2 are regulated to control the resultant MWCNT length. It is found that Fe_2O_3 is reduced to Fe_3O_4 and FeO after contacting with $\text{C}_2\text{H}_2:\text{N}_2$ flow, resulting in formation of MWCNTs with tips anchoring on iron carbide clusters. Later, Lee et al. (2003) could synthesize well-aligned MWCNTs with high purity by pyrolysis of C_2H_2 at 800 °C with the presence of iron (II) phthalocyanine. The synthesized MWCNTs exhibit a bamboo-like structure with good crystallinity. It is also reported that the growth rate of well-aligned MWCNTs could be enhanced with an increase in C_2H_2 concentration. With those typical examples, such pyrolytic method has been recognized as one of the most practical routes appropriate for mass production of MWCNTs. As a result, most of commercially available MWCNTs are synthesized by many manufacturers, such as Hyperion Catalysis International, Inc. (Cambridge, MA). Meanwhile, Carbon Nanotech Research Institute (CNRI), a subsidiary of Mitsui Chemical has planned to develop a large scale production of 120 t of MWCNTs per annum. In addition, Applied Sciences, Inc. (API) and Showa Denko (SDK), have been successful in a large scale production of MWCNTs with relatively large diameters and a wide distribution in the range 70–200 nm. However, it should be noted that synthesis of those carbon nanomaterials from such gaseous raw materials would possibly be upset by the unstable supply.

2.2 Liquid carbon source

Instead of gaseous raw materials, various kinds of liq-

uid containing carbon atoms, for example acetone, benzene, ethanol, toluene and high-molecular weight hydrocarbons, have been employed for synthesizing carbonaceous nanomaterials with different properties. Some kinds of liquid carbon sources would be intentionally prepared while others would be available as liquid by-products or wastes received from some specific industrial processes (Ago et al., 2000; Endo et al., 2001; Afre et al., 2006; Alves et al., 2011; Li et al., 2012). For investigation of formation mechanism, Ago et al. (2000) used a vertical flow reactor for synthesizing single and multi-walled carbon nanotubes by the catalytic reaction of colloidal solutions of metal nanoparticles. They made use of a reverse micelle solution of Co–Mo nanoparticles dissolved in toluene as raw material and injected the solution directly into a reactor of which temperature was maintained at 1200 °C. Therefore, it could be implied that such liquid precursor would be vaporized to provide clusters of carbon atoms as building blocks (Sun and Li, 2004; Yuan et al., 2007; Sowichai et al., 2012). The growth of SWCNTs was observed when the small amount of thiophene was added in the colloidal solution (1 wt.%). However, when they added 10 wt.% of thiophene, only MWCNTs can be grown from the self-assembly process. For mechanism investigation, it was found that carbon nanotubes contained metal nanoparticles encapsulated at the tip so that the tip-growth model was discussed.

Meanwhile, in many countries petrochemical industries have also produced some useful products necessary for our daily life but they also generate some hydrocarbon wastes which are mainly in liquid form. In general, as-received heavy hydrocarbon residue which is a highly aromatic material received as a bottom product after the distillation of petroleum could also be fed into a furnace or boiler for the generation of heat or “lighting up” facility in many coal-fired power plants. Certainly, such by-product of petroleum industries has great potential as feedstock in making carbon materials because it contains a large amount of carbon-rich molecules. As a typical example, slop oil which is a residual waste obtained from a petrochemical plant in Thailand was fractionated using a laboratory distilling unit could be separated into some fractions based on their boiling points as shown in **Fig. 1**. Light fraction contains hydrocarbons with boiling point lower than 170 °C while the middle and large fractions are separated at 150–320 and > 300 °C, respectively. It could be clearly observed that the fractionated hydrocarbons exhibit different appearance because of their compositions which could be decomposed for generating carbon clusters after subject to sufficient thermal energy (Endo et al., 2001; Andrews et al., 2002; Dai, 2002). Anyway, the main drawback of residual hydrocarbons is its high initial viscosity. In addition, it usually contains relatively high amounts of pollutants and particularly sulfur which forms sulfur dioxide

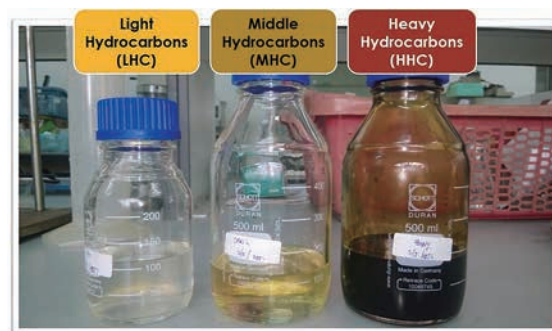


Fig. 1 Physical appearance of each fraction of liquid hydrocarbon waste (slop oil) obtained from petrochemical process.

upon combustion. Li et al. (2012) reported that the growth temperature plays an important role in determining the formation of SWCNTs. However, different characteristics of SWCNTs synthesized from heavy oil when compared with the small hydrocarbons would be attributed to the formation process which did not proceed through C₂ carbon units. It should also be noticed that effects of impurities in such waste on the synthesis of CNPs would be of concern so that many current strategies have been explored by adapting from some existing technologies. For example, the bottom product of a crude distillation unit in a petroleum refinery process usually contains high contents of sulfur and mercury compounds (Mohammed et al., 2012; Zubaidey et al., 2013; Khairi et al., 2015). Typically, various methods including chemical adsorption, gas stripping and chemical precipitation are employed for removing mercury from crudes and other hydrocarbon liquids to avoid the problems of poisoning. Meanwhile, sulfur removal with sorbent beds or chemical scrubbing has also been used with new supporting methods, such as microwave irradiation, for scavenging the sulfur content from liquid hydrocarbons in prior to their processing. In addition, effect of hydrocarbon chain length on the synthesis and the final quality of CNTs is also important issue though it is still ambiguously understood. Basically, the longer chain hydrocarbons would possibly be decomposed, resulting in formation of a broad spectrum of small hydrocarbons and carbon clusters with different specific molecular weights. Such hydrocarbons would undergo different reaction routes, resulting in formation of either arranged graphitic nanostructures or amorphous forms (Alberts 1997; Endo et al., 2001; Andrews et al., 2002; Dai 2002; Prasek et al., 2011; Mishra et al., 2012). In comparison with other carbon sources, such as methane, acetylene and ethanol, those hydrocarbons with broad molecular weight distribution would provide both crystalline and amorphous carbon nanostructures as could be confirmed by Raman spectroscopic analyses (Lee et al., 2003; Liu et al., 2003; Puengjinda et al., 2009).

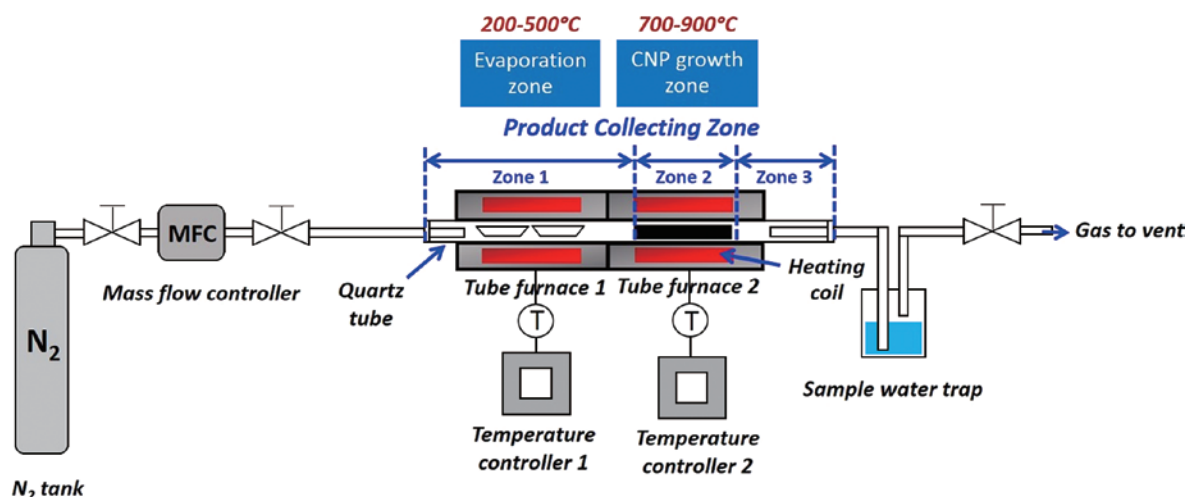


Fig. 2 Schematic diagram of reactor system for synthesizing carbonaceous nanomaterials from hydrocarbon feedstock.

Therefore, some pre-treatment would be essential for controlling the final quality or purity of CNPs which are synthesized from those hydrocarbon wastes.

In general, a typical set-up employed for synthesizing carbonaceous nanomaterials from such hydrocarbons would consist of a reactor equipped with raw material feeding and product collection as shown in Fig. 2. Feedstock would be introduced into the reactor by many means, such as spraying nozzle, ultrasonic nebulizer or even static container (Vilatela et al., 2015; Chaisitsak et al., 2007; Charinpanitkul et al., 2009b). Some inert carrier gas would be supplied into the reactor for carrying the hydrocarbon precursor which would be vaporized by regulated heating with a designated ramp rate for ensuring the steady flow of carbon sources into the reaction zone. The self-assembly reaction would be stimulated by a control of sufficiently high temperature zone within the reactor (Colomer et al., 2000; Barreiro et al., 2006; Charinpanitkul et al., 2009b; Puengjinda et al., 2009; Sano et al., 2012). During the formation of carbonaceous nanomaterials within the reactor, complicated phenomena, such as convective diffusional flow, thermophoresis and decomposition, would play a competitive role in regulating the production yield and characteristics of the resultant products. As a typical example, SEM micrographs of carbonaceous nanomaterials synthesized from fractionated hydrocarbon wastes and its mother liquor (slop oil) were depicted in Fig. 3. It could be clearly observed that synthesized products collected from different location of the reactor exhibit different apparent characteristics. Carbonaceous nanomaterials collected from Zone 1 where temperature was a little bit higher than the boiling point of slop oil mainly consist of spherical carbon nanocapsules (CNCs) which contain metal nanoparticle inside. Meanwhile, the highest thermal energy supply in Zone 2 would result in formation of well aligned MWCNTs with rather

uniform diameter because of enhanced self-assembly reaction. However, at Zone 3 where the remaining precursors would further undergo the self-assembly reaction but would be discouraged by the convective flow, resulting in formation of a mixture of MWCNTs and amorphous carbon nanospheres (CNSs). Further analyses on characteristics of resultant products obtained from different location in the reactor in cooperation with synthesizing conditions (temperature, ratio of feedstock and catalyst, flow rate of carrier gas and so on) would be taken into account for elucidating the formation mechanism of such carbonaceous nanomaterials. Most of previous works agree with a postulation that metal catalysts which would be intentionally supplied into the reactor would exist in active liquid form which would adsorb carbon molecular clusters onto its surface and then catalyze the self-assembly reaction, resulting in formation of carbonaceous nanostructures which contain those catalytic metal nanoparticles inside (Bai et al., 2003; Emmenegger et al., 2003; Barreiro et al., 2006; Prasek et al., 2011). However, other concrete evidence from in situ characterization would still be required for clear understanding on such phenomenon.

2.3 Solid carbon source

In general sense, plastic is considered as a nuisance which could provide many negative consequences, such as destruction of mangrove ecosystem due to its non-dissociation property in nature. Thin plastic bags have no recyclable value and are abandoned or by packing refuse in it (Tarig et al., 2013). Converting such plastic wastes into valuable products, such as carbon nanotubes (CNTs) could be an important and profitable option for industry and for environmental protection. Recently many research works focusing on synthesis of CNTs and other nanostructure derivatives through thermal decomposition of

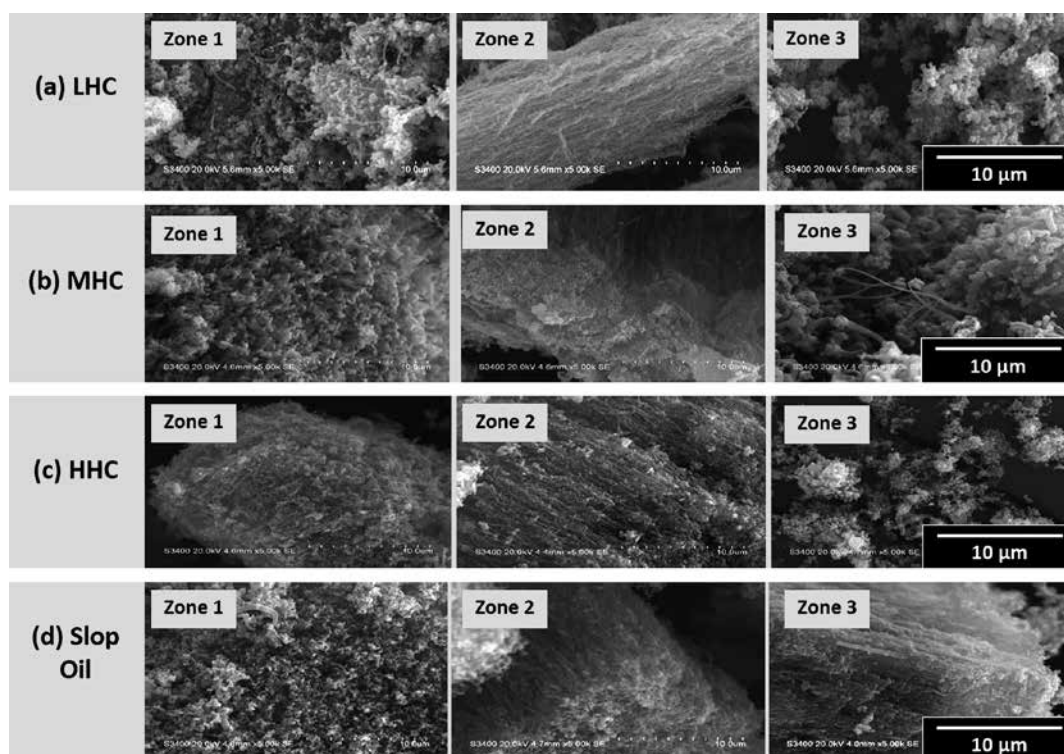


Fig. 3 SEM micrographs of CNTs prepared from (a) low boiling point hydrocarbon (LHC), (b) medium boiling point hydrocarbon (MHC), (c) high boiling point hydrocarbon (HHC) and (d) slop oil under a synthesizing temperature of 900 °C.

plastic wastes, such as polypropylene (PP), low density polyethylene (LDPE), high density polyethylene (HDPE), polyacrylate (PC), polyvinyl chloride (PVC), polystyrene (PS) and polyethyleneterephthalate (PET) with the presence of specific catalysts have been reported (Zhang et al., 2008; Quan et al., 2010; Zhuo et al., 2010; Mishra et al., 2012; Yang et al., 2012; Savant et al., 2013; Acomb et al., 2014; Bajad et al., 2015; Nahil et al., 2015). Within those previous works, usage of low-cost alternative feedstocks which are post-consumer plastic wastes for CNT production has been demonstrated. Sufficient concentrations of carbon-containing species (either hydrocarbons alone or a mixture of hydrocarbon, CO and CO₂) as well as hydrogen and water molecules could be generated from the thermal decomposition of those plastic wastes. Then stand-alone pyrolysis of such plastic wastes or pyrolysis followed by premixed combustion of resulting gaseous pyrolyzates leads to CNT growth on catalytic surfaces. For example, Zhang et al. (2008) used combustion method for synthesis of CNTs using Ni compound/organic-modified montmorillonite and polypropylene (PP) as a source. They reported that with the increment of temperature, PP began to decompose to form carbon clusters which would diffuse around Ni nanoparticles, which could facilitate the growth of CNTs due to root-growing mechanism (Liu et al., 2003). Later, Mishra et al. (2012) have tried to use PE and MA-PP as precursor for synthesis of CNTs by

mixing PE with PP using ferrocene or Ni as catalyst in a stainless steel autoclave heated at 700 °C for 100 min. They reported that CNTs with average diameter of about 160 nm were synthesized with negligible generation of toxic or corrosive reagents. In addition, effect of synthesizing temperature on catalytic conversion of those plastic wastes to carbonaceous nanomaterials could be manifested through changes of catalyst particle size which is intentionally loaded into the synthesizing reactor (Bazargan and McKay, 2012; Altalhi et al., 2013). As a result, it should be noted that effluents of such plastic waste treating system are gases with substantial amounts of carbon monoxide, light hydrocarbons and hydrogen (Acomb et al., 2014). Therefore, it may be possible to utilize such gaseous by-products for power generation. Some new gas turbine technologies, such as Siemens G-class Gas Turbines, could work under flexible load conditions which such gaseous by-products with CO content could be effectively controlled (Engelber et al., 2004). In addition, the conversion of such gaseous by-products to reactive chemicals, such as alcohol and liquid hydrocarbons would be achievable by chemical reactions prior to its utilization as feed materials for CNT production (Andrews et al., 2002). These previous works would reveal that usage of such commodity plastic wastes with appropriate catalysts is a potential mean for synthesizing CNTs with competitive cost. However, due to the complexity of experimental

process, exact formation process of CNTs still needs further research.

Meanwhile, because of the increasing demand of electronic applicant usage, printed circuit board (PCB), which typically consists of 15 % epoxy resin, 30 % glass cloth filament, 22 % copper coils, metal (Sn, Pb, Fe, Ni, etc.) and Br, has become a serious social problem. One possible method for recovering both organic and non-organic fractions from PCB is pyrolysis technique so that some research works on conversion of PCB wastes have been reported (Jie et al., 2008; Quan et al., 2010; Mankhand et al., 2012). It is demonstrated that PCB waste pyrolysis could provide liquid products containing high concentrations of phenol-group species. Hollow-centered and straight CNTs with outer diameter of ~338 nm could be directly synthesized by pyrolysis of PCB pyrolysis oil using ferrocene as catalyst at 900 °C under nitrogen atmosphere. CNTs with nominal length of several microns could be observed with the presence of amorphous carbon nanoparticles (Quan et al., 2010). The external surface of porous carbonaceous nanomaterials prepared from carbonization of KOH-treated resin at 700 °C is full of cavities with BET specific surface area of 1214 m²/g and micropore volume of 0.41 cm³/g, respectively.

Eventually, it should be noted that scaled-up industrial system has also been explored especially for utilization of useful energy released during the synthesis of carbonaceous nanomaterials from such industrial wastes. Such exothermally released energy will offset the energy required to pyrolyze the industrial waste and to preheat the synthesizing system, resulting in a great improvement of the overall energy-efficiency. Thus, it would possibly help minimize the production cost of carbonaceous nanomaterials (Thostenson et al., 2001; Paradise and Goswami 2007; Prasek et al., 2011; de Volder et al., 2013). As mentioned above, comprehensive analyses of synthesized products within those different synthesizing process would still be required for ensuring the economically justifiable production of such carbonaceous nanomaterials.

3. Present advancement of carbonaceous nanomaterial applications

As mentioned above, applications of carbon nanotubes (CNTs) including their derivatives, such as carbon nanocapsules (CNCs), carbon nanohorns (CNHs) and graphenes have been an emerging subject of considerable research attempts owing to their unique mechanical, thermal, electrical and optical properties (Andrews et al., 2002; Zeng et al., 2006; Paradise and Goswami, 2007; Iijima, 2012; de Volder et al., 2013). Owing to those advantages, CNTs hold great promise as fundamental building blocks for nanoelectronics, field emitters, drug

delivery system, sensors and energy storage devices. For sustainable and secure continuity of the carbonaceous nanomaterial production, broad spectra of promising applications have been examined by many research teams around the world. Therefore, a substantial number of works done for exploring what might be the key characteristics of such carbon nanomaterials for each specific requirement of their usage are available. Using a comprehensive collection of literatures, promising applications involving with some specific technical requirements, such as antibiotic removal, spilled oil handling and pollutant gas detection were summarized in this review.

3.1 Fundamental applications

As fundamental applications, carbonaceous nanomaterials could be employed in their primitive form as they are produced or in modified form as other composites, which would require additional processing (Andrews et al., 2002; Yang et al., 2005; Zeng et al., 2006; Xu et al., 2007; Tusi et al., 2010; Iijima, 2012). Applications of such carbonaceous nanomaterials with specific purposes would be metal catalyst support, pollutant removal and so on. Based on our search through SCOPUS database, it seems that there are a variety of fundamental applications but three main categories have drawn attentions of many researchers because of some specific emerging needs from industrial and environmental viewpoints (Dai, 2002; de Volder et al., 2013).

3.1.1 Catalyst supports

Industrial sector generally requires robust catalysts made of precious metal species which are generally embedded onto the surface of some supporting materials. Among various materials, carbon is recognized as an excellent candidate due to its stability and compatibility (Bazargan and McKay, 2012; Nahil et al., 2015). For example, Yang et al. (2005) prepared spherical carbon particles or carbon spherules for accommodating Pt nanoparticles which was employed as electrocatalyst in direct methanol fuel cells (DMFCs). Their microscopic analyses revealed that K₂PtCl₆ with ethylene glycol could reduce size of the Pt nanoparticles with faceted crystalline structure. Aggregation and activity of the Pt nanoparticles are dependent on the surface properties of the carbon spherules. It should be noted that with cyclic voltammetry and galvanostatic polarization analyses the Pt/HCS catalyst could exhibit a higher catalytic activity in the electrooxidation of methanol than that of commercial ones. Then Xu et al. (2007) had also tried to deposit Pt or Pd on carbon microspheres (CMS), which could be used for methanol and ethanol oxidation in alkaline media. The results show that noble metal electrocatalysts supported on carbon microspheres give better performance than that supported on

carbon black. It is well known that Pd is not a good electrocatalyst for methanol oxidation, but it shows excellently higher activity and better steady-state electrolysis than Pt for ethanol electrooxidation in alkaline media. The results confirmed a synergistic effect by the interaction between Pd and carbon microspheres which could exert a great potential in direct ethanol fuel cells application. Meanwhile, Tusi et al. (2010) examined hydrothermal carbonization process for preparing composite of CNTs and PtRu nanoparticles, which were respectively generated from starch as carbon source and platinum and ruthenium salts as catalysts, with the presence of KOH or TPAOH (tetrapropylammonium hydroxide) for pH control. Based on comprehensive analyses using SEM/EDX, TGA, XRD and cyclic voltammetry, they reported that carbon PtRu nanocomposites prepared from TPAOH were more active for methanol oxidation than those prepared from KOH due to the pore volume and mesoporous structure. More recently Nahil et al. (2015) has reported that the pyrolysis with catalytic reforming of waste polypropylene with the presence of Ni-composite catalysts could provide multi-walled carbon nanotubes as a by-product of hydrogen production. They found that injection of steam with the presence of Ni–Mn–Al catalyst and MWCNTs would play a crucial role for achieving an optimal hydrogen production. Because of abundant surface area available for accommodating metal catalysts and the presence functional groups, MWCNTs could provide preferable yield of hydrogen as well as promoting decomposition of pollutants, such as phenol (Sano et al., 2012; Nahil et al., 2015). With such typical examples, it could be implied that carbonaceous nanomaterials would be a good candidate for supporting catalyst but clear understanding on their synergistic functions is still under investigation.

3.1.2 Water pollutant removal

Leakage of some chemicals employed in many human activities including agricultures and health remediation has been recognized as one of emerging threats to the world. Among those pollutants, it happens that antibiotics lead to tremendously serious consequence to the eco-system (Lu et al., 2005b; Grobert, 2007; Ji et al., 2009; Wang et al., 2009; Sowichai et al., 2012; Zhang et al., 2012). Though some conventional adsorbents, such as activated carbon or zeolite, are commercially available there are some drawbacks related to post-handling would draw research attentions to explore other new candidates. Therefore, some carbonaceous nanomaterials with special properties have been developed as novel adsorbent. From a viewpoint of adsorption kinetics, CNTs with ordered pore structure could make it easier for the diffusion of pollutants to adsorption sites when compared to conventional activated carbon (AC) with random pore structure. It should be noted that ACs generally contain micropores,

which are seldom available for the access of relatively large organic molecules. Lu et al. (2005b) studied the adsorption of trihalomethanes to CNTs and powdered activated carbon (PAC). They reported that CNTs reached adsorption equilibrium much faster than PACs, which would be attributed to the different porous structures of CNTs and PAC. The more uniform pore structure of CNTs would be beneficial for the diffusion of pollutants into the inner pores. Based on experimental investigation on adsorption of tetracycline to CNTs, graphite and activated carbon done by Ji et al. (2009), the adsorption affinity of tetracycline decreased in the order of graphite/SWNT > MWNT >> AC upon normalization for adsorbent surface area. These finding results would be attributed to the weaker adsorption of tetracycline to AC of which adsorption affinity was greatly influenced by the accessibility of available adsorption sites. Meanwhile, the remarkably strong adsorption of tetracycline to CNTs can be attributed to the strong adsorptive interactions (van der Waals forces, π - π EDA interactions, cation- π bonding) with the graphene surface of CNTs.

Then Sowichai et al. (2012) synthesized magnetic carbon nanoparticles (M-CNPs) from a mixture of glycerol and ferrocenes. The synthesized nanomaterials which mainly consisted of CNTs were used as an adsorbent for removal of tetracycline dissolved in simulated waste water. It was found that the adsorption capacity on M-CNPs was strongly dependent upon contact time and adsorption temperature. The increase in the adsorption temperature would result in the increase in both adsorption capacity and rate. However, the adsorption equilibrium would be achieved within 180 min regardless of adsorption temperature. Meanwhile, Zhang et al. (2012) examined the adsorption kinetics of phenanthrene and biphenyl on granular activated carbon (GAC) and CNTs. They reported that external mass transfer controlled the adsorption of organic compound to CNTs, while intraparticle diffusion dominated in the adsorption of organic compounds onto ACs. As a result, in well mixed systems, CNTs are superior to ACs in terms of sorption kinetics. Based on those typical examples of previous investigation, there are sufficient evidences revealing that regardless of their morphology, carbonaceous nanomaterials would be a good candidate for water pollution removal.

3.1.3 Spilled oil handling

More recently spreading news of many incidents of damaged pipeline and liner containing hydrocarbons which were spilled into the environment would clearly reveal that such spilled oil pollution could exert tremendously serious destruction of the eco-system. Spreading of spilled oil layer on natural water resources usually occurs after the oil discharge from emission sources and starting contact with water-surface. Rate of spreading

would be dependent upon oil characteristics, such as surface tension, viscosity, density, speed and environmental conditions, such as direction of wind, and water currents. Spreading would increase the oil covering surface area which would prevent the exposure to the sunlight and air, resulting in serious collapse of the eco-system. Therefore, development of effective adsorbent technology for handling such problem has gained an increasing interest from many research teams in many countries (Walkup et al., 1969; IPIECA, 1991; Albert, 1997; Wei and Molloy 2003; White and Molloy, 2003; Wang et al., 2007; Ren et al., 2011; Liu et al., 2015).

In general, natural inorganic sorbents, such as clay, glass, perlite, sand, vermiculite, wool, and volcanic ash would be employed for adsorbing those spilled oil. Those adsorbents would be able to absorb from 4 to 20 times their weight of oil. On the other hand, organic materials can be used on land and are not adaptable to water use for oil spill cleanup. More recently some synthetic sorbents includes man-made materials that are similar to plastics, such as polyurethane, polyethylene, polypropylene, and nylon fibers, which could exhibit superior adsorption capability as much as 70 times their weight of oil. However, those synthetic sorbents possess some drawbacks, especially their reusability and difficulties in their handling until they are disposed of properly (IPIECA, 1991). It appears that carbonaceous nanomaterials could be suited to adsorb spilled oils that can perpetrate or wick within their tortuous surface (Wang et al., 2007; Ren et al., 2011; Liu et al., 2015). Such adsorbents could be employed like sponges to collect oil by capillary action or suction, attributed to large surface area, the chemical affinity of the sorbents for the spilled oil, and chemical constituents including their porosity, molecular structure and change in volume (Ren et al., 2011). Absorbents work best on light, less viscous oils, while adsorbents work best on heavy, sticky, more viscous oils. For actual demonstration, the authors have also employed a freeze drying method to prepare sponge composites made of polyvinyl acetate (PVA) and MWCNTs. **Fig. 4** illustrated the appearance of 2 different sponge samples which the first was prepared from a mixture PVA and MWCNTs and the other from a similar mixture with addition of carboxymethyl cellulose (CMC). It could be clearly observed that the sponge prepared from the PVA/MWCNT/CMC exhibited stable porous structure with only insignificant shrinkage. Such stronger structure could be explained by the evidences obtained from microscopic analyses as shown in **Fig. 5**. With the presence of CMC, MWCNTs were uniformly dispersed within the PVA matrix, resulting in formation of fibrous network which could endure the external forces and could recover to its initial dimension after the external forces were released. Finally, with oil adsorption test, both sponge samples could exhibit impressive perfor-

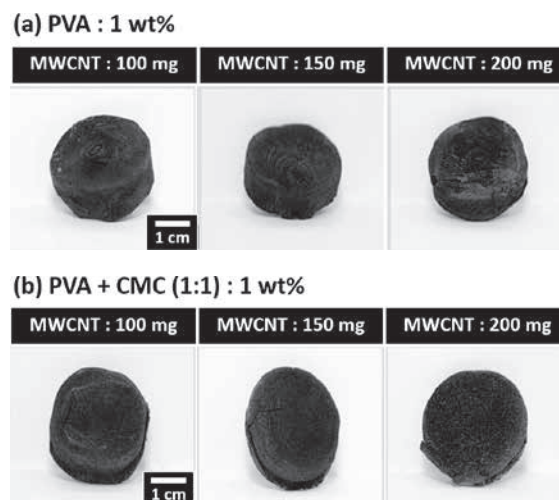


Fig. 4 Appearance of MWCNT sponge prepared by freeze drying with (a) 1 wt% of PVA and (b) 1 wt% of PVA/CMC mixture.

mance in collecting spilled oil within their porous structures. **Fig. 6** is a typical example of slop oil adsorption using the PVA/WMCNT/CMC sponges. In good agreement with other previous works, such composite sponge could exhibit a superior adsorption capability of about 60 times their weight of oil. Therefore, based on these evidences, it would be considered that carbonaceous nanomaterials could be a good alternative for many fundamental applications.

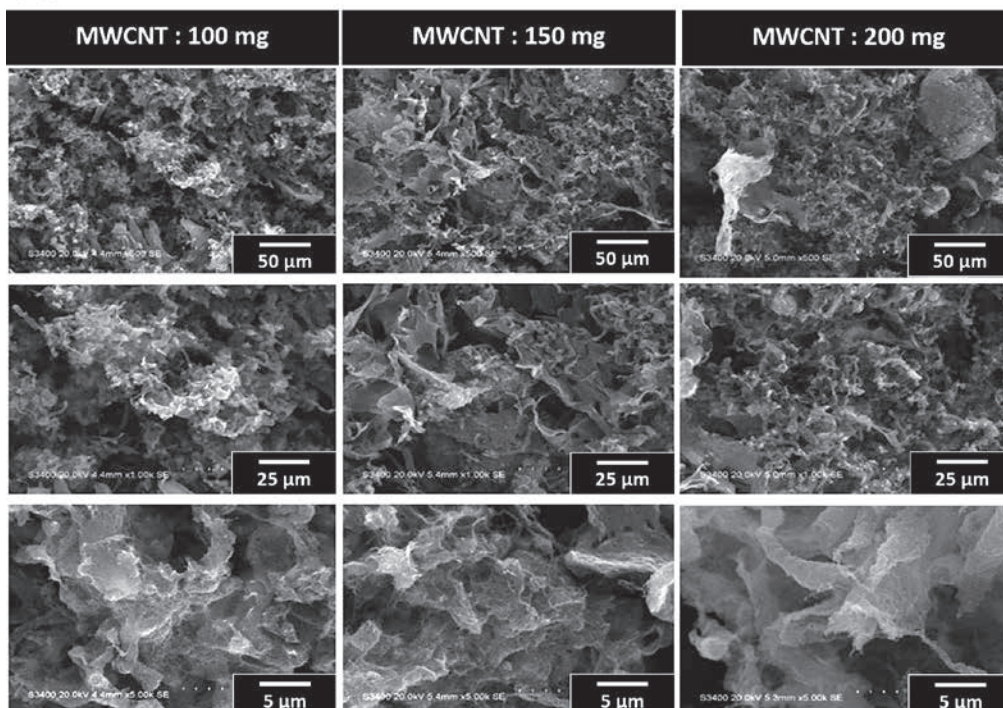
3.2 Novel applications

Different from fundamental applications, transformation of carbonaceous nanomaterials into distinguishable forms would lead to some novel applications which would hardly be achieved by using their primitive forms. It could be expected that derivation of novel applications of carbonaceous nanomaterials by integration with other technologies, such as sensor or quantum electronic technology, would cover much broader perspectives (Bittencourt et al., 2006; Espinosa et al., 2007; Balazsi et al., 2008; Hashishin, and Tamaki, 2008; Ghasempour and Zad, 2009). In this review, some typical examples of novel applications of carbonaceous nanomaterials are summarized.

3.2.1 Pollutant gas detection

Various gaseous pollutants have been emitted from many sources which are related to industrial manufacturing or daily living of human. Preventive actions against natural or artificial emission of some toxic exhausted gas have been accomplished by many research teams around the world (Bittencourt et al., 2006; Espinosa et al., 2007; Balazsi et al., 2008; Hashishin and Tamaki, 2008). With the excellent conductivity, carbonaceous materials would

(a) PVA : 1 wt%



(b) PVA + CMC (1:1) : 1 wt%

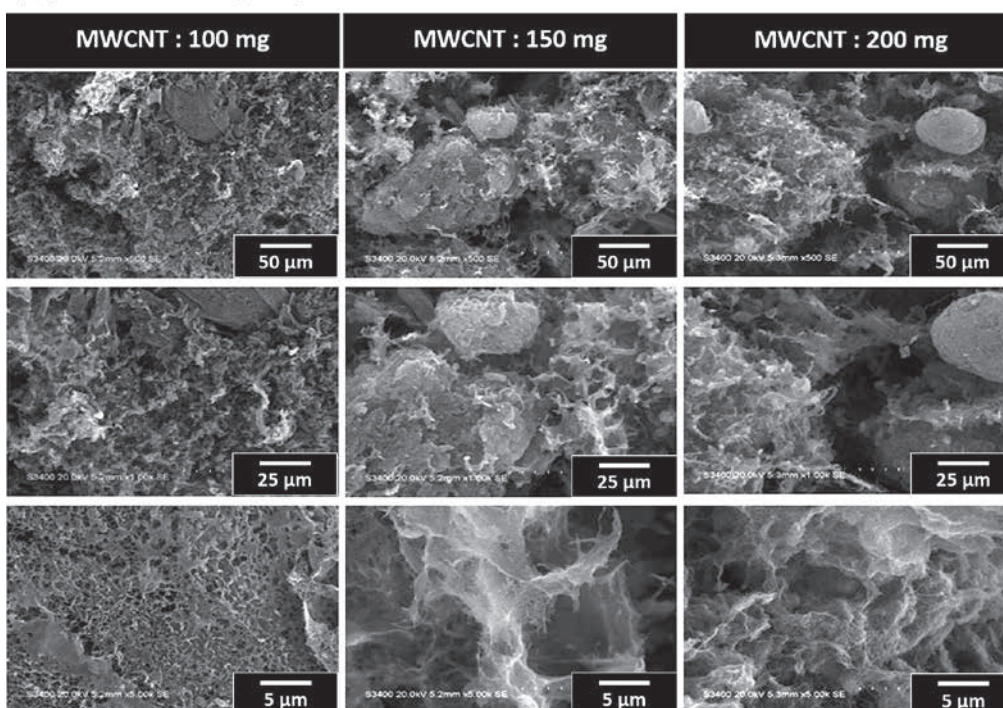


Fig. 5 SEM micrographs of MWCNT sponge prepared with (a) 1 wt% of PVA and (b) 1 wt% of PVA/CMC mixture.

be hybridized with some semi-conductor nanoparticles for improving sensing capability. Here are some typical examples of previous works which made of carbonaceous nanomaterials which could detect some toxic gaseous pollutants (NO_x, SO_x and VOC).

Bittencourt et al. (2006) prepared active layers for gas

sensing applications by adding oxygen plasma functionalised multi-walled carbon nanotubes (MWCNTs) to WO₃ and using the drop-coating deposition method. Two different ratios of MWCNTs in WO₃ (1/100 and 1/1000) were considered and the response of these sensors towards toxic gases such as nitrogen dioxide, carbon monoxide

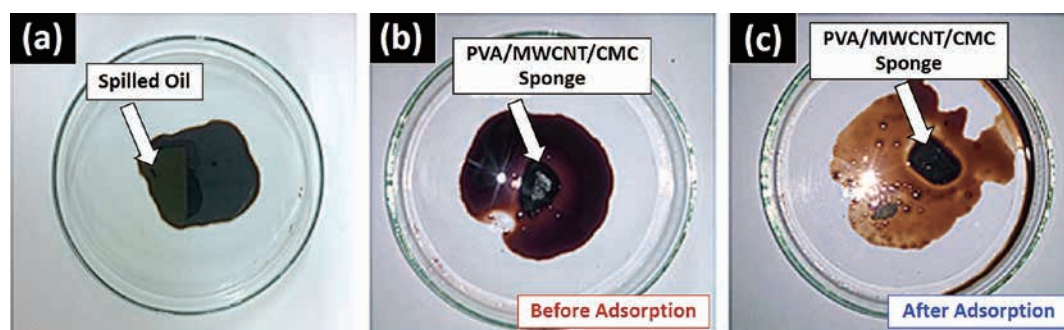


Fig. 6 Typical experiment on spilled oil adsorption using PVA/MWCNTs/CMC sponge. (a) spilled oil, (b) spilled oil with PVA/MWCNTs/CMC sponge just before adsorption, and (c) spilled oil after adsorption by PVA/MWCNTs/CMC sponge.

and ammonia was compared with that of WO_3 and MWCNTs gas sensors. It was found that the addition of a suitable quantity of MWCNTs in a WO_3 film can lower the sensor operating temperature to room temperature. The response of the hybrid films to NO_2 could be enhanced when only a few MWCNTs were added into the WO_3 films. Furthermore, hybrid films were able to detect ammonia which is very difficult to detect by using pure WO_3 and MWCNTs gas sensors, when operated at 150°C . Then Espinosa et al. (2007) investigated response to NO_2 of three different type of metal oxide (SnO_2 , WO_3 or TiO_2) prepared with the presence of a low amount of oxygen-functionalized MWCNTs. It was reported that the responsiveness towards NO_2 of these metal oxide/MWCNT hybrid films could considerably be improved. Meanwhile, the sensors based on hybrid SnO_2 /MWCNTs films present excellent sensitivity towards NO_2 when operated at room temperature. The results suggest that there should be an optimum amount of carbon nanotubes to be added to each specific metal oxide in order to enhance sensitivity.

Later, Hashishin and Tamaki (2008) also prepared MWCNT- WO_3 composite by directly growing MWCNTs on Au electrode by means of thermal CVD following by an impregnation by a suspension of H_2WO_3 on the surface of as-grown MWCNTs. After calcinations in argon at 400°C for 3 h, the composite was fabricated as sensor for testing its responses to NO_2 . The MWCNTs- WO_3 composite sensor could exhibit good sensor response ($R_a/R_g = 3.8$ at 200°C , whereas R_a is the resistance of sensor in air and R_g is that in NO_2 -containing atmosphere). The sensor response was greatly improved with MWCNT- WO_3 composite, comparing with that of MWCNT sensor ($R_a/R_g = 1.05$) which would be ascribed to formation of p-n junction, between MWCNT(p) and WO_3 (n), and thus improvement of NO_2 adsorption.

3.2.2 Electrode material

As promising novel applications, electronic devices have been proposed and developed for various purposes,

such as supercapacitor, dye-sensitized solar cell, hydrogen fuel cell and so on (Yoon et al., 2000; Soneda et al., 2003; Liu et al., 2005; Lee et al., 2008; Ramasamy et al., 2008). In those devices, electrode materials have been considered as a key issue for improving such device performance. Among various carbonaceous materials, such as activated carbon, disordered carbon, mesoporous carbon and MWCNTs are under close scrutiny for use as a promising electrode material. For instance, in electrical double layer capacitors (EDLC), composites involving, carbon or CNT and RuO_2 or MnO_2 compounds, have been developed for usage as electrode materials. In some preliminary studies involving MWCNTs and MnO_2 composites focused on optimal composition of MWCNTs and their rate capability for few cycles, and showed their promising performance (Yoon et al., 2000; Liu et al., 2005). It is well recognized that long cycle and high rate stability of an energy storage system are very important criteria for its applications as supercapacitors. However, long cycle performance at a considerably higher charge–discharge current has not been reported so far. Meanwhile, for counter-electrode of dye-sensitized solar cell application, carbon based materials, i.e. fullerene and SWCNTs have also been investigated as cost-effective and simpler alternatives. Catalytic activity towards iodine ion reduction has been investigated on carbon based counter-electrodes (Soneda et al., 2003). So far, an overall energy conversion efficiency of such solar cell device has still been below that of conventional Pt counter electrode DSSCs. However, it has also been suggested that Pt counter electrode in DSSC could be replaced by carbonaceous nanomaterials without affecting the energy conversion efficiency. Despite high catalytic activity towards iodine ion reduction, carbonaceous counter-electrode would probably exert some risk to the stability of DSSCs (Ramasamy et al., 2008). Since the electrodes made up of carbonaceous nanomaterials, prolong exposure in corrosive iodine redox electrolyte would be expected to result in the detachment of loosely bounded particles from rest of the electrode,

thereby promoting the dark current and degrade the overall device performance. Nevertheless, the stability of carbon counter-electrode in DSSC through optimization of electrolyte composition and device fabrication process would be further explored.

4. Summary

Because of the increasing global consumption, an exponential increase in industrial production activities inevitably results in overwhelming remain of industrial waste. As a result, increasing attentions of research and development teams in various countries have led to development of novel methodologies to utilize such industrial waste for production of carbonaceous nanomaterials instead of using as alternative energy sources. Meanwhile, for sustainable and secure continuity of the carbonaceous nanomaterial production, broad spectra of promising applications have also been examined. Among those emerging applications, utilization of carbonaceous nanomaterials in pollution control and prevention has been focused worldwide. Therefore, in this review, relevant research works focusing on catalytic pyrolysis of carbonaceous industrial waste for carbon nanomaterial production were comprehensively analyzed and summarized. In addition, broad spectra of promising applications involving with antibiotic removal, spilled oil adsorption, pollutant gas detection and electrode materials were also reviewed. Based on comprehensively reviewed literatures, it would be considered that carbonaceous nanomaterials could be potentially produced from various industrial wastes and they would be a good alternative for many fundamental and novel applications. Linkages between their characteristics and dominating phenomena taking place in those applications would be important research issues for further exploration.

Acknowledgement

Main support from the Silver Jubilee Fund of Chulalongkorn University through the Climate Change and Disaster Management Research Cluster (CU 56-357-CC) is gratefully acknowledged. Partial support from the Institutional Research Grant (IRG5780014) of TRF and Chulalongkorn University (Contract No. RES_57_411_21_076) is also acknowledged.

References

Acomb J.C., Wu C., Williams P.T., Control of steam input to the pyrolysis-gasification of waste plastics for improved pro-

- duction of hydrogen or carbon nanotubes, *Appl. Catal. B: Environ.*, 147 (2014) 571–584.
- Afre R.A., Soga T., Jimbo T., Kumar M., Ando Y., Sharon M., Somani P.R. and Umeno M., Carbon nanotubes by spray pyrolysis of turpentine oil at different temperatures and their studies, *Microporous. Mesoporous Mater.*, 96 (2006) 184–190.
- Ago H., Komatsu T., Ohshima S., Kuriki Y., Yumura M., Dispersion of metal nanoparticles for aligned carbon nanotube arrays, *Appl. Phys. Lett.*, 77(2000) 79–81.
- Alberts P.H., Petroleum and individual polycyclic aromatic hydrocarbons. Hoffman D.J., et al. Editors, *Handbook of ecotoxicology*, Lewis, Boca Raton (FL), 1997, p. 330–356.
- Altalhi T., Kumeria T., Santos A., Losic D., Synthesis of well-organised carbon nanotube membranes from non-degradable plastic bags with tuneable molecular transport: Towards nanotechnological recycling, *Carbon*, 63 (2013) 423–433.
- Alves J.O., Zhuo C., Levendis Y., Tenório J.A.S., Catalytic conversion of wastes from the bioethanol production into carbon nanomaterials, *Catalytic conversion of wastes from the bioethanol production into carbon nanomaterials*, *Appl. Catal. B: Environ.*, 106 (2011) 433–444.
- Andrews R., Jacques D., Qian D., Rantell T., Multiwall Carbon Nanotubes: Synthesis and Application, *Acc. Chem. Res.*, 35 (2002) 1008–1017.
- Arora N., Sharma N.N., Arc discharge synthesis of carbon nanotubes: Comprehensive review, *Diam. Rel. Mater.*, 50 (2014) 135–150.
- Auer E., Freund A., Pietsch J., Tacke T., Carbons as supports for industrial precious metal catalysts, *Appl. Catal. A: General*, 173 (1998) 259–271.
- Bai S., Li F., Yang Q.H., Cheng H.M., Bai J.B., Influence of ferrocene/benzene mole ratio on the synthesis of carbon nanostructures, *Chem. Phys. Lett.*, 376 (2003) 83–89.
- Bajad A., Tiwarib S., Vijayakumara R., Synthesis and characterization of CNTs using polypropylene waste as precursor, *Mater. Sci. Eng. B.*, 194 (2015) 68–77.
- Balázs C., Sedláčková K., Llobet E., Ionescu R., Novel hexagonal WO₃ nanopowder with metal decorated carbon nanotubes as NO₂ gas sensor, *Sensors Actuators B: Chemical*, 133(2008) 151–155.
- Bandow S., Kokai F., Takahashi K., Yudasaka M., Qin L.C., Iijima S., Interlayer spacing anomaly of single-wall carbon nanohorn aggregate, *Chem. Phys. Lett.*, 321 (2000) 514–519.
- Barreiro A., Selbmann D., Pichler T., Biedermann K., Gemming T., Rummeli M.H., Schwalke U., Büchner B., On the effects of solution and reaction parameters for the aerosol-assisted CVD growth of long carbon nanotubes, *Appl. Phys. A*, 82 (2006) 719–725.
- Bazargan A., McKay G., A review—Synthesis of carbon nanotubes from plastic wastes, *Chem. Eng. J.*, 195 (2012) 377–391.
- Bittencourt C., Felten A., Espinosa E.H., Ionescu R., Llobet E., Correig X., Pireaux J.J., WO₃ films modified with functionalised multi-wall carbon nanotubes: Morphological, compositional and gas response studies, *Sensors Actuators B: Chemical*, 115 (2006) 33–41.

- Chaisitsak S., Nukeaw J., Tuantranont A., Parametric study of atmospheric-pressure single-walled carbon nanotubes growth by ferrocene-ethanol mist CVD, *Diam. Relat. Mater.*, 16 (2007) 1958–1966.
- Charinpanitkul T., Sano N., Muthakarn P., Tanthapanichakoon W., Enhancing effect of monoolein surfactant on carbon nanoparticle synthesis by arc discharge in liquid, *Mater. Res. Bull.*, 44 (2009a) 324–327.
- Charinpanitkul T., Sano N., Puengjinda P., Klanwan J., Akrapattangkul N., Tanthapanichakoon W., Naphthalene as an alternative carbon source for pyrolytic synthesis of carbon nanostructures, *J. Anal. Appl. Pyro.*, 86 (2009b) 386–390.
- Charinpanitkul T., Tanthapanichakoon W., Regeneration of activated carbons saturated with pyridine or phenol using supercritical water oxidation method enhanced with hydrogen peroxide, *J. Ind. Eng. Chem.*, 17 (2011) 570–575.
- Colomer J.F., Stephan C., Lefrant S., van Tendeloo G., Willems I., Kónya Z., Fonseca A., Laurent C., Nagy J.B., Large-scale synthesis of single-wall carbon nanotubes by catalytic chemical vapor deposition (CCVD) method, *Chem. Phys. Lett.*, 317 (2000) 83–89.
- Dai H., Carbon nanotubes: opportunities and challenges, *Surf. Sci.*, 500 (2002) 218–241.
- de Volder M.F.L., Tawfick S.H., Baughman R.H., Hart A.J., Carbon Nanotubes: Present and Future Commercial Applications, *Science*, 339 (2013) 535–539.
- Emmenegger C., Bonard J.M., Maun P., Sudan P., Lepora A., Grobety B., Zuttel A., Schlupbach L., Synthesis of carbon nanotubes over Fe catalyst on aluminium and suggested growth mechanism, *Carbon* 41 (2003) 539–547.
- Endo M., Kim Y.A., Takeda T., Hong S.H., Matusita T., Hayashi T., Dresselhaus M.S., Structural characterization of carbon nanofibers obtained by hydrocarbon pyrolysis, *Carbon* 39 (2001) 2003–2010.
- Engelbert C., Fadok J., Fuller R., Lueneburg B., Introducing the 1S.W501G Single-Shaft Combined Cycle Reference Power Plant, *Proceedings of ASME Power*, 2004, Baltimore, Maryland.
- Espinosa E.H., Ionescu R., Chambon B., Bedis G., Sotter E., Bittencourt C., Felten A., Pireaux J.J., Correig X., Llobet E., Hybrid metal oxide and multiwall carbon nanotube films for low temperature gas sensing, *Sensors Actuators B: Chemical*, 127 (2007) 137–142.
- Ghasempour R., Zad A.I., Hybrid multiwalled carbon nanotubes and trioxide tungsten nanoparticles for hydrogen gas sensing, *J. Phys. D: Applied Phys.*, 42 (2009) 165105.
- Gong J., Feng J., Liu J., Jiang Z., Chen X., Mijowska E., Wen X., Tang T., Catalytic carbonization of polypropylene into cup-stacked carbon nanotubes with high performances in adsorption of heavy metallic ions and organic dyes, *Chemical Engineering Journal*, 248 (2014) 27–40.
- Grobert N., Carbon nanotubes—becoming clean, *Mater. Today*, 10 (2007) 28–35.
- Guo J., Wang X., Yao Y., Yang X., Liu X., Xu B., Structure of nanocarbons prepared by arc discharge in water, *Mater. Chem. Phys.*, 105 (2007) 175–178.
- Hashishin T., Tamaki J., Conductivity-Type Sensor Based on CNT-WO₃ Composite for NO₂ Detection, *J. Nanomater.*, 2008 (2008) 1–4.
- Iijima S., Helical microtubules of graphitic carbon, *Nature*, 354 (1991) 56–58.
- Iijima S., Nanocarbon Materials: Synthesis and Structure Characterizations, *Proceeding of the 2nd Workshop on Nanoscience : Carbon-related Systems and Nanomaterials*, NCKU, Tainan, Taiwan (2012).
- IPIECA. A Guide to Contingency Planning for Oil Spill on Water, Report Series, Vol.2, 1991.
- Jang J., Bae J., Fabrication of polymer nanofibers and carbon nanofibers by using a salt-assisted microemulsion polymerization, *Angew. Chemie*, 43 (2004) 3803–3806.
- Ji L.L., Chen W., Duan L., Zhu D.Q., Mechanisms for strong adsorption of tetracycline to carbon nanotubes: A comparative study using activated carbon and graphite as adsorbents, *Environ. Sci. Technol.*, 43 (2009), 2322–2327.
- Jie G., Shun L.Y., Xi L.M., Product characterization of waste printed circuit board by pyrolysis, *J. Anal. Appl. Pyrolysis*, 83 (2008) 185–189.
- Khairi A.N.S., Yusof N.A., Abdullah A.H., Mohammad F., Removal of Toxic Mercury from Petroleum Oil by Newly Synthesized Molecularly-Imprinted Polymer, *Int. J. Mol. Sci.*, 16 (2015) 10562–10577.
- Kim N.S., Lee Y.T., Park J.H., Vertically Aligned Carbon Nanotubes Grown by Pyrolysis of Iron, Cobalt, and Nickel Phthalocyanines, *J. Phys. Chem. B*, 107(2003) 9249–9255.
- Kroto H.W., Heath J.R., O'Brien S.C., Curl R.F., Smalley R.E., C₆₀: Buckminsterfullerene, *Nature*, 318 (1985) 162–163.
- Kusaba M., Tsunawaki Y., Production of single-wall carbon nanotubes by a XeCl excimer laser ablation, *Thin Solid Films*, 506 (2006) 255–258.
- Lebel L.L., Aissa B., Khakani M.A.E., Therriault D., Preparation and mechanical characterization of laser ablated single-walled carbon-nanotubes/polyurethane nanocomposite microbeams, *Comp. Sci. Technol.*, 70 (2010) 518–524.
- Lee Y.T., Kim N.S., Park J.H., Han J.B., Choi Y.S., Ryu H., Lee H.J., Temperature-dependent growth of carbon nanotubes by pyrolysis of ferrocene and acetylene in the range between 700 and 1000 °C, *Chem. Phys. Lett.*, 372 (2003) 853–859.
- Lee W.J., Ramasamy E., Lee D.Y., Song J.S., Performance variation of carbon counter electrode based dye-sensitized solar cell, *Solar Energy Mater. Solar Cells*, 92 (2008) 814–818.
- Li X., Lei Z., Ren R., Liu J., Zuo X., Dong Z., Wang H., Wang J., Characterization of carbon nanohorn encapsulated Fe particles, *Carbon*, 41 (2003) 3068–3072.
- Li Y., Wang H., Wang G., Gao J., Synthesis of single-walled carbon nanotubes from heavy oil residue, *Chem. Eng. J.*, 211 (2012) 255–259.
- Liu B.C., Lee T.J., Lee S.H., Park C.Y., Lee C.J., Large-scale synthesis of high-purity well-aligned carbon nanotubes using pyrolysis of iron(II) phthalocyanine and acetylene, *Chem. Phys. Lett.*, 37 (2003) 55–59.
- Liu H.Y., Wang K.P., Teng H.S., A simplified preparation of mesoporous carbon and the examination of the carbon accessibility for electric double layer formation, *Carbon* 43 (2005) 559–566.

- Liu X., Yang Y., Lin X., Xu B., Zhang Y., Deoiled asphalt as carbon source for preparation of various carbon materials by chemical vapor deposition, *Fuel Process. Technol.*, 87 (2006) 919–925.
- Liu T., Chen S., Liu H., Oil Adsorption and Reuse Performance of Multi-Walled Carbon Nanotubes, *Procedia Engineering*, 102 (2015) 1896–1902.
- Lu Y., Zhu Z.P., Liu Z.Y., Carbon-encapsulated Fe nanoparticles from detonation-induced pyrolysis of ferrocene, *Carbon*, 43 (2005a) 369–374.
- Lu C.S., Chung Y.L., Chang K.F., Adsorption of trihalomethanes from water with carbon nanotubes. *Water Res.*, 39 (2005b) 1183–1189.
- Mankhand T.R., Singh K.K., Gupta S.K., Das S., Pyrolysis of Printed Circuit Boards, *Inter. J. Metal. Eng.*, 1(2012) 102–107.
- Mishra N., Das G., Ansaldo A., Genovese A., Malerba M., Povia M., Ricci D., Fabrizio E.D., Zitti E.D., Sharon M., Sharon M., Pyrolysis of waste polypropylene for the synthesis of carbon nanotubes, *J. Anal. Appl. Pyro.*, 94 (2012) 91–98.
- Mohammed A.D., Isah A.G., Umaru M., Ahmed S., Abdullah Y.N., Comparative study on sulphur reduction from heavy petroleum- Solvent extraction and microwave irradiation approach, *Inter. J. Energy Environ.*, 3 (2012) 949–960.
- Montoro L.A., Lofrano R.C.Z., Rosolen J.M., Synthesis of single-walled and multi-walled carbon nanotubes by arc-water method, *Carbon*, 43 (2005) 200–203.
- Morales N. J., Goyanes S., Chilotte C., Bekeris V., Candal R.J., Rubiolo G.H., One-step chemical vapor deposition synthesis of magnetic CNT–hercynite (FeAl_2O_4) hybrids with good aqueous colloidal stability, *Carbon*, 61(2013) 515–524.
- Nahil M.A., Wu C., Williams P.T., Influence of metal addition to Ni-based catalysts for the co-production of carbon nanotubes and hydrogen from the thermal processing of waste polypropylene, *Fuel Proc. Technol.*, 130 (2015) 46–53.
- Paradise M., Goswami T., Carbon nanotubes—Production and industrial applications, *Mater. Desgn.*, 28 (2007) 1477–1489.
- Parkansky N., Boxman R.L., Alterkop B., Zontag I., Lereah Y., Barkay Z., Single-pulse arc production of carbon nanotubes in ambient air, *J. Phys. D: Appl. Phys.*, 37 (2004) 2715–2722.
- Popov V.N., Carbon nanotubes: properties and application, *Mater. Sci. Eng.: R: Reports*, 43 (2004) 61–102.
- Prasek J., Drbohlavova J., Chomoucka J., Hubalek J., Jasek O., Adam V., Kizek R., Methods for carbon nanotube synthesis—review, *J. Mater. Chem.*, 21 (2011) 15872–15884.
- Puengjinda P., Sano N., Tanthapanichakoon W., Charinpanitkul T., Selective synthesis of carbon nanotubes and nanocapsules using naphthalene pyrolysis assisted with ferrocene, *J. Ind. Eng. Chem.*, 15 (2009) 375–380.
- Qiu J., Chen G., Li Z., Zhao Z., Preparation of double-walled carbon nanotubes from fullerene waste soot by arc-discharge, *Carbon*, 48 (2010) 1312–1320.
- Quan C., Li A., Gao N., Synthesis of carbon nanotubes and porous carbons from printed circuit board waste pyrolysis oil, *J. Hazard. Mater.*, 179 (2010) 911–917.
- Ramasamy E., Won Jae Lee W.J., Lee D.Y., Song J.S., Spray coated multi-wall carbon nanotube counter electrode for tri-iodide reduction in dye-sensitized solar cells, *Electrochem. Commun.*, 10 (2008) 1087–1089.
- Ren X., Chen C., Nagatsu M., Wang X., Carbon nanotubes as adsorbents in environmental pollution management: a review, *Chem. Eng. J.*, 170 (2011) 395–410.
- Sano N., Akazawa H., Kikuchi T., Kanki T., Separated synthesis of iron-included carbon nanocapsules and nanotubes by pyrolysis of ferrocene in pure hydrogen, *Carbon*, 41 (2003) 2159–2162.
- Sano N., Charinpanitkul T., Kanki T., Tanthapanichakoon W., Controlled synthesis of carbon nanoparticles by arc in water method with forced convective jet, *J. Appl. Phys.*, 96 (2004) 645–649.
- Sano N., Hori Y., Yamamoto S., Tamon H., A simple oxidation–reduction process for the activation of a stainless steel surface to synthesize multi-walled carbon nanotubes and its application to phenol degradation in water, *Carbon* 50 (2012) 115–122.
- Satishkumar B.C., Govindaraj A., Rao C.N.R., Bundles of aligned carbon nanotubes obtained by the pyrolysis of ferrocene-hydrocarbon mixtures: role of the metal nanoparticles produced in situ, *Chem. Phys. Lett.*, 307 (1999) 158–162.
- Sawant S.Y., Somani R.S., Panda A.B., Bajaj H.C., Formation and characterization of onions shaped carbon soot from plastic wastes, *Mater. Lett.*, 94 (2013) 132–135.
- Serp P., Feurer R., Kalck P., Kihn Y., Faria J.L., Figueiredo J.L., Chemical vapour deposition process for the production of carbon nanospheres, *Carbon*, 39 (2001) 621–626.
- Soneda Y., Toyoda M., Hashiya K., Yamashita J., Kodama M., Hatori H., Inagaki M., Huge electrochemical capacitance of exfoliated carbon fibers, *Carbon*, 41 (2003) 2680–2682.
- Sowichai K., Supothina S., Nimitrakoolchai O.U., Seto T., Otani Y., Charinpanitkul T., Facile method to prepare magnetic multi-walled carbon nanotubes by in situ co-precipitation route, *J. Ind. Eng. Chem.*, 18(2012), 1568–1571.
- Sun X., Li Y., Colloidal Carbon Spheres and Their Core/Shell Structures with Noble-Metal Nanoparticles, *Angew. Chemie*, 43 (2004) 597–601.
- Thostenson E.T., Ren Z., Chou T.W., Advances in the science and technology of carbon nanotubes and their composites: a review, *Comp. Sci. Technol.*, 61 (2001) 1899–1912.
- Tsai Y.Y., Su J.S., Su C.Y., He W.H., Production of carbon nanotubes by single-pulse discharge in air, *J. Mater. Proces. Technol.*, 209 (2009) 4413–4416.
- Tusi M.M., Brandalise M., Verjúlío-Silva R.W.R., Correa O.V., Villalba J.C., Anaissi F.J., Neto A.O., Linardi M., Spinacé E.V., Preparation of PtRu/C electrocatalysts by hydrothermal carbonization using different carbon sources, *Proceeding of the 10th Inter. Symp. “Scientific Bases for the Preparation of Heterogeneous Catalysts”* edited by Gaigneaux E.M., Devillers M., Hermans S., Jacobs P., Martens J., Ruiz P. (2010)
- Vijayaraghavan G., Stevenson K.J., Synergistic assembly of dendrimer-templated platinum catalysts on nitrogen-doped carbon nanotube electrodes for oxygen reduction, *Langmuir*, 23 (2007) 5279–5282.

- Vilatela J., Rabanal M., Cervantes-Sodi F., A Spray Pyrolysis Method to Grow Carbon Nanotubes on Carbon Fibres, Steel and Ceramic Bricks., *J Nanosci. Nanotech.*, 15 (2015) 2858–2864.
- Walkup P.C., Polentz L.M., Smith J.D., Peterson P.L., Study of equipment and methods for removing oil from harbor waters, *Proceedings of Joint Conference on Prevention and Control of Oil Spills*, 15–17 December 1969, New York, 237–248.
- Wang S.G., Liu X.W., Gong W.X., et al. Adsorption of fulvic acids from aqueous solutions by carbon nanotubes, *J. Chem. Technol. Biotechnol.*, 82 (2007) 698–704.
- Wang X., Tao S., Xing B., Sorption and Competition of Aromatic Compounds and Humic Acid on Multiwalled Carbon Nanotubes, *Environ. Sci. Technol.*, 43(2009) 6214–6219.
- Wei Q.F., Mather R.R., Fotheringham A.F., Yang R.D., ESEM Study of Oil Wetting Behaviour of Polypropylene Fibres, *Spill Sci. Technol. Bull.*, 46 (2003) 780–783.
- White I.C., Molloy F., Factors that Determine the Cost of Oil Spills, *Proceeding of International Oil Spill Conference 2003*, Vancouver, Canada, 6–11 April 2003.
- Xiao Y., Liu Y., Cheng L., Yuan D., Zhang J., Gu Y., Sun G., Flower-like carbon materials prepared via a simple solvothermal route, *Carbon*, 44 (2006) 1589–1591.
- Xu C., Cheng L., Shen P., Liu Y., Methanol and ethanol electro-oxidation on Pt and Pd supported on carbon microspheres in alkaline media, *Electrochem. Commun.*, 9 (2007) 997–1001.
- Yang R., Qiu X., Zhang H., Li J., Zhu W., Wang Z., Huang X., Chen L., Monodispersed hard carbon spherules as a catalyst support for the electrooxidation of methanol, *Carbon* 43 (2005) 11–16.
- Yang W., Sun W.J., Chu W., Jiang C.F., Wen J., Synthesis of carbon nanotubes using scrap tyre rubber as carbon source, *Chinese Chem. Lett.*, 23 (2012) 363–366.
- Yao Z., Zhu X., Li X., Xie Y., Synthesis of novel Y-junction hollow carbon nanotrees, *Carbon*, 45 (2007) 1566–1570.
- Yoon S., Lee J.W., Hyeon T., Oh S.M., Electric Double-Layer Capacitor Performance of a New Mesoporous Carbon, *J. Electrochem. Soc.* 147 (2000) 2507–2512.
- Yuan D., Xu C., Liu Y., Tan S., Wang X., Wei Z., Shen P.K., Synthesis of coin-like hollow carbon and performance as Pd catalyst support for methanol electrooxidation, *Electrochem. Commun.*, 9 (2007) 2473–2478.
- Zeng Q., Li Z., Zhou Y., Synthesis and Application of Carbon Nanotubes, *J. Nat. Gas Chem.*, 15 (2006) 235–246.
- Zhang H., Ding Y., Wu C., Chen Y., Zhu Y., He Y., Zhong S., The effect of laser power on the formation of carbon nanotubes prepared in CO₂ continuous wave laser ablation at room temperature, *Physica B: Condensed Matter*, 325 (2003) 224–229.
- Zhang J., Li J., Cao J., Qian Y., Synthesis and characterization of larger diameter carbon nanotubes from catalytic pyrolysis of polypropylene, *Materials Letters*, 62 (2008) 1839–1842.
- Zhang S.J., Shao T., Kose H.S., Karanfil T., Adsorption kinetics of aromatic compounds on carbon nanotubes and activated carbons, *Environ.Toxic. Chem.*, 31(2012) 79–85.
- Zhuo C., Hall B., Richter H., Levendis Y., Synthesis of carbon nanotubes by sequential pyrolysis and combustion of polyethylene, *Carbon*, 48 (2010) 4024–4034.
- Zubaidy I.A.H., Tarsh F.B., Darwish N.N., Majeed B.S.S.A., Sharafi A.A., Chacra L.A., Adsorption Process of Sulfur Removal from Diesel Oil Using Sorbent Materials, *J. Clean Energy Technol.*, 1 (2013) 66–68.

Author's short biography

Konrat Kerdnawee



Konrat Kerdnawee obtained her Bachelor in Chemical Engineering from King Mongkut's University of Technology Thonburi (KMUTT) in 2012. At the present she is conducting her Ph.D. in Center of Excellence in Particle Technology (CEPT), Department of Chemical Engineering, Faculty of Engineering, Chulalongkorn University. Her research background in the field of carbon nanoparticles, such as carbon nanotubes. She can be synthesized magnetic-carbon nanoparticles using pyrolysis method and study on application of these materials for removal pollutant in water.

Chompoopitch Termvidchakorn



Chompoopitch Termvidchakorn received her Bachelor in Chemical Engineering from Chulalongkorn University in 2013. Now she is conducting her Ph.D. in Center of Excellence in Particle Technology (CEPT), Department of Chemical Engineering, Faculty of Engineering, Chulalongkorn University. Her present research involve to synthesis of single-walled carbon nanohorns and their catalytic performance for sugar conversion.

Pacharaporn Yaisanga



Pacharaporn Yaisanga obtained her Bachelor in Chemical Engineering from Mahidol University in 2012. At present she is conducting her Master in Center of Excellence in Particle Technology (CEPT), Department of Chemical Engineering, Faculty of Engineering, Chulalongkorn University. Her interest is in carbon nanotube composite membrane synthesis for carbon dioxide capture.

Jirapat Pakchamsai



Jirapat Pakchamsai received his Bachelor in Nano Engineering from Chulalongkorn University in 2015. During his internship in May-June 2014 at Department of Chemical Engineering, Kyoto University he performed the synthesis of Fe-single-walled carbon nanohorns (Fe-SWCNHs) composites via Gas-Injected Arc-In-Water (GI-AIW) method and studied the influence of Au-Addition on some physical properties of carbon nanoparticles. He is a member of Center of Excellence in Particle Technology (CEPT), Department of Chemical Engineering, Faculty of Engineering, Chulalongkorn University. His present research is emphasized on the synthesis of single-walled carbon nanohorns via Gas-Injected Arc-In-Water (GI-AIW) method and their application of antibiotics adsorption.

Author's short biography



Cheewapon Chookiat

Cheewapon Chookiat will receive his Bachelor in Nano Bachelor in Nano Engineering from Chulalongkorn University in October 2015. During his two-month internship in 2014, he conducted a research on Freeze-Drying technology at Division of Food Science and Biotechnology, Department of Agriculture, Kyoto University, Kyoto, Japan. Now he is a member of Center of Excellence in Particle Technology (CEPT), Department of Chemical Engineering, Faculty of Engineering, Chulalongkorn University. His present research is emphasized on the synthesis of single-walled carbon nanohorns via Gas-Injected Arc-In-Water (GI-AIW) method and their application of antibiotics adsorption.



Apiluck Eiad-ua

Apiluck Eiad-ua is an Assistant Professor of College of Nanotechnology, King Monkut's Institute of Technology Ladkrabang (KMITL). He received Bachelor in Chemical Engineering from Prince of Songkla University in 2001, Master in Chemical Engineering from Chulalongkorn University in 2004, and Doctor in Frontier Material from Nagoya Institute of Technology in 2011, respectively. He had experiences to work in National Institute of Advanced Industrial Science and Technology (AIST), Japan for 2 years and National Metal and Material Technology Center (MTEC) for 10 months. He joined KMITL with present research interest on Synthesis and Application of Nanoporous Materials since 2011.



Winadda Wongwiriyan

Winadda Wongwiriyan is an Assistant Professor of College of Nanotechnology, King Mongkuts's Institute of Technology Ladkrabang. She received her Bachelor, Master and Ph.D. in Electronic Engineering from Osaka University in 2003, 2005 and 2008, respectively. She also experienced a one-year postdoctoral fellowship at Institute of Carbon Science and Technology, Shinshu University. Her previous and current research interest has been focused on synthesis of carbon nanomaterials and their applications in sensor and energy storage devices.



Weerawut Chaiwat

Weerawut Chaiwat is a Lecturer in Environmental Engineering and Disaster Management Program, affiliated with School of Interdisciplinary Studies, Mahidol University, Kanchanaburi Campus, Thailand. He received his Bachelor in Chemical Engineering from Chulalongkorn University, Thailand, in 2003, and Master and Ph.D. in Chemical Engineering from Kyoto University, Japan, in 2007 and 2010, respectively. He also experienced a two-year postdoctoral fellowship at Fuels and Energy Technology Institute, Curtin University, Perth, Australia, during 2010-2012. His research interest has been focused on thermo-chemical conversion technology of biomass and hydrocarbon wastes to bio-fuels and value-added carbonaceous materials.

Author's short biography



Sakhon Ratchahat

Sakhon Ratchahat received his Bachelor and Master Degree in Chemical Engineering from Chulalongkorn University. During his Master study, he conducted research on synthesis of carbon microspheres from native starch by hydrothermal process. He worked as research assistant at Center of Excellence in Particle Technology, Chulalongkorn University for 2 years before pursuing his Ph.D. Now he is a Ph.D. student at Sekiguchi laboratory, Graduate School of Science and Engineering, Tokyo Institute of Technology, Japan. The research is Solar Gasification of Biomass in Catalytic Molten Salt Reactor.



Kajornsak Faungnawakij

Kajornsak Faungnawakij is a principal researcher and a director of Nanomaterials and Nanosystems Engineering Research Unit at NANOTEC, NSTDA. He received his B.Eng. (ChE with first-class honor) from Prince of Songkla University in 2001, and D.Eng. (ChE) from Chulalongkorn University in 2005. During 2005–2007, he held a researcher position at Japan Science and Technology Agency, and a postdoctoral fellow at Kyoto University. He has worked in the fields of nanocatalysis in biorefinery, published > 65 research articles, and filed > 25 patents. He has received some prestigious awards, including a “Distinguished Young Chemist Award 2010” and a “Young Scientist Award 2011”.



Komkrit Suttioponparnit

Komkrit Suttioponparnit is a researcher in Environmental Research and Management Department, PTT Research and Technology Institute, Thailand. He received his Bachelor Degree in Chemical Engineering from Srinakharinwirot University in 2001 and subsequently pursued his Master and Doctoral Degree in Chemical Engineering from Kasetsart University in 2003 and 2011, respectively. His present research interest is on Nanotechnology for Environmental Sustainability, particularly in the areas focusing on the utilization of petroleum and petrochemical by-products for synthesis of carbon-based nanomaterials, synthesis of nanocatalysts for pollution treatment, and the development of nanomaterials for heavy metals sensing in environment.



Tawatchai Charinpanitkul

Tawatchai Charinpanitkul is Associate Professor of Chemical Engineering, and Director of Center of Excellence in Particle Technology, Chulalongkorn University. He received Bachelor in Chemical Engineering from Chulalongkorn University in 1986, and Master and Doctor in Chemical System Engineering from University of Tokyo in 1989 and 1992, respectively. His research interest is focused on Synthesis and Application of Carbonaceous and Zinc Nanoparticles, and Biomass Technology. He has published 110 technical papers. In recognition of dedication, he was bestowed Royal Decorations, the highest being the Knight Grand Cordon (Special Class) of the Most Exalted Order of the White Elephant.

Aerosol Delivery of siRNA to the Lungs. Part 2: Nanocarrier-based Delivery Systems[†]

Susanne R. Youngren-Ortiz¹, Nishant S. Gandhi¹,
Laura España-Serrano¹ and Mahavir B. Chougule^{1,2*}

¹ Translational Drug Delivery Research (TransDDR) Laboratory, Department of Pharmaceutical Sciences,
The Daniel K. Inouye College of Pharmacy, University of Hawaii at Hilo, USA

² Natural Products and Experimental Therapeutics Program, The Cancer Research Center, University of Hawaii at Manoa, USA

Abstract

In this article, applications of engineered nanoparticles containing siRNA for inhalation delivery are reviewed and discussed. Diseases with identified protein malfunctions may be mitigated through the use of well-designed siRNA therapeutics. The inhalation route of administration provides local delivery of siRNA therapeutics to the lungs for various pulmonary diseases. A siRNA delivery system can be used to overcome the barriers of pulmonary delivery, such as anatomical barriers, mucociliary clearance, cough clearance, and alveolar macrophage clearance. Apart from naked siRNA aerosol delivery, previously studied siRNA carrier systems include those of lipidic, polymeric, peptide, or inorganic origin. These delivery systems can achieve pulmonary delivery through the generation of an aerosol via an inhaler or nebulizer. The preparation methodologies for these siRNA nanocarrier systems will be discussed herein. The use of inhalable nanocarrier siRNA delivery systems have barriers to their effective delivery, but overcoming these constraints while formulating a safe and effective delivery system will offer unique advances to the field of inhaled medicine.

Keywords: siRNA, nanocarrier, nanoparticle, aerosolization, pulmonary, lung

1. Introduction

siRNA has potential therapeutic applications in treating ‘undruggable’ diseases via post-transcriptional downregulation of target gene expression. The mechanisms of RNAi have been comprehensively reviewed (Fellmann C. and Lowe S.W., 2014; Fire A. et al., 1998; Hannon G.J., 2002; Kim D.H. and Rossi J.J., 2007). The siRNA possess a specific sequence that is complementary with its target mRNA and induces site-specific cleavage and subsequent inhibition of intracellular protein synthesis. The synthesis of siRNAs is relatively simple compared to other therapeutic classes because it does not require a cellular expression system, complex protein purification, or refolding schemes (Amarzguoui M. et al., 2005). A major advantage of siRNA over small molecule drugs or protein therapeutics is that the sequences can be rapidly designed for highly specific inhibition of the target of interest.

Pulmonary diseases such as asthma, lung cancer, cystic fibrosis, pulmonary hypertension, and chronic obstructive pulmonary disorder (COPD) have potential siRNA therapeutic targets (Amarzguoui M. et al., 2005; Burnett J.C. and Rossi J.J., 2012; Kanasty R. et al., 2013). However, due to the high negative charge density and the relatively large size of the siRNA molecules, naked siRNA molecules are not able to enter cells efficiently (Reischl D. and Zimmer A., 2009). Thus, delivery systems for siRNA need to be developed to successfully protect and deliver these agents. Nevertheless, siRNA delivery systems are likely to have instability issues that cause premature release of the nucleic acids, especially with systems that incorporate their cargo through electrostatic interactions. Pulmonary delivery of siRNA faces major challenges that involve decreased correlation between *in vitro* and *in vivo* experiments, difficulty in translation from animal models to humans, and administration routes used in animal studies that are non-applicable for human use (Lam J.K.-W. et al., 2012). Another challenge in siRNA therapy is the possibility of off-target effects induction.

This second part of a two part review article focuses on the pulmonary route of administration, siRNA loaded non-viral particulates for pulmonary or nasally inhaled delivery systems, and preparation techniques for siRNA

[†] Received 11 January 2016; Accepted 17 February 2016
J-STAGE Advance Publication online 30 April 2016

¹ 200 West Kawili Street, Hilo, Hawaii 96720, USA

² Honolulu, Hawaii 96813, USA

* Corresponding author: Mahavir B. Chougule;

E-mail: mahavir@hawaii.edu

TEL: +1-808-981-4519 FAX: +1-808-981-4520

loaded nanoparticles (Youngren-Ortiz S.R. et al., 2016). While the previous part covered the rationale for the use of various siRNA delivery systems, this part will focus on the preparation of siRNA loaded nanocarrier systems including examples of their pulmonary delivery.

2. Non-viral delivery of siRNA to the lung

siRNA is a highly negative charged, hydrophilic, and large-sized (approximately 13.3 kDa) macromolecule that cannot cross biological membranes to reach their target sites. Viral vectors have previously demonstrated cell uptake and siRNA efficacy, however, major limitations to human therapeutic delivery exist, such as uncontrolled viral replication, immunogenicity, tumorigenicity, and toxicity (Thomas C.E. et al., 2003). Due to these concerns, non-viral delivery systems have been developed and successfully used to deliver siRNA. An ideal siRNA delivery system should (1) condense siRNA into nanosized particles, (2) protect siRNA from enzymatic degradation, (3) facilitate cellular uptake, (4) promote endosomal escape to release siRNA to the cytoplasm where the RNA-induced silencing complex (RISC) is located, (5) have negligible effects on gene silencing activity or specificity and (6) have negligible toxicity (Lam J.K.-W. et al., 2012; Merkel O.M. and Kissel T., 2011). Non-viral delivery systems include naked siRNA, and delivery vectors such as lipids, polymers, peptides, and inorganic materials, as shown in Fig. 1.

2.1 siRNA delivery

2.1.1 Introduction

Unformulated or naked siRNA involves the delivery of siRNA without the use of a delivery vehicle or carrier. Advantages of this strategy include the ease of preparation and the facility of delivery by inhalation, intratracheal, or intranasal routes. A major disadvantage of this strategy is that the delivered siRNA is susceptible to poor cell targeting and uptake, and to degradation within the

airways. As discussed in part 1 of the review article, the major barriers for the delivery of siRNA to the lung include the presence of mucus, alveolar fluid, alveolar macrophages, and mucociliary clearance. Unfavorable physicochemical properties of siRNAs (negative charge, large molecular weight) and instability in plasma (half-life 10 min) also poses major delivery challenges (Ren Y. et al., 2010). Furthermore, after being transported intracellularly into the lysosomes via endocytosis, siRNA gets degraded in the lysosomes which diminishes the activity of siRNA therapeutics (Tseng Y.-C. et al., 2009). Since unmodified siRNA is prone to enzymatic degradation, new methods such as chemical modification of siRNA have been developed to increase stability. The chemical modification also improves specificity and potency, and reduces the immune response and off-target effects (Watts J.K. et al., 2008).

2.1.2 RNA modifications & preparation methods

The local delivery of siRNA is particularly well-suited for lung disease and infection therapy (De Fougères A. and Novobrantseva T., 2008). The direct instillation of siRNA into the lungs through intranasal or intratracheal routes results in direct contact with lung epithelial cells. Non-modified siRNA's can also induce nonspecific activation of immune system through the Toll-like receptor 7 pathway (Whitehead K.A. et al., 2009a). However, chemical modifications can be introduced into the RNA duplex structure which can enhance biological stability without adversely affecting gene-silencing activity and prevent nonspecific immune activation. Some of the modifications include incorporation of 2'-O-methyl modifications into the sugar structure of selected nucleotides within both the sense and antisense strands. The therapeutic efficacy of delivered siRNA can also be improved using conjugation of small molecules or peptides to the sense strand of siRNA. Several other modifications have been reported to eliminate the off-target effects such as phosphorothioate or boranophosphate introduction (Gandhi N.S. et al., 2014).

In a recent study, Antagomir-122 was synthesized from a hydroxyproline-linked cholesterol solid support and 2'-O-methyl phosphoramidites. On administration a marked decrease in endogenous miR-122 levels in the liver was observed (Krützfeldt J. et al., 2005). This and such other newer strategies have shown promise in protecting the siRNA against degradation by endonucleases thus allowing them to reach their site of action.

There are 3 main methods used for the production of siRNA *in vitro* which includes 1) chemical synthesis, 2) *in vitro* transcription of small RNA's and 3) *in vitro* transcription of long RNA's produced by the digestion with Dicer enzyme (Aalto A.P. et al., 2007). The *in vitro* chemical synthesis of siRNAs involves *in vitro* transcription and digestion of long dsRNAs by an RNase III family enzyme (e.g. Dicer, RNase III). These production methods

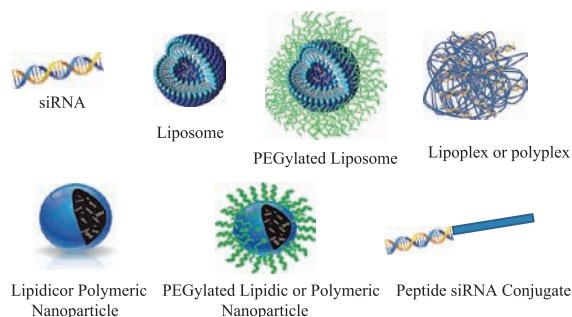


Fig. 1 Schematic of different non-viral siRNA delivery vectors.

require the design of siRNA sequences before siRNA preparation. Recently, Aalto et al. utilized an *in vitro* system using the combination of T7 RNA polymerase and RNA-dependent RNA polymerase (RdRP) of bacteriophage f6 to generate siRNA molecules. They further used an *in vivo* RNA replication system to produce siRNA. This system was based on carrier state bacterial cells containing the f6 polymerase complex which can result in unlimited amounts of siRNA up to 4.0 kb in size. Unmodified or modified siRNA can be prepared with simple reconstitution within normal saline or 5 % dextrose solution for inhalation delivery. Aerosolization of the siRNA solution can be conducted using a nebulizer. A new class of naked siRNA has been developed by Hamasaki et al., termed ribophorin II (PnkRNATM) and nkRNA[®] as shown in Fig. 2 (Hamasaki T. et al., 2012). This novel class of RNAi agents was synthesized as single-stranded RNA on a solid phase that, following synthesis, self-anneal into a unique helical structure containing a central stem and two loops (Merkel O.M. et al., 2014). Furthermore, a naked and unmodified novel RNAi agent, such as RPN2-PnkRNA, which has been selected as a therapeutic target for lung cancer when delivered via inhalation resulted in efficient inhibition of tumor growth without any significant toxicity.

2.1.3 Examples of siRNA delivery

Luciferase expressing mice were treated by intratracheal administration of 10 nmol siRNA duplex or 10 nmol phosphorothioate locked antisense oligonucleotide free

nucleic acids (Moschos S.A. et al., 2011). *Ex vivo* luminescence imaging elucidated organ associated luciferase knock-down. IVIS imaging of oligonucleotides labeled with Cy5 combined with confocal microscopy was used to determine their biodistribution (Moschos S.A. et al., 2011). Upon administration, the oligonucleotides underwent fast systemic distribution by transcytosis and renal clearance. The kidney and liver uptake of the phosphorothioate locked nucleic acid antisense oligonucleotides caused gene knockdown in these organs. However, protein expression was not downregulated in purified lung tissue cells (Moschos S.A. et al., 2011). The reduced therapeutic efficacy of free RNA supports observations by another group, who concluded that intratracheally delivered free TNF- α siRNA post-hemorrhage was inefficient in reducing the symptoms in a septic shock model of acute lung injury (Lomas-Neira J. et al., 2012). After bleomycin triggered pulmonary fibrosis was induced in mice with transgenic expression of human TGF- β 1, 5 mg/kg TGF- β 1 siRNA or a scrambled control was delivered intratracheally. This study found that siRNAs sequences shared by human and rodents successfully knocked down TGF- β 1 expression in human derived cell lines and significantly inhibited pulmonary fibrosis *in vivo* (D'alessandro-Gabazza C.N. et al., 2012).

2.2 Lipid-based delivery systems

2.2.1 Introduction

Lipid-based delivery systems are commonly used to deliver siRNA *in vitro* or *in vivo* (Tseng Y.-C. et al., 2009). Most often, cationic lipids or liposomes are used to form complexes, termed lipoplexes with anionic siRNA through spontaneous electrostatic interaction. Commercial siRNA transfection agents are commonly lipid-based systems, including OligofectamineTM, TransIT-TKO, Lipofectamine[®] RNAiMAX, and DharmaFECT (Bitko V. et al., 2005; Heidel J.D. et al., 2007; Tompkins S.M. et al., 2004; Wang J.-C. et al., 2010). A major challenge of using lipid-based siRNA delivery systems is their toxicity and non-specific activation of inflammatory cytokines and interferon responses (Wu S.Y. and Mcmillan N.A., 2009). Since aerosolization is a high shear stress process, the stability of the liposomes should be monitored since this process may cause physical and chemical changes that can lead to early siRNA release and degradation of the siRNA (Gaspar M.M. et al., 2008). Lipid based delivery systems for siRNA include liposomes, solid lipid nanoparticles (SLN) and nanostructured lipid carriers (NLC).

SLN are prepared by replacing the oil of the fat emulsion by a solid lipid or a blend of solid lipids, which makes the lipid matrix of the SLN solid at room and body temperature (Cavalli R. et al., 1997; Kalariya M. et al., 2005; Schwarz C. et al., 1994; Siekmann B. and Westesen K.,

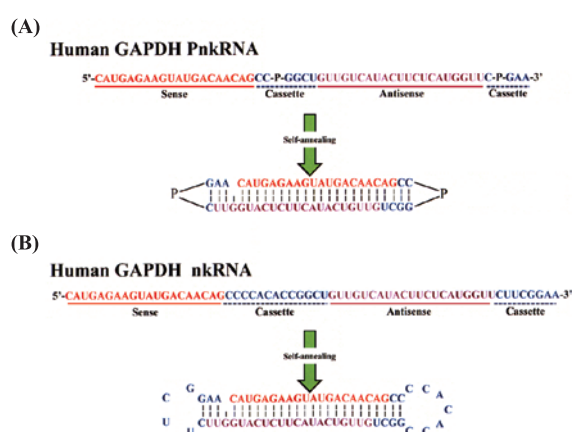


Fig. 2 Structure of novel PnkRNA (A) and nkRNA (B) RNAi therapeutic agents. Both PnkRNA (A) and nkRNA (B) were prepared as single stranded RNA oligomers that then self-anneal as shown by Hamasaki et al. Nucleotides shown in red indicate sense strand of the target (GAPDH), nucleotides shown in violet are the antisense strand, and nucleotides shown in blue are the loop cassettes. P indicates a proline derivative. Reprinted through open access agreement under the Creative Commons Attribution (CC BY) license from Ref. (Hamasaki T. et al., 2012).

1994). SLN are composed of 0.1–30 % w/w lipid dispersed in an aqueous solution of 0.5–5 % w/w surfactant as a stabilizing agent (Pardeike J. et al., 2009; Weber S. et al., 2014). SLN provide physical stability, chemical stability, controlled release, and low cytotoxicity if appropriate excipients are utilized (Wissing S. et al., 2004). SLN can be produced without the use of organic solvents and can be scaled up. Disadvantages of SLN are low loading capacity and premature release during storage (Mehnert W. and Maeder K., 2012). These events occur because the low ordered lipid modification of the particle matrix after production transforms to the highly ordered β -modification during storage. The β -modification is characterized by perfect crystal lattice with few imperfections and therefore, little room is left for siRNA storage. In order to overcome these issues, a second generation of lipid nanoparticles, the NLC were developed. NLC have a solid lipid matrix at room and body temperature and consist of a blend of solid lipid and oil, preferably at a ratio of 70:30 up to a ratio of 99.9:0.1 (Mehnert W. and Maeder K., 2012; Patel A.R. et al., 2013; Patlolla R.R. et al., 2010). Through mixing different kinds of lipids, a less ordered matrix with more room for active compounds is achieved (Mehnert W. and Maeder K., 2012).

2.2.2 Preparation methods

2.2.2.1 Cationic lipoplexes

Cationic lipids or liposomes can spontaneously form complexes with negatively charged siRNA through electrostatic interactions to form lipoplexes (**Fig. 3**). Complexation of cationic lipids and siRNA occurs through the negatively charged siRNA interaction with the positively charged lipids. This interaction causes neutralization of the cationic lipids, causing them to aggregate and encapsulate the siRNA (Bochicchio S. et al., 2014). It is necessary to optimize the lipid composition, lipids to siRNA ratio and the lipoplexes preparation methods, in order to improve stability and delivery efficiency while reducing possible adverse effects. Lipoplexes often have good transfection efficiency due to their efficient interaction with the negatively charged cell membranes as shown in **Fig. 3**. However, lipoplexes generally display poor stability and reproducibility when compared to other lipid based siRNA delivery systems, such as liposomes or SLN (De Fougères A.R., 2008). Another disadvantage is that cationic lipids are typically more toxic than neutral lipids (Dokka S. et al., 2000). To shield the positive charge of the cationic lipids, hydrophilic polymers such as PEG have been used to reduce inflammatory response.

Lipoplexes are not stable in liquid suspension for long-term storage, as shown by several studies in which the lipoplexes aggregate (Anchordoquy T.J. et al., 1997; Felgner P.L. et al., 1995). This leads to the requirement of preparation immediately prior to administration or to im-

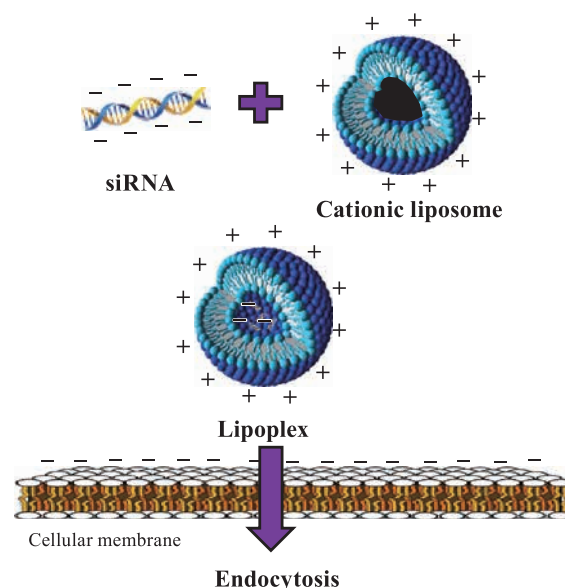


Fig. 3 Cationic liposome and anionic siRNA interaction forming a lipoplex. The cationic lipoplex interacts with the negatively charged cellular membrane leading to enhanced delivery within the cells via endocytosis.

prove lipoplex stability through the use of high pH diluents, sucrose gradients, and conjugation of PEG to the surface of lipoplexes (Caplen N.J. et al., 1995; Felgner P.L. et al., 1995; Gao X. and Huang L., 1996; Hoffland H. et al., 1996; Hong K. et al., 1997). Lyophilization is another method for intervening this issue that has been shown to inhibit aggregation for long-term storage of nucleic acid formulations (Allison S.D. and Anchordoquy T.J., 2001; Allison S.D. et al., 2000; Anchordoquy T.J. et al., 1997). Lyophilization allows for storage at room temperature, and therefore is preferred over freezing due to cost reduction in transportation and storage, and improved stability of biomolecules resulting from the removal of non-freezable water associated with most biomolecules (Umraniya Y. et al., 1995). Lyophilization can cause liposome fusion and phase separation during the drying and rehydration steps (Crowe J.H. and Crowe L.M., 1988). To overcome these problems, cryoprotectants, such as carbohydrates, are used. Cryoprotectants limit mechanical damage and rupture of the lipid bilayer, caused by ice crystals, during the freeze-drying and the rehydration process by maintaining the membrane in a flexible state (Allison S.D. and Anchordoquy T.J., 2000).

2.2.2.2 Liposomes

The basic steps of loaded liposome production include (1) lipid hydration, (2) regulation of liposome size, and (3) removal of non-encapsulated drug (Samad A. et al., 2007).

Lipid hydration can be achieved through mechanical methods, organic solvent methods, or detergent removal

methods (Bochicchio S. et al., 2014; Youngren S. et al., 2013). Mechanical methods for lipid hydration are based on using a rotating evaporator to form a thin-layer of phospholipids onto the wall of the rotating vessel. The layer is hydrated with an aqueous buffer solution that contains the siRNA to load while the vessel rotates. The process forms multilamellar vesicles, which can further be sonicated, extruded, or homogenized to form small unilamellar vesicles. Glass beads may be used to optimize the process by allowing the creation of thinner lipid films by increasing surface area. These thinner lipid films allows for higher hydration efficiency and siRNA entrapment. Lipid hydration by organic solvent methods requires the melting of lipids within an organic solvent followed by exposure to an aqueous phase that is then separated by evaporation. If the starting point is an organic solvent immiscible with the aqueous phase, then it is possible to use the reverse-phase evaporation vesicles technique, where the intermediate state is represented by emulsions. The lipid solution in an organic solvent with the aqueous buffer is sonicated to obtain a water-in-oil (W/O) emulsion. Controlled evaporation of the organic solvent leads to the formation of unilamellar vesicles. When most of the organic solvent is removed, a gel is formed, and it has to be agitated to transform into a viscous fluid that contains liposomes. The gel collapse coincides with the conversion of the W/O emulsion in the liposome form. If the starting point is an organic solvent miscible with water, then it is possible to continue with a precipitation stage. An aqueous buffer is added to the miscible organic solvent to dilute it, leading to the precipitation of lipids which then aggregate to form liposomes. The speed of the dilution passage can be adjusted to obtain desirable liposomal particle size, with faster dilution passages being associated with smaller particle size of formed vesicles.

Detergent removal methods for lipid hydration form micellar structures that engulf more lipids as the detergent is removed to form unilamellar vesicles. This method is less efficient for low molecular weight compounds than other lipid hydration methods (Tarkunde S.V. et al., 2014). Since this method has not been studied for large hydrophilic compounds like siRNA molecules, it is assumed that liposomal formulation of siRNA using this method is not suitable (Bochicchio S. et al., 2014).

Size optimization and removal of free siRNA should be performed following the lipid hydration step. Size of liposomes should be adjusted based on the siRNA that needs to be incorporated. This may be achieved through (1) extrusion at low or medium pressure through dimensionally defined pores, (2) fractionation of a heterogeneous population by centrifugation or size-exclusion chromatography, and (3) homogenization to obtain smaller sized liposomes (Bochicchio S. et al., 2014). Examples of extrusion devices are the Avanti Mini-Extruder and Nano

DeBEE high pressure homogenizer shown in **Fig. 4**. Other mechanical dispersion methods include sonication, freeze-thawed liposomes, lipid-film hydration by shaking or freeze drying, or dried reconstituted vesicles (Çağdaş M. et al., 2014). The non-encapsulated siRNA can be removed by dialysis, ultrafiltration via ultracentrifugation, gel chromatography, and ionic-exchange resins (Bochicchio S. et al., 2014).

Methods of encapsulating siRNA in liposomes include simple mixes of siRNA with pre-assembled liposomes, pre-condensation of siRNAs before liposome encapsulation, direct hydration of a lipid thin-film layer with a siRNA solution, and the ethanol dilution method (Bochicchio S. et al., 2014). A pre-assembled liposome can be complexed with siRNA with a simple mixture method. This method is not suitable for PEGylated liposomes, since siRNA is unable to penetrate the PEGylated lipid bilayer efficiently (Gutbier B. et al., 2010). In this case, the siRNA would bind to the liposomal surface, which causes premature release of the siRNA from the liposome *in vivo*. To achieve a siRNA PEGylated liposome loaded using the simple mixture method, the siRNA and the non-PEGylated liposomes can be incubated to form the siRNA liposome complex and subsequent incubation with PEG-lipids at elevated temperatures. The PEG-lipids would be inserted within the lipid bilayer, which can be verified by measuring zeta potential (Whitehead K.A. et al., 2009b). An alternative is to covalently bind PEG chains to the siRNA liposome complexes after simple mixture loading of the siRNA. An example of this surface modification is the binding of PEG to the amine functional groups of the cationic cholesterol polyamine (CDAN) component of a liposomes using a pH-sensitive oxime linkage that decomposes at pH < 5.5 (Carmona S. et al., 2009). This technique, known as the “ABCD paradigm”, overcomes drawbacks of other PEGylation methods, in that there is adequate siRNA encapsulation, PEGylation elicits a stealth behavior, and the PEG chain release of the liposomes within the endosomal compartments leads to a pH triggered endosomal escape (Kostarelos K. and Miller A.D., 2005).

Another technique involves pre-condensation of siRNA with protamine, a natural cationic polypeptide, along with high molecular weight polyanions, such as hyaluronic acid, at a ratio allowing for negatively charged nanoparticles (Li S.D. and Huang L., 2009). The high molecular weight polyanion is used to provide resistance to reticulo-endothelial clearance instead of PEG (Kim S.S. et al., 2010). These complexes are then incubated with cationic liposomes to form the siRNA encapsulated liposomes. Alternatively, siRNAs can be pre-condensed with calcium phosphate nanoparticles followed by the cationic liposomal coating and PEG-lipids (Li J. et al., 2010).

The direct hydration of a thin-film lipid layer with

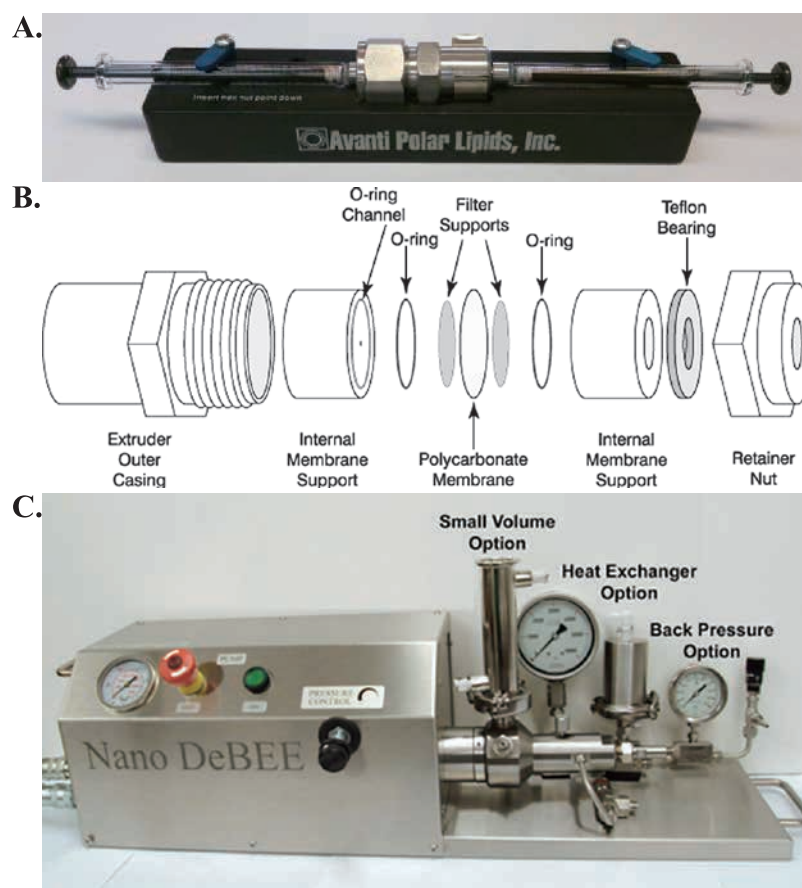


Fig. 4 Avanti Mini-Extruder (A), Avanti Mini-Extruder internal schematic (B), and Nano DeBEE high-pressure homogenizer (C).

siRNA solution allows for encapsulation of siRNA within the aqueous core of a liposome. Addition of a concentrated solution of siRNA to a dry thin lipid film layer allows for the incorporation of the siRNAs into the internal cationic space of a lipidic bilayer (Buyens K. et al., 2009). Since siRNA is present during the formation of the liposomes, approximately 50 % of the siRNA is encapsulated as it is uniformly distributed across cationic lipids, including the internal and external lipid bilayers. An alternative approach involves the formation of a monophasic solution of siRNAs and DOTAP in water/methanol/chloroform mixture that leads to a perfect complex between the negative charge of siRNA and the positive charge of the cationic lipids (Podesta J.E. and Kostarelos K., 2009). Once excess water and chloroform are added, a phase separation occurs. siRNA/DOTAP micelles stay in the organic phase and the aqueous/methanol phase can be discarded. The neutral PEGylated lipids are added along with water and then the organic solvent can be removed by evaporation. The liposomes can then be extruded for further size control (Bochicchio S. et al., 2014).

The ethanol dilution method for directly hydrating the lipid layer is an alternative method of direct hydration. Cationic PEGylated liposomes are mixed with siRNA in

the presence of a critical concentration of ethanol (approximately 40 %) in the aqueous buffer (Semple S.C. et al., 2001). At this ethanol concentration, liposomes are destabilized and their membrane structural integrity is compromised, allowing siRNA to uniformly penetrate the liposomes and associate with the positive charges on the lipids. Ethanol concentration is pivotal since if it is at an inadequate level, the siRNAs would not be able to efficiently penetrate the lipid bilayer. If the ethanol concentration is too high, liposomal aggregation would occur. The ethanol is removed by dialysis or tangential filtration following siRNA loading, forming the PEGylated cationic liposomes containing approximately 50 % of the originally added siRNA. Stabilized Nucleic Acid Lipid Particles, or SNALPs, is a widely recognized example of liposomal complexes prepared using the ethanol dilution method (Morrissey D.V. et al., 2005). A cationic lipid is protonated at low pH of 4–5 within the ethanol of the complex formation buffer, but is neutral when the acidic buffer is exchanged with a physiological buffer at pH 7.4. The advantages of cationic lipids are that siRNAs bound to the external surface of the liposome are detached when neutralized. The released siRNAs can be washed away from the complexes, together with ethanol, during the

buffer exchange procedure. The final complexes can have a final siRNA complexation and encapsulation efficiency of around 90 %. Other complexes of siRNA/PEGylated liposomes are prepared similarly to SNALPs only that they contain other cationic lipids and termed as Lipidoid Nanoparticles (Akinc A. et al., 2008; Love K.T. et al., 2010). This process is carried out with a combination of siRNAs in aqueous buffer with an equal volume of lipids (cationic, neutral, and PEGylated lipids), dissolved in butanol, the mixture is lyophilized and the lyophilized matrix is rehydrated (Akinc A. et al., 2008; Wu S.Y. and Mcmillan N.A., 2009).

2.2.2.3 Solid lipid nanoparticles and nanostructured lipid carriers

SLN formulations are composed of solid lipids, emulsifiers, and water (Mehnert W. and Maeder K., 2012). A schematic of SLN preparation detailing the types of components and feed solutions used is shown in **Fig. 5**. NLC formulations are composed of solid lipids, oil, surfactant, and water (Mehnert W. and Maeder K., 2012). Lipids are used in a broad sense to include triglycerides, partial glycerides, fatty acids, steroids, and waxes. All classes of emulsifiers have been used to stabilize the lipid dispersion. Particle agglomeration may be efficiently prevented through the combination of emulsifiers selected in respect to charge and molecular weight. The use of physiologic lipids within the lipid matrix decreases the possibility of acute or chronic toxicity. The choice of emulsifier heavily depends on the administration route.

Initially, high shear homogenization and ultrasound are dispersing techniques used for the production of solid lipid nanodispersions. Despite both methods being common due to their ease of use, dispersion quality is poor due to

the presence of microparticles and metal contamination.

High pressure homogenization is a reliable and powerful technique for the preparation of SLN. High pressure homogenization has been used for the production of nanoemulsions for parenteral nutrition; therefore these homogenizers are available from several manufacturers with varying sizes. The scalability of this technique is highly efficient. High pressure homogenizers force liquid with 100–2000 bar pressure through a narrow orifice with size of approximately a few micrometers. Due to the narrowed orifice, the fluid accelerates on a very short distance to a high velocity of over 1000 km/h. High shear stress and cavitation forces disrupt the particles down to the nanoparticle size range. Typically, the lipid contents are between 5–10 % and even higher lipid concentrations up to 40 % have been successfully homogenized to lipid nanodispersions. A preparation step that incorporates drug into the bulk lipid by dissolving or dispersing the drug in the lipid melt followed by hot or cold homogenization techniques are used to prepare SLN.

Hot homogenization, or the homogenization of an emulsion, is performed at temperatures above the melting point of the lipid. The pre-emulsion of siRNA loaded lipid melt and the aqueous emulsifier phase is obtained using a high shear mixing device, such as an Ultra-Turrax homogenizer. The quality of the pre-emulsion affects the quality of the final product to a high degree since it is desirable to obtain droplets within the size range of a few micrometers. The higher temperature leads to a lower particle size because of the decreased viscosity of the inner phase. However, high temperatures may increase the degradation of the siRNA or the SLN. The homogenization step may be repeated several times to achieve the desired particle size, keeping in mind that the high pressure homogenization equipment increases the temperature of the sample approximately 10 °C for 500 bar. Increasing the homogenization pressure and number of cycles over the recommended 500–1500 bar 3–5 cycles, respectively causes a particle size increase of the lipid nanocarriers due to particle coalescence as a result of high kinetic energy of the particles. The primary product of hot homogenization is a nanoemulsion due to the liquid state of the lipid. Cooling the nanoemulsion sample to a lower temperature forms the solid particles. Lipid crystallization is slowed due to the small particle size and the incorporation of emulsifiers, therefore the sample may remain as a supercooled melt for several months.

Cold homogenization is a high pressure milling of a suspension of solid lipids. Effective temperature control and regulation is needed in order to ensure the unmolten state of the lipid due to the increase in temperature during homogenization. Cold homogenization has been developed to overcome temperature induced drug degradation, drug distribution into the aqueous phase during homoge-

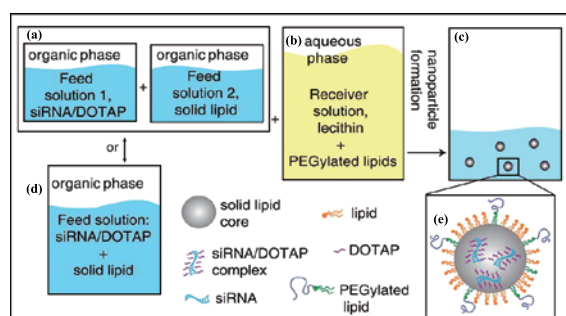


Fig. 5 Schematic of SLN preparation with encapsulated siRNA. Feed solutions 1 and 2 pictured in (a) are sequentially added to the receiver solution pictured in (b). SLNs form following evaporation of organic solvents, as shown in (c). Alternatively, siRNA/DOTAP complex and tristearin are solubilized in CHF, as shown in (d), and then added to the aqueous receiver solution. A schematic drawing of SLN is presented in (e). Reprinted with permission from Ref. (Lobovkina T. et al., 2011). Copyright (2011) American Chemical Society.

nization, and the complexity of the crystallization step of the nanoemulsion leading to several modification or supercooled melts associated with hot pressure homogenization. The first preparatory step that includes the dispersing of the drug in the melt of bulk lipid is followed by a rapid cooling step within liquid nitrogen or dry ice. In this step, the high rate of cooling causes the formation of a homogenous distribution of the drug within the lipid matrix. The solid, siRNA containing lipid is then milled to microparticles. Ball or mortar milling typically results in particle sizes of 50–100 micrometers. Low temperatures increase the fragility of the lipid and causes particle comminution, or the reduction in particle size. The solid lipid microparticles are dispersed in a chilled emulsifier solution. Then the pre-suspension is subjected to high pressure homogenization at or below room temperature. Compared to hot homogenization, generally larger particle sizes and broader size distribution are obtained in cold homogenized samples. The method of cold homogenization minimizes the thermal exposure of the sample, but it does not fully avoid it due to the melting of the lipid/siRNA mixture during the initial step.

SLN can be prepared by solvent emulsification or evaporation techniques by precipitation in o/w emulsions. Lipophilic material is dissolved in a water-immiscible organic solvent that is emulsified within an aqueous phase. Once the solvent evaporates, precipitation of the lipid in the aqueous phase forms a nanoparticle dispersion.

SLN can be prepared by the dilution of microemulsions. Since there are varying opinions on the structure and dynamics of a microemulsion, a detailed review on the subject has been published (Moulik S. and Paul B., 1998). A microemulsion can be envisioned as a two-phase system composed of an inner and outer phase, such as o/w microemulsions. They are prepared by stirring an optically clear mixture at 65–70 °C composed of a low melting fatty acid, an emulsifier, co-emulsifiers, and water. The hot microemulsion is dispersed in cold water (2–3 °C) under stirring. Typical volume ratios of the hot microemulsion to cold water are between 1:25 to 1:50. The dilution process is determined by the composition of the microemulsion. The droplet structure is already contained in the microemulsion, therefore no energy is required to achieve nanoparticle sized particles. The temperature gradient, pH, and the composition of the micro emulsion determine the product quality. High-temperature gradients facilitate rapid lipid crystallization and prevent aggregation. The dilution step constrains the lipid to a considerably lower concentration level than high pressure homogenization based formulations.

Lyophilization increases the chemical and physical stability of SLN over an extended period of time. Transformation of the SLN into a solid form prevents crystal growth by Ostwald ripening and avoids hydrolysis reac-

tions. Lyophilization is also possible for SLN formation of dry powders for inhalation or for reconstitution for nebulizer delivery. The solid state of the lyophilized SLN will have increased chemical and physical stability compared to the aqueous lipid dispersion. Two additional transformations between the formulations are necessary and may cause stability problems. The first transformation from aqueous dispersion to powder involves the freezing of the sample and the evaporation of water under vacuum. Freezing of the sample may cause stability problems due to the freezing out effect which results in changes in the osmolarity and the pH. The second transformation, resolubilization, involves low water and high particle content and high osmotic pressure that could facilitate particle aggregation.

The lipid content of the SLN dispersion should not exceed 5 % to prevent an increase in particle size because direct content of lipid particles is decreased in more diluted samples. The protective effect of the surfactant can be compromised during lyophilization. Diluted SLN dispersions will also have higher sublimation velocities and a higher specific area. The addition of cryoprotectants will be necessary to decrease SLN aggregation and to obtain a better redispersion of the dry product. Typical cryoprotective agents are sorbitol, lactose, mannose, trehalose, glucose, and polyvinylpyrrolidone. They decrease the osmotic activity of water and crystallization and favor a glassy state of the frozen sample. Cryoprotectants are place holders that prevent contact between discrete lipid nanoparticles and they interact with polar head groups of the surfactants and serve as a pseudo hydration shell.

As an alternative to lyophilization, spray drying can be used to transform an aqueous SLN dispersion into a dry product (Chougule M. et al., 2007, 2008; Patel G. et al., 2009). Spray drying can cause particle aggregation due to high temperatures, shear forces, and partial melting of the particles, therefore it is recommended to use lipids with melting points > 70 °C. The incorporation of carbohydrates and low lipid content improve the preservation of the colloidal particle size during spray drying. The melting of the lipid can be minimized by using ethanol-water mixtures as a dispersion medium instead of pure water due to the lower inlet temperatures.

2.2.3 Examples of lipid-based delivery systems

Functional genomic studies to study novel targets for lung cancer or other diseases have commonly utilized commercially available cationic lipid transfection reagents, including Lipofectamine RNAiMAX (Ramachandran S. et al., 2013), Lipofectamine2000 (Cao W. et al., 2012; Chen G. et al., 2012; Fourtounis J. et al., 2012; Huang B. et al., 2013; Liu Y. et al., 2013; Matsubara H. et al., 2012; Nishimura Y. et al., 2014; Rahman M.A. et al., 2013; Wang Y. et al., 2013; Zhang Y.-P. et al., 2012) and HiPerfect (Fourtounis J. et al., 2012). Other groups have made

lipoplexes composed of phospholipids and cholesterol with particle size of approximately 100 nm that have shown higher cellular internalization in lung cancer cells than with Lipofectamine2000, but had higher cytotoxicity. Oxime ether lipid nanoparticles with particle size of 150–220 nm transfected cells more efficiently with serum present than conventional liposomal formulations (Biswas S. et al., 2011).

A myeloid cell leukemia 1 (Mcl1)-specific siRNA administered in a lung metastases model at 0.21 mg/kg was delivered by a microsyringe intratracheally four times on alternating days starting at 5 days post intravenous (i.v.) injection of either B16 or Lewis Lung Carcinoma cells (Shim G. et al., 2013). In this study cationic nanoliposomes with particle size of 200 nm were prepared using the thin-film hydration technique and were composed of the various lipid ratio of EDOPC, DOTAP, DOTMA, DC-Cholesterol, DOPE, and Cholesterol (Shim G. et al., 2013). The thin-films were hydrated with 1 ml of 20 mmol/l HEPES (pH 7.4), and the resulting nanoliposomes were extruded through 0.2 μ m polycarbonate membrane filters three times using an extruder (Shim G. et al., 2013).

An intranasally delivered liposome formulation containing a novel siRNA sequence against the epithelial sodium channel (ENaC) α subunit was developed and evaluated by Clark et al. (Clark K.L. et al., 2013). Liposomes administered intranasally caused significant ENaC downregulation without TLR3, 8, or 9 activation, thereby supporting that the effects were induced by RNAi (Clark K.L. et al., 2013).

An aerosolized liposomal formulation was developed by Mainelis et al., who prepared liposomes composed of egg phosphatidylcholine: 1,2-dipalmitoyl-sn-glycero-3-phosphatidylcholine:cholesterol containing doxorubicin and antisense oligonucleotides or siRNA targeted against multidrug resistance-associated protein 1 (MRP1). This group used these formulations to evaluate the delivery of a nose-only small animal exposure chamber (Mainelis G. et al., 2013). Mainelis et al. characterized the aerosolized particles and found that the change of mean particle size was insignificant during the 1 hour of continuous aerosolization. It was shown that, of the nebulized formulation, 1.4 % at each port was available for inhalation and the lung retention was higher than in the injected samples (Mainelis G. et al., 2013). The lung tumor model was prepared by intratracheal administration of luciferase expressing A549-luc cells followed by detection of tumor growth by luminescence imaging. After inhalation treatment with antisense oligonucleotides and doxorubicin combination, the tumor volumes were 90 % reduced, compared to 40 % after doxorubicin i.v. injection (Mainelis G. et al., 2013).

2.3 Polymer-based delivery systems

2.3.1 Introduction

Polymers for use in nanoparticle drug delivery systems should be biocompatible in terms of non-toxicity, non-antigenicity, biodegradability, and biocompatibility. The natural polymers that have commonly been used for preparation of polymeric nanoparticles are albumin, chitosan, dextran, gelatin, lectins, and sodium alginate (Tekade R.K. and Chougule M.B., 2013; Tekade R.K. et al., 2014; Youngren S.R. et al., 2013). There are many synthetic polymers available, while some are still under development. The well-known synthetic polymers include Poly (ε-caprolactone) (PECL), polylactide (PLA), polystyrene, polyglycolide (PGA), Poly(lactide co- glycosides (PLGA), polyanhydrides, polyorthoesters, polycyanoacrylates, polycaprolactone, polyglutamic acid, polymaleic acid, poly(N-vinyl pyrrolidone), poly(methyl methacrylate), poly(vinyl alcohol), poly(acrylic acid), polyacrylamide, polyethylene glycol, and polymethacrylic acid. Polymeric nanoparticles include nanocapsules, which contain a reservoir core surrounded by a solid material shell, or nanospheres, which are solid matrix particles (Vauthier C. and Bouchemal K., 2009). Polymeric siRNA carriers are capable of swelling due to hydration and release siRNA by diffusion. Another physicochemical mechanism of release is by enzymatic degradation of the polymer at the delivery site, thus releasing the siRNA from the core. The siRNA may also dissociate causing de-adsorption or release. An advantage of the use of polymers as a siRNA delivery systems is the possibility of chemical modifications, which include the synthesis of block polymers and comb polymers or attachment of targeting moieties (Glasgow M.D. and Chougule M.B., 2015). Disadvantages of polymer delivery systems stem from the use of organic solvents in production processes that leave residues, polymer cytotoxicity, and obstruct scalability of the production process. Another disadvantage of peptide based polymer inhaled delivery systems is their ability to increase the elastic and viscous moduli of lung fluid and mucus, decreasing mucociliary clearance, which can complicate many diseases states (Innes A.L. et al., 2009; List S.J. et al., 1978; Marriott C. et al., 1982).

2.3.2 Preparation methods

The preparation methods of polymeric nanoparticles from a polymeric dispersion include emulsification/ solvent diffusion, solvent evaporation, nanoprecipitation, salting out, dialysis, and supercritical fluid (SCF) technology methods. The preparation methods of polymeric nanoparticles from polymerization of monomers are emulsion (including mini- and micro-), interfacial polymerization, and controlled/living radical polymerization (C/ LRP). Ionic gelation and coacervation are methods for

polymeric nanoparticle preparation from hydrophilic polymers.

2.3.2.1. Emulsion and diffusion techniques

Emulsions are typically formed by two immiscible phases and a surface active agent and some form of dispersive force. Polymer precipitation from emulsion droplets can be achieved by removing the polymer solvent through solvent evaporation, fast diffusion after dilution, or salting out (Vauthier C. and Bouchemal K., 2009). These methods lead to formation of nanospheres when performed on simple oil-in-water emulsions. Oil containing nanocapsules can be obtained by adding oil in the polymer solution composing the emulsion droplets.

Emulsification and solvent diffusion is a modified version of the solvent evaporation method (Niwa T. et al., 1994). The encapsulating polymer is dissolved in a partially water soluble solvent such as propylene carbonate and saturated with water to ensure the initial thermodynamic equilibrium of both liquids. In order to produce the precipitation of the polymer and the consequent formation of nanoparticles, it is necessary to promote the diffusion of the solvent of the dispersed phase by dilution with an excess of water when the organic solvent is partly miscible with water or with another organic solvent in the opposite case. The polymer-water saturated solvent phase is emulsified in an aqueous solution containing stabilizer, leading to solvent diffusion to the external phase. Resultant nanospheres or nanocapsules will be formed dependent on the oil-to-polymer ratio. The solvent is removed by evaporation or filtration.

This technique allows for high encapsulation efficiencies (> 70 %), high batch-to-batch reproducibility, eliminates the need for homogenization, ease of scale-up, and narrow size distribution. A disadvantage of this method is that it requires high volumes of water that has to be removed from the suspension and the leakage of water-soluble entrapped therapeutic agent drugs into the external saturated-aqueous phase during emulsification causes a reduction in entrapment efficiency (Reis C.P. et al., 2006). This method has moderate efficiency in the entrapping hydrophilic molecules, therefore it may have limited applications for siRNA delivery systems.

Emulsion polymerization can be used to prepare nanoparticles by monomer polymerization. It is a fast and easily scalable nanoparticle preparation method. The continuous organic phase methodology involves the monomer dispersion into an emulsion, inverse microemulsion, or into a non-solvent of the monomer (Nagavarma B. et al., 2012; Reis C.P. et al., 2006). Surfactants or protective soluble polymers were used in the initial stages of polymerization to prevent aggregation. Since this method utilizes toxic organic solvents, surfactants, monomers, and initiators that can be leached from the formed nanoparticles,

this method has been used sparingly in recent years (Nagavarma B. et al., 2012).

An alternate approach was developed because of the conventional method disadvantages of having non-biodegradable polymer and difficult procedure. Poly(methylmethacrylate) (PMMA), poly (ethylcyanoacrylate) (PECA), and poly (butylcyanoacrylate) nanoparticles were produced by a surfactant dispersion within an organic phase consisting of cyclohexane, n-pentane, and toluene (Nagavarma B. et al., 2012). The monomer is dissolved in the aqueous continuous phase and surfactants or emulsifiers are not required. Initiation occurs when collision happens between the monomer molecules and the initiator molecule, which could be an ion or a free radical, within the continuous phase (Nagavarma B. et al., 2012). Alternatively, the monomer molecule itself can be converted into an initiating radical by high-energy radiation, such as γ -radiation, ultraviolet, or strong visible light. Polymer chains form, according to a mechanisms of anionic polymerization, when collision occurs between the initiated monomer ions or monomer radicals and other monomer molecules. Solid particle formation and phase separation may occur before or after the polymerization reactions (Kreuter J., 1982; Vauthier C. et al., 2003).

The mini-emulsion polymerization method has been developed using a wide range of polymer materials (Arias J. et al., 2001; Ham H.T. et al., 2006; Ziegler A. et al., 2009). A typical mini-emulsion polymerization formulation contains water, monomer mixture, co-stabilizer, surfactant, and initiator. The key difference between emulsion polymerization and mini-emulsion polymerization is the use of a low molecular mass compound as the co-stabilizer and also the use of a high-shear device. Mini-emulsions are critically stabilized, require a high-shear to reach a steady state, and have an interfacial tension much greater than zero (Rao J.P. and Geckeler K.E., 2011).

Micro-emulsion polymerization is used to prepare nanosized polymeric particles that involves a kinetically different process than other emulsion methods (Mishra S. and Chatterjee A., 2011). Although these processes both produce high molar mass colloidal polymeric particles, the particle size achievable for micro-emulsion based techniques is much smaller than for other emulsion based techniques. For micro-emulsion polymerization, typically a water soluble initiator, is placed into the aqueous phase of a thermodynamically stable micro-emulsion containing swollen micelles (Nagavarma B. et al., 2012). These spontaneously formed thermodynamically stable micelles are where polymerization commences. This process relies on large quantities of surfactant systems, which have an interfacial tension at the oil/water interface close to zero. The particles formed are completely coated with surfactant because of this high concentration of surfactant.

Polymer chains are first formed only in some droplets, as the initiation cannot be attained in all droplets simultaneously. Then, the osmotic and elastic influence of the chains destabilize the fragile micro-emulsions and typically lead to an increase in the particle size, the formation of empty micelles, and secondary nucleation. Very small lattices of particle size of 5–50 nm are formed with the presence of empty micelles. Critical factors of the kinetics of micro-emulsion polymerization and the resultant polymeric nanoparticle properties are the concentration of initiator, surfactant, monomer, and reaction temperature (Fessi H. et al., 1989; Nagavarma B. et al., 2012).

2.3.2.2 Solvent evaporation

The first step of the solvent evaporation technique involves the preparation of a polymer solution prepared in volatile solvents and emulsions. Ethyl acetate is the solvent of choice because it has a better toxicological profile when compared to the other widely used solvents, dichloromethane and chloroform (Rao J.P. and Geckeler K.E., 2011). The primary emulsion is transformed into a colloidal nanoparticle suspension following the evaporation of the solvent from the polymer, which is facilitated through the diffusion of the emulsion's continuous phase (Nagavarma B. et al., 2012). The conventional methods involve the formation of primary single emulsions, such as oil-in-water (o/w) or the formation of double-emulsions, such as (water-in-oil)-in-water (w/o)/w. Nanocarriers formed through this method utilize high-speed homogenization or ultra-sonication with subsequent solvent evaporation through continuous magnetic stirring or under vacuum. The resultant semi-solid particles may undergo ultracentrifugation and be washed with distilled water to collect and purify the nanocarriers. The resultant nanocarriers may then be freeze-dried with a suitable cryoprotectant and stabilizing agent. Particle sizes of these nanocarriers are dependent on the type and concentration of stabilizer, homogenizer speed, and polymer concentration. Reduction of particle size can be achieved through high-speed homogenization and ultra-sonication.

2.3.2.3 Nanoprecipitation

Nanoprecipitation, or the solvent displacement method, involves the precipitation of preformed polymer from an organic solution and the diffusion of the organic solvent in the aqueous medium with or without a surfactant (Barichello J.M. et al., 1999; Fessi H. et al., 1989; Galindo-Rodriguez S. et al., 2004; Ganachaud F. and Katz J.L., 2005). The polymer is dissolved in a water miscible solvent of intermediate polarity, leading to the precipitation of spherical nanocarriers. This phase is injected into a stirred aqueous solution containing a stabilizer as a surfactant. Polymer deposition on the interface between the water and the organic solvent, caused by fast diffusion of

the solvent, leads to instant formation of stable nanocarriers in suspension (Quintanar-Guerrero D. et al., 1998). In order to facilitate the suspension formation, the first step is to perform phase separation with a completely miscible solvent that is also a non-solvent for the polymer (Vauthier C. et al., 2003). This nanoprecipitation technique allows the preparation of nanocapsules when a small volume of nontoxic oil is incorporated in the organic phase. Considering the oil-based central cavities of the nanocapsules, high loading efficiencies of hydrophobic drugs are often reported. This technique spontaneously produces emulsification because of the high diffusion rates in result of limiting water-miscible solvents (Nagavarma B. et al., 2012). Spontaneous emulsification is not observed if the coalescence rate of the formed droplets is sufficiently high due to certain instability when mixed in water of some water-miscible solvents. Acetone/dichloromethane is used to dissolve drugs and increase their entrapment. However, dichloromethane increases particle size and has toxicological issues. This method is appropriate for lipophilic drugs; therefore its usefulness for siRNA nanocarriers is limited by low entrapment efficiency.

2.3.2.4 Salting out

The salting out effect causes the separation of a water miscible solvent from an aqueous solvent (Reis C.P. et al., 2006). This procedure is considered a modified emulsification/solvent diffusion method. Drug and polymer are first dissolved in a solvent, like acetone, which is then emulsified with the salting-out agent into an aqueous gel. Salting-out agents include electrolytes, such as magnesium chloride or calcium chloride, or non-electrolytes, such as sucrose with a colloidal stabilizer such as polyvinylpyrrolidone or hydroxyethylcellulose (Nagavarma B. et al., 2012). Induction of nanoparticle formation occurs when the oil/water emulsion is diluted with enough water or aqueous solution to enhance the diffusion of acetone into the aqueous phase (Reis C.P. et al., 2006). Salting out agent selection is highly influential in the drug encapsulation efficiency (Nagavarma B. et al., 2012). Formed polymeric nanoparticles are purified by cross-flow filtration to remove the solvent and salting out agent (Nagavarma B. et al., 2012).

An advantage of the salting out method is that it minimizes stress to protein encapsulates (Jung T. et al., 2000; Lambert G. et al., 2001; Nagavarma B. et al., 2012). The salting out procedure is useful for heat sensitive substances since it does not require increased temperature. The multiple washing steps pose a disadvantage when considering entrapment efficiency. The greatest disadvantage of this method is that it is used exclusively for lipophilic drugs, therefore its application to siRNA is low.

2.3.2.5 Dialysis

Nanocarriers with small particle size and narrow particle size distribution can be prepared by dialysis (Fessi H. et al., 1989; Kostag M. et al., 2010; Rao J.P. and Geckeler K.E., 2011). Polymer dissolved in an organic solvent is placed within a dialysis tube with desired molecular weight cut off (Nagavarma B. et al., 2012). Dialysis is then performed against a non-solvent miscible with the former miscible solvent. The use of the dialysis membrane or semi-permeable membranes allow the passive transport of solvents to slow down the mixing of the polymer solution with a non-solvent (Nagavarma B. et al., 2012). The displacement of the solvent inside the membrane is followed by the progressive aggregation of the polymer due to a loss of solubility and the formation of homogeneous suspensions of nanoparticles. The mechanism of nanocarrier formation by dialysis method is based on a mechanism similar to that of nanoprecipitation. The solvent used in the preparation of the polymer solution affects the morphology and particle size distribution of the nanoparticles.

2.3.2.6 Supercritical fluid technology (SCF)

Supercritical fluid technology has allowed for the use of more environmentally friendly solvents for the preparation of polymeric nanocarriers with high purity (Kawashima Y., 2001; York P., 1999). Supercritical fluid and dense gas technology are expected to offer an effective technique of nanoparticle preparation because it avoids most of the drawbacks of traditional techniques, such as presence of organic solvent (Nagavarma B. et al., 2012).

The production of nanoparticles using supercritical fluids has two principles. The first is the rapid expansion of supercritical solution (RESS). The second principle is the rapid expansion of supercritical solution into liquid solvent (RESOLV). In traditional RESS, the solute is dissolved in a supercritical fluid, followed by the rapid expansion of the formed solution across a capillary nozzle or an orifice into ambient air. The resultant high degree of super saturation and rapid pressure reduction in the expansion results in homogenous nucleation and formation of dispersed particles (Nagavarma B. et al., 2012). Mechanistic studies of different model solutes for the RESS process indicate that within the expansion jet, both micrometer-sized and nanometer particles are present (Weber M. and Thies M.C., 2002). A few studies were carried out on the production of nanoparticles using RESS. Poly (perfluoropolyetherdiamide) droplets produced from the rapid expansion of CO₂ solutions. The RESS experimental apparatus consists of three major units: a high pressure stainless steel mixing cell, a syringe pump, and a pre-expansion unit. A solution of polymer in CO₂ is prepared at ambient temperature. The solution is heated isobarically to the pre-expansion temperature

while pumped through pre-expansion unit before the solution reaches the nozzle. At this point, the supercritical solution is now allowed to expand through the nozzle, at ambient pressure. The concentration and degree of saturation of the polymer have a considerable effect on the particle size and morphology of the particles for RESS (Blasig A. et al., 2002; Chernyak Y. et al., 2001; Lim K.T. et al., 2005; Sane A. and Thies M.C., 2007).

A RESS modification, known as RESOLV, involves the expansion of the supercritical solution into a liquid solvent instead of ambient air (Rao J.P. and Geckeler K.E., 2011; Sun Y.P. et al., 2005). The RESS technique results in microscaled sized particles rather than nanoparticles. In order to overcome this drawback, RESOLV was developed. In RESOLV, the liquid solvent suppresses the particle growth in the expansion jet, thus making it possible to obtain primarily nanosized particles (Meziani M.J. et al., 2004; Nagavarma B. et al., 2012; Sun Y.P. et al., 2005).

2.3.2.7 Interfacial polymerization

Interfacial polymerization is one of the most established methods for the preparation of polymeric nanoparticles (Gaudin F. and Sintez-Zydowicz N., 2008; Landfester K. et al., 2010). In interfacial polymerization, there is step-wise polymerization of two reactive monomers or agents, which are dissolved respectively in two phases (continuous and dispersed), and the reaction takes place at the interface of the two liquids (Karode S. et al., 1998). Hollow polymeric nanoparticles were synthesized with the use of interfacial cross-linking reactions as polyaddition, polycondensation, or radial polymerization (Crespy D. et al., 2007; Danicher L. et al., 2000; Sarkar D. et al., 2005; Scott C. et al., 2005). Polymerization of monomers at the oil/water interface of an oil-in-water micro-emulsion produce oil-containing nanocapsules (Fallouh N.a.K. et al., 1986). The organic solvent, which is completely miscible with water, served as a monomer vehicle and the interfacial polymerization of the monomer was believed to occur at the surface of the oil droplets that formed during emulsification (Aboubakar M. et al., 1999; Gallardo M. et al., 1993; Vauthier C. and Bouchemal K., 2009). The use of acetone or acetonitrile, which are aprotic solvents, was recommended for nanocapsule preparation (Nagavarma B. et al., 2012). Alternatively, protic solvents, such as ethanol, m-butanol and isopropanol, were found to also induce the formation of nanospheres (Nagavarma B. et al., 2012; Puglisi G. et al., 1995). Nanocapsules containing aqueous water can be formed by the interfacial polymerization of monomers in water-in-oil interface and precipitated out forming the nanocapsule shell (Gasco M. and Trotta M., 1986; Watnasirichaikul S. et al., 2000). Therefore, siRNA containing nanocapsules can be formed using the interfacial polymerization of monomers in water-in-oil microemulsions.

2.3.2.8 Controlled/living radical polymerization (C/LRP)

The primary restrictions of radical polymerization are due to unavoidable radical to radical termination reactions and cause a lack of control over the molar mass, the end functionalities, and the overall macromolecular structure (Nagavarma B. et al., 2012). The C/LRP processes are based on previous polymerization techniques and opens new prospects in polymeric nanoparticle preparation (Matyjaszewski K. and Xia J., 2001; Nagavarma B. et al., 2012; Zetterlund P.B. et al., 2008; Zetterlund P.B. et al., 2007). The growing public concern over environmental impacts and the growth of hydrophilic polymer applications in medicine have sparked interest in C/LRP process. These factors have given rise to green chemistry techniques and created a demand for environmentally and chemically benign solvents such as water and supercritical carbon dioxide (Nagavarma B. et al., 2012). Industrial radical polymerization in aqueous dispersed systems and specifically in emulsion polymerization is widely used. The primary goal was to control the characteristics of the polymer to modulate their function, molar mass, molar mass distribution, and structure. Implementation of C/LRP in aqueous dispersed systems, results in the formation of polymeric nanoparticles with precise particle size and size distribution control (Braunecker W.A. and Matyjaszewski K., 2007; Nagavarma B. et al., 2012). Among the available controlled/living radical polymerization methods successfully and extensively studied methods include nitroxide-mediated polymerization (NMP), atom transfer radical polymerization (ATRP), and reversible addition and fragmentation transfer chain polymerization (RAFT) (Dire C. et al., 2008; Min K. et al., 2009; Nicolas J. et al., 2007; Rieger J. et al., 2010; Siegwart D.J. et al., 2009; Zhou X. et al., 2007). The size of the resultant polymeric nanoparticles depends on the type of control agent, control agent concentration, monomer, initiator, and the emulsion type.

2.3.2.9 Hydrophilic polymer ionic gelation/coacervation

Polymeric nanoparticles are prepared by using biodegradable hydrophilic polymers such as chitosan or gelatin as shown in **Fig. 6**. In this method, the positive charged amino groups of the polymer interacts with the negatively charged triphosphate to form coacervates with a size in the nanometer range (Calvo P. et al., 1997a; Calvo P. et al., 1997b; Dustgania A. et al., 2008). Coacervates are formed as a result of electrostatic interaction between two aqueous phases, whereas ionic gelation involves the material undergoing transition from liquid to gel due to ionic interaction conditions at room temperature (Nagavarma B. et al., 2012).

2.3.3 Examples of polymer-based delivery systems

Chitosan is a generally regarded as safe (GRAS) excip-

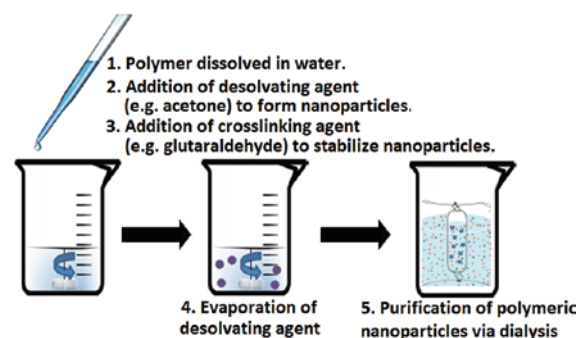


Fig. 6 Diagram showing the preparation of polymeric nanoparticles using the coacervation (desolution) technique.

ient and a natural polysaccharide (Keefe D., 2011; Mao S. et al., 2010). However, its applications in siRNA delivery systems have been hindered due to poor water solubility and low transfection efficiency (Merkel O.M. et al., 2014). An inhalable chitosan/siRNA dry powder composed of unmodified chitosan was prepared using the supercritical CO₂ technique followed by manual grinding in an investigation by Okuda et al. (Okuda T. et al., 2013). Water, ethanol and CO₂ solvents were combined in a compressed column (35 °C, 25 MPa). This supercritical CO₂ technique embodies tolerable conditions for the precipitation of powders capable of reconstitution without siRNA or nanoparticle degradation. The hydrodynamic particle sizes and zeta potentials of the developed chitosan particles were shown to be maintained throughout and after the powder formation process (Okuda T. et al., 2013). Bio-distribution of intratracheally administered Cy5.5 labeled siRNA formulations, including the nanoparticle suspension, the dry powder, and the free/naked siRNA were monitored. The efficiency of the delivered siRNA was measured in a lung metastases model of colon26/Luc cells by luciferase downregulation. The dry powder particles had highest knockdown efficiency, however they had higher lung clearance than the nanoparticle suspension (Okuda T. et al., 2013). This study is one of the few reports that describe the formulation of an inhalable dry powder containing siRNA.

Another dry powder formulation prepared using a double emulsion solvent evaporation method was designed by Jensen et al., where siRNA was entrapped within DOTAP-modified PLGA nanoparticles (Jensen D.K. et al., 2012; Jensen D.M. et al., 2010). The total concentration of DOTAP and PLGA in chloroform was kept constant and the optimal formulation contained 25 % (w/w) DOTAP by varying the weight/weight (w/w) percentage of DOTAP. The particles were spray dried with mannitol and an aerodynamic size of $3.69 \pm 0.18 \mu\text{m}$ obtained, which is within the optimal size range for deep lung deposition, and did not exhibit aggregation or coalescence

(Jensen D.K. et al., 2012; Jensen D.M. et al., 2010). During spray drying, the sugar alcohol remained in its crystalline state, as determined by X-ray powder diffraction analysis, and therefore functioned as a stabilizer. The hydrodynamic diameters and cellular uptake remained unchanged before and after freeze-drying according to statistical analysis, which supported the conclusion that spray-drying is a powerful technique for engineering siRNA nanoparticle dry powder formulations (Jensen D.K. et al., 2012).

PLGA poly[vinyl-3-(dialkylamino) alkylcarbamate-co-vinyl acetate-co-vinyl alcohol]-graft-poly(D,L-lactide-co-glycolide), (DEAPA-PVA-g-PLGA), that contained covalently modified positively charged side groups for siRNA complexation was prepared by Benfer et al. (Benfer M. and Kissel T., 2012). The H1299 NSCLC cellular uptake of DEAPA-PVA-g-PLGA/siRNA nanoparticles increased after addition of surfactant and was internalized mostly by clathrin-mediated endocytosis (Benfer M. and Kissel T., 2012). Merkel et al. also showed that DEAPA-PVA-g-PLGA/siRNA nanoparticles remain in the lung for extended periods of time when compared to gold-standard PEI-formulated or free siRNA. Thus, making the formulation applicable for intratracheal administration (Zheng M. et al., 2012). To prepare the inhalable dry DEAPA-PVA-g-PLGA/siRNA nanoparticle powder, the freeze-drying protocol was optimized. Cryoprotectants, such as dextrose, hydroxypropyl-beta-cyclodextrin, lactosucrose, polyvinylpyrrolidone (PVP), sucrose, and trehalose can be used to stabilize the nanoparticles. Although particles freeze-dried in the cryoprotectant 10 % glucose were about 150 nm in particle size after reconstitution, the particles freeze-dried in the cryoprotectant 10 % saccharose were much larger with a particle size of 250 nm. However, the freeze-dried larger particles showed more similar and efficient cellular uptake when compared to freshly prepared nanoparticles (Zheng M. et al., 2012). It was demonstrated that gene downregulation efficacy was preserved through the freeze-drying process as assessed after reconstitution of the nanoparticles (Zheng M. et al., 2012). These findings are similar to those of a study by Kasper et al. who showed that cryoprotectant concentrations of 12 % and higher can prevent PEI/DNA polyplex aggregation which retains their transfection efficiency after redispersion (Kasper J.C. et al., 2011).

Luo et al. synthesized salbutamol-modified guanidylated chitosan and subsequently formed polyplexes targeted to lung smooth muscle cells for potential applications in asthma or COPD (Luo Y. et al., 2012). The formulations were nebulized with an Aeroneb® Pro nebulizer (Aerogen, Galway, Ireland) and then the collected condensate was administered intratracheally with a PennCentury microsprayer to transgenic mice expressing enhanced green

fluorescent protein (EGFP) (Luo Y. et al., 2012). The animals were treated daily with 5 µg of siRNA 3 days, and *in vivo* knockdown was quantified by confocal laser scanning microscopy (CLSM) of tissue sections and by Western blot. The targeted formulation achieved a 40 % gene downregulation (Luo Y. et al., 2012).

Atelocollagen, a highly purified and pepsin-treated type I collagen obtained from calf dermis also raised interest for its use in pulmonary delivery of siRNA (Merkel O.M. et al., 2014). Protein and siRNA polyplexes were prepared by mixing during a 16h incubation and were administered intratracheally to Wistar or EGFP expressing rats (Liu S. et al., 2012). The therapeutic gene target was syntaxin4, which regulates the function of mucosal-type mast cells and is one of the soluble membrane N-ethylmaleimide-sensitive factor attachment protein receptor (SNARE) proteins. Following siRNA treatment, syntaxin4 knockdown significantly decreased granule contents release from rat mucosal mast cells. Rats were sensitized and challenged with ovalbumin (OVA) following the allergic mouse model protocols to elicit symptoms of asthma. The rats were then intratracheally instilled with atelocollagen siRNA complexes once a day for 5 days. These treatments decreased the rat mast cell protease-II (RMCP-II) levels in the bronchoalveolar lavage fluid (BALF) and prevented asthmatic airway constriction. Therefore, the authors concluded that syntaxin 4 knockdown prevents degranulation and stabilizes mucosal mast cells (Liu S. et al., 2012).

Spermine, a naturally occurring polymer consisting of small linear tetra-amines with two primary and two secondary amines, is popular for the delivery of nucleic acids (Merkel O.M. et al., 2014). Endogenous spermines play a key role in the compact packaging of cellular DNA, this property is exploited artificially in nucleic acid delivery (Eliyah H. et al., 2006; Jiang H.L. et al., 2011). Due to the short molecules and the resultant rigidity of spermine, unmodified spermine does not efficiently compact siRNA (Merkel O.M. et al., 2014; Pavan G.M. et al., 2010). Jiang et al. prepared glycerol propoxylate triacrylate-spermine (GPT-SPE) and shRNA polyplexes that had a particle size of 160 nm and had a zeta potential of +9 mV. Human NSCLC was mimicked using a KrasLA1 model and administered 8 mg of GPT-SPE and 0.8 mg of shRNA (scrambled or Akt1 shRNA) twice a week for 4 weeks as aerosol (Jiang H.L. et al., 2011). The authors did not discuss whether the preparation and delivery processes had an effect on the polyplex physico-chemical characteristics. In a later study, GPT-SPE delivered shRNA against the same target. The same nose-only exposure chamber was used but administered half of the previous dose (0.4 mg) DNA as an aerosol (scrambled or Akt1 shRNA) twice a week over a timeframe of 4 weeks (Hong S.-H. et al., 2012). Aerosol delivery of Akt1 shRNA suppressed lung tumor growth

and the authors elucidated the mechanism of action (Hong S.-H. et al., 2012). The same group conducted another later study, which used the GTE-SPE polymer for sodium-dependent phosphate co-transporter 2b (NPT2b) siRNA delivery via nose-only inhalation (Hong S.-H. et al., 2013). The animals were treated for four weeks with 0.5 mg of siRNA twice a week. Aerosolized NPT2b siRNA downregulated NPT2b expression levels as detected via Western blotting, densitometric analysis and qPCR, and significantly increased the pro-apoptotic protein levels. The activation of apoptosis was confirmed in TUNEL positive cells, and PCNA and VEGF levels were decreased after knockdown of Akt1 (Hong S.-H. et al., 2013).

Choi et al. synthesized a conjugate of dexamethasone and PEI (DEXA-PEI) polyplex to target the cellular nucleus via interaction with the glucocorticoid receptor (Choi M. et al., 2013). This concept was previously explored, but the novelty of this approach was induction of the model of acute lung inflammation by the instillation of baked SiO₂ nanoparticles (Choi M. et al., 2013; Mi Bae Y. et al., 2007). siRNA against macrophage migration inhibitory factor (MIF) was complexed with DEXA-PEI and particles obtained had a particle size of 355 nm, whereas PEI/siRNA complexes aggregated to a particle size of > 600 nm. These particles were administered intratracheally with either 2.5 µg or 10 µg siRNA per animal and were shown to decrease pulmonary inflammation and the MIF mRNA and Muc5ac expression after treatment with conjugated and nonconjugated PEI complexes 72 h post-administration of the polyplexes (Choi M. et al., 2013).

2.4 Peptide-based delivery vectors

2.4.1 Introduction

Protein transduction domains (PTDs) are short amino acid chains that interact with the plasma membrane that allows for cellular uptake that can be used for siRNA delivery. Obtaining controlled siRNA cellular delivery through the use of peptides as carriers can overcome siRNA delivery constraints, which include poor bioavailability and clinical efficacy. Chemical conjugation of cationic peptide cell penetrating peptides (CPP) to siRNA has facilitated enhanced siRNA tissue delivery and cellular internalization. The TAT protein from HIV-1 which was discovered to be responsible for the cellular uptake of the virus was of interest of drug delivery scientists. Since that time, a variety of CPPs have been developed to facilitate the cellular uptake transport of therapeutic molecules including siRNA (Lam J.K.-W. et al., 2012). Covalent peptide to siRNA disulfide bond formation attachment, or non-covalent electrostatic interactions between the siRNA and peptide to form complexes can be used to prepare

siRNA peptide conjugates (Lam J.K.-W. et al., 2012). Their mechanism of action is also expected to vary due to the sequence diversity of different CPPs. These peptides function to improve cellular delivery by efficient transport across the cellular membrane or promote endosomal escape (Endoh T. and Ohtsuki T., 2009). The activities of different CPPs have been reviewed elsewhere (Deshayes S. et al., 2005; Meade B.R. and Dowdy S.F., 2007).

2.4.2 Preparation methods

Double stranded siRNA, with or without modification, can form stable or cleavable peptide conjugates using a range of different conjugation chemistries (Jeong J.H. et al., 2008). Designing conjugation schemes include selection of linkage chemistry, spacer molecule, and orientation of the siRNA and peptide components (Zatsepin T. et al., 2005). There are two main strategies for synthesizing siRNA peptide conjugates: the total stepwise solid-phase synthesis and the solution-phase or solid-phase fragment coupling of peptides with oligonucleotides that have been prepared individually on solid supports (Corey D.R., 2004). Stable linkages may be prepared from either method, but fragment coupling of peptides is necessary for cleavable disulfide linkages.

The most common conjugation chemistries have involved fragment coupling in aqueous solution. Peptide and siRNA fragments are prepared on their own solid supports by conventional automated solid-phase synthesis procedures. Each fragment requires a masked functional group to be incorporated during the assembly, which can be released chemoselectively during a simple deprotonation step. A specific chemical reaction is then initiated in aqueous medium between the functional group on the oligonucleotide and that on the peptide to produce the desired conjugate. An advantage of the fragment-coupling method is that both components can be purified, for example by HPLC, before conjugation so that the conjugation product can be easily identifiable. This method's disadvantage is that the aqueous conditions of conjugation sometimes need to be modified to maintain the solubility of both components and the conjugate product. A reaction of a cysteine-substituted siRNA with a thioester-substituted peptide produces a stable amide linkage through the mechanism of native ligation. Another method involves the reaction of an aldehyde-containing siRNA with a cysteine-containing peptide, forming a thiazolidine linkage, or with an aminooxy peptide forming an oxime linkage, or with a hydrazinopeptide forming a hydrazine. An aldehyde oligonucleotide is unstable and must be generated by periodate treatment of a cis-diol substituted siRNA just before conjugation (Hermanson G.T., 2013).

The most straightforward method of fragment conjugation involves the synthesis of the siRNA component with an alkyl thiol linker on either of the 5' or 3'-end

forming a 3'-thiopropyl or a 5'-thiohexyl linker (Turner J.J. et al., 2006). Following activation with pyridylsulfide, the siRNA can be coupled to a peptide. These thiol-functionalized siRNA can be reacted with a cysteine-containing peptide to form a cleavable disulfide linkage or with a bromoacetyl-substituted peptide to form a stable thioether linkage. A maleimide derivative of the peptide can also be prepared for the reaction with a thiol-substituted siRNA via a Michael-type addition reaction (Hermanson G.T., 2013).

2.4.3 Examples of Peptide-based Deliver Vectors

The PTDs and cell penetrating peptides are small (10–30 amino acid), positively charged molecules that usually contain arginine and lysine. Arginine and lysine amino acids provide primary and secondary amine functional groups in their side chains that can be protonated for electrostatic interaction with siRNA and cellular membranes to enhance the cellular permeability (Merkel O.M. et al., 2014). Delivery of siRNA using a short peptide conducted by Oh et al. who used R3V6 peptides, which were composed of 3 arginines and 6 valines (Merkel O.M. et al., 2014; Oh B. and Lee M., 2014). Ternary complexes were formed with sphingosine-1-phosphate lyase (SIPLyase), a recombinant high mobility group box-1 box A peptide (HMGB1A), siRNA, and R3V6 (siSIPLyase/HMGB1A/R3V6). Premixture of siRNA and HMGB1A avoided aggregation and formed particles with sizes below 200 nm that elicited an anti-inflammatory effect (Oh B. and Lee M., 2014). These ternary complexes were tested *in vitro* and delivered siRNA into non-phagocytosing LA-4 lung epithelial cells more efficiently than PEI and Lipofectamine, inferring that their uptake mechanisms were not based on phagocytosis (Merkel O.M. et al., 2014; Oh B. and Lee M., 2014). Intratracheal administration of the ternary complexes reduced the SIPLyase level efficiently in an LPS-induced BALB/c ALI model. The cell penetrating peptides, TAT and double TAT (dTAT) was used for siRNA delivery by Baoum et al. (Baoum A. et al., 2012). To form the complexes, siRNA was mixed with the poly-cations and then CaCl_2 was added to the mixture in order to compact the siRNA and to decrease the hydrodynamic diameters of the particles (Baoum A. et al., 2012). Following i.v. injection of the complexes, high gene knockdown was observed in the lung (Baoum A. et al., 2012). These results suggest that formulating these siRNA complexes for pulmonary delivery by inhalation, would allow for high local concentration while keeping high accumulation in the lungs.

2.5 Inorganic-based delivery systems

2.5.1 Introduction

Various promising inorganic delivery systems have

been investigated for the delivery of siRNA devised for diagnostic and therapeutic purposes. They include carbon nanotubes and metals such as iron oxide, quantum dots, gold and silica (Chen S. et al., 2014). Mesoporous silica based nanoparticles (MSN) have been widely investigated as carriers for siRNA based targeted drug delivery systems (Chen A.M. et al., 2009; Radu D.R. et al., 2004). The MSN are chemically stable, safe and biodegradable which makes it a promising gene delivery carrier. (Borm P. et al., 2006; Finnie K.S. et al., 2008). MSN also possess several advantages over other inorganic carriers, such as capability to encapsulate higher amounts of drugs due to large pore volumes and improved stability due to their inorganic oxide framework (Slowing, Ii et al., 2007).

2.5.2 Examples of inorganic-based delivery systems

Taratula et al. prepared MSNs with a 3-mercaptopropyl modification for labeling with Cy5.5 and with pyridylthiol for conjugation of a lutein hormone releasing hormone (LHRH) peptide via a PEG spacer and for attaching thiol modified siRNA (Merkel O.M. et al., 2014; Taratula O. et al., 2011b). The MSNs pores were loaded with either doxorubicin or cisplatin with two types of siRNA for a chemotherapeutic combination therapy, as shown in **Fig. 7**. The MRP1 and BCL2 siRNA were selected based on their target mRNA's role in suppression of pump and non-pump cellular chemoresistance. An orthotopic model of lung cancer was established by intratracheal installation of luciferase expressing A549 cells (Garbuzenko O.B. et al., 2010). Nanoparticle accumulation in the mouse lungs was detected by whole body fluorescence imaging and revealed that inhalation administration prevented the MSN systemic circulation delivery and thus limited their accumulation elsewhere in the body (Taratula O. et al., 2011b).

The same group further utilized the modified MSN's to

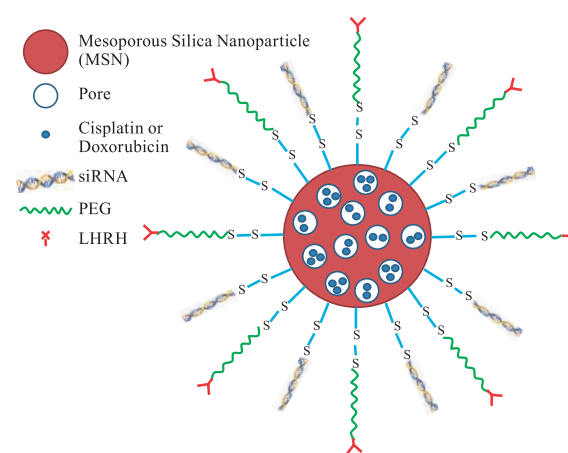


Fig. 7 Co-delivery of siRNA and anticancer agents using mesoporous silica nanoparticles (MSN) The surface engineered approach consists of surface bound siRNA and PEG-LHRH.

co-deliver anticancer drugs [doxorubicin (DOX) or cisplatin (CIS)], suppressor of pump resistance (siRNA targeting MRP-1 mRNA), and suppressor of non-pump cellular resistance (siRNA targeting BCL2 mRNA) using tumor targeting moiety LHRH peptide. The inhalation delivery of LHRH targeted MSN-drug complexes carrying both BCL2 and MRP1 siRNA (LHRH-PEG-siRNA-DOX-MSN) showed that 73.6 % of MSN was retained in lung compared to 5 % when i.v. injected (Taratula O. et al., 2011a). Also, after i.v. administration MSN-based DDS was found to be accumulated mainly in liver (73 %), kidneys (15 %) and spleen (7 %) while inhalation delivery resulted in significant reduction in accumulation to only 17 %, 9 % and 1 % in liver, kidneys and spleen respectively.

3. Ongoing clinical trials on aerosolized siRNA based medicines

Excellair™ from ZaBeCor Pharmaceuticals (Bala Cynwyd, Pennsylvania, USA) is an inhaled siRNA for the treatment of asthma. This siRNA functions as a spleen tyrosine kinase (Syk) inhibitor thereby inhibiting the transcription factors regulated by Syk. Syk is involved in the signaling from the B-cell receptor and regulates the downstream signaling cascades that ultimately leads to the activation of several proinflammatory transcription factors. Thus, the specific Syk inhibition by Excellair™ is designed to reduce the inflammation associated with asthma. In a phase I study, patients with asthma received the inhaled siRNA therapeutic for 21 consecutive days (Watts J.K. and Corey D.R., 2010). The drug was well tolerated in all asthma patients, with no serious adverse side effects. Moreover, 75 % of the patients treated reported improvement of breathing or reduced rescue inhaler use, while placebo patients reported no such improvement. These results helped propel Excellair™ into a phase II clinical trials in 2009, however these results are not available (De Backer L. et al., 2015).

Alnylam Pharmaceuticals (Cambridge, Massachusetts, USA) developed a nebulizer and nasal spray delivered siRNA therapeutic. The ALN-RSV01 siRNA was designed for the treatment of respiratory syncytial virus (RSV) targeting the nucleocapsid protein is indicated for prophylactic treatment against RSV infections in healthy patients (NCT00496821) and for treating RSV infection in lung transplant patients (NCT00658086 and NCT01065935). The ALN-RSV01 siRNA is composed of a double-stranded RNA duplex with 19 base pairs of complementary and 2-nt dT overhangs at both 3' ends (Alvarez R. et al., 2009; Devincenzo J. et al., 2008).

RSV is the leading cause of hospitalization of infants, infecting approximately 70 % of infants under a year old.

A RSV vaccine is not available for pediatric patients due to the potential teratogenicity and reduced effectiveness (Burnett J.C. et al., 2011). RSV may also produce severe respiratory diseases like pneumonia in immunocompromised adolescents and adults, and in the elderly (Devincenzo J. et al., 2010). RSV replicates in the outermost layer of the airway epithelium, including regions lining the nasal passages, trachea, and the bronchioles (Devincenzo J.P., 2009). The anti-viral efficacy of ALN-RSV01 was demonstrated by the reduced infection rate in healthy patients and by reducing the daily symptoms in lung transplantation patients (Devincenzo J. et al., 2010; Zamora M.R. et al., 2011). This example clearly shows the advancement that siRNA brings to clinical care by providing safe and efficacious treatment options.

4. Conclusions and future directions

The therapeutic potential of siRNA in the treatment of lung diseases has yet to be fully explored. The use of inhalable nanoparticulate siRNA delivery systems have barriers to their effective delivery, such as degradation by RNase, mucociliary clearance, cough clearance, and alveolar macrophage clearance, but overcoming these constraints will offer unique advances to the field. Important parameters to consider in aerosolized siRNA formulation design and development are the particle, aerosol, physico-chemical, stability, targeted site, and lung physiological properties.

siRNA carrier systems for aerosol delivery include those of naked siRNA formulation, lipidic, polymeric, peptide, or inorganic origin. Lipid-based delivery systems, such as liposomes or solid lipid nanoparticles have received attention for inhaled pulmonary delivery by using endogenously present phospholipids and surfactant-like lipids. Polymer-based siRNA delivery systems can be composed of biocompatible polymers which may be chemically modified to improve cellular delivery, internalization, and intracellular release. Peptide-based siRNA delivery vectors improve the poor bioavailability and clinical efficacy associated with naked siRNA delivery. Inorganic-based delivery systems allows for the unique delivery of siRNA for diagnostic and therapeutic purposes at higher payloads compared to other delivery systems. Safety of these formulations must be proven through various laboratory and clinical studies. *In vitro* techniques for characterizing aerosolized pulmonary siRNA delivery systems include dissolution tests, inertial cascade impaction, delivered dose uniformity assays, laser diffraction, and laser Doppler velocimetry. *Ex vivo* techniques such as the isolated perfused lung model can be used to identify inhaled particulate distribution. *In vivo* techniques like scintigraphy and pharmacokinetic/

pharmacodynamics analysis can give even more insight to the distribution, safety, and efficacy of a pulmonary inhaled siRNA nanocarrier. The vigorous work researchers have completed regarding the local pulmonary inhaled delivery of siRNA in various models of lung disease. Two inhalable therapeutic siRNA products have entered clinical trials. More clinically relevant preclinical studies utilizing biocompatible and safe siRNA delivery vehicles will provide inhalable aerosolized siRNA delivery vehicles for future clinical studies. Overall, recent work focused on inhalation delivery of siRNA for the treatment of pulmonary disorders has demonstrated the feasibility of this approach. The rapid progress in this area of research would facilitate the translation to the clinic.

Acknowledgements

The authors acknowledge the support of the National Institute of General Medical Science of the National Institutes of Health under award number SC3GM109873. The authors acknowledge Hawai'i Community Foundation, Honolulu, HI 96813, USA, for research support on lung cancer, mesothelioma, and asthma projects (Leahi Fund 15ADVC-74296) in 2015, 2013, and 2011, respectively. The authors would like to acknowledge the 2013 George F. Straub Trust and Robert C. Perry Fund of the Hawai'i Community Foundation, Honolulu, HI 96813, USA, for research support on lung cancer. The authors also acknowledge a seed grant from the Research Corporation of the University of Hawai'i at Hilo, Hilo, HI 96720, USA, and The Daniel K. Inouye College of Pharmacy, University of Hawai'i at Hilo, Hilo, HI 96720, USA, for providing start-up financial support to their research group. The authors acknowledge the donation from Dr. Robert S. Shapiro, MD, Dermatologist, Hilo, HI 96720, USA in support of development of nanotechnology based medicines.

References

- Aalto A.P., Sarin L.P., Van Dijk A.A., Saarma M., Poranen M.M., Arumae U. and Bamford D.H., Large-scale production of dsRNA and siRNA pools for RNA interference utilizing bacteriophage phi6 RNA-dependent RNA polymerase, *RNA*, 13 (2007) 422–429.
- Aoubakar M., Puisieux F., Couvreur P., Deyme M. and Vauthier C., Study of the mechanism of insulin encapsulation in poly (isobutylcyanoacrylate) nanocapsules obtained by interfacial polymerization, *Journal of biomedical materials research*, 47 (1999) 568–576.
- Akinc A., Zumbuehl A., Goldberg M., Leshchiner E.S., Busini V., Hossain N., Bacallado S.A., Nguyen D.N., Fuller J. and Alvarez R., A combinatorial library of lipid-like materials for delivery of RNAi therapeutics, *Nature biotechnology*, 26 (2008) 561–569.
- Allison S.D. and Anchordoquy T.J., Mechanisms of protection of cationic lipid DNA complexes during lyophilization, *Journal of pharmaceutical sciences*, 89 (2000) 682–691.
- Allison S.D. and Anchordoquy T.J., Maintenance of nonviral vector particle size during the freezing step of the lyophilization process is insufficient for preservation of activity: Insight from other structural indicators, *Journal of pharmaceutical sciences*, 90 (2001) 1445–1455.
- Allison S.D., De Molina M. and Anchordoquy T.J., Stabilization of lipid/DNA complexes during the freezing step of the lyophilization process: The particle isolation hypothesis, *Biochimica et Biophysica Acta (BBA)-Biomembranes*, 1468 (2000) 127–138.
- Alvarez R., Elbashir S., Borland T., Toudjarska I., Hadwiger P., John M., Roehl I., Morskaya S.S., Martinello R., Kahn J., Van Ranst M., Tripp R.A., Devincenzo J.P., Pandey R., Maier M., Nechev L., Manoharan M., Kotelianski V. and Meyers R., RNA interference-mediated silencing of the respiratory syncytial virus nucleocapsid defines a potent antiviral strategy, *Antimicrob Agents Chemother*, 53 (2009) 3952–3962.
- Amarzguoui M., Rossi J.J. and Kim D., Approaches for chemically synthesized siRNA and vector-mediated RNAi, *FEBS Letters*, 579 (2005) 5974–5981.
- Anchordoquy T.J., Carpenter J.F. and Kroll D.J., Maintenance of transfection rates and physical characterization of lipid/DNA complexes after freeze-drying and rehydration, *Archives of biochemistry and biophysics*, 348 (1997) 199–206.
- Arias J., Gallardo V., Gomez-Lopera S., Plaza R. and Delgado A., Synthesis and characterization of poly (ethyl-2-cyanoacrylate) nanoparticles with a magnetic core, *Journal of Controlled Release*, 77 (2001) 309–321.
- Baoum A., Ovcharenko D. and Berkland C., Calcium condensed cell penetrating peptide complexes offer highly efficient, low toxicity gene silencing, *Int J Pharm*, 427 (2012) 134–142.
- Barichello J.M., Morishita M., Takayama K. and Nagai T., Encapsulation of hydrophilic and lipophilic drugs in PLGA nanoparticles by the nanoprecipitation method, *Drug development and industrial pharmacy*, 25 (1999) 471–476.
- Benfer M. and Kissel T., Cellular uptake mechanism and knock-down activity of siRNA-loaded biodegradable DEAPA-PVA-g-PLGA nanoparticles, *European Journal of Pharmaceutics and Biopharmaceutics*, 80 (2012) 247–256.
- Biswas S., Knipp R.J., Gordon L.E., Nandula S.R., Gorr S.U., Clark G.J. and Nantz M.H., Hydrophobic oxime ethers: A versatile class of pDNA and siRNA transfection lipids, *ChemMedChem*, 6 (2011) 2063–2069.
- Bitko V., Musiyenko A., Shulyayeva O. and Barik S., Inhibition of respiratory viruses by nasally administered siRNA, *Nature medicine*, 11 (2005) 50–55.
- Blasig A., Shi C., Enick R.M. and Thies M.C., Effect of concentration and degree of saturation on RESS of a CO₂-soluble fluoropolymer, *Industrial & engineering chemistry research*, 41 (2002) 4976–4983.

- Bochicchio S., Dalmoro A., Barba A.A., Grassi G. and Lamberti G., Liposomes as siRNA delivery vectors, *Current drug metabolism*, 15 (2014) 882–892.
- Borm P., Klaessig F.C., Landry T.D., Moudgil B., Pauluhn J., Thomas K., Trotter R. and Wood S., Research strategies for safety evaluation of nanomaterials, part V: Role of dissolution in biological fate and effects of nanoscale particles, *Toxicol Sci*, 90 (2006) 23–32.
- Braunecker W.A. and Matyjaszewski K., Controlled/living radical polymerization: Features, developments, and perspectives, *Progress in Polymer Science*, 32 (2007) 93–146.
- Burnett J.C. and Rossi J.J., RNA-based therapeutics: Current progress and future prospects, *Chemistry & biology*, 19 (2012) 60–71.
- Burnett J.C., Rossi J.J. and Tiemann K., Current progress of siRNA/shRNA therapeutics in clinical trials, *Biotechnology Journal*, 6 (2011) 1130–1146.
- Buyens K., Demeester J., De Smedt S.S. and Sanders N.N., Elucidating the encapsulation of short interfering RNA in pegylated cationic liposomes, *Langmuir*, 25 (2009) 4886–4891.
- Çağdaş M., Sezer A.D. and Bucak S., Liposomes as potential drug carrier systems for drug delivery, 2014.
- Calvo P., Remuñan-López C., Vila-Jato J.L. and Alonso M.J., Chitosan and chitosan/ethylene oxide-propylene oxide block copolymer nanoparticles as novel carriers for proteins and vaccines, *Pharmaceutical Research*, 14 (1997a) 1431–1436.
- Calvo P., Remun Lopez C., Vila Jato J. and Alonso M., Novel hydrophilic chitosan polyethylene oxide nanoparticles as protein carriers, *Journal of Applied Polymer Science*, 63 (1997b) 125–132.
- Cao W., De Oliveira Ribeiro R., Liu D., Saintigny P., Xia R., Xue Y., Lin R., Mao L. and Ren H., EZH2 promotes malignant behaviors via cell cycle dysregulation and its mRNA level associates with prognosis of patient with non-small cell lung cancer, *PloS one*, 7 (2012) e52984.
- Caplen N.J., Alton E.W., Middleton P.G., Dorin J.R., Stevenson B.J., Gao X., Durham S.R., Jeffery P.K., Hodson M.E. and Coutelle C., Liposome-mediated CFTR gene transfer to the nasal epithelium of patients with cystic fibrosis, *Nature medicine*, 1 (1995) 39–46.
- Carmona S., Jorgensen M.R., Kolli S., Crowther C., Salazar F.H., Marion P.L., Fujino M., Natori Y., Thanou M. and Arbuthnot P., Controlling HBV replication *in vivo* by intravenous administration of triggered PEGylated siRNA-nanoparticles, *Molecular pharmaceutics*, 6 (2009) 706–717.
- Cavalli R., Caputo O., Carlotti M.E., Trotta M., Scarnecchia C. and Gasco M.R., Sterilization and freeze-drying of drug-free and drug-loaded solid lipid nanoparticles, *International journal of pharmaceutics*, 148 (1997) 47–54.
- Chen A.M., Zhang M., Wei D., Stueber D., Taratula O., Minko T. and He H., Co-delivery of doxorubicin and Bcl-2 siRNA by mesoporous silica nanoparticles enhances the efficacy of chemotherapy in multidrug-resistant cancer cells, *Small*, 5 (2009) 2673–2677.
- Chen G., Kronenberger P., Teugels E., Umelo I.A. and De Grève J., Targeting the epidermal growth factor receptor in non-small cell lung cancer cells: The effect of combining RNA interference with tyrosine kinase inhibitors or cetuximab, *BMC medicine*, 10 (2012) 28.
- Chen S., Ni B., Huang H., Chen X. and Ma H., siRNA-loaded pegylated porous silicon nanoparticles for lung cancer therapy, *Journal of Nanoparticle Research*, 16 (2014) 1–8.
- Chernyak Y., Henon F., Harris R.B., Gould R.D., Franklin R.K., Edwards J.R., Desimone J.M. and Carbonell R.G., Formation of perfluoropolyether coatings by the rapid expansion of supercritical solutions (RESS) process. Part 1: Experimental results, *Industrial & engineering chemistry research*, 40 (2001) 6118–6126.
- Choi M., Lee M. and Rhim T., Dexamethasone-conjugated polyethylenimine/mif siRNA complex regulation of particulate matter-induced airway inflammation, *Biomaterials*, 34 (2013) 7453–7461.
- Chougule M., Padhi B. and Misra A., Nano-liposomal dry powder inhaler of tacrolimus: Preparation, characterization, and pulmonary pharmacokinetics, *Int J Nanomedicine*, 2 (2007) 675–688.
- Chougule M., Padhi B. and Misra A., Development of spray dried liposomal dry powder inhaler of dapsone, *AAPS PharmSciTech*, 9 (2008) 47–53.
- Clark K.L., Hughes S.A., Bulsara P., Coates J., Moores K., Parry J., Carr M., Mayer R.J., Wilson P. and Gruenloh C., Pharmacological characterization of a novel ENaCa siRNA (GSK2225745) with potential for the treatment of cystic fibrosis, *Molecular Therapy—Nucleic Acids*, 2 (2013) e65.
- Corey D.R., Synthesis of oligonucleotide-peptide and oligonucleotide-protein conjugates, (Eds), *Bioconjugation protocols*, Springer, 2004, pp. 197–206.
- Crespy D., Stark M., Hoffmann-Richter C., Ziener U. and Landfester K., Polymeric nanoreactors for hydrophilic reagents synthesized by interfacial polycondensation on miniemulsion droplets, *Macromolecules*, 40 (2007) 3122–3135.
- Crowe J.H. and Crowe L.M., Factors affecting the stability of dry liposomes, *Biochimica et Biophysica Acta (BBA)-Biomembranes*, 939 (1988) 327–334.
- D’alessandro-Gabazza C.N., Kobayashi T., Boveda-Ruiz D., Takagi T., Toda M., Gil-Bernabe P., Miyake Y., Yasukawa A., Matsuda Y. and Suzuki N., Development and preclinical efficacy of novel transforming growth factor- β 1 short interfering RNAs for pulmonary fibrosis, *American journal of respiratory cell and molecular biology*, 46 (2012) 397–406.
- Danicher L., Frère Y. and Le Calvé A., Synthesis by interfacial polycondensation of polyamide capsules with various sizes. Characteristics and properties, *Macromolecular Symposia*, Wiley Online Library, 2000.
- De Backer L., Cerrada A., Pérez-Gil J., De Smedt S.C. and Raemdonck K., Bio-inspired materials in drug delivery: Exploring the role of pulmonary surfactant in siRNA inhalation therapy, *Journal of Controlled Release*, (2015).
- De Fougères A. and Novobrantseva T., siRNA and the lung: Research tool or therapeutic drug?, *Curr Opin Pharmacol*, 8 (2008) 280–285.
- De Fougères A.R., Delivery vehicles for small interfering RNA *in vivo*, *Human gene therapy*, 19 (2008) 125–132.
- Deshayes S., Morris M., Divita G. and Heitz F., Cell-penetrating

- peptides: Tools for intracellular delivery of therapeutics, *Cellular and Molecular Life Sciences CMLS*, 62 (2005) 1839–1849.
- Devincenzo J., Cehelsky J.E., Alvarez R., Elbashir S., Harborth J., Toudjarska I., Nechev L., Murugaiah V., Van Vliet A. and Vaishnav A.K., Evaluation of the safety, tolerability and pharmacokinetics of ALN-RSV01, a novel RNAi antiviral therapeutic directed against respiratory syncytial virus (RSV), *Antiviral research*, 77 (2008) 225–231.
- Devincenzo J., Lambkin-Williams R., Wilkinson T., Cehelsky J., Nochur S., Walsh E., Meyers R., Gollob J. and Vaishnav A., A randomized, double-blind, placebo-controlled study of an RNAi-based therapy directed against respiratory syncytial virus, *Proceedings of the National Academy of Sciences*, 107 (2010) 8800–8805.
- Devincenzo J.P., Harnessing RNA interference to develop neonatal therapies: From nobel prize winning discovery to proof of concept clinical trials, *Early Hum Dev*, 85 (2009) S31–35.
- Dire C., Magnet S., Couvreur L. and Charleux B., Nitroxide-mediated controlled/living free-radical surfactant-free emulsion polymerization of methyl methacrylate using a poly (methacrylic acid)-based macroalkoxyamine initiator, *Macromolecules*, 42 (2008) 95–103.
- Dokka S., Toledo D., Shi X., Castranova V. and Rojanasakul Y., Oxygen radical-mediated pulmonary toxicity induced by some cationic liposomes, *Pharmaceutical research*, 17 (2000) 521–525.
- Dustgania A., Vasheghani Farahani E. and Imani M., Preparation of chitosan nanoparticles loaded by dexamethasone sodium phosphate, *Iranian Journal of Pharmaceutical Sciences*, 4 (2008) 111–114.
- Eliyahu H., Siani S., Azzam T., Domb A.J. and Barenholz Y., Relationships between chemical composition, physical properties and transfection efficiency of polysaccharide–spermine conjugates, *Biomaterials*, 27 (2006) 1646–1655.
- Endoh T. and Ohtsuki T., Cellular siRNA delivery using cell-penetrating peptides modified for endosomal escape, *Advanced drug delivery reviews*, 61 (2009) 704–709.
- Fallouh N.A.K., Roblot-Treupel L., Fessi H., Devissaguet J.P. and Puisieux F., Development of a new process for the manufacture of polyisobutylcyanoacrylate nanocapsules, *International Journal of Pharmaceutics*, 28 (1986) 125–132.
- Felgner P.L., Tsai Y.J., Sukhu L., Wheeler C.J., Manthorpe M., Marshall J. and Cheng S.H., Improved cationic lipid formulations for in vivo gene therapy, *Annals of the New York Academy of Sciences*, 772 (1995) 126–139.
- Fellmann C. and Lowe S.W., Stable RNA interference rules for silencing, *Nature cell biology*, 16 (2014) 10–18.
- Fessi H., Puisieux F., Devissaguet J.P., Ammoury N. and Benita S., Nanocapsule formation by interfacial polymer deposition following solvent displacement, *International journal of pharmaceutics*, 55 (1989) R1–R4.
- Finnie K.S., Waller D.J., Perret F.L., Krause-Heuer A.M., Lin H.Q., Hanna J.V. and Barbé C.J., Biodegradability of sol-gel silica microparticles for drug delivery, *Journal of Sol-Gel Science and Technology*, 49 (2008) 12–18.
- Fire A., Xu S.Q., Montgomery M.K., Kostas S.A., Driver S.E. and Mello C.C., Potent and specific genetic interference by double-stranded RNA in *Caenorhabditis elegans*, *Nature*, 391 (1998) 806–811.
- Fourtounis J., Wang I.-M., Mathieu M.-C., Claveau D., Loo T., Jackson A.L., Peters M.A., Therien A.G., Boie Y. and Crackower M.A., Gene expression profiling following NRF2 and KEAP1 siRNA knockdown in human lung fibroblasts identifies CCL11/Eotaxin-1 as a novel NRF2 regulated gene, *Respir Res*, 13 (2012) 92.
- Galindo-Rodriguez S., Allemann E., Fessi H. and Doelker E., Physicochemical parameters associated with nanoparticle formation in the salting-out, emulsification-diffusion, and nanoprecipitation methods, *Pharmaceutical research*, 21 (2004) 1428–1439.
- Gallardo M., Couaraze G., Denizot B., Treupel L., Couvreur P. and Puisieux F., Study of the mechanisms of formation of nanoparticles and nanocapsules of polyisobutyl-2-cyanoacrylate, *International journal of pharmaceutics*, 100 (1993) 55–64.
- Ganachaud F. and Katz J.L., Nanoparticles and nanocapsules created using the ouzo effect: Spontaneous emulsification as an alternative to ultrasonic and high shear devices, *ChemPhysChem*, 6 (2005) 209–216.
- Gandhi N.S., Tekade R.K. and Chougule M.B., Nanocarrier mediated delivery of siRNA/miRNA in combination with chemotherapeutic agents for cancer therapy: Current progress and advances, *J Control Release*, 194 (2014) 238–256.
- Gao X. and Huang L., Potentiation of cationic liposome-mediated gene delivery by polycations, *Biochemistry*, 35 (1996) 1027–1036.
- Garbuzenko O.B., Saad M., Pozharov V.P., Reuhl K.R., Mainelis G. and Minko T., Inhibition of lung tumor growth by complex pulmonary delivery of drugs with oligonucleotides as suppressors of cellular resistance, *Proceedings of the National Academy of Sciences of the United States of America*, 107 (2010) 10737–10742.
- Gasco M. and Trotta M., Nanoparticles from microemulsions, *International journal of pharmaceutics*, 29 (1986) 267–268.
- Gaspar M.M., Bakowsky U. and Ehrhardt C., Inhaled liposomes—current strategies and future challenges, *Journal of Biomedical Nanotechnology*, 4 (2008) 245–257.
- Gaudin F. and Sintez-Zydowicz N., Core-shell biocompatible polyurethane nanocapsules obtained by interfacial step polymerisation in miniemulsion, *Colloids and Surfaces A: Physicochemical and Engineering Aspects*, 331 (2008) 133–142.
- Glasgow M.D. and Chougule M.B., Recent developments in active tumor targeted multifunctional nanoparticles for combination chemotherapy in cancer treatment and imaging, *Journal of Biomedical Nanotechnology*, 11 (2015) 1859–1898.
- Gutierrez B., Kube S.M., Reppe K., Santel A., Lange C., Kaufmann J., Suttrop N. and Witzensath M., RNAi-mediated suppression of constitutive pulmonary gene expression by small interfering RNA in mice, *Pulmonary pharmacology & therapeutics*, 23 (2010) 334–344.
- Ham H.T., Choi Y.S., Chee M.G. and Chung I.J., Singlewall carbon nanotubes covered with polystyrene nanoparticles by

- in situ miniemulsion polymerization, *Journal of Polymer Science Part A: Polymer Chemistry*, 44 (2006) 573–584.
- Hamasaki T., Suzuki H., Shirohzu H., Matsumoto T., D'alessandro-Gabazza C.N., Gil-Bernabe P., Boveda-Ruiz D., Naito M., Kobayashi T. and Toda M., Efficacy of a novel class of RNA interference therapeutic agents, *PloS one*, 7 (2012) e42655.
- Hannon G.J., RNA interference, *Nature*, 418 (2002) 244–251.
- Heidel J.D., Liu J.Y.-C., Yen Y., Zhou B., Heale B.S., Rossi J.J., Bartlett D.W. and Davis M.E., Potent siRNA inhibitors of ribonucleotide reductase subunit RRM2 reduce cell proliferation in vitro and in vivo, *Clinical Cancer Research*, 13 (2007) 2207–2215.
- Hermanson G.T., *Bioconjugate techniques*, Academic press, 2013.
- Hofland H., Shephard L. and Sullivan S.M., Formation of stable cationic lipid/DNA complexes for gene transfer, *Proceedings of the National Academy of Sciences*, 93 (1996) 7305–7309.
- Hong K., Zheng W., Baker A. and Papahadjopoulos D., Stabilization of cationic liposome-plasmid DNA complexes by polyamines and poly (ethylene glycol)-phospholipid conjugates for efficient in vivo gene delivery, *FEBS letters*, 400 (1997) 233–237.
- Hong S.-H., Kim J.-E., Kim Y.-K., Minai-Tehrani A., Shin J.-Y., Kang B., Kim H.-J., Cho C.-S., Chae C. and Jiang H.-L., Suppression of lung cancer progression by biocompatible glycerol triacrylate–spermine-mediated delivery of shakt1, *International journal of nanomedicine*, 7 (2012) 2293.
- Hong S.-H., Minai-Tehrani A., Chang S.-H., Jiang H.-L., Lee S., Lee A.-Y., Seo H.W., Chae C., Beck Jr G.R. and Cho M.-H., Knockdown of the sodium-dependent phosphate co-transporter 2b (NPT2b) suppresses lung tumorigenesis, *PloS one*, 8 (2013) e77121.
- Huang B., Zhou H., Wang X. and Liu Z., Silencing satb1 with siRNA inhibits the proliferation and invasion of small cell lung cancer cells, *Cancer Cell Int*, 13 (2013).
- Innes A.L., Carrington S.D., Thornton D.J., Kirkham S., Rousseau K., Dougherty R.H., Raymond W.W., Caughey G.H., Muller S.J. and Fahy J.V., *ex vivo* sputum analysis reveals impairment of protease-dependent mucus degradation by plasma proteins in acute asthma, *American journal of respiratory and critical care medicine*, 180 (2009) 203–210.
- Jensen D.K., Jensen L.B., Koocheki S., Bengtson L., Cun D., Nielsen H.M. and Foged C., Design of an inhalable dry powder formulation of DOTAP-modified PLGA nanoparticles loaded with siRNA, *J Control Release*, 157 (2012) 141–148.
- Jensen D.M., Cun D., Maltesen M.J., Frokjaer S., Nielsen H.M. and Foged C., Spray drying of siRNA-containing PLGA nanoparticles intended for inhalation, *J Control Release*, 142 (2010) 138–145.
- Jeong J.H., Mok H., Oh Y.-K. and Park T.G., siRNA conjugate delivery systems, *Bioconjugate chemistry*, 20 (2008) 5–14.
- Jiang H.L., Lim H.T., Kim Y.K., Arote R., Shin J.Y., Kwon J.T., Kim J.E., Kim J.H., Kim D., Chae C., Nah J.W., Choi Y.J., Cho C.S. and Cho M.H., Chitosan-graft-spermine as a gene carrier in vitro and in vivo, *Eur J Pharm Biopharm*, 77 (2011) 36–42.
- Jung T., Kamm W., Breitenbach A., Kaiserling E., Xiao J. and Kissel T., Biodegradable nanoparticles for oral delivery of peptides: Is there a role for polymers to affect mucosal uptake?, *European Journal of Pharmaceutics and Biopharmaceutics*, 50 (2000) 147–160.
- Kalariya M., Padhi B.K., Chougule M. and Misra A., Clobetasol propionate solid lipid nanoparticles cream for effective treatment of eczema: Formulation and clinical implications, *Indian J Exp Biol*, 43 (2005) 233–240.
- Kanasty R., Dorkin J.R., Vegas A. and Anderson D., Delivery materials for siRNA therapeutics, *Nature materials*, 12 (2013) 967–977.
- Karode S., Kulkarni S., Suresh A. and Mashelkar R., New insights into kinetics and thermodynamics of interfacial polymerization, *Chemical engineering science*, 53 (1998) 2649–2663.
- Kasper J.C., Schaffert D., Ogris M., Wagner E. and Friess W., Development of a lyophilized plasmid/LPEI polyplex formulation with long-term stability—a step closer from promising technology to application, *Journal of Controlled Release*, 151 (2011) 246–255.
- Kawashima Y., Nanoparticulate systems for improved drug delivery, *Advanced drug delivery reviews*, 47 (2001) 1–2.
- Keefe D., Agency response letter GRAS notice no. GRN 000397, 2011, FDA (U.S. Food and Drug Administration) <<http://www.fda.gov/Food/IngredientsPackagingLabeling/GRAS/NoticeInventory/ucm287638.htm>> accessed 29.02.2016.
- Kim D.H. and Rossi J.J., Strategies for silencing human disease using RNA interference, *Nature Reviews Genetics*, 8 (2007) 173–184.
- Kim S.S., Peer D., Kumar P., Subramanya S., Wu H., Asthana D., Habiro K., Yang Y.G., Manjunath N., Shimaoka M. and Shankar P., RNAi-mediated CCR5 silencing by LFA-1-targeted nanoparticles prevents HIV infection in BLT mice, *Mol Ther*, 18 (2010) 370–376.
- Kostag M., Köhler S., Liebert T. and Heinze T., Pure cellulose nanoparticles from trimethylsilyl cellulose, *Macromolecular symposia*, Wiley Online Library, 2010.
- Kostarelos K. and Miller A.D., Synthetic, self-assembly ABCD nanoparticles; a structural paradigm for viable synthetic non-viral vectors, *Chemical Society Reviews*, 34 (2005) 970–994.
- Kreuter J., On the mechanism of termination in heterogeneous polymerization, *Journal of Polymer Science: Polymer Letters Edition*, 20 (1982) 543–545.
- Krützfeldt J., Rajewsky N., Braich R., Rajeev K.G., Tuschl T., Manoharan M. and Stoffel M., Silencing of microRNAs *in vivo* with ‘antagomirs’, *nature*, 438 (2005) 685–689.
- Lam J.K.-W., Liang W. and Chan H.-K., Pulmonary delivery of therapeutic siRNA, *Advanced drug delivery reviews*, 64 (2012) 1–15.
- Lambert G., Fattal E. and Couvreur P., Nanoparticulate systems for the delivery of antisense oligonucleotides, *Advanced drug delivery reviews*, 47 (2001) 99–112.
- Landfester K., Musyanovych A. and Mailänder V., From polymeric particles to multifunctional nanocapsules for

- biomedical applications using the miniemulsion process, *Journal of Polymer Science Part A: Polymer Chemistry*, 48 (2010) 493–515.
- Li J., Chen Y.-C., Tseng Y.-C., Mozumdar S. and Huang L., Biodegradable calcium phosphate nanoparticle with lipid coating for systemic siRNA delivery, *Journal of Controlled Release*, 142 (2010) 416–421.
- Li S.D. and Huang L., Nanoparticles evading the reticuloendothelial system: Role of the supported bilayer, *Biochim Biophys Acta*, 1788 (2009) 2259–2266.
- Lim K.T., Subban G.H., Hwang H.S., Kim J.T., Ju C.S. and Johnston K.P., Novel semiconducting polymer particles by supercritical fluid process, *Macromolecular rapid communications*, 26 (2005) 1779–1783.
- List S.J., Findlay B.P., Forstner G. and Forstner J., Enhancement of the viscosity of mucin by serum albumin, *Biochem. J.*, 175 (1978) 565–571.
- Liu S., Nugroho A.E., Shudou M. and Maeyama K., Regulation of mucosal mast cell activation by short interfering RNAs targeting syntaxin4, *Immunology and cell biology*, 90 (2012) 337–345.
- Liu Y., Dong Q.-Z., Wang S., Fang C.-Q., Miao Y., Wang L., Li M.-Z. and Wang E.-H., Abnormal expression of pygopus 2 correlates with a malignant phenotype in human lung cancer, *BMC cancer*, 13 (2013) 346.
- Lobovkina T., Jacobson G.B., Gonzalez-Gonzalez E., Hickerson R.P., Leake D., Kaspar R.L., Contag C.H. and Zare R.N., In vivo sustained release of siRNA from solid lipid nanoparticles, *ACS Nano*, 5 (2011) 9977–9983.
- Lomas-Neira J., Perl M., Venet F., Chung C.-S. and Ayala A., The role and source of TNF- α in hemorrhage induced priming for septic lung injury, *Shock (Augusta, Ga.)*, 37 (2012) 611.
- Love K.T., Mahon K.P., Levins C.G., Whitehead K.A., Querbes W., Dorkin J.R., Qin J., Cantley W., Qin L.L. and Racie T., Lipid-like materials for low-dose, in vivo gene silencing, *Proceedings of the National Academy of Sciences*, 107 (2010) 1864–1869.
- Luo Y., Zhai X., Ma C., Sun P., Fu Z., Liu W. and Xu J., An inhalable β_2 -adrenoceptor ligand-directed guanidylated chitosan carrier for targeted delivery of siRNA to lung, *J Control Release*, 162 (2012) 28–36.
- Mainelis G., Seshadri S., Garbuzenko O., Han T., Wang Z. and Minko T., Characterization and application of a nose-only exposure chamber for inhalation delivery of liposomal drugs and nucleic acids to mice, *Journal of aerosol medicine and pulmonary drug delivery*, 26 (2013) 345–354.
- Mao S., Sun W. and Kissel T., Chitosan-based formulations for delivery of DNA and siRNA, *Advanced drug delivery reviews*, 62 (2010) 12–27.
- Marriott C., Beeson M.F. and Brown D.T., Biopolymer induced changes in mucus viscoelasticity, (Eds), *Mucus in health and disease—ii*, Springer, 1982, pp. 89–92.
- Matsubara H., Sakakibara K., Kunimitsu T., Matsuoka H., Kato K., Oyachi N., Dobashi Y. and Matsumoto M., Non-small cell lung carcinoma therapy using mTOR-siRNA, *International journal of clinical and experimental pathology*, 5 (2012) 119.
- Matyjaszewski K. and Xia J., Atom transfer radical polymerization, *Chemical reviews*, 101 (2001) 2921–2990.
- Meade B.R. and Dowdy S.F., Exogenous siRNA delivery using peptide transduction domains/cell penetrating peptides, *Advanced drug delivery reviews*, 59 (2007) 134–140.
- Mehnert W. and Maeder K., Solid lipid nanoparticles production, characterization and applications, *Advanced Drug Delivery Reviews*, 64 (2012) 83–101.
- Merkel O.M. and Kissel T., Nonviral pulmonary delivery of siRNA, *Accounts of chemical research*, 45 (2011) 961–970.
- Merkel O.M., Rubinstein I. and Kissel T., siRNA delivery to the lung: What's new?, *Adv Drug Deliv Rev*, 75 (2014) 112–128.
- Meziani M.J., Pathak P., Hurezeanu R., Thies M.C., Enick R.M. and Sun Y.P., Supercritical fluid processing technique for nanoscale polymer particles, *Angewandte Chemie International Edition*, 43 (2004) 704–707.
- Mi Bae Y., Choi H., Lee S., Ho Kang S., Tae Kim Y., Nam K., Sang Park J., Lee M. and Sig Choi J., Dexamethasone-conjugated low molecular weight polyethylenimine as a nucleus-targeting lipopolymer gene carrier, *Bioconjugate Chemistry*, 18 (2007) 2029–2036.
- Min K., Gao H., Yoon J.A., Wu W., Kowalewski T. and Matyjaszewski K., One-pot synthesis of hairy nanoparticles by emulsion ATRP, *Macromolecules*, 42 (2009) 1597–1603.
- Mishra S. and Chatterjee A., Novel synthesis of polymer and copolymer nanoparticles by atomized microemulsion technique and its characterization, *Polymers for Advanced Technologies*, 22 (2011) 1593–1601.
- Morrissey D.V., Lockridge J.A., Shaw L., Blanchard K., Jensen K., Breen W., Hartsough K., Machemer L., Radka S. and Jadhav V., Potent and persistent in vivo anti-HBV activity of chemically modified siRNAs, *Nature biotechnology*, 23 (2005) 1002–1007.
- Moschos S.A., Frick M., Taylor B., Turnpenny P., Graves H., Spink K.G., Brady K., Lamb D., Collins D. and Rockel T.D., Uptake, efficacy, and systemic distribution of naked, inhaled short interfering RNA (siRNA) and locked nucleic acid (LNA) antisense, *Molecular Therapy*, (2011).
- Moulik S. and Paul B., Structure, dynamics and transport properties of microemulsions, *Advances in Colloid and Interface science*, 78 (1998) 99–195.
- Nagavarma B., Yadav H.K., Ayaz A., Vasudha L. and Shivakumar H., Different techniques for preparation of polymeric nanoparticles—a review, *Asian J. Pharm. Clin. Res*, 5 (2012) 16–23.
- Nicolas J., Ruzette A.-V., Farcet C., Gérard P., Magnet S. and Charleux B., Nanostructured latex particles synthesized by nitroxide-mediated controlled/living free-radical polymerization in emulsion, *Polymer*, 48 (2007) 7029–7040.
- Nishimura Y., Takiguchi S., Ito S. and Itoh K., Evidence that depletion of the sorting nexin 1 by siRNA promotes HGF-induced MET endocytosis and MET phosphorylation in a gefitinib-resistant human lung cancer cell line, *International journal of oncology*, 44 (2014) 412–426.
- Niwa T., Takeuchi H., Hino T., Kunou N. and Kawashima Y., In vitro drug release behavior of D, L-lactide/glycolide copolymer (PLGA) nanospheres with nafarelin acetate prepared

- by a novel spontaneous emulsification solvent diffusion method, *Journal of pharmaceutical sciences*, 83 (1994) 727–732.
- Oh B. and Lee M., Combined delivery of HMGB-1 box a peptide and siRNA in animal models of acute lung injury, *J Control Release*, 175 (2014) 25–35.
- Okuda T., Kito D., Oiwa A., Fukushima M., Hira D. and Okamoto H., Gene silencing in a mouse lung metastasis model by an inhalable dry small interfering RNA powder prepared using the supercritical carbon dioxide technique, *Biological and Pharmaceutical Bulletin*, 36 (2013) 1183–1191.
- Pardeike J., Hommoss A. and Mueller R.H., Lipid nanoparticles (SLN, NLC) in cosmetic and pharmaceutical dermal products, *International Journal of Pharmaceutics*, 366 (2009) 170–184.
- Patel A.R., Chougule M.B., Townley I., Patlolla R., Wang G. and Singh M., Efficacy of aerosolized celecoxib encapsulated nanostructured lipid carrier in non-small cell lung cancer in combination with docetaxel, *Pharmaceutical research*, 30 (2013) 1435–1446.
- Patel G., Chougule M., Singh M. and Misra A., Nanoliposomal dry powder formulations, *Methods in enzymology*, 464 (2009) 167–191.
- Patlolla R.R., Chougule M., Patel A.R., Jackson T., Tata P.N.V. and Singh M., Formulation, characterization and pulmonary deposition of nebulized celecoxib encapsulated nanostructured lipid carriers, *Journal of Controlled Release*, 144 (2010) 233–241.
- Pavan G.M., Mintzer M.A., Simanek E.E., Merkel O.M., Kissel T. and Danani A., Computational insights into the interactions between DNA and siRNA with “rigid” and “flexible” triazine dendrimers, *Biomacromolecules*, 11 (2010) 721–730.
- Podesta J.E. and Kostarelos K., Chapter seventeen-engineering cationic liposome: siRNA complexes for in vitro and in vivo delivery, *Methods in enzymology*, 464 (2009) 343–354.
- Puglisi G., Fresta M., Giammona G. and Ventura C., Influence of the preparation conditions on poly (ethylcyanoacrylate) nanocapsule formation, *International Journal of Pharmaceutics*, 125 (1995) 283–287.
- Quintanar-Guerrero D., Allemann E., Fessi H. and Doelker E., Preparation techniques and mechanisms of formation of biodegradable nanoparticles from preformed polymers, *Drug Development and Industrial Pharmacy*, 24 (1998) 1113–1128.
- Radu D.R., Lai C.Y., Jeftinija K., Rowe E.W., Jeftinija S. and Lin V.S., A polyamidoamine dendrimer-capped mesoporous silica nanosphere-based gene transfection reagent, *J Am Chem Soc*, 126 (2004) 13216–13217.
- Rahman M.A., Amin A.R., Wang D., Koenig L., Nannapaneni S., Chen Z., Wang Z., Sica G., Deng X. and Shin D.M., RRM2 regulates Bcl-2 in head and neck and lung cancers: A potential target for cancer therapy, *Clinical Cancer Research*, 19 (2013) 3416–3428.
- Ramachandran S., Krishnamurthy S., Jacobi A.M., Wohlford-Lenane C., Behlke M.A., Davidson B.L. and McCray P.B., Efficient delivery of RNA interference oligonucleotides to polarized airway epithelia in vitro, *American Journal of Physiology-Lung Cellular and Molecular Physiology*, 305 (2013) L23–L32.
- Rao J.P. and Geckeler K.E., Polymer nanoparticles: Preparation techniques and size-control parameters, *Progress in Polymer Science*, 36 (2011) 887–913.
- Reis C.P., Neufeld R.J., Ribeiro A.J. and Veiga F., Nanoencapsulation i. Methods for preparation of drug-loaded polymeric nanoparticles, *Nanomedicine: Nanotechnology, Biology and Medicine*, 2 (2006) 8–21.
- Reischl D. and Zimmer A., Drug delivery of siRNA therapeutics: Potentials and limits of nanosystems, *Nanomedicine: Nanotechnology, Biology and Medicine*, 5 (2009) 8–20.
- Ren Y., Kang C.S., Yuan X.B., Zhou X., Xu P., Han L., Wang G.X., Jia Z., Zhong Y., Yu S., Sheng J. and Pu P.Y., Co-delivery of as-miR-21 and 5-FU by poly(amidoamine) dendrimer attenuates human glioma cell growth in vitro, *J Biomater Sci Polym Ed*, 21 (2010) 303–314.
- Rieger J., Zhang W., Stoffelbach F.O. and Charleux B., Surfactant-free RAFT emulsion polymerization using poly (n, n-dimethylacrylamide) trithiocarbonate macromolecular chain transfer agents, *Macromolecules*, 43 (2010) 6302–6310.
- Samad A., Sultana Y. and Aqil M., Liposomal drug delivery systems: An update review, *Current drug delivery*, 4 (2007) 297–305.
- Sane A. and Thies M.C., Effect of material properties and processing conditions on RESS of poly (l-lactide), *The Journal of supercritical fluids*, 40 (2007) 134–143.
- Sarkar D., El-Khoury J., Lopina S.T. and Hu J., An effective method for preparing polymer nanocapsules with hydrophobic acrylic shell and hydrophilic interior by inverse emulsion radical polymerization, *Macromolecules*, 38 (2005) 8603–8605.
- Schwarz C., Mehnert W., Lucks J. and Müller R., Solid lipid nanoparticles (SLN) for controlled drug delivery. I. Production, characterization and sterilization, *Journal of Controlled Release*, 30 (1994) 83–96.
- Scott C., Wu D., Ho C.-C. and Co C.C., Liquid-core capsules via interfacial polymerization: A free-radical analogy of the nylon rope trick, *Journal of the American Chemical Society*, 127 (2005) 4160–4161.
- Semple S.C., Klimuk S.K., Harasym T.O., Dos Santos N., Ansell S.M., Wong K.F., Maurer N., Stark H., Cullis P.R. and Hope M.J., Efficient encapsulation of antisense oligonucleotides in lipid vesicles using ionizable aminolipids: Formation of novel small multilamellar vesicle structures, *Biochimica et Biophysica Acta (BBA)-Biomembranes*, 1510 (2001) 152–166.
- Shim G., Choi H.-W., Lee S., Choi J., Yu Y.H., Park D.-E., Choi Y., Kim C.-W. and Oh Y.-K., Enhanced intrapulmonary delivery of anticancer siRNA for lung cancer therapy using cationic ethylphosphocholine-based nanolipoplexes, *Molecular Therapy*, 21 (2013) 816–824.
- Sieglwart D.J., Srinivasan A., Bencherif S.A., Karunanidhi A., Oh J.K., Vaidya S., Jin R., Hollinger J.O. and Matyjaszewski K., Cellular uptake of functional nanogels prepared by inverse miniemulsion ATRP with encapsulated proteins, carbohy-

- drates, and gold nanoparticles, *Biomacromolecules*, 10 (2009) 2300–2309.
- Siekman B. and Westesen K., P234 solid lipid nanoparticles stabilized by tyloxapol, *European Journal of Pharmaceutical Sciences*, 2 (1994) 177.
- Slowing, Ii, Trewyn B.G. and Lin V.S., Mesoporous silica nanoparticles for intracellular delivery of membrane-impermeable proteins, *J Am Chem Soc*, 129 (2007) 8845–8849.
- Sun Y.P., Meziani M.J., Pathak P. and Qu L., Polymeric nanoparticles from rapid expansion of supercritical fluid solution, *Chemistry-A European Journal*, 11 (2005) 1366–1373.
- Taratula O., Garbuzenko O.B., Chen A.M. and Minko T., Innovative strategy for treatment of lung cancer: Targeted nanotechnology-based inhalation co-delivery of anticancer drugs and siRNA, *J Drug Target*, 19 (2011a) 900–914.
- Taratula O., Garbuzenko O.B., Chen A.M. and Minko T., Innovative strategy for treatment of lung cancer: Targeted nanotechnology-based inhalation co-delivery of anticancer drugs and siRNA, *Journal of Drug Targeting*, 19 (2011b) 900–914.
- Tarkunde S.V., Gujar K., Harwalkar M. and Gambhire M., Liposome—a novel drug delivery, *Int. J. Pure App. Biosci*, 2 (2014) 92–102.
- Tekade R.K. and Chougule M.B., Formulation development and evaluation of hybrid nanocarrier for cancer therapy: Taguchi orthogonal array based design, *BioMed Research International*, 2013 (2013) 18.
- Tekade R.K., Youngren-Ortiz S.R., Yang H., Haware R. and Chougule M.B., Designing hybrid onconase nanocarriers for mesothelioma therapy: A taguchi orthogonal array and multivariate component driven analysis, *Molecular pharmaceuticals*, 11 (2014) 3671–3683.
- Thomas C.E., Ehrhardt A. and Kay M.A., Progress and problems with the use of viral vectors for gene therapy, *Nature Reviews Genetics*, 4 (2003) 346–358.
- Tompkins S.M., Lo C.-Y., Tumpey T.M. and Epstein S.L., Protection against lethal influenza virus challenge by RNA interference in vivo, *Proceedings of the National Academy of Sciences of the United States of America*, 101 (2004) 8682–8686.
- Tseng Y.-C., Mozumdar S. and Huang L., Lipid-based systemic delivery of siRNA, *Advanced drug delivery reviews*, 61 (2009) 721–731.
- Turner J.J., Williams D., Owen D. and Gait M.J., Disulfide conjugation of peptides to oligonucleotides and their analogs, *Current protocols in nucleic acid chemistry*, (2006) 4.28. 21–24.28. 21.
- Umrana Y., Nikjoo H. and Goodfellow J., A knowledge-based model of DNA hydration, *International journal of radiation biology*, 67 (1995) 145–152.
- Vauthier C. and Bouchemal K., Methods for the preparation and manufacture of polymeric nanoparticles, *Pharmaceutical research*, 26 (2009) 1025–1058.
- Vauthier C., Dubernet C., Fattal E., Pinto-Alphandary H. and Couvreur P., Poly (alkylcyanoacrylates) as biodegradable materials for biomedical applications, *Advanced Drug Delivery Reviews*, 55 (2003) 519–548.
- Wang J.-C., Lai S., Guo X., Zhang X., De Crombrughe B., Sonnylal S., Arnett F.C. and Zhou X., Attenuation of fibrosis in vitro and in vivo with SPARC siRNA, *Arthritis research & therapy*, 12 (2010) R60.
- Wang Y., Chen L., Huang G., He D., He J., Xu W., Zou C., Zong F., Li Y. and Chen B., Klotho sensitizes human lung cancer cell line to cisplatin via PI3k/Akt pathway, *PloS one*, 8 (2013) e57391.
- Watanasirichaikul S., Davies N.M., Rades T. and Tucker I.G., Preparation of biodegradable insulin nanocapsules from biocompatible microemulsions, *Pharmaceutical research*, 17 (2000) 684–689.
- Watts J.K. and Corey D.R., Clinical status of duplex RNA, *Bioorg Med Chem Lett*, 20 (2010) 3203–3207.
- Watts J.K., Delevey G.F. and Damha M.J., Chemically modified siRNA: Tools and applications, *Drug discovery today*, 13 (2008) 842–855.
- Weber M. and Thies M.C., Understanding the RESS process, *Supercritical Fluid Technology in Materials Science and Engineering: Syntheses, Properties, and Applications*, (2002) 387–427.
- Weber S., Zimmer A. and Pardeike J., Solid lipid nanoparticles (SLN) and nanostructured lipid carriers (NLC) for pulmonary application: A review of the state of the art, *European Journal of Pharmaceutics and Biopharmaceutics*, 86 (2014) 7–22.
- Whitehead K.A., Langer R. and Anderson D.G., Knocking down barriers: Advances in siRNA delivery, *Nat Rev Drug Discov*, 8 (2009a) 129–138.
- Whitehead K.A., Langer R. and Anderson D.G., Knocking down barriers: Advances in siRNA delivery, *Nature Reviews Drug Discovery*, 8 (2009b) 129–138.
- Wissing S., Kayser O. and Müller R., Solid lipid nanoparticles for parenteral drug delivery, *Advanced drug delivery reviews*, 56 (2004) 1257–1272.
- Wu S.Y. and Mcmillan N.A., Lipidic systems for in vivo siRNA delivery, *The AAPS journal*, 11 (2009) 639–652.
- York P., Strategies for particle design using supercritical fluid technologies, *Pharmaceutical science & technology today*, 2 (1999) 430–440.
- Youngren-Ortiz S.R., Gandhi N.S., España-Serrano L. and Chougule M.B., Aerosol delivery of siRNA to the lungs. Part 1: Rationale for gene delivery systems, *KONA Powder and Particle Journal*, 33 (2016) 63–85.
- Youngren S., Mulik R., Jun B., Hoffmann P., Morris K. and Chougule M., Freeze-dried targeted mannoseylated selenium-loaded nanoliposomes: Development and evaluation, *AAPS PharmSciTech*, 10.1208/s12249-013-9988-3 (2013) 1–13.
- Youngren S.R., Tekade R.K., Gustilo B., Hoffmann P.R. and Chougule M.B., STAT6 siRNA matrix-loaded gelatin nanocarriers: Formulation, characterization, and *ex vivo* proof of concept using adenocarcinoma cells, *Biomed Res Int*, 2013 (2013) 858946.
- Zamora M.R., Budev M., Rolfe M., Gottlieb J., Humar A., Devincenzo J., Vaishnav A., Cehelsky J., Albert G., Nochur S., Gollob J.A. and Glanville A.R., RNA interference therapy in lung transplant patients infected with respi-

- ratory syncytial virus, *Am J Respir Crit Care Med*, 183 (2011) 531–538.
- Zatsepin T., Turner J., Oretskaya T. and Gait M., Conjugates of oligonucleotides and analogues with cell penetrating peptides as gene silencing agents, *Current pharmaceutical design*, 11 (2005) 3639–3654.
- Zetterlund P.B., Kagawa Y. and Okubo M., Controlled/living radical polymerization in dispersed systems, *Chemical reviews*, 108 (2008) 3747–3794.
- Zetterlund P.B., Nakamura T. and Okubo M., Mechanistic investigation of particle size effects in TEMPO-mediated radical polymerization of styrene in aqueous miniemulsion, *Macromolecules*, 40 (2007) 8663–8672.
- Zhang Y.-P., Li W.-B., Wang W.-L., Liu J., Song S.-X., Bai L.-L., Hu Y.-Y., Yuan Y.-D. and Zhang M., siRNA against plasminogen activator inhibitor-1 ameliorates bleomycin-induced lung fibrosis in rats, *Acta Pharmacologica Sinica*, 33 (2012) 897–908.
- Zheng M., Librizzi D., Kilic A., Liu Y., Renz H., Merkel O.M. and Kissel T., Enhancing in vivo circulation and siRNA delivery with biodegradable polyethylenimine-graft-polycaprolactone-block-poly(ethylene glycol) copolymers, *Biomaterials*, 33 (2012) 6551–6558.
- Zhou X., Ni P. and Yu Z., Comparison of RAFT polymerization of methyl methacrylate in conventional emulsion and miniemulsion systems, *Polymer*, 48 (2007) 6262–6271.
- Ziegler A., Landfester K. and Musyanovych A., Synthesis of phosphonate-functionalized polystyrene and poly (methyl methacrylate) particles and their kinetic behavior in miniemulsion polymerization, *Colloid and polymer science*, 287 (2009) 1261–1271.

Author's short biography



Susanne R. Youngren-Ortiz

Susanne R. Youngren-Ortiz is a Ph.D. candidate the Daniel K. Inouye College of Pharmacy of the University of Hawai'i at Hilo. She obtained her Bachelor of Science Degree in Pharmaceutical Sciences with specialization in Industrial and Physical Pharmacy and minors in Chemistry and Statistics from Purdue University. Her dissertation research project investigates the optimal delivery and the evaluation of cellular effects of therapeutic nanocarriers for the treatment of asthma. She has authored original research articles, review articles, and book chapters. She is an active member of the American Association of Pharmaceutical Scientists (AAPS) and has chaired the University of Hawaii AAPS Student Chapter.

Author's short biography



Nishant S. Gandhi

Nishant S. Gandhi is a Ph.D. candidate at the Daniel K Inouye College of Pharmacy UH Hilo. He has completed his B.Pharm and M.Pharm from University of Pune in India. He has also worked as a chemist at Aristo Pharmaceuticals in Bhopal, India. He is currently working on developing novel nanotechnology based drug delivery systems for the treatment of lung cancer in Dr. Chougule's lab at the DKICP. He has authored publications including original research articles, review articles and book chapters. He is currently an active member of the American Association of Pharmaceutical Scientist (AAPS) and professional pharmacy fraternity "Phi Delta Chi" Gamma theta chapter of the DKICP. He has served as the chair of the University of Hawaii AAPS Student Chapter.



Laura Espana-Serrano

Dr. Laura Espana-Serrano is a Research Associate in the Translational Drug Delivery Research laboratory in the department of Pharmaceutical Sciences of the Daniel K. Inouye College of Pharmacy at the University of Hawaii at Hilo. She obtained her PhD in Biochemistry and Molecular Biology from the *Complutense* University of Madrid, Spain. She has nine years of experience in the fields of Cellular and Molecular Biology of Cancer and Psychiatric diseases. She has authored original research publications and review articles, and she is a member of the National Postdoctoral Association and the American Association of Pharmaceutical Scientists.



Mahavir B. Chougule

Dr. Mahavir B. Chougule is an Associate Professor of the Department of Pharmaceutical Sciences at the Daniel K. Inouye College of Pharmacy, University of Hawaii at Hilo. He is also Associate Member of Natural Products and Experimental Therapeutics Program, University of Hawaii Cancer Research Center. Dr. Chougule's translational drug delivery research laboratory investigates the use of newer combination of therapeutic agents, siRNA, proteins and targeted nanotechnology based formulations for treatment of lung cancer, breast cancer, mesothelioma, neuroblastoma, colon cancer and asthma. Dr. Chougule has 26 publications, 8 patents, 6 review articles, 7 book chapters and 2 editorial articles. His publications have received more than 700 citations with an h-index of 15. He delivered 17 invited talks and 63 scientific presentations at international conferences. He served as a grant reviewer on the NIH, DOD, and international review panels. He is also serving as a member of editorial boards on 7 international journals including AAPS PharmSciTech, Drug Development and Industrial Pharmacy, Journal of Nanopharmaceutics and Drug Delivery and Advanced Science, Engineering and Medicine. Dr. Chougule is a recipient of several awards including recent American Association of Cancer Research Minority-Serving Institution Faculty Scholar in Cancer Research Award, USA. He is an active member of American Association of Cancer Research and American Association of Pharmaceutical Scientists.

Toward Low-Temperature Coal Gasification: Experimental and Numerical Studies of Thermochemical Coal Conversion Considering the Interactions between Volatiles and Char Particles[†]

Cheng-Yi Li^{1,2}, Li-Xin Zhang^{1,3}, Shinji Kudo⁴,
Jun-ichiro Hayashi^{1,4} and Koyo Norinaga^{1,4,*}

¹ Interdisciplinary Graduate School of Engineering Sciences, Kyushu University, Japan

² China Tianchen Engineering Corporation (TCC), China

³ Xi'an Thermal Power Research Institute Co. Ltd., China

⁴ Institute for Materials Chemistry and Engineering, Kyushu University, Japan

Abstract

A novel triple-bed combined circulating fluidized-bed (TB-CFB) coal gasifier, consisting of a downer (pyrolyzer), a bubbling fluidized bed (gasifier), and a riser (combustor) was proposed for realizing low-temperature coal gasification. Several key thermochemical reactions were extracted from those expected in the downer unit: the reforming of refractory tar in both the gas phase and over the char surface, and the steam gasification of the nascent char. This review highlights our recent progress, both experimental and numerical, in studies of thermochemical coal conversion including the various reaction processes, by employing a drop-tube reactor that well approximates the reaction environment in a downer reactor. This discussion can be utilized in designing TB-CFBs and optimizing their operation.

Keywords: coal gasification, simulation, fluidized-bed reactor, tar reforming, drop-tube reactor, reactor modeling

1. Introduction

Coal plays an important role in meeting current world energy demands, and should continue to do so in the near future. The development of techniques for the higher-efficiency clean utilization of coal, such as coal gasification, is becoming an increasingly active area of research (Li C.Z., 2006). Currently, many coal gasification technologies are based on partial combustion at temperatures above 1200 °C. High temperature provides significant advantages for realizing the very fast thermochemical conversion of coal into syngas, but also offers the added expense of chemical energy of the fuel due to heating. The cold gas efficiency can be raised theoretically further by decreasing O₂ consumption while increasing steam or CO₂ consumption, which would result in gasification

operations at lower temperature. Low-temperature gasification with higher cold gas efficiency has received widespread attention in recent years (Hayashi et al., 2014).

The low-temperature gasification of coal is conducted at temperatures well below 1000 °C. Fixed- and fluidized-bed gasifiers, as the main reactor systems for low-temperature gasification, have been developed toward the commercial production of power. The low temperatures, however, inevitably result in slower coal conversion into syngas. The novel Lurgi fixed-bed gasifiers suffer from high tar yields in the product gases (Li X.T. et al., 2004), and the processing rates are slow compared with entrained- and fluidized-beds (Hobbs et al., 1993). Fluidized beds now find wide application in coal gasification (Li X.T. et al., 2004). However, due to their high degree of solids mixing and particle entrainment, a single fluidized bed cannot achieve high solids conversion, as observed with the U-gas[®] gasifier (Goyal and Rehmat, 1992). Therefore, it is necessary to develop a novel gasification technology with higher cold gas efficiency.

Recently, a triple-bed combined circulating fluidized-bed reactor (TB-CFB) system, consisting of a downer (pyrolyzer), a bubbling fluidized bed (BFB, gasifier), and a riser (combustor), as shown in **Fig. 1**, was proposed

[†] Received 2 December 2015; Accepted 8 February 2016
J-STAGE Advance Publication online 30 April 2016

^{1,4} Kasuga-koen 6-1, Kasuga, Fukuoka 816-8580, Japan

² No. 1, Jingjin Road, Beichen District, Tianjin 300400, China

³ No. 99 Yanxiang Road, Xi'an 710054, China

* Corresponding author: Koyo Norinaga;

E-mail: norinaga@cm.kyushu-u.ac.jp

TEL: +81-92-583-7794 FAX: +81-92-583-7793

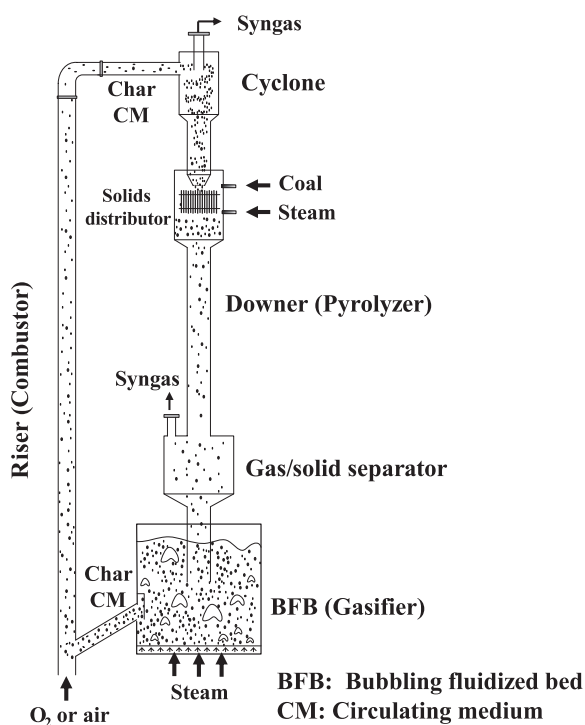


Fig. 1 Schematic diagram of the triple-bed combined circulating fluidized-bed reactor system.

(Guan, et al., 2010a; Guan, et al., 2010b; Guan et al., 2011; Fushimi et al., 2011; Zhang, et al., 2013a; Zhang, et al., 2013b). In brief, the downer was added to a dual-bed circulating fluidized reactor system, after the riser (combustor) and before the BFB gasifier. Fresh coal was fed, mixed with hot circulating solids for the riser, including recycled char and the circulating medium, and rapidly pyrolyzed in the downer at around 900 °C. The resultant tar was simultaneously and rapidly decomposed into syngas and/or coke over the nascent and recycled chars. Then, the tar-free char was separated from the syngas, sent to the BFB gasifier, and gasified without the negative effect of the volatiles-char interaction. The char gasification and volatiles reforming are thus expected to be decoupled under this reactor system. The endothermic and exothermic processes were separated in this system to realize the concept of low-temperature gasification with high cold gas efficiency.

As one important part of the reactor system, the novel downer reactor was expected to decompose tar and thus avoid the detrimental effects of tar on the subsequent char gasification and downstream system operation. After the coal is fed, coal, char particles, and gases flow concurrently in the downer. Several key thermochemical reactions were extracted from the coal conversion involved in the downer: the reforming of tar, the steam gasification of the nascent char, and complex interactions between the volatiles and char. The focus of this review is to highlight our recent understanding of thermochemical coal conver-

sion in the downer reactor of the TB-CFB system, together with some future perspectives.

2. In situ tar reforming process

Tar, an undesirable product of gasification, is defined as the products heavier than C_6 compounds, such as benzene, that can be condensed at ambient temperature. Its reforming is mandatory for power generation and liquid production (Hayashi et al., 2014). Liquid scrubbing techniques and catalytic reforming methods suffer from undesirable overall thermal efficiency loss and/or catalyst deactivation because of the deposition of chlorine/sulfur compounds and carbon (Abu El-Rub et al., 2004a; Devi, et al., 2002; Simell et al., 1997). Thus, it is necessary to develop a tar reforming system with high thermal efficiency and without catalyst poisoning or deactivation. The effective decomposition of tar compounds over biomass/coal-derived chars has been frequently reported (Abu El-Rub, 2008; Gilbert et al., 2009; Kerkkaiwan et al., 2015; Kerkkaiwan et al., 2013; Sun et al., 2011). Naphthalene, representative of the most refractory compounds among tar constituents, was decomposed almost completely over chars or charcoals from different biomass/coal within a short gas residence time (less than 0.25 s) in a fixed-bed reactor (Abu El-Rub et al., 2004b; Fuentes-Cano et al., 2013). Except for benzene and naphthalene, tar constituents were completely decomposed over the coke accumulated in nanoporous alumina within a gas residence time of 0.03 s (Hosokai et al., 2005). These studies demonstrate the potential of utilization of char for tar elimination.

The in situ tar reforming process is one of the key thermochemical phenomena in the downer reactor of the TB-CFB system. Matsuhara et al. (2010) used a two-stage reactor to realize the in situ reforming of nascent tar from the rapid pyrolysis of brown coal over char obtained from the same coal. The results showed that the released tar can be decomposed over the char completely at 900 °C. This indicated the potential for the rapid and complete decomposition of tar over a char surface due to an intensive tar-char interaction. However, the characteristics of the char and reaction conditions of the two-stage reactor system are different from those of the downer reactor, through which coal, char particles, and gases are concurrently flowing. In the downer reactor, the in situ reforming of nascent tar occurs over the nascent char from the rapid pyrolysis of the same coal. In addition, it is not possible to use a fixed char bed to realize the decomposition of tar in the continuously operating TB-CFB system.

In our recent study (Zhang et al., 2013b), a drop-tube reactor (DTR) was employed to simulate reaction environments similar to those in the downer reactor. An

Australian brown coal (Loy Yang, hereafter referred to as LY) was co-fed with char (LYC) or partially gasified char (GLYC) into the DTR, and the effects of the char properties, char concentration in the blended sample, peak temperature, and feeding rate related to the solid hold-up on the tar decomposition were investigated.

The yields of heavy tar for in situ reforming at different concentrations of char are shown in **Fig. 2**. The results are compared with predicted values by assuming the independent thermoconversion of coal and char. The results show that the observed heavy tar yields were 0.4–0.5 mol-C/100-mol-C-(LY + LYC/GLYC) lower than the corresponding predicted values at whole blending ratios of LY and LYC/GLYC fed into the DTR. The differences between their yields are direct evidence of nascent tar decomposition through intensive tar-char interactions. Coking/coke gasification and direct steam reforming are two current possible mechanisms proposed to explain the phenomenon in which the tar is decomposed over the char surface (Hosokai et al., 2008; Matsuhara et al., 2010). It is more reasonable that coking gasification is the main contributor to nascent tar decomposition over a char surface in non-catalytic tar reforming, compared with the direct steam reforming of tar, because the direct steam reforming reactions occur to a lesser extent than coking if catalysts are not used. The nascent tar from the pyrolysis of LY was decomposed by coking over the char from the flash pyrolysis of the same coal, and the char/coke was simultaneously gasified with steam. The steam gasification of the char/coke created new active sites to maintain the tar coking over the char surface. It is noted that the direct steam gasification of tar also is an important role of in situ tar reforming. LY contains abundant Na^+ and Ca^{2+} , and these alkali and alkaline earth metal (AAEM) species that remain in the resultant char are considered to play cata-

lytic roles in the steam gasification of char/coke. This means that higher AAEM contents would be favorable for maintaining the coking activity of the char, and thus, to some extent, the higher coking activity of the char would promote more tar conversion into soot/coke over the char surface.

3. In situ steam gasification of char gasification

The steam gasification of char, as a gas-solid thermochemical conversion, is the rate-determining step (Mühlen et al., 1985) for the entire coal gasification process. The process has been studied by many researchers to understand the kinetics and mechanisms of both non-catalytic and catalytic reactions using fixed- (Haga and Nishiyama, 1988) and fluidized-bed reactors. H_2 is the main inhibitor in the steam gasification of char (Lussier et al., 1998; Yang and Duan, 1985); the rate of steam gasification in the presence of H_2 is lower by an order of magnitude or more than in its absence. However, recent studies (Hayashi et al., 2000, 2002) have shown that pyrolysis-derived volatiles, including tar, are much stronger inhibitors than H_2 in the steam gasification of char, because of the volatiles-char interactions.

The gasification of AAEM-loaded coals has been investigated. Bayarsaikhan et al. (2005) found that the inherent Na^+ and Ca^{2+} species increased the initial gasification rate of the nascent char under a steam atmosphere by more than 80 % in a drop-tube/fixed-bed reactor system. Mašek et al. (2009) reported that catalytic steam gasification proceeded extensively even under conditions in which the gasification of the unloaded coal was retarded by coexisting tarry compounds and char. In addition, higher AAEM contents have also been shown to be favorable for maintaining the coking activity of the char, promoting the in situ steam reforming of tar over the char surface. Therefore, the in situ steam gasification of AAEM-loaded char under volatiles-char interactions is worth studying.

AAEM species are generally loaded on low rank coals using water-soluble precursors such as NaCl (Takarada et al., 1989; Wu et al., 2005), Na_2NO_3 (Yamashita et al., 1991), $\text{Ca}(\text{NO}_3)_2$ (Ohtsuka and Tomita, 1986), CaCl_2 (Yamashita et al., 1992), $\text{Ca}(\text{CH}_3\text{COO})_2$ (Ohtsuka and Tomita, 1986; Tyler and Schafer, 1980), KCl (Liu and Zhu, 1986), or K_2CO_3 (Liu and Zhu, 1986; Tristantini et al., 2015). Kajita et al. (2010) reported that Na^+ and K^+ were irreversibly transferred from the char to the mineral matter (alumina) when contacting with each other at 800 °C. Irreversible reactions between the AAEM and fluidizing medium/circulating medium not only diminish the catalytic action, but also bring about problems in downstream

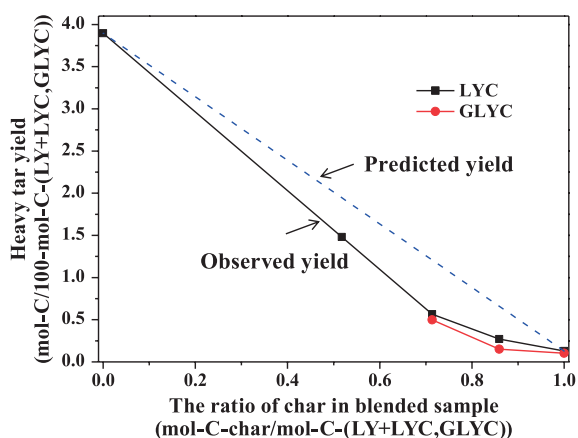


Fig. 2 Heavy tar yields of in situ tar reforming at different char ratios on a (LY + LYC, GLYC)-fed carbon basis. Reprinted with permission from Ref. (Zhang, et al., 2013b). Copyright: (2013) Elsevier B.V.

operations. For example, the defluidization and agglomeration of bed materials occur in fluidized beds because of the formation of Na/K silicates with melting point temperatures below 1000 °C. Therefore, Ca-containing materials are the most promising catalyst precursors for the steam gasification of char. It is noteworthy that a slurry of coal and water usually becomes acidic as a result of the dissolution of organic acidic compounds from brown coal. CaCO_3 and Ca(OH)_2 (which become more soluble in the slurry) have also been reported for use as catalysts in the steam gasification of char (Kim et al., 2013; Ohtsuka and Asami, 1996, 1997; Ohtsuka and Tomita, 1986). Ohtsuka et al. (1997) reported that the catalytic activity of Ca^{2+} from CaCO_3 was higher than that from Ca(OH)_2 in a thermobalance reactor. The reported results, however, were obtained at a low heating rate; the reactor system could not provide a heating rate as high as that achieved in the downer reactor for coal gasification. The higher heating rate causes more rapid thermal cracking and provides more active sites on the char particles for steam gasification. AAEM species can better catalyze the gasification of nascent char, as well as the in situ reforming of volatiles over the char surface, even in a short reaction time. Ca-catalyzed gasification is also known to slow as the process of char conversion proceeds (Liu and Zhu, 1986; Ohtsuka and Asami, 1996, 1997). Possible mechanisms (Radovic et al., 1984) include the sintering of CaO or CaCO_3 and crystalline growth.

In our recent study (Zhang, et al., 2013a), inexpensive materials were selected as catalyst precursors, such as NaCO_3 and Ca(OH)_2 . The catalytic effects of Na^+ and Ca^{2+} from these inexpensive materials on the in situ steam gasification of char from the rapid pyrolysis of low rank coal (Adaro coal from Indonesia, hereafter referred to as AD) were investigated.

The net conversions of the primary chars from Na^+ and Ca^{2+} loaded ADs (AD-Na and AD-Ca, respectively) with different concentrations of the catalysts after in situ steam gasification in the DTR are shown in **Fig. 3**. Here the results with both Na^+ and Ca^{2+} were co-loaded AD (AD-Ca-Na) were also shown. The net conversion of the primary char X_{char} is defined by

$$X_{\text{char}} = \frac{(\text{primary char yield}) - (\text{char yield from DTR})}{\text{primary char yield}} \times 100\%$$

X_{char} is the difference in the extent of carbon deposition between the char and steam gasification of char carbon together with the deposited carbon. **Fig. 3** shows X_{char} as a function of temperature. X_{char} for AD at 900–950 °C is less than 10 %, and catalysis by the inherent AAEM species, if any, was insignificant. However, X_{char} for the catalyst-loaded coals was in the range from 15 to 45 %, and the process of steam gasification within 3 s was clear.

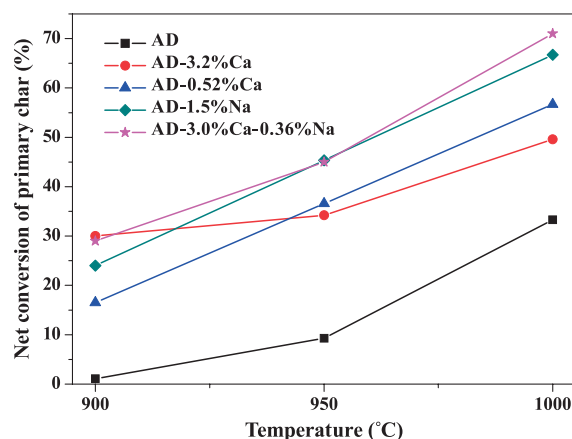


Fig. 3 The net conversions of primary char of AD, AD-3.2%Ca, AD-0.52%Ca, AD-1.5%Na, and AD-3.0%Ca-0.36%Na after in situ steam gasification at 900–1000 °C in the DTR. Reprinted with permission from Ref. (Zhang, et al., 2013a). Copyright: (2013) Elsevier B.V.

The X_{char} value increases in the order $\text{AD} < \text{AD-Na} < \text{AD-Ca} < \text{AD-Ca-Na}$, indicating that AD-Ca-Na had the highest reactivity under the current conditions. Some other studies (Ohtsuka and Tomita, 1986; Takarada et al., 1989) reported that the Na in Australian brown coal at 650 °C exerted a smaller catalytic effect than Ca in the same coal at the same catalyst content (5 %).

The X_{char} results for AD-3.2%Ca and AD-0.52%Ca (of which concentrations of Ca are 3.2 and 0.52 wt%, respectively) show that the Ca^{2+} in the former was more active than that in the latter at 900 °C, but less active at 1000 °C. It is generally accepted that the activity of AAEM catalysts increases with increasing loading and then levels off at a certain point. Increases in the catalyst concentration tend to bring about increases in the size of the catalytic particles, coarsening them through agglomeration and/or coalescence. Thus, a higher Ca content causes more facile coarsening of the catalyst particles (Cazorla-Amoros et al., 1993; Radovic et al., 1983). In addition, although the initial Ca content in the AD-0.52%Ca was only about 1/6 of that in the AD-3.2%Ca, the activity seemed to be equivalent with that in the AD-3.2%Ca at 950 °C, and thus, even higher at 1000 °C. This means that both the specific and overall activities of Ca were reduced by increasing the Ca loading on the AD from 0.52 % to 3.2 % for in situ steam gasification at 950–1000 °C.

It is noteworthy that X_{char} for AD-3.0%Ca-0.36%Na was as high as 71 % and much higher than that for AD-3.2%Ca, although their Ca contents were nearly equivalent. Compared with catalytic effect of AD-1.5%Na, the difference in X_{char} between AD-3.0%Ca-0.36%Na and AD-3.2%Ca is attributed mainly to either the activity of Na or synergy due to the coexistence of Na and Ca that could suppress the coarsening of the Ca catalyst particles.

4. Kinetic modeling coupled with CFD approach accounting for volatiles-char interactions

Coal conversion incorporating the volatiles-char interactions proceeds via a number of complex parallel reactions, and produces a wide range of products such as char, soot, light hydrocarbons, and both single and polycyclic aromatic hydrocarbons. The volatiles-char interaction has been frequently reported for different reactor systems, and the results show that the interaction has a significant role in inhibiting char gasification and promoting nascent tar decomposition. (Hayashi et al., 2014; Li C.Z., 2013). However, those studies focused on laboratory-based experimental investigations only. Kajitani et al. (2013) proposed a kinetic model incorporating the volatiles-char interaction, which reproduced the experimental findings from coal conversion very well, including the effects of the Na concentration in the char during steam gasification. It can also be used in designing any industrial fluidized-bed gasifier in the presence of volatile-char interactions. Although no studies have been performed, the development of a mathematical model based on the experimental results for coal conversion, including the volatiles-char interactions in the downer reactor of a TB-CFB system, should be considered.

4.1 Kinetic model

The lumping component model, an approach in which complex mixtures with large numbers of compounds are lumped into smaller groups of pseudo-components, is widely employed to provide a tractable number of kinetic equations and estimate kinetic parameters. To date, it has been mainly applied in investigations of hydrogenation or the catalytic cracking of heavy oil (Lan et al., 2009; Theologos and Markatos, 1993).

In our recent study (Li C.Y. et al., 2015), it was employed for the first time to estimate kinetic parameters in complex coal conversion environments, including volatiles-char interactions, which were approximated for the downer reactor of the TB-CFB system. A network among lumps in the DTR is proposed as shown in **Fig. 4**. Under our conditions, it is assumed that the coal sample has already been converted into tar, carbon gases, char, and soot by primary pyrolysis at the top non-isothermal zone of the DTR (at 500–900 °C) (Jamil et al., 2004; Sathe et al., 1999). The carbon conversion reactions in the isothermal zone of the DTR were simulated, and the feedstock was lumped into tar, carbon gases, char, and soot derived from the primary pyrolysis of the coal. The possible main reactions in the DTR were considered to be thermal cracking/steam reforming of the volatiles, gasification, and the volatiles-char interactions. The kinetic parameters

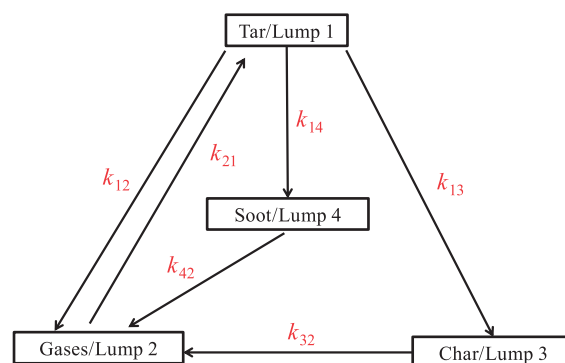


Fig. 4 Schematic diagram of the four-lump reaction network in the DTR coal conversion process accounting for the volatiles-char interaction. Reprinted with permission from Ref. (Li C.Y. et al., 2015). Copyright: (2015) Elsevier B.V.

of the four-lump model were estimated through a mathematical model integrated with a four-order Runge-Kutta method.

4.2 Kinetic model coupled with a computational fluid dynamics (CFD) approach

In the downer reactor of the TB-CFB system, coal, char particles, and gases flow concurrently. Gas-solid two-phase mixed flows are key phenomena and of particular interest for understanding the downer reactor. Ropelato et al. (2005) proposed an Eulerian-Eulerian approach for predicting fluid dynamics in the downer reactor, with good agreement between the experimental data and model predictions. Fushimi et al. (2012) also used an Eulerian-Eulerian method to investigate the degree of solid-solid mixing in the downer unit by simulating the hydrodynamics of hot sand, cold sand, and air, as well as the heat transfer among them. The simulation results agreed well with the experimental observations. An Eulerian-Lagrangian method (CFD-DEM) was applied by Zhao et al. (2007) to simulate gas-solid flows in a 2-dimensional downer reactor, and the predicted macro-scale flow structure had good agreement with the experiments. The published works can successfully predict fluid dynamics in the downer reactor with good agreement between experimental data and model predictions. The data can be useful, but the models only include numerical simulations of gas-solid flows in the downer reactor for coal conversion without considering the chemical reactions. Thus, a CFD approach for gas-solid flows combined with a chemical kinetic model for coal conversion that accounts for the volatiles-char interactions in the downer reactor is urgently needed.

An Eulerian-Eulerian model was employed to simulate the fluid dynamics of gas-solid flow environments approximated for the downer reactor. Six global chemical

reactions with the corresponding kinetics parameters derived from the lumping model were considered in the simulation. The proposed CFD model gave acceptable predictions of gas-solid flows with carbon conversion reactions in the DTR in the presence of volatiles-char interactions (Li C.Y. et al., 2015).

The mass fraction distribution of the four lumps obtained from the simulation is illustrated in **Fig. 5**. In the carbon thermo-conversion process, in situ reforming of tar over the char surface occurred, and resulted in the mass fraction of tar decreasing gradually from inlet to outlet. For char particles, steam gasification is a main pathway for conversion, and their mass fraction also decreases. In contrast, the mass fraction of carbon gases increases very quickly along the DTR. This can be explained by the production of carbon gases through tar cracking and the gasification of both char and soot, which occur at faster rates than that of tar pyrolysis to produce tar.

In addition, the effects of reaction temperature, solid hold-up, and steam partial pressure on tar consumption along the DTR are shown in **Fig. 6**. It is very clear that about 85 % of the tar is consumed at a rapid rate near the DTR entrance zone. Furthermore, the reaction temperature and solid hold-up are two significant factors in tar decomposition, whereas the steam partial pressure has little effect.

5. Conclusions

This manuscript describes the potential of the downer reactor for coal conversion, including tar reforming and char gasification, in a triple-bed combined circulating fluidized-bed reactor system. A drop-tube reactor was employed to simulate the reaction environment approximated in the downer reactor, wherein coal, char particles, and gases are concurrently flowing. Increasing the reaction temperature, feeding rate, and char concentration enhanced the tar decomposition. Inexpensive raw materials such as Na_2CO_3 and $\text{Ca}(\text{OH})_2$ effected good catalytic performance for the steam gasification of the char. Finally, a kinetic model with four lumps (gases, tar, char, and soot) and six reactions encompassing the volatiles-char interactions was developed and successfully integrated with a CFD approach to simulate the gas/particle flow in the DTR.

Acknowledgements

This work was in part supported financially by the New Energy and Industrial Technology Development Organization (NEDO), Japan and MOST-JST, Strategic International Collaborative Research Program, SICORP. In addition, Li-Xin Zhang and Cheng-Yi Li gratefully acknowledge financial supports given by the China Scholar-

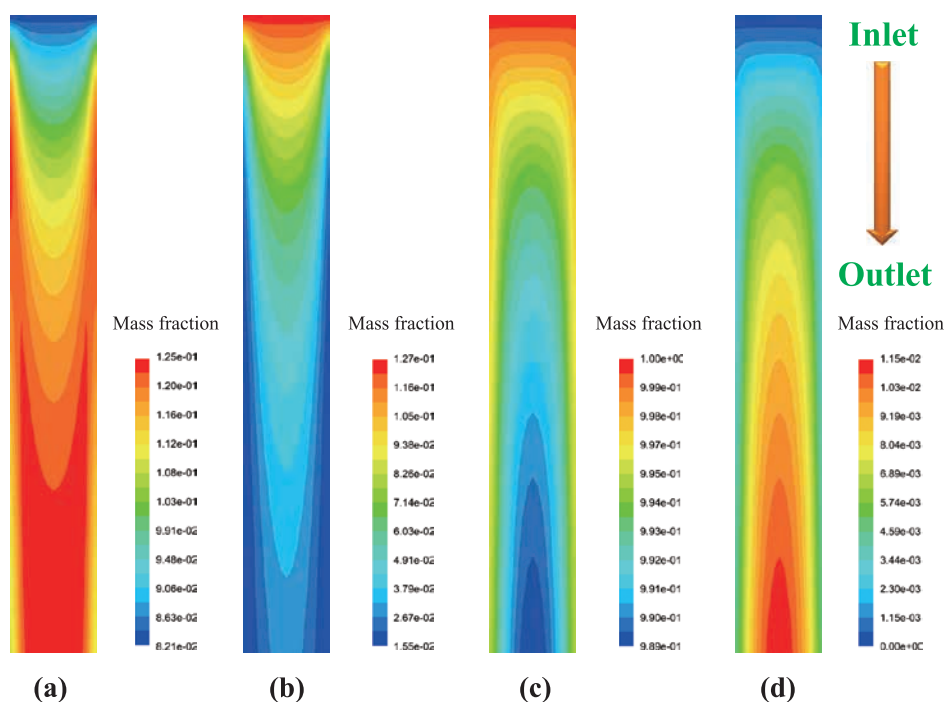


Fig. 5 The contours of different lumps derived from the CFD simulation (in run 4, (a) carbon gases; (b) tar; (c) char; (d) soot; Sum of mass fractions of gas phases = 1; Sum of mass fractions of solid phases = 1) Reprinted with permission from Ref. (Li C.Y. et al., 2015). Copyright: (2015) Elsevier B.V.

ship Council (CSC Program) and the Kyushu University Global COE program (G-COE Program). The authors are grateful to Professor Hsiu-Po Kuo and Dr An-ni Huang at Department of Chemical and Materials Engineering, Chang Gung University, Taipei for their valuable suggestions for mixed phase flows.

Nomenclature

AAEM	alkali and alkaline earth metal
AD	Adaro coal
BFB	bubbling fluidized bed
CFD	chemical fluid dynamics
DTR	drop-tube reactor
GLYC	partially gasified Loy Yang coal char
LY	Loy Yang coal
LYC	Loy Yang coal char
TB-CFB	triple-bed combined circulating fluidized-bed reactor
X_{char}	net conversion of the primary char

References

- Abu El-Rub Z., Bramer E.A., Brem G., Review of Catalysts for Tar Elimination in Biomass Gasification Processes, *Industrial & Engineering Chemistry Research*, 43 (2004a) 6911–6919. <http://doi.org/10.1021/ie0498403>
- Abu El-Rub Z., Bramer E.A., Brem G., Modeling of tar reduction in biomass fuelled gasification using biomass char as a catalyst, In *Proceeding of Conference and Technology Exhibition on Biomass for Energy, Industry and Climate Protection*, (2004b) 530–541. http://www.abuelrub.com/uploads/7/2/4/0/7240057/canada_2004.pdf
- Abu El-Rub Z., Biomass Char As an in-Situ Catalyst for Tar Removal in Gasification Systems, PhD thesis, Twente University, Enschede, The Netherlands March 2008.
- Bayarsaikhan B., Hayashi J., Shimada T., Sathe C., Li C., Tsutsumi A., Chiba T., Kinetics of steam gasification of nascent char from rapid pyrolysis of a Victorian brown coal, *Fuel*, 84 (2005) 1612–1621. <http://doi.org/10.1016/j.fuel.2005.02.008>
- Cazorla-Amoros D., Linares-Solano A., Salinas-Martinez de Lecea C., Nomura M., Yamashita H., Tomita A., Local structure of calcium species dispersed on carbon: influence of the metal loading procedure and its evolution during pyrolysis, *Energy & Fuels*, 7 (1993) 625–631. <http://doi.org/10.1021/ef00041a010>
- Devi L., Ptasiński K.J., Janssen F.J.J.G., A review of the primary measures for tar elimination in biomass gasification processes, *Biomass and Bioenergy*, 24 (2002) 125–140. [http://doi.org/10.1016/S0961-9534\(02\)00102-2](http://doi.org/10.1016/S0961-9534(02)00102-2)
- Fuentes-Cano D., Gómez-Barea A., Nilsson S., Ollero P., Decomposition kinetics of model tar compounds over chars with different internal structure to model hot tar removal in biomass gasification, *Chemical Engineering Journal*, 228 (2013) 1223–1233. <http://doi.org/10.1016/j.cej.2013.03.130>
- Fushimi C., Guan G., Nakamura Y., Ishizuka M., Tsutsumi A., Matsuda S., Suzuki Y., Hydrodynamic characteristics of a large-scale triple-bed combined circulating fluidized bed, *Powder Technology*, 209 (2011) 1–8. <http://doi.org/10.1016/>

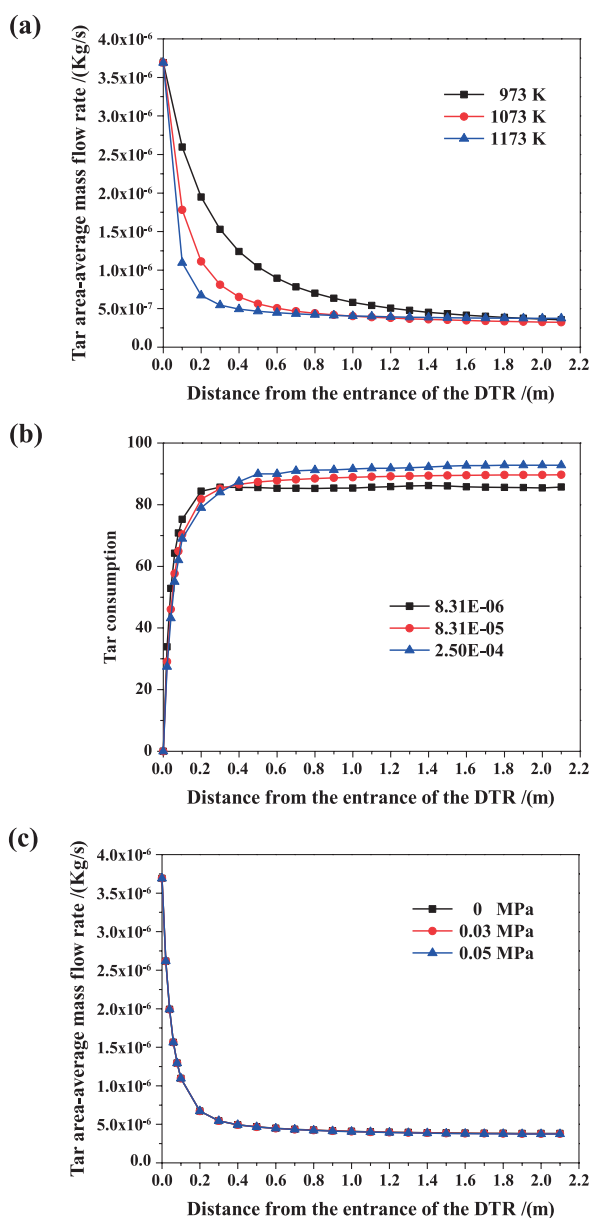


Fig. 6 The effect of reaction conditions on tar consumption as a function of the distance from the entrance of the DTR: (a) temperature; (b) solid hold-up; and (c) steam partial pressure (Li C.Y. et al., 2015). Reprinted with permission from Ref. (Li C.Y. et al., 2015). Copyright: (2015) Elsevier B.V.

- j.powtec.2011.01.018
- Fushimi C., Guan G., Nakamura Y., Ishizuka M., Tsutsumi A., Suzuki Y., Wang C.-H., Mixing behaviors of cold-hot particles in the downer of a triple-bed combined circulating fluidized bed, *Powder Technology*, 221 (2012) 70–79. <http://doi.org/10.1016/j.powtec.2011.12.017>
- Gilbert P., Ryu C., Sharifi V., Swithenbank J., Tar reduction in pyrolysis vapours from biomass over a hot char bed, *Biore-source Technology*, 100 (2009) 6045–6051. <http://doi.org/10.1016/j.biortech.2009.06.041>
- Goyal A., Rehmat A., Fuel Evaluation for a Fluidized-Bed Gasification Process (U-GAS), In *Clean Energy from Waste and Coal* (1992) 58–71. <http://doi.org/10.1021/bk-1992-0515.ch005>
- Guan G., Fushimi C., Tsutsumi A., Prediction of flow behavior of the riser in a novel high solids flux circulating fluidized bed for steam gasification of coal or biomass, *Chemical Engineering Journal*, 164 (2010a) 221–229. <http://doi.org/10.1016/j.cej.2010.08.005>
- Guan G., Fushimi C., Tsutsumi A., Ishizuka M., Matsuda S., Hatano H., Suzuki Y., High-density circulating fluidized bed gasifier for advanced IGCC/IGFC—Advantages and challenges, *Particuology*, 8 (2010b) 602–606. <http://doi.org/10.1016/j.partic.2010.07.013>
- Guan G., Fushimi C., Ishizuka M., Nakamura Y., Tsutsumi A., Matsuda S., Wang C.-H., Flow behaviors in the downer of a large-scale triple-bed combined circulating fluidized bed system with high solids mass fluxes, *Chemical Engineering Science*, 66 (2011) 4212–4220. <http://doi.org/10.1016/j.ces.2011.06.006>
- Haga T., Nishiyama Y., Influence of structural parameters on coal char gasification, *Fuel*, 67 (1988) 748–752. [http://doi.org/10.1016/0016-2361\(88\)90144-5](http://doi.org/10.1016/0016-2361(88)90144-5)
- Hayashi J.I., Iwatsuki M., Morishita K., Tsutsumi A., Li C.Z., Chiba T., Roles of inherent metallic species in secondary reactions of tar and char during rapid pyrolysis of brown coals in a drop-tube reactor, *Fuel*, 81 (2002) 1977–1987. [http://doi.org/10.1016/S0016-2361\(02\)00128-X](http://doi.org/10.1016/S0016-2361(02)00128-X)
- Hayashi J.I., Kudo S., Kim H.S., Norinaga K., Matsuoka K., Hosokai S., Low-temperature gasification of biomass and lignite: Consideration of key thermochemical phenomena, rearrangement of reactions, and reactor configuration, *Energy and Fuels*, 28 (2014) 4–21. <http://doi.org/10.1021/ef401617k>
- Hayashi J.I., Takahashi H., Iwatsuki M., Essaki K., Tsutsumi A., Chiba T., Rapid conversion of tar and char from pyrolysis of a brown coal by reactions with steam in a drop-tube reactor, *Fuel*, 79 (2000) 439–447. [http://doi.org/10.1016/S0016-2361\(99\)00179-9](http://doi.org/10.1016/S0016-2361(99)00179-9)
- Hobbs M.L., Radulovic P.T., Smoot L.D., Combustion and gasification of coals in fixed-beds, *Progress in Energy and Combustion Science*, 19 (1993) 505–586. [http://doi.org/10.1016/0360-1285\(93\)90003-W](http://doi.org/10.1016/0360-1285(93)90003-W)
- Hosokai S., Hayashi J.-I., Shimada T., Kobayashi Y., Kuramoto K., Li C.-Z., Chiba T., Spontaneous Generation of Tar Decomposition Promoter in a Biomass Steam Reformer, *Chemical Engineering Research and Design*, 83 (2005) 1093–1102. <http://doi.org/10.1205/cherd.04101>
- Hosokai S., Kumabe K., Ohshita M., Norinaga K., Li C., Hayashi J.-I., Mechanism of decomposition of aromatics over charcoal and necessary condition for maintaining its activity, *Fuel*, 87 (2008) 2914–2922. <http://doi.org/10.1016/j.fuel.2008.04.019>
- Jamil K., Hayashi J.I., Li C.-Z., Pyrolysis of a Victorian brown coal and gasification of nascent char in CO₂ atmosphere in a wire-mesh reactor, *Fuel*, 83 (2004) 833–843. <http://doi.org/10.1016/j.fuel.2003.09.017>
- Kajita M., Kimura T., Norinaga K., Li C.-Z., Hayashi J.I., Catalytic and Noncatalytic Mechanisms in Steam Gasification of Char from the Pyrolysis of Biomass, *Energy & Fuels*, 24 (2010) 108–116. <http://doi.org/10.1021/ef900513a>
- Kajitani S., Tay H.-L., Zhang S., Li C.-Z., Mechanisms and kinetic modelling of steam gasification of brown coal in the presence of volatile-char interactions, *Fuel*, 103 (2013) 7–13. <http://doi.org/10.1016/j.fuel.2011.09.059>
- Kim H., Kudo S., Tahara K., Hachiyama Y., Yang H., Norinaga K., Hayashi J.I., Detailed Kinetic Analysis and Modeling of Steam Gasification of Char from Ca-Loaded Lignite, *Energy & Fuels*, 27 (2013) 6617–6631. <http://doi.org/10.1021/ef401688h>
- Krerkkaiwan S., Mueangta S., Thammarat P., Jaisat L., Kuchonthara P., Catalytic Biomass-Derived Tar Decomposition Using Char from the Co-pyrolysis of Coal and Giant Leucaena Wood Biomass, *Energy & Fuels*, 29 (2015) 3119–3126. <http://doi.org/10.1021/ef502792x>
- Krerkkaiwan S., Tsutsumi A., Kuchonthara P., Biomass derived tar decomposition over coal char bed, *ScienceAsia*, 39 (2013) 511. <http://doi.org/10.2306/scienceasia1513-1874.2013.39.511>
- Lan X., Xu C., Wang G., Wu L., Gao J., CFD modeling of gas-solid flow and cracking reaction in two-stage riser FCC reactors, *Chemical Engineering Science*, 64 (2009) 3847–3858. <http://doi.org/10.1016/j.ces.2009.05.019>
- Li C.Y., Appari S., Zhang L.X., Huang A.N., Kuo H.P., Kudo S., Hayashi J.-I., Norinaga K., Modeling of gas/particle flow in coal conversion with a drop tube reactor using a lumped kinetic model accounting volatiles-char interaction, *Fuel Processing Technology*, 138(2015) 588–594. <http://dx.doi.org/10.1016/j.fuproc.2015.06.043>
- Li C.Z., Importance of volatile-char interactions during the pyrolysis and gasification of low-rank fuels—A review, *Fuel*, 112 (2013) 609–623. <http://doi.org/10.1016/j.fuel.2013.01.031>
- Li C.Z., Special Issue—Gasification: a Route to Clean Energy, *Process Safety and Environmental Protection*, 84 (2006) 407–408. <http://doi.org/10.1205/psep.ed.0606>
- Li X.T., Grace J.R., Lim C.J., Watkinson A.P., Chen H.P., Kim J.R., Biomass gasification in a circulating fluidized bed, *Biomass and Bioenergy*, 26 (2004) 171–193. [http://doi.org/10.1016/S0961-9534\(03\)00084-9](http://doi.org/10.1016/S0961-9534(03)00084-9)
- Liu Z., Zhu H., Steam gasification of coal char using alkali and alkaline-earth metal catalysts, *Fuel*, 65 (1986) 1334–1338. [http://doi.org/10.1016/0016-2361\(86\)90099-2](http://doi.org/10.1016/0016-2361(86)90099-2)
- Lussier M.G., Zhang Z., Miller D.J., Characterizing rate inhibition in steam/hydrogen gasification via analysis of adsorbed hydrogen, *Carbon*, 36 (1998) 1361–1369. [http://doi.org/10.1016/S0008-682X\(98\)00084-9](http://doi.org/10.1016/S0008-682X(98)00084-9)

- 1016/S0008-6223(98)00123-7
- Mašek O., Hosokai S., Norinaga K., Li C.Z., Hayashi J.I., Rapid gasification of nascent char in steam atmosphere during the pyrolysis of Na- and Ca-Ion-exchanged brown coals in a drop-tube reactor, *Energy and Fuels*, 23 (2009) 4496–4501. <http://doi.org/10.1021/ef900235e>
- Matsuhara T., Hosokai S., Norinaga K., Matsuoka K., Li C.Z., Hayashi J.I., In-situ reforming of tar from the rapid pyrolysis of a brown coal over char, *Energy and Fuels*, 24 (2010) 76–83. <http://doi.org/10.1021/ef9005109>
- Mühlen H.-J., van Heek K.H., Jüntgen H., Kinetic studies of steam gasification of char in the presence of H₂, CO₂ and CO, *Fuel*, 64 (1985) 944–949. [http://doi.org/10.1016/0016-2361\(85\)90149-8](http://doi.org/10.1016/0016-2361(85)90149-8)
- Ohtsuka Y., Asami K., Ion-Exchanged Calcium from Calcium Carbonate and Low-Rank Coals: High Catalytic Activity in Steam Gasification, *Energy & Fuels*, 10 (1996) 431–435. <http://doi.org/10.1021/ef950174f>
- Ohtsuka Y., Asami K., Highly active catalysts from inexpensive raw materials for coal gasification, *Catalysis Today*, 39 (1997) 111–125. [http://doi.org/10.1016/S0920-5861\(97\)00093-X](http://doi.org/10.1016/S0920-5861(97)00093-X)
- Ohtsuka Y., Tomita A., Calcium catalysed steam gasification of Yallourn brown coal, *Fuel*, 65 (1986) 1653–1657. [http://doi.org/10.1016/0016-2361\(86\)90264-4](http://doi.org/10.1016/0016-2361(86)90264-4)
- Radovic L.R., Walker Jr. P.L., Jenkins R.G., Catalytic coal gasification: use of calcium versus potassium, *Fuel*, 63 (1984) 1028–1030. [http://doi.org/10.1016/0016-2361\(84\)90329-6](http://doi.org/10.1016/0016-2361(84)90329-6)
- Radovic L.R., Walker P.L., Jenkins R.G., Importance of catalyst dispersion in the gasification of lignite chars, *Journal of Catalysis*, 82 (1983) 382–394. [http://doi.org/10.1016/0021-9517\(83\)90205-1](http://doi.org/10.1016/0021-9517(83)90205-1)
- Ropelato K., Meier H.F., Cremasco M.A., CFD study of gas-solid behavior in downer reactors: An Eulerian-Eulerian approach, *Powder Technology*, 154 (2005) 179–184. <http://doi.org/10.1016/j.powtec.2005.05.005>
- Sathe C., Pang Y., Li C.Z., Effects of heating rate and ion-exchangeable cations on the pyrolysis yields from a Victorian brown coal, *Energy and Fuels*, 13 (1999) 748–755. <http://doi.org/10.1021/ef980240o>
- Simell P., Kurkela E., Stahlberg P., Hepola J., Catalytic hot gas cleaning of gasification gas, *Catalysis Today*, 27 (1997) 3–68. [http://doi.org/10.1016/0920-5861\(95\)00172-7](http://doi.org/10.1016/0920-5861(95)00172-7)
- Sun Q., Yu S., Wang F., Wang J., Decomposition and gasification of pyrolysis volatiles from pine wood through a bed of hot char, *Fuel*, 90 (2011) 1041–1048. <http://doi.org/10.1016/j.fuel.2010.12.015>
- Takarada T., Nabatame T., Ohtsuka Y., Tomita A., Steam gasification of brown coal using sodium chloride and potassium chloride catalysts, *Industrial & Engineering Chemistry Research*, 28 (1989) 505–510. <http://doi.org/10.1021/ie00089a001>
- Theologos K.N., Markatos N.C., Advanced modeling of fluid catalytic cracking riser-type reactors, *AIChE Journal*, 39 (1993) 1007–1017. <http://doi.org/10.1002/aic.690390610>
- Trisanti D., Supramono D., Suwignjo R.K., Catalytic Effect of K₂CO₃ in Steam Gasification of Lignite Char on Mole Ratio of H₂/CO in Syngas, *International Journal of Technology*, 6 (2015) 22. <http://doi.org/10.14716/ijtech.v6i1.208>
- Tyler R.J., Schafer H.N.S., Flash pyrolysis of coals: influence of cations on the devolatilization behaviour of brown coals, *Fuel*, 59 (1980) 487–494. [http://doi.org/10.1016/0016-2361\(80\)90175-1](http://doi.org/10.1016/0016-2361(80)90175-1)
- Wu H., Li X., Hayashi J.I., Chiba T., Li C.-Z., Effects of volatile-char interactions on the reactivity of chars from NaCl-loaded Loy Yang brown coal, *Fuel*, 84 (2005) 1221–1228. <http://doi.org/10.1016/j.fuel.2004.06.037>
- Yamashita H., Nomura M., Tomita A., Local structures of metals dispersed on coal. 4. Local structure of calcium species on coal after heat treatment and carbon dioxide gasification, *Energy & Fuels*, 6 (1992) 656–661. <http://doi.org/10.1021/ef00035a018>
- Yamashita H., Yoshida S., Tomita A., Local structures of metals dispersed on coal. 3. Na K-edge XANES studies on the structure of sodium gasification catalyst, *Industrial & Engineering Chemistry Research*, 30 (1991) 1651–1655. <http://doi.org/10.1021/ie00055a037>
- Yang R.T., Duan R.Z., Kinetics and mechanism of gas-carbon reactions: Conformation of etch pits, hydrogen inhibition and anisotropy in reactivity, *Carbon*, 23 (1985) 325–331. [http://doi.org/10.1016/0008-6223\(85\)90118-6](http://doi.org/10.1016/0008-6223(85)90118-6)
- Zhang L.X., Kudo S., Tsubouchi N., Hayashi J.I., Ohtsuka Y., Norinaga K., Catalytic effects of Na and Ca from inexpensive materials on in-situ steam gasification of char from rapid pyrolysis of low rank coal in a drop-tube reactor, *Fuel Processing Technology*, 113 (2013a) 1–7. <http://doi.org/10.1016/j.fuproc.2013.03.009>
- Zhang L.X., Matsuhara T., Kudo S., Hayashi J.I., Norinaga K., Rapid pyrolysis of brown coal in a drop-tube reactor with co-feeding of char as a promoter of in situ tar reforming, *Fuel*, 112 (2013b) 681–686. <http://doi.org/10.1016/j.fuel.2011.12.030>
- Zhao Y., Cheng Y., Ding Y., Jin Y., Understanding the hydrodynamics in a 2-dimensional downer by CFD-DEM simulation, In *The 12th International Conference on Fluidization—New Horizons in Fluidization Engineering*, 2007.

Author's short biography



Cheng-Yi Li

Cheng-Yi Li received his PhD by accomplishing a study on modelling and simulation on reacting flow included in thermochemical conversion process of coal in 2015 at Kyushu University. He received his bachelor and master degrees at China University of Mining and Technology (Beijing) and currently working at China Tianchen Engineering Corporation as a process engineer for designing and developing advanced chemical plants in different fields, such as coal gasification plant, petrochemical plant and so on.



Li-Xin Zhang

Li-Xin Zhang received his PhD by accomplishing a study on the decomposition characteristics of tar derived from low temperature gasification of brown coal over coexisting char in 2013 at Kyushu University. He received his bachelor and master degrees at China University of Mining and Technology (Beijing) and currently working at Xi'an Thermal Power Research Institute Co. Ltd. (P.R. China) for developing coal-based poly-generation system and advanced coal power generation system.



Shinji Kudo

Shinji Kudo is an assistant professor at Institute for Materials Chemistry and Engineering, Kyushu University. He obtained his Ph.D. in Chemical Engineering from Kyoto University (2010) where he studied catalyst and reactor design for hydrogen production by steam reforming of methanol. He was an assistant professor at Research and Education Center of Carbon Resources, Kyushu University in 2010–2012, and moved to the present position in 2013. His current research focus is on thermochemical conversion of lignocellulosic biomass and lignite for production of syngas, valuable chemicals, carbonaceous materials, and coke.



Jun-ichiro Hayashi

Jun-ichiro Hayashi has been a professor of Institute for Materials Chemistry and Engineering, Kyushu University, since 2009, and also Director of Research and Education Center of Carbon Resources, Kyushu University, since 2012. He received his doctoral degree (Engineering) from Kyushu University in 1996. He was an associate professor (1996–2005), and then professor (2005–2009) of Hokkaido University. His major academic field is chemical engineering and chemical reaction engineering. His research area ranges over upgrading and conversion of carbon resources, carbon/inorganic materials, and environmental technologies.



Koyo Norinaga

Koyo Norinaga has been an Associate Professor of Institute for Materials Chemistry and Engineering, Kyushu University since 2009. He received his doctoral degree in 1999 in applied chemistry at Hokkaido University. He was an assistant professor at Tohoku University (1999–2002), a senior scientist (Humboldt fellow) at Karlsruher Institute of Technology (Karlsruhe, Germany, 2002–2006), and an associate professor at Hokkaido University (2006–2009). His research covers modeling and simulation of chemically reacting flows, including pyrolysis of light hydrocarbons, gasification and combustion of coal and biomass, and CVD/CVI of carbon and silicon carbide for composite material production.



Synthesis of Nanoparticles by Laser Ablation: A Review[†]

Myungjoon Kim¹, Saho Osone², Taesung Kim^{1,3},
Hidenori Higashi² and Takafumi Seto^{2*}

¹ School of Mechanical Engineering, Sungkyunkwan University, Korea

² Faculty of Natural System, Kanazawa University, Japan

³ SKKU Advanced Institute of Nano Technology (SAINT), Sungkyunkwan University, Korea

Abstract

Laser ablation is a method for fabricating various kinds of nanoparticles including semiconductor quantum dots, carbon nanotubes, nanowires, and core shell nanoparticles. In this method, nanoparticles are generated by nucleation and growth of laser-vaporized species in a background gas. The extremely rapid quenching of vapor is advantageous in producing high purity nanoparticles in the quantum size range (< 10 nm). In this review, the formation mechanism of nanoparticles by laser ablation is summarized. Recent progress on the control of nanoparticle size and the challenges for functional nanoparticle synthesis by advanced laser ablation technology are then discussed.

Keywords: laser ablation, nanoparticle, quantum dot, nanocarbons

1. Introduction

Nanoparticles have a variety of unique properties that are not observable in bulk materials (Buzea et al., 2007). The most critical characteristic of nanoparticles is that the properties (electrical, optical, magnetic, and so on) depend strongly on the size and size distribution of the particles (Kim et al., 2014). For example, silicon nanoparticles are photoluminescent in the visible spectrum at room temperature (Kenemitsu, 1995; Yoshida et al., 1998); the wavelength of the emitted light can be controlled with the particle size (Orie et al., 2003a). Nano-sized titania particles have also gathered attention as building blocks for photovoltaic devices (O'regan and Gratzel, 1991) and for photocatalytic applications (Fujishima and Honda, 1972). The photochemical properties of titania nanoparticles also have a strong dependence on particle size as well as on crystal structure. Many kinds of nanoparticles exhibit special characteristics (ferromagnetism, paramagnetism, pinned emission, fluorescence, spin quantum effect, etc.) when the size of a particle is at the nanoscale level (Zheng et al., 2004; Kim et al., 2011; Kim et al., 2014). The spe-

cial characteristics are significantly impacted by the size and size distribution of the particles.

Various nanoparticle fabrication methods have been developed with the bottom-up approach in the liquid phase (including sol-gel and chemical reduction) as well as vapor phase (such as physical/chemical vapor deposition and flame synthesis). Each fabrication method has advantages and disadvantages. Liquid phase methods are cost-effective and are used for synthesizing various kinds of nanoparticles with well-controlled structures at the laboratory scale. Vapor phase processes are superior at synthesizing high purity nanoparticles by means of the continuous flow reactor. In both of the liquid and gas bottom-up processes, solid nanoparticles are generated from the nucleation of supersaturated species that are prepared by precursor reactions and/or evaporation of solids. Laser ablation is a method that utilizes laser (which is an acronym for light amplification by stimulated emission of radiation) as an energy source for ablating solid target materials. In this process, extremely high energy is concentrated at a specific point on a solid surface to evaporate light-absorbing material. The term 'ablation' refers to the removal of surface atoms and involves not only a single photon process (breaking the chemical bonds) but also multiphoton excitation (thermal evaporation). High-purity nanoparticles can be generated by laser ablation because the purity of the particles is basically determined by the purity of the target and ambient media (gas or liquid) without contamination from the reactor. However, it is difficult to control size distribution, agglomeration, and

[†] Received 25 January 2016; Accepted 22 March 2016
J-STAGE Advance Publication online 30 April 2016

^{1,3} 300 Cheoncheon-dong, Jangan-gu, Suwon, Gyeonggi, 440-746, Korea

² Kakuma-machi, Kanazawa, Ishikawa 920-1192, Japan

* Corresponding author: Takafumi Seto;

E-mail: t.seto@staff.kanazawa-u.ac.jp

TEL: +81-76-234-4815 FAX: +81-76-264-6239



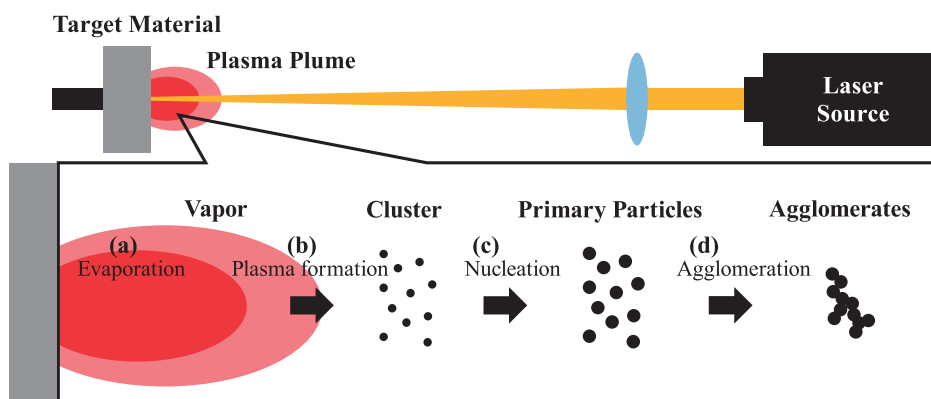


Fig. 1 Schematic of particle generation procedure in the laser ablation process.

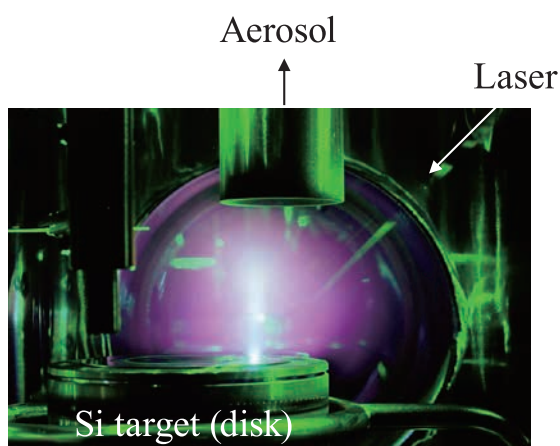


Fig. 2 Laser-induced plume of silicon in low pressure.

crystal structure in the conventional laser ablation process since nanoparticles are built by random (Brownian) motion of molecules. Therefore, several advanced laser ablation techniques have been developed for fabricating morphology-controlled nanoparticles. In this review, laser ablation-based nanoparticle formation processes and their mechanisms are briefly discussed, followed by a review of recent studies of laser ablation techniques for synthesizing various kinds of nanoparticles. Finally, advanced laser ablation processes for synthesizing functional nanomaterials with highly controlled nanostructures are introduced.

2. Nanoparticle formation by laser ablation

2.1 Basic concept of laser ablation

Fig. 1 is a schematic of the nanoparticle formation process by laser ablation. When the laser beam is focused on the surface of a solid target material in the ambient media (gas or liquid), the temperature of the irradiated spot rapidly increases, vaporizing the target material. The colli-

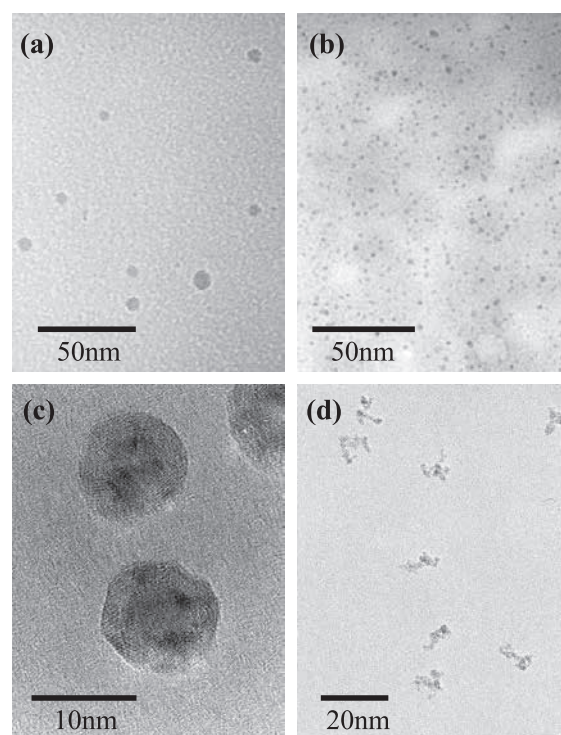


Fig. 3 Typical transmission electron micrographs of laser ablation-generated (a) silicon, (b) carbon and (c) surface-oxidized nickel nanoparticles. (d) Aggregates of nickel nanoparticles as a result of coagulation and necking.

sions between the evaporated species (atom and clusters) and the surrounding molecules result in excitation of the electron state coupled with light emission and generation of electrons and ions, forming a laser-induced plasma plume (Fig. 2). The plasma structures (size of the plume and its emission spectrum) depend on the target material, ambient media (liquid or gas), ambient pressure, and laser conditions. Fig. 3 shows typical transmission electron micrographs of nanoparticles generated by laser ablation of various materials. In general, laser ablation in low-pressure background gas is preferable for creating a large plume and works well in generating small particles (Fig. 3(a)).

Laser ablation in liquid is employed to confine the plasma plume in a small region to directly disperse nanoparticles in the liquid phase (**Fig. 3(b)**). In any case, the ambient media must be carefully selected because the laser-generated particles easily react with surrounding molecules to create complexes such as oxides and other undesirable species (**Figs. 3(b) and (c)**). Coagulation is another critical phenomena that must be finely controlled in the later stages of nanoparticle formation. Since laser-generated particles have a very clean surface, agglomerated particles create chemical bonds at the contact point (neck), which significantly compromise the properties of primary particles (**Fig. 3(d)**, Sakiyama et al., 2004). The low-pressure gas process is advantageous not only for reducing the size of the primary particles but also for preventing coagulation.

2.2 Laser

For the fabrication of nanoparticles of the desired size and structure, the selection of a suitable laser system is one of the most critical decisions. The evaporation rate of the target material is generally determined by the laser parameters (laser source, wavelength, fluence, pulse width and frequency), the light absorption efficiency of the target material, and the condition of the ambient media. Laser energy per unit area on the target material is defined as fluence of the laser F , which is given as,

$$F = \frac{I}{A} \quad (1)$$

where I [J/pulse] is the laser power and A [m²] is the area of the laser spot. In the case of silicon nanoparticle formation using the double harmonic wave of the Nd:YAG laser (wavelength of 532 nm), a laser with a fluence (F) of more than several J/cm² is frequently used. The wavelength of the laser is another important parameter that determines the absorption efficiency of the target. The absorption depth and spot (focusing) area are also influenced by laser wavelength (Friedrich et al., 1998). In early studies of nanoparticle synthesis by laser ablation, excimer lasers in the ultraviolet spectrum (193 nm for ArF, 248 nm for KrF) are often used as a light source (Yoshida et al., 1996; Shinde et al., 2000). Recently, Q-switch pumped pulsed YAG (Yttrium Aluminum Garnet) lasers are more commonly used for laser ablation because they do not require hazardous gases. The wavelength of Nd:YAG laser (1,064 nm for fundamental wave) can be changed by employing nonlinear optical crystals. For example, 532 nm for second harmonic generation and 355 nm for third harmonic and other frequency mixing are possible. Overall, it is difficult to attain stable ablation using the fundamental wave because of the weaker light absorption in the infrared region (Lu et al., 2008). Torrisi et al. (2003) investigated the effect of wavelength on laser ablation of

solid Cu using a 1064 nm Nd:YAG laser and a 308 nm XeCl excimer laser. They showed that UV laser is more efficient at evaporating the copper atoms, even though infrared radiation has higher ionic kinetic energy and higher plasma temperature. Lu et al. (2008) calculated the evaporation thresholds of Si and estimated them to be 2×10^{10} W/cm² for a 266 nm wavelength laser and 4×10^{11} W/cm² for a 532 nm wavelength laser. Short pulse lasers (nanoseconds) with less energy density have also been used to generate Si nanoparticles. As an example, Seto et al. (2001b) generated Si nanoparticles with a 5 ns pulsed Nd:YAG laser (532 nm) with an average fluence of 16 J/cm² (about 3×10^9 W/cm²). The pulse width of the laser is also another important parameter that determines peak energy. Recently picosecond (Lau et al., 2014) and femtosecond lasers (Fischer et al., 2015) have been applied to enhance the photon absorption efficiency of the target surface to break chemical bonding.

2.3 Change in the temperature by laser irradiation

When the target surface is irradiated with short laser pulses, the absorbed photon energy is transferred to the solid lattice as a form of thermal (internal) energy. Heat transfer in the electron and lattices subsystems can be characterized by the following one-dimensional, two-temperature diffusion equations with temperatures of electron T_e and lattices T_i (Chichkov et al., 1996).

$$C_e \frac{\partial T_e}{\partial t} = -\frac{\partial Q(z)}{\partial z} - \gamma(T_e - T_i) + S \quad (2)$$

$$C_i \frac{\partial T_i}{\partial t} = \gamma(T_e - T_i) \quad (3)$$

$$Q(z) = -k_e \frac{\partial T_e}{\partial z}, \quad S = I(t)A\alpha \exp(-\alpha z) \quad (4)$$

where C_e and C_i are the heat capacities of the electron and lattices subsystems, z is perpendicular direction to the heat surface, $Q(z)$ is the heat flux, γ is the electron-phonon coupling strength, S is the laser source term, k_e is the heat conductivities of the electron, $I(t)$ is the laser intensity, A is the absorbance of the sample, and $1/\alpha$ can be defined as the optical penetration depth.

Equations (2–4) can be modified for the laser pulse width. In the case of nanosecond laser pulses, T_e is assumed to be equal to T_i (Chichkov et al., 1996) due to the duration of the laser pulse being much larger than the lattice heating time. Then equations (2–4) can be reduced to

$$C_i \frac{\partial T_i}{\partial t} = \frac{\partial}{\partial z} \left(k_o \frac{\partial T}{\partial z} \right) + I(t)A\alpha \exp(-\alpha z) \quad (5)$$

where, k_o is the conventional equilibrium thermal conduc-

tivity of a substance.

2.4 Nucleation and particle growth

Since the laser-vaporized materials are very rapidly quenched from extremely high temperatures (> 5000 K) to room temperature (usually shorter than $50 \mu\text{s}$ after the laser pulse; Wen et al., 2006), nanometer-sized particles form by supersaturated vapor nucleation at the edge of the laser plume (**Fig. 1(c)**). The change in the number concentration of vaporized material (monomer), clusters, and particles can be given by the general dynamic equation (Pratsinis and Kim, 1989) by considering nucleation, condensation, and coagulation. Numerical simulations of the solutions to the general dynamic equation have been conducted for predicting the size distribution of nanoparticles generated by the ablation process (Wen et al., 2007; Kuroda et al., 2012). It should be noted that there are significant contributions of electron and ion species on the nucleation process, *i.e.* ion-induced nucleation in the laser ablation process. As a result, the particles generated by the laser ablation were electrically charged (Seto et al., 2003). However, it is still difficult to reproduce the rapid change in the size distribution due to nucleation and growth of the laser-vaporized materials. To experimentally analyze the particle formation process, advanced in-situ observation techniques are necessary. Emission spectroscopy of plumes (Geohegan et al., 1998) is one in-situ measurement technique for investigating the dynamics of particle formation. The mobility analyzing technique may also be applied to investigate the effect of particle generation conditions on the size distribution as discussed later in this review.

3. Synthesis of various kinds of nanoparticles by laser ablation

3.1 Semiconductor quantum dot

A semiconductor quantum dot is a nanocrystal that exhibits quantum properties such as tunable light emission driven by the quantum confinement effect (Canham, 2000) and single electron transport phenomena (Tilke et al., 2001). There are some reports on the synthesis of II–VI and III–V semiconductor quantum dots by laser ablation such as formation of GaAs nanocrystals (Perriere et al., 2001), ZnSe and CdS quantum dots (Anikin et al., 2002), CdSe and CdTe nanoparticles (Ruth and Young, 2006) that can be applied to the study of optical imaging therapy (Wolfbeisref, 2015). However, the laser ablation process for composite materials is challenged in controlling the stoichiometry and crystallinity in the process for rebuilding laser-vaporized elements. Group-IV ele-

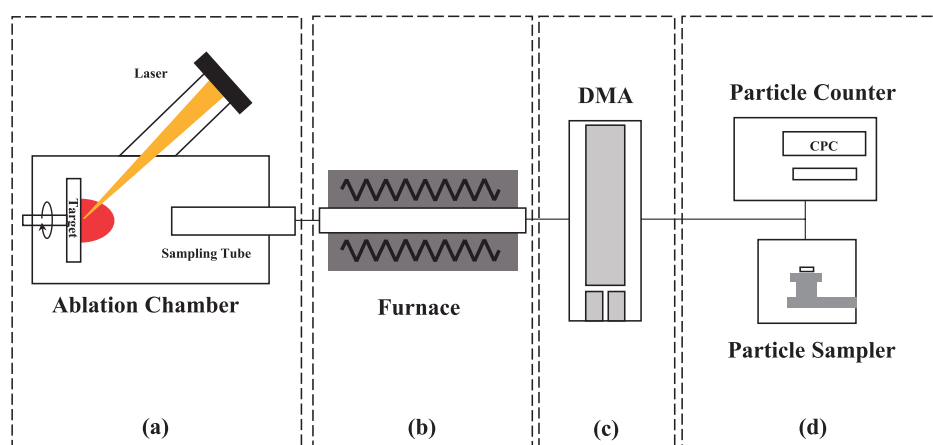
ments such as silicon and germanium and carbon nanoparticles are single element semiconductors. Silicon and carbon are abundant (non-rare metal) elements that exhibit a variety of unique properties when the particle sizes are in the nanometer range. Therefore, we will focus on the synthesis of silicon and carbon nanoparticles in this review.

Table 1 lists laser ablation studies on silicon nanoparticle synthesis. Okada and Iijima (1991) measured the oxidation rate of silicon nanoparticles generated by laser ablation and found that the oxidation rate drops with decreasing particle size. They used a YAG laser of 12 millisecond pulse width and produced 20–500 nm particles under pressures of 0.75 to 3 Pa. Yoshida et al. (1996) synthesized silicon crystallites in gas between pressures of 333 to 1330 Pa using an argon-fluoride (ArF) excimer laser (193 nm wavelength, 12 ns pulse width, fluence 1 J/cm^2). They showed mean diameter of particle can be varied as a function of the He background gas pressure. The mean diameter calculated from the SEM images were about 23 nm at 333 Pa, 36 nm at 432 Pa, and 52 nm at 665 Pa. Pressure effects on particle size in laser ablation generation was studied in more detail by Seto et al. (2003) through particle classification with a low pressure differential mobility analyzer (low pressure DMA, LPDMA, see later section). Suzuki et al. (2001) investigated the suitability of LPDMA as a size classification tool for the silicon nanoparticles generated by laser ablation under low-pressure conditions. They compared the mode size and the geometrical standard deviation (GSD) of silicon nanoparticles with and without LPDMA size classification. The GSD was significantly reduced from 1.6 (as-prepared) to 1.2 for particles as small as 4 nm after classification by LPDMA. The results indicate that size classification is effective for generating the monodispersed nanoparticles that can be used to clarify the relationship between quantum properties and size.

Another important factor affecting the quantum properties of Si nanoparticles is their crystallinity. Unfortunately, laser ablation tends to generate amorphous agglomerates which have poor (broad) optical properties (Hirasawa et al., 2004). Gas phase annealing is an effective method to improve crystallinity and the shape of the Si nanoparticles. **Fig. 4** shows laser ablation process coupled with gas phase annealing, particle classifying, and particle measurement systems. Since laser ablation systems have good compatibility with gas flow reactors and other instruments as shown in **Fig. 4.**, particle morphologies (size, shape and crystallinity etc.) can be controlled in the aerosol phase. Hirasawa et al. (2004) investigated the change in the crystallinity of Si nanoparticles by Raman spectroscopy and TEM as a function of the gas-phase annealing temperature. They also employed LPDMA for size selection and studied the size-dependent crystalli-

Table 1 Silicon nanoparticle synthesis studies using pulsed laser ablation method (A: annealing, m: mean, M: mode)

Author	Laser Source	Pressure	Additional Process	Particle	Particle size
Okada and Iijima 1991	YAG	0.75~3.0 Pa			20~500 nm
Yoshida et al. 1996	ArF excimer	333~1330 Pa			3~100 nm
		333 Pa		Aggregates	(m) 23 nm
		434 Pa		Aggregates	(m) 36 nm
		666 Pa		Aggregates	(m) 52 nm
Seto et al. 2001a	Nd:YAG	666 Pa	DMA	Primary	2~7 nm
Seto et al. 2001b	Nd:YAG	666 Pa	DMA	Primary	(M) 7, 10 nm
Suzuki et al. 2001	Nd:YAG	666 Pa		Primary	(M) 6 nm
		666 Pa	DMA	Primary	(M) 3.8 nm
Seto et al. 2003	Nd:YAG	333 Pa		Aggregates	~70 nm
		666 Pa		Aggregates	~120 nm
		280 Pa	DMA	Primary	(M) 5 nm
		334 Pa	DMA	Primary	(M) 4 nm
		380 Pa	DMA	Primary	(M) 4 nm
		380 Pa	DMA	Aggregates	(M) > 6 nm
		434 Pa	DMA	Primary	(M) 4 nm
		434 Pa	DMA	Aggregates	(M) > 6 nm
Orii et al. 2003a	Nd:YAG	931 Pa	(A) 900 °C, DMA	Primary	(M) 3~6 nm
Orii et al. 2003b	Nd:YAG	931 Pa	(A) 900 °C, DMA	Primary	(M) 6.9 nm
Hirasawa et al. 2004	Nd:YAG	1000 Pa	(A) 300 °C, DMA	Primary	(M) > 14 nm
		1000 Pa	(A) 500 °C, DMA	Primary	(M) 11.2 nm
		1000 Pa	(A) 700 °C, DMA	Primary	(M) 10.3 nm
		1000 Pa	(A) 900 °C, DMA	Primary	(M) 10 nm
Hirasawa et al. 2006	Nd:YAG	1000 Pa	DMA	Primary	7~14 nm

**Fig. 4** Schematic of nanoparticle synthesis process using laser ablation, which is composed of (a) particle generation, (b) gas phase annealing, (c) particle classifying, and (d) particle measurement.

zation process of Si nanoparticles in the gas phase. Based on their analysis, for Si nanoparticles (< 10 nm), gas phase annealing over 900 °C is effective in improving both crystallinity and shape as a result of sintering. The size-classified, spherical, and single crystal Si nanoparticles generated by

the method exhibited sharp photoluminescence (PL) that was tunable with the size of Si nanoparticles (Orii et al., 2003a, b). The PL spectra of Si nanoparticles showed that peak energy increased from 1.34 to 1.79 eV with a drop in particle size from 7 to 3 nm, and full width at half maxi-

mum (FWHM) of the PL drops to approximately 0.22 eV as a result of size classification by the LPDMA.

3.2 Metal and oxide nanoparticles

Metal and metal oxide nanoparticles also display various unique features that have potential for electrical, magnetic, catalytic, and optical applications. Some studies on the synthesis of metal and metal oxide nanoparticles by laser ablation are listed in **Table 2**. Kawakami et al. (2002) produced gold nanoparticles by laser ablation under helium gas under pressures of 3 to 90 kPa. They generated a film by directly depositing the gold nanoparticles on the substrate by generating an aerosol-jet. The microstructure of the gold film changed from porous to high density with increasing pressure. As a result, the electrical resistivity of the film changed from $10^{-1} \Omega\text{cm}$ (3 kPa) to $10^{-5} \Omega\text{cm}$ (50 kPa). Dikovska et al. (2013) also synthesized silver nanoparticles by laser ablation under high vacuum conditions ($\sim 10^{-5}$ torr). They investigated the influence of Nd:YAG laser wavelength on the size of

generated particles. They reported that a shorter wavelength (266 nm) was better at generating smaller particles (4 nm in diameter) and that it exhibited surface plasmon resonance.

Magnetic nanoparticles from transition metals and metal alloys have also been synthesized by laser ablation. Since magnetic properties are strongly influenced by purity, crystallinity, and particle size of the nanoparticles, advanced laser ablation (**Fig. 4**) is significantly more capable of controlling nanoparticle morphologies. Sakiyama et al. (2004) fabricated Ni particles of a select size coated with a NiO shell with the laser ablation method. They also applied the aerosol process, i.e., LPDMA size classification, and gas phase annealing to improve Ni nanoparticle morphology. A Ni/NiO core shell structure was successfully generated by the oxidation of Ni nanoparticles. Seto et al. (2004, 2005) investigated the magnetic properties of Ni/NiO nanoparticles generated by this method using a superconducting quantum interference device (SQUID) magnetometer at room temperature. Ferromagnetism was observed with a film comprising nickel particles larger

Table 2 Metallic nanoparticle synthesis studies using pulsed laser ablation method (A: annealing, m: mean, M: mode, S: shell thickness)

Author	Laser Source	Material	Pressure	Additional Process	Particle	Particle size
Shinde et al. 2000	Excimer	Fe_xO_y , SrM	266 Pa	Cold Finger		30~60 nm
			266 Pa	Cold Finger		15~100 nm
Seto et al. 2001a	Nd:YAG	TiO_x	2.6~13.3 kPa	DMA	Primary	10~50 nm
Hirasawa et al. 2002	Nd:YAG	TiO_x	1.73 kPa	DMA	Primary	(M) 5.9 nm
			1.73 kPa	(A) 500 °C, DMA	Primary	(M) 4.9 nm
			1.73 kPa	(A) 650 °C, DMA	Primary	(M) 4.4 nm
			1.73 kPa	(A) 800 °C, DMA	Primary	(M) 6.9 nm
			1.73 kPa	(A) 900 °C, DMA	Primary	(M) 14.3 nm
Harano et al. 2002	Nd:YAG	TiO_x	101.3 kPa		Aggregates	10~50 nm, 100~1000 nm
Kawakami et al. 2002	Nd:YAG	Au	3 kPa	DMA	Primary	(M) 8 nm
			7 kPa	DMA	Primary	(M) 13 nm
			20 kPa	DMA	Primary	(M) 20 nm
			30 kPa	DMA	Primary	(M) 30 nm
			50 kPa	DMA	Primary	(M) 75 nm
			90 kPa	DMA	Primary	(M) 80 nm
Sakiyama et al. 2004	Nd:YAG	Ni/NiO	1 kPa	DMA	Aggregates	
			1 kPa	(A) 400~800 °C, DMA	Primary	5~20 nm (S) 2 nm
Seto et al. 2006	Nd:YAG	CoPt	1 kPa	(A) 1000 °C, DMA	Primary	(M) 14 nm
Seto et al. 2007	Nd:YAG	CoPt/SiO ₂	1 kPa	(A) 1000 °C, DMA	Primary	(M) 7 nm, (S) 2 nm
Niu et al. 2012	KrF excimer	FeNi	High vacuum 266 Pa		Primary Aggregates	(M) 4 nm (M) 6 nm
Dikovska et al. 2013	Nd:YAG	Ag	$\sim 10^{-3}$ Pa		Primary	(M) 4~11 nm

than 6.2 nm in core diameter. In contrast, smaller Ni nanoparticles with core diameters of 3 nm exhibited superparamagnetism. They reported that the formation of an antiferromagnetic NiO shell is effective for controlling the manifestation of superparamagnetism in the nanometer-sized ferromagnetic Ni core.

Another approach for overcoming the superparamagnetic limit is to synthesize highly anisotropic magnetic alloy nanoparticles such as fct FePt and CoPt. Alloy nanoparticles of Co and Pt were synthesized by laser ablation by varying the Co:Pt ratio of the target (Seto et al., 2006). Their EDX results showed that the composition of the generated particles could be controlled by the target composition. The magnetization of the laser-synthesized CoPt particles (83.7 emu/g) was almost double that of bulk CoPt (44 emu/g). They also observed a weak exchange coupling at the interface between the ferromagnetic core (CoPt) and antiferromagnetic shell (CoO). Seto et al. (2007) also investigated the influence of shell material by synthesizing a non-magnetic SiO₂ shell by laser ablation of a multi-component target comprising Co, Pt and SiO₂. Metal oxide and metal composite nanoparticles have also been generated by laser ablation. Shinde et al. (2000) also synthesized iron oxides and strontium ferrite (SrM) with the laser ablation method and evaluated the magnetic characteristics.

Vapor phase synthesis of titania (TiO₂) nanoparticles has been extensively investigated since they have photo-voltaic and photocatalytic applications (Harano et al., 2002; Pallotti et al., 2015). Seto et al. (2001a) synthesized TiO_x particles by Nd:YAG laser ablation of a TiO₂ target in a background gas (He) with pressure ranging from 2.6 to 13.3 kPa. They observed increases in the mobility diameter due to agglomeration as the pressure increased. High-resolution TEM analysis of the nanostructures of the generated revealed that the metallic (Ti) core was covered with a sub-stoichiometric shell structure with a thickness of several nanometers. Hirasawa et al. (2002) also synthesized TiO_x nanoparticles by laser ablation and investigated the effect of aerosol post-annealing temperatures of up to

900 °C. They reported an increase in the primary particle diameter due to sintering and change in crystallinity from amorphous form to anatase and rutile, which was confirmed by Raman scattering. They also discussed the non-stoichiometric phase of TiO_x particles such as Ti₂O₃. More recently, Tsuji et al. (2012) investigated the effect of nucleation (particle formation) temperature on the morphology of TiO₂ nanoparticles generated by the laser oven process (laser ablation in a tubular furnace).

3.3 Nanocarbons and nanowires

The benefit of non-equilibrium laser ablation nucleation processes is that it can generate various kinds of crystal phases and allotropes that are not seen in the normal (equilibrium) synthesis processes. **Fig. 5** shows transmission electron micrographs of nanometer scale carbon allotropes (nanocarbons) such as carbon nanotubes (CNTs, **Fig. 5(a)**), onion-like carbon (**Fig. 5(b)**), and nano-diamonds (**Fig. 5(c)**) synthesized by laser ablation. Since laser ablation is superior at generating high-purity and nanometer-sized metal particles, it is also suitable as a catalyst for the growth of single walled carbon nanotubes (SWCNTs) on the substrate. For example, Kohno et al. (2004) generated Co/Mo and Co/Pt alloy nanoparticles by laser ablation and investigated the ethanol-CVD growth of the CNT on the substrate. In another development, laser ablation in a high temperature flow reactor (laser oven method) has been widely used to generate high-purity SWCNTs (Puretzky et al., 2000). References on carbon-related nanomaterial synthesis using gas-phase laser ablation are arranged in **Table 3**. Compared to conventional CVD formation on substrates, the laser oven method has an affinity for generating SWCNTs with low level of defects in a continuous flow-type generator.

As an example of nanocarbon generation in a flow-type generator, a simple and continuous one-step system using the laser oven method generated a SWCNT aerosol (Klanwan et al., 2010). A graphite target containing Ni and Co was ablated by pulsed laser in the tubular furnace

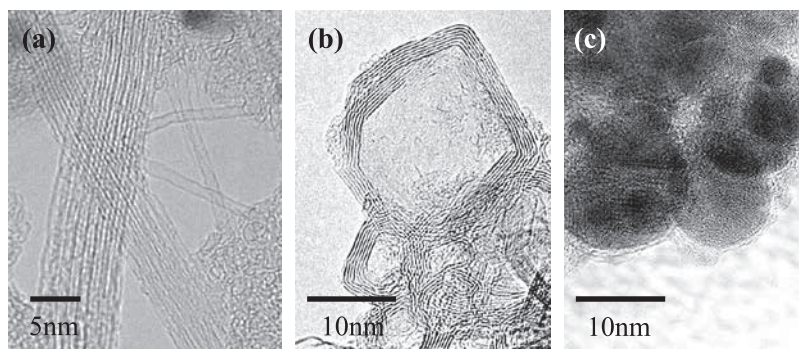


Fig. 5 Transmission electron micrographs of nanocarbons generated by laser ablation. (a) Onion-like carbon, (b) carbon nanotubes, and (c) diamond-like nanoparticles.

at temperatures of 25 to 1080 °C. The generated SWCNTs (< 2 nm in diameter, **Fig. 5(a)**) were carried by atmospheric pressure nitrogen gas for on-line analysis of their size distribution using the scanning mobility particle sizer (SMPS). Other types of carbon allotropes have been synthesized by advanced laser ablation methods. Inoue et al. (2012) synthesized onion-like carbon nanoparticles (**Fig. 5(b)**) using a graphite target with a cavity that confined the generated particles so they can be irradiated by multiple laser beams. As a result of periodic laser beam irradiation of the gas-suspended carbon particles in the cavity, the phase transition from amorphous carbon nanoparticles to the orderly concentric graphitic shell structure was identified. Seto et al. (2014) also showed that the present method is capable of synthesizing a variety of unique nanostructured carbons including diamond-like carbon (**Fig. 5c**). They evaluated the change in the density of the carbon nanoparticles during the laser-induced phase transition.

4. Summary—Achieving large-scale production of nanoparticles by laser ablation

In this review, the formation mechanism and examples of nanoparticle synthesis by laser ablation were discussed. As mentioned previously, the properties of the nanoparticles depend strongly on size and size uniformity. Advanced laser ablation methods can generate size- and shape-controlled nanoparticles by post processing (**Fig. 4**), but that, at the same time, significantly reduces the production yield. In addition, laser ablation is disadvantaged by high input energy (Kushnir et al., 2008) and the small laser-irradiating area for evaporating the target materials. Therefore, laser ablation applications have been limited to exploring unique properties of new types of nanoparticles. To achieve large-scale production of nanoparticles by laser ablation, it is necessary to generate

morphology-controlled nanoparticles without subsequent post-processing.

Laser ablation has an affinity for synthesizing anisotropic nanomaterials such as carbon nanotubes (Karthikeyan et al., 2009), nanorods (Tian et al., 2013) and nanowires (Rao et al., 2003) in the large-scale. In these processes, high-purity catalysts that are small in size and have good crystallinity play an important role in the anisotropic growth of such one-dimensional nanomaterials. In addition, laser ablation has good compatibility with aerosol flow systems and with the benefit of being capable of continuously producing large quantities of nanoparticles as well as nanoparticle-based nanomaterials. There are also several reports on the production of colloidal metal nanoparticles in a liquid flow system (Muttaqin et al., 2015). Such metal nanoparticles have applications as bio-markers.

Size classification by LPDMA is advantageous, not only for obtaining size-classified particles, but also for measuring the size distribution of nanoparticles in the gas phase process. Therefore, it can be implemented as a process monitor for optimizing process parameters (pressure, flow rate, temperature etc.). The size distribution of nanoparticles generated by laser ablation can be measured when an LPDMA is coupled with a particle detector such as an aerosol electrometer (Seto et al., 2001b). Quantum-sized particles (< 10 nm) with a relatively narrow size distribution can be generated by laser ablation under low pressure conditions without post-processing. For this purpose, an LPDMA/electrometer system can be used for exploring the optimum conditions to obtain nanoparticles with the desirable size distribution.

Acknowledgements

The authors are grateful for support by JSPS KAKENHI Grant Number 15K14200.

Table 3 Carbon nanoparticle synthesis studies using pulsed laser ablation method in a flow reactor (H: heating, D: diameter, L: length, M: mode)

Author	Laser Source	Structure	Pressure	Additional Process	Size
Puretzky et al. 2000	Nd:YAG	SWNTs	66.5 kPa	(H) 1000 °C	200 nm/s growth rate
	XeCl	SWNTs	66.5 kPa	(H) 1000 °C	
Klanwan et al. 2010	Nd:YAG	SWNTs	101.3 kPa	(H) 25~1080 °C	(D) < 2 nm, (L) > 500 nm
Inoue et al. 2012	Nd:YAG	Amorphous	101.3 kPa	Flat target	(M) 83 nm
		Onion-like	101.3 kPa	Cavity target	(M) 18 nm
Seto et al. 2014	Nd:YAG	Onion-like	101.3 kPa	Flat target	
		Diamond-like		Cavity target	

References

- Anikin K.V., Melnik N.N., Simakin A.V., Shafeev G.A., Voronov V.V., Vitukhnovsky A.G., Formation of ZnSe and CdS quantum dots via laser ablation in liquids, *Chemical Physics Letters*, 366 (2002) 357–360.
- Buzea C., Pacheco I.I., Robbie K., Nanomaterials and nanoparticles: Sources and toxicity, *Biointerphases*, 2 (2007) MR17–MR71.
- Chichkov B.N., Momma C., Nolte S., Von Alvensleben F., Tünnermann A., Femtosecond, picosecond and nanosecond laser ablation of solids, *Applied Physics A*, 63 (1996) 109–115.
- Dikovska A.O., Alexandrov M.T., Atanasova G.B., Tsankov N.T., Stefanov P.K., Silver nanoparticles produced by PLD in vacuum: Role of the laser wavelength used, *Applied Physics A*, 113 (2013) 83–88.
- Fischer D., Schwinghammer K., Sondermann C., Lau V.W., Mannhart J., Lotsch B.V., Laser ablation of molecular carbon nitride compounds, *Applied Surface Science*, 349 (2015) 353–360.
- Friedrich C., Keynton R., Vasile M., Warrington R., Development of a core curriculum in miniaturization technologies, *Journal of Engineering Education*, 87 (1998) 567–574.
- Fujishima A., Honda K., Electrochemical photolysis of water at a semiconductor electrode, *Nature*, 238 (1972) 37–38.
- Geohegan D.B., Poretzky A.A., Duscher G., Pennycook S.J., Photoluminescence from gas-suspended SiO_x nanoparticles synthesized by laser ablation, *Applied Physics Letters*, 73 (1998) 438–440.
- Harano A., Shimada K., Okubo T., Sadakata M., Crystal phases of TiO₂ ultrafine particles prepared by laser ablation of solid rods, *Journal of Nanoparticle Research*, 4 (2002) 215–219.
- Hirasawa M., Seto T., Orii T., Aya N., Shimura H., Synthesis of size-selected TiO_x nanoparticles, *Applied Surface Science*, 197–198 (2002) 661–665.
- Hirasawa M., Orii T., Seto T., Effect of insitu annealing on physical properties of Si nanoparticles synthesized by pulsed laser ablation, *Applied Physics A*, 79 (2004) 1421–1424.
- Inoue A., Seto T., Otani Y., Onion-like carbon nanoparticles generated by multiple laser irradiations on laser-ablated particles, *Carbon*, 50 (2012) 1116–1122.
- Kawakami Y., Seto T., Yoshida T., Ozawa E., Gold nanoparticles and films produced by a laser ablation/gas deposition (LAGD) method, *Applied Surface Science*, 197–198 (2002) 587–593.
- Kim B.H., Lee N., Kim H., An K., Park Y.I., Choi Y., Shin K., Lee Y., Kwon S.G., Na H.B., Park J.-G., Ahn T.-Y., Kim Y.-W., Moon W.K., Choi S.H., Hyeon T., Large-scale synthesis of uniform and extremely small-sized iron oxide nanoparticles for high-resolution t1 magnetic resonance imaging contrast agents, *Journal of the American Chemical Society*, 133 (2011) 12624–12631.
- Kim B.H., Hackett M.J., Park J., Hyeon T., Synthesis, characterization, and application of ultrasmall nanoparticles, *Chemistry of Materials*, 26 (2014) 59–71.
- Klanwan J., Seto T., Furukawa T., Otani Y., Charinpanitkul T., Kohno M., Hirasawa M., Generation and size classification of single-walled carbon nanotube aerosol using atmospheric pressure pulsed laser ablation (AP-PLA), *Journal of Nanoparticle Research*, 12 (2010) 2747–2755.
- Kohno M., Orii T., Hirasawa M., Seto T., Murakami Y., Chiashi S., Miyauchi Y., Maruyama S., Growth of single-walled carbon nanotubes from size-selected catalytic metal particles, *Applied Physics A*, 79 (2004) 787–790.
- Kuroda S., Kaihara S., Fujii Y., Kinoshita T., Adachi M., Modeling of particle generation in laser ablation plasma, *Journal of Aerosol Science*, 50 (2012) 38–56.
- Lau M., Haxhiaj I., Wagener P., Intartaglia R., Brandi F., Nakamura J., Barcikowski S., Ligand-free gold atom clusters adsorbed on graphene nano sheets generated by oxidative laser fragmentation in water, *Chemical Physics Letters*, 610–611 (2014) 256–260.
- Lu Q., Mao S.S., Mao X., Russo R.E., Theory analysis of wavelength dependence of laser-induced phase explosion of silicon, *Journal of Applied Physics*, 104 (2008) 083301.
- Niu X., Murray P., Sarangan A., Synthesis of Fe–Ni bimetallic nanoparticles from pixel target ablation: Plume dynamics and surface characterization, *Journal of Nanoparticle Research*, 14 (2012) 1–8.
- Okada R., Iijima S., Oxidation property of silicon small particles, *Applied Physics Letters*, 58 (1991) 1662–1663.
- O'regan B., Gratzel M., A low-cost, high-efficiency solar cell based on dye-sensitized colloidal TiO₂ films, *Nature*, 353 (1991) 737–740.
- Orii T., Hirasawa M., Seto T., Tunable, narrow-band light emission from size-selected Si nanoparticles produced by pulsed-laser ablation, *Applied Physics Letters*, 83 (2003a) 3395–3397.
- Orii T., Hirasawa M., Seto T., Aya N., Onari S., Temperature dependence of photoluminescence from mono-dispersed Si nanoparticles, *The European Physical Journal D—Atomic, Molecular, Optical and Plasma Physics*, 24 (2003b) 119–122.
- Pallotti D.K., Ni X., Fittipaldi R., Wang X., Lettieri S., Vecchione A., Amoroso S., Laser ablation and deposition of titanium dioxide with ultrashort pulses at 527 nm, *Applied Physics B*, 119 (2015) 445–452.
- Poretzky A.A., Geohegan D.B., Fan X., Pennycook S.J., Dynamics of single-wall carbon nanotube synthesis by laser vaporization, *Applied Physics A*, 70 (2000) 153–160.
- Ruth A.A., Young J.A., Generation of CdSe and CdTe nanoparticles by laser ablation in liquids, *Colloids and Surfaces A: Physicochem. Eng. Aspects*, 279 (2006) 121–127.
- Sakiyama K., Koga K., Seto T., Hirasawa M., Orii T., Formation of size-selected Ni/NiO core-shell particles by pulsed laser ablation, *J. Phys. Chem. B*, 108 (2004) 523–529.
- Seto T., Kawakami Y., Suzuki N., Hirasawa M., Kano S., Aya N., Sasaki S., Shimura H., Evaluation of morphology and size distribution of silicon and titanium oxide nanoparticles generated by laser ablation, *Journal of Nanoparticle Research*, 3 (2001a) 185–191.
- Seto T., Kawakami Y., Suzuki N., Hirasawa M., Aya N., Laser synthesis of uniform silicon single nanodots, *Nano Letters*,

- 1 (2001b) 315–318.
- Seto T., Orii T., Hirasawa M., Aya N., Fabrication of silicon nanostructured films by deposition of size-selected nanoparticles generated by pulsed laser ablation, *Thin Solid Films*, 437 (2003) 230–234.
- Seto T., Koga K., Akinaga H., Takano F., Sakiyama K., Hirasawa M., Orii T., Laser synthesis and magnetic properties of monodispersed core–shell nanoparticles, *Applied Physics A*, 79 (2004) 1165–1167.
- Seto T., Akinaga H., Takano F., Koga K., Orii T., Hirasawa M., Magnetic properties of monodispersed Ni/NiO core–shell nanoparticles, *The Journal of Physical Chemistry B*, 109 (2005) 13403–13405.
- Seto T., Koga K., Akinaga H., Takano F., Orii T., Hirasawa M., Laser ablation synthesis of monodispersed magnetic alloy nanoparticles, *Journal of Nanoparticle Research*, 8 (2006) 371–378.
- Seto T., Koga K., Takano F., Akinaga H., Orii T., Hirasawa M., Murayama M., Synthesis of magnetic CoPt/SiO₂ nanoparticles, *Journal of Physics: Conference Series*, 59 (2007) 255–258.
- Seto T., Inoue A., Higashi H., Otani Y., Kohno M., Hirasawa M., Phase transition and restructuring of carbon nanoparticles induced by aerosol laser irradiation, *Carbon*, 70 (2014) 224–232.
- Shinde S.R., Kulkarni S.D., Banpurkar A.G., Nawathey-Dixit R., Date S.K., Ogale S.B., Magnetic properties of nanosized powders of magnetic oxides synthesized by pulsed laser ablation, *Journal of Applied Physics*, 88 (2000) 1566–1575.
- Suzuki N., Makino T., Yamada Y., Yoshida T., Seto T., Mono-dispersed, nonagglomerated silicon nanocrystallites, *Applied Physics Letters*, 78 (2001) 2043–2045.
- Tilke A.T., Simmel F.C., Blick R.H., Lorenz H., Kotthaus J.P., Coulomb blockade in silicon nanostructures, *Progress in Quantum Electronics*, 25 (2001) 97–138.
- Torrisi L., Gammino S., Andò L., Nassisi V., Doria D., Pedone A., Comparison of nanosecond laser ablation at 1064 and 308 nm wavelength, *Applied Surface Science*, 210 (2003) 262–273.
- Tsuji M., Seto T., Otani Y., Effect of surrounding gas temperature on the morphological evolution of TiO₂ nanoparticles generated by laser ablation in tubular furnace, *Journal of Nanoparticle Research*, 14 (2012) 674–683.
- Wen S.B., Mao X., Greif R., Russo R.F., Radiative cooling of laser ablated vapor plumes: Experimental and theoretical analyses, *Journal of Applied Physics*, 100 (2006) 053104.
- Wen S.B., Mao X., Greif R., Russo R.E., Experimental and theoretical studies of particle generation after laser ablation of copper with a background gas at atmospheric pressure, *Journal of Applied Physics*, 101 (2007) 123105.
- Wolfbeis O.S., An overview of nanoparticles commonly used in fluorescent bioimaging, *Chemical Society reviews*, 44 (2015) 4743–4768.
- Yoshida T., Takeyama S., Yamada Y., Mutoh K., Nanometer—sized silicon crystallites prepared by excimer laser ablation in constant pressure inert gas, *Applied Physics Letters*, 68 (1996) 1772–1774.
- Yoshida T., Yamada Y., Orii T., Electroluminescence of silicon nanocrystallites prepared by pulsed laser ablation in reduced pressure inert gas, *Journal of Applied Physics*, 83 (1998) 5427–5432.
- Zheng J., Zhang C., Dickson R.M., Highly fluorescent, water-soluble, size-tunable gold quantum dots, *Physical Review Letters*, 93 (2004) 077402.

Author's short biography



Myungjoon Kim

He received his Bachelor of Science degree in Mechanical Engineering from Sungkyunkwan University, Korea in 2009. Currently, he is a candidate of combined master's and doctorate program in the School of Mechanical at Sungkyunkwan University. His research is focused on the numerical analysis on particle suspended in fluid.

Author's short biography



Saho Osone

She received her Bachelor of Engineering degree in Chemical Engineering from Kanazawa University, Japan in 2007. She received her Master of Engineering in Chemical Engineering from Kanazawa University, Japan in 2009. Currently, she is working at Takeda Pharmaceutical Company Limited. She is also a doctoral course student at Kanazawa University. Her research is focused on nanoparticle material synthesis by gas phase processes and measurement of aerosol nanoparticles.



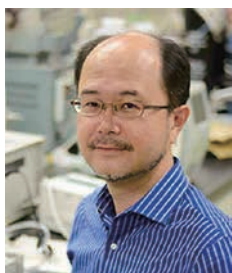
Taesung Kim

He received his Bachelor of Science degree in Mechanical Engineering from Seoul National University, Korea in 1994. He received his Master of Science, and Doctor of Philosophy degrees in Mechanical Engineering from Minnesota University, USA in 1998, and 2002, respectively. Dr. Kim currently works as professor in the School of Mechanical Engineering and adjunct professor in the SKKU Advanced Institute of Nano Technology at Sungkyunkwan University in Suwon, Korea. His research interests include nanoparticle synthesis, development of applications related with bio aerosol, Chemical Mechanical Polishing, and thin film synthesis.



Hidenori Higashi

He received his Bachelor of Engineering degree in Chemical Engineering from Kyushu University, Japan in 1994. He received his Master of Engineering, and Doctor of Engineering degrees in Chemical Engineering from Kyushu University, Japan in 1996, and 2001, respectively. From 1997 to 2004, he worked as a Research Associate at Kyushu University. From 2004, he works as an Assistant Professor (2004 to 2015) and as an Associate Professor (from 2016), Faculty of Natural System, Institute of Science and Engineering, Kanazawa University, Japan. His research topics cover broad area in supercritical fluid technology, aerosol science and technology.



Takafumi Seto

He received the Doctoral degree in Engineering from Hiroshima University at 1996. From 1997 to 2007, he worked at Mechanical Engineering Laboratory (from 2001, National Institute of Industrial Science and Technology (AIST)). From 2007, he works as an Associate Professor (2007 to 2013) and as a Professor (2013 to now), Kanazawa University, Faculty of Natural System, Institute of Science and Engineering, Kanazawa University, Japan. His research topics cover broad area in aerosol science and technology such as nanoparticle synthesis, classification, transport phenomena, electrostatics, instrumentation, and laser ablation.

Deficiencies in Traditional Oral Dosage Forms and the Emergence of Controlled-Release Powder Manufacturing[†]

Martin G. Teresk¹, Cory J. Berkland^{1,2} and Nathan H. Dormer^{1*}

¹ Orbis Biosciences, Inc., USA

² Department of Pharmaceutical Chemistry, University of Kansas, USA

Abstract

The importance of providing safe and effective delayed- and extended-release oral formulations that can replace products requiring multiple administrations has been continually cited as an area in need of improvement for pharmaceutical companies. Such controlled release challenges become especially critical when they must be adapted for paediatrics, those suffering from dysphagia, or patients with specific dosage administration limitations. More often than not, lack of palatability and taste-masking compound this formulation challenge. Many particulate approaches show promise, but can be fraught with broad particle size distributions, initial drug burst, poor drug entrapment efficiency, low drug loading, and limited scalability. Here, we summarize the key factors that drive formulation development of format-flexible controlled-release oral powders, and the manufacturing aspects involved with some of the foremost marketed products, including next-generation single-step layered powder manufacturing (below).

Keywords: powder, particle, microsphere, taste-masking, paediatric, controlled-release

1. The dosage form problem

The importance of providing safe, effective, and proven medicines for populations with dysphagia, such as children, geriatrics, and those suffering from debilitating illnesses, has been continually cited as an area in need of improvement for pharmaceutical companies and the providers who administer their product (Bergstrom D. et al., 2004; Bhardwaj S. and Hayward M., 1996; Cram A. et al., 2013; Dickens D.S. et al., 2008; Engelen L. et al., 2005; Imai E. et al., 1995; Ivanovska V. et al., 2014; Lopez F.L. et al., 2015; Matsui D., 2007; Milne C.P. and Bruss J.B., 2008; Rocca J.G. and Park K., 2004; Sugao H., 1997; Tyle P., 1993). The widespread lack of dispersed format oral products, however, forces clinicians and pharmacists to use alternative solutions to treat their patients that are not always backed by supporting bioavailability, stability, and safety studies. Tablets are sometimes administered extemporaneously by crushing the dosage form and mixing with food or drink. Not only are these delivery methods inconsistent, they often lead to dosing errors, decreased

bioavailability or efficacy, and non-adherence because of foul-tasting active pharmaceutical ingredients (APIs) (Jayanthi B. and Manna P., 2011; Osterberg L. and Blaschke T., 2005; Sansom L., 1999; Schier J. et al., 2003).

Due to taste and efficacy concerns, The Institute for Safe Medical Practices (ISMP) has issued a “Do Not Crush” list, which highlights over 400 dosage forms that cannot be compounded due to special controlled-release properties, taste-masking, or API protection (Bergstrom D. et al., 2004; Bhardwaj S. and Hayward M., 1996; Dickens D.S. et al., 2008; Engelen L. et al., 2005; Imai E. et al., 1995; Matsui D., 2007; Milne C.P. and Bruss J.B., 2008; Rocca J.G. and Park K., 2004; Sugao H., 1997; Tyle P., 1993). Lack of titratable and palatable formulations affects over half of the global population (under 18 and over 65 years of age) and can subject patients to avoidable adverse events (Jayanthi B. and Manna P., 2011; Osterberg L. and Blaschke T., 2005; Sansom L., 1999; Schier J. et al., 2003). Of all medication-related hospitalizations that occur in the United States, between one-third and two-thirds are the result of poor medication adherence (Matsui D., 2007; Milne C.P. and Bruss J.B., 2008). Current dosing regimens for populations with dysphagia or those unwilling to take traditional tablets or capsules suffer because many current oral formulations fail to simultaneously address the critical aspects discussed below (Griffith R., 2005; Wright D., 2002).

[†] Received 18 April 2016; Accepted 16 June 2016
J-STAGE Advance Publication online 30 July 2016

¹ Lenexa, KS 66214, USA

² Lawrence, KS 66045, USA

* Corresponding author: Nathan H. Dormer;
E-mail: nate@orbisbio.com
TEL: +1-913-544-1199

1.1 Palatability

Many APIs are extremely bitter and coating efforts can be ineffective or result in an unpleasant mouth feel due to irregular surface features. Approximately half of patients with organoleptic sensitivities refuse to take their medicine, with the large majority of those reporting bad taste as the single major reason for non-compliance (Matsui D., 2007). Sweeteners alone are often unable to overcome the extremely unpleasant taste of many active ingredients in syrups and suspensions (Bergstrom D. et al., 2004; Bhardwaj S. and Hayward M., 1996; Dickens D.S. et al., 2008). Moreover, efforts to mask flavors using coatings, agglomeration, or microencapsulation often result in poorly-controlled, heterogeneous particle distributions that result in a gritty or granular mouth feel. Ideally, a highly palatable dosage form will consist of taste-masking with a smooth mouthfeel while maintaining other controlled release properties.

1.2 Titratable dosing

Different ages, weights, body mass indices, and metabolically-impaired individuals require considerable dosing precision that is not linearly scaled (Milne C.P. and Bruss J.B., 2008). Because medication errors are common in six percent of pediatric hospitalizations, dose titration is critical, as a “one-size-fits-all” dosing is ineffective in children due to their developmental variability (Cram A. et al., 2013; Ivanovska V. et al., 2014; Lopez F.L. et al., 2015). and can prove deleterious for geriatric patients with hepatic or renal impairment.

1.3 Controlled-release kinetics

Achieving controlled-release kinetics with tablets is a relatively simple process, as the size and form factor of the dosage form lends to using robust coating methods, sometimes with several layers (Jayanthi B. and Manna P., 2011; Sansom L., 1999). Capsules have the advantage of being injection moulded, extruded, or die pressed with gelatines and other controlled-release polymers in a repeatable, high-throughput manner, enabling large doses of medication in a modest form factor. Tablets are simply pressed by traditional means, then coated with subsequent layers of controlled-release components, which makes translation of specialised functions (e.g. delayed or extended release) simple with a pill format (Jayanthi B. and Manna P., 2011; Sansom L., 1999). The major problem, however, is the size of such dosage forms, which renders them impracticable to certain patient populations.

2. Challenges with traditional oral dosage forms

Universal technology hurdles exist independently of drug or indication even for adult populations, and thus substantially impede development of optimal therapeutics for those with special dosing considerations. Specifically, for pediatric drugs, companies must meet all standard pharmaceutical benchmarks (bioavailability, shelf life, safety, and efficacy) but also consider palatability, dosing accuracy, and age-appropriate formats. Through the Best Pharmaceuticals for Children Act, Pediatric Research Equity Act, and EMEA Pediatric Investigation Plans, the industry is either incentivized or in some cases required to perform pediatric studies (2002, 2003, 2006; Cram A. et al., 2013). Internal capabilities for this development are limited, and many companies do not have the capacity to make pediatric formulations. This emphasizes the need for scalable, flexible, cost-effective formulation platforms for practical, palatable, age-appropriate, and accurate dosing to create safer medications that enhance compliance at any age. While advances in pediatric-centric dosage formats take to market, adults with dysphagia will also secure the benefits of research and development efforts focused on providing alternative formats to historical solid oral dosage forms.

2.1 Size burden of tablets and capsules

Data from marketed pharmaceutical products indicates that the average size of a controlled- or extended-release tablet is nearly 1.5 cm in length (Pharmacircle, 2016). Physiological studies demonstrate that swallowing becomes increasingly difficult when the dimension of the object being ingested reaches more than 50 % of the oesophageal diameter, which is 2.0 cm for the prototypical adult (Harb J., 2015). By this logic, the average controlled-release tablet is too large to be swallowed comfortably. The merits residing in pills and capsules is that they contain the volumetric space to (1) deliver a large payload of API, (2) utilize elaborate controlled-release mechanisms (such as ion-exchange, micro-pumping mechanisms, etc.), and (3) circumvent many shelf stability challenges. These merits, however, fall short of benefitting a significant fraction of the world population simply due to the form factor size.

2.2 Taste and consistency burden of syrups, suspensions, elixirs, and solutions

Where large tablets and capsules present swallowing and administration challenges, liquid formats succeed in dose titration most of the time. The advantages beyond ease of dosing are limited in traditional syrups, however.

Liquid formats (1) are not extended-release, (2) have little-to-no taste-masking, (3) and can contain API particles prone to settling and aggregation if not reconstituted properly prior to administration, which have resulted in risks to patient safety (Bergstrom D. et al., 2004; Cram A. et al., 2013; Ivanovska V. et al., 2014; Lopez F.L. et al., 2015; Matsui D., 2007; Milne C.P. and Bruss J.B., 2008). Recent advances (which will be discussed later in this article) have enabled extended release and taste-masking of orally-administered APIs, but the breadth of application currently covers less than one percent of marketed drugs.

2.3 Alternatives to traditional dosage forms

As a technical resolution to the large format of controlled-release pills and capsules, the foul taste of traditional syrups and suspensions, and the lack of controlled-release options for APIs tableted and encapsulated in nearly 85 % of marketed drugs (**Table 1**) (Maalouf N., 2013; Vummaneni V. and Nagpal D., 2012), many pharmaceutical and contract manufacturing organizations (CMOs) are focusing research and development efforts on controlled-release powder formats, which combine the stability of solid oral dosage forms and dose titration advantages of liquids. These tablet alternatives address many of the deficiencies discussed earlier, but can still be fraught with inadequacies such as multiple-step manufacturing and inconsistent particle sizes.

3. Controlled-release powders

Micro- and nanoparticulate powders are manufactured with a myriad of processes, but the primary motivation is integration of controlled-release mechanisms to govern particle disintegration and API dissolution. The requirement of achieving controlled release universally relies on physical sequestration of the API via one or more physicochemical mechanisms, which typically requires multiple steps. A powder form factor, however, can present unique challenges to achieving controlled release coatings due to (1) the high surface area of particles, (2) irregular sizes of particles within the powder, and (3) the number of process steps required to ensure predictable performance and reasonable quality of the final product. Though, taste-masking can still be achieved with powders when a coating or other chemical modification is applied. Here, we discuss the salient manufacturing steps for current and next-generation dosage forms (**Table 2**) (Cram A. et al., 2013; Maalouf N., 2013; Vummaneni V. and Nagpal D., 2012).

3.1 Coated drug granules

The most straightforward method for achieving taste-masking and controlled release with powders employs a two-step process in which a precursor particle is manufactured by various means, then coated with one or more layers containing controlled-release materials (**Fig. 1**).

Table 1 Overall dosage form landscape for most-prescribed medications

Types of Pediatric/ Geriatric/ Dysphagia-Friendly Formulations	Of Most- Prescribed Drugs (%)	Taste Masking Methods	Disadvantage	Advantage	Major Technologies and Companies Practicing in Each Dosage form Space
Suspension	13.0	coating, microencapsulation, ion exchange resin, inclusion complexes, granulation, adsorption, prodrug, bitterness inhibitors, multiple emulsion, gel formation	Easy to swallow, can be taste- masked, though most form factors of these types are not (see exceptions at right).		TPG/Adare: Microcaps [®] , Liquitard [®] . Tris: OralXT [™] , LiquiXR [™] Cipla: Sprinkles [®] , Orbis: Optimum [®]
Granules/Powder	2.8				
Orally Disintegrating Tablet (ODT)	3.0				TPG/Adare: Advatab [®] , Diffucaps [®] . Tris: ODTXR [™] . SPI: Actimask [®] . Catalent: Zydis [®] . Cima: OraSolv [®] , Durasolv [®] , Lyoc [™]
Chewable Tablet	4.2				
Sublingual/Lingual	0.6				Tris: ChewableXR [™] . SPI: Actimask [®]
Tablet	42.7	Inherently no taste-masking: drug freely/rapidly available	Does not help those with dysphagia	Taste-masking available	TPG/Adare, Catalent, Capsugel/ Bend Reserach, Allergan/Actavis, Pfizer, GlaxoSmithKline, Bayer, Procter & Gamble, Johnson & Johnson, Bristol Myers Squibb, AstraZeneca, Impax, SPI,
Capsule	18.0				
Solution/Syrup	15.0				
Elixir	0.8			No swallowing difficulty for those with dysphagia	

Table 2 Various manufacturing technologies that rely on particles and powders as final dosage form

Powder-Based Technology	Manufacturing Considerations	Form Factor	Proprietor of Technology	Flagship Formulations Approved or In Pipeline
Optimum [®]	Single-step microencapsulation, uniform particle size distribution (100s-1000s μ m), scalable, dosage and format flexible, enables combination therapy	Microspheres and Microcapsules	Orbis Biosciences	prednisone, guaifenesin, ibuprofen
DETERx [®]	Multi-step production (drug-wax complex, particle fabrication, coating), dosage and format flexible, less uniform size distribution, abuse deterrent formulation	Hydrophobic matrix as physical or diffusional barrier	Collegium Pharmaceutical	oxycodone, oxymorphone, hydrocodone, morphine, methylphenidate
LiquiTime [®]	Multi-step production (granulation, coating, drying), non-uniform granule size distribution, size limited (> 100 μ m), dosage and format flexible	Traditional 2-Step Coating of particles	Flamel Technologies	guaifenesin, ibuprofen
Microcaps [®] (Used alone and in Liquitard [®] , AdvaTab [®])	API particles complexed with controlled-release matrix	Drug-coated powder	Adare Pharmaceuticals	tenofovir disoproxil fumarate, potassium chloride, paracetamol
Diffucaps [®]	Multi-step production (granulation, coating, drying), non-uniform granule size distribution, size limited (> 500 μ m), dosage and format flexible	Minitablets	Adare Pharmaceuticals	propranolol, methylphenidate, cyclobenzaprine
Sprinkles [®]		Minitablets	Cipla	lopinavir, ritonavir
OralXR+ TM (Used alone and in LiquiXR TM , ChewableXR TM , ODTXR TM , StripsXR TM)	Multi-step production (resin priming, drug loading, resinate wash, drying), requires acidic or basic drug chemical structure, relies on proprietary resin beads	Solid suspension or ODT	Tris Pharma	amphetamine, codeine/chlorpheniramine polistirex, dextromethorphan
XR Technologies (RDIM, DTRS [®] , and KCTP TM)			Neos Therapeutics	methylphenidate
ORaSol [®] , DuraSol [®] , Lyoc TM	API granules co-lyophilized with matrix	ODT	Cima Labs	loperamide, clozapine, prednisolone
Actimask [®]		ODT	SPI Pharmaceuticals	paracetamol, ibuprofen
Zydis [®]		ODT	Catalent Pharma Solutions	lorazepam, loratadine, piroxicam, olanzapine

Precursor particles can either be (1) finely-milled API crystals, (2) crystalline or amorphous API co-mixed with inert bases or controlled-release materials, or (3) an entirely inert core without API. These three types of precursors can be manufactured by one or more means, which include traditional vibratory methods, congealing/spinning disk atomization, prilling, hot-melt extrusion (HME) and spheronization, aqueous dispersion, blending/bulking, electrohydrodynamic spraying (EHDS), or spray drying (Ambike A.A. et al., 2005; Cloupeau M. and Prunet-Foch B., 1994; Eldem T. et al., 1991; Gharsallaoui A. et al., 2007; Hancock B.C. et al., 2003; Passerini N. et al., 2006;

Vehring R., 2007; Yurteri C.U. et al., 2010). Material selection for the precursor particle relies on process capabilities, desired end-product controlled-release properties, API thermal and oxidative stability and desired physical properties (surface features, density, friability, hardness, etc). Once the precursor microparticulate is manufactured, the product, in some instances, can be considered “finished.”

If taste-masking, delayed-release, or stability-enabling properties are required, the precursor particle advances to subsequent traditional coating steps using fluidized beds, Würster coaters, dry polymer coating, spray coating, pan

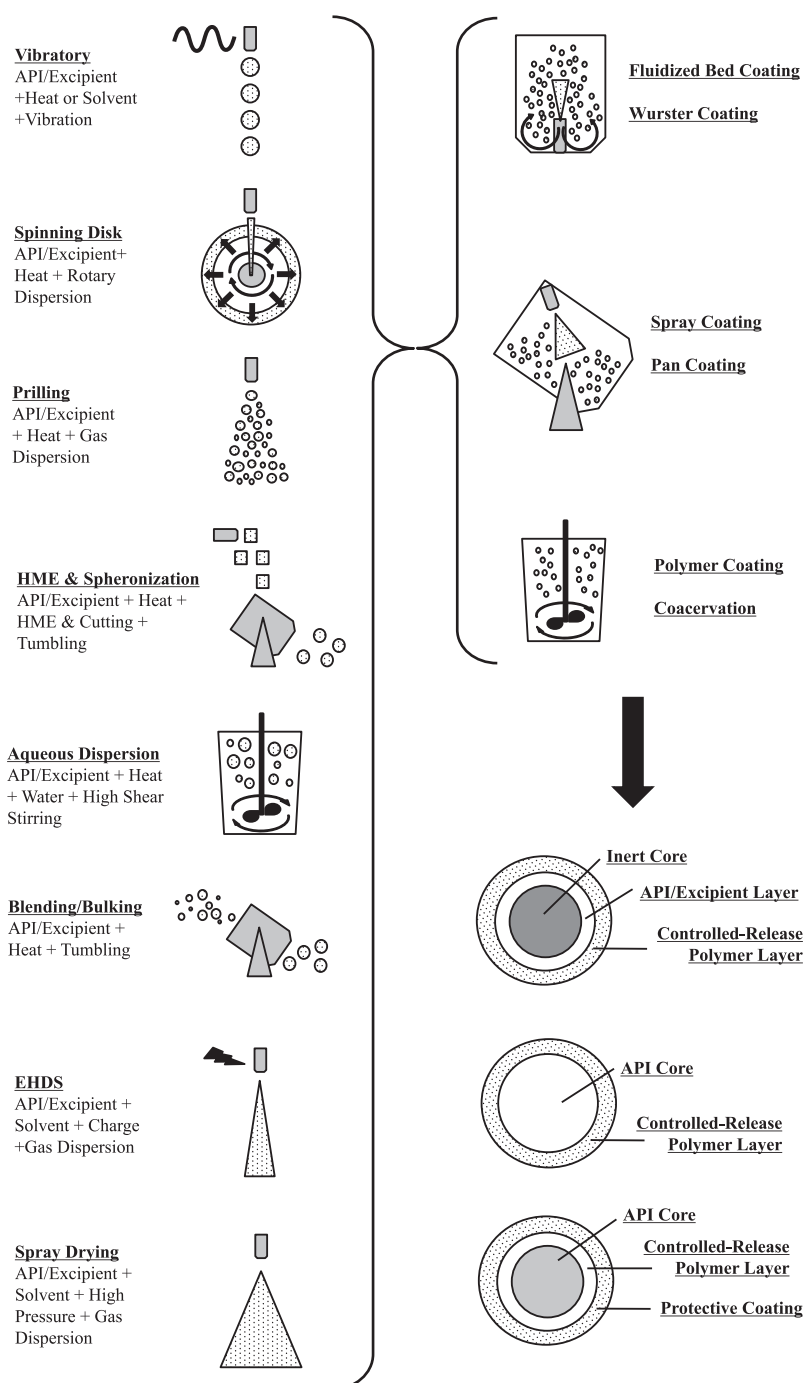


Fig. 1 Powder creation and coating has traditionally been at least a two-step process, but provides great flexibility in end product dosage form and function. Each technique gives a different particle size range, with vibratory techniques creating the largest powders, and spray drying the smallest powders.

coating, or coacervation (Dewettinck K. and Huyghebaert A., 1999; Gouin S., 2004; Jono K. et al., 2000; Lopez F.L. et al., 2015; Sastry S.V. et al., 2000). Materials of choice for the secondary coating steps are selected for reasons commensurate with precursor particles (i.e. material compatibility, controlled-release behaviour, and stability). The final dosage form can then be bottled for resuspension at time of use, packaged in sachets or sprinkle capsules, placed in dissolving tongue strips, co-lyophilized with

other materials for orally-disintegrating tablets (ODTs), or reconstituted in syrup if liquid stability is not an issue (**Table 2**).

The history of manufacturing controlled-release powders by adding one or more coating steps to API-rich cores is no less than colossal, and for this reason we have provided a high-level overview with references to detailed reviews. These techniques are, however, divergent from state-of-the art techniques that focus on chemical modifi-

cation of the API and/or substrate to which it is affixed via ion exchange resins (Elder D.P., 2005; Fazal U.-R. and Khan S.N., 2012; Pande S.V. et al., 2011). The main advantages that these methods can yield are (1) enabling liquid stability, and (2) deterring abuse of scheduled APIs, such as opiates and amphetamines. While revolutionary, drug complexation employs a number of manufacturing steps that far surpasses that of simple bead layering, and include and still usually include a final coating step (Dewettinck K. and Huyghebaert A., 1999; Gouin S., 2004; Jono K. et al., 2000; Lopez F.L. et al., 2015; Sastry S.V. et al., 2000). Here, we look in detail at two processes.

3.2 Granules with increased lipophilicity

Collegium Pharmaceutical's manufacturing process achieves extended release with abuse-deterrent properties via two major steps (1) API solubility reduction and (2) API carrier dispersion. (Eldem T. et al., 1991; Passerini N. et al., 2006) An optional third step is, unequivocally, coating for added protection of the particle contents.

Solubility reduction can be achieved by either reducing the overall charge of the API molecule, forming a salt between the API and a lipid moiety, forming a complex between API and metal cation, complexation with cyclodextrins, or covalently modifying the molecule with ester or amide linkages.

Following solubility reduction, the modified API is dissolved in a molten wax or lipid with or without the assistance of co-solvents. Suitable materials include fatty alcohols, fatty esters, fatty acid glycerides, hydrogenated oils, and stearates. The final powder is then made via traditional means using congealing, extrusion/spheronization, prilling, or aqueous dispersion (**Fig. 1**) (Eldem T. et al., 1991; Passerini N. et al., 2006). Optional coatings can then be added by traditional means used for coated drug granules with one or more controlled-release polymers for taste-masking or API protection (Dewettinck K. and Huyghebaert A., 1999; Gouin S., 2004; Jono K. et al., 2000; Lopez F.L. et al., 2015; Sastry S.V. et al., 2000).

3.3 Ion exchange resin complexation

Similar to Collegium's DETERx technology, Tris Pharma and Neos Therapeutic's technologies also use a drug-tethering concept, but also provide liquid stability and extended-release. The manufacturing methods between Tris and Neos are very similar (**Fig. 2**), but are described here in brief. The main premise with these two technologies is reliance on an ion-exchange complex between API and inert substrate (Elder D.P., 2005; Fazal U.-R. and Khan S.N., 2012; Mehta K. et al., 2012; Pande S.V. et al., 2011).

The first major step includes manufacturing of a resin

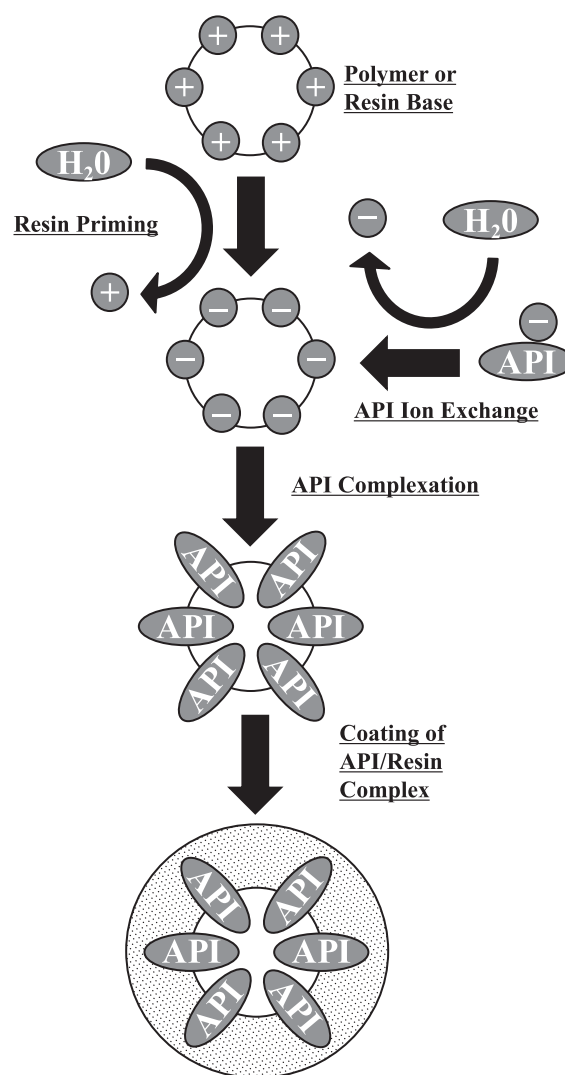


Fig. 2 Tris, Neos, and Collegium all use ion-exchange type processes for powder precursors, but Collegium disperses the API-complex in lipids and waxes that constitute the particle bulk, whereas Tris and Neos place thin coatings over the API-resin complex. All three techniques provide controlled-release, taste-masking, and abuse deterrence.

microparticulate with charged moieties. Resin particles can be created through traditional processes such as suspension polymerisation with polystyrene, methacrylate, or acrylonitrile salts or variants thereof. Resins can be cationic or anionic in nature, depending on whether the API to be complexed is weakly or strongly acidic or basic. The resin must then be primed to ion exchange with the API.

The second step incorporates the ion exchange process during which the API of interest is ionized by salt removal, then complexed to the resin microparticle precursor by itself or with other additives that enhance stability or solubility, such as sugars. This process creates a bond between the API and resin that is more physically and chemically robust than mixing and emulsifying processes in traditional powder extrusion and layering discussed

previously. Following this, the resin is (1) washed to eliminate unreacted API, then (2) dried for the final formulary step.

Just as in traditional powder-coating methods, a final step focuses on securing the complexed API to the resin by coating with controlled-release polymers that provide diffusional control or pH-responsiveness, or layered with lipids and waxes. Following the drug-resin coating, the powder is ready for final format packaging, which may include compressing into ODTs, filling in sachets, titrating into capsules, or bottling into liquid suspensions. Because taste is only perceived when the API is in solution, ion exchange resins provide taste-masking because the API is sequestered to the inert substrate.

3.4 Next generation powder manufacturing

Developing controlled-release powders, to date, has employed combinations of manufacturing mechanisms and complex chemistry, which achieve substantial advantages over traditional pill and capsule formats, enabling extended- and delayed-release liquid suspensions and powder sachets, while providing taste-masking as-is, in a liquid constituent, or further compounded into ODTs or dissolving strips. The major criticisms of these methods, however, focus on the sheer number of process steps and excipients with undefined long-term safety and toxicology profiles (such as polystyrene). Thus, it comes as no surprise that manufacturers are investigating less complex chemistry and single-step manufacturing methods for producing controlled-release powders.

One such technology platform, Precision Particle Fabrication technology, also known as Optimum technology, comes from Orbis Biosciences. The manufacturing scheme creates microsphere and microcapsule powders with high drug loading while maintaining the ability to process into a variety of extended-release, delayed-release, and taste-masked formats (Berkland C. et al., 2007a, 2007b; Pack D.W. et al., 2004a, 2003, 2001, 2002, 2004b).

The approach first creates either (1) a homogenous API-excipient mixture or suspension (i.e. for non-layered microspheres), or (2) separate core and drug-free shell solutions (i.e. for coated microspheres) (**Fig. 3**). High-shear mixing under controlled heat is added, after which the contents are transferred through heat-traced process lines and sprayed through a nozzle with (1) vibrational excitation to produce uniform droplets and (2) stabilizing anti-solvent stream to reduce the diameter of the exiting jet. The platform is capable of processing a variety of liquids, melts, polymer mixtures, slurries, and solutions of various viscosities and thermal properties. Unlike other encapsulation techniques, Optimum's central advantage is the ability to, in a single step, manufacture multi-kilogram batches of microcapsules (core and coating) having nominal diameters around 100 μm and API content up to 80 % by volume. Controlled-release formulations in the pipeline using this next-generation powder technology are APIs such as Ibuprofen, Guaifenesin, Prednisone, and Ritonavir, where the titratable dosing and flexibility allows for unparalleled dissolution matching against reference listed drugs (RLDs). The simultaneous advantages of this manufacturing method are (1) produc-

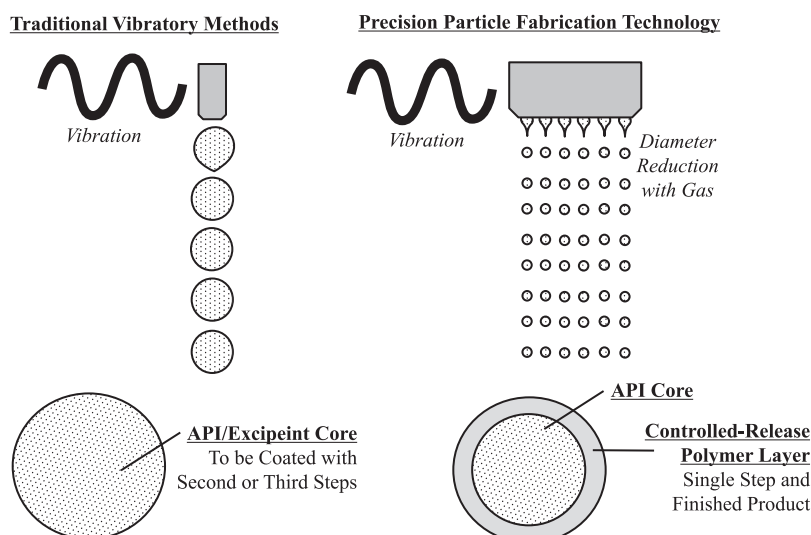


Fig. 3 Precision Particle Fabrication Technology, also known as Optimum technology, creates monodisperse powders just as traditional vibratory methods, but with (1) highly reduced diameters and (2) single-step manufacturing of coatings, which conserves time and resources of historical powder manufacturing techniques. There is also no need for complex chemistry beyond the controlled-release polymers used. Depending on the formulation steps used to incorporate the API, abuse deterrence with Optimum technology is possible, while taste-masking and controlled release are also present.

tion of uniform, monodisperse powders, (2) single-step manufacturing, (3) the ability to control a wide range of therapeutic classes, (4) no requirement for API modification or complexation, (5) no requirement for processing solvents, (6) controlled-release with high API content, and (7) particle sizes that are indiscernible to the patient.

Such high API loading and entrapment is made possible because the Optimum fabrication method can process suspensions and high viscosity mixtures while shearing the molten stream to less than 1/5 of the nozzle orifice before layered droplet breakup and hardening.

4. Formulation examples

Here, we will look closely at specific formulation examples representing some of the highlighted techniques for producing controlled-release powder formulations. Approaches detailed include hot-melt extrusion paired with spinning disk atomization, fluidized bed coating, ion exchange resins, and precision particle fabrication technology. Depending on the steps involved, either an immediate-, delayed-, or extended-release formulation is achieved.

4.1 Azithromycin

This example outlines manufacture of immediate-release microspheres containing azithromycin via hot melt extrusion and spinning disk atomization (Appel L. et al., 2005).

A mixture consisting of 370 g microcrystalline wax, 90 g Pluronic® F87, and 90 g stearyl alcohol was added to a glass beaker in a water bath, and was melted over 60 minutes at 93 °C. Following melting, 450 g azithromycin dihydrate was added such that the anticipated batch size was 1.0 kg with a theoretical drug loading of 45 %. This mixture was mixed for an additional 25 minutes.

Using a gear pump, the molten azithromycin solution was transferred at 250 mL/min onto the center of a spinning disk atomizer, which was rotating at 8000 rpm heated to 100 °C. The microparticles solidified mid-air via convection, were collected in a lined vessel, and determined to have a mean diameter of 190 µm.

Following manufacture, the powder was dissolution tested with a United States Pharmacopeia (USP) Type II apparatus (Fig. 4), which demonstrates the immediate-release nature of the un-coated formulation.

4.2 Cetirizine

This example outlines manufacture of delayed-release microcapsules containing cetirizine via hot melt extrusion, spinning disk atomization, then fluidized bed coat-

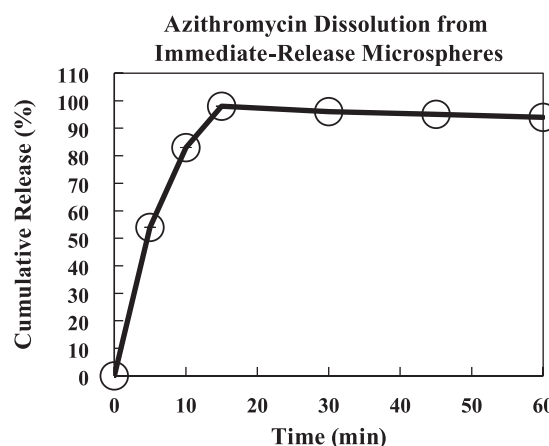


Fig. 4 Dissolution of uncoated azithromycin microspheres created with spinning disk atomization. Paddle speed was 50 rpm in a 37 °C vessel with simulated gastric fluid. Image created from tabulated dissolution data in US 2005/0152982 A1 (Appel L. et al., 2005).

ing.(Appel L. et al., 2012) The manufacture is largely the same as the previous example, with the exception of adding a second coating step to make delayed-release microcapsules.

A mixture consisting of 750 g Compritol® 888 and 62.5 g Pluronic® F127 was added to sealed stainless steel tank, and was melted over 40 minutes at 90 °C with heating fluid circulating through the tank's jacket. The molten solution was stirred at 75 rpm for 5 minutes. Following melting, 250 g cetirizine and 187.5 g of croscarmellose sodium was added such that the anticipated batch size was 1.25 kg with a theoretical drug loading of 20 %. This mixture was stirred for an additional 5 minutes with a high speed homogenizer.

Using nitrogen, the tank was pressurized to 103 kPa to transfer the molten cetirizine solution at 145 g/min onto the center of a spinning disk atomizer, which was rotating at 5500 rpm heated to 90 °C. The microparticles solidified mid-air via convection, were collected in a lined vessel.

The cetirizine-containing microparticles were then coated with a 15 % solution of Surelease® E77050 for 150 minutes in a Glatt GPCG-1 fluidized bed coater equipped with a Würster column set to 15 mm. Circulating air (~17.9 L/s) and bed temperatures were kept at an average of 63 °C and 46 °C, respectively, while the coating was applied between 3.8 and 7.4 g/min at 220 kPa.

Following manufacture, the powder was dissolution tested with a United States Pharmacopeia (USP) Type II apparatus (Fig. 5), which demonstrates the delayed-release nature of the coated formulation.

4.3 Potassium chloride

This example outlines manufacture of extended-release microcapsules containing potassium chloride via coacer-

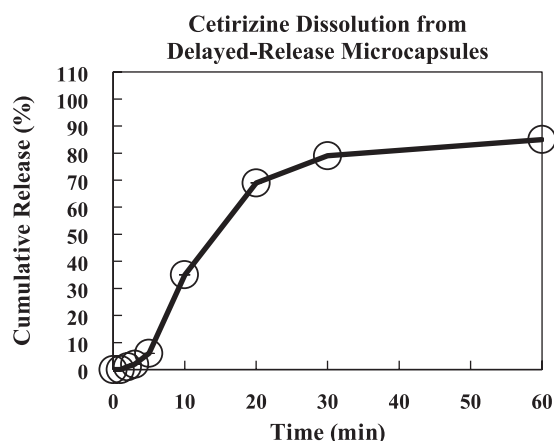


Fig. 5 Dissolution of coated cetirizine microcapsules created with spinning disk atomization and Würster coating. Paddle speed was 50 rpm in a 37 °C vessel with simulated mouth buffer. Image created from tabulated dissolution data in US 8,236,349 B2 (Appel L. et al., 2012).

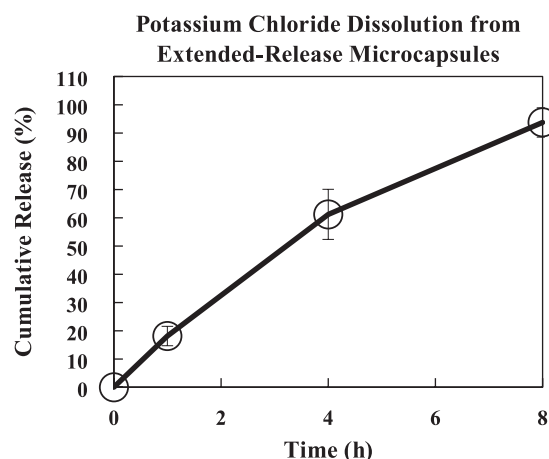


Fig. 6 Dissolution of single-coated potassium chloride microcapsules created with ion-exchange resins. Paddle speed was 100 rpm in a 37 °C vessel with purified water. Image created from tabulated dissolution data in US 5,422,122 (Powell T.C., 1995).

vation, fluidized bed coating (Powell T.C., 1995).

A mixture consisting of 567 kg of potassium chloride crystals between 300 µm and 600 µm in diameter were first mixed with 3312 L of cyclohexane, 83.5 kg of ethylcellulose, and 58 kg of polyethylene. The contents were then heated under agitation until all of the components were in solution. The solution was then cooled to achieve initial coating of the potassium chloride crystals, filtered under vacuum, then dried in a fluidized bed, resulting in single-layer microcapsules less than 850 µm in diameter. A second coating is applied in a fluidized bed coater with a solution consisting of 6.9 kg of hydroxypropylcellulose in 35 L purified water, such that the anticipated batch size was 715 kg with a theoretical drug loading of 79 %.

Following manufacture, the powder was dissolution tested with a United States Pharmacopeia (USP) Type II apparatus (**Fig. 6**), which demonstrates the extended-release nature of the dual-coating formulation.

4.4 Dextromethmorphan

This example outlines manufacture of immediate-release microparticles containing dextromethmorphan via ion exchange resins (Hirsh J. et al., 2005).

First, 1.0 kg of an ion exchange resin, Amberlite® IRP69, was added to 4.75 L of deionized water heated to 90 °C, and was mixed well before adding 300 g of dextromethmorphan HBr. The solution was allowed to mix for 120 minutes to facilitate binding. Next, the resin particles were isolated via vacuum filtration, washed with 10 L of heated deionized water, then re-suspended in another 3 L of heated deionized water. An additional 300 g of dextromethmorphan HBr was then added to the 3 L volume under mixing, which continued for an additional 120 minutes.

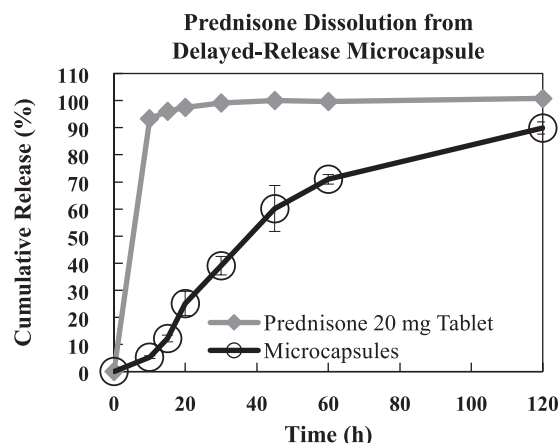


Fig. 7 Dissolution of uncoated dextromethmorphan microparticles created with ion exchange resins. Paddle speed was 50 rpm in a 37 °C vessel with 0.1 N HCl. At 1 hour, the buffer pH was increased to 6.8. Image created from tabulated dissolution data in US 2005/0181050 A1 (Hirsh J. et al., 2005).

Following second stage binding, the reaction mixture was cooled overnight, filtered, washed three times with 10 L volumes of heated deionized water, and dried at 45 °C until substantially free of water as determined by a moisture analyzer. The resulting microparticles had a drug load of approximately 31 %.

Following manufacture, the powder was dissolution tested with a United States Pharmacopeia (USP) Type II apparatus (**Fig. 7**), which demonstrates the immediate-release nature of the un-coated formulation.

4.5 Methylphenidate

This example outlines manufacture of an extended-release microparticle formulation containing methylphe-

nidate via ion exchange resins and fluidized bed coating (Mehta K. et al., 2012). The manufacture is largely the same as the previous example, with the exception of adding second and third coating steps to make extended-release microcapsules. The entire formulation, however, uses single-coated, dual-coated, and drug-free diluent particles to achieve the extended release profile.

First, 3.1 kg of methylphenidate HCl was solubilized in 80 L of purified water with continuous mixing, before adding 7.7 kg of Amberlite® IRP69. This solution was allowed to mix 60 minutes before being filtered, rinsed, and dried until water content was between 3 % and 7 %. The methylphenidate-resin complex was milled and sieved such that particles under 410 µm were isolated for the next step.

In a secondary containment system, 657 g of Kollidon® K30 was dissolved in 2.7 L of purified water, to which the methylphenidate resin complexes were added under mixing until the Kollidon® solution gained nearly 8 % in weight. The slurry was dried until the moisture content was between 15 % and 25 %, milled and sieved a second time to yield particles under 410 µm, dried until water content was between 3 % and 7 %, then milled and sieved a third time to yield particles under 410 µm. The resulting product were single-coated particles.

Dual coated particles were manufactured by applying a second coat to the methylphenidate resin complexes detailed above. A solution consisting of 2.1 kg of purified water, 56 g triacetin, and 3.4 kg Kollicoat® SR30D was prepared and fed to a fluid bed processor with Würster column to coat approximately 3.9 kg of methylphenidate particles from the previous coating step. This was performed until the particles achieved 30 % weight gain. As a last step, the dual-coated methylphenidate ion exchange complex was dried for 5 hours at 60 °C before being passed for a fourth time through a 410 µm mesh screen.

The third component, diluent microparticles, were prepared by mixing 125 g Poloxamer® 188, 34.4 kg sugar, 965 g sodium citrate, 1.3 kg anhydrous citric acid, 500 g sodium benzoate, and 200 g sucralose to 1.8 L purified water in a high shear granulator. The granules were dried until the water content was below 1.5 %, then milled and sieved through an 850 µm mesh screen.

The entire extended release composition consisted of starch, xanthan gum, talc, flavor, and silicon dioxide such that the diluent granules, single-coated granules, and dual-coated granules, approximated 75 %, 1.7 %, and 9.9 % of the total dry weight, respectively.

Following manufacture, the above components were reconstituted to an equivalent of 60 mg methylphenidate in water, and administered to healthy adults. Mean plasma concentration of methylphenidate was compared to adults administered two 30 mg dose of the RLD product (**Fig. 8**), which demonstrates the extended-release nature of the dual-coated formulation.

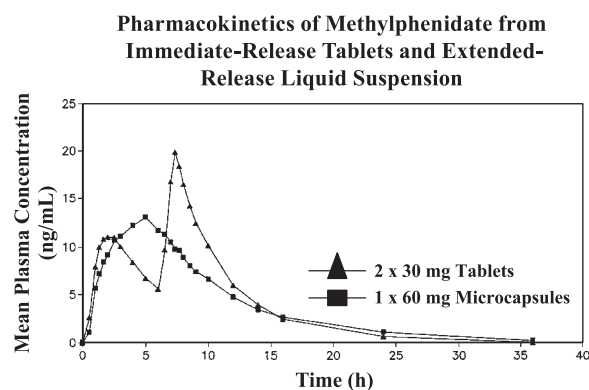


Fig. 8 Pharmacokinetics of a suspension of single-coated, dual-coated, and diluent methylphenidate microcapsules. Plasma concentration was also compared to administration of two 30 mg RLD tablets. The data demonstrate that the microcapsule suspension maintains plasma concentration of methylphenidate as two separately-dosed tablets would. Image reproduced from US 8,287,903 B2 (Mehta K. et al., 2012).

4.6 Prednisone

This example outlines manufacture of taste-masked microspheres containing prednisone via precision particle fabrication (Berkland C. and Singh M., 2014, 2015; Berkland C. et al., 2014). The manufacture is largely the same as the previous example, with the exception of using a dual chamber nozzle for simultaneous coating to yield delayed-release microcapsules.

A mixture consisting of 120 g glyceryl monostearate and 50 g sorbitan monostearate was melted at 95 °C under constant stirring in a jacketed glass reactor under constant mixing. Following, 20 g Eudragit® EPO was added until dispersed. This mixture was allowed to mix for 2 hours, followed by addition of 10 g of prednisone.

The resulting solution was transferred to a 200 mL stainless steel syringe loaded onto a Harvard Apparatus PHD Ultra syringe pump. The syringe was maintained at 80 °C and the contents were injected to primary chamber of a single-barrel stainless steel precision particle fabrication nozzle heated to 80 °C. The flow rate of the prednisone solution was 35 mL/h. such that the anticipated batch size was 200 g with a theoretical prednisone loading of 5.0 %. A third chamber was fed filtered ambient nitrogen at 3.0 L/min to stabilize the droplet breakup. The nozzle was subjected to a frequency of 1.0 kHz with an amplitude of 1.0 Volts, peak-to-peak (Vpp).

The microspheres solidified mid-air via convection and were collected in a stainless steel vessel lined with a 2 mm poly-bag. Resulting particles had a mean size of 180 µm in diameter.

Following manufacture, the powder was dissolution tested with a United States Pharmacopeia (USP) Type II apparatus (**Fig. 9**) and compared to an RLD syrup, which

demonstrates the delayed-release nature of the single-step coated formulation.

4.7 Guaifenesin

This example outlines manufacture of extended-release microspheres containing guaifenesin via precision particle fabrication (Berkland C. and Singh M., 2014, 2015; Berkland C. et al., 2014), where a coating step is not included to achieve extended release.

A mixture consisting of 1360 g carnauba wax, 200 g stearic acid, and 20 g ethylcellulose was melted at 95 °C under constant stirring in a stainless steel mixing vessel. After the molten mixture was formed, 640 g of guaifenesin was incorporated until a homogenous solution was formed such that the anticipated batch size was 1.0 kg with a guaifenesin loading was 32 %.

The resulting solution was pressurized with filtered nitrogen and fed at 1.0 kg/h through a mass flow controller, to the primary chamber of a stainless steel 12-barrel precision particle fabrication nozzle heated to 95 °C. A secondary chamber was fed filtered ambient nitrogen at 3.6 L/min to stabilize the droplet breakup. The nozzle was subjected to a frequency of 1.4 kHz with an amplitude of 1.0 Vpp.

The microspheres solidified mid-air via convection and were collected in a stainless steel vessel lined with a 2 mm poly-bag. Resulting particles had a mean size of 150 µm in diameter.

Following manufacture, the powder was dissolution tested with a United States Pharmacopeia (USP) Type II apparatus (**Fig. 10**) and compared to an RLD tablet, which demonstrates the extended-release nature of the un-coated formulation.

4.8 Ibuprofen

This example outlines manufacture of extended-release microspheres containing ibuprofen via precision particle fabrication (Berkland C. and Singh M., 2014, 2015; Berkland C. et al., 2014), where a coating step is not included to achieve extended release.

A mixture consisting of 3150 g carnauba wax, 250 g stearic acid, and 100 g ethylcellulose was melted at 95 °C under constant stirring in a sealed 30 L stainless steel mixing vessel with high shear homogenizer. After the molten mixture was formed, 1500 g of ibuprofen was incorporated until a homogenous solution was formed such that the anticipated batch size was 5.0 kg with an ibuprofen loading was 30 %.

The resulting solution was pressurized with filtered nitrogen and fed at 2.0 kg/h through heat-traced process lines and distributed to five mass flow controllers, feeding the primary chambers of five stainless steel 12-barrel precision particle fabrication nozzles heated to 95 °C. The

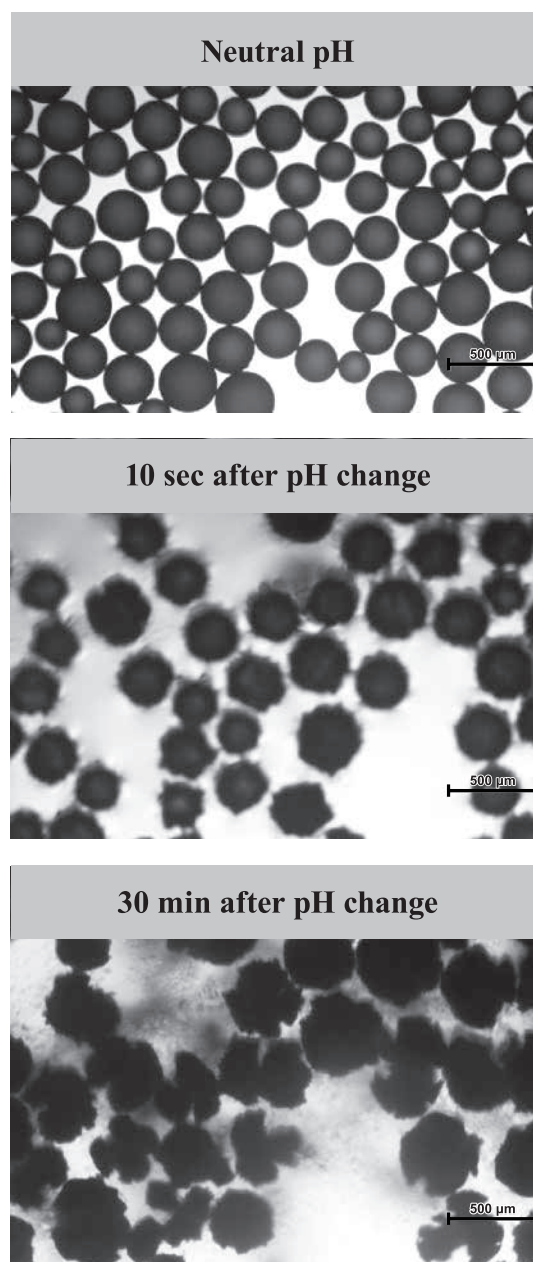
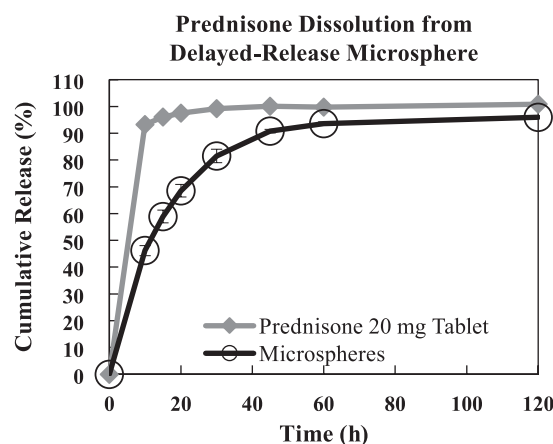


Fig. 9 (Top) Dissolution of coated prednisone microcapsules created with precision particle fabrication. Paddle speed was 75 rpm in a 37 °C vessel with 0.1 N HCl. Data are compared to the RLD tablet. (Bottom) Microsphere rupture *in vitro* after pH change.

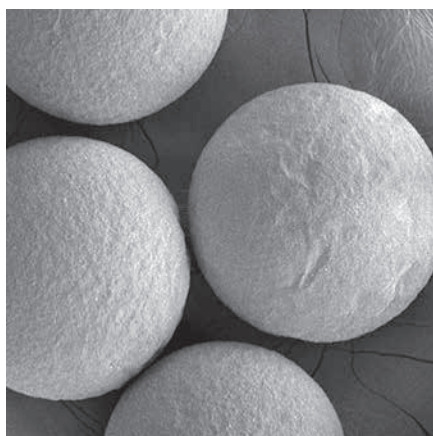
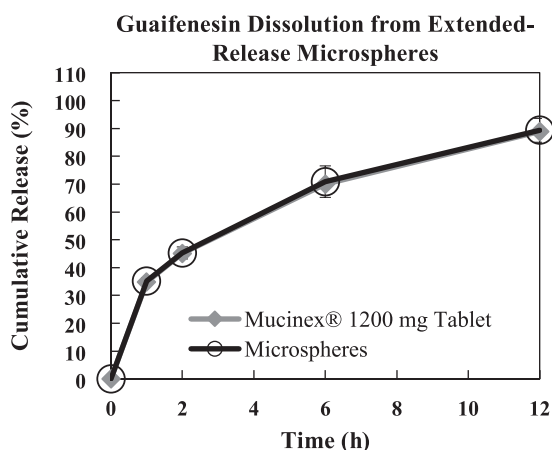


Fig. 10 (Top) Dissolution of uncoated guaifenesin microspheres created with precision particle fabrication. Paddle speed was 75 rpm in a 37 °C vessel with 0.1 N HCl. Data are compared to the RLD tablet, where the microsphere formulation has an F2 (similarity factor) of 97.2. (Bottom) Scanning electron micrograph image of guaifenesin microspheres with a mean size of 150 µm in diameter.

five secondary nozzle chambers were each fed filtered ambient nitrogen at 5 L/min/nozzle to stabilize the droplet breakup. The nozzles were subjected to a frequency of 2.0 kHz with an amplitude of 0.6 Vpp.

The microspheres solidified mid-air via convection inside an enclosed 825 L jacketed stainless steel vessel chilled with heat transfer fluid to a temperature of 15 °C. Resulting particles had a mean size of 120 µm in diameter.

A similar formulation was also made on a single-barrel precision particle fabrication nozzle that with a composition of 45 % carnauba wax, 25 % stearic acid, and 30 % ibuprofen.

Following manufacture, the powders were dissolution tested with a United States Pharmacopeia (USP) Type II apparatus (**Fig. 11**) and compared to an RLD tablet, which demonstrates the extended-release nature of the un-coated formulations.

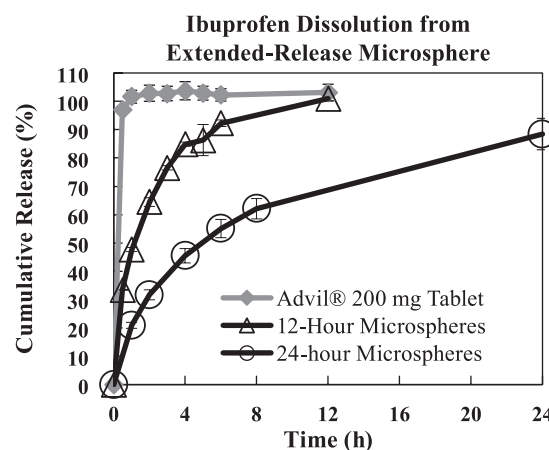


Fig. 11 Dissolution of uncoated 12-hour and 24-hour extended-release ibuprofen microspheres created with precision particle fabrication. Paddle speed was 75 rpm in a 37 °C vessel with 0.05 M SLS. Data are compared to the RLD tablet.

4.9 Ritonavir

This example outlines manufacture of taste-masked microcapsules containing ritonavir via precision particle fabrication (Berkland C. and Singh M., 2014, 2015; Berkland C. et al., 2014). The manufacture is largely the same as the previous example, with the exception of using a dual chamber nozzle for simultaneous coating to yield delayed-release microcapsules.

A mixture consisting of 40 g stearic acid and 10 g Eudragit® EPO was melted at 95 °C under constant stirring in a stainless steel mixing vessel. This mixture would comprise the microcapsule shell feed.

A second vessel was prepared where 42.5 g of polyethylene glycol 1500 was melted at 80 °C. Following, 7.5 g of ritonavir was incorporated until a homogenous dispersion was formed. This mixture would comprise the microcapsule core feed.

The resulting solutions were each transferred to 50 mL stainless steel syringes loaded onto a Harvard Apparatus PHD Ultra syringe pumps. The syringes were maintained at 80 °C and the contents were simultaneously injected to primary and secondary chambers of a single-barrel stainless steel precision particle fabrication nozzle heated to 80 °C. The flow rates of the prednisone-free shell and prednisone-containing core were set to 30 mL/h and 20 mL/h, respectively, such that the anticipated batch size was 90 g with a theoretical prednisone loading of 6.7 %. A third chamber was fed filtered ambient nitrogen at 2.5 L/min to stabilize the droplet breakup. The nozzle was subjected to a frequency of 1.0 kHz with an amplitude of 1.0 Vpp.

The microcapsules solidified mid-air via convection and were collected in a stainless steel vessel lined with a

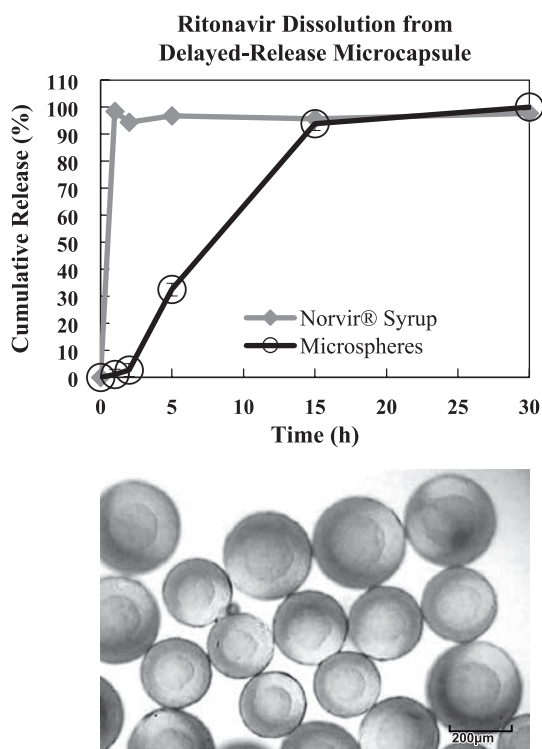


Fig. 12 Dissolution of coated delayed-release ritonavir microcapsules created with precision particle fabrication. Paddle speed was 75 rpm in a 37 °C vessel with 0.1 N HCl for the first 2 minutes, then 0.05 M SLS. Data are compared to the RLD syrup.

2 mm poly-bag. Resulting particles had a mean size of 250 µm in diameter.

Following manufacture, the powder was dissolution tested with a United States Pharmacopeia (USP) Type II apparatus (**Fig. 12**) and compared to an RLD syrup, which demonstrates the delayed-release nature of the single-step coated formulation.

5. Conclusion

Though traditional oral dosage forms such as pills, capsules, caplets, and tablets work for many individuals, a significant fraction of the world's population suffers from dysphagia, taste sensitivities, or an unwavering avoidance to taking oral medication of any format. As these patients are afflicted with acute or chronic illnesses, sometimes a lack of format flexibility and dosage options limits treatment, and in the worst circumstances, prevents it.

An emergence in manufacturing of controlled-release powders has taken place over the last decade, replacing large tablets with dispersible and dose-flexible alternatives that can be supplied in sachets, sprinkled in food, or suspended in liquid. The methods for making controlled release powders vary, but typically include forming an API/excipient core precursor then coating with one or

more controlled-release layers for a finished product. Contemporary techniques incorporate chemical modification and sequestration of the API, prior to secondary coating steps. Next-generation techniques eliminate the need for multiple steps, achieving even coatings while maintaining monodisperse size distributions and high API content at small overall particle size to enhance palatability and mouth-feel. Though the number of powder alternatives that are available for currently approved medications is limited, a rising number of pharmaceutical companies and manufacturing organizations are incorporating controlled-release powder manufacturing to their portfolios to address the growing dosage form problem for paediatric and geriatric patients. In an age where “bigger is better,” for nearly everything in culture, the opposite is unquestionably becoming true for powders, where “less is more” in terms of dosage form size, manufacturing steps, and process chemistry.

Nomenclature

D	particle size (µm)
l	length (m)
m	mass (kg)
P	pressure (Pa)
t	time (s)
Δt	time duration
T	temperature (K)
V	volume (L)
μ	gas (Pa s)
ρ_g	density (kg m ⁻³)
V_{pp}	volts, peak-to-peak

References

- Best pharmaceuticals for children act, Public Law 107–109, Washington, DC, 2002.
- Ambike A.A., Mahadik K.R., Paradkar A., Spray-dried amorphous solid dispersions of simvastatin, a low T_g drug: *In vitro* and *in vivo* evaluations, *Pharmaceutical Research*, 22 (2005) 990–998.
- Appel L., Friesen D.T., Lachapelle E.D., Konagurthu S., Falk R.F., Reo J.P., Taste-masked drugs in rupturing multiparticulates, Google Patents, <https://www.google.com/patents/US8236349> (2012).
- Appel L., Ray R., Newbold D., Lyon D., West J., Friesen D., Mccray S., Crew M., Lo J., Controlled release multiparticulates formed with dissolution enhancers, Google Patents, <https://www.google.com/patents/US20050152982> (2005).
- Bergstrom D., McNally E., Freeman S., The growing pediatrics

- market, Pharmaceutical Executive, (2004).
- Berkland C., Pollauf E., Raman C., Silverman R., Kim K., Pack D.W., Macromolecule release from monodisperse PLG microspheres: Control of release rates and investigation of release mechanism, *Journal of Pharmaceutical Sciences*, 96 (2007a) 1176–1191.
- Berkland C., Pollauf E., Varde N., Pack D.W., Kim K., Mono-disperse liquid-filled biodegradable microcapsules, *Pharmaceutical Research*, 24 (2007b) 1007–1013.
- Berkland C., Singh M., Sustained release particle formulations, Google Patents, <https://www.google.com/patents/US20140294980> (2014).
- Berkland C., Singh M., Taste masking drug formulations, Google Patents, <https://www.google.com/patents/WO2015130760A1?cl=en> (2015).
- Berkland C., Singh M., Dormer N., Tramadol particle formulations and methods, Google Patents, <https://www.google.com/patents/WO2014205228A1?cl=en> (2014).
- Bhardwaj S., Hayward M., Palatable pharmaceutical compositions, SmithKline Beecham Corporation, (1996).
- Cloupeau M., Prunet-Foch B., Electrohydrodynamic spraying functioning modes: A critical review, *Journal of Aerosol Science*, 25 (1994) 1021–1036.
- Cram A., Bartlett J., Heimlich J., Oral multiparticulates as a flexible solid dosage form approach for paediatric use, *BioPharm Asia*, (2013).
- Dewettinck K., Huyghebaert A., Fluidized bed coating in food technology, *Trends in Food Science & Technology*, 10 (1999) 163–168.
- Dickens D.S., Sinsabaugh D., Fahner J.B., Characteristics of pediatric chemotherapy medication errors in a national error reporting database, *Cancer*, 112 (2008) 445–446; author reply 446.
- Eldem T., Speiser P., Hincal A., Optimization of spray-dried and -congealed lipid micropellets and characterization of their surface morphology by scanning electron microscopy, *Pharmaceutical Research*, 8 (1991) 47–54.
- Elder D.P., Pharmaceutical applications of ion-exchange resins, *Journal of Chemical Education*, 82 (2005) 575.
- Engelen L., De Wijk R.A., Van Der Bilt A., Prinz J.F., Janssen A.M., Bosman F., Relating particles and texture perception, *Physiol Behav*, 86 (2005) 111–117.
- Fazal U.-R., Khan S.N., Therapeutic applications of ion exchange resins, in: Inamuddin D. and Luqman M. (Eds), *Ion exchange technology ii: Applications*, Springer Netherlands, Dordrecht, 2012, pp. 149–168.
- Gharsallaoui A., Roudaut G., Chambin O., Voilley A., Saurel R., Applications of spray-drying in microencapsulation of food ingredients: An overview, *Food Research International*, 40 (2007) 1107–1121.
- Gouin S., Microencapsulation: Industrial appraisal of existing technologies and trends, *Trends in Food Science & Technology*, 15 (2004) 330–347.
- Griffith R., Managing difficulties in swallowing solid medications: The need for caution., *Nurse Presc*, 3 (2005) 201–203.
- Hancock B.C., Colvin J.T., Mullarney M.P., Zinchuk A.V., Pharmaceutical powders, blends, dry granulations, and immediate-release tablets, *Pharmaceutical technology*, (2003) 64–80.
- Harb J., Why so many pills are too big to swallow: And why it's safe to crush or cut up some, but not others., (2015)
- Hirsh J., Fleming A., Rariy R., Dosage forms using drug-loaded ion exchange resins, Google Patents, <https://www.google.com/patents/US20050181050> (2005).
- Imai E., Hatae K., Shimada A., Oral perception of grittiness, *Journal of Textural Studies*, 26 (1995) 561–576.
- Ivanovska V., Rademaker C., Van Dijk L., Mantel-Teeuwisse A., Pediatric drug formulations: A review of challenges and progress, *Pediatrics*, 134 (2014).
- Jayanthi B., Manna P., Per oral extended products – an overview, *J App Pharm Sci*, 1 (2011) 50–55.
- Jono K., Ichikawa H., Miyamoto M., Fukumori Y., A review of particulate design for pharmaceutical powders and their production by spouted bed coating, *Powder Technology*, 113 (2000) 269–277.
- Lopez F.L., Ernest T.B., Tuleu C., Gul M.O., Formulation approaches to pediatric oral drug delivery: Benefits and limitations of current platforms, *Expert Opinion on Drug Delivery*, 12 (2015) 1727–1740.
- Maalouf N., Developing patient-centric drug formulations to meet patient needs, (2013).
- Matsui D., Current issues in pediatric medication adherence, *Paediatr Drugs*, 9 (2007) 283–288.
- Mehta K., Tu Y.H., Perumal A., Orally effective methylphenidate extended release powder and aqueous suspension product, Google Patents, <https://www.google.com/patents/US8287903> (2012).
- Milne C.P., Bruss J.B., The economics of pediatric formulation development for off-patent drugs, *Clin Ther*, 30 (2008) 2133–2145.
- Osterberg L., Blaschke T., Adherence to medication, *New Engl J Med*, 353 (2005).
- Pack D.W., Berkland C., Cox A., Kim K., Three-month, zero-order piroxicam release from monodispersed double-walled microspheres of controlled shell thickness, *Journal of Biomedical Materials Research Part A*, 70A (2004a) 576–584.
- Pack D.W., Berkland C., Kim K., PLG microsphere size controls drug release rate through several competing factors, *Pharmaceutical Research*, 20 (2003) 1055–1062.
- Pack D.W., Berkland C., Kim K.K., Fabrication of PLG microspheres with precisely controlled and monodisperse size distributions, *Journal of Controlled Release*, 73 (2001) 59–74.
- Pack D.W., Berkland C., King M., Cox A., Kim K., Precise control of PLG microsphere size provides enhanced control of drug release rate, *Journal of Controlled Release*, 82 (2002) 137–147.
- Pack D.W., Berkland C., Kipper M.J., Narasimhan B., Kim K.K., Microsphere size, precipitation kinetics and drug distribution control drug release from biodegradable polyanhydride microspheres, *Journal of Controlled Release*, 94 (2004b) 129–141.
- Pande S.V., Kshirsagar M.D., Chandewar A.V., Ion exchange resins pharmaceutical applications and recent advancement, 2011, 2 (2011).
- Passerini N., Albertini B., Perissutti B., Rodriguez L., Evalua-

- tion of melt granulation and ultrasonic spray congealing as techniques to enhance the dissolution of praziquantel, *International Journal of Pharmaceutics*, 318 (2006) 92–102.
- Pediatric research equity act, Public Law 108–155, Washington DC, 2003.
- Pharmacircle, (2016), www.pharmacircle.com, from www.pharmacircle.com.
- Powell T.C., Controlled release potassium chloride tablet, Google Patents, <https://www.google.com/patents/US5422122> (1995).
- Regulation no. Ec 1901/2006, Ec E.P.a.T.C., Brussels, (2006).
- Rocca J.G., Park K., Oral drug delivery: Prospects and challenges, *Drug Development and Delivery*, 4 (2004) No.4. <http://www.drug-dev.com/Main/Back-Issues/187.aspx>.
- Sansom L., Oral extended-release products, *Aust Prescr*, 22 (1999) 88–90.
- Sastry S.V., Nyshadham J.R., Fix J.A., Recent technological advances in oral drug delivery – a review, *Pharmaceutical Science & Technology Today*, 3 (2000) 138–145.
- Schier J., Howland M., Hoffman R., Nelson, Fatality from administration of labetalol and crushed extended-release nifedipine, *Annals of Pharmacotherapy*, 37 (2003) 1420–1423.
- Sugao H., Taste masking of bitter drug powder without loss of bioavailability by heat treatment of wax-coated microparticles, *Journal of Pharmaceutical Sciences*, 87 (1997).
- Tyle P., Effect of size, shape and hardness of particles in suspension on oral texture and palatability, *Acta Psychologica*, 84 (1993) 111–118.
- Vehring R., Pharmaceutical particle engineering via spray drying, *Pharmaceutical Research*, 25 (2007) 999–1022.
- Vummaneni V., Nagpal D., Taste masking technologies: An overview and recent updates, *International Journal of Research in Pharmaceutical and Biomedical Sciences*, 3 (2012) 510–525.
- Wright D., Medication administration in nursing homes, *Nurse Std*, 16 (2002) 33–38.
- Yurteri C.U., Hartman R.P.A., Marijnissen J.C.M., Producing pharmaceutical particles via electrospraying with an emphasis on nano and nano structured particles—a review, *KONA Powder and Particle Journal*, 28 (2010) 91–115.

Author's short biography



Martin G. Teresk

Martin Teresk, PhD, joined Orbis after completing five years at Gilead Sciences, where he served as a process development chemist. Martin's expertise resides in designing, developing, and validating robust and commercially viable processes for the manufacturing of active pharmaceutical ingredients. He holds a PhD in Organic Chemistry from University of Texas at Austin and a BS in Chemistry from Purdue.



Cory J. Berkland

Cory Berkland, PhD, has been developing microencapsulation and drug delivery capabilities for more than a decade. Cory has a PhD in Chemical and Biomolecular Engineering from the University of Illinois, Urbana-Champaign, where he co-invented and developed the Orbis technology. Cory is a Professor of Pharmaceutical Chemistry and Chemical and Petroleum Engineering at The University of Kansas.



Nathan H. Dormer

Nathan Dormer, PhD, leads the formulation team at Orbis Biosciences. He has more than 8 years of experience developing a variety of controlled-release solutions using microsphere techniques. He received his BS in Chemical Engineering from The University of Kansas before completing his PhD in Bioengineering from The University of Kansas with NIH-sponsored training in drug delivery and protein stability. He has authored a number of publications and book chapters relating to microspheres.

A Review of Advanced Ball Mill Modelling[†]

Luís Marcelo Tavares

¹ *Department of Metallurgical and Materials Engineering, COPPE, Universidade Federal do Rio de Janeiro, Brazil*

Abstract

In the early 1990s the discrete element method (DEM) was used for the first time to simulate media motion in tumbling mills. Although it has been over a quarter of a century since this tool was first used to predict media motion it has not yet reached maturity to be used in predicting product size distribution and throughput of tumbling mills. However, there has not been shortage of attempts to do so. The literature is relatively vast in the topic and researchers who embark in this area of research will find it difficult to understand the current status of development and also the similarities and fundamental differences that exist amongst the various approaches that have been proposed and pursued over the years. The paper reviews the literature on the application of models based on distributed collision energy information to predict size reduction in tumbling mills, in particular ball mills, analyzing critically various approaches proposed, their limitations and achievements, identifying areas that still require development until the technology becomes ready for being used for optimizing and designing ball mills. Finally, the advances recently accomplished on the approach proposed by the author and his co-workers are then reviewed in greater detail.

Keywords: modeling, discrete element method, ball mills, mechanistic

1. Introduction

In spite of the development and increase in popularity of several other technologies, such as vertical roller mills, stirred media mills and high-pressure grinding rolls, ball mills still retain a significant part of their importance in grinding, being widely used from minerals and cement, to chemicals and ceramics. The operation of a ball mill is a capital- and energy-intensive process, so that even marginal improvements in their efficiency result in immense benefits to the industry. These mills are more often of the tumbling type, but also include planetary and vibratory mills, which have all in common the analogous type of motion of the loose grinding media. It has been long recognized that in order to reduce their size, materials require the application of energy in some form. This recognition led to attempts to relate energy and size reduction from the latter part of the 19th century (von Rittinger, 1867; Kick, 1885) throughout the 20th century (Bond, 1952; Charles, 1957), and even more recently (Morrell, 2004).

These different approaches have one thing in common: they use a single number to describe energy in grinding.

This number, the specific energy, is the ratio between the power and the throughput in the case of continuous systems, or the power multiplied by the grinding time per unit mass of powder or ore in batch mills. Given typically in kWh/t, it has long been recognized as the most important descriptor of the contribution of the process to the outcome of comminution. The importance of specific energy and the knowledge on how mill power can be controlled by varying mill design and operating variables, has allowed engineers design mills and improve a large number of operations throughout the 20th century (Herbst and Fuerstenau, 1980). These so-called energy-size reduction relationships were originally only used as one-size descriptors of comminution (Bond, 1952), but with the advent of the size-mass balance, or population balance model (Herbst and Fuerstenau, 1980), improvements from this type of relationships also became useful to describe the change of the entire size distribution from the feed to the product.

A more in-depth look at ball mill operation clearly suggests the richness of the information hidden behind the value of specific energy in an operation, which should be regarded as merely an average number. The emphasis on this number suggests, in principle, that it would not matter how the material receives energy, just the amount. Single-particle breakage has allowed us to gain insights into this by analyzing the different outcomes if a particle receives energy in the form of a single high-energy im-

[†] Received 23 May 2016; Accepted 13 June 2016
J-STAGE Advance Publication online 30 August 2016
¹ Cx. Postal 68505, CEP 21945-970, Rio de Janeiro, RJ, Brazil
E-mail: tavares@ufrj.br
TEL: +55-21-2290-1544 Ext. 246

pact from the grinding media, or from a multitude of very low-energy impacts, which have very different outcomes (Pauw and Maré, 1988; Tavares, 2004). Evidence of this also appears in the form of the empirical equations that have been used to account for several variables in grinding in tumbling mills that are part of the design method of Bond (Rowland and Kjos, 1980), as well as to the need for the user to conduct additional batch grinding tests to fit some of the model parameters in the case of the scale-up method proposed by Herbst and Fuerstenau (1980).

As such, great value can be gained by using distributed information on specific comminution energies, rather than averages. Such information has already been available from careful experimentation or, more commonly, simulations using the discrete element method (DEM), which conveniently allows predicting the distribution of collision energies in a mill (Weerasekara et al., 2013), creating an alternative to the lumped specific energy information used to date to describe size reduction in mills. DEM makes it possible to predict how collisions vary in magnitude and frequency as the geometry, the ball charge and the mill speed are varied. Therefore, instead of correlating each individual parameter such as mill diameter, filling, speed and ball size, for instance, to the product size, one can directly take into account the record of the collisions and their influence on the particle size distribution in the mill.

There has been no shortage in the last 25 years or so of approaches to use such distributed collision energy information in modelling ball mills. However, it is not straightforward to identify how they differ, their benefits and challenges in their goal of replacing the traditional energy-size reduction methods such as Bond's (Bond, 1952) or population balance model (PBM) formulations (Herbst and Fuerstenau, 1980; Austin et al., 1984). The present work focuses primarily on the research dedicated to predict particle breakage in ball mills, analyzing in particular DEM-based approaches to predict size reduction in mills, called here "advanced models". As such, this review does not directly cover other aspects that are also necessary to predict grinding in continuous systems, such as material transport and internal classification, which also were the object of much research throughout the last quarter of century.

2. Advanced mill modelling prior to DEM

The first attempts in coupling impact energy information to particle breakage data to predict grinding have been made in the late 1980s and early 1990s. These were used to predict the functions that make up the traditional population balance model. The greatest difficulty at the time was associated to the collection of information on

the collision energies in the mill. Yashima et al. (1988) and Nomura et al. (1991) estimated the size-dependent rates of breakage of particles contained in ball mills using single-particle slow compression data and experimental measurements of impact energy spectra using load sensors positioned in the shell of a lab mill, showing some qualitative agreement. Cho (1987) and Höfler and Herbst (1990) demonstrated how both the breakage rate and the breakage distribution functions varied with collision energy, using data from particle bed breakage tests and impact energy spectra from tests in a batch mill. Their work proposed that the breakage function B_{ij} commonly used in the traditional population balance model could be interpreted as the weighed-average of the energy-dependent breakage distribution function values $B_{ij}(E_{m,k})$, giving (Cho, 1987)

$$B_{ij} = \sum_{k=1}^n p(E_{m,k}) B_{ij}(E_{m,k}) \quad (1)$$

where $p(E_{m,k})$ is the fraction of collisions with specific energy level $E_{m,k}$. This equation could be used, associated to the breakage rate or selection function (S_i) to predict grinding in a batch mill using the equation (Austin et al., 1984)

$$\frac{dw_i}{dt} = -S_i w_i + \sum_{j=1}^{i-1} S_j b_{ij} w_j \quad (2)$$

where w_i is the fraction of particles in size class i at time t and b_{ij} is the breakage function in density form, so that $b_{ij} = B_{ij} - B_{i-1,j}$.

This is certainly a more logical and intuitive approach than assuming a constant breakage distribution function, as used in the traditional PBM formulation of ball milling. These approaches, however, had the serious limitation of requiring impact energy data, which was very difficult to estimate experimentally. In the case of Cho (1987), the distribution of collision energies was back-calculated from batch grinding data, so that it should be understood as only a proof of concept of the modeling approach.

3. Role of DEM in advanced mill modelling

A major advance in the modeling of ball mills became possible through the development of the discrete element method. DEM provides a numerical procedure for solving Newton's second law with an appropriate contact relationship that can be applied to describe the motion of each grinding medium contained in the mill charge to predict element position, velocity and forces of interaction over time. Very good reviews of the method when applied to comminution can be found elsewhere (Cleary, 1998; Weerasekara et al., 2013). The relevance of the method when applied to milling lies in its ability to account for

the effects of a number of variables explicitly, including mill speed, mill filling, ball size distribution and liner configuration. It was first applied to simulate ball milling by Mishra and Rajamani (1992), who originally described media motion in two dimensions. The technique is now packaged in a number of commercial as well as open source software, being able to describe media motion in three dimensions, which is critical to provide the quantitative information required for mill simulation (Powell and McBride, 2006; Morrison and Cleary, 2008).

In DEM, particles are either considered undeformable (hard) or deformable (soft) (O’Sullivan, 2011). The latter, in which particles are allowed to overlap, is the most commonly used. It is supported by proper constitutive laws describing the contacts, with Hertz-Mindlin being the most commonly used (Weerasekara et al., 2013).

Algorithms that allow describing particle breakage inside the DEM environment are more recent developments, and include the discrete grain breakage (Herbst and Potapov, 2004), the bonded particle model (Potyondy and Cundal, 2004) and the particle replacement (Cleary, 2001). As such, DEM with the proper description of particle breakage appeared as a complete and empiricism-free solution to the current approaches used in modeling ball mills, since it does not only allow describing media motion, but also breakage of particles inside the charge (Morrison and Cleary, 2008). Indeed, as a proof of concept, some researchers have demonstrated that it is possible to include particles in mill simulations and follow them as they tumble and are progressively broken by the balls. Indeed, Herbst and Potapov (2004) included polyhedral particles that broke inside the charge, Metzger and Glasser (2013) described breakage of particles inside a batch mill using the bonded particle model, while Delaney et al. (2013) described breakage of particles in a pilot mill using the particle replacement method. Unfortunately, this intuitive approach is not yet feasible to be used in any realistic way to simulate industrial ball mills, since breakage algorithms add to the already high computational demand for simulating these mills and also can lead to an “explosion” on the number of particles in the simulations, making computation unfeasible at this time. However, such techniques are quickly reaching maturity for application in simulation of a number of crusher types (Cleary and Sinnott, 2015; Quist and Evertsson, 2016; Barrios and Tavares, 2016). With increasing computation power, these techniques will become, however, gradually more applicable to tumbling mills, in particular of the autogenous and semi-autogenous type, given that the autogenous media not only also transfers energy but also undergoes breakage.

DEM simulation of industrial tumbling mills can represent a challenge even in the absence of breakage in the DEM environment. This is because the powder or ore

particles are much finer in size than the grinding media, leading to difficulty in keeping track of the immense number of particles contained in full-scale mills, besides the need to reduce the time step to avoid overlapping the media with the smallest powder particles (Cleary and Morrison, 2011). The first limitation can be illustrated with a simple example: the most common tumbling mill used in the lab is the Bond ball mill, used to measure the widely used Bond ball mill work index (Bond, 1952). The mill dimensions, 30 cm in diameter and 30 cm in length, and the test conditions are standardized, with a maximum ball size of 40 mm and an ore top size of 3.35 mm. With less than 300 balls, it poses no challenge in running the simulations, if only grinding media are included (**Fig. 1**). For such a small mill and operating at both low mill filling (20 %) and powder filling (50 %), one could include also the powder charge. Indeed, for a typical powder size distribution, it would be possible to include particles as fine as about 0.5 mm before running out of memory using today’s desktop computers, since it could take as much as 10 GB of computer memory to run them, for instance, in a commercial software such as EDEM® (DEM Solutions, UK) which is substantial (**Fig. 1**). However, if the case of a large-diameter industrial mill is considered, which could have, for instance, 8 m of internal diameter, the user would already run out of memory if he included particles with the top size in the feed, if the same ball and particle size distributions simulated in the laboratory mill are used. Moreover, this is only considering a 30 cm slice of the mill, which could have more than two billion elements with sizes above 0.5 mm (**Fig. 1**).

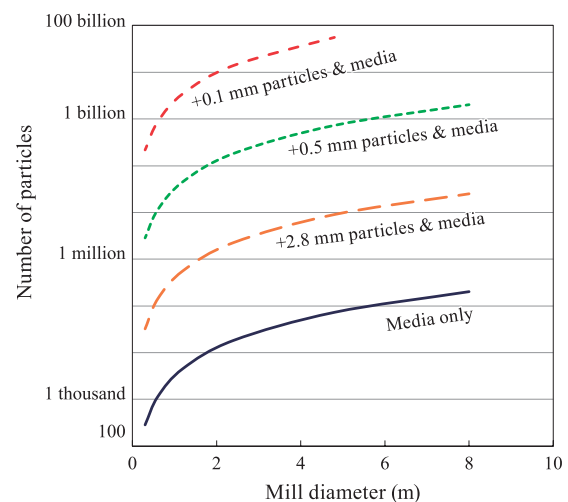


Fig. 1 Number of particles used in simulating 30 cm slices of mills with different diameters (balls in size range of 40–15 mm) and powder following the cumulative size distribution given by $\text{Passing} = (x/3.35)^{0.5}$, where particle size x is given in mm (20 % ball filling, 50 % interstitial powder filling). Powder finer than designated size is accumulated in the informed size.

Nevertheless, it is worth mentioning that the increase in computing power in recent years has enticed researchers to include both grinding media and powder in some simulations of small ball mills, which has been particularly useful to understand the collision frequencies and energies involved in media-particle contacts (Cleary and Morrison, 2011; Wang et al., 2012; Capece et al., 2014). This type of simulations, however, represents a challenge in gathering collision information, since the event of a particle being nipped by two colliding media is logged as two separate collisions of lower magnitude.

One pragmatic solution to this in the case of ball mills is to simplify the problem by not including the ore or powder particles in DEM, only the grinding media in the simulations, calculating the product size distribution and the mill capacity in a post-processing stage using a PBM scheme on the basis of the frequencies and magnitudes of collisions, that is, the collision energy spectrum, experienced by particles in the mill. The key advantage of this approach is that the milling environment can be decoupled from the ore or powder in size reduction, while the main challenge is related to the fact that the mass of material and sizes of particles involved in each of the collisions are not known. Also, this approach is only valid whenever the contribution of the ore or powder particles in transferring energy and inducing breakage in other particles is negligible, which is a valid assumption in the case of ball mills. As such, DEM would be given the role of only providing information on the mechanical environment in the mill, since the ore particles would not appear explicitly in the simulations. Powell et al. (2008) called these ore particles “sub-DEM particles”, since they would be the background material that is subjected to the collisions through being entrapped between the colliding media, but would not appear in the DEM simulations explicitly.

In order to ensure that predictions of the collision energy spectra under these circumstances are realistic, it is important to ensure that DEM simulations can predict mill media motion accurately. This problem is not straightforward since the absence of powder (ore) in the DEM simulations would need to be compensated by modifying some—if not all—of the contact parameters that govern the contacts between balls and between them and the mill liners. This can only be accomplished by proper contact parameter estimation, which is reviewed elsewhere (Mishra and Murty, 2001). As such, the user should be aware that apparent contact parameters and not standard parameters for steel-steel contacts (whenever steel media are used), for instance, should be used in these simulations, given the dissipative effect of the background powder. Typically, the presence of powder increases the rolling and sliding friction of the ball charge, while it reduces the coefficient of restitution in the Hertz-Mindlin model. Obvious challenges are associated to the variation

of the motion of the charge as particles become finer. This evidently further complicates matters when using data from batch milling to calibrate DEM contact parameters, which is common.

It is common to select contact parameters in DEM simulations so as to match the power predicted to the one measured either in a batch or an industrial mill. However, caution should be exercised in not using it as the only target when selecting values of contact parameters in ball mill simulations. It is known that several sets of plausible contact parameters can approximately match the measured mill power, but with reasonably distinct patterns of media motion (Martins et al., 2012; Chagas et al., 2015). Positions of toe and shoulder of the charge, monitored by video recordings of batch mills fitted with a transparent end covers (Moys et al., 2000; Venugopal and Rajamani, 2001), the position and velocity of an instrumented ball (Martins et al., 2012) or of an irradiated ball using positron emission particle tracking (PEPT) (Govender et al., 2013; Chagas et al., 2015), are excellent alternatives to be used in conjunction with net mill power to calibrate contact parameters for effective mill simulations.

Once the mill geometry, velocity and the charge size distribution have been defined, and the various material and contact parameters selected, the mill can then be simulated. It is important to ensure, though, that a steady motion of the media has been established, which takes several revolutions if the charge is initially in repose. After this is established, the mill can then be simulated for a sufficient period of time to give a consistent output, which is about two revolutions (Powell et al., 2008), during which detailed information on the collisions are recorded. At this point the simulation is interrupted and the interactions between grinding media and between them and the mill liners are binned for analysis at a post-processing stage. This analysis provides the probability distributions, which in effect are the rates at which grinding media interact. The question then arises about the collision energy information that will be harnessed from DEM. Three options have been considered by researchers:

- the dissipated energy
- the maximum impact energy
- the kinetic energy

The dissipated energy, also called energy loss, results from the inelastic contact between grinding media or grinding media and an ore particle, that mimics dissipative processes such as plastic deformation or breakage. It is calculated as the integral of the damping forces with respect to the displacements over a whole contact period, accounting for the contributions of both the normal (n) and the shear (s) components of the contact:

$$E = E_n + E_s = \int_0^{t_{\text{contact}}} F_n d\zeta_n + \int_0^{t_{\text{contact}}} F_s d\zeta_s \quad (3)$$

where F_n and F_s are the components of the contact force in the normal and shear directions, respectively, and t_{contact} is the total contact time during a collision.

The maximum impact energy, characterizing the maximum stress experienced in the collision, is the integral of the contact force and displacement in the normal direction when the overlap between two particles reaches the maximum (Wang et al., 2012).

The kinetic energy in the collision between two grinding media is calculated by $1/2 m_b v_{ij}^2$, where v_{ij} ($= v_i - v_j$) is the relative normal velocity of the two grinding media at the collision and m_b is average ball mass ($= (m_{b,i} + m_{b,j})/2$) for media-media collision or the mass of one ball for ball-liner collision, whereas the reduced mass, given by ($= 2m_{b,i}m_{b,j}/(m_{b,i} + m_{b,j})$) is also often used (Kwan et al., 2005).

It is convenient, for comparison purposes, to represent distributions of collision energies in the form of cumulative distribution functions $P(E)$ and total frequency of collisions ω . Cumulative distributions are illustrated in **Fig. 2** for different liner configurations in a batch mill. Whenever necessary the distribution of collision energies in density form in the mill $p(E)$ may be calculated from the cumulative distribution, with $p(E) = dP(E)/dE$.

Finally, when grinding is carried out wet, the presence of water would also influence the contact parameters. As such, coupling of DEM and techniques such as computational fluid dynamics (CFD) or smoothed particle hydrodynamics (SPH) would allow realistic description of the influence of the fluid medium (Cleary et al., 2006). The fidelity of the simulation models able to predict breakage will then determine whether or not it is feasible to still use

predictions from ball-only DEM simulations or coupled DEM-CFD or DEM-SPH simulations to predict media motion. In this case it is important to acknowledge the effect of the presence of water on dampening the collisions (Mayank et al., 2015).

4. DEM-based models of mills

4.1 Models that use lumped information from DEM

Resorting to empiricism, some researchers have attempted to couple either the total or an average collision energy or power obtained using DEM to breakage rates or other measures of breakage intensity from batch grinding experiments (Kano and Saito, 1998; Mori et al., 2004; Kwan et al., 2005; Lee et al., 2010).

One interesting approach has been used by Herbst (2004) to predict mill power using DEM and then use it to scale-up the energy-specific breakage rates proposed by Herbst and Fuerstenau (1980) to solve the equation

$$\frac{dw_i}{d\bar{E}_m} = -S_i^E w_i + \sum_{j=1}^{i-1} S_j^E b_{ij} w_j \quad (4)$$

where b_{ij} is the breakage function back-calculated from batch grinding tests, and $\bar{E}_m = P\theta/H$ is the specific energy, where H is the mill hold-up, θ is the residence time and P is the mill power, estimated using DEM.

The obvious advantage of this approach lies in the fact that DEM captures the influence of liner configuration in mill power, which is not taken into account using power models such as those from Rowland and Kjos (1980). However, in analogy to the traditional population balance models, it does not use distributed collision energy information in predicting mill performance. Further, since the contributions of material and machine are not properly decoupled, this approach becomes significantly more limited when compared to other advanced models of ball mills discussed as follows.

4.2 PBM formulations based on particle bed breakage

One of the first attempts to apply DEM to ball mill modeling was by Rajamani and co-workers at the University of Utah (Rajamani et al., 1993), who described batch grinding using the expression

$$\frac{dM_i}{dt} = -\omega \sum_{k=1}^n p(E_k) m_{i,k} + \omega \sum_{j=1}^{i-1} \sum_{k=1}^n p(E_k) m_{j,k} b_{ij}(E_k) \quad (5)$$

where N is the number of collision energy classes, ω is the frequency of collisions, $p(E_k)$ is the fraction of collisions of magnitude E_k , $m_{i,k}$ is the mass of particles in size

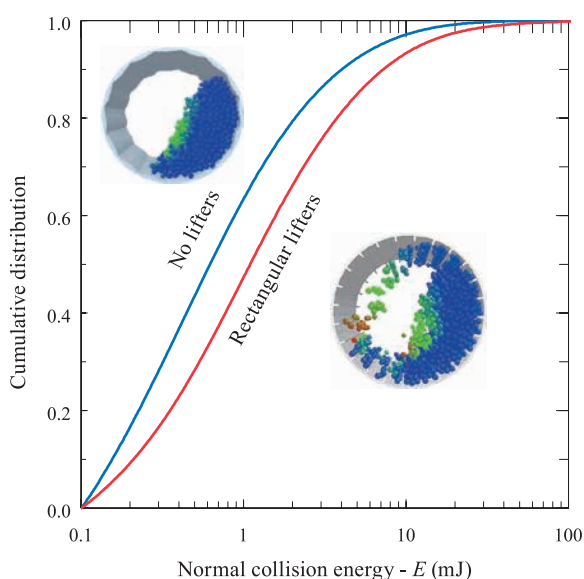


Fig. 2 Collision energy distributions for a 0.6 m diameter mill with different liner profiles balls at 67 % of critical speed, 30 % mill filling and 25 mm steel balls.

interval i broken in a single collision of energy E_k , M_i is the mass of particles in the i th size interval and $b_{ij}(E_k)$ is the breakage function for j th size interval particles generated from collisions of magnitude E_k .

Rajamani et al. (1993) were able to predict reasonably well the size distribution from grinding limestone in a 25 cm-diameter mill, but only at short grinding times, on the basis of 2D DEM simulations. The limitation of short grinding times was due to the fact that only breakage of the top size fraction was predicted.

This equation, however, does not take into account the instantaneous mass fraction of size i in the mill. This was corrected with the introduction of the term M_i/H as the mass fraction of material contained in size class i , or w_i , in an updated version of the model by Datta and Rajamani (2002), given by

$$\frac{dw_i}{dt} = \frac{\omega}{H} \sum_{k=1}^n \left[p(E_k) \left(-m_{i,k} w_i + \sum_{j=1}^{i-1} m_{j,k} b_{ij}(E_k) w_j \right) \right] \quad (6)$$

The model uses information on the broken mass of particles $m_{i,k}$ at a given collision energy and the energy-specific breakage function, both obtained from drop weight tests with 4-layer particle beds, following the procedure originally proposed by Höfler and Herbst (1990). The broken mass was also described as logarithmic function of the specific collision energy.

The model has been validated by comparisons between measured and calculated size distributions in batch grinding of limestone in mills with diameters from 25 to 90 mm, with reasonable agreement (Datta and Rajamani, 2002). However, a correction factor of 0.8 to both appearance and disappearance terms in Eqn. 6 was needed to fit experimental data. The authors attributed this to the inefficiency of the mill.

Datta and Rajamani (2002) recognized that, in a mill, a particle bed between two colliding balls will be composed of something between a monolayer and several layers of material, and not the 4-layer bed considered in their experiments.

One key limitation of this approach is associated to the fact that it relies heavily on data from breakage of particle beds. This mode of breakage varies as a function of particle size distribution in the bed, impact energy, ball size and number of layers, but covering all these by experiments would be too time-consuming. Indeed, this approach also relies on estimates of broken mass, which are both function of material (type, particle size) and environment (ball size and collision energy), which is not desired for modeling purposes.

The approach by Datta and Rajamani (2002) has been used more recently by Wang et al. (2012) to predict results from batch grinding tests. In this study, the authors compared the type of energy information used in the simulations and also included not only the grinding media in the

DEM simulations, but also medium-sized particles to mimic the powder.

The approach reviewed herein assumed that impacts of all energies contribute to breakage, which is not a reasonable assumption since single particle impact tests have shown that a minimum impact energy must be overcome to cause body breakage (Tavares, 2007). Further, particles may sustain damage and become weaker due to impacts that are insufficient to cause outright breakage but may break after a succession of impacts. Finally, this modeling approach does not decouple properly surface from body breakage of ore particles.

4.3 Microscale PBM formulations based on breakage probability

Recognizing the limitations of earlier approaches, some researchers have chosen to use single-particle breakage as the basis of their modeling. The first comprehensive approach along this line has been proposed by King and Bourgeois (1993) and later presented in a modified form by King (2001). It was based on measurements of fracture energies of individual particles (Fig. 3), determined using the impact or ultrafast load cell (Tavares and King, 1998; Tavares, 2007), and on the equivalence between body breakage probability and the fracture energy distribution.

King and Bourgeois (1993) accounted for the fact that the following outcomes could occur when a particle is hit by grinding media:

- If the energy is insufficient to cause fracture, the particle will remain intact inside the charge.
- If the energy is sufficient to cause fracture, the particle will undergo primary breakage and rebreakage (secondary breakage), until all energy is dissipated.

The basis of their approach is the postulate that the breakage functions actually effective in the multiparticle

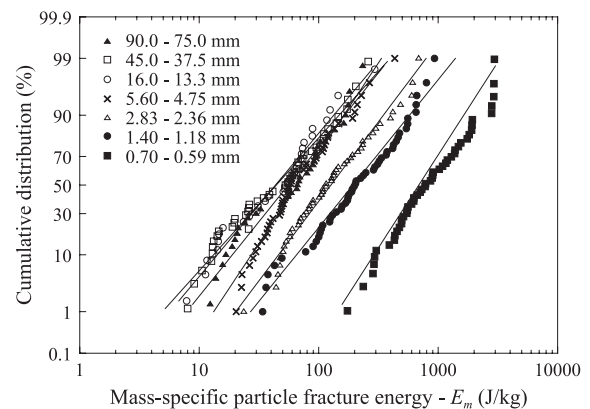


Fig. 3 Distribution of particle fracture energies of a gneiss rock over a range of sizes, with a lognormal fit (Eqn. 8). Reprinted with permission from Tavares and Neves (2008). Copyright: (2008) Elsevier Ltd.

environment of a ball mill can be synthesized from the universal single-particle breakage functions once the patterns of energy distribution and stress application are known in a bed of particles that is subject to impact (King and Bourgeois, 1993). The power of this approach is that it avoids the limitations of the particle-bed based approaches, reviewed in section 4.2, that cannot properly cover through experimentation the different bed configurations encountered in practice. On the other hand, one of its limitations is associated to the need for testing single particles at fine sizes, which is both time consuming and inconvenient. Besides that, small sample size statistics can also be considered a limitation of this method (Herbst, 2004).

King (2001) proposed that the breakage rate function of particles contained in size class i could be expressed by

$$S_i = \int_0^\infty p(E) m_i^*(E) \int_0^1 F_i(eE) p(e) de dE \quad (7)$$

where $p(E)$ is the distribution of collision energies, estimated using DEM, $p(e)$ is the energy partition amongst particles within the bed, which accounts for the fact that when identical particles are stressed within a bed, they do not necessarily receive the same amount of energy. $F_i(eE)$ is the distribution of fracture energies of particles in size class i , and $m_i^*(E)$ is the mass of particles captured in an impact of magnitude E .

King and Bourgeois (1993) demonstrated that the model was able to describe qualitatively the results of batch grinding experiments, but fell short to provide accurate enough descriptions of particle capture and energy split in the bed. They based their predictions on 2D DEM simulations. Nevertheless, this work pioneered the microscale approaches to modeling ball mills.

More recently, Crespo (2011) pursued some aspects of this approach by considering the distribution of particle fracture energies and a perceived distribution of collision energies in a ball mill. While the work demonstrated the capability of his approach of predicting non-first order breakage rates for coarse particles, it suffered from important limitations. Further, it used very simple descriptions of the breakage function, with rather severe simplifications, besides oversimplified descriptions of particle capture probability, which were back-calculated from batch grinding data.

Both of these approaches considered that the distribution of particle fracture energies could be described using the lognormal distribution, which has been demonstrated elsewhere to be able to describe such data properly (King and Bourgeois, 1993; Tavares and King, 1998). It is given by

$$F_i(E_m) = \frac{1}{2} \left[1 + \operatorname{erf} \left(\frac{\ln E_m - \ln E_{m50,i}}{\sqrt{2\sigma^2}} \right) \right] \quad (8)$$

where $E_{m50,i}$ is the median particle fracture energy and σ^2

is the variance. The variation of the median fracture energy of the material with particle size could be well described using the expression (Tavares and King, 1998)

$$E_{m50,i} = E_\infty \left[1 + \left(\frac{d_o}{x_i} \right)^\phi \right] \quad (9)$$

where x_i is the representative size of particles contained in the i th class, E_∞ , d_o and ϕ are model parameters that should be fitted to experimental data. In some cases the variance σ^2 in Eqn. 8 is also found to vary with particle size and a relationship to describe it has been proposed elsewhere (Carvalho and Tavares, 2013).

A related approach was used by Bwalya et al. (2001) to predict breakage rates in autogenous grinding. The authors considered the distribution of fracture energies of the particles, described with a modified version of the Weichert (1992) breakage probability function derived from single particle breakage in a drop weight tester and collision energies for short grinding times using 2D DEM. Breakage was generally overpredicted compared to an experimental mill, although the model correctly predicted the reduction in breakage rates as a function of particle size. With this approach they were also able to predict the non-first order rates of breakage of coarse particles in a mill.

Another modification of the Weichert (1992) breakage probability function that became very popular was proposed by Vogel and Peukert (2004):

$$F_i(E_m) = 1 - \exp[-f_{\text{mat}} x_i (E_m - E_{m,\min})] \quad (10)$$

where f_{mat} and $x_i E_{m,\min}$ are constants representing material parameters which should be fit to data, in which $E_{m,\min}$ is the threshold energy, below which particles will not suffer body breakage.

Recently, Tuzcu and Rajamani (2011) proposed another expression for predicting the energy-specific breakage rates for powder in a batch mill on the basis of Eqn. 10, giving

$$S_i^E = k' \omega \sum_{k=1}^n p(E_{m,k}) F_i(E_{m,k}) \frac{E_k}{\sum_{k=1}^n E_k} \quad (11)$$

which would be used to solve the batch grinding equation

$$\frac{dM_i}{dt} = -S_i^E \frac{M_i}{H} + \sum_{j=1}^{i-1} S_j^E b_{ij}^E \frac{M_j}{H} \quad (12)$$

in which k' is a constant that includes the captured mass and all other unmodeled effects (Tuzcu and Rajamani, 2011), $F_i(E_{m,k})$ is the probability of fracture of particles in size i at the applied specific collision energy $E_{m,k}$, described using Eqn. 10. They were able to predict well breakage of coarse particles (top size of 31.8 mm) in a 0.9 m diameter batch mill, using Eqns. 11 and 12 and collision energy spectra from 2D DEM simulations.

Capece et al. (2014) proposed yet another method to

calculate the breakage rates, also using Eqn. 10:

$$S_i = f_{\text{mat}} x_i \omega \sum_{k=1}^n p(E_{m,k}) (E_{m,k} - E_{m,\min}) \quad (13)$$

where $E_{m,k}$ is the specific energy in the k th collision. The authors proposed to conduct batch grinding experiments with various narrow-size feeds, then 3D DEM simulations with grinding media and powder particles of these sizes and then fit the material parameters (f_{mat} , $x E_{m,\min}$) on the basis of Eqn. 13. The breakage function was back-calculated from data of these batch grinding tests and Eqn. 2. The authors were able to fit one set of material parameters to several experiments with alumina, which demonstrates the relevance of their approach, which circumvents the challenge of estimating the mass of material captured by including the powder particles in the simulations. It has, however, limited predictive capability for finer powder sizes, which are known to be broken in beds and not as individual particles, and for which simulations would require significant computer effort. This approach has similarities to the one proposed by Concas et al. (2006).

Some of the assumptions in these formulations are:

i. The approach of King and Bourgeois (1993) and Crespo (2011) assumed that particles are involved in each collision that happens in the mill. This means that each collision nips some material regardless of the location of the collision. This is generally considered to be a valid assumption if the fractional mill filling of the media interstices is equal to 1 or higher. The approaches of Tuzcu and Rajamani (2011) and Capece et al. (2014) do not require this assumption by including powder particles in the simulations.

ii. Approaches of King and Bourgeois (1993), Crespo (2011) and Tuzcu and Rajamani (2011) did not account for the fact that particles that do not break in the impacts become progressively weaker, which significantly affects the chances of particle breakage (Bwalya et al., 2001; Tavares, 2009). As such, the model assumes that the fracture energy distribution of particles contained in a given size class remains unchanged as grinding progresses.

iii. Essentially all approaches assume that breakage of particles due to abrasion (surface breakage) is negligible and no contribution of shearing of particles during ball-to-ball or ball-to-wall collisions exists.

iv. The contents of the mill are assumed to be perfectly mixed, that is, the size distribution of the particle bed caught between two colliding balls is the same as the prevailing distribution in the entire mill. This assumption is perceived to be valid for dry grinding where internal classification is not as prevalent as in wet grinding. Bwalya et al. (2001), on the other hand, assumed that the probability of a particle being involved in a collision in a tumbling mill is a function of particle surface area.

v. The fracture energy or breakage probability of a par-

ticle does not vary if it was produced as a progeny of a low-energy or a high-energy stressing event.

By using the breakage probability, these approaches actually included an additional variable to particle size in the population balance model formulation, which is the energy required for (body) breakage, called particle fracture energy.

4.4 Microscale PBM formulations describing different breakage mechanisms

A number of approaches have been proposed that tackle some of the limitations of these earlier models. The commonality amongst them is the fact that they attempt to describe in greater detail the response of the ore or powder to the different fragmentation mechanisms, which could be listed as:

1. Body breakage: the integrity of the original particle is completely lost;
2. Surface breakage, further described as:
 - a. Attrition or abrasion: mass loss at the surface of rounded rocks as other particles slide over them or they slide over the liner, or as a result of predominantly normal low-energy collisions;
 - b. Chipping: loss of corners, edges and larger asperities from small scale breakage for irregular shaped particles;
 - c. Rounding: preferential and higher abrasive mass loss from sliding at the corners and edges of blocky particles.

The occurrence of either depends on the intensity and mode of stressing. As such, the approaches reviewed in this section also have in common the vision that, since the contributions of the milling environment and of the ore are appropriately decoupled, the same modeling framework can be used to describe different types of comminution machines, and not only tumbling ball mills.

4.4.1 Unified comminution model

This model framework, proposed by Powell et al. (2008) from the University of Cape Town and called unified comminution model (UCM), proposes modeling any size reduction machine by coupling the mechanical environment in the size reduction equipment, obtained using DEM, to data that describes the different fundamental modes of breakage, and tools that characterize the influence of slurry in wet milling, namely CFD and SPH. It employs the population balance framework to mathematically combine the particles and their associated breakage products into a mass balance per time step. For a single component (or material class) and batch operation, it can be expressed as

$$\frac{dM_i}{dt} = - \sum_{d=1}^N \lambda_i(E_d) M_i - \sum_{r=1}^S \lambda_i(E_r) M_i + \sum_{j=1}^{i-1} \left[\sum_{d=1}^N \lambda_j(E_d) M_j(E_d) b_{ij}(E_d) + \sum_{r=1}^S \lambda_j(E_r) M_j(E_r) b_{ij}(E_r) \right] \quad (14)$$

where $\lambda_i(E)$ is the net breakage frequency at energy E for the size class i , given by $\lambda_i(E) = \lambda_i^{\text{DEM}}(E) / \lambda_i^{\text{exp}}(E)$, in which $\lambda_i^{\text{DEM}}(E)$ is the DEM collision frequency at energy E for size class i and $\lambda_i^{\text{exp}}(E)$ is the mean number of collisions required to break particles in size class i with collision energy E . N and S are, respectively, the number of normal and shear energy bins and M_i is the mass of material contained in size i in the mill.

The model recognizes that depending on the magnitude of the collision energy on a particle three different outcomes could occur (Powell et al., 2008):

- i. Single hit (body) breakage—for a collision with sufficient energy to break the particle, so that the lower limit for this is defined as E_{crit} .
- ii. Multiple impact (body) breakage—the energy of a single impact is too low to break the rock, however, as it is hit more times at this energy it has an increasing probability of breakage. As a result of this, the model requires to track the histories of individual particles (Powell and McBride, 2006).
- iii. No bulk damage—the impact energy is too low to cause any bulk damage to the rock. The upper limit for this is defined as E_0 .

The strength of the approach is its generality and the fact that it recognizes several of the important “pieces of the puzzle” that were missing in earlier approaches. However, the authors admitted that several voids existed that limited the feasibility of applying the model at the time, including the lack of information on apportioning the energy between colliding media, the left-over energy-input power not accounted for in particle damage and the description of breakage of the sub-DEM material. Several features of the model make it more aligned with requirements of modeling autogenous and semi-autogenous mills than ball mills, since the three different outcomes listed above may only be applicable to ore particles simulated in DEM. It is worth noting that the original approach proposed to describe breakage of sub-DEM particles was acknowledged by the authors to be fairly crude, based on relating energy dissipated in the collisions coupled to the standard Bond ball mill method (Powell et al., 2008).

A first demonstration of a simplified form of the model to calculate breakage rates of a full-scale ball mill has been presented more recently (Powell et al., 2011), although it has not yet been validated for this type of mill.

4.4.2 Virtual comminution machine

Another approach recently proposed in this category is the virtual comminution machine (VCM), by Morrison and Cleary (2008) from the University of Queensland and the CSIRO, respectively. Also meant to be a framework to deal with different size reduction processes, the VCM is the one that has evolved the most in coupling DEM to a description of the slurry flow and discharge classification, given by smoothed particle hydrodynamics (SPH) (Cleary et al., 2006). This approach also had the additional feature of providing a model to describe rounding by means of parameterised super-quadric particles (Cleary and Morrison, 2016) and fines generation by attrition. Further, it also describes weakening by repeated impacts (called incremental breakage by the authors), using the model proposed by Morrison et al. (2007), which is another modification of Eqn. 10 by Vogel and Peukert (2004), given by

$$F_i(E_m) = 1 - \exp \left[-b^* \sum_{k=1}^n (E_m - fE_0) \right] \quad (15)$$

If E_m is lower than E_0 , the contribution from $(E_m - E_0)$ is zero. b^* is a material parameter which may contain the particle size i . f is a parameter, characterizing the fraction of E_0 at which cracks will stop propagating, which was included in a recent revision of the model to improve fitting to data (Cleary and Morrison, 2016).

It is understood that the model predicts breakage of the sub-DEM material using a population balance approach, although the equations used have not been published by the authors. As such, it is unclear how particle capture of sub-DEM particles is addressed, although recent work in which not only grinding media but also fine particles are included in the simulations sheds light into this (Cleary and Morrison, 2011). Indeed, the researchers recognized that developments that remained to be done included dealing with the presence of fine material in ball mills (Weerasekara et al., 2013).

Many of the capabilities of the model are relatively recent and significant testing and validation is still required to demonstrate the predictive capabilities of the VCM. The developers recognize that good quality characterization of breakage behaviour of the specific rocks being used by all the breakage mechanisms is required and that the VCM is only as good as both its numerical model and ore characterization components (Weerasekara et al., 2013).

Amongst the modelling approaches in the literature of tumbling mills, the VCM is the one that already describes the greatest variety of outcomes from breakage listed in the beginning of this section. Evidently, many of the features of the model, in particular the rounding capability, are particularly suited for predicting size reduction in autogenous and semi-autogenous mills, but would also be useful to predict ball milling with a coarse feed.

4.4.3 Other approaches

Another interesting approach proposed has been to predict breakage by coupling DEM to a tool, called discrete grain breakage (DGB) (Herbst and Potapov, 2004), and computational fluid dynamics (CFD) to describe the slurry flow in the mill. This approach, called High Fidelity Simulation (HFS), attempts to connect single-particle breakage response to mill performance. It has also been proposed as a general approach for predicting different types of crushers and mills, but has been restricted in application to full-scale mills due to the very significant computational effort associated to its use.

More recently, a refinement of the single-particle based approach by King and Bourgeois (1993) was proposed by the author and his research team at the Universidade Federal do Rio de Janeiro (UFRJ). First, the weakening by repeated impacts and the breakage of particles at much lower impact energies is incorporated in the model. In analogy to the other models presented in this section, it also describes surface and body breakage, using (body) breakage probability to distinguish between the two. This model is presented in greater detail in the following section.

Finally, it is worth noting that the approach proposed by Tuzcu and Rajamani (2011) also distinguished body and surface breakage mechanisms, although it described the later in a fairly simplistic manner, assuming a constant proportion of fines produced by this mechanism as grinding time progressed in a batch mill.

4.5 UFRJ mechanistic model

Following the footsteps of the work originally carried out at the University of Utah during the early 1990s (King and Bourgeois, 1993), the research group at UFRJ proposed yet another DEM-based approach to model comminution machines. The model is based on the combination of DEM that is used to describe the mechanical environment in the comminution machine, to a myriad of empirical and semi-empirical models that describe the different breakage modes and that are fitted to particle breakage data, and also to models that describe how sub-DEM particles are captured and how the collision energy is split among particles when they are assembled in beds. These pieces of the puzzle are then put together using two models: the microscale population balance model, which keeps track of the mass balance of particles in each size and ore composition class, and an expression that describes the variation of the distribution of particle fracture energies inside the machine as comminution progresses, called fracture energy convolution. This latter is based on the continuum damage model of particle breakage (Tavares and King, 2002) and the distribution of particle fracture energies (Fig. 3). Both equations will vary according to

the mode of operation of the comminution device, if batch or continuous, and also according to the mixing conditions that prevail.

The model considers that when particles suffer an impact, some of them undergo catastrophic (body) breakage and some do not. If stresses are insufficient to cause body breakage, they will undergo surface breakage (abrasion/chipping) and will also become progressively weaker.

The batch grinding process equation can be derived from a more general formulation of the traditional population balance model applied to the microscale description of size reduction processes (Carvalho and Tavares, 2009). The equation that describes the rates of changes in mass of material contained in size class i is

$$\begin{aligned} \frac{dw_i}{dt} = \frac{\omega}{H} & \left\{ -w_i \int_0^\infty m_i^*(E) p(E) \int_0^1 [1 - b_{ij}(eE)] F_i(eE, t) p(e) de dE \right. \\ & + \sum_{j=1}^{i-1} w_j \int_0^\infty m_j^*(E) p(E) \int_0^1 b_{ij}(eE) F_j(eE, t) p(e) de dE \\ & \left. - D_{i,s}(t) + A_{i,s}(t) \right\} \end{aligned} \quad (16)$$

where H is the powder or ore load, also called mill hold-up, w_i is the mass fraction of particles contained in size class i in the mill at time t , ω is the frequency of stressing events, $p(E)$ is the distribution of stressing energies E in the mill, $m_i^*(E)$ is the mass of particles contained in size class i captured in each collision event of magnitude E and $p(e)$ is the function that represents the energy split among particles nipped in a bed. $b_{ij}(eE)$ is the body breakage function in density form, dependent on stressing energy (Tavares and Carvalho, 2009) and $A_{i,s}$ and $D_{i,s}$ are functions that characterize the appearance and disappearance due to surface breakage, omitted for brevity, and presented elsewhere (Carvalho and Tavares, 2013). The product eE is the fraction of the collision energy that is absorbed by each particle captured in an impact event.

The body breakage function is described on the basis of expressions that account for the effect of particle size and stressing energy on the size distribution of the progeny fragments. The reduction in size of the progeny with increasing applied energy has been described very successfully using the t_{10} -procedure. The size distribution from impacts at a specific energy E_m on particles contained in size class j is calculated by first estimating the fraction of material passing $1/10^{\text{th}}$ of the original particle size, called t_{10} , using the expression (Tavares, 2009)

$$t_{10,j} = A \left[1 - \exp \left(-b' \frac{E_m}{E_{m50b,j}} \right) \right] \quad (17)$$

where A and b' are model parameters and $E_{m50b,j}$ is the median mass-specific particle fracture energy of the par-

ticles that are broken as a result of an impact of magnitude E_m . When the collision energy is higher than the fracture energy of the toughest particle contained in size class j , then $E_{m50b,j} = E_{m50,j}$, otherwise it should be calculated numerically (Tavares and Carvalho, 2009). The validity of Equation (17) has been demonstrated elsewhere (Tavares, 2009).

From the t_{10} value, calculated using Eqn. 17, it is then possible to estimate the proportions passing (t_n values) of different fractions of the original parent size for each collision energy and particle size investigated. This is done with the aid of a model that is based on the incomplete beta function (Carvalho and Tavares, 2013). The cumulative breakage function is then calculated from $B_{ij}(E_m) = \text{interp}(t_{10}, t_n)$.

In the case of batch operation, Eqn. 16 should be solved simultaneously with the equation that describes how the fracture probability distribution of particles contained in each size i varies with time, given by

$$F_i(E, t + \Delta t) = \frac{G_i F_i^*(E, t + \Delta t) + H_i F_i(E, 0) + I_i F_i(E, t)}{G_i + H_i + I_i} \quad (18)$$

where G_i is the fraction of material in the size class that has been damaged but remained in the original size range, H_i is the fraction that appeared due to body and surface breakage, and I_i is the fraction that was not captured in the time interval, with expressions given elsewhere (Carvalho and Tavares, 2013).

The fracture probability distribution of the original material $F_i(E, 0)$ can be, generally, described well using the lognormal distribution, given by Eqn. 8. In some cases, an upper truncation of the distribution is also necessary (Carvalho and Tavares, 2013). The median particle fracture energy varies according to size through Eqn. 9, and $E_{50,i} = E_{m50,i} \bar{m}_{p,i}$. The mean weight of a particle contained in size class i may be estimated by $\bar{m}_{p,i} = \rho \beta x_i^3$, where ρ is the material specific gravity and β the volume shape factor.

Also, the standard deviation of the lognormal distribution of particle fracture energies (Eqn. 8) can vary with size and the variation can be described using an expression analogous to Eqn. 9 (Carvalho and Tavares, 2013).

In Eqn. 18 $F_i(E, t)$ is the distribution of fracture energies of the material contained in size class i that did not suffer any impact event during the time interval, whereas $F_i^*(E, t + \Delta t)$ is the distribution of fracture energies of the particles in size class i that were captured in a collision event, but did not fracture, being given by the convolution equation

$$F_i^*(E, t + \Delta t) = \frac{\int_0^{E_i^*} p(E') \int_0^1 \left\{ \frac{F_i[E / (1-D), t] - F_i(eE', t)}{1 - F_i(eE', t)} \right\} p(e) de dE'}{\int_0^{E_i^*} p(E') dE'} \quad (19)$$

and

$$D = \left[\frac{2\gamma(1-D)}{(2\gamma-5D+5)} \frac{eE'}{E} \right]^{\frac{2\gamma}{5}} \quad (20)$$

where E_i^* is the maximum fracture energy of particles contained in class i , which is equal to the value that satisfies $F_i(E_i^*) = 1$ as comminution progresses (Tavares and Carvalho, 2009) and γ is a parameter that characterizes the amenability of the material to breakage by repeated impacts, which is typically independent of particle size (Tavares, 2009). The model is able to account for the fact that particles that are stressed but do not fracture in a collision event will become progressively weaker. The model does not have an explicit damage threshold, since the amount of damage sustained by particles becomes progressively smaller as the ratio between the collision energy (eE') and their fracture energy (E) approaches zero.

Illustration of application of Eqns. 18 to 20 to material ground in a batch mill (**Fig. 4**) demonstrates the progression of the distribution of fracture energies of the remaining material in the top size range. It shows the predominant effect of survival of the toughest particles, along with the weakening of a fraction of the population of the particles.

The mass of material captured (m_i^*) between two grind-

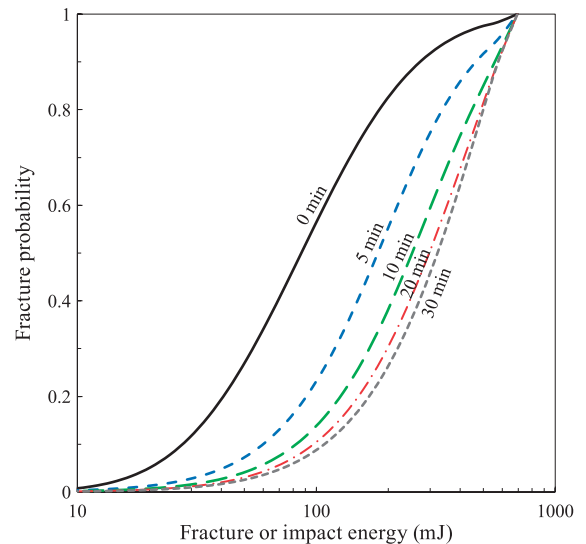


Fig. 4 Predicted variation of particle fracture energies of 9.5×6.3 mm granulate particles with grinding time in a 0.3 m diameter batch mill with 25 mm steel balls, 67 % of critical speed and 30 % mill filling. Reprinted with permission from Tavares and Carvalho (2009). Copyright: (2009) Elsevier Ltd.

ing media elements may be estimated from the product of the number of particles caught between the two grinding media ($N_{\text{cap},i}$) and the average weight of the particles ($\bar{m}_{p,i}$), $m_i^* = \bar{m}_{p,i} N_{\text{cap},i}$.

Given the evidence from earlier work (Höfler, 1990), that particles in an unconfined bed normally only break when they are typically squeezed down to one or two layers between grinding media, particles are modeled as a packed monolayer bed. If particles had spherical shapes, and if they were arranged according to a dense hexagonal packing, then the number of particles captured as a function of radius from the center of impact could be estimated by (Barrios et al., 2011a)

$$N_{\text{cap},i} = \frac{1}{4} + \frac{3}{4} \left(\frac{2r_c}{x_i} \right)^2 \quad \text{for } r_c \geq x_i / 2$$

$$= 1 \quad \text{for } r_c < x_i / 2 \quad (21)$$

where r_c is the radius of the bed, also called radius of capture, and x_i is the mean size of the particles caught by the colliding steel ball, estimated from the geometric mean of sieves sizes containing the fraction.

A model has been proposed by Barrios et al. (2011a) to calculate this radius of capture on the basis of diameters of colliding grinding media, size of particles, their strength and impact energies. An illustration of the effect of impact energy and particle size on the radius of capture is presented in Fig. 5. This model has also been used by other researchers (Powell et al., 2011) to estimate mass captured of sub-DEM material in mill simulations. The validity of the model in describing the mass of material captured and the energy distribution in the bed inside the milling environment, however, has not yet been demon-

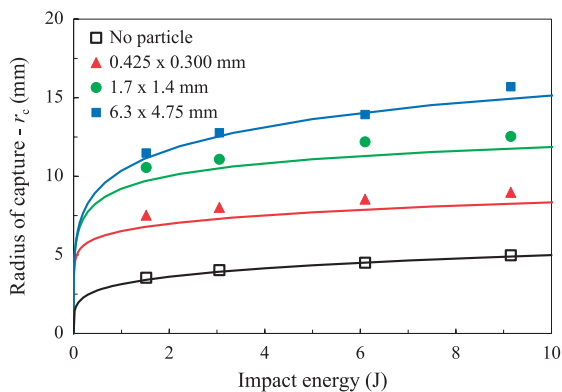


Fig. 5 Radius of capture in the contact between balls of different sizes and a monolayer bed of particles contained in the size range sitting on a flat anvil for different particle sizes and impact energies. Symbols present experiments and lines the model fit. Reprinted with permission from Weerasekara et al. (2013). Copyright: (2013) Elsevier Ltd.

strated, but is the subject of ongoing work in the author's laboratory.

In the description of the energy split function in the bed $p(e)$, it is considered that the stressing energy is split equally among particles positioned in the bed, so that $p(e) = \delta(e - 1/N_{\text{cap},i})$, where δ is the Dirac delta function. However, another more complex expression has also been proposed to describe the energy split in a more realistic way (Barrios et al., 2011a).

The size-discretized Equations (16) and (18) are solved simultaneously at each time step using a finite difference scheme. Time steps are typically in the order of 0.01 s, but should be chosen to be as small as necessary to guarantee that particles take part in no more than one collision event in the interval.

The sensitivity of the model to the geometry of the impact makes it worthwhile to log separately collisions between each two elements in contact, forming a matrix of probability distributions of collision energies.

The model has demonstrated to be capable of predicting non-first order breakage rates of coarse particles (Tavares and Carvalho, 2009) and also of describing the effects of several design and operating variables in milling in

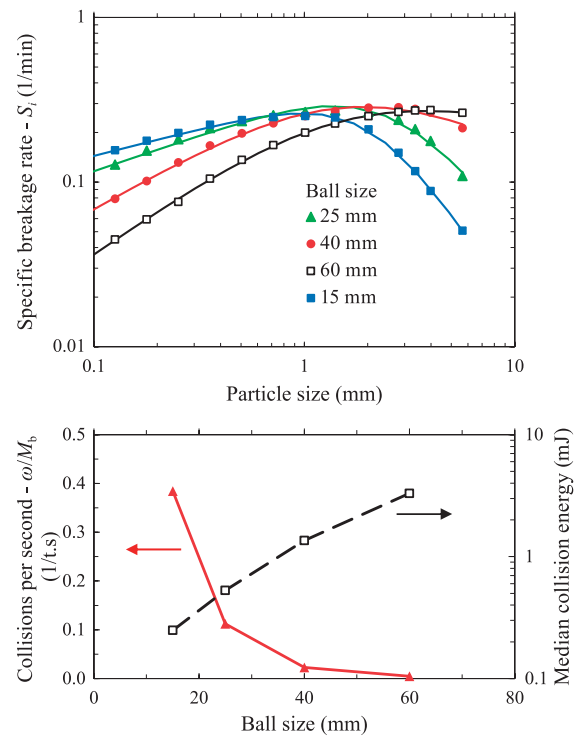


Fig. 6 Simulated breakage rates for a copper ore as a function of particle and steel ball size for a ball mill (top) and DEM median impact energy and collision frequency as a function of ball size (bottom), where M_b is the mass of the ball charge (30 % mill filling and 67 % of critical speed in a 0.3 m diameter mill). Reprinted with permission from Carvalho and Tavares (2013). Copyright: (2013) Elsevier Ltd.

breakage rates (Carvalho and Tavares, 2013). The effect of ball size on specific breakage rates predicted using the model is illustrated in Fig. 6, and shows that the model is capable of accounting for the shift in the size corresponding to the maximum breakage rate with a change in ball size, which has been widely documented in the literature (Austin et al., 1984; Katubilwa and Moys, 2009). Smaller ball sizes produce less energetic impacts and each impact captures fewer particles, being also less efficient at nipping coarser particles. Offsetting these effects that tend to decrease the specific rate of breakage as ball size decreases is the increased frequency of impacts that results from the larger number of smaller balls in the mill, also shown in the figure.

Additional work has demonstrated that grinding of multi-component mixtures in continuous mills can also be simulated using the model (Carvalho and Tavares, 2009), although the validity of the predictions has not yet been demonstrated. Detailed model validation is underway in the authors laboratory (Rodríguez, 2016), and Fig. 7 illustrates results that demonstrate that the model can predict batch grinding well even at prolonged times.

Unlike the UCM and the VCM, the mechanistic mill model describes single hit breakage and incremental breakage with no distinction, since it accounts for the distribution of fracture energies of the material and uses Eqn. 17 to characterize intensity of breakage in both cases. As such, it is truly a two-variable model, since not only sizes of particles change as grinding progresses, but also their fracture energies.

Besides considering the assumptions i, iv, and v of the earlier single-particle based models (4.3), the UFRJ mechanistic mill model does not yet account for the interaction of particles of different sizes in the bed, in spite of evidences that this has been found relevant in the past (Schönert, 1979).

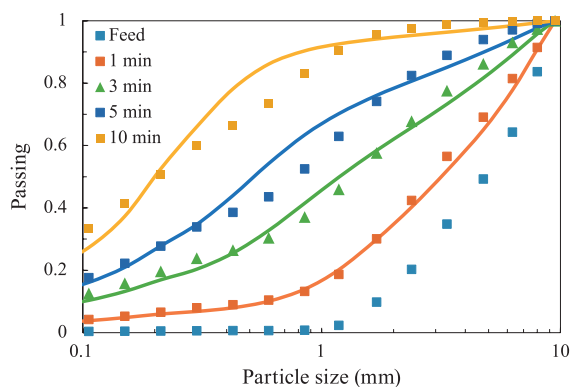


Fig. 7 UFRJ mechanistic model validation in dry batch grinding of granulite. Symbols are experimental data and lines model predictions (0.3 m mill, 40 mm steel balls, 30 % filling, 100 % interstitial filling, 67 % of critical speed).

5. Discussion

5.1 Fracture probability distributions

Several approaches reviewed require information on fracture probability distributions and their variation with particle size. Different models (Tavares and King, 1998; Vogel and Peukert, 2004; Rozenblat et al., 2012) have been proposed to describe this variation. Several authors (King and Bourgeois, 1993; Tavares and Carvalho, 2009; Crespo, 2011) used the lognormal distribution (Eqn. 8) and the relationship describing the variation of the median fracture energy with size given by Eqn. 9, which have demonstrated to be capable of describing material response over a range of sizes (Tavares and King, 1998; Tavares and Neves, 2008).

The approach proposed by Vogel and Peukert (2004) and the Weibull distribution has attracted significant attention, being used, either directly or modified, in describing breakage probability in several approaches (Concas et al., 2006; Morrison and Cleary, 2008; Tuzcu and Rajamani, 2011; Capece et al., 2014), in particular owing of its simplicity, with only two fitting parameters. This model (Eqn. 10) identifies a threshold collision energy below which no body breakage would occur. Although the model has explicitly the number of impacts, so that it can describe weakening by repeated impacts, a more appropriate modification has been proposed by Morrison et al. (2007) that more appropriately describes this effect.

As such, given its popularity, it is important to analyze the approach of Vogel and Peukert (2004) in greater detail. Solving Eqn. 10 considering the case in which particles are impacted at exactly their median fracture energy, so that $F_i(E_{m50}) = 0.5$ in Eqn. 10, gives

$$E_{m50,i} = x_i E_{m,min} \left[1 + \left(\frac{k''}{x_i} \right) \right] \quad (24)$$

where $k'' = \ln(2)/f_{mat} x_i E_{m,min}$.

The similarity between Equations (24) and (9) is evident, with the key difference that the median fracture energy is inversely proportional to particle size in Eqn. 24 (−1 power), whereas it was found to vary, according to material, from −0.8 to about −2.5 for geological materials (Tavares and King, 1998; Tavares and Neves, 2008). As such, the model given by Eqns. 9 and 10 provides not only a more realistic description of the variation of breakage probability with size but also allows decoupling the variability in the breakage probability distributions from the effect of size in the median fracture energy. It has, however, more parameters (four in total, in contrast to only 2 in Eqn. 10) that need to be fitted from experimental data on breakage probability or fracture energy distributions for a range of sizes. This data can be collected with reason-

able convenience at intermediate and coarse sizes (Dan and Schubert, 1990; Tavares and King, 1998; Rozenblat et al., 2012) but no robust solution appeared yet to deal with breakage of fine particles, although some alternatives have been proposed (Marktscheffel and Schönert, 1986; Barrios et al., 2011b; Ribas et al., 2014). Nevertheless, Eqn. 10 can be a good compromise between complexity and capability to describe reality for using in earlier stages of development of advanced models of milling, in particular when the model developer has little access to data on particle breakage probability.

5.2 Collision energies

As discussed earlier, at least three options exist in regard to the collision energies from DEM for advanced mill simulations. It is, however, important to match the information on the collision that is obtained in DEM with the information from single-particle breakage (Powell et al., 2008). For instance, not all energy involved in a collision is absorbed by individual particles and/or a bed, leading to a rebound that could lead to additional breakage.

Several researchers (Datta and Rajamani, 2002; Tavares and Carvalho, 2009; Capece et al., 2014) use the dissipated energies as the basis of their simulations. Using the model approach and data by Datta and Rajamani (2002), Wang et al. (2012) concluded that the kinetic energies in the collision were the type of information that could most reliably predict the batch mill performance. The use of the dissipated energy is considered valid in the UFRJ Mechanistic Model since the energies that are used to model fracture probabilities (Eqn. 8) and energy-specific breakage function (Eqn. 18) already account only the absorbed by the particles (Tavares, 1999). However, the authors recognize a mismatch can occur between the sum of dissipated energy and the total energy computed by the center of gravity of the charge, in particular as mill diameters increase (Carvalho and Tavares, 2013).

Normal and shear components of the collisions contribute to breakage and should be considered in the model predictions. Indeed, these appear explicitly in the UCM equations (Powell et al., 2008) and are used actively to describe the different outcomes of breakage as part of the VCM (Morrison and Cleary, 2016). Other authors (Datta and Rajamani, 2002; Tuzcu and Rajamani, 2012) simply group the two components and deal with the combined spectrum. However, the actual roles of normal and shear components in the different modes of breakage are not yet entirely clear (Powell and McBride, 2006), in particular when dealing with surface breakage. Originally the UFRJ model only used the normal components of the collision (Tavares and Carvalho, 2009), but the latest version of the model, with an improved description of surface breakage, also includes the shear component (Rodriguez, 2016).

5.3 Other

Simulations using the discrete element method have been used to investigate mixing between grinding media and ore charge. Cleary and Morrison (2011) included powder at different proportions to investigate its effect on the motion of charge and collision spectra in a laboratory ball mill. They showed that particles were not uniformly distributed, but tended to concentrate at the shoulder region at very low powder fillings. At higher powder fillings, namely above 100 %, mixing between grinding media and powder was good, thus justifying the approximation used in nearly all the advanced models. The only model that does not explicitly consider this assumption is the VCM (Morrison and Cleary, 2008), although outcomes from relaxing this assumption have not yet been presented.

One of the first observations from DEM simulations of mills is that the frequency of high-energy impacts, such as those reproduced in standard drop weight tests (Napier-Munn et al., 1996) is very small, shedding light into the importance of low-energy collisions and, therefore, to weakening by repeated impacts and to surface breakage. Whereas the former has attracted significant attention (Tavares and King, 2002; Morrison et al., 2007), descriptions of surface breakage are still in their infancy, in particular if compared to volume breakage. In spite of some recent worthwhile attempts (Morrison and Cleary, 2008; Yahyei et al., 2015), a need exists to study this mode of breakage in greater detail in the future to properly inform advanced mill models. Indeed, it is important to recognize that surface breakage can be understood as either the result of normal collisions that are of insufficient magnitude to cause body breakage (Tavares and Carvalho, 2009), or to collisions that are predominantly of the shear type, although this distinction is seldom made by researchers. The lack of proper descriptions and understanding of breakage by either pure or predominant shear have so far prevented its implementation in the UFRJ mechanistic model (Carvalho and Tavares, 2013).

Nearly all advanced approaches use some form of population balance framework to mathematically combine the particles and their associated breakage products into a mass balance per time step. Several of the approaches (King, 2001; Datta and Rajamani, 2002; Capece et al., 2014) use the linear population balance model equation, e.g., Eqn. 2 in the case of the batch mill, with the only difference that breakage and selection functions are calculated on the basis of data from DEM simulations. Other approaches (King and Bourgeois, 1993; Tavares and Carvalho, 2009) use a different formulation of the population balance model equations, called microscale population balance model, since breakage mechanisms and collision energy spectra are convoluted in the equations.

Amongst the approaches that consider the breakage probability (fracture energies), only the UFRJ Mechanistic Model (Tavares and Carvalho, 2009) addresses its change as the result of both breakage of particles and weakening of the unbroken particles. Indeed, this model can be, potentially, used to predict the fracture energies of particles that leave the mill, which can impact downstream processes.

Models differ even at the most fundamental level of definition of body breakage. Whereas several follow the definition used in all traditional population balance model formulations of breakage as departure from the original size range that contains the particle (Datta and Rajamani, 2002; Capece et al., 2014), other formulations (King and Bourgeois, 1993; Tavares and Carvalho, 2009) consider breakage as the loss of a substantial part of the particle weight, taken arbitrarily as 10 % (Dan and Schubert, 1990). As such, it accounts for the fact that when a particle suffers body breakage, fragments from it can remain in the original size range.

It is evident from this review that very important advances have been made, in particular in the last 10 years, in advanced ball mill modeling. The approaches that are progressing further are those that account for breakage probability and also that distinguish the different breakage mechanisms. However, important challenges remain, in particular related to connecting single particle breakage response at fine sizes to milling response, both batch and continuous, and to modeling surface breakage. It is the opinion of the author that it will reach maturity in the next several years, following on the footsteps of other already mature applications of DEM, such as in transfer chute design and liner design for preventing ultraprojection of grinding media.

6. Conclusions

- Several approaches have been proposed since the late 1980s to describe beyond mean breakage rates, breakage functions and specific comminution energy, size reduction in tumbling mills.
- Since the 1990s these approaches evolved significantly, given the contribution of the discrete element method (DEM) in describing the mechanical environment in mills.
- In spite of the increase in computing power, modeling ball mills is still better described considering only the grinding charge and not the powder in the DEM simulations, relaying on post-processing the data using a proper population balance formulation to predict grinding.
- Several of the initial approaches in advanced modeling relied exclusively on particle bed data to describe breakage. In spite of their simplicity, they became less popular given the lack of description of breakage prob-

ability and also the difficulty of representing all combinations that would be found in practice.

- Models that rely on single particle breakage and (body) breakage probability have gained popularity in recent years and were pioneered by the work of King and Bourgeois (1993). The approaches differ by the expressions used to describe breakage probability. Several of these models have adopted the formulation of Vogel and Peukert (2004), although more flexible alternatives exist.
- A limited number of approaches decouple body and surface breakage, and only one approach (VCM) describes explicitly rounding of coarse particles due to surface breakage, which could be relevant in ball milling of oversized feeds.
- A very limited number of approaches account for weakening by repeated unsuccessful collisions.
- The approach proposed in the author's laboratory describes how breakage probability varies due to breakage and weakening of the particles. This approach also includes sub-models that successfully describe the different mechanisms (body and surface breakage, but not rounding), as well as the mass of powder captured in each collision, besides efficient solution algorithms that have been used to predict grinding over a range of conditions. As such, this is the only two-variable model, in which the material can change not only its size class, but also its fracture energy as grinding progresses.
- The important progress in recent years suggests advanced models of ball mills will reach some level of maturity in upcoming years.

Nomenclature

A	model parameter of Eqn. 17
$A_{i,s}$	function describing birth by surface breakage
b'	model parameter of Eqn. 17
b''	parameter of Eqn. 15
B_{ij}	cumulative body breakage function
b_{ij}	body breakage function in density form
$B_{ij}(E_{m,k})$	cumulative energy-specific breakage function for j th size interval
$b_{ij}(E_{m,k})$	energy-specific breakage function in density form for j th size interval
D	damage sustained by a particle
$D_{i,s}$	disappearance function for surface breakage
d_o	parameter in Eqn. 9
e	variable representing the fraction of the collision energy absorbed by a particle

E	collision energy	k''	constant in Eqn. 24
E'	collision energy (integration variable)	M_b	mass of the ball charge
E_{crit}	lowest magnitude of collision energy required to break a particle	m_b	mass of one grinding medium or reduced mass in a collision
E_i^*	maximum fracture energy of particles contained in class i	$m_{b,i}$	mass of i th ball in a collision
E_k	impact energy in k th collision or mean collision energy in k th class	M_i	mass of particles in the i th size interval
E_m	specific collision energy	$m_i(E)$	broken mass of particles in size class i resulting from an impact of magnitude E
\bar{E}_m	mean specific comminution energy	$m_i^*(E)$	mass of particles contained in size class i captured in each stressing event of magnitude E
$E_{m,k}$	specific energy in the k th collision or mean collision energy in k th class	$\bar{m}_{p,i}$	mean weight of a particle contained in size class i
$E_{m,min}$	parameter in Eqn. 10, which represents the threshold specific energy for body breakage	N	number of normal collision energy bins
$E_{m50,i}$	median mass-specific particle fracture energy of particles in size class i	n	number of collision energy bins
$E_{m50b,i}$	median fracture energy of particles in size class i that are broken as a result of impact of magnitude E_m	$N_{cap,i}$	number of particles contained in size class i captured in a collision event
E_n	normal portion of the collision energy	P	mill power predicted by DEM
E_o	parameter of Eqn. 15, representing the energy below which particles do not fracture	$P(E)$	cumulative distribution of collision energies
erf	error function	$p(E)$	distribution of collision energies in density form
E_s	shear portion of the collision energy	$p(e)$	energy split among particles in each collision
$E_{50,i}$	median particle fracture energy of particles in size class i	$p(E_{m,k})$	distribution of specific collision energies in density form
E_∞	parameter in Eqn. 9, representing the median fracture energy of infinitely coarse particles	r_c	radius of capture of the bed
f	parameter of Eqn. 15, characterizing the fraction of E_o in which cracks will stop propagating	S	number of shear collision energy bins
$F_i(E,0)$	fracture probability distribution of the original material in size class i	S_i	selection or breakage rate of particles in size i
$F_i(E_m)$	fracture probability distribution of particles contained in size i at a specific collision energy E_m	S_i^E	energy-specific selection function
$F_i^*(E,t)$	distribution of fracture energies of the particles in size class i that were captured in an impact event, but did not fracture	t	time
f_{mat}	parameter in Eqn. 10	$t_{contact}$	total contact time during a collision
F_n	normal component of the contact force	t_n	fraction of material body broken to $1/n^{th}$ of the parent size
F_s	shear component of the contact force	t_{10}	fraction of material body broken to $1/10^{th}$ of the parent size
G_i	fraction of material in size class i that has been damaged but remained in the original size range	v_i	velocity of grinding medium i in a collision
H	powder or ore load, also called mill hold-up	v_{ij}	relative velocity of grinding media i and j
H_i	fraction of material that appeared in size class i due to body and surface breakage	$w_i(t)$	mass fraction of particles contained in size class i in the mill at time t
I_i	fraction of material that in size class i was not captured in the time interval	x	particle size
k'	constant in Eqn. 11	x_i	mean size of particles in size class i

Greek symbols

β	volume shape factor
γ	damage accumulation parameter (Eqn. 20)
δ	Dirac delta function
θ	mean residence time

$\lambda_i(E)$	net breakage frequency at energy E for the size class i
$\lambda_i^{\text{DEM}}(E)$	DEM collision frequency at energy E for size class i
$\lambda_i^{\text{exp}}(E)$	mean number of collisions required to break the particle with collision energy E
ξ	deformation of media during a collision
ρ	specific gravity
σ	standard deviation of the log-normal distribution of particle fracture energy (Eqn. 8)
ϕ	parameter in Eqn. 9
ω	frequency of collisions

References

- Austin L.G., Klimpel R.R., Luckie P.T., Process engineering of size reduction, AIME, New York, 1984.
- Barrios G.K.P., Carvalho R.M. de Tavares L.M., Modeling breakage of monodispersed particles in unconfined beds, *Minerals Engineering*, 24 (2011a) 308–318.
- Barrios G.K.P., Carvalho R.M. de Tavares L.M., Extending breakage characterisation to fine sizes by impact on particle beds, *Transactions of the Institution of Mining and Metallurgy C*, 120 (2011b) 37–44.
- Barrios G.K.P., Tavares L.M., A preliminary model of high pressure roll grinding using the discrete element method and multi-body dynamics coupling, *International Journal of Mineral Processing* (2016), doi: 10.1016/j.minpro.2016.06.009.
- Bond F.C., The third theory of comminution, *Transactions of AIME*, 193 (1952) 484–494.
- Bwalya M.M., Moys M.H., Hinde A.L., The use of discrete element method and fracture mechanics to improve grinding rate prediction, *Minerals Engineering*, 14 (2001) 565–573.
- Capece M., Bilgili E., Davé R.N., Formulation of a physically motivated specific breakage rate parameter for ball milling via the discrete element method, *AIChE Journal*, 60 (2014) 2404–2415.
- Carvalho R.M., Tavares L.M., Dynamic modeling of comminution using a general microscale breakage model. *Computer-Aided Chemical Engineering*, 27 (2009) 519–524.
- Carvalho R.M., Tavares L.M., Predicting the effect of operating and design variables on breakage rates using the mechanistic ball mill model, *Minerals Engineering*, 43–44 (2013) 91–101.
- Chagas A.S., Carvalho R.M., Bbosa L., Mainza A., Tavares L.M., Calibration of DEM contact parameters for tumbling mills using PEPT. *Proceedings, 14th European Symposium on Comminution and Classification, Gothenburg, 2015*, pp. 1–6.
- Charles R.J., Energy-size reduction relationships in comminution, *Transactions of the AIME*, 208 (1957) 80–88.
- Cho H., Breakage mechanisms in size reduction, Ph.D. thesis, University of Utah, 1987.
- Cleary P.W., Predicting charge motion, power draw, segregation wear and particle breakage in ball mills using discrete element methods, *Minerals Engineering*, 11 (1998) 1061–1080.
- Cleary P.W., Recent advances in DEM modeling of tumbling mills, *Minerals Engineering*, 14 (2001) 1295–1319.
- Cleary P.W., Sinnott M., Morrison R.D., Prediction of slurry transport in SAG mills using SPH fluid flow in a dynamic DEM based porous media, *Minerals Engineering*, 19 (2006) 1517–1527.
- Cleary P.W., Morrison R.D., Understanding fine ore breakage in a laboratory scale ball mill using DEM, *Minerals Engineering*, 24 (2011) 352–366.
- Cleary P.W., Morrison R.D., Comminution mechanisms, particle shape evolution and collision energy partitioning in tumbling mills, *Minerals Engineering*, 86 (2016) 75–95.
- Cleary P.W., Sinnott M.D., Simulation of particle flows and breakage in crushers using DEM: Part 1—Compression crushers, *Minerals Engineering*, 74 (2015) 178–197.
- Concas A., Lai N., Psiu M., Cao G., Modelling of comminution processes in Spex mixer/mil, *Chemical Engineering Science*, 61 (2006) 3746–3760.
- Crespo E.F., Application of particle fracture energy distributions to ball milling kinetics, *Powder Technology*, 210 (2011) 281–287.
- Dan C.C., Schubert H., Breakage probability, progeny size distribution and energy utilization of comminution by impact, *Aufbereitungs-Technik*, 31 (1990) 241–247.
- Data A., Rajamani R.K., A direct approach of modeling batch grinding in ball mills using population balance principles and impact energy distribution, *International Journal of Mineral Processing*, 64 (2002) 181–200.
- Delaney G.W., Cleary P.W., Morrison R., Loveday B., Predicting breakage and the evolution of rock size and shape distributions in Ag and SAG mills using DEM, *Minerals Engineering*, 50–51 (2013) 132–139.
- Govender I., Cleary P.W., Mainza A.N., Comparisons of PEPT derived charge features in wet milling environments with a friction-adjusted DEM model, *Chemical Engineering Science*, 97 (2013) 162–175.
- Herbst J.A., A microscale look at tumbling mill scale-up using high fidelity simulation, *International Journal of Mineral Processing*, 74S (2004) S299–S306.
- Herbst J.A., Fuerstenau D.W., Scale-up procedure for continuous grinding mill design using population balance models, *International Journal of Mineral Processing*, 7 (1980) 1–31.
- Herbst J.A., Potapov A.V., Making a discrete grain breakage model practical for comminution equipment performance simulation, *Powder Technology*, 143–144 (2004) 145–150.
- Höfler A., Fundamental breakage studies of mineral particles with an ultrafast load cell device, Ph.D. thesis, University of Utah, 1990.
- Höfler A., Herbst J.A., Ball mill modeling through microscale fragmentation studies: fully monitored particle bed comminution versus single impact tests, *Proceedings, 7th European Symposium on Comminution, Ljubljana, 1990*, v. 1, pp. 381–397.
- Kano J., Saito F., Correlation of powder characteristics of talc during planetary ball milling with the impact energy of the balls simulated by the particle element method, *Powder*

- Technology, 98 (1998) 166–170.
- Katubilwa F.M., Moys M.H., Effect of ball size distribution on milling rate, *Minerals Engineering*, 22 (2009) 1283–1288.
- Kick F., *Des Gesetz der Proportionalem wider-stand und Seine Anwendung*, Felix, Leipzig, 1885.
- King R.P., Modeling and simulation of mineral processing systems, Butterworth-Heinemann, 2001.
- King R.P., Bourgeois F.S., A new conceptual model for ball milling. Proceedings, 18th International Mineral Processing Congress, Sydney, 1993, pp. 81–86.
- Kwan C., Mio H., Chen Y., Ding Y., Saito F., Papadopoulos D., Bentham A., Ghadiri M., Analysis of the milling rate of pharmaceutical powders using the distinct element method (DEM), *Chemical Engineering Science*, 60 (2005) 1441–1448.
- Lee L., Cho H., Kwon J., Using the discrete element method to analyze the breakage rate in a centrifugal/vibration mill, *Powder Technology*, 198 (2010) 364–372.
- Marktscheffel M., Schönert K., Liberation of composite particles by single particle compression, shear and impact loading, Proceedings, 6th European Symposium on Comminution, Nuremberg, 1986.
- Martins S., Li W., Radziszewski P., Faucher A., Makni S., Experimental and simulated ball in a tumbling mill—a comparison, *Minerals Engineering*, 43–44 (2012) 79–94.
- Mayank K., Narasimha M., Govender I., Two way coupled CFD-DEM model to predict tumbling mill dynamics, Proceedings, International Semi-Autogenous Grinding and High-Pressure Roll Grinding Technology, Vancouver, 2015, paper #28.
- Metzger M.J., Glasser B.J., Simulation of the breakage of bonded agglomerates in a ball mill, *Powder Technology*, 237 (2013) 286–302.
- Mishra B.K., Murty C.V.R., On the determination of contact parameters for realistic DEM simulations of ball mills, *Powder Technology*, 115 (2001) 290–297.
- Mishra B.K., Rajamani R.K. The discrete element method for the simulation of ball mills, *Applied Mathematical Modeling*, 16 (1992) 598–604.
- Morrell S., An alternative energy–size relationship to that proposed by Bond for the design and optimisation of grinding circuits, *International Journal of Mineral Processing*, 74 (2004) 133–141.
- Mori H., Mio H., Kano K., Saito F., Ball mill simulation in wet grinding using a tumbling mill and its correlation to grinding rate, *Powder Technology*, 143–144 (2004) 230–239.
- Morison R.D., Cleary P.W., Towards a virtual comminution machine, *Minerals Engineering*, 21 (2008) 770–781.
- Morrison R.D., Shi F., Whyte R., Modelling of incremental rock breakage by impact—For use in DEM models, *Minerals Engineering*, 20 (2007) 303–309.
- Moys M.H., van Nierop M.A., van Tonder J.C., Glover G., Validation of the discrete element method (DEM) by comparing predicted load behavior to a grinding mill with measured data, *Developments in Mineral Processing*, Elsevier, 2000, v. 13, pg. C3–39–C3–44.
- Napier-Munn T.J., Morrell S., Morrison R.D., Kojovic T., *Mineral Comminution Circuits: Their Operation and Optimization*, JKMRRC Monograph Series in Mining and Mineral Processing, Brisbane, 1996.
- Nomura S., Hosada K., Tanada T., An analysis of selection function for mills using balls as grinding media. *Power Technology*, 68 (1991) 1–12.
- O’Sullivan C., *Particulate discrete element modelling: a geomechanics perspective*, Spon Press, v. 4, 2011.
- Pauw O.G., Maré M.S., The determination of optimum impact-breakage routes for an ore, *Powder Technology*, 54 (1988) 3–13.
- Potyondy D.O., Cundall P.A., A bonded-particle model for rock, *International Journal of Rock Mechanics and Mining Sciences*, 41 (2004) 1329–1364.
- Powell M.S., Govender I., McBride A.T., Applying DEM outputs to the unified comminution model, *Minerals Engineering*, 21 (2008) 744–750.
- Powell M.S., McBride A.T., What is required for DEM simulations to model breakage in mills? *Minerals Engineering*, 19 (2006) 1013–1021.
- Powell M.S., Weerasekara N.S., Cole S., LaRoche R.D., Favier J., DEM modeling of liner evolution and its influence on grinding rate in ball mills, *Minerals Engineering*, 24 (2011) 341–351.
- Quist J., Evertsson C.M., Cone crusher modelling and simulation using DEM, *Minerals Engineering*, 85 (2016) 92–105.
- Rajamani R.K., Agrawala S., Mishra B.K., Mill scaleup: ball collision frequency and collision energy density in laboratory and plant-scale mills, Proceedings, 18th International Mineral Processing Congress, Sydney, 1993, pp. 103–107.
- Ribas L., Cordeiro G.C., Toledo Filho R.D., Tavares L.M. Measuring the strength of irregularly-shaped fine particles in a microcompression tester, *Minerals Engineering*, 65 (2014) 149–155.
- Rodriguez V.A., Validation of the UFRJ mechanistic ball mill model, M.S. Thesis, Universidade Federal do Rio de Janeiro, 2016 (in Portuguese).
- Rowland C.A., Kjos D.M., Rod and ball mills, in: Mular A.L., Bhattu R.B. (Eds.) *Mineral Processing Plant Design*, AIME, 1980, pp. 239–278.
- Rozenblat Y., Grant E., Levy, Kalman H., Tomas J., Selection and breakage functions of particles under impact loads, *Chemical Engineering Science*, 71 (2012) 56–66.
- Schönert K., Aspects of physics of breakage relevant to comminution, Proceedings of the 4th Tewksbury Symposium, Melbourne, 1979, pp. 3.1–3.9.
- Tavares L.M., Energy absorbed in breakage of single particles in drop weight testing, *Minerals Engineering*, 12 (1999) 43–50.
- Tavares L.M., Optimum routes for particle breakage by impact, *Powder Technology*, 142 (2004) 81–91.
- Tavares L.M., Breakage of single particles: quasi-static, in: Salman A.D., Ghadiri M., Hounslow M.J. (Eds.), *Handbook of Particle Breakage*, Elsevier, 2007, v. 12, pp. 3–68.
- Tavares L.M., Analysis of particle fracture by repeated loading as damage accumulation, *Powder Technology*, 190 (2009) 327–339.
- Tavares L.M., Carvalho R.M., Modeling breakage rates of coarse particles in ball mills, *Minerals Engineering*, 22

- (2009) 650–659.
- Tavares L.M., King R.P., Single-particle fracture under impact loading, *International Journal of Mineral Processing*, 54 (1998) 1–28.
- Tavares L.M., King R.P., Modeling particle breakage by repeated impacts using continuum damage mechanics, *Powder Technology*, 123 (2002) 138–146.
- Tavares L.M., Neves P.B., Microstructure of quarry rocks and relationships to particle breakage and crushing, *International Journal of Mineral Processing*, 87 (2008) 28–41.
- Tuzcu E.T., Rajamani R.K., Modeling breakage rates in mills with impact energy spectra and ultra fast load cell data, *Minerals Engineering*, 24 (2011) 252–260.
- Venugopal R., Rajamani R.K., 3D simulation of media motion in tumbling mills by the discrete element method, *Powder Technology* (2001) 157–166.
- Vogel L., Peukert W., Determination of material properties relevant to grinding by practicable labscale milling tests, *International Journal of Mineral Processing*, 74S (2004) S329–338.
- Von Rittinger P.R., *Lehrbuch der Aufbereitungs Kunde*, Ernst and Korn, Berlin, 1867.
- Wang M.H., Yang R.Y., Yu A.B., DEM investigation of energy distribution and particle breakage in tumbling ball mills, *Powder Technology*, 223 (2012) 83–91.
- Weerasekara N.S., Powell M.S., Cleary P.S., Tavares L.M., Evertsson M., Morrison R.D., Quist J., Carvalho R.M., The contribution of DEM to the science of comminution, *Powder Technology*, 248 (2013) 3–24.
- Weichert R., Application of defect statistics and fracture mechanics for describing comminution processes, *Zement-Kalk-Gips* 45 (1992), 51–57.
- Yahyei M., Weerasekara N.S., Powell M.S., Characterization of superficial breakage using multi-size pilot mills, *Minerals Engineering*, 81 (2015) 71–78.
- Yashima S., Hashimoto H., Kanda Y., Sano S., Measurement of kinetic energy of grinding media in a tumbling ball mill. *Proceedings of the 16th International Mineral Processing Congress*, Stockholm, 1988, pp. 299–309.

Author's short biography



Luís Marcelo Tavares

Luís Marcelo Tavares is a Professor at the Department of Metallurgical and Materials Engineering of Universidade Federal do Rio de Janeiro. He received his bachelor's degree in Mining Engineering (honours) and his master's degree from Universidade Federal do Rio Grande do Sul. In 1997 he was awarded a Ph.D. degree in Extractive Metallurgy at the University of Utah under the supervision of the late Professor R.P. King. He has been a member of the faculty of the Universidade Federal do Rio de Janeiro (Brazil) since 1998, where he is head of the Laboratório de Tecnologia Mineral and has been Department chairman. His research interests include advanced models of comminution, particle breakage, physical concentration, classification, iron ore processing and development of pozzolanic materials. He is a founding member of the Global Comminution Collaborative (GCC) and has received a number of awards from the Brazilian Association of Metallurgy, Materials and Mining (ABM).

A Review of the Modeling of High Pressure Grinding Rolls[†]

Samira Rashidi¹, Raj K. Rajamani^{1*} and Douglas W. Fuerstenau²

¹ Department of Metallurgical Engineering, College of Mines and Earth Sciences, University of Utah, USA

² Hearst Memorial Mining Building, University of California, USA

Abstract

High Pressure Grinding Rolls (HPGR) technology is accepted as an energy-efficient and cost-effective alternative for treating specific mineral ore types. HPGR technology has been advancing within manufacturing facilities and research centers since its first installation in 1985. Over the last three decades much of the literature on HPGR have focused on the industrial applications and trade-off studies in comparison with semi-autogenous and ball milling circuits. Literature on fundamental studies of HPGR technology has been very limited. This paper aims to provide a review of the modeling of high pressure grinding rolls.

Keywords: HPGR, modeling, interparticle breakage, particles compression, comminution

1. Introduction

More than thirty years have passed since the first industrial installation of high pressure grinding rolls (HPGR). Through this time, HPGR technology has advanced on many technical fronts. Nowadays, it is accepted as a standard technology for certain types of ore materials (Battersby et al., 1992; Patzelt, 1992).

The development of HPGR technology originated from the fundamental studies that the late Prof. Schönert, the inventor of HPGR, and his colleagues performed on interparticle breakage (Schönert, 1985, 1988). From his extensive research on single-particle breakage under compression and impact loading, Schönert (1988) concluded that the highest efficiency for particle breakage is only possible through slow compression loading of single particles. Schönert then extended his research to the breakage of beds of particles in a piston-die press. He observed that confined particle-bed breakage was less energy efficient than single-particle breakage yet was far more efficient than tumbling mill grinding (See Fig. 1). The dominant factors affecting the energy efficiency of the particle-bed stressing in a confined environment include the form of energy distribution to particles and the particle/particle interaction (Abouzeid and Fuerstenau, 2009).

Following this finding, the same results obtained in particle-bed loading could be repeated in a continuous

mode with a small-scale HPGR. This led to a patent being issued to Schönert in 1977 (German Patent Number DE-2708053). In an oral history interview, Schönert stated that his patent was for a process and not for a machine¹⁾. Schönert's patent was for a process that compressed a bed of particles to a certain pressure that may require deagglomeration of the product. He immediately began negotiations for licensing his patent to two German manufacturers, Polysius (currently known as thyssenkrupp Industrial Solutions) and KHD, to produce the required roller mills for industrial applications. Manufacturing an industrial-scale machine that would operate under the specific conditions of dry grinding circuits, found particularly in cement plants, proved to require extensive design and development. One of the challenges that led both companies to expend a substantial amount of effort was resolving how to handle wear rate on the rolls. Later, Köppern, another German manufacturer that had developed the technology of roller presses for the briquetting process, further contributed in promoting the HPGR technology. Briquetting machines are used for the compaction of granular materials that may share a few similarities with HPGR machines.

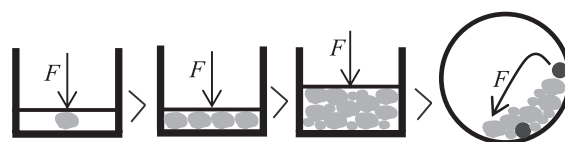


Fig. 1 The order of energy efficiency for different modes of breakage.

[†] Received 25 September 2015; Accepted 9 June 2016
J-STAGE Advance Publication online 30 August 2016

¹ Salt Lake City, UT 84112, USA

² Berkeley, CA 94720, USA

* Corresponding author: Raj K. Rajamani;

E-mail: raj.rajamani@utah.edu

TEL: +1-801-581-3107 FAX: +1-801-581-4937

¹⁾ Schönert's interview is published in the appendix on pages 599 to 629 of Fuerstenau's oral history (Fuerstenau, 2011).

At this point it might do well to comment on the terminology that has been used to designate high compression particle-bed comminution. When publishing in English, Schönert tended to call the technology either “high compression roller mills” or “high-pressure roller mills”, HPRM. Other designations were also used for the high pressure grinding technology with respect to a wide range of applications from coarse crushing to very fine grinding, such as ‘high pressure roller crusher’, HPRC. The generic term that has been widely settled upon is HPGR, high pressure grinding rolls, and is used in this paper as well. It should be noted that each manufacturer has its own registered trade name for their particular HPGR.

Quite rapidly, HPGRs were widely installed in cement plants throughout Germany and Europe. Schönert stated that he believed the rapid installations of energy-efficient HPGRs were due to the high cost of electrical power in Germany (Fuerstenau, 2011). The first major application of HPGRs by the mining industry was at the diamond mines of DeBeers in South Africa. The motivation in this case was the enhanced liberation of diamonds with HPGRs (Fuerstenau, 2011). The strong development and design efforts by the manufacturers led to an increasing number of installations in a wider range of industries.

The rapid utilization of HPGR technology in industrial applications led to publications that mainly presented general information about new installations, benefits achieved, as well as challenges. However, there were very few publications by manufacturers at the early stage of development that discussed the scale-up of HPGRs. That said, Schönert and his students at the Technical University of Clausthal were actively involved in the fundamental research that helped delineate interparticle breakage phenomena in a HPGR through systematic studies with a piston-die apparatus and a 200 mm diameter by 100 mm length lab-scale HPGR (Otte, 1988; Schönert, 1988, 1991; Schönert and Lubjuhn, 1990; Norgate and Weller, 1991; Lubjuhn and Schönert, 1993; Reichardt and Schönert, 2003). Schönert also developed fundamental relationships for defining the scale-up factors for the design of HPGR units. Additionally, by capturing high-speed videos, Schönert investigated the behavior of particle beds inside a HPGR (Schönert, 1991; Lubjuhn and Schönert, 1993).

By the early 1990s, Fuerstenau and his research team focused on this energy-efficient grinding technology by utilizing a single-particle roll mill as well as a 200 mm by 100 mm high pressure grinding rolls at the University of California, Berkeley, USA. They studied the effect of HPGR operating parameters and developed fundamental models to simulate high pressure breakage phenomena. (Fuerstenau et al., 1991; Fuerstenau et al., 1993; Fuerstenau et al., 1996; Fuerstenau and Abouzeid, 2007). As access to laboratory-scale HPGRs became prevalent, more research was dedicated to studying various aspects of high

pressure grinding performance and attendant models (Austin et al., 1993; Lim et al., 1996b; Rashidi, 2014).

Although the majority of research about HPGR technology is limited to lab-scale units due to the large capacity of these machines, Klein and his research team at the University of British Columbia have been able to demonstrate interesting pilot-scale results through running tests in a 750 mm by 220 mm HPGR unit manufactured by Köppern (Drozdiak et al., 2011; Nadolski et al., 2011; Rosario et al., 2011). Daniel (2002) also obtained valuable information about HPGR scale-up through extensive tests using different sizes of HPGR machines.

As HPGR became accepted as a standard grinding technology, much of the research was generally directed toward establishing dimensionless numbers for characterizing grinding operations (Klymowsky and Liu, 1997; Daniel, 2003; Mcken and Williams, 2006; Morrell, 2006). Some research was also focused on applying discrete element modeling (DEM) to high pressure grinding techniques (Djordjevic and Morrison, 2006; Barrios et al., 2014). Even though DEM models are computationally demanding, they provide visual insight into the nature of particle breakage in the gap between the rolls.

Overall, HPGR is not yet considered mature in terms of modeling. In fact, modeling publications tend to be limited and scattered without proper verification. That being said however, there has not been a high demand within the industry for additional investigation and research on HPGR modeling. Rather, industrial publications show that the current focus is on developing new applications for HPGR technology as well as alternatives for improving the well-accepted layouts of this technology (Burchardt et al., 2011; Van der Meer, 2011).

This paper aims to review the evolution of the modeling since the introduction of this technology. We emphasize only those models that have the potential for further development in the future.

2. Principle of high pressure grinding

The energy efficiency of comminution methods is determined by the mobility or confinement of the particles being comminuted (Fuerstenau and Kapur, 1995). Schönert (1996) clearly showed that the most energy-efficient method of breakage is the direct application of force to a single particle or at least a monolayer of particles. The breakage of particles in a confined bed is the second most energy-efficient method of comminution, at least at low reduction ratios (Gutsche, 1993). As exemplified by ball milling, loose-bed comminution has the lowest efficiency, which is due to the hit-and-miss mode of energy transfer during particle/ball impacts. Schönert quickly realized the opportunity of increasing the energy

efficiency of comminution by employing particle-bed breakage.

The efficiency of this method comes from the direct transfer of energy to particles and the highly localized interparticle stresses that are generated at the contact points of each particle in the bed (De, 1995). In other words, particles are stressed by each other provided that the average size of the largest particle is smaller than the width and height of the bed and the applied force is higher than the particle strength (Schönert, 1988, 1991). During compression of the particle bed, smaller particles fill the void space and thereby participate in the transfer of energy and the breaking and re-breaking of larger particles to a certain fineness (Klymowsky, 2009). This mode of breakage requires fewer particles to be in contact with the grinding medium, that is, the roll surface (Klymowsky, 2009).

There is, however, a negative aspect of particle-bed grinding, namely a retardation effect. Grinding virtually comes to a halt in highly compressed beds at sufficiently high pressure. This was shown by Fuerstenau et al. (1996) in a detailed study of confined particle-bed breakage of brittle materials whilst using a piston-die apparatus. It seems that the presence of a sufficient amount of fines in the bed and the buildup of an isostatic-like pressure field can lead to a near cessation of particle breakage, as illustrated in **Fig. 2**. Schönert and Mueller (1990) developed an expression that gives the fraction of narrowly-sized feed particles that are broken as a function of compaction energy, including a maximum fraction that can be broken. For efficient HPGR comminution, this points to operating HPGRs at low reduction ratios and to the removal of fines in recycle systems if the HPGR is to produce a finished product.

A system consisting of rolls that operates at high pressure was conceived by Schönert to translate the breakage of a confined particle-bed into a continuous form. The three key criteria for this system include direct transfer of particles inside the machine, direct discharge of the product, and the capability of adjusting the level of the applied force and thereby the energy input (Schönert, 1991). The basic principle is similar to briquetting machines that operate with pressures low enough to compact the particles without necessarily increasing the portion of fines (Schewechten and Mulburn, 1990). When it comes to particle bed comminution however, a high grinding pressure is required in order to compress the bed of particles to a bulk specific gravity of 70 to 85 percent of the ore's specific gravity, which will cause the particles to break and thereby generate fines in the product (Schönert, 1988).

An HPGR machine consists of a pair of counter-rotating rolls, which are mounted in a very sturdy frame. While the bearing block of one roll is fixed, the other one can float linearly to adjust the gap between the two rolls as the material properties, such as particle size distribu-

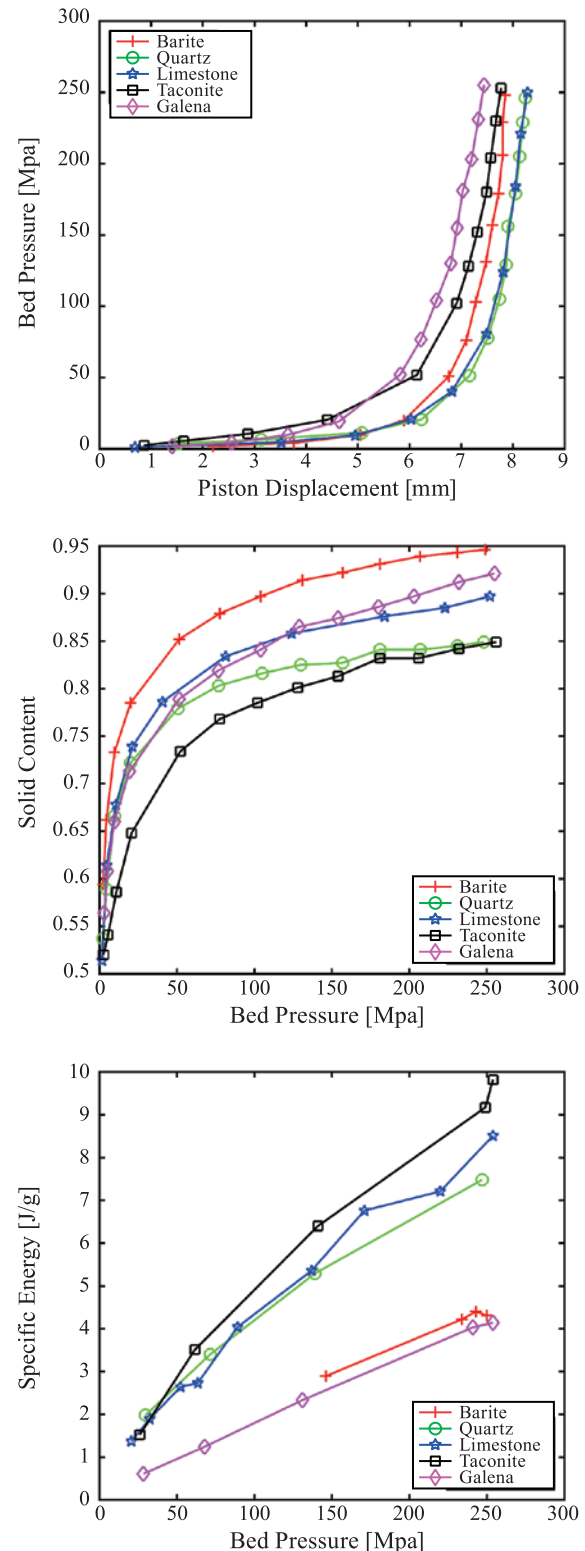


Fig. 2 The isostatic-like pressure field in confined particle-bed breakage shown in piston-die tests (Adapted from Gutsche, 1993).

tion, moisture, and hardness, change. A hydro-pneumatic spring system applies the grinding force directly on the particle bed via the floating roll. Larger gap openings result in higher grinding pressures. The extent of the gap

opening is controlled by the preset grinding force and initial gap. Each roll unit is normally equipped with a single drive motor that powers the roll through a gearbox. Feed material is introduced from the top, passes through the gap where it experiences the grinding force, and then leaves the machine from the bottom in the form of either free-flowing particulates (as with quartz) or as a compacted cake (as with limestone, dolomite, coal, etc.).

In a confined mode of particle-bed breakage, energy absorption is a main factor for the size-reduction process (Schönert, 1996). The specific grinding force has a direct effect on the amount of energy absorbed to a certain level, beyond which the bed is saturated and little-to-no breakage occurs (Fuerstenau et al., 1996; Schönert, 1996).

Fig. 3 shows a schematic illustration of the multiple zones that particles pass through in between the two counter-rotating rolls. Feed material first enters the acceleration zone (also known as the de-aeration, the pre-crushing, or the pre-grinding zone) (Schwechten and Mulburn, 1990; Austin et al., 1993; Lubjuhn and Schönert, 1993) and transfers through the feed hopper into the next zone, where particle-bed breakage under high pressure occurs. This transfer is accompanied with compaction during which, re-arrangement of the particles takes place and smaller particles fill the void space between the larger ones. Air that is trapped in the void space, leaves the particle bed from the top. Primarily governed by gravity at the beginning, the downward movement of the feed can be resisted by the rate of the upward airflow. For this reason, efficient ventilation is critical to optimal operation of the HPGR, especially in bigger units. Particles get compacted as they move through and, hence, friction forces between particle/particle as well as particle/roll surface increases, which assists with the acceleration of the particle bed. Bulk density also increases as material goes down the HPGR, where it may reach up to 85 percent of

the ore's specific gravity.

The zone that starts with the nip angle is called the grinding zone (also known as the compression zone). True interparticle breakage takes place in the grinding zone, where the particles bed is exposed to the highest grinding pressure. The grinding zone is limited to the shortest distance between the two rolls namely the working gap and, on the other hand, the critical gap, which is defined by the nip angle. The nip angle is influenced by the material properties, the roll surface pattern, and the roll speed.

In both research and industrial operation of HPGRs, feed material may either be mono-sized or have a distribution of particles. In research, when comparing energy-efficiency with single-particle breakage, the feed must be narrowly sized. Extensive industrial application of HPGRs has been the comminution of granulated blast-furnace slag in the production of cement. In this case, the particle bed forms as the feed particles are broken in the grinding zone. On the other hand, when it comes to feeds that have a distributed particle size, voids in the particle bed are filled with finer particles as they enter the acceleration zone. This should lead to a somewhat more energy-efficient comminution. Among several factors that affect the performance of HPGR grinding, moisture in the feed has been found to have a significant effect on HPGR operation because it influences friction and adhesion between particles as they are being squeezed in the gap (Fuerstenau and Abouzeid, 1998). Depending on the feed characteristics, optimum moisture content would help with efficient grinding. Moreover, it also helps, up to a certain extent, with the build-up of an autogenous protection layer on the surface of the profiled or studded rolls when treating highly abrasive ores.

The third zone below the working gap is called the relaxation zone. Compacted particles face relatively no pressure as soon as they leave the grinding zone, and

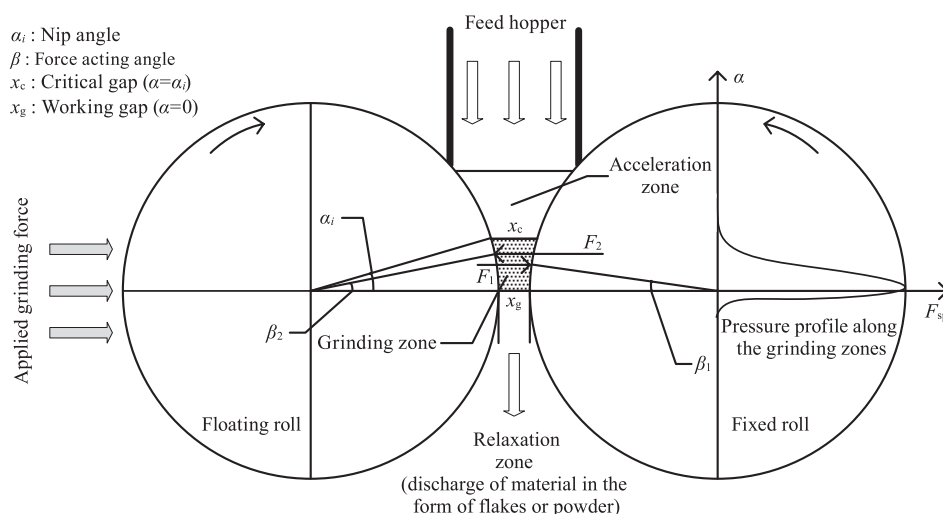


Fig. 3 Schematic of the gap between rolls showing Acceleration, Grinding and Relaxation zones.

therefore, the thickness of the flakes in the discharge tend to expand slightly right after exiting the grinding zone. If necessary, the thickness of the flakes provide a good estimate for the working gap. If, of course, the fine particles do not agglomerate however (as seen in the case of grinding quartz), then the particles exiting the grinding zone will be free flowing.

Material moving between the two rolls is exposed to a gradient of pressure intensity along the gap. Schönert (1991) showed that the grinding pressure increases steeply in the compression zone, with the peak pressure being at the working gap or slightly above it. On the other hand, not all particles along the roll width experience the same pressure intensity. Because of this, multiple breakage modes take place depending on where the particles are passing through the gap and what is their relative size. Those particles in the bed that are larger than the critical gap, will break when they come in contact with the roll surface. This is because they are passing from the acceleration zone to the grinding zone. Depending on the construction of the housing of the rolls, there may also be an edge effect, where some of the feed particles experience partial compression in the grinding zone. In other words, particles passing through the center of the roll width are, due to the pressure gradient across the width, more compacted and therefore leave the rolls with a higher portion of fines than those passing through either end of the rolls.

3. Scale-up and sizing of HPGR

Soon after the introduction of HPGR, Schönert (1985) was the first to publish the key parameters, in the form of equations, for the scale-up of HPGR. Those equations have been widely quoted by others. Throughput, power, and the specific grinding force are the three main scale-up factors required for sizing a HPGR machine. To begin, a series of tests need to be carried out in order to obtain the necessary data for the quantification of the scale-up factors.

The energy efficiency of HPGR is achieved via true interparticle breakage. Measuring the nip angle allows one to suitably define the top size of the feed that would minimize single-particle contact breakage as much as possible and, instead, expose most of the feed to interparticle breakage mode. Any particle larger than the top size is normally broken in the pre-crushing zone repeatedly until being small enough to enter the compression zone. Nip angle is mostly a function of the material properties and both the roll dimensions and surface pattern. If material characteristics inside the grinding zone are known, then the nip angle can also allow one to measure the volumetric flowrate of particles. Klymowsky et al. (2002) used the geometry of the grinding zone to calculate the nip angle,

α_i :

$$\alpha_i = \cos^{-1} \left(1 - \left(\frac{\delta_g}{\delta_F} - 1 \right) * \left(\frac{x_g}{1000D} \right) \right) \quad (1)$$

The nip angle theme is central to the models proposed in the literature. Austin et al. (1993, 1995) showed that the specific grinding pressure has an inverse effect on the specific throughput. Depending on the specific grinding pressure and the compressibility of the ore bed, the operating gap takes on a value of its own. Austin et al. (1993, 1995) also showed that a higher pressure reduces the working gap and thereby diminishes the volumetric flow through the rolls. The relationship that Austin et al. (1993, 1995) derived between the relative gap (x_g/D) and the specific throughput (see Eqn. 7 for definition) is as follows:

$$\dot{m}_c = \frac{x_g}{1000D} (1 - \theta_g) \cos \alpha_i + (1 - \theta_g) \cos \alpha_i (1 - \cos \alpha_i) \quad (2)$$

Austin et al. (1993, 1995) relationship allows one to determine the nip angle and the critical gap (the distance between the two rolls at the nip angle) by fitting Eqn. 2. Several grinding tests with similar conditions under at least three substantially different levels of operating pressure are needed to find the linear relationship between the specific throughput and the relative gap. For details, refer to Dhawan et al. (2012). The nip angle, depending entirely on the feed characteristics and roll surface pattern, ranges from 4 degrees up to 10 or 11 degrees (Scheweichten and Mulburn, 1990; Schönert, 1991; Lim and Weller, 1999).

The HPGR mass flowrate is proportional to the dimensions of the rolls because the geometry of the gap is directly related to the capacity of the machine. Schönert (1985) and Schönert and Lubjuhn (1990) quantified this relationship as follows:

$$M = \rho (1 - \theta_g) x_g u_m L 3.6 = \delta_g x_g u_m L 3.6 \quad (3)$$

Eqn. 3 is well quoted in the literature and is called the continuity equation. The mass flow between the rolls is illustrated in **Fig. 4**. As can be seen, Eqn. 3 can hold true as long as the cake (product) density remains constant along the roll width and the phenomenon of the edge effect is neglected (Lubjuhn and Schönert, 1993). Only small HPGR machines, with the roll diameter less than 300 mm, can provide uniform compaction through the roll width. As a result, a more practical approach to define mass flowrate is to conduct actual measurement during the operation. The volumetric flowrate can then be defined as follows (Schönert, 1988):

$$V = \frac{M}{\rho} \quad (4)$$

With replacing Eq. 3, Schönert (1988) showed that the

volumetric flowrate is a function of the rolls geometry and material characteristic:

$$V = (1 - \theta_g) x_g u_m L 3.6 = k \left(\frac{u_m}{u} \right) V_p \quad (5)$$

With $k = (1 - \theta_g)(x_g/1000 D)$ being a material constant, knowing that the working gap is linearly related to the roll diameter of a given material, and assuming material velocity is equal to the roll velocity, volumetric flowrate can be measured based on the roll dimensions and the roll speed within a good approximation. Schönert (1988) called V_p the potential volumetric flow rate that replaces Eqn. 5, given as:

$$V_p = uLD \quad (6)$$

In order to minimize the influence of the machine size on the measured throughput, the specific throughput parameter was introduced. The specific throughput parameter, also widely known as “m-dot” in the industry, provides the expected throughput for a HPGR, with 1 m diameter and 1 m length rolls running at 1m/s peripheral speed (Klymowsky et al., 2002):

$$\dot{m}_c = \frac{x_g}{D} * \delta_g * 3.6 \quad (7)$$

The necessary data to calculate \dot{m}_c can be measured from the flake density, δ_g , in the HPGR discharge. At the same time however, this formula can only be used for lab-scale machines as long as the edge effect is negligible. For this reason, the following formula is more practical for real applications:

$$\dot{m}_f = \frac{M}{uLD} \quad (8)$$

The value obtained from Eqn. 8 provides information about the response of the material to high pressure grinding. It should be noted that certain parameters, such as feed properties and specifics of the HPGR machine, influences the value. For more details refer to Rashidi (2014). Practice has shown that the specific throughput rate is influenced by the size of the machine, often caused by the size distribution of feed particles and the internal friction between particles (Burchardt et al., 2011). Evidently, larger feed sizes in the plant-scale HPGRs could behave differently under compression than finer feeds in pilot-scale HPGRs. This is the reason that most manufacturers prefer to run scale-up tests in large units because it minimizes the effect of machine size as much as possible.

In the interparticle mode of breakage, grinding occurs when the compressive force is higher than the particle strength. A higher specific grinding force increases the rate of fines generated in the product at a diminishing rate (Schönert, 1996), as discussed in Section 2. The optimum

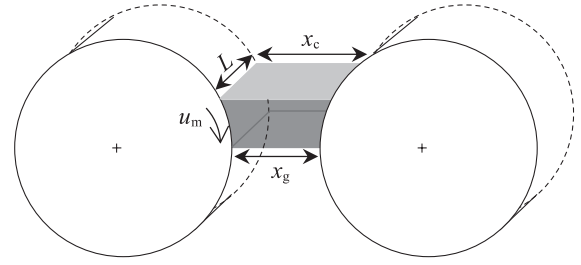


Fig. 4 Schematic of gap geometry in HPGR.

HPGR specific grinding force can be defined via HPGR grinding tests. It is broadly discussed across the HPGR publications that the compressive milling force is the main controlling parameter for the fineness of the HPGR product. The specific grinding pressure is considered to be one of the scale-up factors as the effect from the roll dimensions is taken off through dividing the milling force by the roll width and length:

$$F_{sp} = \frac{F}{DL10^6} \quad (9)$$

The specific grinding force is the average force applied on the projected area of the rolls. At the same time however, there is a pressure gradient along the width. Further, the pressure across the gap rises to a very high value at the center of the working gap and then drops very quickly. De and Fuerstenau (2012) presented a model for calculating the pressure profile across the gap at different angular positions in the vicinity of the nip angle. This study, verified with a piston-die apparatus, showed that the maximum pressure inside the bed can reach as high as 200 to 250 MPa (De, 1995). Schönert and Lubjuhn (1990) estimated it to be 40 to 60 times the applied specific grinding force:

$$F_{max} = \left(\frac{1}{\alpha_f C_F} \right) F_{sp} \quad (10)$$

Extensive results from lab-scale to industrial-size machines show that the required power for driving rolls increases with the specific grinding force. HPGRs are designed in such a way that the grinding force is applied on the floating roll, perpendicular to the projected area of the roll. The applied force is split into two force components: tangential and radial. The tangential component creates a torque on the roll, which determines the required power to drive the roll. One of the rolls is normally exposed to less force compared to the other one, however Schönert (1988) simplifies it by assuming that equal force is applied to both rolls. Therefore, the total torque needed to drive both rolls is given by:

$$T = 2 \left(\frac{D}{2} \right) F \sin \beta = DF\beta \quad (11)$$

The point at which the grinding force is applied on the roll is determined by the force-acting angle β . The force-acting angle should be less than the nip angle in order to efficiently apply the grinding force on the particle bed. The power required for driving the roll is determined by the force and the force-acting angle. With $\sin \beta = \beta$ for small angles, the power is calculated as follows:

$$P = \omega T = \left(2\pi \frac{u_r}{60}\right)(DF\beta) = 2\beta V_p F_{sp} = 2\beta u F \quad (12)$$

There are several necessary measurements to define the scale-up factors, which include the specific throughput, the optimum specific grinding force in relation to the required fineness, and the specific power consumption, that can be determined through a series of tests. **Fig. 5** summarizes the interrelationship between the scale-up parameters. HPGR design and, to a great extent, material properties majorly affect these parameters. Overall, the scale-up of HPGRs has not faced any significant changes since the introduction of the technology.

4. Particle breakage modeling

Developing a realistic mathematical model for the size reduction in HPGRs has really not been possible due to a variety of reasons. The fact that HPGR was put into commercial use so quickly and given the restricted access to scale-up as well as the industrial datasets are just a few of the reasons why the progress in this area has been slow. In this section, those models that have shown potential for further development are discussed.

As was pointed out, grinding in interparticle bed breakage is directly controlled by the specific energy input. With respect to HPGR grinding, Fuerstenau et al. (1993) showed that the reduction ratio for a single pass of material varies linearly with the specific energy input, which holds true for a limited range:

$$\frac{X_f}{X_{50}} = jE_{sc} + e \quad (13)$$

Unlike in ball milling, the residence time for individual particles in the bed is the same in HPGR. All particles in

the feed experience a fixed-time of residence (Fuerstenau et al., 1991). Even then, Gutsche and Fuerstenau (2004) showed that similar to ball mills, the self-similar behavior holds true for the product size distribution of the HPGR. In other words, different product cumulative size distributions follow one master curve (Fuerstenau and Kapur, 1995) when expressed as a function of relative size (size of particle divided by the product median size) which is given by:

$$F(x, E) = \bar{Z} \left(\frac{x}{X_{50}} \right) \quad (14)$$

Utilizing the self-similarity concept, some researchers proposed that by fitting an empirical master curve to the self-similar distributions, the product size distribution can be easily predicted at any specific energy input as long as the median size is determined (Lim et al., 1996a; Daniel, 2002). Based on these observations, Fuerstenau et al. (1991) modified the ball mill grinding kinetics equation in terms of the cumulative energy input instead of the grinding time to predict the product size distributions in HPGR:

$$\frac{dM_i(E)}{dE} = -S_i^E M_i(E) + \sum_{j=1}^{i-1} b_{i,j} S_j^E M_j(E); j = 1, \dots, i-1 \quad (15)$$

Assuming the breakage function can be normalized, the specific selection function can then be based on the actual energy that goes into grinding by incorporating an energy dissipation exponent, y , (Fuerstenau et al., 1991):

$$S_i = S_i^E \frac{P}{E_{sc}^y}; \quad 0 \leq y < 1 \quad (16)$$

For this full batch-grinding model, both selection function and breakage function had to be back-calculated from experimental data, resulting in a total of eight exponents and constants to be simultaneously fitted (Fuerstenau et al., 1991; Fuerstenau et al., 1993). An important finding was that the specific selection function is nearly constant, independent of particle size, in contrast to ball milling. This should be expected since the same amount of energy is transmitted to all particle sizes in confined particle-bed comminution. This model was successfully verified using the experimental data obtained in a lab-scale HPGR that was developed in collaboration between Prof. Schönert at the Technical University of Clausthal and Prof. Fuerstenau at the University of California, Berkeley (Gutsche, 1993). This lab unit with 200 mm diameter by 100 mm width rolls can process sample as small as 10 kg. This machine was later handed over to the University of Utah under the supervision of Prof. Rajamani.

The assumption of using the energy-normalized selection function for grinding in HPGRs could only hold true for low specific energy input where there is a linear function between the energy input and the fineness of the

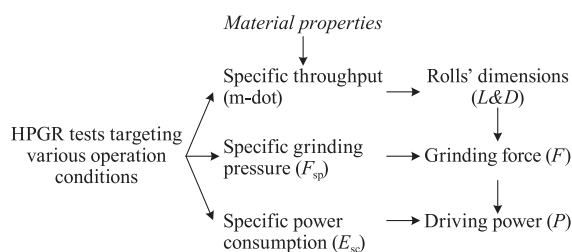


Fig. 5 Interrelationship between HPGR scale-up parameters.

product. Unlike ball milling, where energy is a direct function of time, higher specific energy in particle-bed breakage does not necessarily relate to a higher reduction ratio (Austin et al., 1993). Moreover, the application of this model needs to be further investigated for larger machines where, for a given specific energy input, the product size distribution varies along the rolls width.

In a separate study, Austin and Trubelja (1994) modified the roll crusher model to predict the action of grinding in HPGR. The roll crusher model was previously developed by Austin et al. (1980). It should be noted that grinding in roll crushers is completely different from HPGR grinding. In roll crushers, the gap is fixed and no compressive pressure is applied to the rolls. Hence, breakage occurs through contact with the rolls. Individual particles larger than the gap repeatedly break into smaller sizes until they pass through the rolls.

Austin et al. (1993) defined two sets of selection functions based on the geometry of the gap in a HPGR. The first selection function was defined for large particles broken by contact, which normally happens above the critical gap in the acceleration zone. This selection function was normalizable by the working gap as a function of specific grinding force and therefore, the energy input. The second selection function was defined for particles with equal or smaller size compared to the critical gap, which are nipped into the compression zone and broken by inter-particle stresses. It is important to note that the largest particle present in the feed is defined by the working gap. Austin and Trubelja (1994) at the time did not suggest any particular compression selection function and, instead, used an equation based on the calculated particle size distribution to determine this selection function. Later, Schneider et al. (2009) incorporated the specific grinding pressure into Austin's model and defined the compression selection function.

Austin and Trubelja (1994) proposed a sequential discrete-size model to simulate the product size distribution. It is based on two sets of particle-size distributions: particles that are left unbroken and are denoted as P_i and particles that enter from larger size fractions after breakage and are denoted as P_i^* . With $(1 - a_i)$ and $(1 - a_i')$ to be the mass of the fraction of particles left unbroken after nipping (pre-crushing) and compression, respectively, the product size distribution is then calculated as follows:

$$P_i = \begin{cases} (1 - a_i)(1 - a_i'); & i = 1 \\ (1 - a_i)(1 - a_i')P_i^*; & 1 < i \leq n \end{cases} \quad (17)$$

where,

$$P_i^* = \begin{cases} 0; & i = 1 \\ -a_i^*b_{i,1} + \sum_{j=1}^{i-1} b_{i,j}a_j^*P_j^*; & 1 < i \leq n \end{cases} \quad (18)$$

with

$$a_i^* = a_i + a_i'(1 - a_i) \quad (19)$$

Similarly, two sets of normalizable breakage functions were considered based on the two modes of breakage, namely contact (nipping) and compression. To simplify the model however, they assumed that the values for both breakage functions are the same. The experimental data used for fitting the model were obtained in a 100 mm by 30 mm lab-scale HPGR manufactured by Polysius (Austin et al., 1993). To verify this model, Schneider et al. (2009) used six sets of experimental data that were obtained in a 250 mm in diameter by 100 mm in length lab-scale HPGR equipped with studded rolls, also manufactured by Polysius.

The multi-component model developed by Austin and Trubelja (1994) is primarily empirical and employs a large number of model parameters. It is difficult to regenerate the results by back-calculations unless some constraints are imposed on some of the model parameters. Also, the edge effect that is a characteristic of larger machines is not addressed in this model.

Since the dominant form of breakage in a HPGR unit is particle-bed comminution, feed properties, especially feed size distribution profoundly influences the final product size distribution. Various arrangements of particles in the bed lead to distinctive stressing patterns under the force loading, which accordingly result in different product size distributions. This led Liu and Schönert (1996) to pursue the application of the well-developed population balance models for predicting the product size distribution in a confined particle bed as a function of energy input. They introduced an energy split function in order to determine the energy absorption for each size fraction via an iterative algorithm:

$$k_j = \frac{E_j}{E}, \quad \sum_{j=1}^n k_j M_i(E) = 1 \quad (20)$$

Assuming that breakage and selection functions are characteristic features of material, these two parameters were quantified via controlled tests with mono-sized particles in a piston-die apparatus. Liu and Schönert (1996) tests were focused on brittle material such as quartz. They showed that the influence of the energy input increases as the distribution of particle sizes widens. However, due to the complex iterative nature of the method, Liu and Schönert (1996) did not recommend it for a wide feed size distribution since the errors between the measured and the fitted values would inherently increase.

Klymowsky and Liu (1997) further developed Liu and Schönert's model to simulate the entire spectrum of product size distribution for an industrial HPGR unit. As explained earlier, the final HPGR product is a combined

result of three grinding actions that take place as material passes through the two rolls. Those include pre-crushing, compression, and edge effect. Correspondingly, Klymowsky and Liu (1997) multi-component HPGR model consisted of three steps for quantifying the product size distribution: (1) predicting the resulting particle size distribution in the pre-crushing zone through sequential breakage similar to Austin and Trubelja (1994) method; (2) predicting the resulting particle size distribution in the center using the population balance model similar to Liu and Schönert (1996) model; (3) defining the theoretical particle size distribution for the edge product and solving the energy consumption balance between all three breakage zones based on the fact that a pressure gradient exists between the two rolls.

Klymowsky and Liu (1997) created a large experimental dataset based on a 900 mm diameter by 250 mm pilot-scale HPGR. They set the selection and breakage functions and the energy split function according to the results that Liu and Schönert (1996) had obtained in their ideal particle-bed tests on quartz. Nonetheless, around 10 remaining model parameters still needed fitting via back-calculation. Therefore, to avoid large variations, Klymowsky and Liu (1997) proposed splitting the model parameters into secondary and primary sets. They suggested that secondary parameters should be determined through a few fundamental tests such as running controlled experiments with narrow-sized feed. Then the value for each secondary parameter would be fixed by averaging it over the range obtained in each experimental dataset. Following this, primary parameters could be further refined through a new set of data and an averaging technique would be used to fix a value for each primary model parameter. They showed that simulation results based on this technique were promising. This model was further evaluated by Van der Meer (2010).

Similarly, Morrell et al. (1997b) adopted a modular structure to predict throughput, power, and product size distribution. The product size distributions for three defined breakage zones within a HPGR are independently calculated and combined at the end to produce the final results. To do so, Morrell et al. (1997b) individually applied a modified version of the Whiten-Awachi-Anderson crusher model (Anderson, 1988) for each grinding zone. The Whiten-Awachi-Anderson crusher model features a classification function that defines the probability that particles would break in a crusher based on the preset gap openings given as:

$$C(x) = 1 - \left(\frac{K_2 - x}{K_2 - K_1} \right)^{K_3} \quad (21)$$

Crushers operate in a stepwise action and, therefore, particles bigger than the gap openings (K_2 and K_1 in Eqn. 21) would break repeatedly until become small enough to

pass through the gap without further size reduction. This is similar to the breakage action in the pre-crushing zone, where large particles break sequentially in order to be smaller than the critical gap to enter the grinding zone (Morrell et al., 1997b; Daniel and Morrell, 2004). Morrell et al. (1997a) defined the critical gap based on the geometry of the grinding zones as follows:

$$x_c = 0.5 \left\{ (D + x_g) - \left[(D + x_g)^2 - \frac{4\delta_g D x_g}{\delta_F} \right]^{0.5} \right\} \quad (22)$$

Inside the compression zone, Morrell et al. (1997b) considered two sub breakage mechanism namely edge-effect and compression. While in reality all particles inside the compression zone go under compression to some extent, with the highest force exerted on particles in the center of the gap, in their model, Morrell et al. (1997b) assumed that resulting particles from edge-effect go under single-particle breakage similar to what was assumed for the pre-crushing zone. In order to determine the fraction of particles that undergo the edge effect, Morrell et al. (1997a) defined a split function as follows:

$$f = \gamma \frac{x_g}{L} \quad (23)$$

The classification function used in Whiten-Awachi-Anderson crusher model employs three parameters and with the addition of the fourth parameter, t_{10} , a total of 12 parameters need to be fitted to experimental data to produce the final product size distribution. As shown by Fuerstenau and Kapur (1995), the HPGR product size distribution follows a master curve, which makes it logical to use t_{10} as a breakage characteristic parameter. The value of t_{10} varies with the energy input. However, as mentioned earlier, the energy input and grinding force as the dominant factor for controlling the product fineness, forms a linear relationship for only a limited range.

A large number of the parameters are given fixed values to simplify the approach. However, the remaining critical parameters are determined via conducting breakage characteristics tests such as drop-weight test in addition to HPGR tests. The application of breakage characteristics tests could be referred as an important feature for the Morrell-Tondo-Shi model. Among the parameters, K_2 takes the value of critical gap for the pre-crushing zone and the value of working gap for the portion of material going through the edge-effect zone. In other words, K_2 is the controlling factor for the top size of the product. Meanwhile, the value of K_3 , which is an ore characteristic, is only determined for the compression zone and along with t_{10} has to be fitted to experimental data obtained from HPGR tests. The iterative back-calculation continues until the difference between the simulated and measured energy input reaches a minimum.

Morrell-Tondo-Shi model has been further reviewed by

Daniel (2002) and Benzer et al. (2001) by vast data from various sizes of HPGR machines, putting it in a unique position compared to the rest of the work done so far. Nevertheless, it does not fully include the fundamental breakage mechanism that takes place in the compression zone with respect to all parameters contributing to the final product size distribution.

Torres and Casali (2009) developed a modular structure on the basis of Morrell-Tondo-Shi model to simulate throughput, power, and product size distribution from pilot-scale HPGR tests. Their model for predicting product size distribution shares a similar structure with Morrell-Tondo-Shi model, but with a different approach as it features a discretized system for the particle bed. With this approach, the gap between the two rolls is divided into N blocks. These blocks start from the critical gap and end at the working gap.

To predict the product size distribution, Torres and Casali (2009) benefited from the population balance modeling technique. They assumed that all particles larger than the critical gap would instantaneously break and enter the compression zone along with the rest of the particles that are already small enough to form the feed for the compression zone. The final product size distribution is the combined particle size distributions from each block. The resultant particle size distribution is not only a function of the feed particle size, but also depends upon the position of the particles inside each block in addition to the position of the corresponding block along the gap. Therefore, the population balance model was modified accordingly (Torres and Casali, 2009):

$$u_z \frac{dM_{i,k}(z)}{dz} = -S_{i,k}M_{i,k}(z) + \sum_{j=1}^{i-1} b_{i,j}S_{j,k}M_{j,k}(z) \quad (24)$$

Eqn. 24 results in $N \times n$ matrix of ordinary differential equations with N and n being the total number of blocks and particle size classes, respectively. Torres and Casali (2009) suggested an analytical solution for Eqn. 24 as follows:

$$p_{i,k} = \sum_{j=1}^i A_{ij,k} \exp\left(-\frac{S_{j,k}}{u_z} z\right) \quad (25)$$

where

$$A_{ij,k} = \begin{cases} 0 & i < j \\ \sum_{l=j}^{i-1} \frac{b_{i,l}S_{l,k}}{S_{i,k} - S_{j,k}} A_{il,k} & i > j \\ f_i^{\text{IP}} - \sum_{l=1}^{i-1} A_{il,k} & i = j \end{cases} \quad (26)$$

It was assumed that the breakage function is the same for each particular ore independent of the position inside the compression zone. The breakage function needed to be calibrated with the experimental data. Using the func-

tional format of selection function, three additional parameters including the specific breakage rate, S_i^E , required fitting to experimental data.

Unlike Morrell-Tondo-Shi model, Torres and Casali (2009) considered that compression takes place along the roll width even though the intensity follows a parabola pattern resulting in coarser product towards the ends. However, their model does not offer a way to quantify the fraction of edge product that does not undergo true inter-particle breakage as opposed to those particles passing through the center of the compression zone.

In a simplified approach to apply the population balance model to HPGR grinding, Dundar et al. (2013) assumed that the dominant grinding mechanism in HPGR is true compression bed. Dundar et al. (2013) determined the breakage function through running tests in a piston-die setup using a narrow-size feed. The breakage function parameters were estimated using the Narayanan (1986) single-particle impact breakage model. With the breakage function being considered as the characteristics of materials and constant for each ore type, the selection function was estimated for the total HPGR discharge product via back-calculation. Therefore, the selection function was fitted to experimental HPGR data using Austin et al. (1976) power equation. In contrast to previous models, Dundar et al. (2013) model simplifies the grinding action in HPGRs to only true particle-bed breakage. Although this model does not consider individual grinding actions in industrial HPGRs, the published results are quite promising for further evaluation.

In another effort to simplify the population balance model for compression grinding, Esnault et al. (2015) defined the breakage mechanism of the particle-bed compression as a function of porosity. Porosity in the particle-bed changes with the applied energy. Esnault et al. (2015) assumed that breakage via compression can be defined by the generation of new surface area referring to Rittinger's law:

$$SS(F_{n+1}(x)) - SS(F_n(x)) = \frac{dSS(F(x))}{dE} \frac{dE}{d\theta} (\theta_{n+1} - \theta_n) \quad (27)$$

Esnault et al. (2015) emphasized that the tests for determining the breakage function values need to be performed under low pressure to minimise the occurrence of re-breakage. Esnault et al. (2015) results were based on the fine brittle material, which fits with the applicable range of particle sizes that is suggested for the Rittinger's law. Esnault et al. (2015) noted the increased error for those tests under very high pressure and referred that to the effect of particle cushioning. Even though, grinding in HPGR units is more complicated than piston-die apparatus, Esnault et al. (2015) model provided a great under-

standing for measuring the breakage in particles bed related with porosity.

Looking at overall particle size simulation modeling works (Summarized in **Table 1**); the focus has been mainly on adapting the population balance model that has been well-developed for ball mills to the breakage behavior in HPGR. This approach has had limitations with the fact that particle-bed breakage rate does not necessarily increases with the energy input beyond the saturation point. Results published so far indicate that the ideal controlled way to determine the selection and breakage function for particle-bed breakage is through the use of piston-die apparatus. The major difficulty in such modeling is to include edge effect.

5. HPGR characteristics tests

As discussed earlier, the scale-up studies are mostly based on HPGR testing in pilot-scale machines with at least a minimum of 500 to 700 mm roll diameter. The particle-bed breakage is very sensitive to the feed properties and a real test in a HPGR machine would provide the most realistic results about the response of high compression on any specific material. However, HPGRs are known for their high capacity making it difficult to conduct feasibility studies, requiring large mass of ore material. Even the smallest lab-scale HPGR requires at least 20 to 25 kg material to maintain a long enough feed stream to log data under steady-state operation.

A considerable amount of research has been put into investigating the possibility of running small-scale batch tests as an indication for the amenability of HPGR. Piston-die apparatus represents the batch mode of inter-particle breakage. Besides, it requires a small mass of sample, allows controlled compression, and applies compression at a desired rate. These advantages made the piston-die a standard tool for measuring the breakage rates and the breakage distribution functions in many of the modeling works.

De and Fuerstenau (2012) showed that the rotation angle is the key parameter to define the grinding zone, where the compression happens. They derived an equation to determine this angle based on the load-displacement profile in a piston-die test provided that the nip angle is known (De, 1995):

$$\alpha = \cos^{-1} \left\{ 1 - \frac{h - h_f}{h_0 - h_f} (1 - \cos \alpha_i) \right\} \quad (28)$$

Knowing the angle of rotation, De and Fuerstenau (2012) related the pressure profile in a HPGR to the piston-die test data, and subsequently predicted the scale-up factors of HPGRs including force, torque, working gap, throughput, and the specific energy input. They

also demonstrated that the normalized particle size distributions obtained from a lab-scale HPGR unit and piston-die setup are matching if the specific energy input is kept constant.

Daniel (2003) also presented interesting findings to relate the piston-die operating parameters to lab-scale HPGR operation including the critical gap, working gap, and the grinding force. He showed that the product size distribution in both machines for the same feed size distribution and the same material were matching under the specific energy input range of 2.5–3.5 kWh/t. Similar results have been reported by Kalala et al. (2011). In a novel approach, Rashidi (2014) defined a new series of controlled tests to estimate the selection and breakage functions via running tests in a lab-scale HPGR.

The most practical meaning for a characteristic test would be the formulation of a work index. A value that can show the performance of the HPGR unit to a specific ore regardless of any parameter involved such as feed size distribution and so on. Bond work index is the world-wide known factor that with all the limitations serves as a well-established technique to evaluate the response of tumbling mills to grinding a specific ore. However, this index itself is not directly applicable to HPGR grinding technology. Morrell (2004) formulated a general work index formula that could be applied to numerous grinding equipment including HPGR:

$$W_h = KM_{ih} 4 \left(x_2^{f(x_2)} - x_1^{f(x_1)} \right) \quad (29)$$

Where M_{ih} is a breakage related index (HPGR work index) that is obtained through a specialized test known as SMC Test[®]. However, it is not clear how this parameter is defined and how it is related to the strength of the particles. K is a constant that takes two different values depending on the mode of operation ($K = 1$ for a HPGR in closed circuit with a screen and $K = 1.19$ for an open circuit HPGR). Morrell (2006) showed that the exponent $f(x)$ in Eqn. 29 takes different values depending on the particle size as follows:

$$f(x_i) = - \left(0.295 + \frac{x_i}{1000000} \right) \quad (30)$$

Data that Morrell (2006) used for the verification of this model were obtained through a lab-scale HPGR under the limited range of 2.5–3.5 kWh/t specific energy input. Later, Morrell (2010) introduced a new parameter, S_h , the material strength parameter, in Eqn. 29, in case feed particle size was greater than 25 mm relating to the fact that the particle strength changes with the size:

$$W_h = S_h KM_{ih} 4 \left(x_2^{f(x_2)} - x_1^{f(x_1)} \right) \quad (31)$$

with

Table 1 Summary of HPGR particle size simulation modeling works.

Model structure	Salient features	Areas for improvement	Reference
<ul style="list-style-type: none"> *Modifying ball mill grinding kinetics equation in terms of energy input. *Introducing an energy dissipation component to normalize the specific selection function. 	<ul style="list-style-type: none"> *Important observation that selection function is constant for all particle sizes. *Fully representing the similarities between ball mill and HPGR products. 	<ul style="list-style-type: none"> *Depends on the feed material properties. *Does not address the variation of particle size in different HPGR sizes. *Applicable to low energy input levels. 	Fuerstenau et al., 1991; Fuerstenau et al., 1993
<ul style="list-style-type: none"> *Modifying roll crusher model individually for two dominant breakage mechanisms in HPGRs: Contact and particle-bed. *The final product is a combination of broken and unbroken particles under two separate breakage mechanisms. 	<ul style="list-style-type: none"> *Model accounts for the fact that not all particles break as a result of the bed compression. *It adopts roll crusher model that represents the crushing mode in the acceleration zone. 	<ul style="list-style-type: none"> *Empirical only. *Depends on the feed material properties. *Does not account for the edge-effect (partial compression). 	Austin et al., 1993; Austin and Trubelja, 1994
<ul style="list-style-type: none"> *Providing two mass and energy balance equation to account for the effect of energy adsorption in different size classes. *Selection and function are defined by controlled tests in a piston-die apparatus using mono-sized particles. 	<ul style="list-style-type: none"> *First application of the PBM model for HPGR grinding. *Using controlled confined particle-bed breakage tests to quantify breakage characteristics. 	<ul style="list-style-type: none"> *Not suitable for wide feed size distributions. *Does not consider the pre-crusher and the edge-effect zones. 	Liu and Schönert, 1996
<ul style="list-style-type: none"> *A modular model that introduces an energy distribution function. *HPGR tests are combined with piston-die tests to simulate the product size distributions. 	<ul style="list-style-type: none"> *Accounting for three grinding actions that take place in an industrial HPGR. *Defining the grinding parameters through basic grinding tests. 	<ul style="list-style-type: none"> *Incorporating large number of model parameters. 	Klymowsky and Liu, 1997
<ul style="list-style-type: none"> *A modular model considering three grinding zones in an HPGR. *Adopting cone crusher model individually for each grinding zone. *Applying drop-weight test along with HPGR tests to fit the model. 	<ul style="list-style-type: none"> *Reconciling results from drop-weight test (breakage characteristic test) with the HPGR model. *Widely evaluated in industrial applications based on published material. 	<ul style="list-style-type: none"> *Large number of model parameters. *Does not consider the partial compression in the edge effect zone. *Limited to low energy input levels. 	Morrell et al., 1997a; Daniel and Morrell, 2004
<ul style="list-style-type: none"> *A modular discretized PBM model based on Morrell-Tondo-Shi model. 	<ul style="list-style-type: none"> *Embodied in the model the pressure gradient that exists in the compression zone. 	<ul style="list-style-type: none"> *Depends on the feed material properties. 	Torres and Casali, 2009
<ul style="list-style-type: none"> *Application of population balance model. *Measuring the breakage function via the piston-die test. *Smoothing out selection function based on material and operating conditions. 	<ul style="list-style-type: none"> *Quantifying selection function in accordance with the operating conditions and material properties. 	<ul style="list-style-type: none"> *Does not fully cover the multiple breakage actions in industrial and semi-industrial HPGRs. 	Dundar et al., 2013
<ul style="list-style-type: none"> *Modifying population balance model for the compression-bed breakage based on the creation of new surface area. 	<ul style="list-style-type: none"> *Application of Rittinger's law to define the particle-bed breakage under the compressive load. 	<ul style="list-style-type: none"> *Applicable to low energy input due to the particle cushioning under higher pressure. 	Ensault et al., 2015

$$S_h = 35(x_1 x_2)^{-0.2} \quad (32)$$

Morrell work index is limited to the higher end of specific energy input range, under which there is a linear relationship between energy input and size reduction. This model being empirical keeps evolving.

6. Summary

The modeling of HPGR via the principles of selection and breakage function modeling concept has been partly successful. Many published works show internal consistency with the data generated in their works. However, the difficulty arises when scaling up the lab-model parameters to large machines. The principal difficulty has been the postulation of two different grinding zones in the radial direction and two different zones in the axial direction of the roll. Moreover, an experimental procedure for determining breakage functions independently is lacking. Hence, estimation of numerous parameters befuddles the modeling effort. Next, the models based on a work-index like structure, will have to depend on a single size to represent the entire size distribution. Therefore, more empirical coefficients are introduced in such models. Nevertheless, all the models have explained the internal dynamics of the high compression bed loading and the effect of machine parameters on loading. As of this date, the modeling effort continues to advance.

Nomenclature

a_i	Nipping selection function (Austin model)
a'_i	Compression selection function (Austin model)
$b_{i,j}$	Breakage function
c_F	Material constant
$C(x)$	Classification function
D	Roll diameter [m]
E	Energy input [kWh]
E_j	Energy absorption in size class j [kWh/t]
E_{sc}	Specific energy input [kWh/t]
f	Split function (Morrell-Tondo-Shi model)
f_i^{lp}	Feed fraction factor going under single-particle breakage (Torres-Casali model)
F	Grinding force [N]
$F(x)$	Particle size distribution
$F(x, E)$	Particle size distribution function as a function of specific energy input
F_{sp}	Specific grinding pressure [N/mm ²]

F_{max}	Maximum specific grinding pressure [N/mm ²]
$F(x_i)$	Exponent for Morrell work index formula
h	Particle-bed height at an applied force [mm]
h_0	Initial particle-bed height [mm]
h_f	Final particle-bed height [mm]
j	Particle-bed grindability [t/kWh]
k	Material constant
k_j	Energy split function (Schönert model)
K_1	Whiten-Awachi-Anderson crusher model parameter
K_2	Whiten-Awachi-Anderson crusher model parameter
K_3	Whiten-Awachi-Anderson crusher model parameter
L	Roll length [m]
M	Mass flowrate [t/h]
\dot{m}_c	Specific throughput based on cake characteristic [ts/m ³ h]
\dot{m}_f	Specific throughput based on flowrate [ts/m ³ h]
M_{ih}	Morrell HPGR work index
$M_i(E)$	Mass fraction of particles in size class i per unit of Energy input
$M_{i,k}(z)$	Mass fraction of particles in size class i based on its vertical position (z) in block k
P	Power [kW]
P_i	Mass fraction of particles left unbroken at size i
P_i^*	Mass fraction of particles that enter size i
$p_{i,k}$	Mass fraction of particles entering size i in block k
$SS(x)$	Specific surface function
S_i^E	The energy-normalized selection function at size i
S_i	Selection function at size i
T	Torque [Nm]
u	Roll peripheral speed [m/s]
u_m	Material peripheral velocity in the gap [m/s]
u_r	Roll rotational speed [rpm]
u_z	Material peripheral velocity in the z direction [m/s]
V	Volumetric flowrate [m ³ /h]
V_p	Potential volumetric flowrate [m ³ /h]
W_h	Morrell work index
x	Particle size
x_c	Critical gap at the nip angle [mm]
x_g	Working gap [mm]
X_f	Median size in the feed [μm]
X_{50}	Median size in the product [μm]
x_2	80 percent passing size for product [μm]

x_1	80 percent passing size for feed [μm]
y	Energy dissipation exponent
z	Particle position inside gap (Torres-Casali model)
\bar{Z}	Self-similar distribution function
α	Angle of rotation
α_i	Nip angle
β	Force-acting angle
γ	Split factor (Morrell-Tondo-Shi model)
δ_g	Gap (cake) density [t/m^3]
δ_F	Feed bulk density [t/m^3]
θ	Porosity
θ_g	Gap (cake) porosity
ρ	Material density [t/m^3]
ω	Roll radial velocity [$1/\text{s}$]

References

- Abouzeid A.-Z.M., Fuerstenau D.W., Grinding of Mineral Mixtures in High-Pressure Grinding Rolls, *International Journal of Mineral Processing*, 93 (2009) 59–65.
- Anderson J.S., Napier-Munn, T.J., Power Prediction for Cone Crushers, in: *Third Mill Operators Conference*, AusIMM, Cobar, 1988.
- Austin L.G., Shoji K., Bhatia V.K., Savae K., Klimperl, R., Some Results on the Description of Size Reduction as a Rate Process in Various Mills, *Industrial & Engineering Chemistry Process Design and Development*, 15 (1976) 187–196.
- Austin L.G., Van Orden D.R., Perez J.W., A Preliminary Analysis of Smooth Roll Crushers, *International Journal of Mineral Processing*, 6 (1980) 321–336.
- Austin L.G., Weller R., Lim I.L., Phenomenological Modelling of the High Pressure Grinding Rolls, in: *XVIII International Mineral Processing Congress*, Sydney, 1993, pp. 87–96.
- Austin L.G., Trubelja M.P., The Capacity and Product Size Distribution of High Pressure Grinding Rolls, in: *IV Meeting of the Southern Hemisphere on Mineral Technology*, Concepcion, Chile, 1994, pp. 4–67.
- Austin L.G., Trubeljal M.P., Seebach H.M. Von, Capacity of High-Pressure Grinding Rolls, *Minerals and Metallurgical Processing*, 1995, pp. 65–73.
- Barrios G.K.P., Pérez-prim J., Tavares L.M., A DEM Model of HPGR Operation Using Bed Compression Models Calibrated with a Piston Die Test, in: *9th International Comminution Symposium*, 2014.
- Battersby M.J.G., Kellerwessel H., Oberheuser G., Important Advances in the Development of High Pressure Rolls Comminution for the Minerals Industry, in: *Extractive Metallurgy of Gold and Base Metals*, Kalgoorlie, 1992, pp. 26–28.
- Benzer H., Ergun L., Lynch A.J., Oner M., Gunlu A., Celik I.B., Aydogan N., Modelling Cement Grinding Circuits, *Minerals Engineering*, 14 (2001) 1469–1482.
- Burchardt E., Patzelt N., Knecht J., Klymowsky R., HPGR's in Minerals: What do Existing Operations Tell us for the Future?, in: *Autogenous and Semi-autogenous Grinding Technology Conference*, Vancouver, 2011.
- Daniel M.J., HPGR Model Verification and Scale-up, University of Queensland, 2002.
- Daniel M.J., Particle Bed Compression Comminution using a Piston-die to Predict the Performance of a HPGR, in: *JKMRC Conference*, Brisbane, 2003, pp. 67–83.
- Daniel M.J., Morrell S., HPGR Model Verification and Scale-up, *Minerals Engineering*, 17 (2004) 1149–1161.
- De A.K., Modeling and Optimization of Fine Grinding of Minerals in High-Pressure Roll Mill-Ball Mill Hybrid Comminution Circuits, University of California, Berkeley, 1995.
- De A., Fuerstenau D.W., Simulation of Macroscopic Variables Related to Comminution in High-Pressure Grinding Rolls, in: *XXVI International Mineral Processing Congress (IMPC)*, New Delhi, 2012, pp. 1075–1090.
- Dhawan N., Rashidi S., Latchireddi R., Rajamani R.K., Evaluation of Scale up Factors in a Lab Scale High Pressure Grinding Roll, in: *XXVI International Mineral Processing Congress (IMPC)*, New Delhi, 2012, pp. 1171–1188.
- Djordjevic N., Morrison R., Exploratory Modelling of Grinding Pressure within a Compressed Particle Bed, *Minerals Engineering*, 19 (2006) 995–1004.
- Drozdiak J.A., Klein B., Nadolski S., Bamber A., A Pilot-Scale Examination of a High Pressure Grinding Roll/Stirred Mill Comminution Circuit, in: *Autogenous and Semi-autogenous Grinding Technology Conference*, Vancouver, 2011.
- Dundar H., Benzer H., Aydogan N., Application of Population Balance Model to HPGR Crushing, *Minerals Engineering*, 50–51 (2013) 114–120.
- Esnault V.P.B., Zhou H., Heitzmann D., New Population Balance Model for Predicting Particle Size Evolution in Compression Grinding, *Minerals Engineering*, 73 (2015) 7–15.
- Fuerstenau D.W., Shukla A., Kapur P.C., Energy Consumption and Product Size Distributions in Choke-Fed High-Compression Roll Mills, *International Journal of Mineral Processing*, 32 (1991) 59–79.
- Fuerstenau D.W., Kapur P.C., Gutsche O., Comminution of Minerals in a Laboratory-size, Choke-Fed High-pressure Roll Mill, in: *XVIII International Mineral Processing Congress (IMPC)*, Sydney, 1993, pp. 175–180.
- Fuerstenau D.W., Kapur P.C., Newer Energy-Efficient Approach to Particle Production by Comminution, *Powder Technology*, 82 (1995) 51–57.
- Fuerstenau D.W., Gutsche O., Kapur P.C., Confined Particle Bed Comminution under Compressive Loads, *International Journal of Mineral Processing*, 44–45 (1996) 521–537.
- Fuerstenau D.W., Abouzeid A.-Z.M., The Performance of the High Pressure Roll Mill: Effect of Feed Moisture, *Fizykochemiczne Problemy Mineralurgii*, 32 (1998) 227–241.
- Fuerstenau D.W., Abouzeid A.-Z.M., Role of Feed Moisture in High-Pressure Roll Mill Comminution, *International Journal of Mineral Processing*, 82 (2007) 203–210.

- Fuerstenau D.W., Mineral Processing Engineer and Scientist: in Education, Research, Industry, and International Cooperation, in: an Oral History Conducted by Eleanor Swent in 2001, Regional Oral History Office, The Bancroft Library, University of California, Berkeley, 2011, pp. 599–629.
- Gutsche O., Comminution in Roll Mills, University of California, Berkeley, 1993.
- Gutsche O., Fuerstenau D.W., Influence of Particle Size and Shape on the Comminution of Single Particles in a Rigidly Mounted Roll Mill, *Powder Technology*, 143–144 (2004) 186–195.
- Kalala J.T., Dong H., Hinde A.L., Using Piston-Die Press to Predict the Breakage Behaviour of HPGR, in: Autogenous and Semi-autogenous Grinding Technology Conference, Vancouver, 2011.
- Klymowsky I.B., Liu J., Modelling of the Comminution in a Roller Press, in: XX International Mineral Processing Congress (IMPC), Aachen, 1997a, pp. 141–154.
- Klymowsky I.B., Liu J., Towards the Development of a Work Index for the Roller Press, in: Kawatra (Ed.), SME Comminution Practices Symposium, 1997b, pp. 99–105.
- Klymowsky R., Patzelt N., Knechtz J., Burchardt E., Selection and Sizing of High Pressure Grinding Rolls, in: A.L. Mular, D.N. Halbe, and D.J. Barratt (Eds.), *Mineral Processing Plant Design, Practice, and Control Proceedings*, 2002, pp. 636–668.
- Klymowsky R., HPGR-Accepted Technology in Mining, in: Mining Magazine Congress, Niagara-on-the-Lake, Canada, 2009.
- Lim W.I.L., Morrell S., Tondo L., David D., Modelling the High Pressure Grinding Rolls, in: Mining Technology Conference, Fremantle, (1996a) 169–176.
- Lim W.I.L., Voigt W., Weller K.R., Product Size Distribution and Energy Expenditure in Grinding Minerals and Ores in High Pressure Rolls, *International Journal of Mineral Processing*, 95 (1996b) 539–559.
- Lim W.I.L., Weller K.R., Some Benefits of Using Studded Surfaces in High Pressure Grinding Rolls, *Minerals Engineering*, 12 (1999) 187–203.
- Liu J., Schönert K., Modelling of Interparticle Breakage, *International Journal of Mineral Processing*, 44–45 (1996) 101–115.
- Lubjuhn U., Schönert K., Material Flow in the Acceleration Zone and Throughput of High Pressure Roller Mills, in: XVIII International Mineral Processing Congress (IMPC), Sydney, 1993, pp. 161–168.
- Mcken A., Williams S., An Overview of the Small-Scale Tests Available to Characterise Ore Grindability, in: Autogenous and Semi-autogenous Grinding Technology Conference, Vancouver, 2006.
- Morrell S., Lim W., Shi F., Tondo L., Modelling of the HPGR Crusher, in: Kawatra (Ed.), *Comminution Practices*, 1997a, pp. 117–126.
- Morrell S., Shi F., Tondo L., Modelling and Scale-up of High Pressure Grinding Rolls, in: XX International Mineral Processing Congress (IMPC), Aachen, 1997b, pp. 129–140.
- Morrell S., An Alternative Energy–Size Relationship to that Proposed by Bond for the Design and Optimisation of Grinding Circuits, *International Journal of Mineral Processing*, 74 (2004) 133–141.
- Morrell S., Rock Characterisation for High Pressure Grinding Rolls Circuit Design, in: Autogenous and Semi-autogenous Grinding Technology Conference, Vancouver, 2006.
- Morrell S., Predicting the Specific Energy Required for Size Reduction of Relatively Coarse Feeds in Conventional Crushers and High Pressure Grinding Rolls, *Minerals Engineering*, 23 (2010) 151–153.
- Nadolski S., Bamber A.S., Klein S., Drozdak J., Investigation into Laboratory Scale Tests for the Sizing of High Pressure Grinding Roll, in: Autogenous and Semi-autogenous Grinding Technology Conference, Vancouver, 2011.
- Narayanan S., Single Particle Breakage Tests: A Review of Principles and Applications to Comminution Modelling, *Bull. Proc. Australas. Inst. Min. Metall.*, 291 (1986) 49–58.
- Norgate T.E., Weller K.R., Options for Incorporating High-Pressure Grinding Rolls into Comminution Circuits, in: Fourth Mill Operators' Conference, Burnie, 1991, pp. 19–24.
- Otte O., Polycom High Pressure Grinding Principles and Industrial Application, in: Third Mill Operators' Conference, Cobar, 1988, pp. 131–135.
- Patzelt N., High-Pressure Grinding Rolls, A Survey of Experience, in: IEEE Conference, Dallas, 1992, pp. 149–181.
- Rashidi S., A Study of Energy-Size Relationship and Wear Rate in a Lab-Scale High Pressure Grinding Rolls Unit, The University of Utah, 2014.
- Reichardt B.Y., Schönert K., Interparticle Breakage of Fine Hard Materials by Single and Multiple Compression, *Chemical Engineering & Technology*, 26 (2003) 191–197.
- Rosario P.P., Hall R.A., Grundy M., Klein B., A Novel AG-crusher-HPGR Circuit for Hard, Weathered Ores Containing Clays, in: Autogenous and Semi-autogenous Grinding Technology Conference, Vancouver, 2011.
- Schewechten D., Mulburn G.H., Experiences in Dry Grinding with High Compression Roller Mills for End Product Quality below 20 Microns, *Minerals Engineering*, 3 (1990) 23–34.
- Schneider C.L., Alves V.K., Austin L.G., Modeling the Contribution of Specific Grinding Pressure for the Calculation of HPGR Product Size Distribution, *Minerals Engineering*, 22 (2009) 642–649.
- Schönert K., Sizing of High Pressure Twin Roll Mills, *Zement Kalk Gips*, 12 (1985) 728–730.
- Schönert K., A First Survey of Grinding with High-Compression Roller Mills, *International Journal of Mineral Processing*, 22 (1988) 401–412.
- Schönert K., Lubjuhn U., Throughput of High Compression Roller Mills with Plane and Corrugated Rollers, in: 7th European Symposium on Comminution, Ljubljana, 1990, pp. 149–158.
- Schönert K., Mueller F., Representation of Breakage Fraction and Breakage Function of Inter-particle Stressing, *Aufbereitungs-Technik*, 31 (1990) 248–256.
- Schönert K., The Characteristics of Comminution with High Pressure Roller Mills, *KONA Powder and Particle Journal*, 9 (1991) 149–158.

Schönert K., The Influence of Particle Bed Configurations and Confinements on Particle Breakage, *International Journal of Mineral Processing*, 44–45 (1996) 1–16.

Torres M., Casali A., A Novel Approach for the Modelling of High-Pressure Grinding Rolls, *Minerals Engineering*, 22 (2009) 1137–1146.

van der Meer F., High Pressure Grinding Rolls Scale-up and Experiences, in: XXV International Mineral Processing Congress (IMPC), Brisbane, 2010, pp. 1319–1331.

van der Meer F.P., Feasibility of Dry High Pressure Grinding and Classification, in: Autogenous and Semi-autogenous Grinding Technology Conference. Vancouver, 2011.

Author's short biography



Samira Rashidi

Samira Rashidi received her Ph.D. from the University of Utah in 2014. The principal emphasis of Samira's research has been about improving efficiency of the grinding equipment and circuits via mathematical modeling and simulation. Her Ph.D. research was focused primarily on energy-size relationship and wear-rate measurement in HPGRs under the supervision of Prof. Raj Rajamani. Samira currently is a Process Engineer at thyssenkrupp Industrial Solutions (USA). She is involved in all processing aspects of new and existing grinding systems in the mining, minerals, and cement applications.



Raj K. Rajamani

Raj Rajamani has been on the faculty of the Metallurgical Engineering department of the University of Utah, Salt Lake City, Utah, USA since 1980. Currently he holds the position of professor. His research interest include population balance modeling of tumbling mills, computational fluid dynamics of hydrocyclones, discrete element modeling of semi-autogenous grinding mills, eddy current sorting of metallic particles and modeling of high pressure grinding rolls. He received the Antoine M. Gaudin Award, presented by the Society of Mining, Metallurgy and Exploration Engineers Inc. in the year 2009.



Douglas W. Fuerstenau

After receiving his Sc.D. degree at MIT, Dr. Fuerstenau spent a six-year period teaching at MIT and working in industry, after which time he joined the faculty of the University of California. At Berkeley he established an extensive program of teaching and research in minerals processing, applied surface chemistry and particle technology. With his graduate students and postdoctoral researchers, he has published a wide range of seminal papers in this field. He currently is P. Malozemoff Professor Emeritus of Mineral Engineering in the University of California.

Liquid Flame Spray—A Hydrogen-Oxygen Flame Based Method for Nanoparticle Synthesis and Functional Nanocoatings[†]

Jyrki M. Mäkelä*, Janne Haapanen, Juha Harra, Paxton Juuti and Sonja Kujanpää

[†] *Aerosol Physics Laboratory, Department of Physics, Tampere University of Technology, Finland*

Abstract

In this review article, a specific flame spray pyrolysis method, Liquid Flame Spray (LFS), is introduced to produce nanoparticles using a coflow type hydrogen-oxygen flame utilizing pneumatically sprayed liquid precursor. This method has been widely used in several applications due to its characteristic features, from producing nanopowders and nanostructured functional coatings to colouring of art glass and generating test aerosols. These special characteristics will be described via the example applications where the LFS has been applied in the past 20 years.

Keywords: nanopowder, nanoparticle, functional coatings, flame spray pyrolysis, aerosol

1. Introduction

Nanoparticle powder materials are widely used in the modern industry, they have a variety of technological applications, they are commercially available but frequently custom made for each application using various fabrication methods (Kruis et al., 1998). Thermal gas phase synthesis and particularly aerosol techniques, offer ways to generate nanoparticles via dry industrial processes (Ulrich, 1971; Kruis et al., 1998). Especially flame methods are considered to be optimal for up-scaling (Kammler et al., 2001a; Stark and Pratsinis, 2002; Mueller et al., 2003). Thorough reviews on the flame spray pyrolysis (FSP) techniques for producing nanopowder have been made previously (Pratsinis, 1998; Mädler, 2004; Teoh et al., 2010). The FSP method generates well-defined nanoparticulate material which can be collected as a powder from the exhaust aerosol of the flame (Stepuk et al., 2013; Park and Park, 2015) or sprayed on a surface (Mishra et al., 2014). Apart from nanopowder production, recently the FSP and related techniques have also been used fairly efficiently in various types of coating applications (Mädler et al., 2006a; Tricoli et al., 2008; Pimenoff et al., 2009). With moderately high production rate (ca. g/min), the method is also applicable for covering large surface areas

with thin nanoparticle coating. One of the most recent applications is coating of a heat-sensitive flexible roll-to-roll material, such as paper or paper board, by a direct deposition of flame-generated nanoparticles in order to e.g. adjust the wetting properties of the substrate (Mäkelä et al., 2011; Haapanen et al., 2015).

In this review article, we introduce a distinct FSP technique, Liquid Flame Spray (LFS), which is based on a coflow type hydrogen-oxygen flame. It utilizes pneumatic spraying of a liquid precursor in the burner. Most often hydrogen is used as the atomizing gas, which having a high speed leads to a highly turbulent flame. The turbulent flame in the LFS is steady and robust, it does not require additional side flamelets and, due to the hydrogen, the precursor liquid itself does not need to be a fuel. The LFS has been widely used in several applications due to its characteristic features. Additionally to powder generation and coating applications, the LFS is also feasible as a test aerosol generator, since the utilization of hydrogen as the fuel, the exhaust gas does not contain excessive amounts of carbon containing components. In this review article, these special characteristics will be described via the example applications in which the LFS has been applied in the past 20 years.

2. Method description

Flame spray pyrolysis (FSP), or liquid feed flame spray pyrolysis, is usually defined as a method consisting of a spray of micron-sized liquid precursor droplets and a

[†] Received 23 May 2016; Accepted 18 August 2016

¹ P.O.Box 692, FI-33101 Tampere, Finland

* Corresponding author: Jyrki M. Mäkelä;
E-mail: jyrki.makela@tut.fi
TEL: +358-40-198-1018

flame reactor where the liquid precursor is assumed to evaporate, react and nucleate into nanoparticulate form, as described by e.g. Ulrich (1984), Pratsinis (1998) and Teoh et al. (2010). The history of the FSP has recently been described on a more general level by e.g. Purwanto et al. (2011) and Trommer and Bergmann (2015). The several alternative reaction schemes and particle formation mechanisms occurring in the FSP reactor when fabricating, e.g., metal oxide powder, has been discussed on a general level by Mädler (2004).

We define Liquid Flame Spray (LFS) as one certain type of flame spray pyrolysis, where the combustion gas and oxidizing gas are hydrogen and oxygen, respectively. It is specific, that the combustion gas is also acting as an atomizing gas and no other gaseous components are necessarily needed in the process. It is notable that hydrogen driven flames have also been widely used and studied elsewhere, and utilized by e.g. Sokolowski et al. (1977), Chung and Katz (1985), Cho and Choi (2000), Lee and Choi (2000), and Katusic and Krauss (2011).

The term ‘Liquid Flame Spray’ was originally used by Tikkanen et al. (1994), Tikkanen et al. (1997) and Gross et al. (1999) in connection with an application where art glass was coloured by nanoparticles deposited from the flame onto the surface of a molten glass item. In this article, we have maintained this definition that LFS consists of a liquid precursor atomization by one of the combustion gases, favourably H_2 . This is not an unambiguous definition but it clarifies the division within the family of several flame spray pyrolysis modifications in literature, also described by e.g. Trommer and Bergmann (2015). With this in mind, we have collected **Table 1** to list up papers dealing with LFS, or a very similar technique.

The basic characteristics of the LFS process have been presented by Tikkanen et al. (1997) and Aromaa et al. (2007), and the process fundamentals have been further discussed by Pitkänen et al. (2005), Keskinen et al. (2007a) and Keskinen et al. (2008). A schematic of the LFS-burner is presented in **Fig. 1**.

In the burner nozzle, the speed of the hydrogen flow, as an atomizing gas, is close to the speed of sound. This is advantageous for the atomizing process, as it assists in maximizing the kinetic energy input into the atomizer, where generally small precursor droplets are assumed to be favourable to facilitate evaporation from the droplets. Keskinen et al. (2008) have measured the droplet size distribution of the LFS atomizer with a conclusion that by number, the majority of the generated droplets are in the submicron size range, mass median diameter being at around 3–5 μm .

According to the data by Tikkanen et al. (1997), Pitkänen et al. (2005), Mäkelä et al. (2006) and Keskinen et al. (2007a), the maximum temperature of the LFS flame exceeds 2600 K. A temperature profile obtained with typ-

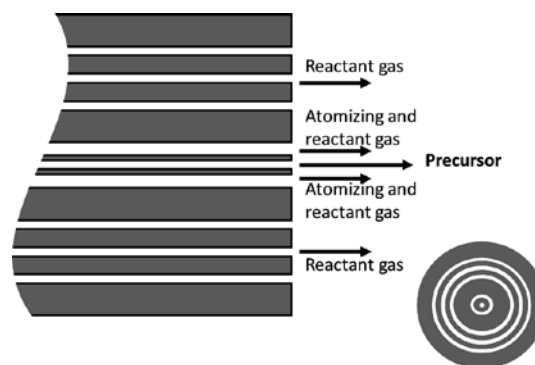


Fig. 1 Liquid Flame Spray burner. Note, that only two of the available coaxial rings for gas flow are necessary for the basic performance of the LFS-method. The rest of the rings may be used to modify the flame or to introduce additional components into the process.

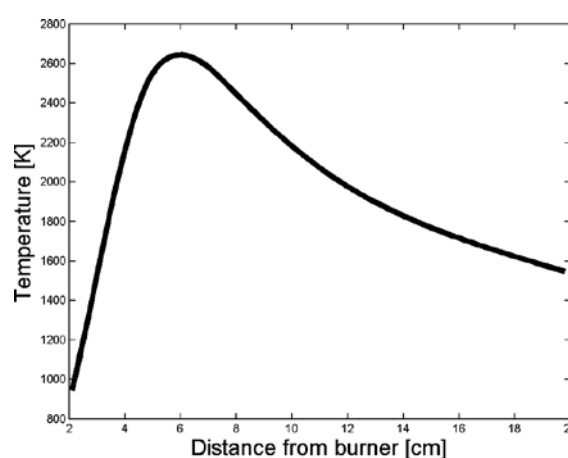


Fig. 2 Temperature in the center axis of a LFS flame with gas volume flow rates of $H_2/O_2 = 20/10$ l/min. According to data from Pitkänen et al. (2005).

ical gas volume flow rates, ($H_2/O_2 = 20/10$ l/min) is presented in **Fig. 2** (Pitkänen et al., 2005). This relatively high temperature level is, again, advantageous to facilitate precursor evaporation and decomposition. Eventually, it is apparent that the variety of feasible precursor liquids that are accessible to the LFS is fairly large.

In most of the studies on the LFS, the ratio of hydrogen and oxygen flow rates has been typically stoichiometric, 2/1, but it can also be easily varied. In the studies by both Cho and Choi (2000) and Lee and Choi (2000) on relatively similar oxy-hydrogen flames, the amount of hydrogen was decreased well below the stoichiometric value. When hydrogen flow rate was varied in the order of 10 % of O_2 , both the flame temperature, increasing with the fraction of H_2 , and the crystal structure of the generated particles were changed. Similar approach with varying H_2/O_2 ratio have been described also by e.g. Kammler et al. (2001b), Hannebauer and Mezel (2003), Dosev et al. (2006), Goldys et al., (2006), Jang et al. (2006), Pikhitsa et al., (2007). Sheen et al. (2009) used an oxy-hydrogen

Table 1 Collection of articles utilizing liquid feed-flame spray pyrolysis combined with H₂/O₂-flame

Reference	Particle compound	Application	Specific
Tikkanen et al., 1997, Surface and Coatings Technol.	Al ₂ O ₃	Process fundamentals	
Pitkänen et al., 2005, IFRF Combustion Journal	SiO ₂	Process fundamentals	
Aromaa et al., 2007, Biomolecular Engineering	TiO ₂	Process fundamentals	
Aromaa et al., 2013, A Nanotechnol Approach, Wiley	Ag, TiO ₂	Process fundamentals	
Cho and Choi, 2000, Journal of Aerosol Science.	SiO ₂	Process fundamentals	SiCl ₄ -precursor
Chung and Katz, 1985, Combustion and Flame	SiO ₂	Process fundamentals	H ₂ /O ₂ /Ar counterflow flame
Harra et al., 2015, Aerosol Science and Technol.	SiO ₂ , TiO ₂	Process fundamentals	Powder form LFS
Harra et al., 2016, AIChE Journal	Al ₂ O ₃	Process fundamentals	Residual particles
Keskinen et al., 2008, Atomization and Sprays	ZrO ₂	Process fundamentals	Spray droplets
Lee and Choi, 2000, Journal of Aerosol Science	SiO ₂	Process fundamentals	SiCl ₄ -precursor
Katusic and Kress 2011, Patent CA2803211 A1.	Ni _x O _y , Mn _x O _y Co _x O _y	Powder generation	
Keskinen et al., 2004, Journal of Materials Res.	Ag, Pd	Powder generation	
Sokolowski et al., 1977, Journal of Aerosol Science	Al ₂ O ₃	Powder and aerosol generation	
Harra et al., 2013, Powder Technology	Fe _x O _y	Powder generation	Photocatalysis
Hartmann et al., 1985, US Patent	TiO ₂ SiO ₂ , Al ₂ O ₃ ,	Powder generation	
Keskinen et al., 2009, Journal of Applied Physics	SnO ₂	Powder generation	Gas sensors
Mäkelä et al., 2004, Journal of Materials Science	Ag, Pd, Fe _x O _y	Powder generation	
Nikkanen et al., 2008, Res. Lett. Nanotechnol	Al ₂ O ₃ , ZrO ₂ , Fe _x O _y	Powder generation	
Nikkanen et al., 2014, Powder Technology	Al ₂ O ₃ , ZrO ₂ , Fe _x O _y	Powder generation	
Dosev et al., 2006, J Aerosol Sci.	Eu:Y ₂ O ₃	Powder generation	Photoluminescence
Goldys et al., 2006, J Am Chem Soc.	Er:Gd ₂ O ₃	Powder generation	Fluorescence
Keskinen et al., 2007b, Catalysis Letters	Pd, Al ₂ O ₃ , La ₂ O ₃	Nanoparticle suspension	Catalysis
Mäkelä et al., 2006, Materials Letters	TiO ₂	Deposit	
Sainiemi et al., 2007, Nanotechnology	SiO ₂	Deposit	Etching mask
Thybo et al., 2004, J Catalysis	Au/TiO ₂	Deposit	Catalysis
Keskinen et al., 2007a, J. of Nanoparticle Research	Ag, TiO ₂	Deposit, Aerosol	Binary particles
Tikkanen et al., 1994, J. of Non-Crystalline Solids	CuO	Class colouring	Coloured glass powder in liquid
Beneq Oy, 2016, Glass Coloration	CoO, Co ₃ O ₄ , CuO, Ag	Glass colouring	
Gross et al., 1999, J of Thermal Spray Technol.	CoO, Co ₃ O ₄ , CuO, Ag	Glass colouring	
Hotoleanu et al., 2002, NOC 2002	SiO ₂ , Al ₂ O ₃ , Er ₂ O ₃	Optical fiber	
Rajala et al., 2003, Rev. Advanced Materials Sci.	La ₂ O ₃ , SiO ₂ , Er ₂ O ₃ , Al ₂ O ₃	Optical fiber	Glass
Tammela et al., 2006, Proceedings of SPIE 6116	SiO ₂ , Al ₂ O ₃ , Er ₂ O ₃	Optical fiber	
Keskinen et al., 2006, Catalysis Letters	Ag, TiO ₂	Functional coating	Anti-bacterial
Ejenstam et al., 2015b, Applied Surface Science	TiO ₂	Functional coating	Corrosion protection
Piispanen et al., 2011, Applied Surface Science	TiO ₂	Functional coating	Glass
Pimenoff et al., 2009, Thin Solid Films	TiO ₂	Functional coating	Glass, Wetting
Stepien et al., 2013b, Wear	TiO ₂	Functional coating	Mechanical
Stepien et al., 2013c, Nanoscale Research Letters	TiO ₂	Functional coating	Mechanical
Valtakari et al., 2016, Nordic Pulp and Paper Res J.	TiO ₂	Functional coating	Microfluidistics on board
Songok et al., 2014, ACS Appl. Mater. and Interfaces	TiO ₂	Functional coating	Microfluidistics on paper
Keskinen et al., 2005, The Electrochemical Society	TiO ₂	Functional coating	Photocatalysis
Valtakari et al., 2013, J Print Media and Technol. Res.	TiO ₂	Functional coating	Printing
Aromaa et al., 2012, J Aerosol Science	TiO ₂	Functional coating	Wetting
Mäkelä et al., 2011, Aerosol Science and Technology	TiO ₂	Functional coating	Wetting
Moghaddam et al., 2015, Holzforschung	TiO ₂	Functional coating	Wetting
Stepien et al., 2011, Applied Surface Science	TiO ₂	Functional coating	Wetting
Stepien et al., 2013a, Langmuir	TiO ₂	Functional coating	Wetting
Teisala et al., 2010, Surface and Coatings Technology	TiO ₂	Functional coating	Wetting
Teisala et al. 2013a, Cellulose	TiO ₂	Functional coating	Wetting
Teisala et al., 2013b, Colloid and Polymer Science	TiO ₂	Functional coating	Wetting
Teisala et al., 2014a, Nordic Pulp and Paper Res J.	SiO ₂ , TiO ₂	Functional coating	Wetting
Teisala et al., 2014b, Cellulose	TiO ₂	Functional coating	Wetting
Tuominen et al., 2014, J. Adhesion Sci. Technol.	SiO ₂	Functional coating	Wetting
Haapanen et al., 2015, Mater. Chem. Physics	SiO ₂ , TiO ₂	Functional coating	Wetting
Teisala et al., 2012, Langmuir	TiO ₂	Functional coating	Wetting fundamentals
Stepien et al., 2012a, Surface and Coatings Technol.	TiO ₂	Functional coating	Wetting; Surface chemistry
Stepien et al., 2012b, Applied Surface Science	SiO ₂ , TiO ₂	Functional coating	Wetting; Surface chemistry

flame to produce coated particles of SnO_2 , SiO_2 and TiO_2 , in binary combinations. Alternatively, if an excess amount of hydrogen will be injected, then the flame will create reducing conditions. In the study by Aromaa et al. (2012), it was found out that an excess amount of hydrogen in the flame may have an effect on the surface chemistry of the generated particles, and the amount of carbon/hydrocarbons on the surface. But in their case the product Ti-compound remained still in the form of TiO_2 . Provided that the hydrogen flow is kept constant, size and temperature of the flame can be affected also by varying the solvent feed rate (Mäkelä et al., 2011), especially for the alcohol based precursors.

The atomization of the liquid precursor usually brings along another issue: the fate of the residue of each precursor droplet sprayed into the flame (Strobel and Pratsinis, 2011; Rosebrock et al., 2013; 2016). If the precursor liquid is sufficiently volatile, the original droplet will evaporate and a reaction in the gas phase will take place producing nanoparticles, as expected. If the precursor liquid is not volatile enough, then a liquid-to-solid reaction will take place in the droplet resulting in the formation of residual particles, as described in Fig. 3.

Depending on the properties of the liquid precursor, e.g. volatility, concentration and temperature of the decomposition, the remaining residual particles may be moderately

large. In the worst case, the residual particle diameter may remain in the order of 100 nm–1 μm . This is not by any means advantageous for the nanopowder production, since the specific surface area of the powder will inevitably be decreased. The importunate problem has recently been solved for the case of conventional methane/oxygen FSP-flame by introducing specific chemical components in the precursor to induce droplet explosion (Strobel and Pratsinis, 2011; Rosebock et al., 2013; Rosebock et al., 2016). In their case, DEGBE (diethylene glycol monobutyl ether) or EHA (2-ethylhexanoic acid) were introduced into the precursor liquid, using concentration levels of 50 % for these chemicals. In the case of our hydrogen driven LFS, it was recently found out that already less than 5 % of EHA in the precursor solution (containing aluminum nitrate) may be sufficient to induce the desired explosion of the precursor droplets, and thereby avoiding residual particle formation (Harra et al., 2016).

3. Applications

3.1 Nanopowder generation

The most widely used application of the FSP is the generation of nanopowders (Ulrich, 1971; Ulrich, 1984). The product material is most often collected by bag filters consisting of e.g. glass fiber material (Kammler et al., 2001a; Stark and Pratsinis, 2002). A commercial process by Degussa/Evonik utilizes a hydrogen-oxygen flame, similarly to the LFS, but typically gaseous precursors, such as SiCl_4 and TiCl_4 (Hartmann et al., 1995). Still, Evonik also uses a liquid fed FSP system, with a preference of hydrogen gas as a fuel, e.g. to produce nanopowders containing lithium compounds (Katusic and Kress, 2011).

The LFS has been used in nanopowder production for e.g. single component (Tikkanen et al., 1997; Mäkelä et al., 2004), binary component (Keskinen et al., 2004; Keskinen et al., 2005) and multicomponent nanopowders (Nikkanen et al., 2008; Nikkanen et al., 2014). In these studies, the particulate matter was collected from the exhaust flow of the flame using an electrostatic precipitator.

Nikkanen et al. (2014) used collected and compacted composite nanopowder made by the LFS to fabricate carbon nanotubes within the porous powder sample. The LFS generated nanopowder has also been used for fabricating magnetic composite nanoparticles in a tube furnace (Harra et al., 2013), in order to produce photocatalytic powder for water purification, and for a study on coating of ceramic nanoparticles with silver in a tube furnace (Harra et al., 2015).

One consequence of the fuel being hydrogen is that the end product will be mostly water vapour. This fact can be utilized in the powder collection, as described by Keskinen

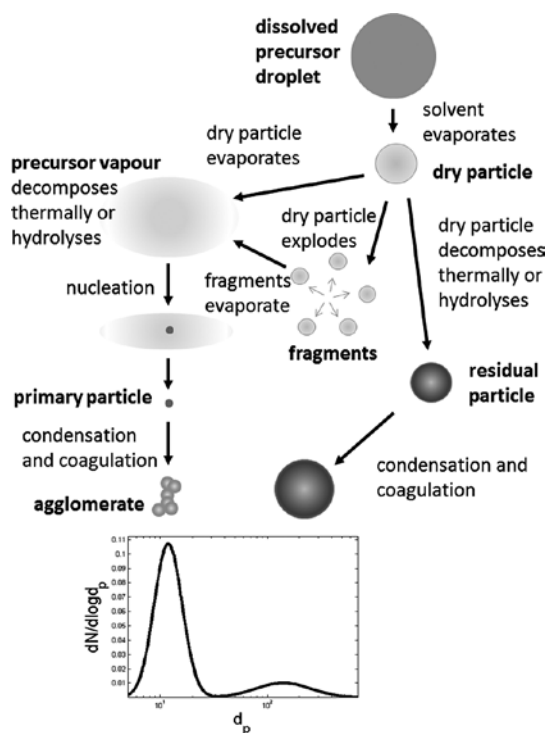


Fig. 3 Schematic of the particle formation mechanisms in a Liquid Flame Spray process. Both agglomerated nanoparticles and larger residual particles will be formed, resulting in a bimodal product particle size distribution. Updated from Aromaa et al. (2013).

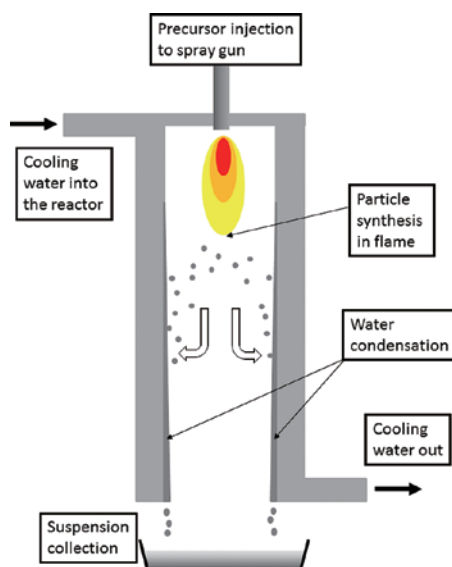


Fig. 4 Collection of the LFS generated nanoparticles into a liquid suspension utilizing combined particle thermophoresis and water vapour condensation due to the cold reactor walls. Adapted from Keskinen et al. (2007b).

et al. (2007b). The principle is illustrated in **Fig. 4**. By introducing a cold walled chamber around the flame, both the nanoparticles and the water vapour can be collected into a suspension via combined nanoparticle thermophoresis and vapour condensation, both of which tend to transport the material towards the cooled walls.

3.2 Test aerosol generation

Aerosol nanoparticle sources with controlled particle size and output concentration are useful for generating test aerosols for e.g. instrument calibration or filter testing (Kulkarni et al., 2011). Also, with combined aerosol measurement and modeling of flow field and aerosol particle dynamics, the data describing the evolution of the aerosol emitted from a localized emission, can be used to assess the exposure of e.g. engineered nanoparticles in a workplace in different release scenarios (Brouwer et al., 2009).

Among the many methods to generate aerosol nanoparticles (Kulkarni et al., 2011), Liquid Flame Spray can be considered an openly operating particle source in an atmospheric pressure. In this respect, the flame can be considered as an exemplary case of a nanoparticle process or potentially also an aerosol source emulating airborne engineered nanoparticle (ENP) release in the workplace. In a typical scenario of occupational health, the particles are usually emitted from the process due to leaks in the ducts or processing chambers or other unintentional release from the process line into the laboratory. Flame technique is one of the most up-scalable techniques for generating nanoparticles to fill large containers for high-volume use of ENPs, or e.g. for arranging a flow split into several ex-

posure chambers. The *in situ* production of nanoparticles in large quantities with a flame, with natural suspension into the air, is a much simpler and effective way to generate a well-defined nanoaerosol than to start with a commercial nanopowder and then de-agglomerate and disperse it into an airborne suspension (Mülhopt et al., 2007).

Monsé et al. (2013; 2014) have characterized the LFS flame and its gaseous emissions in order to test and use it for exposure assessment. The CO₂-emission of the LFS flame is rather small, since the only carbon source is the precursor itself (including solvent). This is advantageous compared to the conventional flames utilizing e.g. methane or acetylene. However, a slight disadvantage in this application arises from nitrogen oxides. If the LFS flame operates normally in the free atmospheric conditions, having immediate access to ambient oxygen in the surroundings of the flame, then, due to the thermal reactions, the NO_x level in the exhaust gas can exceed 1.5 ppm (Monsé et al., 2014). Whereas, the available excess oxygen is typically considered to be advantageous for the nanopowder generation to ensure complete oxidation of the product (Katusic and Kress, 2011), here the excess oxygen is not necessarily crucial. Monsé et al. (2014) succeeded in decreasing the NO_x concentration level below the required 500 ppb by arranging a sheath flow of inert gas around the flame. In their case, the argon flow introduced from the outmost ring in the annular coflow burner kept the flame apart from the oxygen of the ambient air, avoiding excess NO_x formation.

Flame generator can also be used as a test aerosol source in several other purposes such as instrument testing (Mäkelä et al., 2009; Asbach et al., 2009) or filter loading experiments. Once the nanoparticle aerosol has been generated, both large scale industrial filters and smaller scale personal gas mask filters could be considered. In two recent studies (Koivisto et al., 2012; Koivisto et al., 2015), a potential inhalation dose and performance of a loose fitting respiratory filter were evaluated using particle size distribution and concentration data obtained from a LFS generated aerosol in a test room.

3.3 Accumulation of particle deposit

In some applications, as in catalysis, photocatalysis, or gas measurement, granular highly porous material is needed, in order to have large surface area available for reaction to occur on. However, these materials often require that certain degree of solidity needs to be maintained. The porous material for, e.g., gas sensing can be prepared by creating a viscous paste which contains the nanopowder and then performing an appropriate heat treatment to form the final material (Keskinen et al., 2009). The material could also be accumulated by direct

deposition of the nanoparticles from the gas phase (Mädler et al., 2006a; Castillo et al., 2014; Liu et al., 2016).

In our case, the nanoparticle deposition process from the flame onto the substrate is mainly a combination of thermophoresis and diffusion through the boundary layer above the surface:

$$J = -D \frac{dN}{dx} - \frac{0.55N\gamma_{\text{gas}}}{\rho_{\text{gas}}} \frac{1}{T} \frac{dT}{dx} \quad (1)$$

where N denotes the particle number concentration, x distance towards the substrate, γ and ρ the dynamic viscosity and density of the gas, respectively, and D denotes the diffusion coefficient of the particles.

It is convenient to categorize the arrangements of the deposited nanoparticles on the substrate, depending on the morphology of the generated porous material. **Fig. 5** illustrates schematics of some main alternatives. The particles are arranged on the substrate as a sub-monolayer either clearly separate (**Fig. 5a**) or somewhat closer and having contact with each other (**Fig. 5b**). Sainiemi et al. (2007) utilized these two options to create SiO_2 -nanoparticle mask for deep reactive ion etching of silicon wafer in order to fabricate nanopillars on the wafer surface. The particles may also form a porous layer either without sintering (**Fig. 5c**) or with sintering (**Fig. 5d**), or even form a thicker layer (**Fig. 5e**). Finally, the particles may also be embedded in the substrate (**Fig. 5f**), as may occur with softer substrates, such as e.g. polymer or molten glass. The heat of the flame assists the process keeping the substrate soft and thereby enhancing particle penetration into the substrate material. Using polymers as a deposition substrate for nanoparticles to fabricate polymer nanocom-

posites has a high potential for many applications. Recently e.g. plasmonic and phosphorescent-superparamagnetic actuators have been prepared by depositing nanoparticles from the flame into a polymer film (e.g. PMMA) and covering the nanoparticle film with spin coated layer of the same polymer as the substrate, resulting in a nanoparticle layer fully embedded in the polymer (Sotiriou et al., 2013). Also conductive polymer nanocomposites have been fabricated with similar process (Blattmann et al., 2015).

Of the alternatives described in **Fig. 5a–f**, the thin particle layers, such as shown in **Fig. 5a–d**, are possible to be deposited practically onto any material, since the interaction time with the flame and substrate can be very short. Two practical examples have been presented in **Fig. 6a** and **Fig. 6b**. If thicker nanoparticle layers are required, then high nanoparticle concentrations, intensive particle fluxes or longer deposition times are needed. For longer deposition time, it is often also required that the substrate stands heat of the flame relatively well.

The direct deposition process of the LFS generated nanoparticles, as described above, has been studied by Mäkelä et al. (2006), Keskinen et al. (2006) and Keskinen et al. (2007a). It is apparent that along with the accumulation of the nanoparticles, the porous material will be gradually deformed due to the heat treatment. In case of Mäkelä et al. (2006), it was observed that the collected TiO_2 , which originally consisted mostly of anatase, had a tendency to be converted into rutile due to the heat treatment during the deposition process. In **Fig. 6**, a layer of deposited $\text{SiO}_2\text{-Al}_2\text{O}_3$ (90 %/10 %) is shown in different

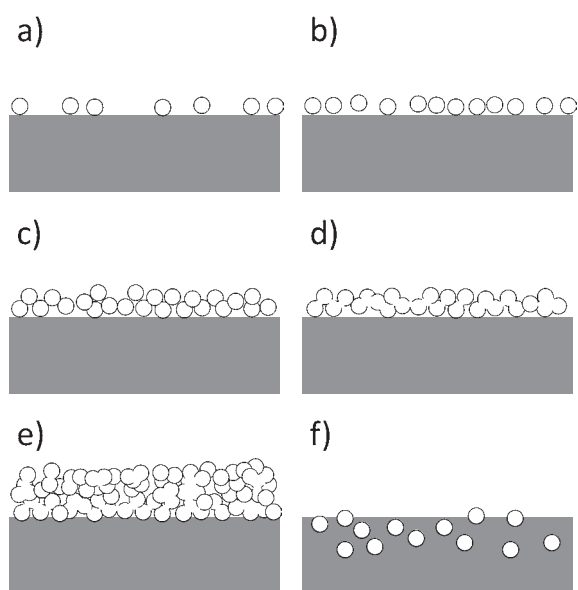


Fig. 5 Schematic illustration of different alternatives for morphology of the nanoparticle deposit.

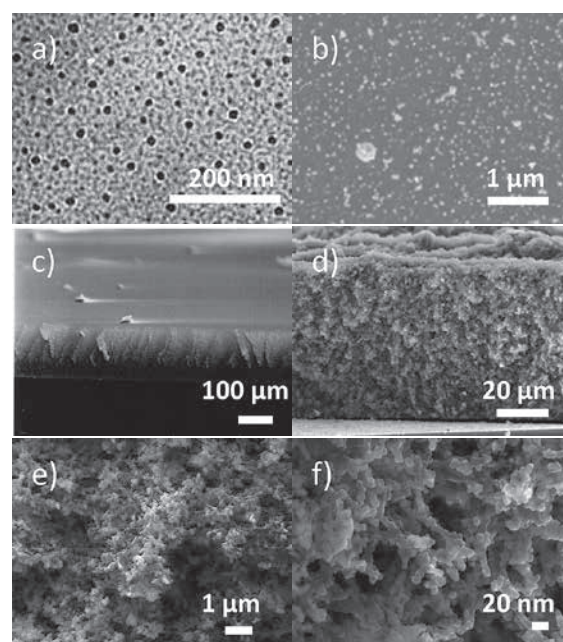


Fig. 6 a–b) Sub-monolayer types of silver nanoparticle deposits, c–f) Accumulation of a thicker porous $\text{SiO}_2\text{-Al}_2\text{O}_3$ nanoparticle layer on a silicon wafer (Mäkelä, 2005).

scales. For the largest magnifications, it is seen that a certain degree of sintering has occurred.

The sintering of the nanoparticles in a similar process, while fabricating nanostructured porous photocatalytic TiO_2 , has been further studied by Thimsen and Biswas (2007) and Thimsen et al. (2008), with a conclusion that the eventual sintering of the porous material under the flame is governed by both the sample temperature and the primary particle size, sintering being enhanced with increasing temperature and with decreasing primary particle size.

It is notable that this deposit of our LFS flame generated particles, shown in **Fig. 6e–f**, has a strikingly similar structure to the one presented by Mädler et al. (2006a), where also thermophoresis is the dominating deposition mechanism, but clearly differs from the more tree-like structure presented by Castillo et al. (2014), where diffusion clearly is the dominating deposition mechanism.

The assembling of the porous nanoparticle layer is highly dependent on the deposited particle morphology and the Peclet number of the flow field. (Mädler et al 2006; Nasiri et al., 2015) The layer thickness and porosity can be individually controlled as shown by e.g. Mädler et al. (2006b). Ballistic deposition of individual particles produces denser layers than those produced by letting agglomerates with low fractal dimension diffuse to the surface.

Comparison of the cross-sectional SEM image of LFS-made TiO_2 layer by Stepien et al. (2013c) and simulations made by Mädler et al. (2006b) indicates that the LFS-made porous TiO_2 -nanoparticle layer consists of deposits of multiple agglomerates produced by flame process. Deposited agglomerates consist of several primary nanoparticles, forming thick layer of nanoparticles with high porosity.

3.4 Glass colouring and processing

In the early history of the LFS, properties of glass material were affected by the deposition of flame generated nanoparticles onto its surface. Here, both art glass colouring and amplifying optical fiber are discussed.

In **Fig. 7a** and **Fig. 7b** the principle of the art glass colouring has been presented. During the high temperature process in molten glass, it is assumed that the nanoparticle will first deposit and plunge into the glass (according to **Fig. 5f**), and then the metal compound will be dissolved into the glass matrix, and finally the ions will be diffused inside the glass material. A typical colouring agent is CoO_3 , which creates a strong blue colour within the soda-lime-silica glass due to dissolved Co^{2+} ions (**Fig. 7b**, Gross et al., 1999). The wavelength from the incoming light, which corresponds to the electronic transition of the metal ion, is absorbed in the glass and thus the

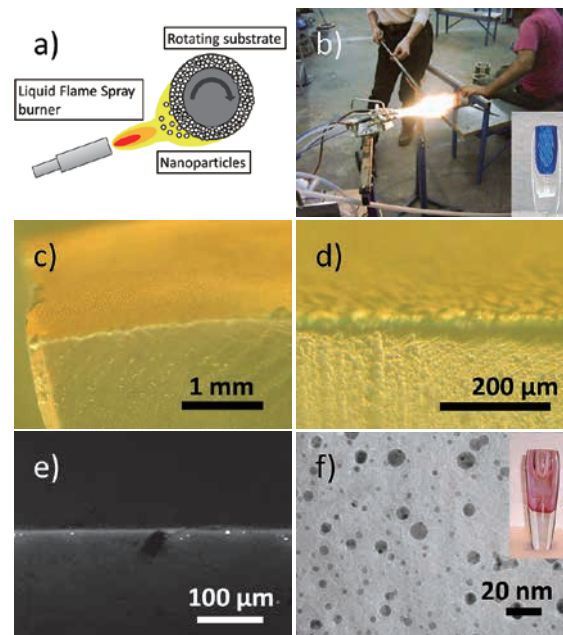


Fig. 7 Glass processing. **a)** Deposition of nanoparticles onto a rotating substrate, an art glass item or an optical fiber preform, **b)** glass colouring in practice, blue colour from CoO_3 nanoparticles, **c–d)** optical micrographs of a cross section of coloured yellow glass (Ag-nanoparticles), **e)** SEM backscattering graph of a cross section of coloured glass (Ag), **f)** TEM graph of in-flame sampled nanoparticles (Au), used for red colour in glass item shown (in insert). Glasswear design by Markus Eerola.

imparting colour will be made up of the remaining wavelengths in the visible spectrum (Bamford, 1977). However, compounds such as silver (**Fig. 7c–e**) and gold (**Fig. 7f**) are known to dissolve and re-nucleate into reduced nanoparticles. There the colour effect will arise from light scattering from the nanoparticles in the glass matrix, being eventually dependent on the final size of the noble metal nanoparticles. In this application, where the LFS flame is in close contact with the glass substrate, the heat from the flame is an essential enabling feature of the process. The heat prevents the molten glass from cooling down temporarily and it also intensifies both the particle diffusion and dissolving inside the glass material. The LFS is also commercially applied in float glass colouring under the trademark nHALO© (Beneq, 2016).

There are also several other LFS applications related to optics, such as doped optical fiber fabrication (Rajala et al., 2003; Tammela et al., 2006), where one needs to be able to control the refractive index of the material (Becker et al., 1999). Here, aluminum, phosphorus and germanium are most often used as additives to silica. Furthermore, the dopant, such as erbium, which is crucial for the amplifying property, also needs to be injected to the fiber preform material. This is most conveniently arranged by a flame-driven nanoparticle deposition process according to

Fig. 7a, resulting in a deposit structure given in **Fig. 5e**. It is also important that when the generated deposit, the actual fiber preform, will be further processed into an optical fiber, having the presence of carbonaceous compounds minimized with the use of hydrogen flame is an advantage (Hotoleanu et al., 2002).

Other optical applications of LFS can be found in fabricating surface plasmon resonance materials (Saarinen et al., 2014). Finally, also functional coatings can be fabricated on glass surfaces, practically by the same mechanisms, using the LFS in a direct deposition process (Pimenoff et al., 2009; Piispanen et al., 2011).

3.5 Functional coatings

In the past 10 years, the Liquid Flame Spray method has been applied to prepare functional coatings by utilizing direct deposition of the nanoparticles from the flame onto the substrate. One of the conventional uses of nanoparticles is catalysis, as described by e.g. Johannessen et al. (2004), where methane was used as fuel to fabricate noble metal based nanoparticles. The LFS has also been used in a somewhat similar application (Keskinen et al., 2007b; Aromaa et al. 2013). Photocatalytic coatings have been fabricated by Keskinen et al. (2005) and Keskinen et al. (2006).

Recently, a slightly less conventional application of the LFS method as a functional coating process has been introduced, where TiO_2 or SiO_2 nanoparticles are deposited onto heat sensitive materials, such as paper or paperboard, in a roll-to-roll scheme, in order to control the wetting of the surface (Teisala et al., 2010; Mäkelä et al., 2011; Stepien et al., 2011; Teisala et al., 2014a; Haapanen et al., 2015). Here, a layer of nanoparticles, with structure and morphology described in **Fig. 5e** has been created. The feasible line speeds for the process are between 50–500 m/min. In the process, the LFS flame is directed towards the moving paperboard. From the model calculations (Aromaa et al., 2012) and from the paper surface temperature measurements using a pyrometer, the surface temperature of the paperboard has been estimated to remain below 300 °C. The nanoparticle flux from the flame ($T = 600\text{--}800\text{ °C}$) onto the paperboard is estimated to be caused mostly by thermophoresis. A SEM-graph of the porous layer, consisting of ca. 20 nm TiO_2 nanoparticles, is shown in **Fig. 8**. According to the analysis of Stepien et al. (2013a), the thickness of the porous coating in the as-prepared form is approximately 600 nm, but the layer can be solidified by a heavy mechanical compression.

Both superhydrophilic (Tuominen et al., 2014) and superhydrophobic (Teisala et al., 2012; Stepien et al., 2012a; Stepien et al., 2012b; Stepien et al., 2013a), coatings have been fabricated using SiO_2 and TiO_2 , respectively. Additionally, their mechanical properties have been tested

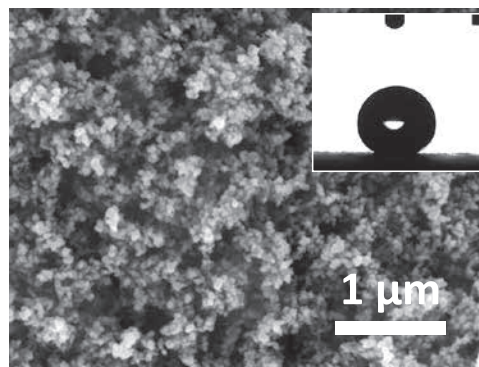


Fig. 8 The porous structure of superhydrophobic TiO_2 nanoparticle deposit on a paperboard (see e.g. Teisala et al. (2014a) and references from thereon). Insert: water droplet on the superhydrophobic paperboard.

(Stepien et al. 2013b; Stepien et al. 2013c), and surface chemistry have been characterized (Stepien et al., 2012a; Stepien et al., 2013a). The results indicate that to achieve, e.g., a full superhydrophobicity on the coating, both surface chemistry and a hierarchical micro-nanostructure is required (Teisala et al., 2012; 2013b). Most interestingly, it is possible to convert the superhydrophobic TiO_2 surface reversibly into superhydrophilic with UV illumination, and back to superhydrophobic with a heat treatment (Teisala et al., 2013a; Teisala et al., 2014b). Surface analysis has shown (Stepien et al., 2013a) that when the coating has been deposited on a paper or a paperboard, there seems to be a layer of carbonaceous compounds on the TiO_2 nanoparticles, which will be chemically converted due to UV. The result has been interpreted so that the flame vaporises some carbonaceous material from the substrate, which will re-condense on the particles, and thereby the surface of the nanoparticles is chemically altered. This indicates that the coating process itself may play a central role in affecting the functionality of the coating.

This control of the switchable surface wetting of heat sensitive substrates, between superhydrophilic and superhydrophobic states, can be further applied in e.g. printability (Valtakari, et al., 2013) and microfluidistic design on roll-to-roll materials (Songok, et al., 2014; Valtakari et al., 2016). Also, hydrophobisation of the surface of wood materials is an important field (Moghaddam et al., 2013; Moghaddam et al., 2014), where direct nanoparticle deposition from the LFS has also been applied successfully (Moghaddam et al., 2015; Moghaddam et al., 2016). Superhydrophobic coatings can also be used to affect the corrosion properties of the surface (Ejenstam et al., 2013; Ejenstam et al., 2015a; Ejenstam et al., 2016), with a potential application field also for nanoparticle coatings (Ejenstam et al., 2015b).

4. Conclusion

We have presented results obtained during the past years on the several applications of the Liquid Flame Spray. As one type of a flame spray pyrolysis, it may be considered to be a conventional method for generating nanopowders from liquid precursors, even though it can utilize a wider range of available precursor compounds due to the help from the hydrogen combustion. Furthermore, due to its characteristics it can easily be applied in direct nanoparticle coating process of even a larger area, and moreover, the combustion product being water vapour instead of carbonaceous compounds gives a clear advantage in specific applications.

Acknowledgements

The authors wish to acknowledge funding from Academy of Finland, project nLABS 2014–2018, and from Finnish Funding Agency for Innovation (Tekes), project NANORATA2 (2011–2014) grant no. 40094/11. The research leading to these results has also received funding from European Union's Seventh Framework Programme FP7/2007–2013/under REA grant agreements n° [CP-IP 211464-2] (NANODEVICE 2009–2013) and n° [280765] (BUONAPART-E 2012–2016). The article reflects only the authors' view and that the Union is not liable for any use that may be made of the information contained therein.

References

- Aromaa M., Keskinen H., Mäkelä J.M., The effect of process parameters on the Liquid Flame Spray generated titania nanoparticles, *Biomolecular Engineering*, 24 (2007) 543–548.
- Aromaa M., Arffman A., Suhonen H., Haapanen J., Keskinen J., Honkanen M., Nikkanen J.-P., Levänen E., Messing M.E., Deppert K., Teisala H., Tuominen M., Kuusipalo J., Stepien M., Saarinen J.J., Toivakka M., Mäkelä J.M., Atmospheric synthesis of superhydrophobic TiO₂ nanoparticle deposits in a single step using Liquid Flame Spray, *Journal of Aerosol Science*, 52 (2012) 57–68.
- Aromaa M., Pimenoff J.A., Mäkelä, J.M., Liquid Flame Spray as a means to achieve nanoscale coatings with easy-to-clean properties, in: Daoud W.A. (Ed.), *Self-Cleaning Materials and Surfaces: A Nanotechnology Approach*, John Wiley & Sons Ltd, Chichester, 2013, pp. 229–252.
- Asbach C., Kaminski H., Fissan H., Monz C., Dahmann D., Mülhopt S., Paur H.-R., Kiesling H.J., Herrmann F., Voetz M., Kuhlbusch T.A.J., Comparison of four mobility particle sizers with different time resolution for stationary exposure measurements, *Journal of Nanoparticle Research*, 11 (2009) 1593–1609.
- Bamford C.R., *Color Generation and Control in Glass*, Elsevier, Amsterdam, 1977.
- Becker P., Olsson N.A., Simpson J.R., *Erbium-Doped Fiber Amplifiers: Fundamentals and Technology*, Academic Press, San Diego, 1999.
- Beneq Oy, 2016, Glass Coloration <<http://beneq.com/glass-coloration.html>> accessed 15.05.2016.
- Blattmann C.O., Sotiriou G.A., Pratsinis S.E., Rapid synthesis of flexible conductive polymer nanocomposite films, *Nanotechnology*, 26 (2015) 125601.
- Brouwer D., van Duuren-Stuurman B., Berges M., Jankowska E., Bard D., Mark D., From workplace air measurement results toward estimates of exposure? Development of a strategy to assess exposure to manufactured nano-objects, *Journal of Nanoparticle Research*, 11 (2009) 1867–1881.
- Castillo J.L., Martin S., Rodriguez-Perez D., Perea A., Garcia-Ybarra P.-L., Morphology and nanostructure of granular materials built from nanoparticles, *KONA Powder and Particle Journal*, 31 (2014) 214–233.
- Cho J., Choi M., Determination of number density, size and morphology of aggregates in coflow diffusion flames using light scattering and local sampling, *Journal of Aerosol Science*, 31 (2000) 1077–1095.
- Chung S.-L., Katz J.L., The counterflow diffusion flame burner: A new tool for the study of the nucleation of refractory compounds, *Combustion and Flame*, 61 (1985) 271–284.
- Dosev D., Guo B., Kennedy I.M., Photoluminescence of Eu³⁺: Y₂O₃ as an indication of crystal structure and particle size in nanoparticles synthesized by flame spray pyrolysis, *J. Aerosol Sci.*, 37 (2006) 402–411.
- Ejenstam L., Ovaskainen L., Rodriguez-Mezoso I., Wågberg L., Pan J., Swerin A., Claesson P.M., The effect of superhydrophobic wetting state on corrosion protection – The AKD example, *Journal of Colloid and Interface Science*, 412 (2013) 56–64.
- Ejenstam L., Swerin A., Pan J., Claesson P.M., Corrosion protection by hydrophobic silica particle-polydimethylsiloxane composite coatings, *Corrosion Science*, 99 (2015a) 89–97.
- Ejenstam L., Tuominen M., Haapanen J., Mäkelä J.M., Pan J., Swerin A., Claesson, P.M., Long-term corrosion protection by a thin nano-composite coating, *Applied Surface Science*, 357 (2015b) 2333–2342.
- Ejenstam L., Swerin A., Claesson P.M., Toward superhydrophobic polydimethylsiloxane-silica particle coatings, *Journal of Dispersion Science and Technology*, 37 (2016) 1375–1383.
- Goldys E.M., Drozdowicz-Tomsia K., Jinjun S., Dosev D., Kennedy I.M., Yatsunenko S., Godlewski M., Optical Characterization of Eu-Doped and Undoped Gd₂O₃ Nanoparticles Synthesized by the Hydrogen Flame Pyrolysis Method, *J. Am. Chem. Soc.*, 128 (2006) 14498–14505.
- Gross K.A., Tikkanen J., Keskinen J., Pitkänen V., Eerola M., Siikamäki R., Rajala M., Liquid flame spraying for glass coloring, *Journal of Thermal Spray Technology*, 8 (1999) 583–589.
- Haapanen J., Aromaa M., Teisala H., Tuominen M., Stepien M., Saarinen J.J., Heikkilä M.J., Toivakka M., Kuusipalo J., Mäkelä J.M., Binary TiO₂/SiO₂ nanoparticle coating for

- controlling the wetting properties of paperboard, *Materials Chemistry and Physics*, 149–150 (2015) 230–237.
- Hannebauer B., Menzel F., The Combustion of SiCl_4 in Hot O_2/H_2 flames, *Z. Anorg. Chem.*, 629 (2003) 1485–1490.
- Harra J., Nikkanen J.-P., Aromaa M., Suhonen H., Honkanen M., Salminen T., Heinonen S., Levänen E., Mäkelä J.M., Gas phase synthesis of encapsulated iron oxide–titanium dioxide composite nanoparticles by spray pyrolysis, *Powder Technology*, 243 (2013) 46–52.
- Harra J., Juuti P., Haapanen J., Sorvali M., Roumeli E., Honkanen M., Vippola M., Yli-Ojanperä J., Mäkelä J.M., Coating of silica and titania aerosol nanoparticles by silver vapor condensation, *Aerosol Science and Technology*, 49 (2015) 767–776.
- Harra J., Kujanpää S., Haapanen J., Juuti P., Hyvärinen L., Honkanen M., Mäkelä J.M., Aerosol Analysis of Residual and Nanoparticle Fractions from Spray Pyrolysis of Poorly Volatile Precursors. Accepted manuscript online: 11 AUG 2016 11:40PM EST | DOI: 10.1002/aic.15449.
- Hartmann W., Mangold H., Kerner D., Flame-hydrolytically produced titanium dioxide mixed oxide, method of its production and its use, US Patent, (1995) 5451390 A.
- Hotoleanu M., Kiiveri P., Tammela S., Särkilahti S., Valkonen H., Rajala M., Kurki J., Janka K., Characteristics of highly doped Er-fibers manufactured by the new direct nanoparticle deposition process, in: 7th European Conference on Networks & Optical Communications (NOC2002), Darmstadt, 2002, pp. 200–204.
- Jang H.D., Chang H., Suh Y., Okuyama K., Synthesis of SiO_2 nanoparticles from sprayed droplets of tetraethylorthosilicate by the flame spray pyrolysis, *Current Applied Physics*, 6, Supplement 1 (2006) e110–e113.
- Johannessen T., Jensen J.R., Mosleh M., Johansen J., Quaade U., Livbjerg H., Flame synthesis of nanoparticles: Applications in catalysis and product/process engineering. *Chemical Engineering Research and Design*, 82 (2004) 1444–1452.
- Kammler H.K., Mädler L., Pratsinis S.E., Flame synthesis of nanoparticles, *Chemical Engineering & Technology*, 24 (2001a) 583–596.
- Kammler, H.K., Mueller, R., Senn, O., Pratsinis, S.E., Synthesis of silica–carbon particles in a turbulent H_2 –air flame aerosol reactor. *AIChE Journal*, 47 (2001b) 1533–1543.
- Katusic S., Kress P., Method for producing mixed oxides comprising lithium, Patent, (2011) CA2803211 A1.
- Keskinen H., Mäkelä J.M., Vippola M., Nurminen M., Liimatainen J., Lepistö T., Keskinen, J., Generation of silver/palladium nanoparticles by liquid flame spray. *Journal of Materials Research*, 19 (2004) 1544–1550.
- Keskinen H., Mäkelä J.M., Hellsten S., Aromaa M., Levänen E., Mäntylä T., 2005. Generation of titania nanoparticles by liquid flame spray for photocatalytic applications, in: Devi A., Fischer R., Parala H., Allendorf M., Hitchman M. (Eds.), *EUROCVI-15: Fifteenth European Conference on Chemical Vapor Deposition*, The Electrochemical Society, Inc., Pennington, 2005, pp. 491–498.
- Keskinen H., Mäkelä J.M., Aromaa M., Keskinen J., Areva S., Teixeira C.V., Rosenholm J.B., Pore V., Ritala M., Leskelä M., Raulio M., Salkinoja-Salonen M.S., Levänen E., Mäntylä T., Titania and titania-silver nanoparticle deposits by Liquid Flame Spray and their functionality as photocatalyst for organic- and biofilm removal, *Catalysis Letters*, 111 (2006) 127–132.
- Keskinen H., Mäkelä J.M., Aromaa M., Ristimäki J., Kanerva T., Levänen E., Mäntylä T., Keskinen J., Effect of silver addition on the formation and deposition of titania nanoparticles produced by Liquid Flame Spray, *Journal of Nanoparticle Research*, 9 (2007a) 569–588.
- Keskinen H., Mäkelä J.M., Heikkinen R., Suopanki A., Keskinen J., Synthesis of Pd-alumina and Pd-lanthana suspension for catalytic applications by one-step Liquid Flame Spray, *Catalysis Letters*, 119 (2007b) 172–178.
- Keskinen H., Aromaa M., Heine M.-C., Mäkelä, J.M., Size and velocity measurements in sprays and particle producing flame sprays, *Atomization and Sprays*, 18 (2008) 1–26.
- Keskinen H., Tricoli A., Marjamäki M., Mäkelä J.M., Pratsinis, S.E., Size-selected agglomerates of SnO_2 -nanoparticles as gas sensors, *Journal of Applied Physics*, 106 (2009) 084316.
- Koivisto A.J., Aromaa M., Mäkelä J.M., Pasanen P., Hussein T., Hämeri K., Concept to estimate regional inhalation dose of industrially synthesized nanoparticles, *ACS Nano*, 6 (2012) 1195–1203.
- Koivisto A.J., Aromaa M., Koponen I.K., Fransman W., Jensen K.A., Mäkelä J.M., Hämeri K.J., Workplace performance of a loose-fitting powered air purifying respirator during nanoparticle synthesis, *Journal of Nanoparticle Research*, 17 (2015) 177–186.
- Kruis F.E., Fissan H., Peled A., Synthesis of nanoparticles in the gas phase for electronic, optical and magnetic applications—a review, *Journal of Aerosol Science*, 29 (1998) 511–535.
- Kulkarni P., Baron P.A., Willeke K., *Aerosol Measurement: Principles, Techniques, and Applications*, John Wiley & Sons, Inc., Hoboken, 2011.
- Lee D., Choi M., Control of size and morphology of nano particles using CO_2 laser during flame synthesis, *Journal of Aerosol Science*, 31 (2000) 1145–1163.
- Liu G., Wong W.S.Y., Nasiri N., Tricoli A., Ultraporous superhydrophobic gas-permeable nano-layers by scalable solvent-free one-step self-assembly *Nanoscale*, 8 (2016) 6085.
- Mädler L., Liquid-fed aerosol reactors for one-step synthesis of nano-structured particles, *KONA Powder and Particle Journal*, 22 (2004) 107–120.
- Mädler L., Roessler A., Pratsinis S.E., Sahn T., Gurlo A., Barsan N., Weimar U., Direct formation of highly porous gas-sensing films by in situ thermophoretic deposition of flame-made Pt/SnO_2 nanoparticles, *Sensors and Actuators B*, 114 (2006a) 283–295.
- Mädler L., Lall A.A., Friedlander S.K., One-step aerosol synthesis of nanoparticle agglomerate films: Simulation of film porosity and thickness, *Nanotechnology*, 17 (2006b) 4783–4795.
- Mäkelä J.M., Keskinen H., Forsblom T., Keskinen, J., Generation of metal and metal oxide nanoparticles by liquid flame spray process, *Journal of Materials Science*, 39 (2004) 2783–2788.
- Mäkelä J.M., Unpublished results, Department of Physics, Tam-

- pere University of Technology, (2005).
- Mäkelä J.M., Hellsten S., Silvonen J., Vippola M., Levänen E., Mäntylä T., Collection of liquid flame spray generated TiO₂ nanoparticles on stainless steel surface, *Materials Letters*, 60 (2006) 530–534.
- Mäkelä J.M., Aromaa M., Rostedt A., Krinke T.J., Janka K., Marjamäki M., Keskinen J., Liquid flame spray for generating metal and metal oxide nanoparticle test aerosol, *Human and Experimental Toxicology*, 28 (2009) 421–431.
- Mäkelä J.M., Aromaa M., Teisala H., Tuominen M., Stepien M., Saarinen J.J., Toivakka M., Kuusipalo J., Nanoparticle deposition from Liquid Flame Spray onto moving roll-to-roll paperboard material, *Aerosol Science and Technology*, 45 (2011) 827–837.
- Mishra Y.K., Kaps S., Schuchardt A., Paulowicz I., Jin X., Gedamu D., Wille S., Pulan O., Adelung R., Versatile fabrication of complex shaped metal oxide nano-microstructures and their interconnected networks for multifunctional applications, *KONA Powder and Particle Journal*, 31 (2014) 92–110.
- Moghaddam M.S., Wälinder M.E.P., Claesson P.M., Swerin A., Multicycle Wilhelmy plate method for wetting properties, swelling and liquid sorption of wood, *Langmuir*, 29 (2013) 12145–12153.
- Moghaddam M.S., Claesson P.M., Wälinder M.E.P., Swerin A., Wettability and liquid sorption of wood investigated by Wilhelmy plate method, *Wood Science and Technology*, 48 (2014) 161–176.
- Moghaddam M.S., Heydari G., Tuominen M., Fielden M., Haapanen J., Mäkelä J.M., Wälinder M.E.P., Claesson P.M., Swerin A., Hydrophobisation of wood surfaces by combining liquid flame spray (LFS) and plasma treatment: dynamic wetting properties, *Holzforschung*, 70 (2015) 527–537. DOI: 10.1515/hf-2015-0148.
- Moghaddam M.S., Wälinder M.E.P., Claesson P.M., Swerin A., Wettability and swelling of acetylated and furfurylated wood analyzed by multicycle Wilhelmy plate method, *Holzforschung*, 70 (2016) 69–77.
- Monsé C., Monz C., Dahmann D., Asbach C., Stahlmecke B., Lichtenstein N., Buchwald K.E., Merget R., Bunger J., Bruning T., Developments for investigations into the health effects of zinc oxide particles, *Gefahrstoffe Reinhaltung der Luft*, 73 (2013) 144–148.
- Monsé C., Monz C., Dahmann D., Asbach C., Stahlmacke B., Lichtenstein N., Buckwald K.-E., Megret R., Bünger J., Brüning T., Development and evaluation of a nanoparticle generator for human inhalation studies with airborne zinc oxide, *Aerosol Science and Technology*, 48 (2014) 418–426.
- Mueller R., Mädler L., Pratsinis S.E., Nanoparticle synthesis at high production rates by flame spray pyrolysis, *Chemical Engineering Science*, 58 (2003) 1969–1976.
- Mülhopt S., Kochev Alavi A., Diabaté S., Paur, H.-R., Aerosol generation for exposure experiments, in: European Aerosol Conference, Association for Aerosol Research, Salzburg, 2007, Abstract T09A019.
- Nasiri N., Elmoe T.D., Liu Y., Qin Q.H., Tricoli A., Self-assembly dynamics and accumulation mechanisms of ultra-fine nanoparticles, *Nanoscale*, 7 (2015) 9859–9867.
- Nikkanen J.-P., Keskinen H., Aromaa M., Järn M., Kanerva T., Levänen E., Mäkelä J.M., Mäntylä T., Iron oxide doped alumina-zirconia nanoparticle synthesis by liquid flame spray from metal organic precursors, *Research Letters in Nanotechnology*, 2008 (2008) 516478.
- Nikkanen J.-P., Harju M., Järn M., Linden J., Rintala J., Messing M.E., Huttunen-Saarivirta E., Saarinen T., Kanerva T., Honkanen M., Aromaa M., Levänen E., Pettersson M., Mäkelä J.M., Deppert K., Mäntylä T., Synthesis of carbon nanotubes on Fe_xO_y doped Al₂O₃–ZrO₂ nanopowder, *Powder Technology*, 266 (2014) 106–112.
- Park H.K., Park K.Y., Control of particle morphology and size in vapor-phase synthesis of titania, silica and alumina nanoparticles, *KONA Powder and Particle Journal*, 32 (2015) 85–101.
- Pimenoff J.A., Hovinen A.K., Rajala M.J., Nanostructured coatings by liquid flame spraying, *Thin Solid Films*, 517 (2009) 3057–3060.
- Piispanen M., Hupa L., Comparison of self-cleaning properties of three titania coatings on float glass, *Applied Surface Science*, 258 (2011) 1126–1131.
- Pikhitsa P.V., Choi M., Yang S., Kim J.-Y., Jang H., Park J.-H., Fast fragmentation of metal oxide nanoparticles via reduction in oxyhydrogen flame, *Applied Physics Letters*, 90 (2007) 163106.
- Pitkänen A., Mäkelä J.M., Nurminen M., Oksanen A., Janka K., Keskinen J., Keskinen H., Liimatainen J.K., Hellstén S., Määttä T., Numerical study of silica particle formation in turbulent H₂/O₂ flame, *IFRF Combustion Journal*, (2005) 200509.
- Pratsinis S.E., Flame aerosol synthesis of ceramic powders, *Progress in Energy and Combustion Science*, 24 (1998) 197–219.
- Purwanto A., Wang W.-N., Okuyama K., Flame Spray Pyrolysis in: Ashgriz. N. (Ed.), *Handbook of Atomization and Sprays*, Springer, New York, 2011, pp. 869–879.
- Rajala M., Janka K., Kykkänen P., An industrial method for nanoparticle synthesis with a wide range of compositions, *Reviews on Advanced Materials Science*, 5 (2003) 493–497.
- Rosebrock C.D., Riefler N., Wriedt T., Mädler L., Tse S.D., Disruptive burning of precursor/solvent droplets in flame-spray synthesis of nanoparticles, *AIChE Journal*, 59 (2013) 4553–4566.
- Rosebrock C.D., Wriedt T., Mädler L., Wegner K., The role of microexplosions in flame spray synthesis for homogeneous nanopowders from low-cost metal precursors, *AIChE Journal*, 62 (2016) 381–391.
- Saarinen J.J., Valtakari D., Haapanen J., Salminen T., Mäkelä J.M., Uozumi J., Surface-enhanced Raman scattering active substrates by liquid flame spray deposited and inkjet printed silver nanoparticles, *Optical Review*, 21 (2014) 339–344.
- Sainiemi L., Keskinen H., Aromaa M., Luosujärvi L., Grigoros K., Kotiaho T., Mäkelä J.M., Franssila S., Rapid fabrication of high aspect ratio silicon nanopillars for chemical analysis, *Nanotechnology*, 18 (2007) 505303. DOI:10.1088/0957-4484/18/50/505303.
- Sheen S., Yang S., Jun K., Choi M., One-step flame method for

- the synthesis of coated composite nanoparticles, *Journal of Nanoparticle Research*, 11 (2009) 1767–1775.
- Sokolowski M., Sokolowska A., Michalski A., Gokieli B., The “in-flame-reaction” method for Al_2O_3 aerosol formation, *Journal of Aerosol Science*, 8 (1977) 219–230.
- Songok J., Tuominen M., Teisala H., Haapanen J., Mäkelä J.M., Kuusipalo J., Toivakka M., Paper-based microfluidics: Fabrication technique and dynamics of capillary-driven surface flow, *ACS Applied Materials & Interfaces*, 6 (2014) 20060–20066.
- Sotiriou G.A., Blattmann C.O., Pratsinis S.E., Flexible, Multifunctional, Magnetically Actuated Nanocomposite Films, *Advanced Functional Materials*, 23 (2013) 34–41.
- Stark W.J., Pratsinis S.E., Aerosol flame reactors for manufacture of nanoparticles, *Powder Technology*, 126 (2002) 103–108.
- Stepien M., Saarinen J.J., Teisala H., Tuominen M., Aromaa M., Kuusipalo J., Mäkelä J.M., Toivakka M., Adjustable wettability of paperboard by liquid flame spray process, *Applied Surface Science*, 257 (2011) 1911–1917.
- Stepien M., Saarinen J.J., Teisala H., Tuominen M., Aromaa M., Kuusipalo J., Mäkelä J.M., Toivakka M., Surface chemical analysis of photocatalytic wettability conversion of TiO_2 nanoparticle coating, *Surface and Coatings Technology*, 208 (2012a), 73–79.
- Stepien M., Saarinen J.J., Teisala H., Tuominen M., Aromaa M., Kuusipalo J., Mäkelä J.M., Toivakka M., Surface chemical characterization of nanoparticle coated paperboard, *Applied Surface Science*, 258 (2012b) 3119–3125.
- Stepien M., Saarinen J. J., Teisala H., Tuominen M., Aromaa M., Haapanen J., Kuusipalo J., Mäkelä J.M., Toivakka M., ToF-SIMS analysis of UV-switchable TiO_2 -nanoparticle-coated papersurface, *Langmuir*, 29 (2013a) 3780–3790.
- Stepien M., Chinga-Carrasco G., Saarinen J.J., Teisala H., Tuominen M., Aromaa M., Haapanen J., Kuusipalo J., Mäkelä J.M., Toivakka M., Wear resistance of nanoparticle coatings on paperboard, *Wear*, 307 (2013b) 112–118.
- Stepien M., Saarinen J.J., Teisala H., Tuominen M., Haapanen J., Mäkelä J.M., Kuusipalo J., Toivakka M., Compressibility of porous TiO_2 nanoparticle coating on paperboard, *Nanoscale Research Letters*, 8 (2013c) 444–449.
- Stepuk A., Krämer K., Stark, W.J., Flame synthesis of complex fluoride-based nanoparticles as upconversion phosphors, *KONA Powder and Particle Journal*, 30 (2013) 267–275.
- Strobel R., Pratsinis S.E., Effect of solvent composition on oxide morphology during flame spray pyrolysis of metal nitrates, *Physical Chemistry Chemical Physics*, 13 (2011) 9246–9252.
- Tammela S., Söderlund M., Koponen J., Philippov V., Stenius, P., The potential of direct nanoparticle deposition for the next generation of optical fibers, in: Digonnet M.J., Jiang S. (Eds.), *Proceedings of SPIE 6116, Optical Components and Materials III*, Society of Photo-Optical Instrumentation Engineers, San Jose, 2006, 61160G.
- Teisala H., Tuominen M., Aromaa M., Mäkelä J.M., Stepien M., Saarinen J.J., Toivakka M., Kuusipalo, J., Development of superhydrophobic coating on paperboard surface using the Liquid Flame Spray, *Surface and Coatings Technology*, 205 (2010) 436–445.
- Teisala H., Tuominen M., Aromaa M., Stepien M., Mäkelä J.M., Saarinen J.J., Toivakka M., Kuusipalo J., Nanostructures increase water droplet adhesion on hierarchically rough superhydrophobic surfaces, *Langmuir*, 28 (2012) 3138–3145.
- Teisala H., Tuominen M., Stepien M., Haapanen J., Mäkelä J.M., Saarinen J.J., Toivakka M., Kuusipalo J., Wettability conversion on the liquid flame spray generated superhydrophobic TiO_2 nanoparticle coating on paper and board by photocatalytic decomposition of spontaneously accumulated carbonaceous overlayer, *Cellulose*, 20 (2013a) 391–408.
- Teisala H., Tuominen M., Aromaa M., Stepien M., Mäkelä J.M., Saarinen J.J., Toivakka M., Kuusipalo J., High- and low-adhesive superhydrophobicity on the liquid flame spray-coated board and paper: structural effects on surface wetting and transition between the low- and high-adhesive states, *Colloid and Polymer Science*, 291 (2013b) 447–455.
- Teisala H., Tuominen M., Haapanen J., Aromaa M., Stepien M., Mäkelä J.M., Saarinen J.J., Toivakka M., Kuusipalo J., Review on Liquid Flame Spray in paper converting: Multifunctional superhydrophobic nanoparticle coatings, *Nordic Pulp and Paper Research Journal*, 29 (2014a) 747–759.
- Teisala H., Tuominen M., Haapanen J., Aromaa M., Stepien M., Mäkelä J.M., Saarinen J.J., Toivakka M., Kuusipalo J., Switchable water absorption of paper via liquid flame spray nanoparticle coating, *Cellulose*, 21 (2014b) 2033–2043.
- Teoh W., Amal R., Mädler, L., Flame spray pyrolysis: An enabling technology for nanoparticles design and fabrication, *Nanoscale*, 2 (2010) 1324–1347.
- Thimsen E., Biswas P. Nanostructured photoactive films synthesized by a flame aerosol reactor, *AIChE Journal*, 53 (2007) 1727–1735.
- Thimsen E., Rastgar N., Biswas P., Nanostructured TiO_2 films with controlled morphology synthesized in a single step process: Performance of dye-sensitized solar cells and photo water splitting, *Journal of Physical Chemistry C*, 112 (2008) 4134–4140.
- Tikkanen J., Eerola M., Rajala M., Coating glass by flame spraying, *Journal of Non-Crystalline Solids*, 178 (1994) 220–226.
- Tikkanen J., Gross K.A., Berndt C.C., Pitkänen V., Keskinen J., Raghu S., Rajala M. Karthikeyan J., Characteristics of the liquid flame spray process. *Surface and Coatings Technology*, 90 (1997) 210–216.
- Tricoli A., Graf M., Mayer F., Kühne S., Hierlemann A., Pratsinis S.E., Micropatterning layers by flame aerosol deposition-annealing, *Advanced Materials*, 20 (2008) 3005–3010.
- Trommer R.M., Bergmann C.P., *Flame Spray Technology: Method for Production of Nanopowders*, Springer, Berlin 2015.
- Tuominen M., Teisala H., Aromaa M., Stepien M., Mäkelä J.M., Saarinen J.J., Toivakka M., Kuusipalo J., Creation of superhydrophilic surfaces of paper and board, *Journal of Adhesion Science and Technology*, 28 (2014) 864–879.
- Ulrich D.G., *Theory of particle formation and growth in oxide*

synthesis flames, *Combustion Science and Technology*, 4 (1971) 47–57.

Ulrich G.D., Flame synthesis of fine particles, *Chemical & Engineering News*, 62 (1984) 22–29.

Valtakari D., Bollström R., Tuominen M., Teisala H., Aromaa M., Toivakka M., Kuusipalo J., Mäkelä J.M., Uozumi J., Saarinen, J.J., Flexographic printing of PEDOT: PSS on

coated papers for printed functionality, *Journal of Print Media and Technology Research*, 2 (2013) 7–13.

Valtakari D., Stepien M., Haapanen J., Teisala H., Tuominen M., Kuusipalo J., Mäkelä J.M., Toivakka M., Saarinen J.J., Planar fluidic channels on TiO₂ nanoparticle coated paper-board, *Nordic Pulp and Paper Research Journal*, 31 (2016) 232–238.

Author's short biography



Jyrki M. Mäkelä

Dr. Jyrki M. Mäkelä is Professor at the Department of Physics, Tampere University of Technology, Finland. He graduated from University of Helsinki, Department of Physics in 1987 and took the degree of PhD at the same department in 1992. During 1992–2000 he worked in the Aerosol Physics Group at University of Helsinki on nanoparticle measurement, mainly in chamber studies and for atmospheric nanoparticle formation. In 2000 he moved to Tampere University of Technology, TUT, as a Lecturer and received a full Professorship there in 2010. Since 2000 he has been leading the Aerosol Synthesis Group at TUT, Aerosol Physics Laboratory, focusing on nanoparticle generation and fabrication of functional surfaces via aerosol synthesis. During 2014–2016 he acted as the Head of the Department of Physics at TUT.



Janne Haapanen

Janne Haapanen is currently working as a researcher and a doctoral student at Tampere University of Technology, Department of Physics, Aerosol Physics Laboratory. He has been working in Prof. Mäkelä's Aerosol Synthesis group since 2009. He received his MSc (Tech.) degree in Technical Physics in 2010 and currently working a researcher and a doctoral student in the same research group. During 2015–2016, he worked as a visiting researcher at Danish Technological Institute, Aarhus, Denmark and at Technical University of Denmark, Kgs. Lyngby, Denmark for 7 months. Main topic of research is functional nanocoatings fabricated by Liquid Flame Spray (LFS) method. He has done research in antibacterial, photocatalytic, superhydrophobic, superhydrophilic, ice-phobic and superamphiphobic nanocoatings by combining several methods with LFS, such as plasma treatment, ALD and silanization.



Juha Harra

Dr. Juha Harra is currently a postdoctoral researcher at the Department of Physics in Tampere University of Technology. He received his Master of Science (Technology) and Doctor of Science (Technology) degrees in Technical Physics from Tampere University of Technology in 2010 and 2015, respectively. During 2016, he worked six months as a visiting scientist in SP Technical Research Institute of Sweden at the Department of Chemistry, Materials and Surfaces in Stockholm. His main research interest is in aerosol physics, including nanoparticle synthesis using gas-phase techniques, real-time measurement of aerosol particles, and particle deposition for functional nanocoatings.

Author's short biography



Paxton Juuti

Paxton Juuti is presently studying Technical Physics as a doctoral student at the Department of Physics, Tampere University of Technology, Finland. He received his BSc (Tech.) degree in 2013 on the topic of nanoparticle sintering and MSc (Tech.) degree in 2015 on real-time monitoring of aerosol synthesis. His research interests include material functionalization via aerosol routes and monitoring of aerosol processes.



Sonja Kujanpää

MSc (Tech.) Sonja Kujanpää graduated from Tampere University of Technology majoring in Advanced Engineering Physics in 2016. The topic of her thesis was “Determination of the mass size distribution of the industrial nanoparticle application produced aerosol”. Today she works as a teacher of mathematical subjects in comprehensive school.

Small-Scale Particle Interactions Are Having Significant Effects on Global Fluidized Bed Behavior[†]

Ray Cocco^{1*}, Allan Issangya¹, S.B. Reddy Karri¹, Tim Freeman²,
Heinrich M. Jaeger³ and Ted M. Knowlton¹

¹ Particulate Solid Research, Inc., USA

² Freeman Technology, UK

³ The James Franck Institute, University of Chicago, USA

Abstract

Fluidized bed design and scale-up depends strongly on particle characteristics such as size, shape, and for Geldart Group A particles, the level of fines (particles smaller than 44 microns). However, recent research has shown that particle clustering has a significant effect on fluidized bed hydrodynamics which impacts how these units should be designed and scaled up. This is especially true with the estimation of the solids entrainment rate and the cyclone collection efficiency. The amount of fines, particle shape and surface morphology play a role on the level of particle clustering in a fluidized bed. The fine particles are an excellent conduit for moving charge as electrons or ions which appear to be the dominant mechanism of electrostatics for Geldart Group A material in a bubbling fluidized bed. This electrostatic force trades off with particle momentum relaxation and rotational to translation momentum transfer with regard to forming a particle cluster. The issue is the quantification of this effect so more precise calculations can be made with particle entrainment rates and cyclone collection efficiency. Preliminary work on particle shear in a packed and fluidized beds, suggest that particle clustering can be measured and may provide a quantifiable metric for the level of particle clustering.

Keywords: powder, particle, fluidization, entrainment, clustering, cohesive forces

1. Introduction

In the design and operation of fluidized beds, particles are assumed to behave independently of each other which results in a fluid-like state once all the particles have been suspended by the fluid. In other words, the factors responsible for dense granular flow such as particle shape, surface roughness, and stress chains nearly disappear once the particles are fluidized. It's a common convention that has limited our understanding of fluidized bed hydrodynamics.

Through the years, this common convention has been challenged. Particle clustering has been postulated as early as in the 1890's where fine-grained granular materials were observed to break up into "droplets" much like a liquid stream (Khamontoff, 1890). Wilhelm and Kwauk (1948) proposed that Geldart Group A particles clustered together, which resulted in the smooth fluidization ob-

served just after the minimum fluidization velocity was achieved. This homogeneous or smooth fluidization is only observed for Geldart Group A particles below the minimum bubbling velocity. Larger particles, such as Geldart Group B particles, exhibit bubbling fluidization at the onset of fluidization. The smaller Geldart Group A particles were viewed as being responsible for particle clustering, which is not evident with larger particles. Geldart and Wong (1987) expanded on this by adding even smaller Geldart Group C particles to a fluidized bed of Geldart Group A particles. The result was a marked decrease in the measured entrainment rate. They suspected that the smaller particles or fines were adhering to the larger particle which affect the drag.

A study by Baeyens et al. (1992) was in agreement with Geldart and Wong's work. Baeyens et al. noted that particles had to be smaller than 40 microns to exhibit this effect on entrainment. This maximum particle size was called the critical particle size and denotes the point where interparticle forces exceed hydrodynamic forces. Subbarao (2010) provided an expression for determining the cluster size which was inline with the findings of Baeyens et al. Jayaweera et al. (1964) found these clusters were stable over a range of two to six particles in size. Clusters larger than six particles were found to split and

[†] Received 1 June 2016; Accepted 1 September 2016

¹ IL60632, USA

² GL20 8DN, UK

³ IL 60637, USA

* Corresponding author: Ray Cocco;

E-mail: ray.cocco@psri.org

TEL: +01-773-523-7227 FAX: +01-773 243-0054

form sub groups of clusters. Fortes et al. (1987) observed similar-sized clusters which were stable up to a Reynolds number of 1800.

Cocco et al. (2010) used a high-speed camera connected to a customized boroscope to reveal these particle clusters in the freeboard region of a fluidized bed containing fluidized catalytic cracking (FCC) equilibrium catalyst with a median particle size of 72 microns and 12 % fines (defined as particle with a size smaller than 44 microns). In fact, 30 % of the particle behavior in the freeboard was found to resemble particle cluster formation with an average particle cluster size of 11 particles. These clusters tended to be small particles or fines adhering to one or two larger particles. This finding was also consistent with similar observations in a fluidized bed of polyethylene powder where 75 % of the particle flow in the freeboard was in the form of particle clusters.

However, Kaye and Boardman (1962) noted that the concentration of particles in a freeboard tends to be too low for the formation of a significant amount of particle clusters. Solids concentrations needed to exceed 0.05 % which is unlikely in a freeboard of a bubbling fluidized bed. Matsen (1982) also concurred that cluster formation and the size of the cluster formation are strongly dependent on the solids concentration.

The same study by Cocco et al. (2010) used the high-speed camera with a boroscope to reveal that particle clusters existed in the fluidized bed as well as above the fluidized bed. The region surrounding a passing bubble showed that most of the particles were behaving as weakly-bound clusters. Cocco et al. suggested that perhaps clusters are formed in the bed and, in part, are subsequently entrained into the freeboard. Particle concentrations in the fluidized bed certainly exceed the criteria of Kaye and Boardman.

Hays et al. (2008) observed that entrainment rates were dependent on fluidized bed height. The taller the bed, the lower the entrainment rate. It was suggested that the reduction in entrainment rates with increasing bed heights was due to a longer growth time with the deeper bed for particle clustering. Hays et al. also added baffles into the fluidized bed and noticed that the entrainment rate increased in a system where small particles (less than 44 microns) were present. The baffles were believed to be responsible for breaking up these weakly-bound clusters. For beds with larger particles, there were not enough particle clusters to exhibit this effect. Both studies further support that particle clusters are mostly formed in the fluidized bed, and that the resulting entrainment rates and particle clustering in the freeboard are the result of particle clusters in the bed becoming ejected into the freeboard.

However, without understanding the underlying nature of the formation of particle clustering, it would be difficult to capture the hydrodynamics of a fluidized bed. This

is more important now than in the past as more fluidized bed challenges are being addressed with computational fluid dynamic (CFD) models. In the past, fluidized bed design and operation was accomplished using empirical correlations which inherently contained the role of particle clustering in the experimental data. With CFD, the model is more fundamentally based, but it is based on the particles as being independent entities which is an incorrect assumption for many systems.

2. Impact of particle clustering on fluidized bed design

The lack of understanding of particle clustering in fluidized beds has compounded the scale-up of these unit operations. One of the key operating costs with fluidized beds are the solids loss rates. In catalytic systems, catalyst loss rates can amount to millions of dollars per year if a fluidized bed is not optimized. Fluidized bed design needs to consider particle attrition and particle collection to manage the loss of solids, which requires knowing the entrainment rate in the freeboard and the grade efficiency of the cyclones.

The entrainment rate is needed for cyclone and dipleg sizing. Under-prediction of the entrainment rates could lead to undersized cyclones prone to dipleg flooding. Over-prediction of the entrainment rate leads to an oversized-dipleg which can result in plugging because of too low of a solids flux moving down the dipleg.

Yet, entrainment rate predictions can be orders of magnitudes different, especially for Geldart Group A particles. Many empirical correlations, which were developed with experimental data already capture the clustering effect, inherently. However, such correlations are system specific. This certainly seems to be the case with the disparity of the entrainment rate from published correlations (Chew et al., 2015). **Fig. 1** illustrates this discrepancy for the entrainment rate prediction using six entrainment rate correlations for FCC powder with 9 % fines in a fluidized bed at a superficial gas velocity of 1 m/s. For the small particles, entrainment fluxes were more than two orders of magnitude different, as shown in **Fig. 1**. Even the trends differ with some correlations showing entrainment significantly increasing with decreasing particle size while other correlations level off. It is likely that the lack of consideration or enough consideration for particle clustering could be a key issue with the discrepancies in these entrainment rate correlations (Chew et al., 2015). Furthermore, such differences can also be found in the calculations of the transport disengagement heights (Cahyadi A. et al., 2015).

Particle clustering can also lead to higher than expected cyclone collection efficiencies. It is hard to see the down

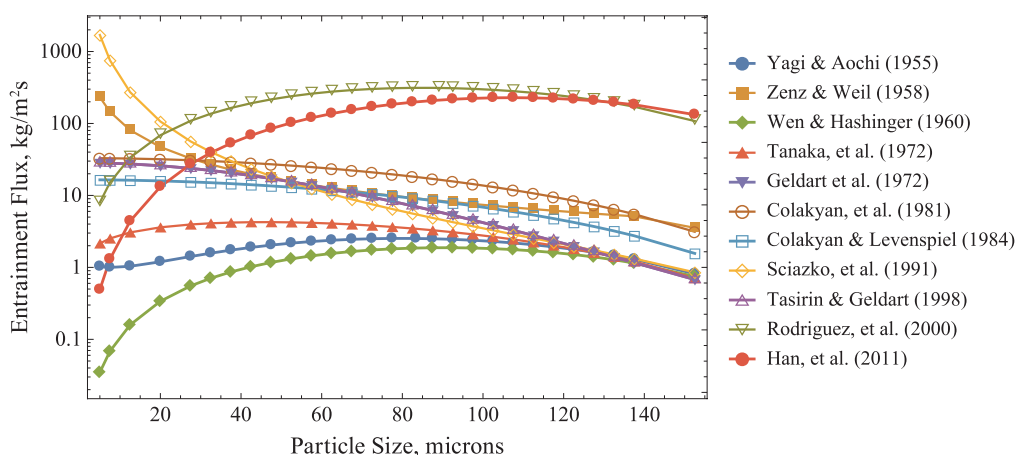


Fig. 1 Entrainment rate calculations based on FCC catalyst powder with 11 % fines in a 3-meter ID \times 12-meter tall fluidized bed with a bed height of 6 meters and superficial gas velocity of 3 m/s at room temperature.

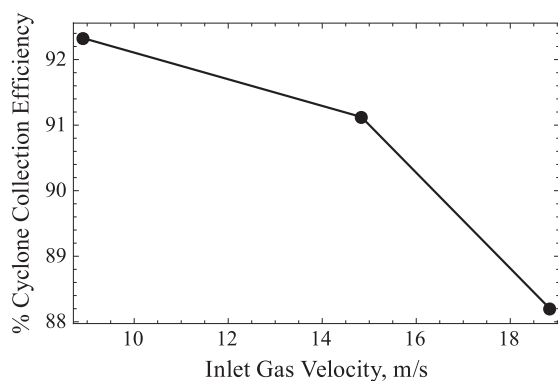


Fig. 2 Cyclone collection efficiency for the collection of titanium dioxide particles in cyclone with a 0.43-m diameter barrel at a solids loading of 0.32 kg solids per m³ of gas.

side of this scenario, but consider what happens when new cyclones are added to this fluidized bed with higher inlet velocities. Higher collection efficiency would be expected but that is not always the case. As shown in **Fig. 2** for a 0.43-m diameter cyclone used in the collection of titania particles, higher inlet velocities resulted in a lower collection efficiency, not higher as expected. The higher inlet velocities were postulated as breaking up particle clusters with the additional trauma to the clusters. These clusters were preserved in the cyclone at the lower velocities. As a result, cyclone collection was influenced by smaller particles at the higher velocity. At the lower inlet velocities, a particle cluster was retained resulting in the cyclone “seeing” a larger “particle” and providing a higher collection efficiency.

Until there is a better understanding of the mechanism of cluster formation and how these clusters behave in fluidized operations, such discrepancies as those shown in **Figs. 2** and **3** will continue. **Fig. 3** illustrates this concept for the simulation of a 0.9-meter diameter fluidized bed of

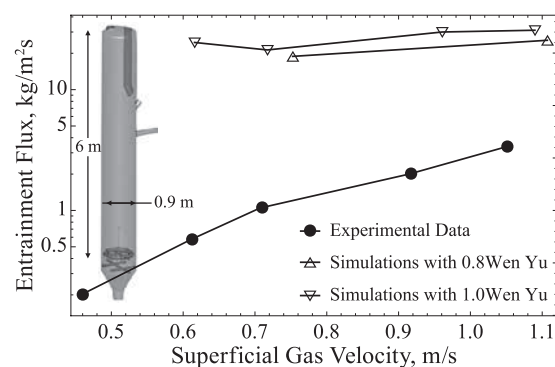


Fig. 3 Log linear plot for the entrainment fluxes from experimental data and Barracuda v16 CFD simulations with 0.8 and 1.0 multipliers on the Wen-Yu drag model for a 0.9-m diameter fluidized bed with a 1.2-meter bed height (at rest).

FCC particles with 9 % fines. As shown in **Fig. 3**, Barracuda CPFD simulations resulted in 20X higher entrainment fluxes than those observed experimentally for a 0.9-meter diameter fluidized bed of FCC catalyst with a 1.2-meter static bed height. Most commercial CFD codes do not account for clustering unless invoked with a drag correction (Yang et al., 2004). Hence, the entrainment rates can be significantly over predicted when CFD is used. Reasonable changes in the drag model may not help either. **Fig. 3** illustrates this using a Wen and Yu drag model with a 0.8 or 1.0 multiplier. The entrainment rates from these simulations were relatively unchanged with respect to the differences with the experimental data. The experimental data are based on the experimental procedures outlined in Issangya et al. (Issangya et al., 2013).

3. Impact of fines levels on particle clustering

As noted by Baeyens et al. (1992), particle clustering in

a fluidized bed was the result of particles with a size smaller than 40 microns. Hays et al. (2008) observed this with a 0.16-m diameter fluidized bed of FCC catalyst (Geldart Group A, $d_{p50} = 72$ microns, $\rho_p = 1500$ kg/m³). As shown in **Fig. 4** where grating-like baffles were added in the bed at 1.6 and 2.5 feet (0.5 and 0.75 meters) above the distributor plate, the entrainment rate was found to increase when superficial gas velocities exceeded 1 m/s. Hays et al. proposed that the higher velocities provided enough shear to break up particle clusters that existed in the bed. Yet, when larger coke particles (Geldart Group B, $d_{p50} = 150$ microns, $\rho_p = 15600$ kg/m³) were used in this unit, little differences in entrainment rates were observed over the whole range of superficial gas velocities, as shown in **Fig. 5**.

Direct evidence of particle clusters was observed and reported by Cocco et al. (2010). Using a modified borescope connected to a high-speed Phantom V7.2 camera,

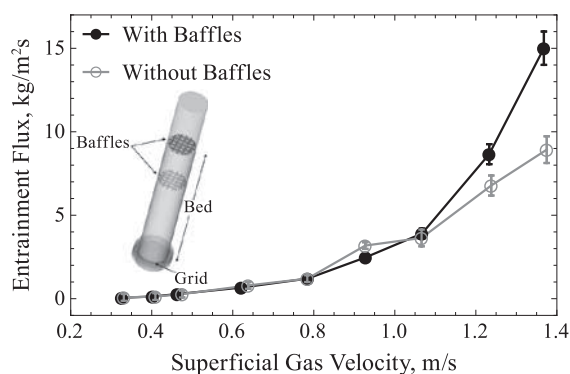


Fig. 4 Entrainment rate versus bed height from a bed of FCC catalyst fines ($d_{p50} = 27$ microns, particle density = 1500 kg/m³) in a 0.15-meter diameter fluidized bed at a superficial gas velocity of 0.56 m/s. Reprinted from Cocco et al., *Journal of Powder Technology* 203 (2010) pp. 3–11 with permission from Elsevier.

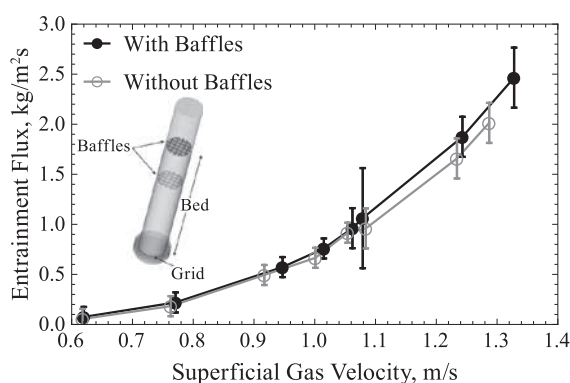


Fig. 5 Entrainment flux from a 0.3-meter diameter bed of fluid coke ($d_{p50} = 150$ microns, particle density = 1600 kg/m³) at a static bed height of 0.7 meters with and without baffles at various superficial gas velocities. Reprinted from Cocco et al., *Journal of Powder Technology* 203 (2010) pp. 3–11 with permission from Elsevier.

Cocco et al. were able to resolve particle clusters well above the bed in the freeboard. The borescope could capture particle and cluster flows beyond the influence of the wall where electrostatics could be more significant. Experiments were performed in a 0.15-m diameter fluidized bed at a superficial gas velocity of 0.6 m/s. As shown in **Fig. 6**, most of the clusters consisted of small particles or fines attached to larger particles. Clusters of only large particles were not typically observed.

Yet, Kaye and Boardman (1962) proposed that particle clustering becomes significant in many systems only where solids concentrations exceed 0.05 %. Such particle concentrations are higher than typically measured in the freeboard region of bubbling fluidized beds at superficial gas velocities of 0.6 m/s. The particle clusters may not be forming in the freeboard to any significant degree, but in the fluidized bed itself. This was confirmed in Cocco et al. (2010) with high-speed video measurements in the fluidized bed. As shown in **Fig. 7**, particle clustering is prolific in a fluidized bed of FCC catalyst particles.

Fig. 7 shows a selected frame from high-speed video captured in a fluidized bed of FCC particles using a modified borescope. The image in **Fig. 7**, is after a bubble passed by the probe where solids volume fractions concentrations are less than that of the bed emulsion. Nearly all the particles were behaving as clusters and small particles appear to have an integral role in the cluster formation. This level of particle clustering has a significant impact on the entrainment rate which is a product of the bubble bursting on top of the bed (Wen & Hashinger 1960).

It is unknown whether the clusters exist in the denser emulsion phase and get ejected into the less dense bubble phase, or if the clusters are solely a product of the bubble phase in the fluidized bed (Cocco et al., 2010). In the first

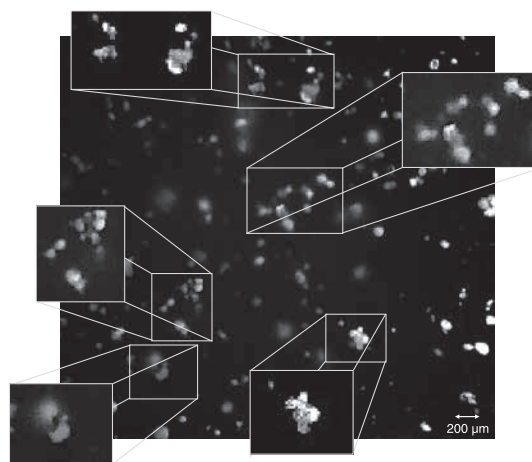


Fig. 6 Selective frame of FCC catalyst in the freeboard region of a 0.15-meter diameter fluidized bed at a superficial gas velocity of 0.61 m/s. Images were collected at 4000 frames per second with a 20 μ s exposure time.

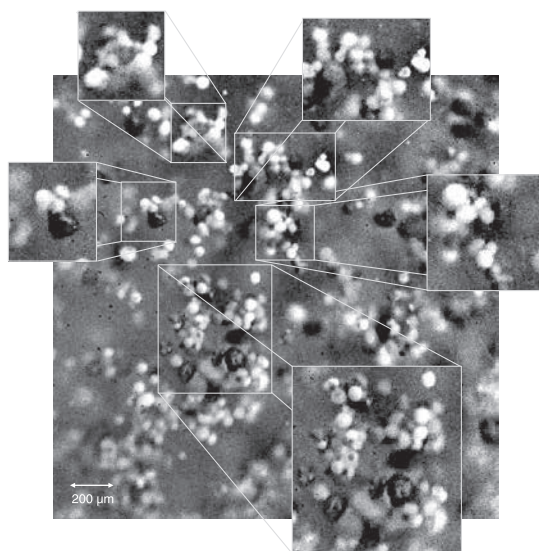


Fig. 7 Selective frame of FCC catalyst in the bed region of a 0.15-meter diameter fluidized bed at a superficial gas velocity of 0.61 m/s. Images were collected at 4000 frames per second with a 20 μ s exposure time.

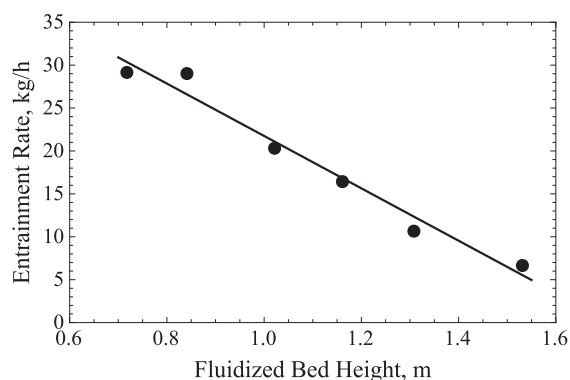


Fig. 8 Entrainment rate versus bed height from a bed of FCC catalyst fines ($d_{p50} = 27$ microns, particle density = 1500 kg/m³) in a 0.15-meter diameter fluidized bed at a superficial gas velocity of 0.56 m/s. Reprinted from Cocco et al., *Journal of Powder Technology* 203 (2010) pp. 3–11 with permission from Elsevier.

case, clustering is prolific and bed hydrodynamics may be strongly coupled to the level of particle clustering. In the second case, clustering may only affect entrainment rates but not bed hydrodynamics.

Hays et al. (2008) also reported that the entrainment rate was strongly dependent on the fluidized bed height. **Fig. 8** shows the measured entrainment rate from a 0.15-m diameter fluidized bed for FCC catalyst powder with 5 % fines at varying bed heights (Cocco et al., 2010; Hays et al., 2008). With the cyclone located well above the transport disengagement height for all cases, the entrainment rate was found to decrease significantly. A doubling of the bed height resulted in a 3.5 times reduction in the entrainment rates. Taller fluidized beds of FCC catalyst particles

resulted in lower entrainment rates than shorter beds. Cocco et al. (2010) suggested that a taller bed provides a longer residence time in the bed for the clusters to get larger. What is unknown is how the concentration of fines in a fluidized bed changes the slope of this relationship.

Fig. 7 illustrates direct evidence of particle clustering in a fluidized bed. **Figs. 4** and **5** show that particle fines (particles smaller than 44 microns) promote the formation of particle clusters which is not unexpected. Fines mobility can be significant in a fluidized bed and serves as a conduit for promotion of particle clustering. However, how do fines promote this particle clustering?

4. Clusters and cohesive forces

The questions to address are how do these clusters affect key design parameters such the entrainment rate and cyclone efficiency. Specifically, what are the underlying forces that promote clustering in a fluidized bed? Possible mechanics for the formation of particle clusters include hydrodynamic interactions (drag minimization) (Geldart, 1987; Zelenko et al., 1996), inelastic grain-grain collision (collisional cooling (Lu et al, 2005; Wang et al., 2009) and viscous dissipation (Subbarao, 1986; Shuyan et al., 2008)), electrostatic forces, capillary bridging or van der Waals forces (Israelachvili, 1992; Podczek, 1998; Visser, 1989).

Royer et al. (2009) investigated some of these effects in granular streams of particles freely falling from a small opening at the bottom of a hopper. For particles in the 50–150 micron range they tracked cluster formation with a high-speed video camera falling alongside the stream. They found that the glass beads developed clusters during a 2.5 meter free fall. These cluster formations were observed in an atmosphere or vacuum suggesting that hydrodynamic interactions may not be a cause. When a similar experiment was performed with 100-micron copper particles, clustering was not observed. If inelasticity was a driving force for clustering, clustering should have been more pronounced as copper has a coefficient of restitution of 0.9 compared to soda glass with a coefficient of 0.97. This together with the fact that the glass particle clusters did not slowly disintegrate during freefall suggested the presence of small cohesive forces in the nano-Newton range.

Clustering in this scenario results when impacting particles cannot escape from the energy well created by attractive forces. In the freefall experiments, the relevant region is right underneath the hopper opening, where the granular kinetic temperature has dropped to a level that clusters are no longer sheared apart, but the collision frequency is still high enough to lead to aggregation. Here, the lighter glass particles did not have enough impact energy to escape after a collision, while the heavier copper

particles did.

Royer et al. confirmed this using Atomic Force Microscopy (AFM) to measure the contact forces directly. They found that the adhesion force was short-ranged (a few nm, i.e. clearly less than 1/1000 of a bead diameter) and a few 10's of nano-Newtons in magnitude. They proposed that the cohesion was due to van der Waals forces or capillary-type interactions from molecularly thin layers of water adsorbed on the particle surfaces. This hypothesis was further confirmed when Royer et al. added Aerosil silica nanoparticles to the surface of the glass beads. The addition of the Aerosil nanoparticles artificially roughened the surface of the glass beads. This resulted in the treated glass beads exhibiting a much reduced adhesion force in the AFM measurements and no longer showing particle clustering in the freefall experiments.

For the glass and metal particles in the experiments by Royer et al., short-range cohesion dominated over longer-ranged charging effects. Electrostatic charging can, of course, become important with other types of insulating particle material. Waitukaitis et al. (2013) performed experiments with freely falling streams of 200–300 micron zirconium dioxide silicate particles, in which they incorporated a Faraday cup at the bottom and had parallel electrodes along the particle free fall. By applying a horizontal electric field, the charge on individual particles could be extracted. Remarkably, while the particle stream as a whole was found to be essentially uncharged, the distribution of charge on individual particles showed broad tails around zero, indicating the existence of particles with large net positive or negative charges, equivalent in magnitude to the charge of several million electrons. It was noted that in these experiments the particle density in the freefall region was adjusted to be low (by using a smaller opening at the bottom of the hopper than Royer et al. used), such that particle-particle collisions were rare. Thus, the particle tracking during freefall was essentially a diagnostic of the triboelectric or contact charging that had occurred during earlier particle-particle contacts, most likely inside the hopper during the outflow process.

Waitukaitis et al. (2013; 2014) were able to show that such contact charging among particles made from the same material involves the transfer of negative charge and that the charging magnitude can be linked directly to the dispersion in particle size, as proposed earlier by Lacks et al. (2007; 2008). Particles smaller than the mean size tend to become charged negatively, while larger particles tend to acquire positive charge. However, at least for zirconium dioxide silicate particles Waitukaitis et al. found that the charge carrier could not have been electrons. The density of electrons in high energy trapped states at the particle surfaces was shown from thermoluminescence measurements to be at least four orders of magnitude too small than needed to account for the observed charging of these

particles.

This suggested that the charge carrier responsible for triboelectric contact charging might be ions, such as OH⁻ ions from the presence of water on the surface of the particles. Pence et al. (1994) and McCarty et al. (2008) have noted the importance of water, and with it OH⁻ ions, on the surface of particles for contact charging. Unless one prepares surfaces under ultra-high vacuum conditions, thin water layers are generally unavoidable. Indeed, even in a vacuum at 10⁻⁶ Torr, a molecularly thin layer of water adsorbs in one second, which is the definition of a Langmuir. However, we caution that to date there is not yet consensus about the precise tribocharging mechanism applicable to granular materials. For example, Baytekin et al. (2011) showed that contact charging of insulating materials can also occur when tiny, nano-sized chunks of solid surface material are transferred during contact.

The surface morphology of particles therefore appears to play a role on several levels as far as clustering is concerned: Asperities may increase the distance two particles can come into proximity, which controls the strength of short-ranged van der Waals and/or capillary forces. In addition, the surface morphology is likely to affect the efficacy of charge transfer during contact, which in turn affects long-ranged electrostatic interactions.

Lee et al. (2015) used high-speed video of 300 micron, free-falling zirconium dioxide silicate particles to explore how electrostatic charging increases the efficiency of particle capture and aggregation processes. They were able to track in detail how particles attract each other over distances of 100's of microns, undergo multiple collisions, and finally stick to each other. Lee et al. were able to model the trajectories between successive collision events as Kepler-like orbits, taking into account the mutual polarization of the particles.

Lee's et al. findings also showed that particles lost some translational kinetic energy upon collision, while particle rotation can have a significant effect. They were able to capture two particles having an electrostatic attraction for each other but clustering failed resulting from the rotation of one of those particles having a less than spherical shape. Asperities from a rough surface could have a similar effect (Wilhelm and Kwauk, 1948).

Lee et al. (2015) also noted that cluster formation often requires multiple bounces to dissipate the kinetic energy such that cohesion can dominate. Clustering was at its lowest probability for the collision of two particles. Collisions of a particle with a pre-existing cluster appeared to be more likely to lead to aggregation, owing to the ability of a cluster to deform internally. In other words, clusters have a lower coefficient of restitution than individual particles.

Thus, in the presence of electrostatic forces, particle clustering appears to be a two-step process. Coulombic

forces between oppositely charged particles or forces arising from polarization of a less-charged particle by a highly charged particle, provide a long-ranged attraction. We note that polarization forces are always attractive, irrespective of the charge polarity on the participating particles. For single-peaked particle size distributions, where the peak of the associated charge distribution from collisions will be near zero charge (Waitukaitis et al. (2014), this means that clusters will tend to be comprised of (near) neutral particles that have aggregated around highly charged ones.

The second step in clustering involves short-ranged cohesive forces. Surface roughness and asperities can lead to more rotational momentum upon collision [Geldart and Wong, 1987; Cocco et al., 2010]. Fines may be less prone to this, as these particles have both less translational and rotational momentum which may also explain why clustering is more evident for many fluidized bed systems with particles smaller than 44 microns.

Longer-ranged electrostatic interactions make it possible to capture and aggregate particles even if they are not undergoing collisions that transfer rotational momentum to translational or by some other similar process. By preventing particle escape during multiple bounces, these interactions also lead to efficient capture when the impact energy would be too large to be sufficiently dissipated during a single collision. This greatly increases the clustering propensity. On the other hand, as clusters grow they eventually reach a size, where, depending on the cohesive strength and the background pressure, they will become large enough that other factors become controlling such as particle shear and drag.

5. Clusters and bulk shear forces

To discern the extent of particle clustering, flow measurements were taken in a 2.5-cm diameter fluidized bed using Freeman Technology's FT4 Powder Rheometer in accordance to ASTM D7891 (2009). If particle clustering is pervasive throughout the emulsion, it should be detectable with the energy required to shear the fluidized bed. If particle clustering is restricted to the region around or below the bubbles, such detection should be limited to the number of bubbles. At low superficial gas velocities near the minimum bubbling velocity, this number should be low and the impact to shear the bed minimal.

The FT4 Powder Rheometer measures the resistance that a powder exerts on a rotating blade as it moves axially through a powder sample which is packed, fluidized or compacted. This resistance, measured as torque and axial force, quantifies the energy needed to rotate the blade. In short, the FT4 provides a measure of the stresses involved when the powder shears at different axial posi-

tions for a packed, compacted or fluidized bed. If clustering is prolific throughout the emulsion of a fluidized bed, then more energy would be needed to shear the solids than for a case where clustering is not significant. Similarly, if clustering is restricted to the region around or below the bubbles, the additional shear should be diluted by the rest of the non-clustering emulsion.

For this study, three samples were examined which consisted of FCC catalyst powder with varying levels of fines concentration (< 44 microns) at 3 % fines (low fines), 12 % fines (medium fines) and 100 % fines (high fines). Analysis consisted of filling a 5-cm diameter cylinder with 25 ml of material. Testing was done at room conditions and replicated for all data points. Testing consisted of measuring the energy needed for rotation in a packed and fluidized bed for up to five times the minimum fluidization velocity.

Fig. 9 shows the results from the permeability testing. As expected for flow through a packed bed, the pressure drop owed to the permeability was five times higher for the high fines case compared to the low or medium fines cases. This level of pressure drop can be typical of cohesive materials which is in agreement with **Figs. 4** and **5** with the comparison of entrainment for Geldart Group A and B materials.

It is interesting that the low and medium fines case had similar permeabilities, with the low fines case showing only a slightly lower pressure drop relative to the medium fines case. **Fig. 10** better illustrates this subtle difference. At low normal stresses (little compaction) this difference is more significant, but as the normal stresses are increased (higher compaction) this difference becomes small. The medium fines case appeared to be insensitive to increases in normal stresses from 2 to 14 kPa, suggesting fines provided a close packed bed upon filling.

This difference is more evident in **Fig. 11** where 15 kPa of normal force on top of a packed bed of particles resulted in a certain level of compaction. The medium fines

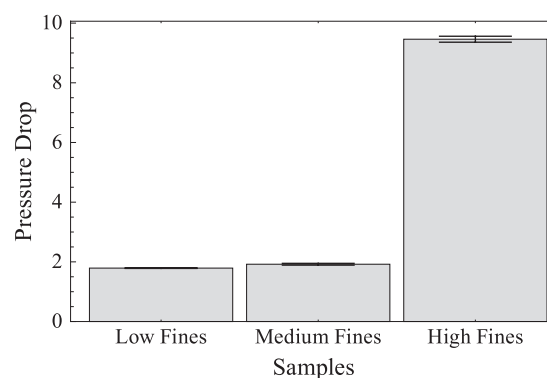


Fig. 9 Permeability testing of low, medium and high fines FCC catalyst with air at a superficial gas velocity of 0.002 m/s at room conditions.

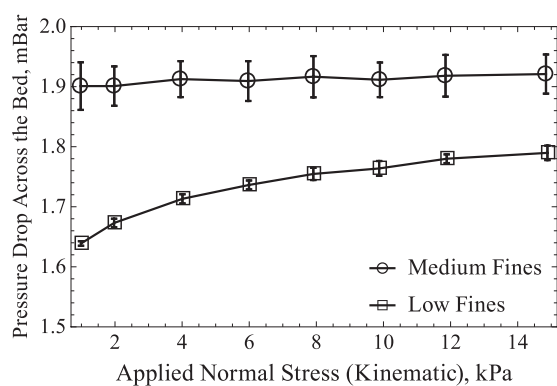


Fig. 10 Permeability testing of low and medium fines FCC catalyst with air at a superficial gas velocity of 0.002 m/s at room conditions with varying normal applied stress (compaction). conditions.

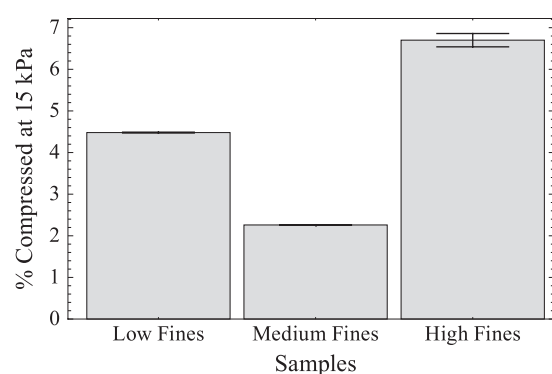


Fig. 11 Percent change in bed height due to compaction at 15 kPa.

case resulted in the least amount of compaction which is in agreement with **Fig. 10**. The less availability of fines results in less of a close pack situation. The high fines case showed the most compaction which is likely the result of weak cohesive forces preventing the bed from approaching a close packed condition with no normal force on the bed. Once force is applied, the cohesive forces are quickly overwhelmed with the applied force.

Consolidation from vibration at a constant amplitude and frequency provided a different trend. The low and medium fines case resulted in comparable consolidation indices (the degree of compaction with mechanical agitation) whereas the level of compaction for the high fines case was three times higher, as shown in **Fig. 12**. This difference suggests that even mild perturbations to the bed can break up the cohesive forces. Thus, if clustering is significant in the bulk, it appears to provide a lower bed density in the non-consolidated state. However, even low levels of energy in the environment seem to break up or reconfigure these clusters.

The most discernible trend with regard to the level of fines was observed with the Basic Flowability Energy (BFE) test. BFE is the energy required to establish a par-

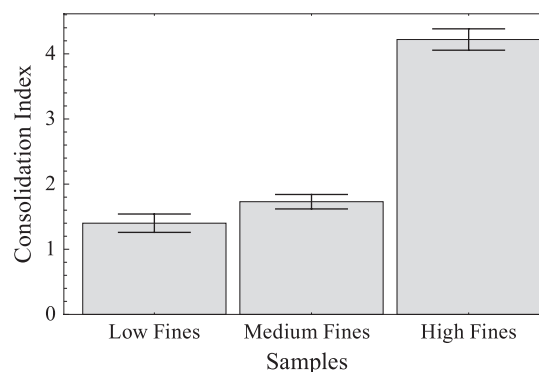


Fig. 12 Measure of the impact that tapping (vibration at constant frequency and amplitude) has on the flow properties of a powder.

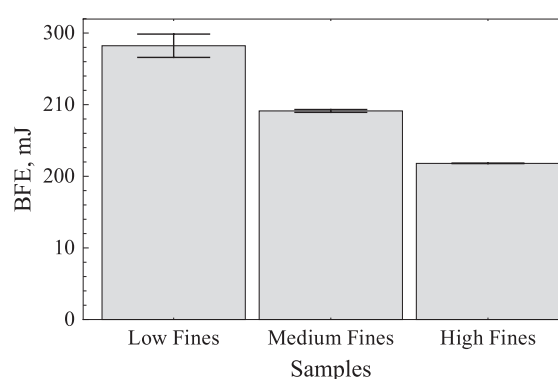


Fig. 13 Basic Flowability Energy for varying level of fines in FCC powder in a packed bed state.

ticular flow pattern in a conditioned, precise volume of powder. This flow pattern is a downward anti-clockwise motion of the blade, generating a compressive, relatively high stress flow mode in a packed bed of powder. The BFE is calculated from the work done in moving the blade through the powder from the top of the vessel to the bottom (i.e. during the downward traverse).

Fig. 13 shows the BFE for the three FCC samples in a packed bed state. The low fines case required the most energy needed for displacing powder. That level of energy decreased as the level of fines concentration increased in the samples suggesting the flowability of the bed becomes easier with increasing fines level. These results are consistent with the increasing formation of clusters with higher fines and resulting in more consolidation during vibration as shown **Figs. 11** and **12**. The granular stresses are less apparent with increasing fines levels. Presumably the higher fines levels provide larger or more clusters which owing to their weak cohesive forces act as a lubricant when under stress.

Indeed, these results suggest that the BFE might provide a trend that can be calibrated to the level of fines concentration which may be an indication of the level of particle clustering in terms of number and/or size. How-

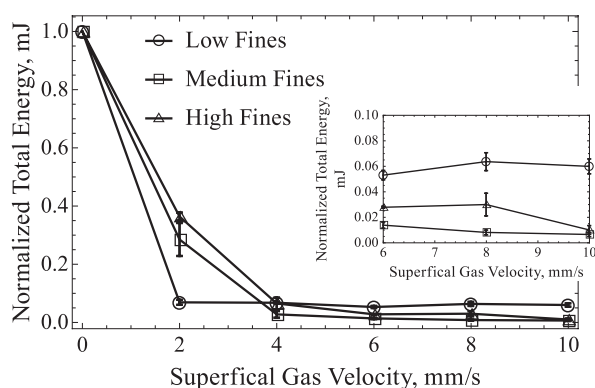


Fig. 14 Energy for varying level of fines in FCC powder with increasing levels of superficial gas velocity through the bed.

ever, the work of Royer et al. (2009) and Waitukaitis et al. (2013) clearly shows that material type and surface morphology have a significant role in the level of particle clustering. Though, the BFE might be able to trend with a cluster level, that trend is most likely to be different for each material with respect to size, surface chemistry, morphology, etc.

Fig. 14 shows the Aerated Energy (AE, the energy measured on the insert when air is being passed through the powder at a specified velocity) needed for rotating the blade with increasing levels of superficial gas velocities. This allows the measurement of the AE from a packed bed to fluidized bed state. The minimum fluidization velocity is apparent with this test and is represented by the leveling off of the normalized total energy needed to rotate the blade (integrated with respect to axial penetration). For the low fines case, the minimum fluidization velocity appeared to be at 0.002 m/s, whereas the high and medium fines case were at 0.004 m/s which is consistent with experimental measurements based on ASTM 7743 (2008).

Above minimum fluidization velocities, the high fines case consistently resulted in more energy needed for the rotating blade with significant cohesive forces prohibiting uniform fluidization. The medium fines case resulted in lower energy requirements compared to the low fines case for superficial gas velocities below 0.01 m/s, as a result of lower permeability and moderate cohesion. At velocities greater than or equal to 0.01 m/s, the trend reversed and more energy was needed for the medium fines case compared to the less cohesive low fines case. However, this may be the result of bed becoming fully fluidized in the low fines case with the onset of bubbling. With higher fines levels, the minimum bubbling velocity increases (Geldart, 1986) and beyond the minimum bubbling velocity, no further improvements in flow properties are observed.

The results from the FT4 tests between the minimum

fluidization and minimum bubbling velocities, suggest that clustering might impede the flow of particles in a homogenous or smoothed fluidized bed. Because bed densities at fluidization are much less than that of a packed bed, the shear forces may be less than the cohesive forces. Hence, the energy needed for rotating the blade increased as it would increase for increasing particle sizes.

From the results presented in **Figs. 9** through **14**, the shear stresses and compaction of a packed bed are influenced by the level of fines concentration. The BFE and AE tests show the best trend with respect to increasing fines concentration, supporting the assumption that clusters could be acting as a lubricant in granular flow of packed beds, yet limiting the extend of homogeneous dispersion in fluidized beds.

The AE test quantifies the energy requirements needed for rotating the blade in a fluidized bed. For measurements between the minimum fluidization and minimum bubbling velocities, higher fines levels appear to coincide as a trend with higher AE requirements. Since the bed is fluidized, the shear stresses associated with particle shape and surface roughness have less of an influence as in the BFE test where results predominantly depend on cohesive strength. Other factors such as particle shapes and structural integrity (i.e., attrition) should also be a consideration.

However, it is still circumstantial that the AE test trends with the level of clusters either by number or size. Additional data are needed to provide that trend either by directionally measuring cluster number and size in a bed under similar conditions and using it for correction to entrainment calculations, or comparing it directly to entrainment data.

The results of the FT4 Powder Rheometer testing suggest that cohesive forces presumably resulting in particle clustering are prolific in the bulk solids and are not confined in the region around or below a bubble. This is evident with the non-monotonic changes in permeability and compaction with increasing fines level where bubbles were not present. The AE testing also suggests particle clusters are not restricted to bubbles as more energy was needed with increasing fines levels below the minimum bubbling velocity under homogenous or smooth fluidization.

6. Conclusions

With particle clustering being linked to the morphological and electrostatic nature of the particle surface, entrainment rate calculations are highly material specific. Coupled with the reflux of particles or clusters in the free-board because of internals such as cyclones and expanded heads, it appears unlikely that a fundamentally-based CFD model would be effective in determining the en-

trainment rate.

Direct evidence of particle clustering in a fluidized bed has been observed. Particle clusters form in the bed and their size may be dependent on the residence time in the bed (i.e., bed height and gas velocity). The mechanism for clustering appears to be resulting from a combination of short-ranged cohesion due to van der Waals or capillary forces and longer-ranged electrostatic interactions, with particles becoming charged by transfer of electrons or, more likely, ions during contact. The small particles or fines provide an effective conduit in moving the charge throughout the fluidized bed. Fines have a higher mobility in fluidized beds. However, rotational movement of a particle could overpower the electrostatic forces, especially for the larger particles. Thus, particles with low sphericity or high surface roughness may be less likely to form particle clusters.

Despite the mechanism, microscopic particle clustering affects the fluidization behavior and has a significant effect on entrainment, a design parameter critical for fluidized bed scale-up. To achieve better accuracy with entrainment rate calculations and with the CFD modeling of entrainment, this clustering needs to be accounted for.

Preliminary testing using the FT4 Powder Rheometer for measuring the energy needed to shear FCC catalyst samples at varying levels of fines concentration in a packed and fluidized bed suggest fines play a role here as well. However, such testing under fluidized conditions relaxes the effects of other factors such as particle shape and surface roughness on the shear stresses. Furthermore, the results of this aeration test found a trend only with the level of fines concentration and not directly with the level of particle clusters which were unknown.

Nonetheless, particle clustering in a fluidized bed appears to be significant throughout the bed and not confined to the bubble, even though visual observations were restricted to the region around the bubble. Permeability, compaction, and unconsolidated shear stress measurements showed a good trend with the level of fines, a promoter of particle clustering, in a packed bed. Furthermore, the AE testing further confirmed this by showing a monotonic trend in energy requirements with increasing fines levels below the minimum bubbling velocity.

Acknowledgements

The authors would like to thank Frank Shaffer and Rupendranath Panday of the US National Energy Technology Laboratory and Alexander Mychkovsky and Steve Ceccio of the University of Michigan for their help with consultation with the development of the boroscope. The authors also thank the US Department of Energy for their funding under DE-FC26-07NT43098 and the US National

Science Foundation for their funding under DMR-CMP-1309611.

References

- ASTM D7743-12, Standard Test Method for Measuring the Minimum Fluidization Velocities of Free Flowing Powders, 2008 ed., ASTM International, West Conshohocken, PA, 1900. doi: 10.1520/D7743.
- ASTM D7891-15, Standard Test Method for Shear Testing of Powders Using the Freeman Technology FT4 Powder Rheometer Shear Cell, 2009, ed., ASTM International, West Conshohocken, PA, 1900. doi: 10.1520/D7891.
- Baeyens J., Geldart D., Wu S.Y., Elutriation of fines from gas fluidized beds of Geldart A-type powders—effect of adding superfines, *Powder technology*, 71 (1992) 71–80.
- Baytekin H.T., Patashinski A.Z., Branicki M., Baytekin B., Soh S., Grzybowski B.A., The mosaic of surface charge in contact electrification, *Science*, 333 (2011) 308–312.
- Cahyadi A., Neumayer A.H., Hrenya C.M., Cocco C.M., Chew J.W., Comparative study of Transport Disengaging Height (TDH) correlations in gas–solid fluidization, *Powder Technology*, 275 (2015) 220–238. doi: 10.1016/j.powtec.2015.02.010.
- Chew J.W., Cahyadi A., Hrenya C.M., Karri S.B.R., Cocco R.A., Review of entrainment correlations in gas-solid fluidization, *Chemical Engineering Journal*, 260 (2015) 152–171. doi: 10.1016/j.ccej.2014.08.086.
- Cocco R.A., Shaffer F., Hays Karri S.B.R., Knowlton T.M., Particle clusters in and above fluidized beds, *Powder Technology*, 203 (2010) 3–11.
- Colakyan M., Catipovic N., Jovanovic G., Fitzgerald T.J., Elutriation from a Large Particle Fluidized Bed with and without Immersed Heat Transfer Tubes, *AIChE Symp. Ser.*, 77 (1981) 66–75.
- Colakyan M., Levenspiel O., Elutriation from fluidized beds, *Powder Technology*, 38 (1984) 223–232.
- Fortes A.F., Joseph D.D., Lundgren T.S., Nonlinear mechanics of fluidization of beds of spherical particles, *Journal of Fluid Mechanics*, 177 (1987) 467–483.
- Geldart D., Cullinan J., Georgiades S., Gilvray D., Pope D.J., The effect of fines on entrainment from gas fluidized beds, *Transactions of the Institution of Chemical Engineers*, 57 (1979) 269–275.
- Geldart D., *Gas Fluidization Technology*, Wiley Interscience, Chichester, (1986), p. 25.
- Geldart D., Wong A.C.Y., Entrainment of particles from fluidized beds of bed of fine powder, *AIChE Symposium Series*, 255 (1987) 1.
- Han Y.L., Chyang C.S., Hsiao W.M., Lo K.C., Effect of fines hold-up in the freeboard on elutriation from a fluidized bed, *J. Taiwan Inst. Chem. Eng.*, 42 (2011) 120–123.
- Hays R., Karri S.B.R., Cocco R.A., Knowlton T.M., Small Particles Cluster Formation in Fluidized Beds and its Effect on Entrainment, *Circulating Fluidized Bed IX*, 9 (2008) 1–5.
- Israelachvili J.N., *Intermolecular and Surface Forces*, 2nd Ed., Academic Press (1992).

- Issangya A., Karri S.B.R., Knowlton T.M., Cocco R.A., Effects of bed diameter, baffles, fines content and operation conditions on pressure fluctuations in fluidized beds of FCC catalyst particles, *Fluidization XIV*, XIV (2013) 1–9.
- Jayaweera K.O.L.F., Mason B.J., Slack G.W., The behavior of clusters of spheres falling in a viscous fluid, *Journal of Fluid Mechanics*, 20 (1964) 121–128.
- Kaye B.M., Boardman R.P., Cluster formation in dilute suspensions, in *Proc. Symp. on the Interaction between Fluids and Particles*, Institution of Chemical Engineers London (1962) 17–21.
- Khamontoff N., Application of photography to the study of structures of trickles of fluid and dry materials, *J. Russ. Phys-Chem. Soc.*, 22 (1890) 281–284.
- Lacks D. J., Levandovsky A., Effect of particle size distribution on the polarity of triboelectric charging in granular insulator systems, *Journal of Electrostatics*, 65 (2007) 107–112. doi: Doi 10.1016/J.Elstat.2006.07.010
- Lacks D.J., Duff N., Kumar S.K., Nonequilibrium accumulation of surface species and triboelectric charging in single component particulate systems, *Physical Review Letters*, 100 (2008) 188305. doi: 10.1103/Physrevlett.100.188305
- Lee V., Waitukaitis S.R., Miskin M.Z., Jaeger H.M., Direct observations of particle interactions and clustering in charged granular streams, *Nature Physics*, 11 (2015) 733–737.
- Lu H.L., Sun Q.Q., He Y.R., Sun Y.L., Ding H.M., Xiang L., Numerical study of particle cluster flow in risers with cluster-based approach, *Chemical Engineering Science*, 60 (2005) 6757–6767.
- Matsen J., Mechanisms of choking and entrainment, *Powder Technology*, 32 (1982) 21–33.
- McCarty L.S., Whitesides G.M., Electrostatic charging due to separation of ions at interfaces: contact electrification of ionic electrets, *Angewandte Chemie International Edition*, 47 (2008) 2188. doi: 10.1002/anie.200701812.
- Pence S., Novotny V., Diaz A., Effect of Surface Moisture on Contact Charge of Polymers Containing Ions, *Langmuir*, 10 (1994) 592. doi: 10.1021/la00014a042.
- Podczek F., Particle-particle adhesion in pharmaceutical powder handling, Imperial College Press (1998).
- Rodriguez J.M., Sanchez J.R., Alvaro A., Florea D.F., Estevez A.M., Fluidization and elutriation of iron oxide particles. A study of attrition and agglomeration processes in fluidized beds, *Powder Technology*, 111 (2000) 218–230.
- Royer J.R., Evans D.J., Oyarte L., Guo Q., Kapit E., Möbius M.E., Waltukaitis S.R., Heinrich J.M., High-speed tracking of rupture and clustering in freely falling granular streams, *Nature*, 459 (2009) 1110–1113. doi: 10.1038/nature08115.
- Sciazzko M., Bandrowski J., Raczek J., On the entrainment of solid particles from a fluidized-bed, *Powder Technology*, 66 (1991) 33–39.
- Shuyan W., Zhiheng S., Huilin L., Long Y., Wentie L., Yonlong D., Numerical predictions of flow behavior and cluster size of particles in riser with particle rotation model and cluster-based approach, *Chemical Engineering Science*, 63 (2008) 4116–4125.
- Subbarao D., Clusters and lean-phase behavior, *Powder Technology*, 46 (1986) 101–107.
- Subbarao D., A model for cluster size in risers, *Powder Technology*, 199 (2010) 48–54. doi: 10.1016/j.powtec.2009.04.015.
- Tanaka I., Shinohara H., Hirose H., Tanaka Y., Elutriation of fines from fluidized bed, *Journal of Chemical Engineering of Japan*, 5 (1972) 51–57.
- Tasirin S.M., Geldart D., The elutriation of fine and cohesive particles from gas fluidized beds, *Chemical Engineering Communications*, 173 (1999) 175–195.
- Waitukaitis S.R., Jaeger H.M., In situ granular charge measurement by free-fall videography, *Review of Scientific Instruments*, 84 (2013) 025104. doi: 10.1063/1.4789496
- Waitukaitis S.R., Lee V., Pierson J.M., Forman S.L., Jaeger H.M., Size -Dependent Same-Material Tribocharging in Insulating Grains, *Physical Review Letters*, 112 (2014) 218001–5. doi: 10.1103/PhysRevLett.112.218001.
- Wang S.Y., Li X., Lu H.L., Yu L., Ding J.M., Yang Z.M., DSMC prediction of granular temperatures of clusters and dispersed particles in a riser, *Powder Technology* 192 (2009) 225–233.
- Wen C.Y., Hashinger R.F., Elutriation of solid particles from a dense-phase fluidized bed, *AIChE J.* 6 (1960) 220–226.
- Wilhelm R.H., Kwauk M., Fluidization of solid particles, *Chemical Engineering Progress* 44 (1948) 201–218.
- Visser J., van der Waals and other cohesive forces affecting powder fluidization, *Powder Technology* 58 (1989) 1–10.
- Yagi S., Aochi T., Elutriation of particles from a batch fluidized bed, *Society of Chemical Engineering (Japan)—Spring Meeting*, 1955.
- Yang N., Wang W., Ge W., Wang L., Li J, Simulation of heterogeneous structure in a circulating fluidized bed-riser by combining the two fluid model with EMMS approach, *Industrial and Engineering Chemistry Research*, 43 (2004) 5548–5561.
- Zelenko V.L., Sergeev Y.A., Tjin T., Iske P.L., Clusters and particle segregation in gas-solid flow through a vertical tube, *Physica A: Statistical Mechanics and its Applications*, 226 (1996) 274–294.
- Zenz P.A., Weil N.A., A theoretical-empirical approach to the mechanism of particle entrainment from fluidized beds, *AIChE J.*, 4 (1958) 472–479.

Author's short biography



Ray Cocco

Ray Cocco holds a Bachelor Degree in Chemical Engineering from University of Florida and a Doctoral Degree in Chemical Engineering from Auburn University. He is a member of ASTM and the AIChE. He worked in reaction engineering and powder technology for 17 years at Dow Chemical. He is currently President and CEO of Particulate Solid Research, Inc. (PSRI) which is a research consortium of 35 companies which focuses on multiphase flows. He serves on several editorial boards including Powder and Bulk Engineering, Powder Technology and Advance Powder Technology. He is also the Chair of the World Congress in Powder Technology in Orlando, Florida in 2018.



Allan Issangya

Allan Issangya holds a Bachelors Degree from Dar es Salaam, Master Degree from University of Leeds and Doctoral Degree from University of British Columbia in Chemical Engineering. He is a member of the AIChE. He has 20 years of experience in fluidization at Particulate Solid Research Inc., with a current position of Technical Leader. He has interest in granular-fluid hydrodynamics in fluidized beds, gas bypassing and bed internals.



S.B. Reddy Karri

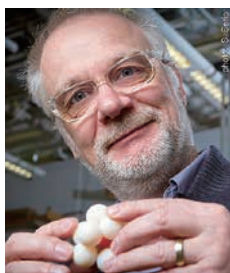
Reddy Karri holds a Master and Doctoral Degrees in Chemical Engineering from New Hampshire. He is a member of the AIChE and Chair of the Particle Technology Forum. He extensively consults and trouble shoots the industrial problems in the energy field. He is currently the Technical Director at Particulate Solid Research, Inc. where he has been for 28 years. He is a recent recipient of the AIChE PTF Fluidization Processing Award in 2014.



Tim Freeman

Tim has a degree in Mechatronics from the University of Sussex in the UK. He is past Chair of the American Association of Pharmaceutical Scientists (AAPS) Process Analytical Technology Focus Group and is a member of the Editorial Advisory Board of Pharmaceutical Technology. He has recently been featured on the Industry Expert Panel in European Pharmaceutical Review magazine. Since 1990, Tim Freeman is Managing Director of powder characterization company Freeman Technology. He was instrumental in the original design and continuing development of the FT4 Powder Rheometer® and through his work with various professional bodies, and involvement in industry initiatives, is an established contributor to wider developments in powder processing.

Author's short biography



Heinrich M. Jaeger

Heinrich Jaeger is the William J. Friedman and Alicia Townsend Professor of Physics at the University of Chicago. He received his Ph.D. in physics in 1987 from the University of Minnesota and has been on the faculty at U Chicago since 1991, directing the Chicago Materials Research Center from 2001–2006, and the James Franck Institute from 2007–2010. He is a fellow of the American Physical Society. Jaeger's current research focuses on self-assembled nanoparticle-based structures, on the rheology of concentrated particle suspensions, and on studies of the packing and flow properties of dry granular materials.



Ted M. Knowlton

Ted Knowlton holds a Bachelor, Master and Doctoral Degrees from Iowa State University in Chemical Engineering. Dr. Knowlton managed IGT's fluidization and solids transport programs after receiving his Ph.D. at Iowa State University in 1971 until 1996. He was the Technical Director of Particulate Solid Research, Inc, from 1996 to 2010. Dr. Knowlton received the Distinguished Service Award from the Fluidization and Fluid-Particle Systems Committee of the AIChE in 1990, the Fluor Daniel Lectureship Award for his contributions to the area of fluidization in November, 1996, and the Thiele Award for outstanding lifelong contributions to the field of Chemical Engineering in 2004.

Advances in Nanoparticle Sizing in Suspensions: Dynamic Light Scattering and Ultrasonic Attenuation Spectroscopy[†]

Wu Zhou^{1,2}, Mingxu Su^{1*} and Xiaoshu Cai¹

¹ Institute of Particle and Two-phase Flow Measurement, Shanghai Key Laboratory of Multiphase Flow and Heat Transfer in Power Engineering, University of Shanghai for Science & Technology, China

² Key Laboratory of Energy Thermal Conversion and Control of the Ministry of Education, Southeast University, China

Abstract

Size characterization of nanoparticles has gained wide concerns in the past decades, but it remains a challenge for measurement in suspensions up to now. The extremely small scales of particle size result in great difficulty for traditional static light scattering method and optical imaging. In addition to the electron microscopy techniques, the dynamic light scattering (DLS) method is another widely used technique for laboratory analysis of samples. Moreover, the ultrasonic attenuation spectroscopy (UAS) technique is also being developed rapidly to provide an alternative method for nanoparticle sizing. This paper focuses on the latest development in the above two technologies for nanoparticle size characterization. As for the former, advances about the image-based DLS technology in recent years are reviewed, including three different kinds of data processing methods and corresponding measuring experiments using standard polystyrene particles. Methodology principles, models and experimental setup were also reviewed for the latter UAS technology. Samples of the same nanoscale silver particles were tested by the above two methods, as well as by transmission electron microscopy. A sample of Antimony Tin Oxide (ATO) nanoparticles has also been adopted for measurements and comparisons. Relatively consistent results can be found by comparing the particle sizes or distributions with various methods. The dramatically reduced measurement time in image-based DLS indicates the potential for real-time and in-situ nanoparticle sizing. UAS also provides a suitable way for nanoparticle size characterization at high concentrations.

Keywords: nanoparticle, size characterization, image-based dynamic light scattering, ultrasonic attenuation spectroscopy, inversion

1. Introductions

Nanoparticles are generally referred to as particles with diameter less than 100 nm, which are also called as ultrafine particles. Ultrafine particles often exhibit some unique effects such as quantum size effect, surface effect, etc., which bring particles many special properties. However, there is no reason to think that here is much difference between a 90 nm and a 110 nm particle in ability and there is little evidence for the cutoff diameter for the ultrafine effect (Donaldson K. et al., 2001). There are broad application prospects for them in catalysis, light filter, light absorption, medicine, magnetic media, new material development, and so on. Detailed studies are essential on

methods of nanoparticle characterization. At present, popular methods used for ultrafine particle sizing include electron microscopy, laser particle sizing (combined with large-angle scattered light reception technology), high-speed centrifugal sedimentation, dynamic light scattering, ultrasonic method, etc. In many cases, ultrafine particles are suspended in a liquid medium to form a suspension, which is the basic state for measurement using dynamic light scattering and ultrasonic method.

Dynamic light scattering (DLS) has also been called as photon correlation spectroscopy, quasi-elastic light scattering, or intensity fluctuation spectroscopy in the past. It was first used for the particle sizing in the early 1970s (Pecora R., 1972; Silbey R. and Deutch J.M., 1972) and then got a booming development in the applications. Tscharnuter W. (2006) has also made a remarkable review on the developments of this technology before the 21st century for particle sizing, including histories, principles, sampling, instrument and measurement.

In conventional DLS method, a photomultiplier tube

[†] Received 25 July 2016; Accepted 17 October 2016

¹ 516 Jungong Road, Shanghai, 200093, China

² Sipailou 2#, Nanjing, 210096, China

* Corresponding author: Mingxu Su;

E-mail: sumx@usst.edu.cn

TEL: +86-021-5527-7764 FAX: +86-021-5527-6854

is used to receive the scattered light from nanoparticles, and a digital correlator is utilized to process the one-dimensional time-series signal to obtain the autocorrelation function of the intensity fluctuation. Features of the autocorrelation function (ACF) curve reflect the Brownian motion characteristics of nanoparticles and thus the information of particle size. Commercial instrument based on DLS has become popular in off-line laboratory analysis. However, in order to obtain accurate ACF results, a large number of data is required. The measuring time usually lasts tens of seconds to hundreds of seconds. It is difficult to realize a real-time and online nanoparticle size measurement in unstable or rapidly changing processes.

Study of DLS method using a CCD (Charge Coupled Device) or CMOS (Complementary Metal Oxide Semiconductor) camera as an area detector was first proposed in the nineties of the last century. Wong A.P.Y. and Wiltzius P. (1993) utilized the scattered light at the same scattering angles on the same ring in a CCD sensor. The space-averaged information was used instead of time averaging, which greatly reduced the measurement time. Kirsch S. et al. (1996) collected the scattered light by a CCD camera at nearly identical scattering vectors. The CCD sensor was equivalent to an array of conventional photon sensors. The measurement accuracy was improved since sequential results of different pixels were averaged based on the conventional time average. However, limited by the frame rate of cameras, the above experiments (Kirsch S. et al., 1996; Wong A.P.Y. and Wiltzius P., 1993) were carried out in pure glycerol as dispersion medium, in which Brownian motion of the nanoparticles was very slow.

In addition, Dynamic Light Scattering Microscopy was proposed by Dzakupas R. and Axelrod D. (2004). A progressive scan CCD was used and exposure through a column of the CCD array was adopted. The rapid access to time- and space- sequence signal of dynamic light scattering was realized. That caused an equivalent effect as increasing of frame rate. In this work, the method was used for nanoparticle sizing in water. Zakharov P. et al. (2006) carried out theoretical and experimental researches in order to suppress complex scattering problems in DLS measurements with the CCD camera.

As the rapid development of computer technology and imaging technology in recent years, the high-speed camera with tens of thousands of frames per second (fps) is available. On the other hand, the developed AOI (area of interest) function in general industrial camera can greatly improve the frame rate by reducing image size. It provides the possibility of nanoparticle sizing in water. In this paper, we are mainly focused on the development of DLS method using image sensors. Three different data processing algorithms were reviewed here for image-based DLS (IDLS) method. The first one is based on the

traditional time-based autocorrelation function. The second one is also based on autocorrelation function but with two-dimensional image cross-correlation. The third one is based on one cross-correlation coefficient between two images in a certain time interval, without the autocorrelation functions. A high-speed camera was used in experiments and the scattered light signal in two-dimensional space, as well as in time series were acquired. Images were manipulated in comparison of the three different data processing methods.

In addition to DLS, the ultrasonic attenuation spectroscopy (UAS) method is also considered to be very promising as a rapid on-line measurement technology for nanoparticle suspension system, which has advantages of simple structure, non-invasive and on-line measurement and being available to relatively dense suspensions.

In the field of theoretical modelling and experimental validation involved, Challis R.E. et al. (2005), Povey M.J.W. (2013) and McClements D.J. and Coupland J.N. (1996) conducted intensive studies from numerical calculation problems of the ECAH model based on scattering theory to the simplification for long wave limit, as well as experimental validations. Hipp A.K. et al. (2002) derived the Core-shell model which was suitable for high concentration conditions. Starting from the elastic ultrasound scattering of particles and by introducing Lambert-Beer principle based on an analogy to the Mie theory in light scattering, Riebel U. (1992) developed a model for large solid particles to depict the particle-wave interactions, including entrainment, scattering, and resonances in the short-wavelength regime. He also concluded theoretically the proper order of importance for high concentration systems as (i) steric, (ii) dependent scattering, and (iii) multiple scattering. Dukhin A.S. and Goetz P.J. (1996) and Dukhin A.S. et al. (1996) presented the coupled-phase model, in which, the Happel cell model was exploited to calculate the drag coefficient and a friction coefficient proportional to the volume fraction was introduced to describe the relationship between the gradient of pressure and the relative speed between the particle and the medium. The resultant DT Series commercial instruments were then released by combining acoustic and electro-acoustic spectroscopy, whose greatest feature is being suitable for measuring highly concentrated colloidal particles which have been able to extend the volume fraction to 30 % or even more. Applications to a wide variety of materials were introduced too. Evans J.M. and Attenborough K. (2002) extended the coupled-phase model by way of including irreversible heat transfer and visco-inertial forces, based on the volume-averaged balance equations. They compared the predictions of the core-shell model and the extended coupled-phase model with measurements of ultrasonic velocity and attenuation in two different emulsions for volume fractions up to

70 %, which showed both models were in good agreements with the experimental results. Recently, Challis R.E. and Pinfield V.J. (2014) proposed a novel way to describe the ultrasonic wave propagation in concentrated slurries, in which a simple effective medium modification to the ECAH/LB was put forward to reflect the hydrodynamic effects involved, while it did not yet cause expected coincident results with those of the core-shell models.

In the characterization of ultrafine particles with UAS, Mougin P. et al. (2001) conducted an in-situ examination of solution phase crystallization processes on two organic compounds: urea and (L)-glutamic acid, in which ultrasonic attenuation spectra were measured by a commercial ultrasonic spectrometer (Ultrazizer by Malvern Instruments Ltd.) with two pairs of transducers operating over a frequency range from 1 MHz to 150 MHz. The experiment was carried out during a cooling process with temperatures from 50 °C to 15 °C (−0.4 °C/min), in which the particle sizes (median diameter 0.023–130.8 μm) and concentrations (0.1–0.81 vol %) were monitored continuously. Hou H. et al. (2010) measured an ultrafine ZnO-H₂O suspension with a mean size of approximately 200 nm, in which a variable-path method and the short-time Fourier transform have been adopted to obtain and extract ultrasonic attenuation spectrum and phase velocity synchronously. Wang X.Z. et al. (2009) carried out the on-line characterization of nanoparticle suspensions using dynamic light scattering, ultrasound spectroscopy and process tomography simultaneously. A silicon nanoparticle (70–100 μm in diameter) suspension with initial volume concentration of 24 % was diluted to prepare a series of samples with eight different concentrations as low as 0.8 vol %, thus the measurement of particle size distribution was implemented at different concentrations, and analysis was highlighted on nonlinear effects of the concentration on the final results. Furthermore, a modification (Liu L., 2009) was presented that in ultrasound particle sizing, factor analysis as a method of dealing with multivariate data can be applied to ultrasound spectra to extract the information of linear dependence of attenuation on concentration and the contribution of frequency to attenuation. On the basis of this work a closed-loop control system was further built to measure and control process parameters (Boonkhao B. and Wang X.Z., 2012).

In this paper, researches of UAS method for nanoparticle sizing are particularly focused on, including the following issues: theories and models for ultrasonic attenuation prediction; inversion method for solving particle size; ultrasonic signal transmission and detection technology. In order to clearly distinguish the ultrafine particles, high-frequency broad-band ultrasonic signals are critical to be utilized, which causes higher requirements from the theoretical model calculation to ultrasound generating and receiving technology.

The rest of this paper is arranged as follows. First, detailed reviews of IDLS and UAS for particle sizing are executed, respectively, including measurement principles, data processing, measuring apparatus, and validations experiments using polystyrene particles with various sizes. Then we focus on the characterizations of nanoscale silver and Antimony Tin Oxide (ATO) particles using IDLS and UAS, comparisons and analyses are then executed to come to the final conclusions.

2. Dynamic light scattering

2.1 Measurement principles and data processing

The principle of particle size measurement by DLS technique is based on the Brownian motion of nanoparticles (King T.A., 1989; Thomas A.J.C., 1991; Tscharnuter W., 2006). For spherical nanoparticles dispersed in solutions, the relationship between diffusion coefficient D_T of the Brownian motion and particle diameter D can be given by Stokes-Einstein equation:

$$D_T = \frac{K_B T}{3\pi\mu D} \quad (1)$$

where, K_B is the Boltzmann constant, T is the absolute temperature and μ is the dynamic viscosity of the dispersion medium. D_T is determined using DLS technology by analysing the scattering signal from nanoparticles, which is illuminated using coherent light beam. The scattering light fluctuate randomly in relation with Brownian motion. Smaller particles move faster and the fluctuation of scattered light intensity is also faster. For monodisperse system, the following autocorrelation function (Tscharnuter W., 2006) can characterize such a steady fluctuation.

$$g^{(2)}(\tau) = 1 + \beta \exp(-2\Gamma\tau) \quad (2)$$

where, τ is the time delay between signals, β is an instrumental constant between 0 and 1. The decay constant Γ is related to the diffusion coefficient of the particles D_T by

$$\Gamma = D_T q^2 \quad (3)$$

where, q is the norm of scattering vector, which indicates the difference between wave vector of the scattered light and the incident light. It is related to the refractive index of the dispersion medium n , the scattering angle θ and the wavelength λ of light by

$$q = \frac{4\pi n}{\lambda} \sin\left(\frac{\theta}{2}\right) \quad (4)$$

2.1.1. IDLS with conventional autocorrelation function

To exploit the information of decay constant Γ and dif-

fusion coefficient D_T from one-dimensional fluctuation information of scattered light $I(t)$, the intensity autocorrelation function will be fitted according to Eqn. 5 as conventional DLS data processing method.

$$G(\tau) = \langle I(t)I(t+\tau) \rangle = \frac{1}{N} \sum_{i=1}^N I(t_i)I(t_i+\tau) \quad (5)$$

In order to obtain reliable and accurate result, averaging was adopted on a large number of time-series data, since the fluctuation goes in a random way. It needs a long time for both data acquisition and data processing. The typical measurement time for the current conventional DLS particle sizer is generally 1–2 minutes, which is difficult to meet the requirements of real-time and online measurement for rapidly changing process. Since the Brownian motion of particles is sensitive to the temperature, a temperature control device is necessary in conventional DLS. It can be generally applicable to off-line analysis in laboratory.

IDLS is proposed to capture the information of Brownian motion using an image sensor (Wang Z.Y. et al., 2014; Xu C.Z. et al., 2015). One pixel or several pixels of the sensor is equivalent to one photomultiplier tube. There are generally hundreds of thousands to millions of pixels in one image sensor. As shown in **Fig. 1**, the image is divided into $i \times j$ grids, which is equivalent to $i \times j$ photomultiplier tubes. $i \times j$ time-series of light intensity signals will be obtained simultaneously. Eqn. 5 will be used to calculate the averaged autocorrelation functions and particle size D , or averaging can also be taken on the results $D_{i,j}$ from each autocorrelation function. This takes the place of conventional averaging on autocorrelation functions from a long time-series signal, so the data acquisition time can be reduced dramatically.

But from the perspective of data processing, the present IDLS still needs a sufficient amount of data and a long processing time to ensure a high accuracy of statistical results. Moreover, as for solutions with low viscosity or small particles, higher requirements are expected on the frequency of image acquisition, which is in other words

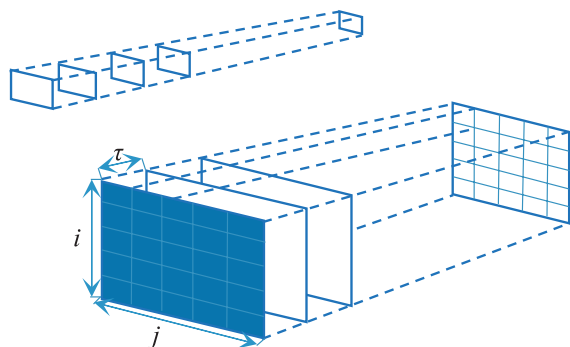


Fig. 1 Images division for data processing (Xu C.Z. et al., 2015).

the frame rate of the camera.

2.1.2. IDLS with ACF from image cross-correlation

Autocorrelation function of discrete-time signals characterizes the similarity between interval signals. It is obtained by correlation processing between one-dimensional signals in a certain time interval. In IDLS method, a camera can capture two-dimensional spatial distribution of light intensity as images, whose similarity can be obtained by image cross-correlation as Eqn. 6.

$$G(\tau) = R(A(m,n), B(m,n)) = \frac{\sum_m \sum_n (A_{m,n} - \bar{A})(B_{m,n} - \bar{B})}{\sqrt{(\sum_m \sum_n (A_{m,n} - \bar{A})^2)(\sum_m \sum_n (B_{m,n} - \bar{B})^2)}} \quad (6)$$

Where, τ is the time delay between two images A and B, both of which have $m \times n$ pixels. That is to say, for a time-series of images, the 2D ACF values at different time delays can be determined by cross-correlation processing between images at the corresponding time delays, such as between the 1st image and the 2nd one, the 1st and the 3rd ... and the 1st and the last one (Liu L.L. et al., 2015; Zhou W. et al., 2015).

Considering three different sizes (79/482/948 nm) of standard polystyrene particles, the theoretical time-dependent autocorrelation functions with $\beta = 1$ can be calculated from Eqn. 1–4, as illustrated in **Fig. 2**. It shows that the autocorrelation function values decrease from 1 to nearly 0 in approximately 2 ms, 20 ms and 40 ms, respectively, for the three sizes of particles. Values close to 0 after the respective times have small effects on the curve fitting. As long as the frame rate of the camera is high enough to characterize the light intensity fluctuation, the data acquisition time will be shortened to be about 2 ms, 20 ms and 40 ms, respectively. If the images are captured in the frame rate of 10000 fps, the number of images required to cover the typical time-scales in auto-

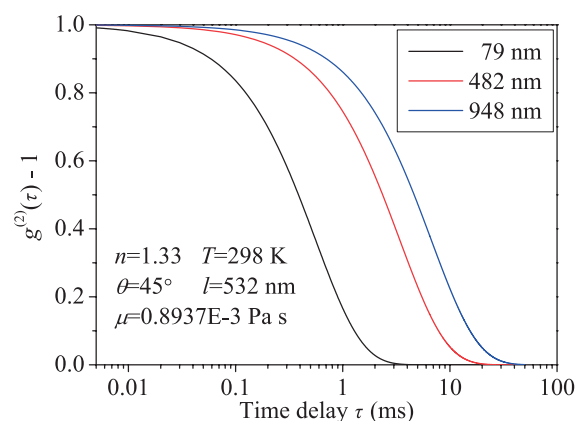


Fig. 2 Theoretical ACF for nanoparticles of different sizes in water (Liu L.L. et al., 2015).

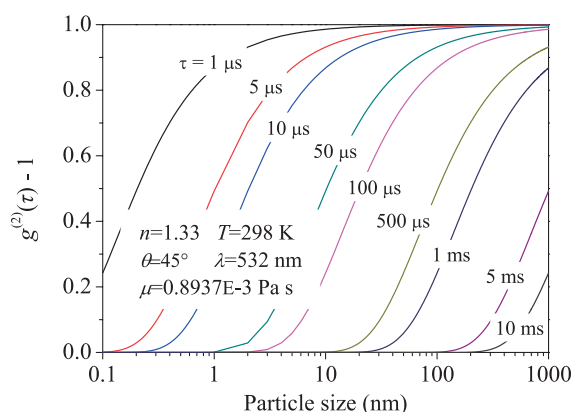


Fig. 3 Variation of theoretical ACF value as particle size at different delayed times (Zhou W. et al., 2015).

correlation function curves should be about 20, 200 and 400 frames. The time intervals between the 1st image and any other image are the corresponding time delays in the 2D ACF. Conventional DLS acquires one value at a time, requiring a longer time-series data to get an averaged result. IDLS utilizes the information on two-dimensional space and the cross-correlation coefficients between images are space-averaged values.

2.1.3. IDLS by one cross-correlation coefficient without ACF

As shown in **Fig. 2**, under the same time delay, the 2D ACF is a monotonically decreasing function of particle size. Larger particles lead to greater correlation coefficient. So the particle size may be determined by one correlation coefficient, which can be obtained by cross-correlation of two-dimensional light intensity signals in a time interval. **Fig. 3** illustrates the variation of correlation coefficient, in another word theoretical ACF value, as particle size under different time delays (from 1 μ s to 10 ms), with the same conditions as **Fig. 2**. It indicates that the data acquisition time can be shortened to the acquisition time of two images, and the data processing time is shortened to the time needed for cross-correlation of these two images.

It should be noticed that the measuring error can be diminished by selecting a proper time interval to maintain a moderate correlation coefficient, since higher accuracy can be achieved at larger slopes of the curves. It shows from **Fig. 3** that more accurate results can be acquired from correlation coefficient in the range 0.15–0.85. Take 200 nm particles for example, the time interval should be in the range from 100 μ s to 2 ms. There are also other parameters, such as scattering angle and laser wave length, which can be adjusted to achieve moderate correlation coefficient.

2.2 Experimental system

Experimental setup was developed to validate and

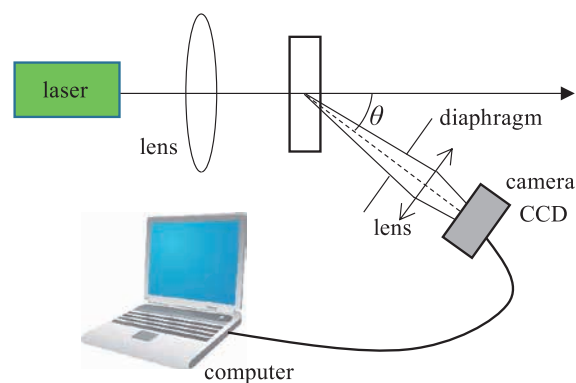


Fig. 4 Schematic drawing of IDLS experimental setup.

compare the above mentioned methods. Schematic drawing of the experimental setup is shown in **Fig. 4**. The measurement system included light source, lenses, sample cell, diaphragm iris, high-speed camera and computer. A green laser diode at 532 nm with 50 mW continuous wave output was used as the light source. The laser beam was focused in the sample cell, just as other commercial DSL nanoparticle sizer has done. The scattered light from the nanoparticles was collected by a lens with focal length of 60 mm. An adjustable diaphragm was applied to define the measured region, with an opening diameter of 0.8 mm in the experiments. Limited scattered light was recorded by a high-speed camera (MotionProX3), instead of a photomultiplier tube in conventional DLS. The camera has an 8-bit CMOS sensor with total effective area of $15.4 \times 12.3 \text{ mm}^2$ and one pixel area of $12 \times 12 \mu\text{m}^2$. The camera was fixed at a 45° angle with the incident light during the experiments.

To avoid the influence of multiple scattering, the solutions were diluted sufficiently to the particle concentration of about 0.1 vol %. The tests were all carried out at room temperature, which was measured during experiments. To meet the requirement of repeatability and measurement accuracy, all of the measurements were repeated five times.

2.3 Validation of IDLS using standard nanoparticles

Standard polystyrene particles (manufactured by Beijing Haianhongmeng Reference Material Technology Co., Ltd.) with three different sizes (79/482/948 nm) were used for validation of the proposed data processing methods. Accuracies were analysed respectively and the measurement times were compared.

2.3.1. Results using conventional ACF

It was noticed from the captured images that the scattering speckle size was about equal to the size of 4×4 pixels in our experiments. The speckle size is also called as one

Table 1 Measured results of standard nanoparticles in different dispersion mediums at different frame rate (Wang Z.Y. et al., 2014)

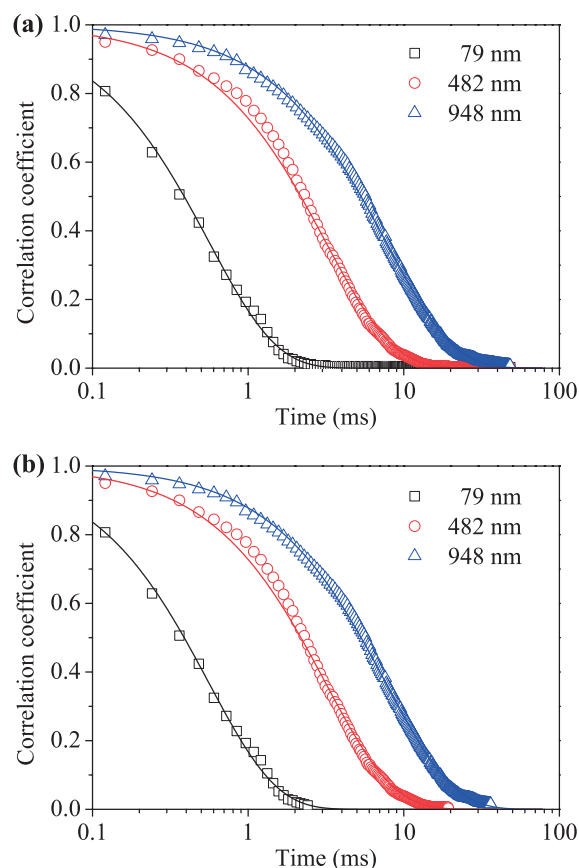
D_N (nm)	Dispersant Frame rate	Distilled water		55 % glycerol water solution					
		8290 fps		8290 fps		4000 fps		2000 fps	
		D_M (nm)	Error (%)	D_M (nm)	Error (%)	D_M (nm)	Error (%)	D_M (nm)	Error (%)
79		74.3	5.9	80.3	1.6	82.3	4.2	84.6	7.1
482		441.7	8.4	485.6	0.8	465.8	3.4	462.5	4.1
948		989.8	4.4	—	—	957.1	0.1	926.5	2.3

“coherence area” or one spot. So the images were divided into grids of the same size of 4×4 pixels. One grid is equal to one photomultiplier tube and one mean size value can be determined from the corresponding time-series intensity fluctuation. Averaged value on all the grids was taken as the final result. First the samples were tested in distilled water using a frame rate of 8290 fps at 200×128 resolution. That is the maximum frame rate of the camera employed here at that resolution. 2000 images were captured continuously in 0.24 s at a time. As shown in **Fig. 2**, 0.24 s is long enough to cover the typical time scale of the ACF for these three samples. The final results are illustrated in **Table 1**. It shows that even the minimum measurement error can reach 4.4 % at 8290 fps in distilled water. The reason is that not enough efficient signals were captured in the typical time scale, especially for small particles. Camera with higher frame rate should be used to improve the accuracy.

However, according to Eqn. 1, the diffusion coefficient of nanoparticles was dependent with the viscosity of dispersion medium. Larger viscosity leads to smaller diffusion coefficient, which can increase the timescale of the autocorrelation function and improve measurement accuracy. Glycerin is a Newtonian fluid with high viscosity, and it is easy to be mixed with water at any ratio. In this work, the glycerol water solution of 55 % mass concentration was adopted as another dispersion medium. The viscosity increased from 0.87×10^{-3} Pa·s in water to 6.15×10^{-3} Pa·s in glycerol-water solution. The measurement results were largely improved at the same frame rate as shown in **Table 1**. No result was obtained for 948 nm particles in glycerol since the Brownian motion was too slow to be detected. In order to investigate the influence of frame rate, tests were also carried out at 4000 fps and 2000 fps in 55 % glycerol-water solution. It shows that the accuracy decreases as the frame rate reduces. In conclusion, the measurement accuracy may be improved by increasing the viscosity of dispersion medium but IDLS using conventional ACF method is greatly affected by the frame rate of the camera.

2.3.2. Results using ACF from image cross-correlation

According to the method described in section 2.1.2, the cross-correlation coefficients between images in a time


Fig. 5 Cross-correlation coefficient and corresponding fitted ACF curves. (a) by 400 images each; (b) by 20, 160 and 300 images, respectively, for 79, 482, 948 nm particles.

series were calculated to compose the ACF curves, as shown in **Fig. 5**. Particles were tested in distilled water at 8290 fps. **Fig. 5(a)** shows fitted ACF curves using 400 images for all the samples. Results in **Table 2** show a higher accuracy as compared with the results in section 2.3.1 at the same conditions, but using less image data. It was caused by grid division in the previous method. The divided grid size was an estimated value, which should be actually different in different locations of the images. The latter method does not require grid division.

Fig. 5(b) shows ACF results using 20, 160, and 300 images, respectively, for 79, 482, 948 nm particles. There is no change in the shape of ACF curves. It indicates that a

Table 2 Measured mean sizes from ACF by image cross-correlation (Liu L.L. et al., 2015)

D_N (nm)	D_M (nm)	Error (%)
79	77.3	2.15
482	452.6	6.10
948	982.4	3.63

certain result can be determined with images captured in the typical time scale duration, which dramatically reduced the acquisition time. In our experimental conditions, the acquisition time were shortened to about 2, 20 and 40 ms, respectively.

2.3.3. Results using one cross-correlation coefficient without ACF

Using the same series of images captured in section 2.3.2, nanoparticle size can be determined from one cross-correlation coefficient between two images in a certain time interval. Two time intervals, 0.25 ms and 0.5 ms, were investigated in our experiments for three different samples, 79/482/948 nm, respectively. The mean particle size can be calculated directly from corresponding cross-correlation coefficient with Eqn. 1–4. Theoretical ACF curves at the above two time intervals and corresponding coefficients are all illustrated in Fig. 6.

The measured results are shown in Table 3. It shows that the measured mean particle size D_M agrees well with corresponding nominal size D_N . The respective relative errors are generally small. It can also be noticed that, with other conditions remaining the same, coefficients at larger slope on the ACF curves lead to higher sensitivity. Take the time interval of 0.5 ms for example, it costs 1 ms to acquire a couple of images and less than 10 ms to process them using a notebook with i7-3612QM quad-core processor. It shows that the acquisition and processing time are both significantly reduced, compared with hundreds seconds in traditional DLS.

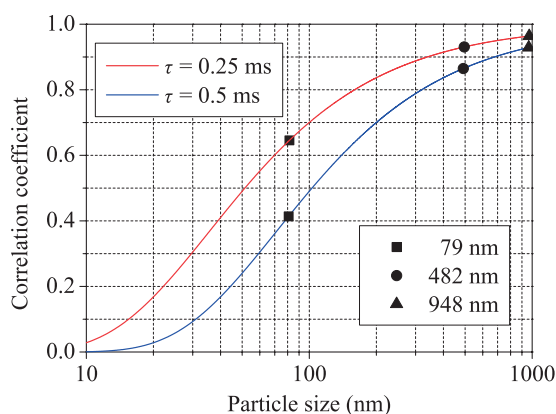

Fig. 6 Mean particle size determination from one cross-correlation coefficient.

Table 3 Measured results using one cross-correlation coefficient

$\tau = 0.25$ ms			$\tau = 0.5$ ms		
D_N (nm)	D_M (nm)	Error (%)	D_N (nm)	D_M (nm)	Error (%)
79	81.5	3	79	80.8	2.3
482	495.6	2.8	482	490.3	1.7
948	970.2	2.3	948	965.7	1.9

3. Ultrasonic attenuation spectroscopy

3.1 Measurement principles

The interaction between ultrasonic beams and particulate two-phase flow is a quite complicated process, in which the sound scattering phenomena must be taken into account in the first place. By assuming small particles as elastic objects, it can be analogous to the light scattering to reach some similar deduction, and certainly the shape of particles, the types of ultrasonic beams and incident angles, as well as the ratio between sound wavelength and particle size could be significant for the description of sound scattering. The analytic solution can usually be obtained for those regular-shaped particles like a sphere, while for more irregular particles the analytic solution is rarely available up to now. Ye Z. et al. (1997) has performed quite a few numerical investigations on acoustic scattering for non-spherical objects from gas, to weak fluid and rigid spheroids, as well as the multiple scattering problems from an ensemble of scatterers (Alvarez A. et al., 1999). However for more cases, a numerical solving method must be relied on. For example, the boundary element method (BEM) can be employed for some special cases like the scattering sound pressure calculation for one or several irregular particles, which could bring us a helpful estimation for the shape effects on sound scattering directive properties and scattering cross section. Except scattering, there are still several important interaction behaviors, relevant with the viscous and thermal dissipations. A further observation of the aforementioned phenomena can help us find obvious intrinsic differences in that the sound scattering merely causes the redirection of acoustic energy away from the incident beam, while the dissipations essentially give rise to the conversion from acoustic energy to heat. Dukhin A.S. and Goetz P.J. (2001) has already pointed out that in fact the scattering and dissipations can be divided into two separated components and analyzed independently, which actually facilitated the understanding of acoustic loss and simplified the mathematical modelling. Typically, a complete mathematical model is still quite necessary in describing all these physical phenomena and establishing the rigorous

relationship between the particle size and the ultrasonic attenuation spectra. Fortunately, much work has been done by quite a few researchers as mentioned in the previous section, among which, the thinking of Epstein P.S. and Carhart R.R. (1953) will be cited in particular to demonstrate a typical procedure of particle sizing.

3.1.1. Ultrasonic attenuation model and calculation

When modelling the interaction between particles and the surrounding sound waves, Epstein P.S. and Carhart R.R. (1953) focused on acoustic scattering and attenuation by droplets suspended in the air. Allegra J.R. and Hawley S.A. (1972) further extended EC's model to solid particles and unified the formulization of ultrasound scattering for particle sizing by fulfilling the ECAH model. As a typical linear scattering theory, their theoretical model fully accounted for the influence on acoustic waves of mixture stickiness and heat dissipation, which coupled to the scattering in the form of viscous waves and heat waves, respectively. By solving the complex wavenumber, the macroscopic phenomena like ultrasonic attenuation and phase shift are judiciously connected with the microscopic process like the interaction between a single particle and surrounding waves. Some numerical validations and predictions were introduced in the previous papers (Su M. and Cai X., 2002; Tebbutt J.S. and Challis R.E., 1996), and an example was stressed to demonstrate the application of the theoretical model for the submicron droplet characterization by using ultrasonic attenuation and phase velocity spectra simultaneously (Su M. et al., 2009).

For a poly-dispersed particle system, the ECAH derived expression for the attenuation coefficient α_s can be given as:

$$\alpha_s = \frac{3\varphi}{16k^2} \sum_{j=1}^N \frac{q_j}{D_j^3} \sum_{n=0}^{\infty} (2n+1) \text{Re}(A_n(D_j, f)) \quad (7)$$

where φ denotes the volume fraction of particles. k is the wavenumber of incident compression wave. D is the diameter of the particle. q_j is the frequency distribution of particles with radii between D_j and D_{j+1} . The summation of series of the compression wave-scattering coefficients A_n (a function of particle diameter D and ultrasonic frequency f) plays the key role for the calculation of the frequency-dependent attenuation coefficients. The solution of A_n finally reduces to a six-order complex linear equations, whose coefficient matrix elements is composed of spherical Bessel and Hankel functions with complex variables as arguments. With the complex argument, a linear increase of the imaginary part of the input parameter leads an exponential variation of these functions. The matrix condition number increases accordingly and the solution of linear equations has numerical instabilities. When function overflow appears for large argument, numerical

matrix solving will fail frequently. The existence of above-mentioned problems seriously confines the applicable range of the ECAH model in numerical implementation in aspects of frequencies and particle size. Pinfield V.J. et al. (2005) once proposed a recurrence relation of Bessel functions involved to express the incident wave in a simulation of acoustic propagation in dispersions. A modified algorithm has also been proposed in detail to fully overcome such a numerical instability problem (Su M. and Cai X., 2002). Avoiding the direct use of Hankel function and constructing new related variables, recurrence relations of both Bessel and Hankel functions are as following:

$$F_n(z) = \frac{2n-1}{z} F_{n-1}(z) - F_{n-2}(z) \quad (8)$$

$$F'_n(z) = F_{n-1}(z) - \frac{n}{z} F_n(z) \quad (9)$$

where z is the argument for Hankel function and n is the order. Several related variables and their derived recurrence formula are introduced.

$$L_n(z) = \frac{F'_n(z)}{F_n(z)} = \frac{F_{n-1}(z)}{F_n(z)} - \frac{n}{z} = \frac{1}{M_n(z)} - \frac{n}{z} \quad (10)$$

$$Q_n(z) = \frac{F''_n(z)}{F_n(z)} = \frac{n-1}{z} \frac{1}{M_n(z)} - \frac{n+1}{z} L_n(z) + \left(\frac{n+1}{z^2} - 1\right) \quad (11)$$

where variable $M_n(z)$ is

$$M_n(z) = \frac{2n-1}{z} - \frac{1}{M_{n-1}(z)} \quad (12)$$

And

$$\begin{cases} M_0(z) = \text{TAN}(z) & \text{for Bessel function} \\ M_0(z) = -i & \text{for Hankel function} \end{cases} \quad (13)$$

The dependence of these variables on the increase of the variable z is demonstrated in **Fig. 7**, which shows that as complex variables increase, the spherical Hankel function and its derivative rapidly decrease toward zero, while the newly constructed variables $L_n(z)$ and $Q_n(z)$ tend to 1 in the end. That is to say, they can be used safely to replace the Hankel function to reduce the condition number and avoid the potential numerical overflow, which is quite crucial for the increase of dimensionless parameter (i.e., a very high frequency). **Fig. 8** illustrates the numerical results using the improved method. It manifests that calculation range extends to the ultrasonic frequency 1~100 MHz with the particle size 1 nm~1000 μm , which indeed covers the major particle size range under poten-

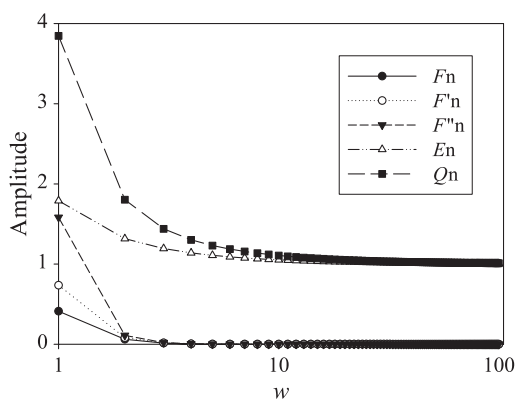


Fig. 7 Variation of different variants with arguments ($n = 1$, $z = w(1 + i)$).

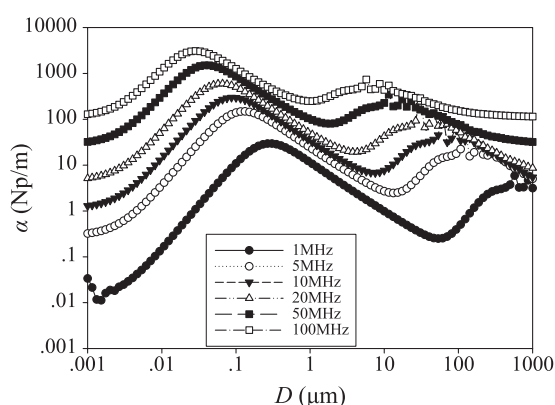


Fig. 8 Predicted ultrasonic attenuation coefficients against particle diameter (0.5 vol % silver aqueous suspension).

tial investigations, although particles outside this range have also been successfully measured. At the same time, it can be observed that the attenuations grow gradually with the increasing frequency. For a fairly small frequency like 1 MHz, a sensitive peak can be found for particles in the submicron range (i.e. 100 nm~1000 nm) due to dissipation mechanism, which indicates the ultrasonic signal would vary with the particle size seriously. With the increasing of frequency, the peak moves towards the smaller particles direction. Thus a broader frequency range can undoubtedly contain more information about the particle size, accordingly in favor of the improvement of resolution of particle sizing.

3.1.2. Data inversion for ultrasonic attenuation

Generally, the inversion algorithms to determine particle size distribution have been classified into two types: dependent and independent modes. The dependent mode algorithm assumes that the particle system to be measured conforms to one or two given size distribution functions, e.g. lognormal or Rosin-Rammler (Allen T., 2003), which are usually characterized by two (unimodal distribution assumption) or five (bimodal distribution assumption) pa-

rameters to be determined by optimization. So far as we know, the BFGS (Broyden-Fletcher-Goldfarb-Shanno) and DFP (Davidon-Fletcher-Powell) are two significant algorithms to perform the optimization process determining the particle size distribution, although they both possess the drawback that optimization might be trapped into the local optimized solutions instead that the global one.

Unlike the competitor, the independent mode algorithm does not assume *a priori* particle size distribution. The particle size solution is obtained directly by solving the Fredholm integral equations discretized into matrix form. By rewriting Eqn. 7 according to its discrete form, the linear equations can be generated in the following form:

$$\frac{3\varphi}{16} \cdot \int_{\Delta D} \frac{1}{k_c^2 D_j^3} \sum_{n=0}^{\infty} (2n+1) \text{Re}(A_n(D_j, f_i)) \cdot dD \cdot \underbrace{\sum_i q(\Delta D_i)}_{\mathbf{q}_i} = \underbrace{a_s(f_i)}_{\mathbf{p}_i} \quad (14)$$

where \mathbf{A} is the coefficient matrix and \mathbf{q} is the discrete particle size frequency distribution, the solution vector. The array \mathbf{p} is the experimental spectrum. It must be noted that the matrix is invariably ill-posed. In addition, solution to such an equation group must obey the non-negative constraint. It requires a regularization method (also known as Twomey algorithm) in order to give stable and real solution \mathbf{q} to ill-posed problems (Tikhonov A.N. and Arsenin V.Y., 1977; Twomey S., 1977).

$$\mathbf{q} = (\mathbf{A}^T \mathbf{A} + \gamma \mathbf{H}) \mathbf{A}^T \mathbf{p} \quad (15)$$

where, \mathbf{H} is the smooth matrix. Furthermore, an Optimum Regularization Technique (ORT) (Brandolin A. et al., 1991) has been put forward by selecting an optimum regularization factor γ_{opt} and appropriately introducing a set of basic cubic splines to reconstruct the distribution in each size bin, which can contribute to reducing the condition number of the coefficient matrix and be beneficial to the smoothness of the solution vector, without altering the linearity characteristic of equations. In fact, the ORT method can be further developed by choosing of an optimized regularization factor γ_{opt} which serves as a balance between the smoothness of the PSD solution and the fitting of the reconstructed spectrum. This has been confirmed in particle sizing using light extinction measurement (Su M. et al., 2007) by introducing the L-curve method (Hanson P.C., 1992), and particle sizing in dense two-phase droplet systems using ultrasonic attenuation and velocity spectra by introducing the Generalized Cross-Validation (GCV) criterion (Su M. et al., 2009).

3.2 Experimental Measurement System

For the purpose of measuring the ultrasonic spectrum based on the insert-substitution method with variable-path

mode (ISO20998-1:2006), an experimental set-up has been developed for acquisition of broad-band ultrasonic signals. As shown in **Fig. 9**, signals were generated and detected by a PR-5800 ultrasonic pulse-echo transmitter/receiver (Parametric, Inc) working with two pairs of broad-band transducers, whose center frequencies were 10 MHz (V312-SU) and 25 MHz (V324-SU), respectively. According to the insert substitution method, the samples under study were injected into two cubic sample cells with thickness of $l_1 = 10$ mm and $l_2 = 20$ mm respectively. Afterward, they encountered successively ultrasonic waves generated from the transducer and the attenuated ultrasonic waves were received by the other transducer on the other side. Temperature of the samples was stabilized at room temperature during the testing to eliminate possible interference on ultrasonic waves.

Two typical ultrasonic time-domain signal are showed in **Fig. 10**, which indicates evidently the differences in amplitude and phase between pure water (for calibration) and the sample suspension. An amplitude spectrum was obtained after processing the raw signal through fast Fourier transform (FFT). Correspondingly, the attenuation could be calculated by path-variation measurement:

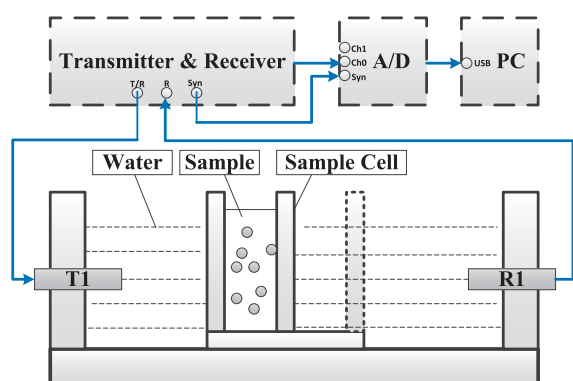


Fig. 9 Sketch map of measurement system.

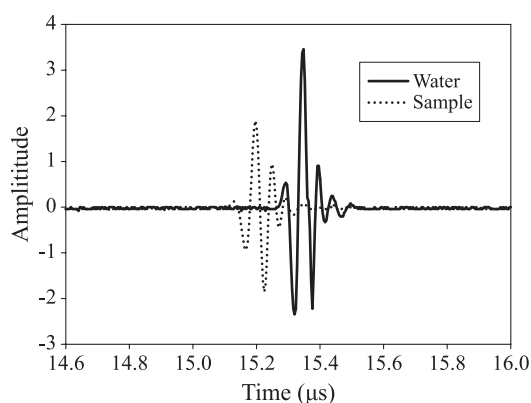


Fig. 10 Ultrasonic pulse signals of water and the sample suspension.

$$\alpha_l = \frac{\ln(A_1 / A_2)}{l_2 - l_1} + \alpha_w \quad (16)$$

where A_1 and A_2 are the amplitude spectra of ultrasonic signals at the sound path length l_1 and l_2 , respectively. α_w is the sound absorption of water.

4. Measurement of polydisperse nanoscale particles

4.1 Nanoscale silver particles

Practical nanoscale silver particles were measured by IDLS using one correlation coefficient and UAS combined with the ORT algorithm, respectively. The nominal mean size was claimed as 20 ± 2 nm by the manufacturer (Shanghai HuZheng Nanotechnology Co., Ltd.).

During IDLS measurement, samples were dispersed in the 75 % glycerol water solution, since the frame rate of the camera used in our work cannot meet the requirement when using water. The viscosity of 75 % glycerol-water at 298 K is 0.03162 Pa·s, which is two orders of magnitude higher than that of water. The refractive index of 75 % glycerol-water is 1.42. Other experimental parameters were set the same as section 2.2. The glycerol-water solution makes it feasible to measure small particles using a lower frame rate. Take the time interval of 1 ms in the measurement, the calculated cross-correlation coefficient is 0.821. Theoretical ACF curve at the delay time of 1 ms is displayed in **Fig. 11**. The particle size corresponding to coefficient of 0.821 is 23.15 nm, which is the measured mean size for the sample of nanoscale silver particles.

The experimental setup and measurement conditions in UAS were introduced in section 3.2, where high frequency ultrasound was adopted. Before testing, the aqueous suspension with 0.5 vol % silver particles experienced a 2-minutes sonication process (FS-300, Shanghai Sonix Ultrasonic Instrument Company). The PSD measured by UAS is illustrated in **Fig. 12**. Furthermore, the volume-based PSD of the same nanoscale silver particles is also represented in **Fig. 12**, which was extracted by analysing their TEM image indicated in **Fig. 13**. It is obvious that the UAS yields a relatively broader size distribution than TEM. This is probably caused by the smoothness operation during the inversion of ultrasonic attenuation spectra to overcome the ill-posed problems inside. Looking back to the size of IDLS, it appears a slightly bigger value compared with the 19.2 nm (Dv_{50}) of UAS and 18.0 nm of TEM analysis. The authors infer that this is due to their rough surfaces slowing the velocity of Brownian motion, which leads to an overestimated result here.

The recovered spectrum and the measured spectrum for UAS are plotted in **Fig. 14**. A good consistence in tendency of variation can be found, while obvious deviations

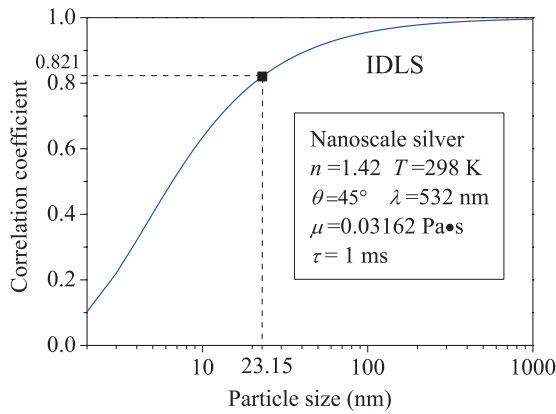


Fig. 11 Measured mean size of nanoscale silver particles by IDLS using one correlation coefficient.

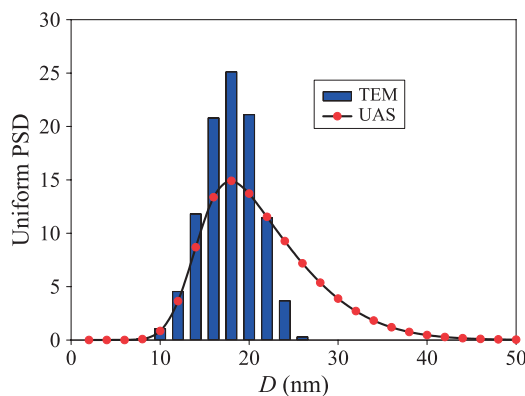


Fig. 12 PSD of the same nanoscale silver particles by UAS and TEM.

occur when the frequency exceeds 25 MHz, which can yield a relative deviation ($\sum \frac{|\alpha_M - \alpha_R|}{\alpha_M} / N$) of 18.2 % between the measured and recovered spectra. Authors inferred that it was likely due to the non-linear loss effect caused by the particle-particle interaction. Thus we calculated the mean distance h between two adjacent particles according to the Woodcock equation, which yielded a value of 71.0 nm (corresponding to the median size of 19.2 nm). Meanwhile the thermal and viscous skin depths (McClements D.J. and Coupland J.N., 1996) at 25 MHz were also provided as $\delta_T = 42.7$ nm and $\delta_V = 107.4$ nm for water. The comparison ($\delta_V > h$) shows that the viscous waves are very likely to exert an effect on the surrounding particles before vanishing, which makes the attenuation spectrum deviate from the prediction of the linear theory (ECAH model), especially over the range of higher frequency. Since the overall trend of recovered spectrum should satisfy the assumption of theoretical model which is merely sensitive to the overall trend, it does not cause significant effect on the inversed results even if the two attenuation values were lost. Thus to some extent such a deviation is acceptable.

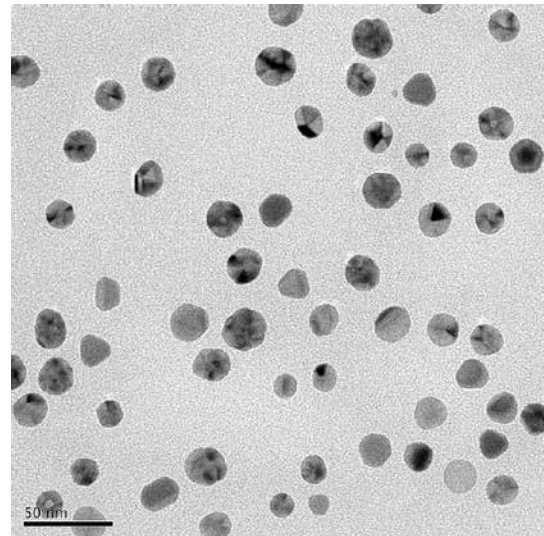


Fig. 13 TEM image of nanoscale silver particles.

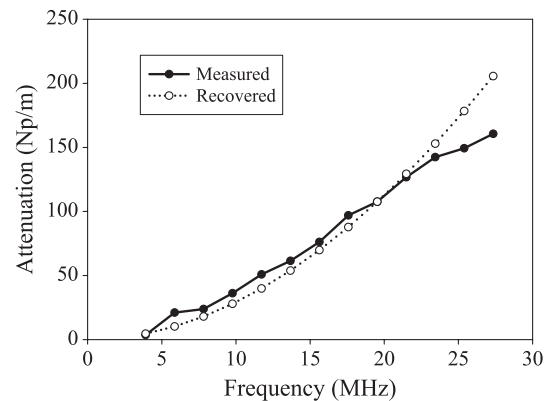


Fig. 14 Recovered and measured ultrasonic spectrum for suspensions of nanoscale silver particles.

4.2 Nanoscale ATO particles

Antimony Tin Oxide (ATO) nanoparticles, as one kind of the advanced materials, has been employed in many industry areas for its attractive properties, such as admirable thermal insulation, unparalleled dispersion, the active resistance, and high performance in wear resistance and safety.

The nanoparticle ATO sample in an aqueous suspension (2 vol %) adopted in our work is also provided by Shanghai HuZheng Nanotechnology Co., Ltd. The particle size distribution of ATO samples measured by ultrasonic attenuation spectrum is ranging from 14.3 nm to 40.6 nm (D_{v01} – D_{v99}), as shown in **Fig. 15**. And the volume median size D_{v50} is around 24.8 nm.

Using the same conditions described in section 4.1, ATO samples are also prepared and measured by IDLS method. To reveal the reliabilities and stabilities of the measurement, 500 couples of images were captured and processed to get 500 data in a very short time. The results

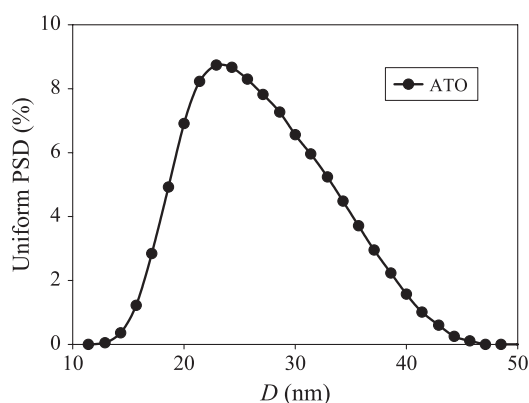


Fig. 15 PSD of nanoscale ATO particles by UAS.

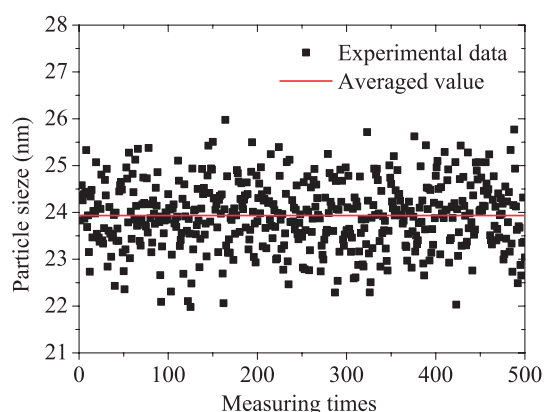


Fig. 16 Mean particle size of nanoscale ATO particles by IDLS.

are shown in Fig. 16, which has the averaged value of 23.9 nm and the standard error of 3.2 %.

According to the values of particle size, the measuring results of ATO samples by IDLS and UAS methods can be considered as in good agreement. However, it can be noticed that the small deviation exists with the results of nanoscale silver particles. The authors would like to clarify that in addition to errors caused by indirect solving algorithms like the mathematic inversion, various definitions and principles among methods could not be ignored when considering the aforementioned deviations. For example, the equivalent projection area diameter (Heywood diameter) is usually used for TEM. The UAS relies on the assumption of spherical sphere to fully interpret the sound scattering behaviour theoretically, which is similar with the IDLS, whereas the latter actually gets the diameter of a ball with the same characteristics of Brownian motion. Strictly speaking, all the principles are aimed at spherical particles, so the measuring results are unavoidably influenced by the sphericity, the surface roughness and other factors, which often exert different influences for different particle characteristics. For example the influences of sphericity on Brownian motion may be crucial compared

to that on ultrasonic attenuation. Consequently, the results presented here also reveal that the size information of nanoscale particles being adequately retrieved by different principles.

5. Final remarks

Two methods (DLS and UAS) with potential for development for nanoscale particles characterization were reviewed. The former is mainly focused on the researches using CCD cameras, which we called as image-based IDS. Three different image processing algorithms were reviewed in detail. At the same time, UAS was addressed to the problems of theoretical modelling (including numerical calculations involved), inversion and experimental signal acquiring and analysis for the broad-band spectrum. Then a sample of nanoscale silver particles with nominal mean size 20 ± 2 nm and ATO was measured by using IDLS, UAS and TEM. The results were reasonable and agreed well with each other. The IDLS method based on one correlation coefficient can avoid acquiring and processing a large number of data in conventional DLS and represent an advantage of ultrafast and stable testing. At the same time, the broad-band ultrasound contains available information on particle size, which can ensure a reasonable and stable result by combining the ORT algorithm. Thus, a potential ultrasound-based technique will be available to permit a fast and invasive measurement for concentrated nanoparticle suspensions without any dilution, where the non-linear effect must be considered carefully.

Acknowledgements

The authors gratefully acknowledge supports from the National Natural Science Foundation of China (51176128, 51576130, 51573093), the Shanghai Science and Technology Commission of China (13DZ2260900) and the Shanghai Municipal Education Commission (14CG46).

Nomenclature

ACF	Autocorrelation Function
DLS	Dynamic Light Scattering
IDLS	Imaged-based Dynamic Light Scattering
TEM	Transmission Electronic Microscopy
UAS	Ultrasonic Attenuation Spectroscopy
A_n	compression wave-scattering coefficients
D	particle size (nm)

D_N	nominal particle size (nm)
D_M	measured particle size (nm)
D_T	diffusion coefficient ($\text{m}^2 \text{s}^{-1}$)
F	Bessel/Hankel function
f	ultrasonic frequency
g	normalized autocorrelation function
G	autocorrelation function
h	mean distance between two adjacent particles (nm)
I	light intensity
k	incident compression wave wavenumber (m^{-1})
K_B	Boltzmann constant (J K^{-1})
l	sound path length (m)
L_n	complex variables related with the ration of the Bessel/Hankel functions and their first derivatives
M_n	complex variables related with the ration of the Bessel/Hankel functions and their second derivative
N	number of frequency in a discrete ultrasonic attenuation spectrum
n	refractive index (–) column number of image pixels (–) order in Hankel function
p	experimental spectrum, with element α_M
q	norm of the scattering vector (m^{-1}) frequency distribution
Q_n	complex variables in the recurrence formula of Bessel/Hankel functions
R	cross-correlation operator
t	time (s)
T	absolute temperature (K)
z	argument for Bessel/Hankel function
α_s	ultrasonic attenuation coefficient (Np m^{-1})
α_M	measured ultrasonic attenuation (Np m^{-1})
α_R	recovered ultrasonic attenuation (Np m^{-1})
β	instrumental constant (–)
Γ	decay constant (s^{-1})
δ_T	thermal skin depth (nm)
δ_V	viscous skin depth (nm)
θ	scattering angle ($^\circ$)
λ	wavelength (nm)
μ	dynamic viscosity (Pa s)
τ	time delay (s)
φ	volume fraction of particles (–)

References

- Measurement and characterization of particles by acoustic methods, part 1: concepts and procedures in ultrasonic attenuation spectroscopy, Switzerland, (ISO20998-1:2006).
- Allegra J.R. and Hawley S.A., Attenuation of sound in suspensions and emulsions: Theory and experiments, *Journal of the Acoustical Society of America*, 51 (1972) 1545–1564.
- Allen T., Powder sampling and particle size determination, Elsevier Science, Amsterdam, 2003.
- Alvarez A., Wang C.C. and Ye Z., A numerical algorithm, of the multiple scattering from an ensemble of arbitrary scatterers, *Journal Of Computational Physics*, 154 (1999) 231–236.
- Boonkhao B. and Wang X.Z., Ultrasonic attenuation spectroscopy for multivariate statistical process control in nanomaterial processing, *Particuology*, 10 (2012) 196–202.
- Brandolin A., García-Rubio L.H., Provedr T., Koehler M.E. and Kuo C., Latex particle size distribution from turbidimetry using inversion techniques, experimental validation, *ACS symposium series*, 472 (1991) 20–33.
- Challis R.E. and Pinfield V.J., Ultrasonic wave propagation in concentrated slurries—the modelling problem, *Ultrasonics*, 54 (2014) 1737–1744.
- Challis R.E., Povey M.J.W., Mather M.L. and Holmes A.K., Ultrasound techniques for characterizing colloidal dispersions, *Reports on Progress in Physics*, 68 (2005) 1541–1637.
- Donaldson K., Stone V., Clouter A., Renwick L. and Macnee W., Ultrafine particles, *Occupational and Environmental Medicine*, (2001) 211–216.
- Dukhin A.S. and Goetz P.J., Acoustic spectroscopy for concentrated polydisperse colloids with high density contrast, *Langmuir*, 12 (1996) 4987–4997.
- Dukhin A.S. and Goetz P.J., Acoustic and electroacoustic spectroscopy characterizing concentrated dispersions emulsions, *Advances in Colloid and Interface Science*, 92 (2001) 73–132.
- Dukhin A.S., Goetz P.J. and Hamlet C.W., Acoustic spectroscopy for concentrated polydisperse colloids with low density contrast, *Langmuir*, 12 (1996) 4998–5003.
- Dzakupas R. and Axelrod D., Dynamic light scattering microscopy. A novel optical technique to image submicroscopic motions. I: Theory, *Biophysical Journal*, 87 (2004) 1279–1287.
- Epstein P.S. and Carhart R.R., The absorption of sound in suspensions and emulsions: I. Water fog in air, *The Journal of the Acoustical Society of America*, 25 (1953) 553–565.
- Evans J.M. and Attenborough K., Sound propagation in concentrated emulsions: Comparison of coupled phase model and core-shell model, *The Journal of the Acoustical Society of America*, 112 (2002) 1911–1917.
- Hanson P.C., Analysis of discrete ill-posed problems by means of the l-curve, *SIAM Rev*, 34 (1992) 561–580.
- Hipp A.K., Storti G. and Morbidelli I., Acoustic characterization of concentrated suspensions and emulsions. 1. Model analysis, *Langmuir*, 18 (2002) 391–404.
- Hou H., Su M. and Cai X., Study on measurement of ultrasonic attenuation and velocity spectra in superfine particle suspensions, *Chinese Journal of Science Instrument*, 31 (2010)

- 241–247.
- King T.A., 7 - photon correlation spectroscopy: Technique and scope, in: Bevington G.A.C. (Eds.), *Comprehensive polymer science and supplements*, Pergamon, Amsterdam, 1989, pp. 911–935.
- Kirsch S., Frenz V., Schärfl W., Bartsch E. and Sillescu H., Multispeckle autocorrelation spectroscopy and its application to the investigation of ultraslow dynamical processes, *The Journal of Chemical Physics*, 104 (1996) 1758–1761.
- Liu L., Application of ultrasound spectroscopy for nanoparticle sizing in high concentration suspensions: A factor analysis on the effects of concentration and frequency, *Chemical Engineering Science*, (2009) 5036–5042.
- Liu L.L., Cai X.S., Zhang J. and Xu C.Z., Research on a novel fast imaging dynamic light scattering method for nanoparticle size measurement, *Acta Optica Sinica*, 35 (2015) 369–375 (In Chinese).
- McClements D.J. and Coupland J.N., Theory of droplet size distribution measurements in emulsions using ultrasonic spectroscopy, *Colloids and Surfaces*, 117 (1996) 161–170.
- Mougin P., Wilkinson D., Roberts K.J. and Tweedie R., Characterization of particle size and its distribution during the crystallization of organic fine chemical products as measured in situ using ultrasonic attenuation spectroscopy, *Journal of the Acoustical Society of America*, 109 (2001) 274–282.
- Pecora R., Quasi-elastic light-scattering from macromolecules, *Annual Review Of Biophysics And Bioengineering*, 1 (1972) 257–276.
- Pinfield V.J., Harlen O.G., Povey M.J.W. and Sleeman B.D., Acoustic propagation in dispersions in the long wavelength limit, *Siam Journal on Applied Mathematics*, 66 (2005) 489–509.
- Povey M.J.W., Ultrasound particle sizing: A review, *Particuology*, 11 (2013) 135–147.
- Riebel U., Characterization of agglomerates and porous particles by ultrasonic spectrometry, *The Fifth European Symposium Particle Characterization*, Nurnberg, (1992).
- Silbey R. and Deutch J.M., Quasi-elastic light-scattering from large macromolecules, *Journal Of Chemical Physics*, 57 (1972) 5010–5011.
- Su M. and Cai X., The numerical study of acoustical attenuation and velocity in the suspension of superfine particles, *Acta Acustica*, 27 (2002) 218–222.
- Su M., Cai X., Xue M., Dong L. and Xu F., Particle sizing in dense two-phase droplet systems by ultrasonic attenuation and velocity spectra, *Science in China Series E-Technological Sciences*, 52 (2009) 1502–1510.
- Su M., Xu F., Cai X., Ren K. and Shen J., Optimization of regularization parameter of inversion in particle sizing using light extinction method, *China Particuology*, 5 (2007) 295–299.
- Tebbutt J.S. and Challis R.E., Ultrasonic wave propagation in colloidal suspensions and emulsions: A comparison of four models, *Ultrasonics*, 34 (1996) 363–368.
- Thomas A.J.C., *Photon correlation spectroscopy: Technique and instrumentation*, Proc Spie, (1991) 2–18.
- Tikhonov A.N. and Arsenin V.Y., *Solution of ill-posed problems*, John Wiley and Sons, New York, 1977.
- Tscharnuter W., *Photon correlation spectroscopy in particle sizing*, (Eds.), *Encyclopedia of analytical chemistry*, John Wiley & Sons, Ltd, 2006, pp. 5469–5485.
- Twomey S., *Introduction to the mathematics of inversion in remote sensing and indirect measurement*, Elsevier, Amsterdam, 1977.
- Wang X.Z., Liu L., Li R.F., Tweedie R.J., Primrose K., Corbett J. and Mcneil-Watson F.K., Online characterisation of nanoparticle suspensions using dynamic light scattering, ultrasound spectroscopy and process tomography, *Chemical Engineering Research & Design*, 87 (2009) 874–884.
- Wang Z.Y., Cai X.S., Xu C.Z. and Liu L.L., Nanoparticle sizing by image processing with dynamic light scattering, *Acta Optica Sinica*, 34 (2014) 282–287 (In Chinese).
- Wong A.P.Y. and Wiltzius P., Dynamic light scattering with a ccd camera, *Review of Scientific Instruments*, 64 (1993) 2547–2549.
- Xu C.Z., Cai X.S., Zhang J. and Liu L.L., Fast nanoparticle sizing by image dynamic light scattering, *Particuology*, 19 (2015) 82–85.
- Ye Z., Hoskinson E., Dewey R.K., Ding L. and Farmer D.M., A method for acoustic scattering by slender bodies .1. Theory and verification, *Journal Of the Acoustical Society Of America*, 102 (1997) 1964–1976.
- Zakharov P., Bhat S., Schurtenberger P. and Scheffold F., Multiple-scattering suppression in dynamic light scattering based on a digital camera detection scheme, *Applied Optics* 45 (2006) 1756–1764.
- Zhou W., Zhang J., Liu L.L. and Cai X.S., Ultrafast image-based dynamic light scattering for nanoparticle sizing, *Review Of Scientific Instruments*, 86 (2015) 115107–115106.

Author's short biography



Wu Zhou

Wu Zhou received her degree from Nanjing University of Science and Technology in 2006 and a Ph.D. in Engineering from Southeast University in 2011. She is now an associate professor in the School of Energy and Power Engineering at the University of Shanghai for Science and Technology. Her research interests include particles and two-phase flow measurement, combustion measurement, mainly by image-based methods. She also interests in mathematical modelling of the above processes. She is a member of Youth Council of the Chinese Society of Particuology.



Mingxu Su

Prof. Mingxu Su received his degree in Power Engineering from Nanjing University of Aeronautics and Astronautics in 1996 and his PhD in Thermal Engineering from the University of Shanghai for Science and Technology, USST in 2002. In the same year, he got a postdoctoral position at UMR 6614 - CORIA in Rouen, France. After that, he went back to the USST being a teacher till now. His main research interests are methods of particle size characterization based on ultrasonic spectroscopy and light scattering theories, as well as the industrial applications on particulate two-phase flow measurement.



Xiaoshu Cai

Prof. Xiaoshu Cai graduated from the Department of Engineering Thermalphysics, Zhejiang University in 1982, and obtained PhD in Department of Power Engineering, Shanghai Institute of Mechanical Engineering in 1991. He became a professor in University of Shanghai for Science and Technology in 1996. Since 1988 he has been engaged in particle sizing and two-phase flow measurement techniques. His current research interests include particles and two-phase flow measurement, combustion measurement, emission and environmental monitoring, as well as power engineering and turbo machinery. He is vice president of Chinese Society of Particuology and president of Shanghai Society of Particuology.

Microstructural Evaluation of $\text{ZrB}_2/\text{ZrO}_2$ Ceramic Powders Prepared by Milling-Assisted Magnesiothermic Reduction of Oxide Raw Materials[†]

Duygu Ağaoğulları*, Özge Balcı, M. Lütfi Öveçoğlu and İsmail Duman

[†] Istanbul Technical University, Faculty of Chemical and Metallurgical Engineering, Department of Metallurgical and Materials Engineering, Particulate Materials Laboratories (PML), Turkey

Abstract

This study reports on the synthesis and microstructural evaluation of $\text{ZrB}_2/\text{ZrO}_2$ ceramic powders prepared by milling-assisted magnesiothermic reduction of oxide raw materials. Powder blends containing ZrO_2 , B_2O_3 and Mg reactants were milled in different type of mills at different durations and were subsequently annealed in a tube furnace under Ar atmosphere. An additional purification step (HCl leaching) was conducted on the milled and annealed samples to obtain only Zr-based products. FactSageTM thermochemical software was used in order to show a preliminary route for the experiments. The effects of milling duration (up to 100 h), milling type (a SPEXTM 8000D Mixer/Mill and a planetary ball mill), excess Mg amount (5–20 wt.%) and annealing duration (6 and 12 h) on the formation and microstructure of the products were examined. The milled, annealed and leached products were characterized using an X-ray diffractometer (XRD), stereomicroscope (SM), scanning electron microscope (SEM) and differential scanning calorimeter (DSC). Pure $\text{ZrB}_2/\text{ZrO}_2$ ceramic powders having particles in size range of 200 nm–1 μm and containing two different crystal structures of ZrO_2 phase (monoclinic and tetragonal) were obtained after milling in the SPEXTM 8000D Mixer/Mill for 30 h, annealing at 1200 °C for 12 h and leaching with 5 M HCl.

Keywords: zirconium diboride, zirconium oxide, boron oxide, ceramic powders, high-energy ball milling, magnesiothermic reduction

1. Introduction

There has been recently a growing interest in ZrB_2 -based ceramics due to their outstanding properties such as high melting point, high electrical and thermal conductivity, as well as excellent chemical inertness, high strength and high thermal shock resistance (Fahrenholtz and Hilmas, 2007; Monteverde et al., 2003). Based on these properties, ZrB_2 -based ceramics are attracting more and more attention in ultrahigh temperature applications where resistance to corrosion, wear and oxidation is demanded (Fahrenholtz and Hilmas, 2007; Zhu et al., 2009a, 2009b). They have been found to be suitable materials in various usage areas such as electrodes, thermowells, molten metal crucibles, armors, thermal protection systems for hypersonic flight, atmospheric re-entry vehicles, rocket propulsion and nose caps (Melendez-Martinez et

al., 2002; Chamberlain et al., 2004; Monteverde et al., 2008; Brouchu et al., 2009). Furthermore, they have been used as wear parts, nozzles, coating on cutting tools and cathodes for electrochemical processing of aluminium (Upadhyay et al., 1997; Opeka et al., 1999). Many of the composite materials have been developed to improve the sinterability and mechanical properties of the ZrB_2 -based materials (Monteverde, 2005; Guo, 2009). Amongst them, $\text{ZrB}_2\text{-ZrO}_2$ ceramics have raised significant concern due to the high contribution of ZrO_2 phase on the densification, oxidation resistance and fracture toughness of the ZrB_2 -based composites (Zhang et al., 2008; Li W. et al., 2009; Zhu et al., 2009a, 2009b; Li et al., 2010).

Many processes are available for the preparation of ZrB_2 or ZrB_2 -based ceramic powders: They have been traditionally produced by high temperature methods using solid-state reactions, borothermal and carbothermal reductions (Zhang et al., 2009; Qiu et al., 2012). Powders and coatings of ZrB_2 have been also produced by electro-metallurgy processes including molten salt electrolysis (Frazer et al., 1975; Malyshev and Gab, 2009). Chemical vapor deposition (CVD) technique has been applied to obtain ZrB_2 coatings by using ZrCl_4 , BCl_3 and H_2 gas

[†] Received 1 July 2015; Accepted 3 September 2015
J-STAGE Advance published online 30 January 2016

[†] Ayazağa Campus, 34469 Maslak, Istanbul, Turkey

* Corresponding author: Duygu Ağaoğulları;
E-mail: bozkurtdur@itu.edu.tr
TEL: +90-212-285-3381 FAX: +90-212-285-3427

mixtures (Gebhardt and Cree, 1965; Greenwood et al., 1966; Deng et al., 2012). In recent years, low-temperature synthesis in an autoclave (Chen et al., 2004; Chen et al., 2012) and self-propagating high-temperature synthesis (SHS) (Radev and Klissurski, 2001; Khanra et al., 2008) methods have been developed to achieve ZrB_2 or ZrB_2 -based ceramic powders. Synthesis of ZrB_2 powders by high-energy ball milling derived mechanochemical reaction has been examined by a group of researchers using the starting materials of ZrO_2 , B_2O_3 and Mg (Setoudeh and Welham, 2006; Guo et al., 2011; Akgün et al., 2011; Jalaly et al., 2013, 2014). The preparation of ZrB_2/ZrO_2 powders was also reported by using high-energy ball milling/annealing processes and/or boro/carbothermal reduction methods (Balci et al., 2012; Qiu et al., 2012). Review in the archival literature showed that mechanochemical route or milling-assisted synthesis processes have been more interesting due to its low-cost, simplicity, high throughput and product quality.

On the other hand, ZrB_2 -based dense bodies have been fabricated by spark plasma sintering (SPS), hot pressing (HP) and pressureless sintering (PS) from the starting powders containing ZrB_2 and some required additives such as SiC, ZrC, ZrO_2 , $MoSi_2$, AlN, B_4C , Al_2O_3 , etc (Guo et al., 2009; Monteverde et al., 2008; Chen et al., 2009; Li B. et al., 2009). Preparation of ZrB_2/ZrO_2 ceramics with these methods have also been investigated using ZrB_2 and ZrO_2 as raw materials (Basu et al., 2002; Zhang et al., 2008; Hong et al., 2008; Zhu et al., 2009b; Li W. et al., 2009). Li W. et al (2009) has reported the fabrication of ZrB_2/ZrO_2 ceramics with various ZrO_2 content by using hot pressing and provided a considerable increase in their fracture toughness values. Zhang et al (2008) has reported the fabrication of ZrB_2/ZrO_2 ceramics by utilizing spark plasma sintering of ZrB_2 and ZrO_2 powders and the increase in their toughness from ZrB_2 -rich layer to ZrO_2 -rich layer due to the phase transformation of ZrO_2 . Thus, ZrB_2/ZrO_2 ceramic powders with fine and homogeneous microstructure can be a potential precursor for the development of ZrB_2 -based dense bodies.

An efficient method should be developed for the synthesis of submicron-sized ZrB_2/ZrO_2 precursors with high purity. Already, it came out as a need for the preparation of their dense bodies since consolidation of ZrB_2/ZrO_2 precursors obtained from oxide raw materials is cheaper than that of their commercial ones. High-energy ball milling which is the main driving force of the displacement or redox/reduction reactions in the mechanical alloying and mechanochemical synthesis processes, has the advantages of enabling rapid preparation for oxide dispersion strengthened alloys, amorphous materials, solid solution alloys, non-equilibrium alloys, intermetallics, compounds, nanocomposites, ceramics and advanced materials that are difficult or impossible to be obtained by

conventional production techniques (Suryanarayana, 2001; El-Eskandarany, 2001). It can be controlled by several parameters such as type of mill, milling speed, milling duration, ball-to-powder weight ratio, milling container, milling atmosphere, milling environment, type, size and size distribution of milling media, etc (Suryanarayana, 2001; El-Eskandarany, 2001). It offers a wide range of options by changing the desired parameters for leading the reactants towards to the size reduction and reaction. So, in the present study, milling-assisted magnesiothermic reduction process was used for the synthesis of the ZrB_2/ZrO_2 ceramic powders from oxide raw materials. Two different types of mills present in the laboratory facilities were employed for the milling process in order to monitor the reaction products of the ZrO_2 - B_2O_3 -Mg powder system. The differences of these mills are speed of rotation, material/diameter of milling media and material/size of milling container, meaning that the efficiency of milling is different for this non-equilibrium processing technique. Subsequently, milled powders were annealed and leached to achieve pure and fine-grained ZrB_2/ZrO_2 ceramic powders.

2. Experimental procedure

Oxide raw materials such as ZrO_2 powders (Alfa AesarTM, in purity of 99.7 %, with an average particle size of 44 μm) and B_2O_3 powders (ETI Mine, in purity of 98 %, with an average particle size of 467 μm) were used in the experiments, respectively as zirconium source and as native boron source for the synthesis of ZrB_2/ZrO_2 ceramic powders. Mg powders (Alfa AesarTM, in purity of 99.7 %, with an average particle size of 145 μm) were utilized as reducing agent in order to yield magnesiothermic reduction of the oxide reactants.

Powder blends containing stoichiometric amounts of reactants were prepared according to the theoretical reduction reaction given in Eq. (1). However, it is already known that the complete reduction of ZrO_2 to ZrB_2 can not be possible considering its high chemical stability (Balci et al., 2012). Thus, the rationale of preferring stoichiometric amount in the preparation of the powder blends is impossibility in the complete reduction and conversion of ZrO_2 to ZrB_2 .



For each run, powder batches were weighed in a PrecisaTM XB320M sensitive balance. The prepared ZrO_2 - B_2O_3 -Mg powder batches were homogenized in a WABTM T2C Turbula blender for 1 h and they are hereafter referred to as-blended (ab) ZrO_2 - B_2O_3 -Mg powders.

As-blended powders were separately milled both in a SPEXTM 8000D Mixer/Mill (6 g powder batch) and in a

FritschTM Pulverisette 5 classic line planetary ball mill (12 g powder batch), with a rotation speed of 1200 and 400 rpm, respectively. Commonly, SPEXTM 8000D Mixer/Mill is employed for exploratory purposes and planetary ball mill is utilized to produce larger quantities of milled powders. In the milling experiments, ball-to-powder weight ratio (BPR) was chosen as 10:1. Milling containers changed according to the type of mills: a hardened steel vial with a capacity of 50 ml was used for the SPEXTM 8000D Mixer/Mill and a zirconia vial with a capacity of 500 ml was used for the planetary ball mill. Hardened steel balls with diameters of 6 mm and zirconia balls with diameters of 10 mm were employed as milling media, respectively. Extent of filling the vial is about 45 % for the utilized mills, knowing that adequate space should be given to the balls and to the particles to move around freely in the vial and to collide each other for getting enough impact energy (Suryanarayana, 2001; El-Eskandarany, 2001). Ar gas (LindeTM, in purity of 99.999 %) was preferred as milling atmosphere. Different milling durations up to 100 h were conducted during the experiments. The milling vials were sealed by evacuating to about 10^{-2} Pa and by back filling with Ar gas in a PlaslabsTM glove box. The milled powders were unloaded again under Ar atmosphere in the same glove-box.

Annealing experiments of the milled $\text{ZrO}_2\text{-B}_2\text{O}_3\text{-Mg}$ powders were carried out in quartz boats which were inserted in a ProthermTM tube furnace, at 1200 °C for 6 and 12 h with a heating and cooling rate of 10 °C/min under Ar gas flow.

Milled and annealed $\text{ZrO}_2\text{-B}_2\text{O}_3\text{-Mg}$ powders were leached with HCl (MerckTM, in concentration of 37 %) under the effect of ultrasonic stirring using a Bandelin SonorexTM RK-100 H ultrasonic bath in order to remove unwanted MgO phase. HCl solutions in concentrations of 3.6 and 5 M were used for the leaching treatments. Leaching parameters such as solid-to-liquid ratio of the solution and duration were selected respectively as 1 g/10 cm³ and 30 min. The solutions containing insoluble solids were subjected to repeated centrifuging in a HettichTM Rotofix 32A centrifuge with a rotation speed of 3500 rpm for 30 min, to repeated decanting and to repeated washing with distilled water. Finally, remained solids were dried under air in a FN 500 stove at 120 °C for 24 h.

The phase compositions of the milled, leached and annealed powders were identified using a BrukerTM D8 Advanced Series X-ray diffractometer (XRD) with $\text{CuK}\alpha$ (1.54060 Å) radiation in the 2θ range of 10–80° incremented at a step size of 0.02° at a rate of 2°/min. International Center for Diffraction Data® (ICDD) powder diffraction files were utilized for the identification of crystalline phases. Thermal property of the milled powders was examined in a TATM Instruments SDT Q600 differential scanning calorimeter (DSC)/thermogravimet-

ric analyser (TGA). DSC/TGA experiments were conducted in alumina crucibles up to a heating temperature of 1200 °C at a rate of 10 °C/min under Ar atmosphere. In order to identify the phases at the exothermic and endothermic peak points, milled powders were heated to 500, 600, 700, 800 and 900 °C in a ThermoscientificTM tube furnace under Ar atmosphere and they were subjected to additional XRD analyses at the same conditions. Microstructural characterizations of the milled, annealed and leached powders were carried out using a ZeissTM Discovery.V12 stereomicroscope (SM) coupled with a ZeissTM Axiocam ERc5s high resolution digital camera and a HitachiTM TM-1000 scanning electron microscope (SEM) operated at 15 kV. For SEM analysis, the specimens were prepared by following the procedure of dissolving the powders in $\text{C}_2\text{H}_5\text{OH}$ (MerckTM, in purity of 99.9 %), syringing them onto a base plate, drying them in air and coating their surfaces with a thin layer of gold using a PolaronTM SC7620 Sputter Coater to enhance their conductivities. Several different regions of the samples were monitored during the SEM analyses: homogeneous distributions of the particles were observed thankful to the milling process conducted for different durations. Thus, representative SEM images of the samples were shown in order to determine the size range of the particles instead of their average size. Lastly, Zr element and also probable Fe impurity, which could be formed as a result of the wear and tear from the hardened steel milling vial and balls, were analyzed in the supernatant liquids by using a Perkin ElmerTM 1100B atomic absorption spectrometer (AAS).

3. Results and discussion

3.1 Thermodynamic calculations

FactSageTM 6.2 thermochemical software was used for the determination of reaction possibility in terms of standard Gibbs free energy change versus temperature relation and for the interpretation of the probable reaction products, in $\text{ZrO}_2\text{-B}_2\text{O}_3\text{-Mg}$ system. The standard Gibbs free energy change versus temperature curve of the $\text{ZrO}_2\text{-B}_2\text{O}_3\text{-Mg}$ system was plotted up to 2000 °C and illustrated in Fig. 1(a).

The reaction has negative free energy change between –930 and –200 kJ in the temperature range of 0–2000 °C, which means that the reduction reaction in Eq. (1) is possible and takes place spontaneously at room temperature and above. However, there is a change in the slope of the curve in Fig. 1(a). The standard Gibbs free energy change of the reaction is between –930 and –775 kJ for the temperatures up to 1095 °C but the slope of the curve increases after this temperature at which Mg boils. Thus, boiling of Mg causes a significant change in the free en-

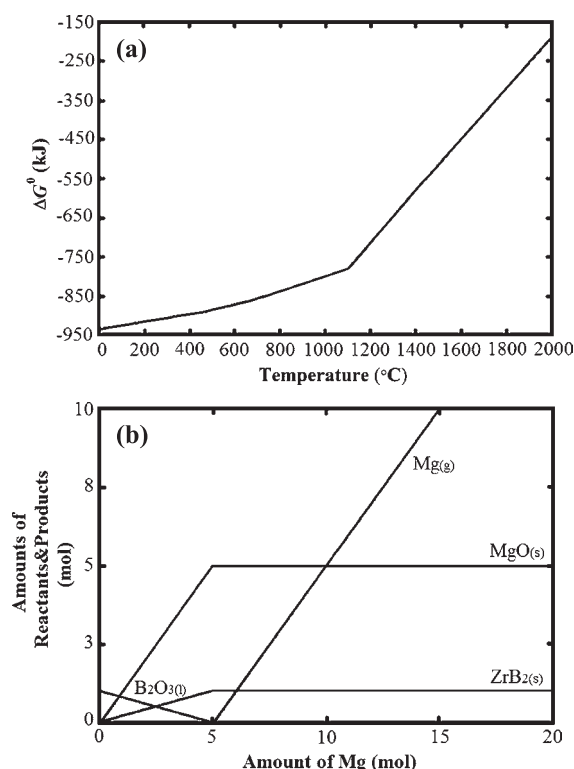


Fig. 1 Thermodynamic calculations of the $\text{ZrO}_2\text{-B}_2\text{O}_3\text{-Mg}$ system obtained from FactSageTM 6.2 thermochemical software for the reaction given in Eq.(1): **(a)** The standard Gibbs free energy change versus temperature curve, and **(b)** Molar amounts of reactants/products varying according to the molar amount of Mg at 1200 °C.

ergy value and hence slows the reaction proceeding. **Fig. 1(b)** shows the FactSageTM plot for the molar amounts of reactants/products varying according to the molar amount of Mg at 1200 °C. Under the stoichiometric amount of Mg (< 5 moles), the molar amounts of ZrB_2 and MgO increase with decreasing amount of unreacted B_2O_3 . When stoichiometric amount of Mg (5 moles) is used in the reaction, B_2O_3 reactant vanishes and 1 mole of ZrB_2 and 5 moles of MgO are obtained as the products. Increasing the molar amount of Mg up to 20 moles does not contribute to the further formation of ZrB_2 and MgO phases because excess amounts of Mg convert into gas phase and leave the system without participating in the reduction reaction. Thus, maximum amounts of ZrB_2 and MgO reaction products can be achieved in the case of using stoichiometric amount of Mg, according to the thermodynamic calculations in **Fig. 1(b)**.

3.2 Milling of the as-blended powders

Fig. 2(a)–(h) displays the XRD patterns of the as-blended powders and those milled in the SPEXTM 8000D Mixer/Mill for different durations (3, 5, 7, 9, 15, 20 and 30 h). As clearly seen from **Fig. 2**, there are no reactions

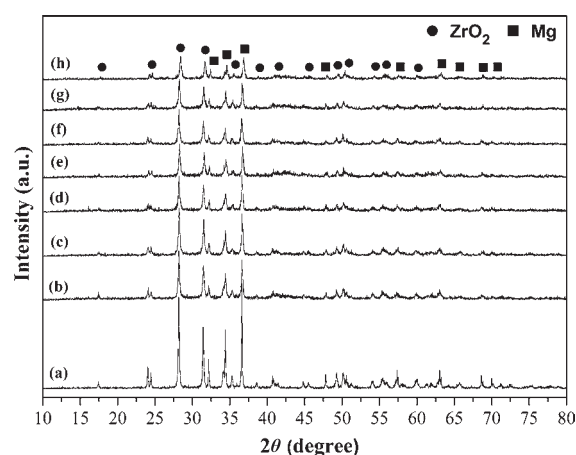


Fig. 2 XRD patterns of the as-blended powders and those milled in the SPEXTM 8000D Mixer/Mill for different durations: **(a)** ab, **(b)** 3 h, **(c)** 5 h, **(d)** 7 h, **(e)** 9 h, **(f)** 15 h, **(g)** 20 h and **(h)** 30 h.

Table 1 The details of the crystal structural parameters of the different phases encountered in this study.

Phase	ICDD Card #	Bravais Lattice	Lattice Parameters (nm)
ZrO_2	89-9066	Primitive Monoclinic	$a = 0.531$ $b = 0.520$ $c = 0.514$
B_2O_3	—	—	—
ZrO_2	50-1089	Primitive Tetragonal	$a = b = 0.359$ $c = 0.515$
Mg	35-0821	Primitive Hexagonal	$a = b = 0.329$ $c = 0.521$
ZrB_2	34-0423	Primitive Hexagonal	$a = b = 0.317$ $c = 0.353$
MgO	45-0946	Face-centered Cubic	$a = b = c = 0.421$

between ZrO_2 , B_2O_3 and Mg even after milling for 30 h because the ZrO_2 and Mg phases are still present in the XRD patterns of the powders. No peaks belonging to the B_2O_3 phase are observed in the XRD pattern of the as-blended $\text{ZrO}_2\text{-B}_2\text{O}_3\text{-Mg}$ powders, probably due to its amorphous nature. Furthermore, any Fe impurity which could be released from the hardened steel vial/balls during milling did not detected in the XRD patterns in **Fig. 2(b)–(h)** since the diffractometer is not capable of analyzing phase amounts under 2 wt.% of the overall sample. **Table 1** presents the details of the crystal structural parameters of the different phases encountered in this study.

Similarly, in a related study reported on the carbothermal reduction of ZrO_2 and B_2O_3 powder blends, there exists no reaction even after milling for 6 h in the SPEXTM

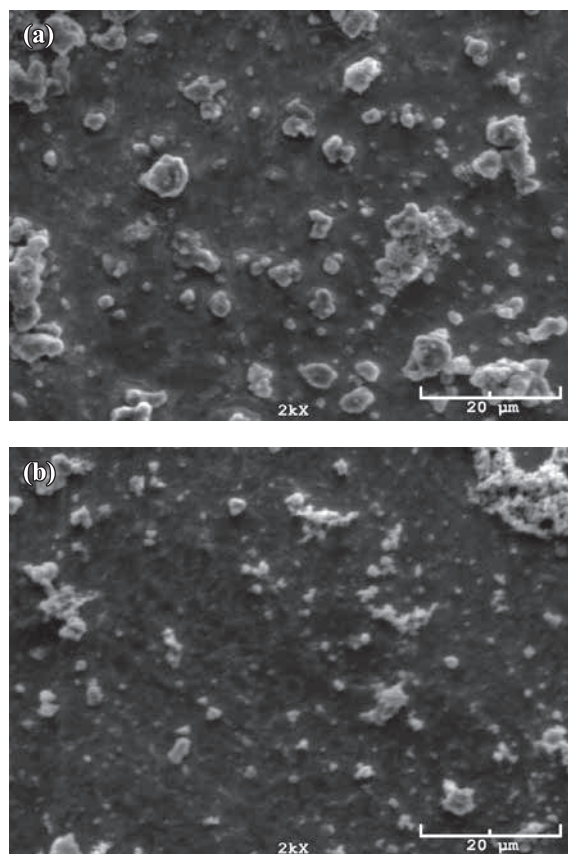


Fig. 3 SEM images of the powders milled in the SPEX™ 8000D Mixer/Mill for different durations: (a) 15 h and (b) 30 h.

8000D Mixer/Mill with a BPR of 10:1 (Balcı et al., 2012). Moreover, ZrO_2 and Mg peaks broadened and their intensities gradually decreased upon increasing the milling time from 0 to 30 h, indicating a gradual decrease in their crystallite sizes and an increase in their lattice strains due to the continuous deformation during milling. There is a visible decrease in the intensities of the ZrO_2 and Mg peaks from 0 to 3 h. However, this decrease is seen less from 3 to 30 h of milling duration. Thus, no change occurred in the phase composition of the powders after milling for 30 h, suggesting that prolonged milling did not contribute to the chemical reaction, but contributed only to the particle size reduction.

Representative SEM images of the powders milled in the SPEX™ 8000D Mixer/Mill for 15 and 30 h are given in **Fig. 3(a) and (b)**. At first view, it is clearly seen from the SEM images that powders milled for 15 and 30 h do not consist of particles with definite and perfect morphologies throughout the structure. **Fig. 3(a)** reveals both the round-shaped particles having sizes smaller than $2\ \mu\text{m}$ and the irregular agglomerates in sizes not larger than $5\ \mu\text{m}$. It is also easily observed from the microstructure in **Fig. 3(a)** that some smaller round-shaped particles are embedded in larger agglomerates. Extended milling to

30 h resulted in the particle size reduction (from $2\ \mu\text{m}$ to $700\ \text{nm}$) and provided the breaking down of the larger agglomerates (from 5 to $2.5\ \mu\text{m}$). Moreover, it was reported in previous studies that repeated fracturing and welding mechanism took place in the vial during milling creates agglomeration and inhomogeneity in the shapes of the particles due to the contact of active and small fresh surfaces at each collision between vial walls/balls and particles (Suryanarayana, 2001; Ağaoğulları et al., 2012a, 2016; Ağaoğulları, 2014).

On the basis of XRD patterns in **Fig. 2** and SEM images in **Fig. 3**, it was understood that milling of stoichiometric amount of ZrO_2 , B_2O_3 and Mg powders in the SPEX™ 8000D Mixer/Mill for 30 h yielded only smaller particles of the reactants without any formation of reduction reaction. Although FactSage™ plot in **Fig. 1(b)** showed that using 20 moles of Mg as starting material rather than 5 moles (stoichiometric amount) did not increase the molar amounts of ZrB_2 and MgO products, milling with the addition of excess amounts of Mg (5, 10, 15 and 20 wt.%) was conducted considering that the thermodynamic calculations exhibit only the equilibrium phase compositions at room and elevated temperatures without taking into account synthesis history and reaction kinetics. As previously known, the impact energy accumulated in the system during milling converts into other types of energies (potential, kinetic, chemical, etc.): these energies are effective in the formation of new structural arrangements which can be deviated from thermodynamic equilibrium states (Suryanarayana, 2001; El-Eskandarany, 2001). In this case, the molar amount of Mg was increased to observe an indication of the reduction reaction. Taking into account that the peak intensities of the ZrO_2 and MgO phases are similar after milling for 7 h with those after milling for 30 h (**Fig. 2(d) and (h)**), experiments with excess Mg amounts were carried out using 7 h of milling duration. **Fig. 4(a)–(d)** illustrates the XRD patterns of the powders milled in the SPEX™ 8000D Mixer/Mill for 7 h with the use of excess amounts of Mg (5, 10, 15 and 20 wt.%), respectively. As seen from **Fig. 4(a)–(d)**, there are still ZrO_2 and Mg phases in the microstructure of the milled powders, definitely in the presence of amorphous B_2O_3 which could not be observed with a distinctive peak by XRD. Also, there are indications of a very small combined peak of ZrB_2 and MgO phases at the 2θ range of 40 – 45° and very small ZrB_2 peaks at the 2θ value of about 34 , 66 and 73° . Amongst the XRD patterns in **Fig. 4(a)–(d)**, the highest intensity of ZrB_2 and MgO phases were obtained when 20 wt.% excess Mg was used in the powder blend. It is expected to detect ZrB_2 and MgO phases in higher intensities than those in **Fig. 4** since the addition of excess Mg could compensate the surface oxidation of the reactants and could trigger the reactants for the desired reaction. However, the tempera-

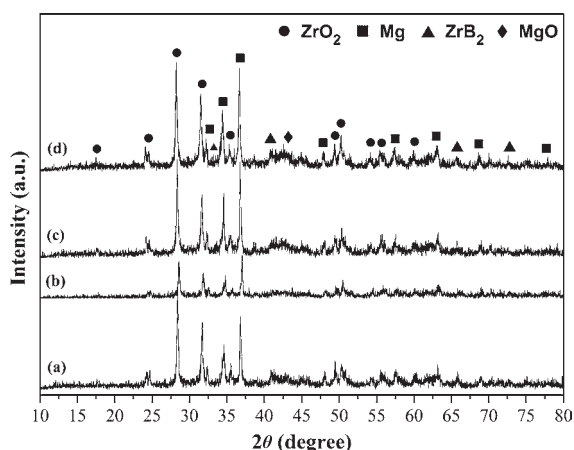


Fig. 4 XRD patterns of the powders milled in the SPEX™ 8000D Mixer/Mill for 7 h with the use of excess amount of Mg: (a) 5 wt.%, (b) 10 wt.%, (c) 15 wt.% and (d) 20 wt.%.

ture increase in the vial arose from the impact energy during milling is not sufficient for activating the ZrO_2 material exhibiting a ceramic character and high chemical stability. If sufficient temperature increase was obtained and hence activation energy barrier was exceeded in the system under the effect of impact energy, there would be a sudden exothermic reaction following to the achievement of adequate particle size reduction. The driving force for this exothermic reaction is ignition occurred at the solid-solid interface of the reduced particles by the help of the high oxygen affinity of Mg. Thus, further ignition of the milled powders should be provided by applying external heat such as annealing.

After obtaining the experimental outputs from milling in the SPEX™ 8000D Mixer/Mill, the type of high-energy ball mill was changed to monitor its effects on the reaction time and product type, considering that the kinetics of the milling process depend on the stress conditions in the milling devices. **Fig. 5(a)–(f)** demonstrates the XRD patterns of the powders milled in the planetary ball mill for 20, 25, 40, 50, 70 and 100 h. According to the XRD patterns in **Fig. 5(a) and (b)**, milled powders for 20 and 25 h contain ZrO_2 and Mg crystalline phases certainly with the amorphous B_2O_3 , revealing that any reaction did not take place till to the end of these durations.

As milling time was increased to 40 h, either a significant decrease in the intensities of the ZrO_2 and Mg phases or small incubations of ZrB_2 and MgO phases were observed (**Fig. 5(c)**). Moreover, the intensity decreases of ZrO_2 and Mg phases are seen sharper for 25 and 40 h milling durations (**Fig. 5(b) and (c)**). Prolonging milling time from 40 h to 50, 70 and 100 h enabled the further size reduction of ZrO_2 and Mg particles but did not enable the formation of complete reduction: ZrB_2 and MgO phases have still very small peak intensities in the pres-

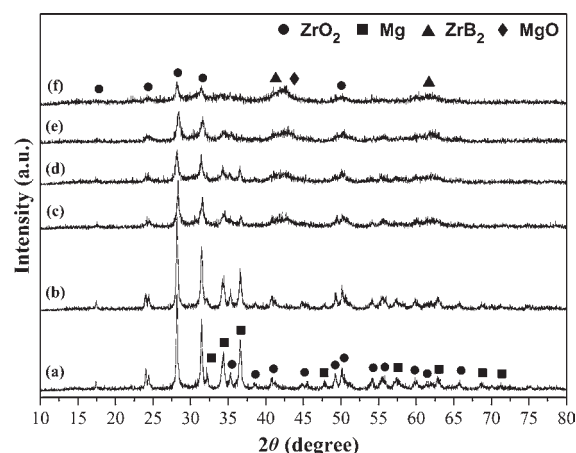


Fig. 5 XRD patterns of the powders milled in the planetary ball mill for different durations: (a) 20 h, (b) 25 h, (c) 40 h, (d) 50 h, (e) 70 h and (f) 100 h.

ence of major ZrO_2 phase. However, Mg peaks almost disappeared due to the continuous deformation. As the XRD analysis results in **Fig. 2(b)–(h)** and **5(a)–(f)** are compared with each other, it is understood that the only difference emerged in the phase type as the incubations of ZrB_2 and MgO. Roughly, these incubations could be expected to occur after milling in the SPEX™ 8000D Mixer/Mill because the rotation speed of this mill is three times higher than that of planetary one which corresponds to a higher impact energy and shorter reaction time. However, there is no indication of ZrB_2 and MgO even after milling for 30 h in the SPEX™ 8000D Mixer/Mill (**Fig. 2(b)–(h)**). The emergence of ZrB_2 and MgO after 40 h milling in the planetary ball mill may be explained by the strong impact forces occurred between ZrO_2 reactant and vial/balls which were made from the same material. It should be also noted that processing parameters of the two mills such as material of milling vial/balls, diameter of the milling balls and milling energy did not match each other and they could not be evaluated in a comprehensive way. Already, the main aim of using two different mills was not to compare their corresponding products in the case of changing one milling parameter by fixing the others, but was to observe the reaction products of the as-blended ZrO_2 - B_2O_3 -Mg powders in two different systems in the within the laboratory facilities.

Representative SEM images of the powders milled in the planetary ball mill for 20, 25, 50 and 100 h are given in **Fig. 6(a) to (d)**, respectively. As seen from **Fig. 6(a) and (b)**, milled powders for 20 and 25 h have irregular-shaped particles in sizes below 20 μm . There is not a very significant difference in the particle sizes of the powders milled for 20 and 25 h (**Fig. 6(a) and (b)**), as compatible with the similar intensities of ZrO_2 and Mg phases in their XRD patterns (**Fig. 5(a) and (b)**).

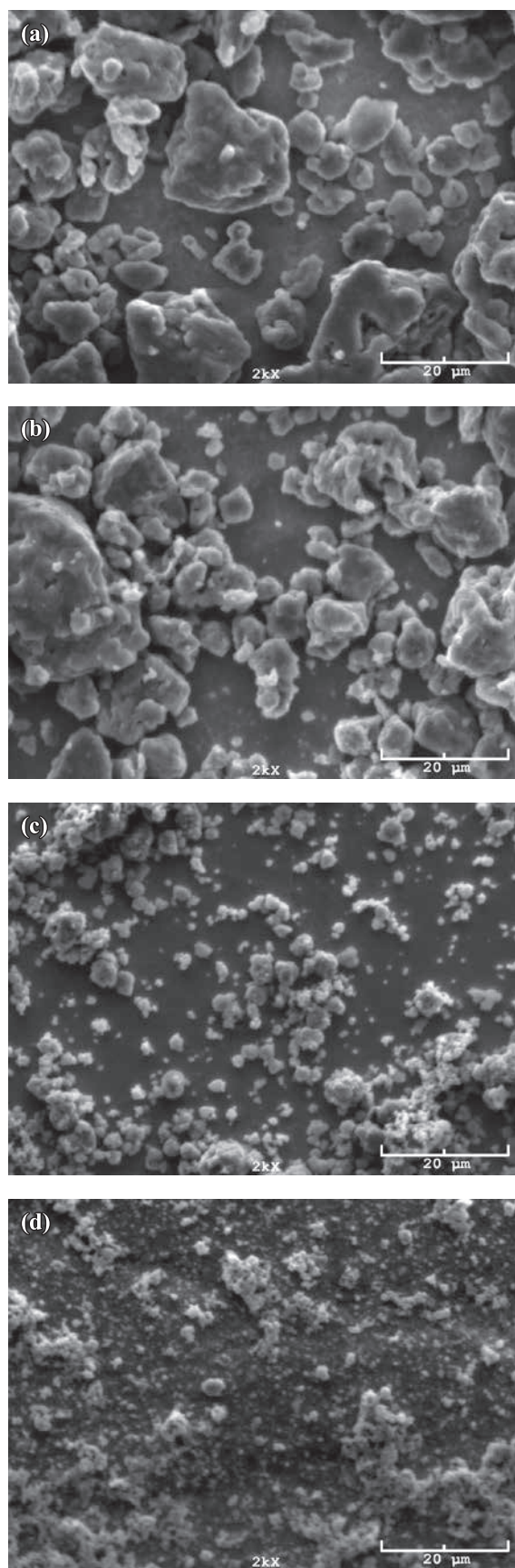


Fig. 6 SEM images of the powders milled in the planetary ball mill for different durations: (a) 20 h, (b) 25 h, (c) 50 h and (d) 100 h.

In other words, further milling for 5 h in planetary ball mill was not adequate to create a remarkable change in the particle size. Besides, the gradual decrease in the particle sizes of the milled powders can be obviously seen from **Fig. 6(b) through (d)**. **Fig. 6(c)** shows agglomerates in sizes not larger than 5 μm and also irregular-shaped particles having sizes below 2 μm . As milling time was increased to 100 h, particle sizes decreased to 2 μm and below (**Fig. 6(d)**). Similar to the microstructures obtained after milling process in the SPEXTM 8000D Mixer/Mill (**Fig. 3(a) and (b)**), agglomeration of powder particles was encountered after milling in the planetary ball mill (**Fig. 6(c) and (d)**). This phenomenon generally prevents the observation of smaller particles throughout the microstructure. Furthermore, approximate particle sizes were obtained after milling for 30 h in the SPEXTM 8000D Mixer/Mill and for 100 h in the planetary ball mill even if milling parameters for two different equipment could not be comparable in regard of the material of milling vial/balls, the diameter of the milling balls and the rotation speed.

3.3 Annealing of the milled powders

After milling processes carried out using different type of mills for different durations, application of an external heat came out as a need for the reduction reaction and for the partial/complete conversion of ZrO_2 to ZrB_2 since milling did not yield the characteristic peaks of ZrB_2 phase even after very long milling durations. Besides, milling the stoichiometric powder blends or those added with 20 wt.% excess Mg in the SPEXTM 8000D Mixer/Mill is considered as more advantageous than milling in the planetary ball mill because similar particle sizes could be achieved at shorter durations by taking into account their independent process parameters. Thus, powders milled for 30 h in the SPEXTM 8000D Mixer/Mill with/without excess Mg amounts were subjected to the subsequent annealing processes. Prior to the annealing, thermal behavior of the sample milled for 30 h was determined by DSC-TGA experiments in order to suggest an annealing temperature.

Fig. 7 shows the DSC-TG scans of the powders milled in the SPEXTM 8000D Mixer/Mill for 30 h. According to the DSC scan, milled powders have an exothermic peak at about 600 $^{\circ}\text{C}$ and a broad endothermic peak at about 900 $^{\circ}\text{C}$. Although powders milled for 30 h have ZrO_2 , B_2O_3 and Mg phases (**Fig. 2(h)**), there are not any endotherms corresponding to the melting of B_2O_3 at 450 $^{\circ}\text{C}$ and melting of Mg at 650 $^{\circ}\text{C}$ in the DSC scan in **Fig. 7**. Instead of these endotherms, there is an exotherm with a sharp peaking point at 600 $^{\circ}\text{C}$ and with an onset temperature of about 400 $^{\circ}\text{C}$. Homogeneous distribution of active ZrO_2 , B_2O_3 and Mg particles in small sizes enabled them

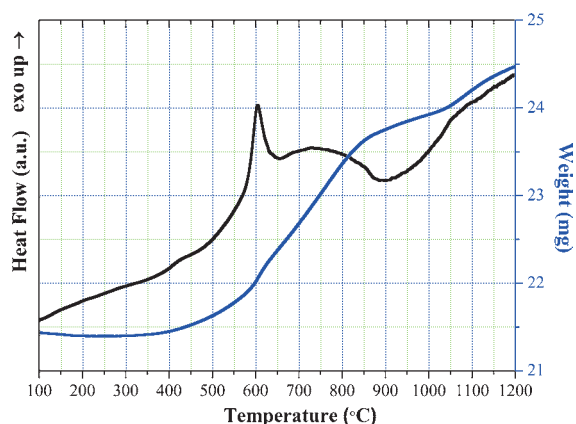


Fig. 7 DSC-TG scans of the powders milled in the SPEX™ 8000D Mixer/Mill for 30 h.

to react with each other rather than their individual melting. Furthermore, the initial weight of the sample increases from 21.45 to 24.50 mg, as seen in the TG scan. In order to reveal the reasons of the exothermic and endothermic peaks, milled powders were just heated to 500, 600, 700, 800 and 900 °C without a holding time and they were cooled instantly down to the room temperature. The XRD patterns of these milled and heated powders are given in **Fig. 8(a) to (e)**. After milled powders were heated to the temperatures of 500, 600, 700 and 800 °C, the microstructure contained ZrO_2 and MgO phases. This means that the exotherm peaking at 600 °C belongs to the oxidation of Mg. This is in good agreement with the TG scan because it has sharp increase (from 21.45 to 23.62 mg) until 850 °C.

Heating of the milled powders to 900 °C resulted in the incubation of ZrB_2 phase (**Fig. 8(e)**), indicating that the endothermic peak is a sign of ZrB_2 formation. As already known, monoclinic ZrO_2 transforms into tetragonal structure at about 1170 °C (Nettleship and Stevens, 1987). However, there is no indication of this transformation in the DSC scan (**Fig. 7**). This phenomenon can be attributed to the non-isothermal fast DSC heating conditions without a holding time, carried out in an alumina crucible in which particles of the reactants placed in a very small volume. Considering the results in **Fig. 7** and **Fig. 8(a)–(e)**, the melting temperature of ZrO_2 (about 2715 °C) and Tamman temperature ($0.4\text{--}0.5 \times T_{\text{melting}}$), the annealing temperature of the milled powders was selected as 1200 °C.

Fig. 9(a) and (b) represent the XRD patterns of the powders milled in the SPEX™ 8000D Mixer/Mill for 30 h and annealed at 1200 °C for 6 and 12 h, respectively. After annealing for 6 h (**Fig. 9(a)**), ZrB_2 and MgO were obtained with their characteristic peaks in the presence of unreacted ZrO_2 phase. However, an amount of monoclinic ZrO_2 phase transformed into tetragonal ($\text{ZrO}_2\text{-t}$) structure. This arose by the help of the holding time for 6 h at 1200 °C because annealing temperature is just a little

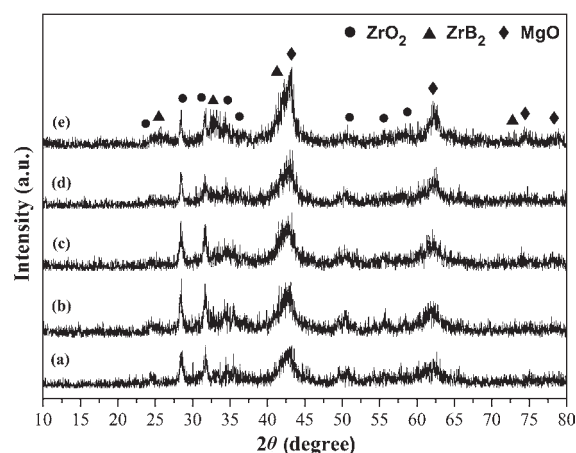


Fig. 8 XRD patterns of the powders milled in the SPEX™ 8000D Mixer/Mill for 30 h and subsequently heated to (a) 500 °C, (b) 600 °C, (c) 700 °C, (d) 800 °C and (e) 900 °C.

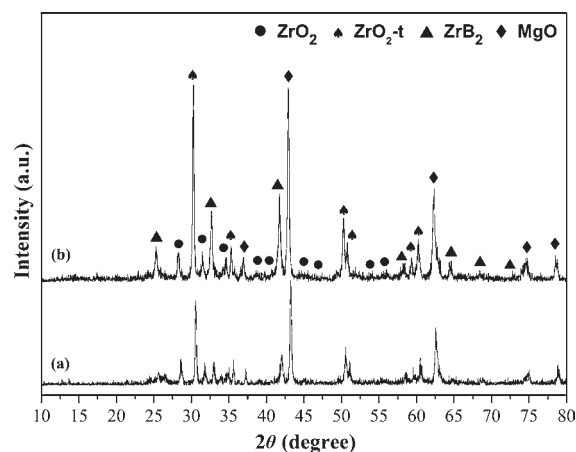


Fig. 9 XRD patterns of the powders milled in the SPEX™ 8000D Mixer/Mill for 30 h and annealed at 1200 °C for different durations: (a) 6 h and (b) 12 h.

higher than the transformation temperature of ZrO_2 (1170 °C). When the annealing time was increased from 6 to 12 h by fixing the temperature, the peak intensities of the ZrB_2 , MgO and $\text{ZrO}_2\text{-t}$ remarkably increased (**Fig. 9(b)**) in the presence of monoclinic ZrO_2 phase which is almost in the approximate amount with that of in **Fig. 9(a)**. Moreover, Fe impurity which could be incorporate into the powders from the hardened steel vial/balls during the milling process did not detected in the XRD patterns even after annealing, meaning that its probable amount is under the detection limit of XRD ($< 2 \text{ wt.}\%$).

Additionally, any emergence of Mg borate compounds such as MgB_4O_7 , $\text{Mg}_2\text{B}_2\text{O}_5$ and $\text{Mg}_3\text{B}_2\text{O}_6$ did not observed in **Fig. 9(a) and (b)** at the end of the annealing processes. It was thought as a probability because Mg/MgO and B_2O_3 can react and form Mg borates in different compositions between the temperatures of 700 and 1000 °C (Ağaoğulları et al., 2012b). Thus, 1200 °C and 12 h can be

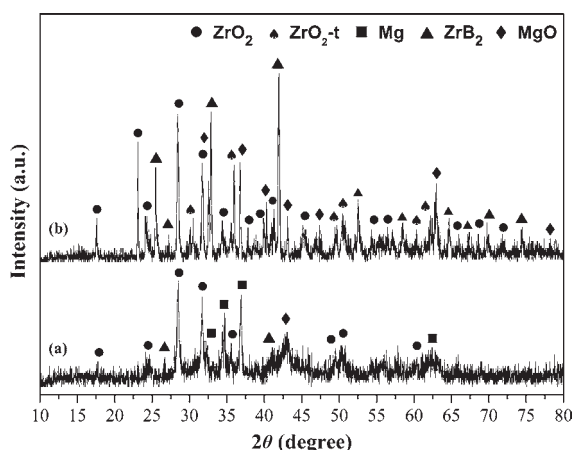


Fig. 10 XRD patterns of the powders: (a) milled in the SPEX™ 8000D Mixer/Mill for 30 h with the use of 20 wt.% excess amount of Mg, and (b) those of annealed at 1200 °C for 12 h.

respectively evaluated as an optimum annealing temperature and annealing time for yielding $\text{ZrB}_2/\text{ZrO}_2$ ceramic powders with an amount of MgO which will be easily leached out using HCl as well as probable Fe impurity. Due to the fact that the higher annealing temperature with a longer annealing duration may cause excess grain growth in the resultant powder particles, annealing parameters were not altered for the following experiments.

Fig. 10(a) and (b) exhibit the XRD patterns of the 20 wt.% excess amount of Mg added powders after milling in the SPEX™ 8000D Mixer/Mill for 30 h and those after annealing at 1200 °C for 12 h, respectively. In comparison with the XRD pattern of the powders milled for 7 h with the same amount of excess Mg (**Fig. 4(d)**), it can be clearly seen that the peak intensities of the ZrO_2 and Mg phases decreased and the incubations of the ZrB_2 and MgO phases increased in very small amounts after milling for 30 h (**Fig. 10(a)**). Thus, there is still no reaction between reactants even after milling for 30 h with the use of 20 wt.% excess amount of Mg.

After annealing of the powders milled for 30 h with the use of 20 wt.% excess amount of Mg at 1200 °C for 12 h (**Fig. 10(b)**), ZrB_2 phase in high peak intensities and MgO occurred in the microstructure in addition to the unreacted monoclinic ZrO_2 and its transformed form ($\text{ZrO}_2\text{-t}$). The utilization of 20 wt.% excess amount of Mg seems to increase the ZrB_2 peak intensities as compared with **Fig. 9(b)**. However, the intensities of the ZrO_2 peaks also increased and hence the $\text{ZrB}_2/\text{ZrO}_2$ intensity ratio decreased with the use of excess Mg. Besides, MgO phase formed in lower amount than that of in **Fig. 9(b)**. The peak intensities of $\text{ZrO}_2\text{-t}$ in **Fig. 10(b)** are significantly lower than those of in **Fig. 9(b)** because excess amount of Mg (20 wt.%) up to a limited level provides ZrO_2 to contribute in the formation of ZrB_2 instead of its transformation

to $\text{ZrO}_2\text{-t}$ during annealing at 1200 °C. However, remained excess amount of Mg evaporated from the system without further participating into the reduction reaction, as compatible with the FactSage™ plot in **Fig. 1(b)**. Thus, annealing of the milled powders containing stoichiometric amounts of reactants can give the ideal route for the production of $\text{ZrB}_2/\text{ZrO}_2$ ceramic powders.

It should be also stated that the thermochemical calculations in **Fig. 1(a) and (b)** performed using FactSage™ 6.2 software for the theoretical reduction reaction given in Eq. (1) conflicted with the experimental outputs of the annealing process, when the obtained products were taken into account. Already, the starting stoichiometric powder blends were prepared in regard of Eq. (1) considering the high stability of ZrO_2 and hence its complexity in the reduction. According to the thermochemical calculations, the reaction products obtained from the stoichiometric amounts of raw materials are only ZrB_2 and MgO. Though, ZrB_2 and MgO in the presence of both monoclinic and tetragonal ZrO_2 were obtained as the reaction products after milling and annealing of the stoichiometric powder blends. So, the reduction reaction of $\text{ZrO}_2\text{-B}_2\text{O}_3\text{-Mg}$ system at 1200 °C should be conformed to the experimental results. The actual reduction reaction rewritten in regard of achieved outputs is given in Eq. (2).



3.4 Leaching of the annealed powders

Following to milling and annealing processes, the reaction products with undesired MgO phase should be purified to achieve fine-grained ceramic powders without any contamination. Thus, leaching treatment was performed using different HCl concentrations (3.6 and 5 M) on the powders milled in the SPEX™ 8000D Mixer/Mill for 30 h and annealed at 1200 °C for 12 h, with the intention of removing the whole MgO present in the microstructure and also probable Fe impurity which was not previously detected by XRD. **Fig. 11(a) and (b)** illustrate the XRD patterns of the leached powders. According to **Fig. 11(a)**, 3.6 M HCl provided the dissolution of MgO but it is still not strong enough for the complete elimination of the undesired phase. As HCl concentration was raised to 5 M, the peak intensities of both monoclinic and tetragonal ZrO_2 and ZrB_2 phases increased without any appearance of MgO (**Fig. 11(b)**).

Subsequent AAS analyses were conducted on the leach solutions decanted from the residual solids in order to detect the dissolved Zr and Fe elements. Since 5 M HCl is highly concentrated, 22 ppm Zr arose from the slight dissolution of ZrO_2 phase was detected in the solution. However, trace amount of Zr was found in the leach solution in the case of using 3.6 M HCl. Furthermore, increasing

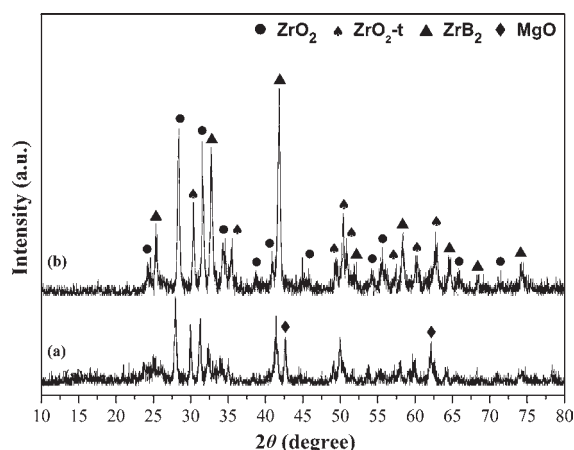


Fig. 11 XRD patterns of the powders milled in the SPEXTM 8000D Mixer/Mill for 30 h, annealed at 1200 °C for 12 h and leached in HCl solution at different concentrations: (a) 3.6 M and (b) 5 M.

the HCl concentration from 3.6 to 5 M increased the dissolution of Fe but not in a significant amount: the detected amounts were about 117 ppm for 3.6 M HCl and 125 ppm for 5 M HCl. In our previous studies about the synthesis of LaB₆ and SmB₆ from La₂O₃-B₂O₃-Mg and Sm₂O₃-B₂O₃-Mg powder blends by mechanochemical reactions in the SPEXTM 8000D Mixer/Mill for 5 h (using the same conditions such as BPR, milling container, media and atmosphere), the supernatant liquids were respectively found to have about 11 and 7.81 ppm Fe after leaching with 3.6 and 4 M HCl (Ağaoğulları et al., 2012a, 2015). In this case, the amount of Fe impurity released from the leached ZrB₂/ZrO₂ ceramic powders is at least ten times higher than those released from the purified LaB₆ and SmB₆ powders due to the higher hardness of ZrO₂ and ZrB₂ compounds. Besides, leaching treatment using 3.6 M was repeated for the obtained ZrB₂/ZrO₂ powders but Fe element was determined as trace amount which was under the detection limit of AAS. Thus, HCl concentrations above 5 M were not applied for leaching of the annealed powders and 5 M HCl was found strong enough to obtain pure ZrB₂/ZrO₂ ceramic powders.

Fig. 12(a)–(d) shows the SM images of the as-blended, milled (in the SPEXTM 8000D Mixer/Mill for 30 h), annealed (at 1200 °C for 12 h) and leached (in 5 M HCl) powders, respectively. Monitoring SM images are beneficial to see the general appearances and colors of the powders and to follow the process in a simple way. As the SM image of the as-blended powders in **Fig. 12(a)** is compared with those in **Fig. 12(b)–(d)**, the change in the colors of the starting materials can be obviously seen and the effect of different treatments can be observed step-by-step.

After milling for 30 h in the SPEXTM 8000D Mixer/Mill, the particles of the reactants were homogeneously distributed throughout the microstructure, Mg particles

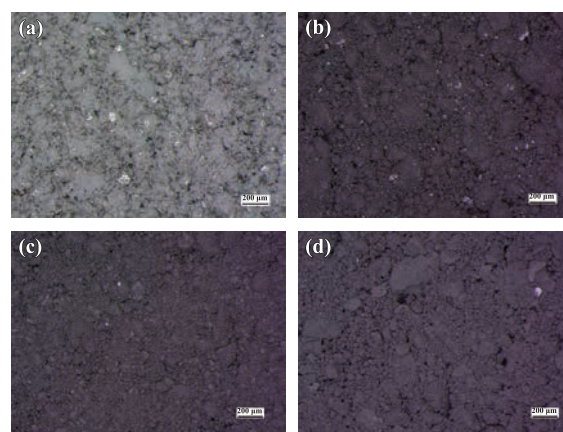


Fig. 12 SM images of the (a) as-blended powders, (b) powders milled in the SPEXTM 8000D Mixer/Mill for 30 h, (c) those annealed at 1200 °C for 12 h and (d) those leached in 5 M HCl.

covered the surfaces of the other reactants and it resulted in a color change in the overall volume (**Fig. 12(b)**). The morphology of the annealed powders (**Fig. 12(c)**) is different than that of milled one (**Fig. 12(b)**). The microstructure turned to a more incorporated and continuous form by the influence of heating with a long holding time. However, the color differences of the Zr-based (ZrO₂, ZrO₂-t and ZrB₂) and MgO particles are clear in **Fig. 12(c)** because Zr-based particles are seen as embedded in the MgO phase. After leaching treatment, the microstructure became a homogeneous form by eliminating the color difference via removing the MgO contamination (**Fig. 12(d)**).

Fig. 13(a) and (b) are the representative SEM images of the powders milled in the SPEXTM 8000D Mixer/Mill for 30 h, annealed at 1200 °C for 12 h and leached in 5 M HCl, at magnifications of 2000 and 8000X, respectively. The general view of the resultant powders containing both monoclinic and tetragonal ZrO₂ and ZrB₂ phases in **Fig. 13(a)** exhibits irregular agglomerates which prevent the observation of smaller particles in the microstructure. **Fig. 13(b)** in higher magnification than **Fig. 13(a)** clearly shows the rounded-shaped particles in sizes ranging between 200 nm and 1 μm. On the basis of **Fig. 13**, it can be said that the final product is in the form of a ceramic powder in which individual particles of the components can be observed, rather than that of a composite powder in which each particle has the similar composition of resultant phases.

Consequently, submicron-sized and pure ZrB₂/ZrO₂ ceramic powders containing two different crystal structures of ZrO₂ phase (monoclinic and tetragonal) were prepared by milling, annealing and leaching processes from ZrO₂-B₂O₃-Mg powder blends. The synthesized precursor material can be utilized as intermediate or final products

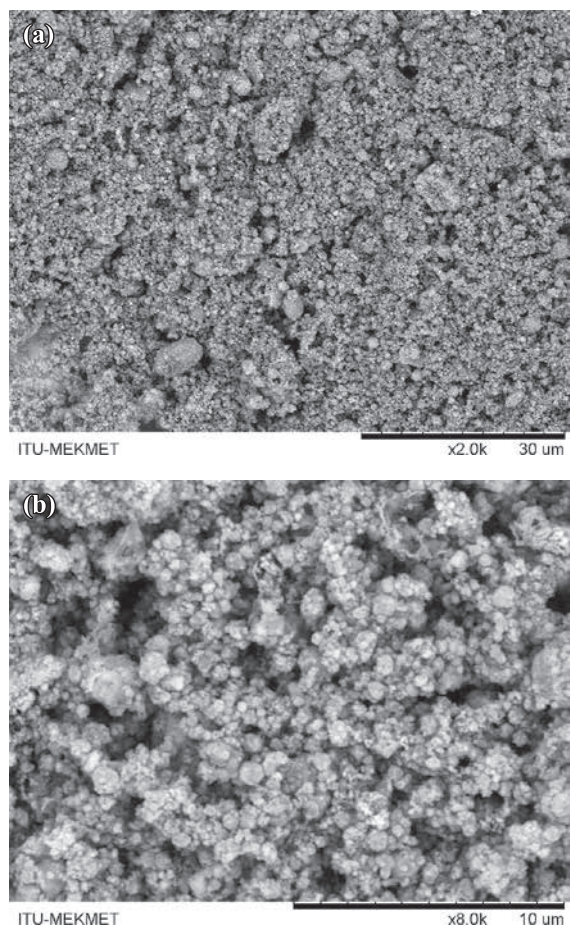


Fig. 13 SEM images of the powders milled in the SPEX™ 8000D Mixer/Mill for 30 h, annealed at 1200 °C for 12 h and leached in 5 M HCl, at different magnifications: (a) 2000X and (b) 8000X.

in different application areas and can lead the way for the further advanced processing techniques to obtain special designated bulk forms of composites.

4. Conclusions

In this study, submicron-sized $\text{ZrB}_2/\text{ZrO}_2$ ceramic powders were successfully synthesized via magnesiothermic reduction of oxide raw materials using a combined process of milling and annealing. An additional HCl leaching step was conducted on the annealed powders for their purification. Based on the results reported in the present study, the following necessary conclusions can be drawn:

- Milling of stoichiometric $\text{ZrO}_2\text{-B}_2\text{O}_3\text{-Mg}$ powder blends in the SPEX™ 8000D Mixer/Mill for 3–30 h did not trigger a reduction reaction since there were still ZrO_2 and Mg phases in the microstructure of the powders. However, it resulted in a gradual reduction in particle sizes. On the other hand, milling of the same blends in the planetary ball mill for 40, 50, 70 and 100 h resulted in the major ZrO_2 and Mg phases

with the minor amounts of ZrB_2 and MgO incubations.

- DSC curve of the milled powders exhibited an exothermic peak at 600 °C and an endothermic peak at 900 °C, respectively corresponding to the oxidation of Mg and incubation of ZrB_2 . The annealing temperature of the milled powders was selected as 1200 °C in regard of DSC-TGA experiments.
- Annealing at 1200 °C for 12 h enabled the milled powders to form ZrB_2 , MgO and both monoclinic and tetragonal ZrO_2 phases.
- Pure $\text{ZrB}_2/\text{ZrO}_2$ ceramic powders having particles in size range of 200 nm–1 μm and containing two different crystal structures of ZrO_2 phase (monoclinic and tetragonal) were obtained after milling in the SPEX™ 8000D Mixer/Mill for 30 h, annealing at 1200 °C for 12 h and leaching with 5 M HCl.

Acknowledgements

This study was supported by “Istanbul Technical University Scientific Research Projects” with the project title of “The Production of IVB Group and Lanthanide Group Metal Borides in Mechanochemical Reaction Medium” and with the project number of 32743. It was also funded by “The Scientific and Technological Research Council of Turkey (TÜBİTAK)” with the project title of “Synthesis of Refractory Metal Borides via Three Different Production Methods from Solid, Liquid and Gas Raw Materials for Various Application Areas; Sintering, Characterization, Comparison of Process and Final Products” and with the project number of 112M470.

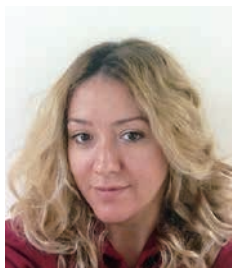
References

- Ağaoğulları D., Synthesis, Development and Characterization of Some Rare-Earth Hexaboride Powders and Their Sintered Products, Ph.D. Thesis, Advisor: Prof. Dr. İsmail Duman, Graduate School of Science, Engineering and Technology, Istanbul Technical University, (2014).
- Ağaoğulları D., Duman İ., Öveçoğlu M.L., Synthesis of LaB_6 powders from La_2O_3 , B_2O_3 and Mg blends via a mechanochemical route, *Ceramics International*, 38 (2012a) 6203–6214.
- Ağaoğulları D., Balcı Ö., Gökçe H., Duman İ., Öveçoğlu M.L., Synthesis of magnesium borates by mechanically activated annealing, *Metallurgical and Materials Transactions A*, 43A (2012b) 2520–2533.
- Ağaoğulları D., Balcı Ö., Öveçoğlu M.L., Suryanarayana C., Duman İ., Synthesis of bulk nanocrystalline samarium hexaboride, *Journal of the European Ceramic Society*, 35 (2015) 4121–4136.
- Ağaoğulları D., Balcı Ö., Öveçoğlu M.L., Duman İ., Preparation

- of LaB₆ Powders via Calciothermic Reduction using Mechanochemistry and Acid Leaching, *KONA Powder and Particle Journal*, 33 (2016) 203–218.
- Akgün B., Çamurlu H.E., Topkaya Y., Sevinç N., Mechanochemical and volume combustion synthesis of ZrB₂, *International Journal of Refractory Metals and Hard Materials*, 29 (2011) 601–607.
- Balcı Ö., Ağaoğulları D., Duman İ., Öveçoğlu M.L., Carbothermal production of ZrB₂-ZrO₂ ceramic powders from ZrO₂-B₂O₃/B system by high-energy ball milling and annealing assisted process, *Ceramics International*, 38 (2012) 2201–2207.
- Basu B., Vleugels J., Biest O., Development of ZrO₂-ZrB₂ composites, *Journal of Alloys and Compounds*, 334 (2002) 200–204.
- Brouchu M., Gauntt B.D., Boyer L., Loehman R.E., Pressureless reactive sintering of ZrB₂ ceramic, *Journal of the European Ceramic Society*, 29 (2009) 1493–1499.
- Chamberlain A.L., Fahrenholtz W.G., Hilmas G.E., High-strength zirconium diboride-based ceramics, *Journal of the American Ceramic Society*, 87 (2004) 1170–1172.
- Chen L., Gu Y., Yang Z., Shi L., Ma J., Qian Y. Preparation and some properties of nanocrystalline ZrB₂ powders, *Scripta Materialia*, 50 (2004) 959–961.
- Chen D., Zhang W., Li X., Hu P., Han J., Hong C., Han W., Microstructural feature and thermal shock behaviour of hot-pressed ZrB₂-SiC-ZrO₂ composite, *Materials Chemistry and Physics*, 116 (2009) 348–352.
- Chen B., Yang L.S., Heng H., Chen J.Z., Zhang L.F., Xu L.Q., Qian Y.T., Yang J., Additive-assisted synthesis of boride, carbide, and nitride micro/nanocrystals, *Journal of Solid State Chemistry*, 194 (2012) 219–224.
- Deng J., Cheng L., Hong Z., Su K., Zhang L., Thermodynamics of the production of condensed phases in the chemical vapor deposition process of zirconium diboride with ZrCl₄-BCl₃-H₂ precursors, *Thin Solid Films*, 520 (2012) 2331–2335.
- El-Eskandarany M.S. Mechanical alloying for fabrication of advanced engineering materials. Norwich, NY: Noyes Publications, 2001.
- Fahrenholtz W.G., Hilmas G.E., Refractory diborides of zirconium and hafnium, *Journal of the American Ceramic Society*, 90 (2007) 1347–1364.
- Frazer E.J., Anthony K.E., Welch B.J., Electrodeposition of zirconium diboride from oxides dissolved in molten cryolite, *Electrodeposition and Surface Treatment*, 3 (1975) 169–177.
- Gebhardt J.J., Cree R.F., Vapor-Deposited Borides of Group IVA Metals, *Journal of the American Ceramic Society*, 48 (1965) 262–267.
- Greenwood N.N., Parish R.V., Thornton P., Metal Borides, *Quarterly Reviews, Chemical Society*, 20 (1966) 441–464.
- Guo S. Densification of ZrB₂-based composites and their mechanical and physical properties: A review, *Journal of the European Ceramic Society*, 29 (2009) 995–1011.
- Guo S., Hu C., Kagawa Y., Mechanochemical processing of nanocrystalline zirconium diboride powder, *Journal of the American Chemical Society*, 94 (2011) 3643–3647.
- Hong C., Zhang X., Li W., Han J., Meng S., A novel functionally graded material in the ZrB₂-SiC and ZrO₂ system by spark plasma sintering, *Materials Science and Engineering: A* 498 (2008) 437–441.
- Jalaly M., Bafghi M.S., Tamizifar M., Gotor F.J., Mechanosynthesis of nanocrystalline ZrB₂-based powders by mechanically induced self-sustaining reaction method, *Advances in Applied Ceramics*, 112 (2013) 383–388.
- Jalaly M., Bafghi M.S., Tamizifar M., Gotor F.J. An investigation on the formation mechanism of nano ZrB₂ powder by a magnesiothermic reaction, *Journal of Alloys and Compounds*, 588 (2014) 36–41.
- Khanra A.K., Pathak L.C., Godkhindi M.M. Double SHS of ZrB₂ powder, *Journal of Materials Processing Technology*, 202 (2008) 386–390.
- Li B., Deng J., Li Y., Oxidation behavior and mechanical properties degradation of hot-pressed Al₂O₃/ZrB₂/ZrO₂ ceramic composites, *International Journal of Refractory Metals and Hard Materials* 27 (2009) 747–753.
- Li B., Deng J., Wu Z., Effect of cutting atmosphere on dry machining performance with Al₂O₃/ZrB₂/ZrO₂ ceramic tool, *International Journal of Advanced Manufacturing Technology*, 49 (2010) 459–467.
- Li W., Zhang X., Hong C., Han W., Han J., Preparation, microstructure and mechanical properties of ZrB₂-ZrO₂ ceramics, *Journal of the European Ceramic Society*, 29 (2009) 779–786.
- Malyshev V.V., Gab A.I., Theoretical fundamentals and practical implementation of electrometallurgical processes of producing disperse zirconium diboride powders and coatings, *Russian Journal of Non-Ferrous Metals*, 50 (2009) 485–491.
- Melendez-Martinez J.J., Dominguez-Rodriguez A., Monteverde F., Melandri C., Portu G., Characterisation and high temperature mechanical properties of zirconium boride-based materials, *Journal of the European Ceramic Society* 22 (2002) 2543–2549.
- Monteverde F., Guicciardi S., Bellosi A., Advances in microstructure and mechanical properties of zirconium diboride based ceramics, *Material Science and Engineering: A*, 346 (2003) 310–319.
- Monteverde F., Progress in the fabrication of ultra-high-temperature ceramics: in-situ synthesis, microstructure and properties of a reactive hot-pressed HfB₂-SiC composite, *Composite Science and Technology*, 65 (2005) 1869–1879.
- Monteverde F., Bellosi A., Scatteia L., Processing and properties of ultra-high temperature ceramics for space applications, *Material Science and Engineering: A*, 485 (2008) 415–421.
- Nettleship I., Stevens R., Tetragonal zirconia polycrystal (TZP)-A review, *International Journal of High Technology Ceramics*, 2 (1987) 1–32.
- Opeka M.M., Talmy I.G., Zaykoski J.A., Mechanical, thermal, and oxidation properties of refractory hafnium and zirconium compounds, *Journal of the European Ceramic Society*, 19 (1999) 2405–2414.
- Radev D.D., Klissurski D., Mechanochemical synthesis and SHS of diborides of titanium and zirconium, *Journal of Material Synthesis Processing*, 9 (2001) 131–136.

- Setoudeh N., Welham N.J., Formation of zirconium diboride (ZrB_2) by room temperature mechanochemical reaction between ZrO_2 , B_2O_3 and Mg, *Journal of Alloys and Compounds*, 420 (2006) 225–228.
- Suryanarayana C., Mechanical alloying and milling, *Progress in Materials Science*, 46 (2001) 1–184.
- Upadhy K., Yang J.M., Hoffmann W.P., Materials for ultrahigh temperature structural applications, *American Ceramic Society Bulletin*, 76 (1997) 51–56.
- Qiu H.Y., Guo W.M., Zou J., Zhang G.J., ZrB_2 powders prepared by boro/carbothermal reduction of ZrO_2 : The effects of carbon source and reaction atmosphere, *Powder Technology*, 217 (2012) 462–466.
- Zhang X., Li W., Hong C., Han W., Han J., A novel development of $\text{ZrB}_2/\text{ZrO}_2$ functionally graded ceramics for ultra-high-temperature application, *Scripta Materialia*, 59 (2008) 1214–1217.
- Zhang G., Guo W., Ni D., Kan Y., Ultrahigh temperature ceramics (UHTCs) based on ZrB_2 and HfB_2 systems: powder synthesis, densification and mechanical properties, *Journal of Physics: Conference Series*, 176 (2009) 012041.
- Zhu T., Li W., Zhang X., Hu P., Hong C., Weng L., Oxidation behavior of $\text{ZrB}_2\text{-SiC-ZrO}_2$ ceramic composites in the temperature range of 800–1200 °C, *Materials Chemistry and Physics*, 116 (2009a) 593–598.
- Zhu T., Li W., Zhang X., Hu P., Hong C., Weng L., Damage tolerance and *R*-curve behavior of $\text{ZrB}_2\text{-ZrO}_2$ composites, *Material Science and Engineering: A*, 516 (2009b) 297–301.

Author's short biography



Duygu Ağaoğulları

Duygu Ağaoğulları received her M.Sc. degree in 2007 and Ph.D. degree in 2014 in Materials Science and Engineering Department from Istanbul Technical University. She worked as a research assistant between 2005 and 2013, and has been affiliated since 2013 in I.T.U. She has been assigned as researcher/scholar in 10 scientific projects. Now, she is working as a postdoctoral scholar in Materials Science and Engineering Department in Stanford University. Her main research activities are powder metallurgy, high-tech boron products and composite materials. She is author/co-author of 21 papers, 1 Patent cited in Web of Science and 75 international conference proceedings.



Özge Balcı

Özge Balcı received her M.Sc. degree in Metallurgical and Materials Engineering from Istanbul Technical University in 2010 and continues her Ph.D. in the same department. She has been assigned as researcher in 4 scientific projects and gained professional fellowships in 3 research projects. She has been as a visiting researcher at IFW Dresden for 6 months during her Ph.D studies. Her main research activities are powder metallurgy, high-tech boron products and composite materials. She is author/co-author of 11 papers and 1 Patent cited in Web of Science and 42 proceedings presented in international conferences.



M. Lütfi Öveçoğlu

Prof. Dr. M. Lütfi Öveçoğlu received his M.Sc. and Ph.D. degrees in Materials Science and Engineering from Stanford University in 1984 and 1987. He has been affiliated with the Department of Metallurgical and Materials Engineering at Istanbul Technical University since 1990. He is the founder and technical director of Particulate Materials Laboratories (PML), a cluster of 9 laboratories. His main research activities are mechanical alloying and mechanochemical synthesis of W-based, Al-based and boride-based materials. He is author/co-author of 145 papers and 1 patent cited in Web of Science, 2 book chapters and 3 edited conference proceedings having about 905 citations.



İsmail Duman

Prof.Dr. İsmail Duman received his M.Sc. degree from Istanbul Technical University in 1978 and Ph.D. degree from Berlin Technical University in 1985 in Metallurgical Engineering. He has been affiliated with Department of Metallurgical and Materials Engineering at Istanbul Technical University since 1980. His main research activities are extractive metallurgy, powder metallurgy, development of high-tech boron products and CVD technologies. He has been the supervisor of 17 M.Sc. and 8 Ph.D. dissertations and he has been assigned as project director or researcher in 23 industrial/scientific research projects. He is author/co-author of 49 papers and 7 Patents cited in Web of Science.

Comparison of Compression and Material Properties of Differently Shaped and Sized Paracetamols[†]

Michal Šimek^{1,2*}, Veronika Grünwaldová² and Bohumil Kratochvíl¹

¹ Department of Solid State Chemistry, University of chemistry and technology Prague, Czech Republic

² Zentiva k.s., Czech Republic

Abstract

Paracetamol is well-known API (active pharmaceutical ingredient) for its bad flow and compression abilities. To improve the compressibility, a high amount of excipient is commonly mixed with paracetamol to create better compressible material. Conversely, we used modified crystallization procedures to prepare plate, irregular and spherical particles from original raw paracetamol to prepare directly compressible API. To expand our screening, several sizes of each shape were prepared and material properties analyzed, mainly the flow and compression abilities, and significant variation of the properties presented; from very poor properties of raw paracetamol to excellent properties of spherical crystals which exhibited ability to be directly compressed without excipient. The analysis also showed very small effect of the size modification on tablet compression and material behavior as the main contribution had the shape alteration and compression force.

Keywords: API, shape modification, particle, properties, compression

1. Introduction

Crystal habit, polymorphism, size and other properties can be modified by the variation of crystallization conditions such as the presence of impurities, ultrasonic frequency, type of solvent and cooling rate (Jordens et al., 2014; Lacmann, 1998). Different crystal habit of a particular drug possesses different in the specific surface and free surface energy. Therefore, they may exhibit different physico-mechanical properties, powder flow and compressibility, which are of pharmaceutical interest (El-Zhry El-Yafi and El-Zein, 2015; Huettnerrauch and Moeller, 1983; Marshall and York, 1991; York, 1983).

Attempts to change the crystal habit and the workability of drugs using alternative crystallization procedures of drugs has been published; for example ibuprofen (Gordon and Amin, 1984), hexamethylmelamine (Gonda, 1985), nitrofurantoin (Marshall and York, 1989) and paracetamol (Ó'Ciardhá et al., 2011). Although, more general influence of several different shapes and sizes of a single API on flowability and compressibility has not yet been presented.

Several shapes and sizes of paracetamol crystals (Form I) were prepared; and their material properties and compressibility compared. We varied the already published different methods of paracetamol crystallization to prepare plates (Garekani et al., 1999), irregular (Kaialy et al., 2014) and spherical (Garekani et al., 2000) paracetamol. Some particle sizes of the described procedures could not have been reproduced; thus, some of the methods were redesigned as described.

2. Materials and methods

Different shapes were prepared from raw paracetamol (Anqui Lu'an Pharmaceutical Co. Ltd, Anqui, Shandong province, China), which was consisted of very small needle-shaped and mainly of irregular particles (**Fig. 3**). This active pharmaceutical ingredient (API) is a widely used over-the-counter analgesic and antipyretic (Aghababian, 2010; Ahmad, 2010). Other used solutions and solids of this work were obtained from Sigma-Aldrich (Sigma-Aldrich Co., Prague, Czech Republic).

2.1 Crystallization procedures

The addition of a second substance, usually a liquid diluent, which reduces the solubility of the solute in the solvent, is one of the common methods of crystallization and it is known as salting-out. The diluent must be misci-

[†] Received 28 July 2015; Accepted 9 November 2015
J-STAGE Advance published online 30 January 2016

¹ Technická 5, 166 28 Prague, Czech Republic

² U Kabelovny 130, 102 37 Prague, Czech Republic

* Corresponding author: Michal Šimek;

E-mail: simekm@vscht.cz

TEL: +420-721-728-186

ble with the crystallization solvent and the solute should be relatively insoluble in it. The preparation of different shapes of paracetamol was driven by the change of the solvent, temperature or usage of additives. The additive inhibited the crystal growth in some directions and produced unusual shapes of the crystal habit. The change of the stirring speed provided different particle size distribution of prepared paracetamols. In every case, the precipitated crystals were collected by filtration using a Büchner funnel under vacuum with no agitation. They were dried for 24 h and stored in tightly closed jars. One size of the original supplied raw paracetamol, two sizes of spheres, three sizes of plates and three sizes of irregulars were prepared (in amount of 30 g) and used for next experiments. Polymorphic purity of prepared samples was tested.

2.1.1 Plates

Paracetamol (50 g) was dissolved in ethanol p.a. (120 ml) at 65 °C. The solution was poured into cooled distilled water (500 ml, 3 °C) with stirring speed 100 rpm to obtain big plates, or 200 rpm to obtain medium plates of paracetamol. After the cooling of the mixture to 25 °C, products were filtered and dried in an oven (80 °C, 24 h). Higher stirring did not produce smaller plates, but irregular shaped particles. To produce smaller plates, the procedure was modified. If methanol was used as a solvent, the procedure led to small plates. Paracetamol (50 g) was dissolved in methanol p.a. (170 ml) at 40 °C. The solution was poured into cooled distilled water (500 ml, 3 °C) with stirring speed 600 rpm. The product was filtered and dried as described.

2.1.2 Irregulars

Paracetamol (50 g) was dissolved in the solution of ethanol p.a. (120 ml) and distilled water (500 ml) at 65 °C. The solution was placed into ice bath and slowly cooled to 25 °C with stirring speed 100 rpm to obtain big irregulars, or 300 rpm to obtain medium irregulars, or 1200 rpm for small irregulars of paracetamol. Products were filtered and dried in an oven (80 °C, 24 h).

2.1.3 Spheres

Paracetamol (50 g) was dissolved in ethanol p.a. (120 ml) at 65 °C. The solution was poured into cooled distilled water (500 ml, 3 °C). The water contained PVP 40000. The stirring speed was set to 200 rpm to obtain medium spheres, or 300 rpm to obtain small spheres of paracetamol. After the cooling of the mixture to 25 °C, products were filtered and dried in an oven (55 °C, 24 h). The big sized particles were not prepared. Although reduction of the stirring speed led to bigger particles, they were contaminated by different shape of particles, mainly irregular and columnar particles.

Table 1 Flow properties and angle of repose

Flow Property	Angle of Repose (degrees)
Excellent	25–30
Good	31–35
Fair—aid not needed	36–40
Passable—may hang up	41–45
Poor—must agitate, vibrate	46–55
Very poor	56–65
Very, very poor	> 66

2.1.4 Bulk volume and tapped volume of powders

Paracetamol (20 g) was placed into a measuring cylinder (250 ml) which was mounted into Sotax TD2 Tap density tester (Sotax Pharmaceutical Testing s.r.o., Prague, Czech Republic) and the apparent volume of the material noted. The machine did 1250 taps and the volume was noted again after tapping. The experiments were in the keeping with European Pharmacopoeia (European Medicines Agency, 2006a).

2.1.5 Angle of repose

Paracetamol (20 g) was placed into a funnel of Pharmatest PTG S-3XY (Pharma test AG, Hainburg, Germany) and depleted, with the secondary stirring of 20 rpm, through a release flap (15 mm) into a measurement plate and the angle of repose from the created powder cone was measured by a detector. The classification system of the powder flowability from European Pharmacopoeia is shown in **Table 1** (European Medicines Agency, 2006b).

2.2 Analysis of particle size and shape

A small amount of paracetamol was fixed on aluminum stubs using the double sided conductive adhesive carbon tapes and sputtered with platinum for 240 s (Sputter SC7640; Quorum Technologies Ltd, Ashford, United Kingdom) and observed with a scanning electron microscope Mira/Tescan LM (Tescan a.s., Brno-Kohoutovice, Czech Republic). Particle size distribution (PSD) was analyzed with image analyse software NIS Elements and *d*-values [lower decil *d*(0.1), median *d*(0.5) and upper decil *d*(0.9)] of particle size distributions were obtained (Šimek et al., 2015).

2.3 DSC analysis

All prepared products was tested of polymorphic purity of paracetamol with differential scanning calorimeter (DSC Pyris 1, Perkin Elmer, Waltham, Massachusetts, USA) was used to determine the solid-state nature of dif-

Table 2 Melting points of paracetamol forms

Form	$T_m/^\circ\text{C}$
I	$168,6 \pm 0,2$
II	$156,4 \pm 0,2$

ferent paracetamols. An accurate weight of each paracetamol powder (4–8 mg) was placed in 40 μL aluminium DSC pan, sealed non-hermetically and heated (range 30–200 $^\circ\text{C}$) at a heating ramp rate of 10 $^\circ\text{C}/\text{min}$ under a nitrogen gas (50 L/min). Before each measurement, the sample was allowed to equilibrate for 5 min at 30 $^\circ\text{C}$. Melting points of known paracetamol forms are shown in **Table 2** (Di Martino et al., 1996).

2.4 Tablet compression

Each of prepared materials was formulated into tablets. Tablets contained only paracetamol (200 mg); no excipient was used. The die wall was cleaned with acetone and prelubricated with 4 % w/w magnesium stearate in acetone before each compression. The compression was carried out using Style one Classic compactor (Medel Pharm Beynost, France) with 7 mm flat faced punches. Ten tablets were produced at compression forces of 5, 10, 15 and 25 kN. Three speeds of compression were used: 25 percent of max speed (87.5 mm/s), 50 percent of max speed (175 mm/s) and 75 percent of max speed (262.5 mm/s). During the compression, punch separation and applied mean force were monitored with Analis software v.2 (Medel Pharm Beynost, France).

2.5 Analyses of compression data

Both force and displacement data from the upper and lower punches were collected from Analis v.2 software during a compression cycle and data were processed to the Heckel equation (Eq. (1)) (Heckel, 1961a, b).

$$\ln\left(\frac{1}{1-D}\right) = kP + A \quad (1)$$

A typical Heckel plot of Eq. (1) is illustrated in **Fig. 1**. Parameter D is the relative density of tablet (the ratio of tablet density to true density of powder) at applied pressure P . k is the slope of the straight line portion of the Heckel plot and the reciprocal of k is the mean yield pressure (Garekani et al., 1999). Since the tablet dimensions were measured in the die, it is referred to as apparent mean yield pressure. The total densification of the powder bed due to die filling and particle rearrangement, D_a , was obtained from the intercept of the linear portion of this plot, A , using Eq. (2).

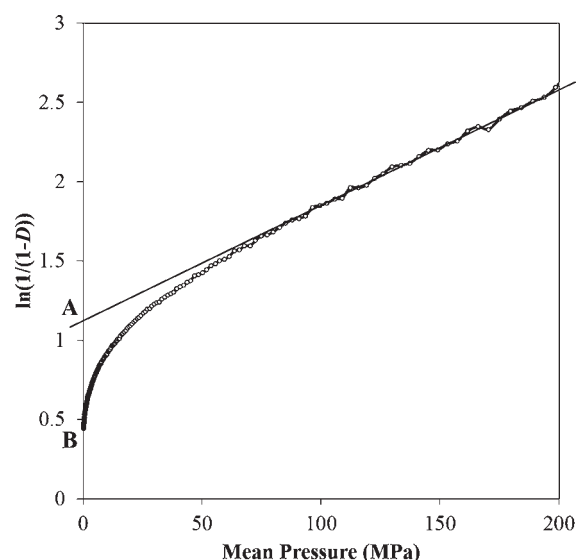


Fig. 1 Heckel plot for paracetamol (Irregular, small) obtained at a compression speed 25 percent and compression force 25 kN.

$$D_a = 1 - e^{-A} \quad (2)$$

From B , the place where the Heckel plot intercepts the $\ln(1/(1-D))$ axis (**Fig. 1**), the density of powder at zero pressure, D_0 , is obtained (Eq. (3)). D_0 can be defined as the densification due to die filling or to initial powder packing.

$$D_0 = 1 - e^{-B} \quad (3)$$

2.6 Measurement of elastic and plastic energy, elastic recovery

For our system in which both punches were mobile, the punch separation was plotted against the mean compression force (Garekani et al., 1999; Gibson, 2009). The area under this curve is the work done or energy. The work done of compression (plastic energy) and expansion work of compression (elastic energy) were calculated using the data collected from Analis v.2 software.

Fig. 2 illustrates a typical force-punch separation. Point A represents the minimal force and maximal punch separation at the beginning of compression. Point B represents the peak force at minimal punch separation, C shows the minimum punch separation and D represents the punch separation after decompression when the force is zero, giving the tablet thickness. The total compression energy is represented by area ABC , and the decompression energy or elastic energy is equal to area under curve CBD . The difference between area ABC and CBD determines the plastic energy (the area under curve ABD).

To calculate the elastic recovery of each tablet in the die we used Eq. (4) (Armstrong and Haines-Nutt, 1972).

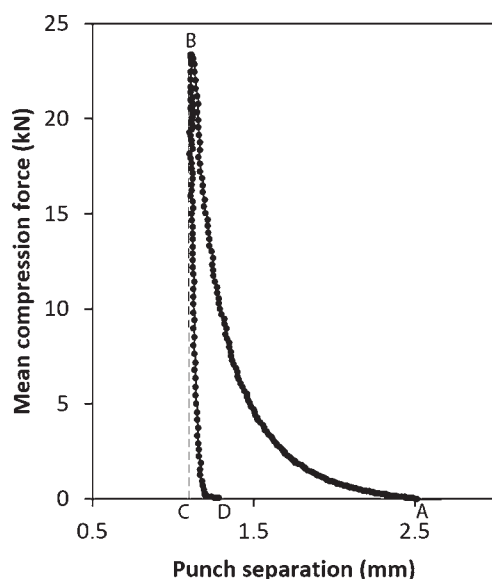


Fig. 2 Force-punch separation plot for paracetamol (Irregular, small) obtained at a compression speed 25 percent and compression force 25 kN.

$$\% \text{ Elastic recovery} = [(H - H_c) / H_c] \times 100, \quad (4)$$

where H_c and H are the thickness of tablet under maximum pressure and after the compression force was removed, respectively (Garekani et al., 1999).

3. Results and discussion

Under the conditions, described in the methodology section, we prepared several samples of paracetamol with different shape (**Fig. 3**). At the first sign, the properties of the materials were mainly relevant to the shape of the crystals and less appropriate to the crystal size.

Particles size distributions of prepared samples, described with d -values, are presented in **Table 3**. Samples of different sizes of each shape were labelled big, medium, or small according to the d -values. The particle size distribution of raw paracetamol was in good keeping with the medium class; and two prepared samples of spherical paracetamols were in keeping with medium and small class.

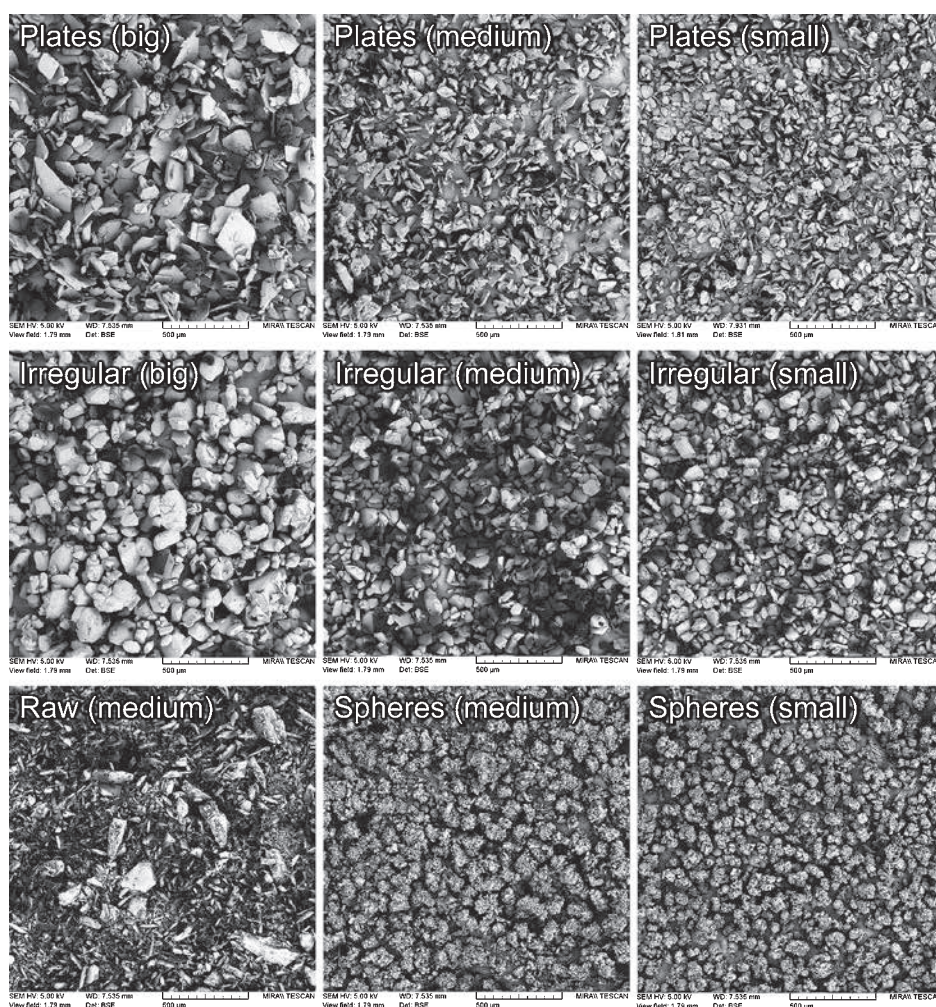


Fig. 3 SEM micrographs of prepared paracetamols and raw paracetamol.

Table 3 Overview of d -values of all prepared paracetamols

Shape	$d(0.1)$ [μm]	$d(0.5)$ [μm]	$d(0.9)$ [μm]
Raw (medium)	17	40	100
Plates (big)	51	113	203
Plates (medium)	37	67	105
Plates (small)	19	40	61
Irregular (big)	51	102	222
Irregular (medium)	44	91	159
Irregular (small)	10	25	57
Spheres (medium)	26	56	103
Spheres (small)	23	39	62

DSC scans of the paracetamols showed only the melting endotherm of paracetamol Form I. No events such as phase transformation or hydration were seen during the crystallization process.

3.1 Bulk volume and tapped volume of powders

The difference between untapped and tapped volume is in the rearrangement of the particles in the bulk of material. The rearrangement mainly consisted of two main events. The first is the movement of the small and very small particles into the space between big particles. It means that samples with a wider PSD, e.g. raw paracetamol, more tended to change the bulk volume according to tapping than paracetamol with a narrow PSD. The second event relates to a crystal shape and orientation of the particles due to the crystal shape. For example, plates can be settled in the bulk in two preferred position—perpen-

dicularly or parallel. Perpendicular position tend to a big inter-particle space, therefore, the volume of material bulk significantly increases. Tapping of plates caused the reorganization of the particles to the parallel position and a significant reduction of the inter-particle space and the overall volume of the bulk were significantly reduced even after several taps. The product was not so dense in comparison to other crystal shapes because the plate particles were not locked together. Conversely, irregular particles and spheres exhibited small change after tapping as the starting position of the particles was very tight due to the very good flow of the particles and very good natural rearrangement, more significant for irregular particles.

The effect of the different sizes of particles was slightly observed for all types of shape. In all cases, smaller particles tended to smaller bulk volume and smaller tapped volume. But overall, the effect of size was very small and negligible.

3.2 Angle of repose

Wide PSD and irregularly-needed shape of raw paracetamol created big contact areas between the particles, thus, the spill of the raw paracetamol was minimal and material was practically only stacked. Even the flow must have been supported by secondary stirring to deplete the material from the funnel to the measurement plate. Similar to the measurement of the bulk and tapped volumes, size variation minimally affected the angle of repose and the main difference was based on the different shape of paracetamol crystals. Plates created big contact areas and, when they run from the funnel to the measurements plates, adhesion forces held particles together, the spread of the particles on the measurement plate was low and the created angle of repose was high. Irregular and spherical

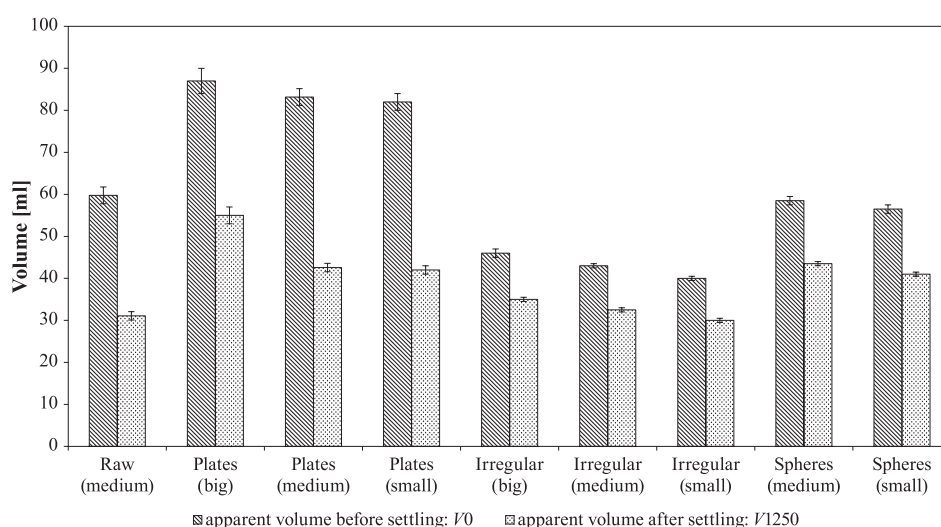


Fig. 4 Bulk volume before the tapping started (V_0) and tapped volume after 1250 taps (V_{1250}) of different shapes of paracetamol crystals with different PSD.

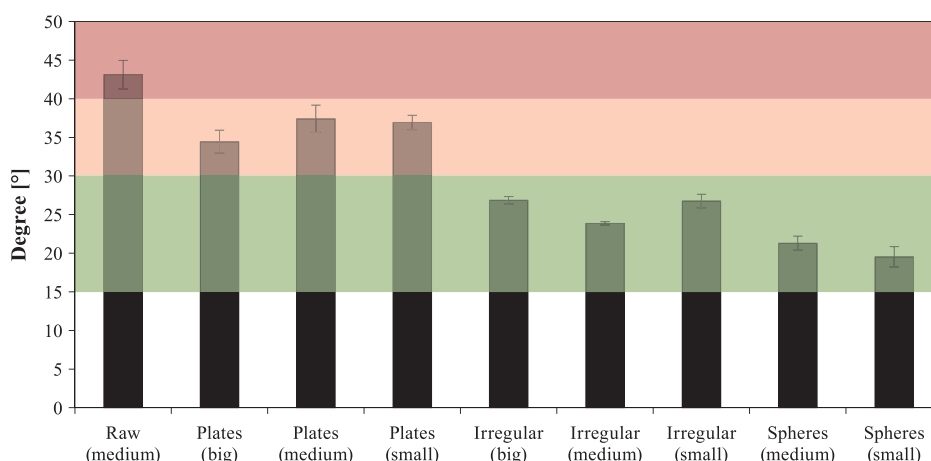


Fig. 5 Angle of repose of different shapes of paracetamol crystals with different PSD.

particles exhibited a free flow into the measurement plate and the angle of repose was very small. The smallest angles of repose were measured for spherical particles and they were even smaller than the values stated in the classification system of the powder flowability (**Table 1**) of European Pharmacopoeia (European Medicines Agency, 2006b).

3.3 Compression properties of paracetamols

Compression of raw, irregular or plate-like crystals of paracetamol produced very weak compacts which had no measureable strength, but they had a high tendency to cap and laminate at all compression forces used. Conversely, spherical crystals produced very strong compacts under the same conditions with no tendency to cap. The strength of these tablets oscillated from 42 N (at compression force 5 kN) to 90 N (at compression force 25 kN).

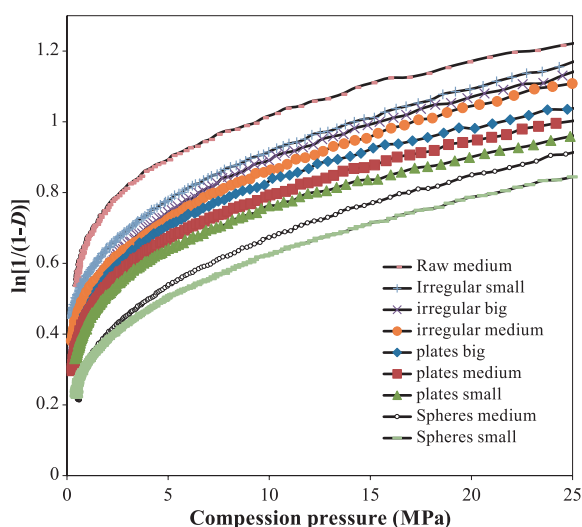


Fig. 6 Heckel plots of different shapes and sizes of paracetamols obtained at compression speed 25 percent.

Crystal shape was the main distributive parameter and size was the minor distributive parameter of the Heckel plots of paracetamols (**Fig. 6**). Irregular and raw paracetamols (irregular particles with a wide PSD) exhibited higher change of densities for given applied pressure than plate-like and spherical paracetamols (**Table 4**). Therefore, the greatest degree of densification during compression was seen for irregular particles, including also raw paracetamol.

Increased frictional and cohesive forces between thin plate-like crystals, due to their large and flat surface, restricted particle sliding and thus reduced densification rate. Additional fragmentation, easier packing or rearrangement occurred at lower pressure. The differentials of $D_a - D_0$ (**Table 4**) also indicated that densification due to die filling and particle rearrangement for the irregular crystals was higher than for plate-like or spherical crystals. Spherical crystals exhibited very good flowability (**Fig. 5**), thus, the die was filled very tight according to the good natural particle rearrangement.

The particle size effect was identical for all paracetamols. Bigger particles tended more to rearrangement at the beginning of compression than smaller particles of the same shape, as illustrated in higher values of the differential $D_a - D_0$ for bigger particles (**Table 4**). It was the most probably caused by higher amount of inter-particle space between bigger than smaller particles. The effect of different particle sizes and shapes was reduced when compression force and speed were increased.

3.4 Elastic recovery and tablet capping analysis

Generally, elastic recovery of tablets most depended on both the shape of particles and compression force; which influenced the total area of permanent bonds created between crystals when compressed. The effect of the force and shape on the elastic recovery of in-die tablets indi-

Table 4 The values D_a-D_0 derived from the Heckel plots of compressed paracetamols

	Irregular			Plates			Raw	Spheres	
	(big)	(med.)	(small)	(big)	(med.)	(small)	(med.)	(med.)	(small)
25 % speed									
5 kN	0.50	0.47	0.41	0.43	0.42	0.36	0.48	0.36	0.35
10 kN	0.44	0.42	0.40	0.42	0.40	0.36	0.44	0.35	0.33
15 kN	0.44	0.41	0.39	0.40	0.39	0.35	0.39	0.34	0.30
20 kN	0.41	0.40	0.36	0.38	0.38	0.34	0.39	0.32	0.30
25 kN	0.38	0.38	0.34	0.37	0.36	0.32	0.39	0.31	0.30
50 % speed									
5 kN	0.42	0.38	0.37	0.41	0.37	0.35	0.40	0.36	0.34
10 kN	0.41	0.38	0.36	0.37	0.36	0.34	0.39	0.32	0.31
15 kN	0.40	0.37	0.36	0.37	0.36	0.32	0.38	0.31	0.30
20 kN	0.39	0.36	0.36	0.36	0.35	0.32	0.37	0.30	0.30
25 kN	0.37	0.31	0.33	0.35	0.34	0.29	0.37	0.30	0.29
75 % speed									
5 kN	0.42	0.38	0.37	0.38	0.36	0.32	0.39	0.34	0.33
10 kN	0.41	0.36	0.35	0.37	0.36	0.32	0.38	0.32	0.30
15 kN	0.41	0.36	0.34	0.36	0.36	0.31	0.37	0.31	0.29
20 kN	0.40	0.32	0.34	0.35	0.33	0.31	0.37	0.30	0.28
25 kN	0.36	0.29	0.33	0.34	0.31	0.27	0.37	0.29	0.28

cated that tablets made from spherical crystals exhibited the lowest elastic recoveries (**Table 5**). Spheres (spherulites) probably fragmented and they created very strong bonds between particles, which were originally very close to each other before compression; due to small bulk volume (**Fig. 4**) and very good powder flow (**Fig. 5**). Irregular particles, which are the most similar in shape to spheres, exhibited different compression behaviour, as irregular particles were single crystals, not made from many small crystals like spherulites of paracetamol, thus the attraction of fragmentation was reduced. Raw paracetamol highly tended to rearrangement of the small particles into the inter-particle space between the big particles when compressed due to high heterogeneity of particle sizes (see in **Fig. 3**); therefore, a lot of the permanent bonds were created. But the heterogeneous distribution of the bonds created in the tablet led to high tendency of capping.

Capping was observed in case of raw, irregular and plates. The degree of capping corresponded with the trend of elastic recovery. Apart from the spheres, the lowest elastic recovery (5.9 %—irregular, small, 5 kN, 25 % speed) led to capping chance up to 86 percent; and the highest elastic recovery (22.4 %—plates, small, 25 kN, 75 % speed) led to 100 percent chance of capping. Spheres

exhibited no sign of capping. Besides the theory of higher fragmentation of the polycrystalline spherules, the most reasonable explanation of this significantly different behaviour may be attributed to the residuals of PVP remaining on the face of the crystals after crystallization. The amount of residual PVP was under detectable limit of DSC analysis; and functioned as particle glue.

The size effect was also observed. Conversely to the effect of particle rearrangement, the effect was not identical for all the shapes. Except the plate-like particles, bigger particles led to higher elastic recovery of tablets. Abnormal behaviour of plates may be assigned to high content of air in the powder bulk (**Fig. 4**).

Lower compression speed probably allowed better reorganization of the crystals at the beginning of compression; therefore, the elastic recovery was higher when higher compression speed applied. Insufficient time to rearrangement the compressed particles caused weaker bonds between particles, thus, tablets more expanded after compression. Moreover, combination of highest compression speeds and highest compression forces caused insufficient time for particle rearrangement which resulted in abnormalities from the trend observed at lower force and speed.

Table 5 Effect of compression force and speed on the elastic recovery of in-die tablets made from all paracetamols

	Irregular			Plates			Raw	Spheres	
	(big) [%]	(med.) [%]	(small) [%]	(big) [%]	(med.) [%]	(small) [%]	(med.) [%]	(med.) [%]	(small) [%]
25 % speed									
5 kN	8.1	7.8	5.9	9.5	9.6	10.2	8.1	4.2	3.5
10 kN	10.5	10.3	7.8	11.6	11.7	13.7	10.4	4.6	4.3
15 kN	14.1	11.7	10.1	11.9	14.0	14.1	10.9	6.5	5.3
20 kN	15.5	12.8	10.9	13.4	14.1	15.2	11.1	6.9	6.1
25 kN	15.1	13.7	11.9	17.1	17.4	19.8	11.7	7.4	6.2
50 % speed									
5 kN	9.5	8.4	7.9	13.0	14.1	14.6	10.9	4.3	4.2
10 kN	11.9	11.8	9.4	15.5	16.3	17.7	11.9	5.2	5.0
15 kN	14.7	13.2	11.4	18.0	18.1	18.4	12.7	6.9	6.1
20 kN	13.4	12.9	12.8	19.2	19.4	19.5	12.9	8.3	7.8
25 kN	11.5	11.6	11.7	18.9	19.5	19.9	13.2	9.4	8.1
75 % speed									
5 kN	10.5	9.4	9.1	14.2	15.1	15.7	11.8	5.5	4.7
10 kN	11.3	11.2	10.1	16.2	16.4	16.9	12.6	6.2	5.7
15 kN	10.7	11.9	10.8	18.5	19.4	20.6	13.1	8.6	6.3
20 kN	10.7	10.9	10.8	19.8	20.8	21.3	13.2	9.2	8.1
25 kN	10.1	10.1	10.0	20.1	22.2	22.4	13.4	9.8	8.3

4. Conclusion

Paracetamol is an active pharmaceutical ingredient known for its bad compression properties. Modified crystallization of paracetamol by a combination of solvents, stirring speed, cooling rate and additives caused a marked modification of the crystal habit and material properties; however, no polymorphic transformation was induced. Raw paracetamol had a wide PSD of irregular particles which caused poor flowability and a high difference of bulk and tapped densities. These properties predetermined this material to be badly compressible, whereas modified crystallization led to the preparation of spherical paracetamol which exhibited precisely opposite behavior.

The comparison of material properties shows that the particles shape, compression force and speed are the main parameters which influenced the compression and quality of prepared tables as well as the material properties. Conversely, different particle size had relatively small influence, which was more reduced with increased compression speed and force.

The most plastic material was the spherical paracetamol. The spherulites, the polycrystalline particles of paracetamol, probably tended to a significant fragmenta-

tion of particles, thus, strong bonds and significantly larger contact area were made between fragmented particles; and probably a non-detectable residuals of PVP after crystallization remained on the surface of particles and functioned as a particle glue. The elastic recovery of tablet, which were made from spherical paracetamol, was very low (from 3.5 to 9.8 percent) and we concluded it was responsible for no capping of these tablets. Other used shapes exhibited high elastic recovery and high probability of the visible capping of produced tablets (at least 86 percent) at all used conditions. The main difference was caused by the shape of the particles and less by the compression speed and force. The particles size had the smaller influence on this property.

Based on the experimental data, crystal manipulation via particle engineering is an efficient tool in producing crystals with optimal physico-mechanical properties to affect the compression behavior of API crystals. This approach might be of interest to those persons who are developing and optimizing the formulation process of poorly compressible APIs. Our further step is to assess the exact fragmentation of different shapes and size of paracetamol by our hot-stage methodology and compare the results with the presented evaluation.

Acknowledgments

The authors thank for financial support from Ministry of Education, Youth and Sports - specific university research (MSMT No 20/2015) for financial support. They also thank L. Krejčík for DSC analyzes and M. Beneš for the help with the Style one compactor.

References

- Aghababian R.V., Essentials of emergency medicine, Jones and Bartlett Publishers, 2010.
- Ahmad J., Hepatology and Transplant Hepatology: A Case Based Approach, Springer, 2010.
- Armstrong N.A., Haines-Nutt R.F., Elastic recovery and surface area in compacted powder systems, *J. Pharm. Pharmacol.*, 24 (1972) 135–136.
- Di Martino P., Guyot-Hermann A.-M., Conflant P., Drache M., Guyot J.-C., A new pure paracetamol for direct compression: the orthorhombic form, *Int. J. Pharm.*, 128 (1996) 1–8.
- El-Zhry El-Yafi A.K., El-Zein H., Technical crystallization for application in pharmaceutical material engineering: Review article, *Asian Journal of Pharmaceutical Sciences*, 10 (2015) 283–291.
- European Medicines Agency, European Pharmacopoeia—Part EP 2.9.34. Bulk density and tapped density of powders, 2006a.
- European Medicines Agency, European Pharmacopoeia—Part EP 2.9.36. Angle of repose, 2006b.
- Garekani H.A., Ford J.L., Rubinstein M.H., Rajabi-Siahboomi A.R., Formation and compression characteristics of prismatic polyhedral and thin plate-like crystals of paracetamol, *Int. J. Pharm.*, 187 (1999) 77–89.
- Garekani H.A., Ford J.L., Rubinstein M.H., Rajabi-Siahboomi A.R., Highly compressible paracetamol: I: crystallization and characterization, *Int. J. Pharm.*, 208 (2000) 87–99.
- Gibson M., Pharmaceutical Preformulation and Formulation, 2, Informa Healthcare USA, Inc., New York, 2009.
- Gonda I., Development of a systematic theory of suspension inhalation aerosols. I. A framework to study the effects of aggregation on the aerodynamic behaviour of drug particles, *International Journal of Pharmaceutics*, 27 (1985) 99–116.
- Gordon R.E., Amin S.I., Crystallization of ibuprofen, Google Patents, 1984.
- Huettenrauch R., Moeller U., Molecular galenics. Part 73. Correlation between the degree of order and the wettability of solids, *Pharmazie*, 38 (1983) 198.
- Jordens J., Gielen B., Braeken L., Van Gerven T., Determination of the effect of the ultrasonic frequency on the cooling crystallization of paracetamol, *Chemical Engineering and Processing: Process Intensification*, 84 (2014) 38–44.
- Kaialy W., Larhrib H., Chikwanha B., Shojae S., Nokhodchi A., An approach to engineer paracetamol crystals by anti-solvent crystallization technique in presence of various additives for direct compression, *Int J Pharm*, 464 (2014) 53–64.
- Lacmann R., Crystallization, Third Edition. J.W. Mullin, Butterworth-Heinemann, Oxford 1997, 527 Seiten, zahlr. Abb. und ISBN 0-7506-3759-5, Chemie Ingenieur Technik, 70 (1998) 1468–1468.
- Marshall P.V., York P., Crystallisation solvent induced solid-state and particulate modifications of nitrofurantoin, *International Journal of Pharmaceutics*, 55 (1989) 257–263.
- Marshall P.V., York P., The compaction properties of nitrofurantoin samples crystallised from different solvents, *International Journal of Pharmaceutics*, 67 (1991) 59–65.
- Ó'Ciardhá C.T., Frawley P.J., Mitchell N.A., Estimation of the nucleation kinetics for the anti-solvent crystallisation of paracetamol in methanol/water solutions, *Journal of Crystal Growth*, 328 (2011) 50–57.
- Šimek M., Grünwaldová V., Kratochvíl B., Hot-stage microscopy for determination of API fragmentation: comparison with other methods, *Pharm. Dev. Technol.*, in press (2015)
- York P., Solid-state properties of powders in the formulation and processing of solid dosage forms, *International Journal of Pharmaceutics*, 14 (1983) 1–28.

Author's short biography



Michal Šimek

In 2012 graduated in Drug synthesis and manufacturing at the Faculty of Chemical Technology, University of Chemistry and Technology in Prague. From 2012 researcher at the University of Chemistry and Technology Prague and researcher at the Solid state department at Zentiva Company in Czech Republic. From 2014, a reviewer for Science Domain international. Research: particle size analysis and science, formulation of solid drugs, crystallization and material science.



Veronika Grünwaldová

In 2002 graduated in chemistry at Prague Institute of Technology. In 2010 Ph.D. graduated in analytical chemistry at the Faculty of Science, Charles University in Prague. Positions: 2002–2006 Institute of Inorganic Chemistry AS CR, researcher; 2003–2006 Academy of Fine Arts, expert consultant; 2007–2012 Zentiva a.s., Analytical scientist; 2012—present Formulation Scientist. Specialization: particles size and morphology, chemical and phase's composition of solid pharmaceutical, forensic and art samples, recently development of generics solid formulation. Methodology: SEM, light microscope, X-ray diffractometer, laser diffractometer and PCCS. Other experimental skills include the use of EDX, X-ray fluorescence, microtome and macro objectives.



Bohumil Kratochvíl

In 1972 graduated in chemistry at the Faculty of Science, Charles University in Prague. In 1985 the transition from the Faculty of Science to the University of Chemistry and Technology, Prague (UCT). Positions : Head of the Department of Solid State Chemistry of the UCT , Vice-dean of the Faculty of Chemical Technology of the UCT and Vice-Rector for Science and Research of the UCT. Editor in Chief of the Chemické Listy journal (1986–2012). Research : Crystallography of coordination, inorganic and small organic compounds , recently application of X-ray diffraction methods in pharmaceutical research , development, production and control. Study of solid pharmaceutical phases: polymorphs, hydrates, cocrystals. Solid dosage forms.

Nanocrystallization of Al Powder by Cryomilling Process[†]

Mohammad Hossein Enayati

[†] Department of Materials Engineering, Isfahan University of Technology, Iran

Abstract

Al5083 powder was subjected to ball milling in liquid nitrogen for 8 h using an attrition ball milling. The evolution of morphology of powder particles and the refinement of grain size were studied by scanning and transmission electron microscopies. The results showed that during cryomilling the morphology of powder particles changed from spherical to equiaxed shape. Additionally, the size of powder particles increased from ~10 μm to ~20 μm with narrower distribution. Simultaneously the cryomilling was associated with a significant reduction of grain size so that the final product after 8 h of cryomilling had a nanocrystalline microstructure (~25 nm) with well-developed high angle grain boundaries. These features were discussed in terms of severe plastic deformation, cold-welding and fracturing of powder particles which occur simultaneously during cryomilling process.

Keywords: cryomilling, aluminium, Al5083, nanocrystalline powder

1. Introduction

Nanocrystalline materials are generally known as those materials that have a crystallite size less than 100 nm. This upper limit of 100 nm is based on the fact that most properties (mechanical/physical/chemical) of materials start to change significantly at this point. Although there are lots of experimental results showing that the change in properties can occur in crystallite size much smaller or in some cases larger than 100 nm.

In conventional coarse-grained polycrystals, with a typical grain size of 10 μm , the fraction of boundaries is very small. In contrast if the grain size reduces to nanocrystalline state (grain size < 10 nm) a high fraction (10^{18} – 10^{21} cm^{-3}) of material is boundaries. As a result, grain boundaries have significant contribution in physical and mechanical properties of nanocrystalline materials. Nanocrystallization leads to the hardness and strength enhancement and improvement of diffusivity, solid solubility, sintering ability and magnetism.

Vapor deposition, plasma processing, gas-condensation, chemical precipitation and crystallisation from the amorphous phase are well established processing routes for obtaining nanocrystalline materials. However, it is well known that mechanical milling (MM) and mechanical

alloying (MA) as solid synthesis routes can also be applied for production of a nanocrystalline as well as nanocomposite powders with high uniformity (Fogagnolo J.B. et al., 2004). Comparison of different preparation methods in terms of cost and productivity demonstrates that MM/MA is the most cost effective route capable of producing nanocrystalline materials in large quantity. It is worth mentioning that powder particles prepared by MA/MM are rarely monocrystals. Instead, MA/MM powders have micrometer dimensions with interior nanometer microstructure. The structure of each particle can be described as a poly-nanocrystalline. The final powder produced by MA/MM can be subsequently either consolidated by standard powder metallurgy techniques into bulk materials with desirable properties or deposited on surfaces of engineering parts using various thermal spraying methods.

It has been proved that grain refinement of powders in MM/MA to the nanometre size is governed by the plastic deformation induced during milling. In general, the grain size decreases continuously with milling time until a minimum (saturation) size is approached (Enayati M.H., 2015; Hellstern E. et al., 1989). Further refinement seems to be difficult to achieve for a fixed set of experimental conditions. Transmission electron microscopy (TEM) observations have revealed that nanocrystallization starts with development of shear bands and dislocations pile-ups at the early stages of milling (Eckert J. et al., 1992; Hellstern E. et al., 1989). With increasing milling time more dislocations are created in the grains leading to a dislocation cell structure and then low-angle boundaries. This stage is finally followed by development of a fully nanocrystal-

Received 20 January 2016; Accepted 3 March 2016

J-STAGE Advance Publication online 30 April 2016

[†] Isfahan 84156-83111, Iran

E-mail: ena78@cc.iut.ac.ir

TEL: +98-311-3915730 FAX: +98-311-3912752



line structure with high-angle grain boundaries (Eckert J. et al., 1992; Cocco G. et al., 1990).

Experimental findings have revealed that the minimum grain size for a given material is a constant value independent of milling conditions. In fact, the minimum grain size is determined by intrinsic properties of materials such as melting temperature, crystal structure and deformation behavior. The milling conditions can only affect the rate at which the grains refine and approach the minimum size. Eckert et al. (1992) observed that the minimum grain size, d_{\min} , in a series of FCC metals including Al, Cu, Ni, Pd, Rh and Ir scales inversely with the melting point, T_m , or the bulk modulus, B , of the respective metals. The higher the T_m or B , the smaller the d_{\min} is obtained. However, no clear inverse correlation between the minimum grain size and melting temperature was obtained for BCC metals Cr, Fe, Nb, W as well as for HCP metals Hf, Zr, Co, Ru. Koch C.C. (1989) observed that only the lower melting temperature FCC metals ($\leq T_m$ for Pd) exhibit an inverse dependence of d_{\min} on T_m .

The dependence of minimum grain size versus melting temperature has been discussed with respect to the competing rates of creating dislocations due to work hardening and recovery phenomena which scale with the melting point (Eckert J. et al., 1992; Benghalem A. and Morris D.G., 1994). Thereby, the minimum grain size achieved by ball milling is determined by the balance between creation and annihilation of dislocations during processing. On basis of this model d_{\min} scales inversely with hardness, proportionally with the stacking fault energy and exponentially with the activation energy for recovery. Hence, the grain size in final material can be controlled by changing the equilibrium rate of dislocation creation and recovery. It has been shown that in ball milling experiments not only the milling time but also further parameters, such as type of the mill machine, the milling tools material, the intensity of milling, the ball-to-powder weight ratio, the milling temperature and the milling atmosphere, may have significant influence on nanocrystallization process.

Experiments show that lowering milling temperature leads to a finer grain size (Koch C.C., 1997). The dependence of d_{\min} on milling temperature has directed researchers to another version of ball milling process known as “cryomilling”. This process benefits from ball milling at cryogenic temperatures. Two different methods have been applied for cryomilling. In most cases, a cryogenic liquid (e.g. liquid N_2) flows continuously inside the mill vessel. The raw materials are ball milled with the cryogenic liquid forming a slurry. In some set-ups the cryogenic temperature during ball milling has been achieved by circulation of cryogenic liquid around the outside surfaces of milling vessel. Basically, cryomilling experiments can be carried out in any type of milling ap-

Table 1 Some physical and mechanical properties of Al5083 alloy

Physical Properties	Value	
Density	2.65 g/cm ³	
Melting Point	843 K	
Electrical Resistivity	$0.058 \times 10^{-6} \Omega \cdot m$	
Thermal Conductivity	121 W/m·K	
Thermal Expansion	$25 \times 10^{-6}/K$	
Mechanical Properties	CW↑	CW↓
Modulus of Elasticity (GPa)	—	72
Proof Stress 0.2 % (MPa)	240	145
Tensile Strength (MPa)	345	300
Shear Strength (MPa)	190	175
Elongation A5 (%)	13	17
Hardness Vickers (HV)	95	70

CW↑ Severely cold worked

CW↓ Slightly cold worked

paratus although the attrition ball mill is often preferred.

Cryomilling process includes several advantages over room temperature ball milling. A benefit of cryomilling is that the rate of diffusional process like annihilation of dislocation is extremely limited at cryogenic temperature. As discussed earlier, under this condition the grain refines with a much higher rate. Hence the milling time required to attain a certain grain size is significantly reduced. Shorter milling time in case of cryomilling implies that a large quantity of powder can be processed in large-scale low-energy ball mills within a reasonable milling time.

The present research was aimed to study the process of nanocrystallization in Al5083 alloy during cryomilling. Synthesis of nanocrystalline structure in different aluminum alloys have been widely investigated but the nanocrystallization in cryomilling condition have been rarely reported. Al5083 alloy is a non-heat treatable aluminum alloy. As a results the strengthening of Al5083 is essentially restricted to cold working/work hardening. However, the strength of Al5083 may be further enhanced by scaling the grains size down to the nano range. Because of excellent combination of engineering properties (see **Table 1**) such as strength, weld ability and corrosion resistance, Al5083 have different applications specifically in chemical industries and marine environments.

2. Materials and methods

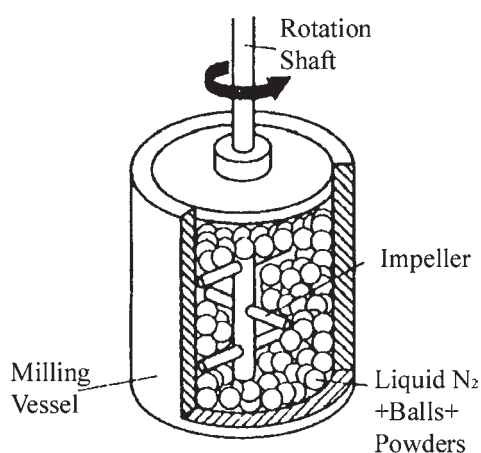
Gas atomized Al5083 powder was used as starting materials. **Table 2** lists the chemical composition of as-received

Table 2 Chemical composition of as-received Al5083 powder

Element	Weight percent
Si	0.15 %
Fe	0.18 %
Cu	0.1 %
Mn	0.7 %
Mg	4.5 %
Zn	0.25 %
Ti	0.05 %
Cr	0.15 %
Al	Balance

Table 3 Cryomilling conditions

Parameter	Value
Weight of Powder	1 kg
Weight of Balls	30 kg
Ball-to-Powder Weight Ratio	30:1
Diameter of Balls	6 mm
Speed of Rotating Shaft	180 rpm
Temperature of Milling Vessel	90 K
Stearic Acid (Surfactant)	0.2 wt%
Milling Time	8 h


Fig. 1 Schematic representation of cryomilling apparatus.

Al5083. The compositions of samples were determined using an energy dispersive X-ray spectrometer (EDX). The main alloying elements in this alloy was found to be Mg with traces of Cr, Zn, Ti, Fe, Cu, Si and Mn. To prevent oxidation or hydration, the powder was stored in vacuum chamber before cryomilling.

Cryomilling was performed in an attrition ball mill. **Fig. 1** shows a schematic configuration of milling apparatus.

This type of mill comprises a static cylindrical vessel with a rotating impeller with which a rather large quantity of powders (several kg) can be processed making it potentially suitable for commercial exploitation. The powder to be milled was placed in a stationary tank with balls and liquid nitrogen. This mixture was then stirred by the shaft with arms, rotating at a high speed of about 180 rpm. **Table 3** shows the cryomilling parameters used in this study.

The milling media including milling tank, shaft, impeller and balls were martensitic stainless steel 440C (Fe-18Cr-1.2C-1Mn-1Si) with a hardness of 60 HRC. A problem with ball milling process is the adhesion of pow-

der particles on milling surfaces reducing the powder yield. The sticking of powders on milling surfaces is caused by severe cold welding of powder. Extensive cold welding also results agglomeration of powder particles which leads to the coarse powder particles. These phenomena are more serious in the processing of ductile materials like aluminum. The adhesion of powders can often be overcome by adding a surface-active agent to the powder mixture in order to inhibit the cold welding process. In this study 0.2 weight percent stearic acid-as a surfactant- was added to the powder mixture. Stearic acid is a waxy solid with chemical formula of $C_{17}H_{35}CO_2H$.

The morphology of powder particles was analyzed in a Philips XL30 FEG scanning electron microscope (SEM) operating at 10 kV. The powder particles size was determined on SEM micrographs using ImageJ software. Powder samples were fixed in small quantities on a sample holder by Ag conductive paint. At least 50 separate particles were chosen for the measurement of powder particle size.

A CM20 transmission electron microscope (TEM) operating at 200 kV was used for observation and characterization of the internal structure of cryomilled Al5083 powders. A small amount of powder sample was dispersed in methanol using ultrasonication for ten minutes. The obtained suspension of particles was lifted on a carbon-coated Cu grid (400 mesh) by dipping the grid in the suspension gently and removing horizontally. The grid was then dried in air for several hours. The resulting specimens showed some thin areas suitable for TEM observation.

3. Results and discussions

Fig. 2 shows SEM images of as-received Al5083 powder particles with different magnifications.

As seen Al5083 particles were spherical in shape with a wide size distribution. The spherical morphology of

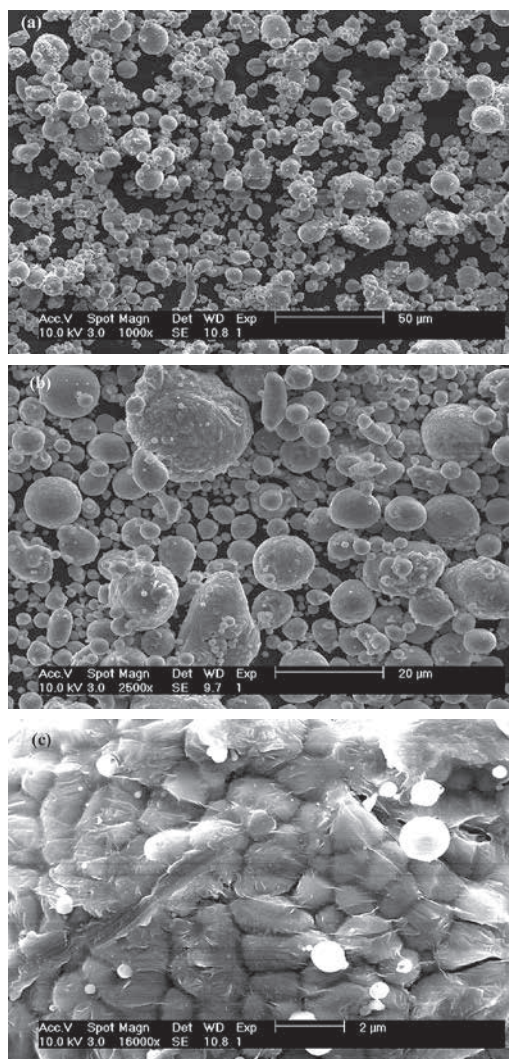


Fig. 2 SEM micrographs of as-received Al5083 powder particles with different magnifications.

as-received powder indicates that the powder was prepared by gas atomization process in which a stream of molten metal is mechanically disintegrated by a jet of high-pressure gas. Under this situation the cooling rate of the molten droplets is sufficiently slow for surface tension forces to spheroidize them before solidification occurs. The surface image of a particle is presented in **Fig. 2c** indicating a typical solidification morphology.

The powder particles size was analyzed on SEM using ImageJ software. The result showed that as-received Al5083 powder particles had a size distribution of 3–15 µm with a mean size of ~10 µm.

Fig. 3 shows SEM images of Al5083 powder particles after 8 h cryomilling. The initial spherical morphology has been destroyed by cryomilling process. Instead a nearly equiaxed morphology was developed. The final product after 8 h of milling time had a narrow size distribution with a mean of ~20 µm indicating that cryomilling has resulted in coarser and more uniform particles.

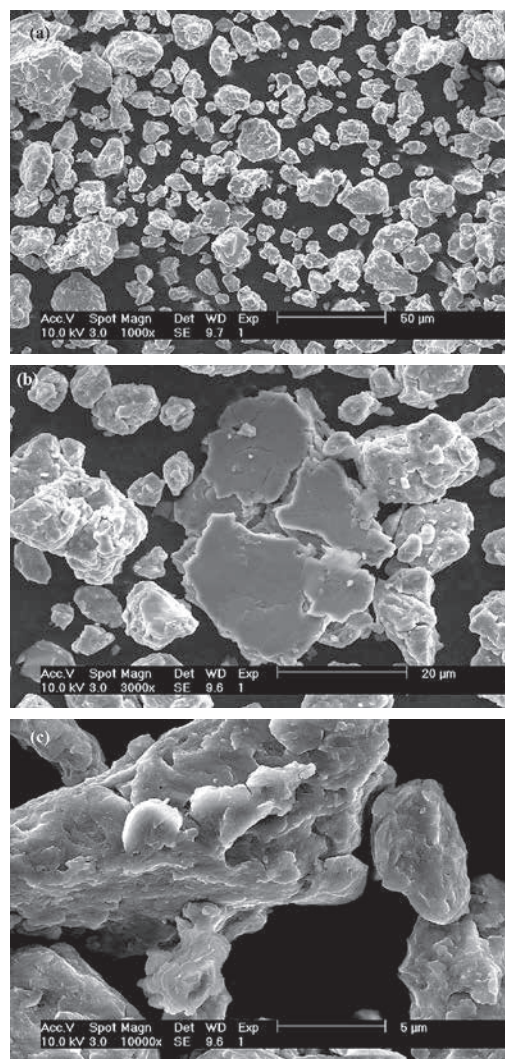


Fig. 3 SEM micrographs of Al5083 powder particles after cryomilling for 8 h.

Changes in particles morphology and microstructure during ball milling of ductile metal powders are produced by two simultaneous processes; cold welding and fracturing. During ball milling clusters of particles are trapped between colliding balls and undergo a high level of impact. If the impact stresses are sufficient, the powder particles plastically deform and flatten (see **Fig. 3b**). As the powder particles are pressed together their surface area increases and the surface oxide films rupture, consequently exposing clean underlying metal. When these fresh surfaces of particles come in contact a metal bond is formed. After a period of milling, particles deform to the extent that cracks initiate, propagate and ultimately fracture the particles. In first stage the cold welding process dominates and as a result the powder particle size continuously increases. This stage can be also termed the agglomeration stage.

The progressive increase in hardness value during the first stage due to the work hardening leads to a decrease

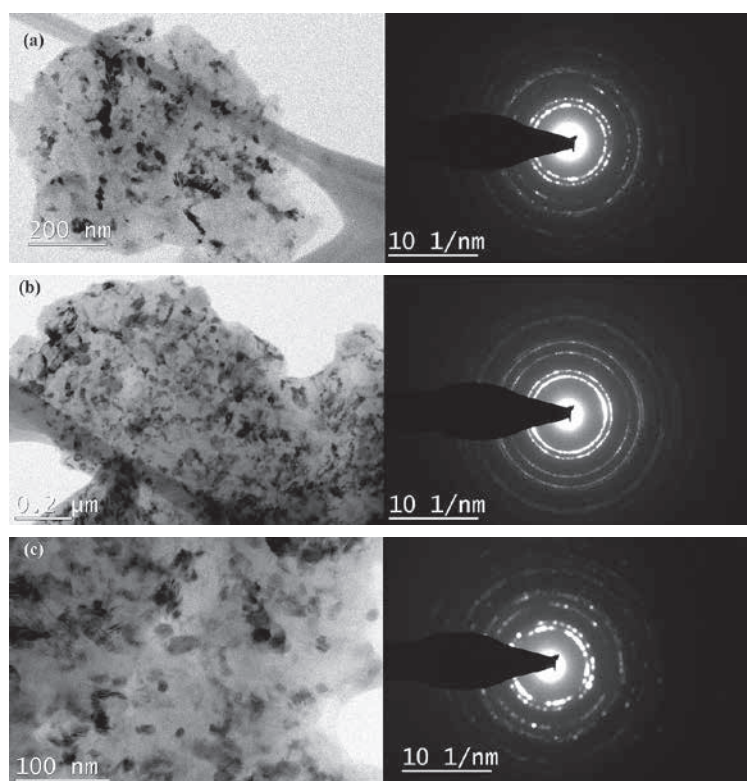


Fig. 4 Bright field (BF) images and selected area diffraction patterns (SADP) of several Al5083 powder particles after cryomilling for 8 h showing a well-developed nanocrystalline structure.

in the ductility of powder particles and therefore, an increased tendency for particle fracture. Thereby, the first stage is followed by the fragmentation stage. During the fragmentation stage the fracturing of particles occurs more readily than cold welding and as a result the powder particle size decreases. The extent of these two events is determined by the mechanical properties of the elemental powders, such as ductility, yield stress and hardness, as well as the magnitude of the impact provided by colliding balls. The last stage is a steady-state stage in which there is a balance between the frequencies of cold welding and fracturing processes so that the average particle size remains unchanged. As illustrated in the following paragraph these three stages are associated with microstructural changes.

The TEM images presented in **Fig. 4** shows bright field (BF) images and selected area diffraction patterns (SADP) of several Al5083 powder particles after cryomilling for 8 h. A well-defined nanocrystalline structure was observed in all particles. The corresponding selected area diffraction patterns exhibited the Debye-Scherrer rings characteristic of a fine grain structure. The BF images suggested that the powder particles had an average grain size of ~ 25 nm. These small grains, in fact, contribute towards the continuous Debye-Scherrer rings in the SADP. Further the SADP included only the Debye-Scherrer rings of fcc Al structure without any indication of a third phase

(e.g. oxide or nitride compounds).

Similar to conventional room-temperature ball milling the transformation of coarse-grained structure to a nano-sized scale during cryomilling includes several successive stages; gradual increasing of dislocation density due to plastic deformation of powder particles, formation of sub-boundaries by annihilation and recovery processes and eventually development of high-angle boundaries by the absorption of more dislocations into the boundaries.

For those cryomilling processes in which the powders are mixed with liquid N_2 , the reaction of constituents with N_2 must be considered. This reaction seems to proceed to a great extent during ball milling as plastic deformation; flattening and fracturing of powder particles repeatedly produce fresh, clean and highly reactive surfaces. The powder- N_2 reaction can be more serious in case of reactive elements such as Al and Ti. However, TEM results in **Fig. 4** do not support this prediction. During cryomilling the nitrogen picked up was found to be 0.11 wt%. Nitrogen dissolved interstitially in Al lattice forming a supersaturated solid solution. It should be noted that because of low temperature, formation of nitrogen-containing dispersoids such as AlN are kinetically improbable, although there is a large driving force for the formation of such compounds (e.g. $\Delta G^{AlN} = -287 \text{ kJ mole}^{-1}$).

However, subsequent heating upon powder consolidation of cryomilled Al5083 can lead to the formation of

various secondary phases including AlN and Al₂O₃. The presence of these precipitates was confirmed in previous studies by atom probe field-ion microscopy (FIM) and high-resolution transmission electron microscopy (HR-TEM) observations but the volume fraction of precipitates was not determined (Zhou F. et al., 2001). Furthermore, the X-ray diffractometry of cryomilled powder after heat treatment showed no traces of secondary phases suggesting that the amount of the dispersoids are virtually very small < 1 vol% (Zhou F. et al., 2001). It is worth noting that the dispersion particles formed during cryomilling acquired nanoscale size ranging from 1–30 nm, with majority of 3–10 nm. The average spacing between the dispersoids was measured to be less than 10 nm. These dispersions were found to be incoherent in nature, highly stable at high temperature and insoluble in matrix. The presence of these finely dispersed particles can play a critical role in retarding grain growth in the nanocrystalline materials through the so-called Zener mechanism even though their volume fraction is low. Furthermore, they could effectively obstruct dislocation motion and therefore reduce the minimum grain size.

4. Conclusions

Similar to conventional room temperature ball milling process cryomilling of aluminum powder led to the nanocrystallization. The ultimate grain size appeared to be similar to that reported for conventional ball milling (25 nm) although the rate of nanocrystallization was found to be much faster. Furthermore, in cryomilling the cold-welding process increased the powder particle size with more uniform morphology compared to as-received powder.

References

- Benghalem A., Morris D.G., Milling and mechanical alloying of copper and some solution alloys seen as a thermomechanical process, *Acta Metallurgica et Materialia*, 42 (1994) 4071–4081, Doi: 10.1016/0956-7151(94)90184-8.
- Cocco G., Soletta I., Battezzati L., Baricco M., Enzo S., Mechanical alloying of the Al–Ti system, *Philosophical Magazine B*, 61 (1990) 473–486, DOI: 10.1080/13642819008219288.
- Eckert J., Holzer J.C., Kril C.E., Johnson W.L., Structural and thermodynamic properties of nanocrystalline fcc metals prepared by mechanical attrition, *Journal of Materials Research*, 7 (1992) 1751–1761, DOI: 10.1557/JMR.1992.1751.
- Enayati M.H., Formation of nanoscale layered structures and subsequent transformations during mechanical alloying of Ni₆₀Nb₄₀ powder mixture in a low energy ball mill, *Kona Powder and Particle Journal*, 32 (2015), 196–206, DOI: 10.14356/kona.2015010.
- Fogagnolo J.B., Robert M.H., Velasco F., Torralba J.M., Aluminium matrix composites reinforced with Si₃N₄, AlN and ZrB₂, produced by conventional powder metallurgy and mechanical alloying, *Kona Powder and Particle Journal*, 22 (2004) 143–150, DOI: 10.14356/kona.2004017.
- Hellstern E., Fechet H.J., Fu Z., Johnson W.L., Structural and thermodynamic properties of heavily mechanically deformed Ru and AlRu, *Journal of Applied Physics*, 65 (1989) 305–310, DOI: 10.1063/1.342541.
- Koch C.C., Materials synthesis by mechanical alloying, *Annual Review of Materials Science*, 19 (1989) 121–143, DOI: 10.1146/annurev.ms.19.080189.001005.
- Koch C.C., Synthesis of nanostructured materials by mechanical milling: problems and opportunities, *Nanostructured Materials*, 9 (1997) 13–22, Doi: 10.1016/S0965-9773(97)00014-7.
- Zhou F., Lee J., Dallek S., Lavernia E.J., High grain size stability of nanocrystalline Al prepared by mechanical attrition, *Journal of Materials Research*, 16 (2001) 3451–3458, DOI: 10.1557/JMR.2001.0474.

Author's short biography



Mohammad Hossein Enayati

M. H. Enayati (PhD, CEng) is a full Professor of materials science at Isfahan University of Technology and Fellow of Institute of Materials, Minerals and Mining (FIMMM), UK. Prof. Enayati's research focuses on the nanostructured and amorphous materials, mechanical alloying and synthesis of advanced materials for thermal spray coating. He has authored several books and numerous articles in well recognized international journals in his field, and has received research funding from a wide variety of agencies. His research has been recognized with numerous awards, most recently from the Iran Nanotechnology Initiative Council and Iranian Nanotechnology Society.

Identification of Optimal Mill Operating Parameters during Grinding of Quartz with the Use of Population Balance Modeling[†]

Evangelos Petrakis*, Elias Stamboliadis and Konstantinos Komnitsas

[†] Technical University of Crete, School of Mineral Resources Engineering, Greece

Abstract

It is known that ball milling is an energy intensive process and great efforts have been made over the years to improve energy efficiency. The use of population balance models (PBMs) can assist in the design of mineral processing circuits and the scale-up of laboratory mill results to full-scale. However, since each model has its own capabilities and limitations, it is believed that a combined use will provide more accurate information for the reliable description of the process.

In this study, the simulation of grinding of quartz is investigated in order to identify the optimal mill operating parameters. With the use of population balance modeling the specific rate of breakage and the cumulative breakage parameters can be determined from mono-size, short grinding time batch tests. The determined breakage parameters were back calculated by minimizing the residual error between experimental and reproduced size distributions. By combining two software packages the back calculated breakage parameters were used for the prediction of the optimum ball filling volume. The proposed procedure can be also applied for the identification of optimal mill operating parameters for other minerals.

Keywords: comminution, breakage rate, ball filling, kinetic models, simulation

1. Introduction

Size reduction is one of the most fundamental operations in the mineral processing industry. The primary purpose of size reduction is to obtain an appropriate product size with the least possible energy consumption. However, it is known that a large share of the energy used in comminution is absorbed by the machine and only a small part is consumed for size reduction. This implies that the existing grinding machines are inefficient and engineers have focused their efforts not only on the design of new and more efficient machines, but also on the development of new approaches for data processing (Yahyaie M. et al., 2015; Umucu Y. et al., 2016).

The main theories that initially described, evaluated and improved the relationship between specific energy and size reduction in comminution are those of Rittinger P.R. (1867), Kick F. (1885) and Bond F.C. (1952). These theories are based on a specific size modulus of the mate-

rial but they do not take into consideration the distribution modulus. Later, Charles R.J. (1957) and Stamboliadis E. (2002) used different breakage models by assuming that both the initial feed and the final product size distributions are expressed by the Gates-Gaudin-Schuhmann (GGS) equation.

During the last decades, considerable work has been done on the optimization of energy consumption in grinding mills using phenomenological grinding kinetics models based on population balance considerations. Population balance modeling is based on first order kinetics and uses two functions, namely the specific rate of breakage S_i and the breakage function $b_{i,j}$ (Herbst J.A. and Fuerstenau D.W., 1980; Austin L.G. et al., 1984). These functions provide the fundamental size-mass balance equation for fully mixed batch grinding operations. Many researchers have underlined the advantages of these functions (Ipek H. and Göktepe F., 2011; Wang X. et al., 2011; Gupta V.K. and Sharma S., 2014), while the scale-up from laboratory data to full-scale mills has also been discussed in a number of recent studies (Fuerstenau D.W. et al., 2003; Deniz V., 2013).

Population balance modeling is the most widely used approach and assumes that the specific rate of breakage is constant and is not affected by the grinding time (Austin

[†] Received 9 January 2016; Accepted 9 March 2016
J-STAGE Advance Publication online 30 April 2016

[†] 73100 Chania, Greece

* Corresponding author: Evangelos Petrakis;

E-mail: vpetraki@mred.tuc.gr

TEL: +30-28210-37608 FAX: +30-28210-06901

L.G. and Bhatia V.K., 1972; Austin L.G. and Bagga P., 1981; Nomura S. et al., 1991). Austin L.G. and Bagga P. (1981) also have shown that the breakage function parameters can be estimated from the size analysis of the products obtained after a short grinding time, using as initial feed a narrow particle size fraction, namely the one size fraction BII method.

The primary concept of simulation balance modeling, which suggests that the breakage function parameters must be estimated before any of the particles are reselected for further breakage, may result in calculation errors (Austin L.G. et al., 1984; Celik M.S., 1988; Bozkurt V. and Özgür I., 2007). The deviation from first-order kinetics is also well known in several cases. Celik M.S. (1988) stated that the breakage rate of anthracite in ball mills exhibited an acceleration, particularly noticeable for long grinding times, due to extensive agglomeration of fines. The acceleration or deceleration of breakage rates of all individual size classes can be determined during wet grinding using the G-H method (Rajamani R.K. and Guo D., 1992). Bilgili E. and Scarlett B. (2005) proposed a phenomenological theory which explains non-first order effects as a result of multi-particle interactions. Instead of the forward experimental estimation of breakage model parameters, the back-calculation method which calculates the model parameters by minimizing the error between experimental and predicted size distributions, is also widely employed. This method uses all available data at the same time and enables reduction of the calculation error. It can be applied in cases where limited data is available and thus the need for carrying out several experiments is minimized. In this regard, Austin L.G. et al. (2007) stated that it is always necessary to confirm that the experimental breakage model parameters reproduce the size distributions and the only way to accomplish this is to use the back-calculation method.

For the design of grinding circuits in mineral processing plants, many equations describing mill power and grinding energy are available. These equations can be categorized into two major groups. The first group describes the relationship between specific energy requirements and size reduction, while the second one relates power draft to mill size. The first group can be represented by the Bond F.C. (1960) test method. This method is widely used both for evaluating the grindability of a material and for determining the power required to drive the mill. However, it uses data from laboratory tests while many empirical correction factors were proposed for the scale-up to larger mills or other operating conditions. With respect to the second group, Herbst J.A. and Fuerstenau D.W. (1973) found out experimentally that a proportional relationship exists between the specific rate of breakage and the specific net mill power for a tumbling mill, which is not affected by the operating parameters. Nomura S. et

al. (1994) also confirmed this relationship.

Two important factors should be determined before carrying out experiments in a mill, namely the ball filling J and the powder filling f_c . J is the ball filling volume, which is the fraction of the mill filled by the grinding media bed (Eqn. (1)), while f_c is the powder filling volume in the mill (Eqn. (2))

$$J = \left(\frac{\text{Volume of solid balls}}{\text{Mill volume}} \right) \cdot \frac{1}{1 - \varepsilon} \quad (1)$$

$$f_c = \left(\frac{\text{Volume of solid powder}}{\text{Mill volume}} \right) \cdot \frac{1}{1 - \varepsilon} \quad (2)$$

where ε is the bed porosity of balls and powder which is assumed to be 40 % for both (Austin L.G. et al., 1984). The fraction of space between the balls at rest that is filled with powder is called interstitial filling U and is calculated by Eqn. (3).

$$U = \frac{f_c}{\varepsilon \cdot J} \quad (3)$$

It is mentioned that when U approaches 1 the impacts are increasingly cushioned by excess particles between grinding media. Considering that a proportional relationship exists between the specific rate of breakage and the specific net mill power, the following Eqns. (4)–(8) can be used to determine the specific rate of breakage S_i (1/min), for each size class i obtained after grinding, as a function of J .

Bond F.C. (1960) proposed the following relationship for wet grinding in overflow ball mills to scale-up results from laboratory tests to larger mills

$$S_i \propto (1 - 0.937 \cdot J), \quad D \geq 2.4 \text{ m} \quad (4)$$

Beeck R. (1970) proposed that for dry grinding of cement the following relationships, based on data from German and U.S plants respectively, could be used.

$$S_i \propto (0.294 - 0.26 \cdot J) \quad (5)$$

$$S_i \propto (0.374 - 0.47 \cdot J) \quad (6)$$

Shoji K. et al. (1982) studied the specific rate of breakage in relation to the ball filling volume for quartz grinding using two tumbling ball mills with different capacity. They proposed the following relationship for mill diameter 0.6 m

$$S_i \propto \left(\frac{1}{1 + 6.6 \cdot J^{2.3}} \right) \cdot e^{-1.20U} \quad (7)$$

Austin L.G. et al. (1984), taking into consideration the differences between various relationships, proposed that for batch dry grinding the following relationship should be used (mentioned here as ‘Bond Modified’)

$$S_i \propto (1 - 0.937 \cdot J) / (1 + 5.95 \cdot J^5) \quad (8)$$

Later, many other research efforts were made to define the relationship between S_i and J under different operating conditions. These studies focused on the determination of S_i using the grinding kinetic model. More specifically, Deniz V. and Onur T. (2002) investigated the breakage kinetics of pumice samples in relation to the powder filling volume in a ball mill, at $J = 20\%$, and found that the maximum normal breakage rate occurred at an interstitial filling U of approximately 0.4. A more recent study by Fortsch D.S. (2006) showed that the reduction of J leads to an increase in capital and installation costs of the milling equipment. He proposed $J = 35\%$ as optimal ball filling volume for cement plants. On the other hand, Metzger M.J. et al. (2009) using silica sand as a test material showed that the lower the ball filling J the higher is the amount of the produced product. They also found that more efficient breakage occurs at ball filling volume $J = 1.5\%$.

The present study through batch kinetic experiments with the use of quartz as test material aims to assess the effect of ball filling volume J on the specific rate of breakage S_i and identify the cumulative breakage function $B_{i,j}$ by keeping the powder filling volume f_c constant. A new methodology is proposed, involving the use of population balance modeling, for the identification of the optimum ball filling during quartz grinding and the scale-up of laboratory mill results to full-scale.

2. Theoretical background

Let's consider a mass of material M in a ball mill that after breakage needs to be divided, by using x_i screens, into $i + 1$ narrow size classes. Normally, for a size class i bounded between two successive screens x_i and x_{i+1} containing a mass fraction $m_i(t)$ at time t , it is assumed that breakage follows a first-order law. That is, the rate of breakage of size i is proportional to the mass of size i in the mill hold up. According to this, the specific rate of breakage S_i is independent of time and since the mill hold up M is constant the following Eqns. (9), (10) are obtained (Austin L.G. and Luckie P.T., 1972; Klimpel R.R. and Austin L.G., 1977):

$$\frac{d[m_i(t)]}{dt} = -S_i \cdot m_i(t) \quad (9)$$

or

$$\log \left[\frac{m_i(t)}{m_i(0)} \right] = \frac{-S_i \cdot t}{2.3} \quad (10)$$

where $m_i(t)$ and $m_i(0)$, are the mass fractions for size class i , at times t and 0 respectively. Thus, a log-linear plot of $m_i(t)$ versus t should result in a straight line and S_i can be

determined from the slope of this line.

The specific rate of breakage depends on the particle size of the mill hold up. Austin L.G. et al. (1984) used the following Eqn. (11) to describe this relationship:

$$S_i = \alpha_T \cdot \left(\frac{x_i}{x_0} \right)^\alpha \cdot Q_i \quad (11)$$

where x_i (mm) is the upper size of size class i , x_0 is the standard size (1 mm), α_T is a parameter depending on milling conditions and α is a characteristic parameter depending on the material properties. More specifically α_T is the specific rate of breakage at size $x_i = 1$ mm and has the same units as S_i (1/min). Q_i is a correction factor, which is 1 for small particles (normal breakage) and less than 1 for too large particles to be nipped and fractured by the grinding media (abnormal breakage). In the abnormal breakage region each material size behaves as it is composed of a weak and a strong fraction (Ipek H. and Göktepe F., 2011). Q_i is calculated by Eqn. (12):

$$Q_i = \left(\frac{1}{1 + (x_i / \mu)^A} \right) \quad (12)$$

where μ is a parameter depending on milling conditions and denotes the particle size when the correction factor is 0.5. A is a positive number that depends on the material type and shows how rapidly the rates of breakage decrease as size increases ($A \geq 0$). The evolution of the specific rate of breakage vs. size is shown in **Fig. 1**.

When a material of size j breaks once, the mass fraction of the broken products with size i can be represented by the breakage function $b_{i,j}$, $i > j$. Thus, $b_{2,1}$ is the mass fraction that is reduced from size 1 into size 2, and so on. The breakage function is usually represented in cumulative form $B_{i,j}$ as,

$$B_{i,j} = \sum_{k=n}^i b_{k,j} \quad (13)$$

where $b_{i,j} = B_{i,j} - B_{i+1,j}$.

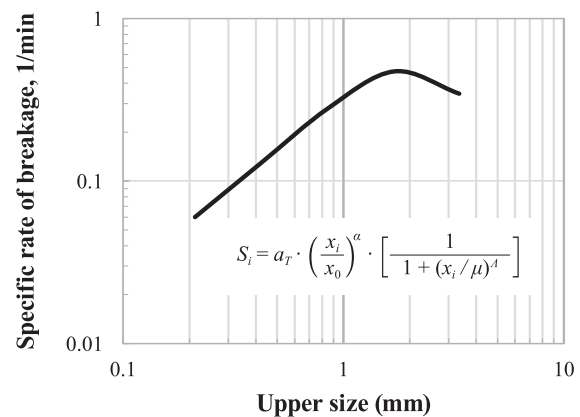


Fig. 1 Evolution of specific rate of breakage versus size.

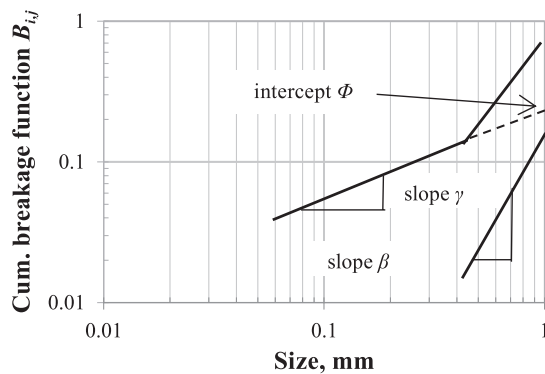


Fig. 2 Cumulative breakage function versus size.

Austin L.G. and Bagga P. (1981) have shown that for short grinding times the values of $B_{i,j}$ can be estimated from the size analysis of the products, using as initial feed a narrow particle size fraction j (the one size fraction BII method):

$$B_{i,j} = \frac{\log[(1 - P_i(0)) / (1 - P_i(t))]}{\log[(1 - P_{j+1}(0)) / (1 - P_{j+1}(t))]} \quad (14)$$

where $P_i(t)$ is the mass fraction less than size x_i at time t .

The above Eqn. (14) presupposes that a small mass fraction of particles with smaller sizes will re-break. Experience suggests that good results are obtained when the selected time of grinding results in a 20 % to 30 % material that is broken out from size j (Austin L.G. et al., 1984).

The cumulative breakage function $B_{i,j}$ can also be represented by the following empirical Eqn. (15) which is the sum of the two straight lines on log-log plot (Austin L.G. and Luckie P.T., 1972):

$$B_{i,j} = \Phi_j \cdot \left(\frac{x_{i-1}}{x_j} \right)^\gamma + (1 - \Phi_j) \cdot \left(\frac{x_{i-1}}{x_j} \right)^\beta \quad (15)$$

where x_j is the top size, $B_{i,j}$ is the cumulative breakage function, γ is the slope of the lower straight line part of curve, β is the slope of the upper part and Φ_j is the intercept, as shown in Fig. 2. γ also, characterizes the relative mass of fines produced after breakage and therefore is related to the grinding efficiency. Generally, the breakage parameters Φ_j , γ and β depend on the properties of the material. Thus, the parameters of the cumulative breakage function, which are determined by laboratory experiments, can be used directly for larger scale mills.

3. Material and methods

The material used in the present experimental study is quartz obtained from the quarry of Assiros, in the vicinity of Thessaloniki, N. Greece, with SiO_2 content 99.1 % and density 2.65 g/cm³. 100 kg of the material was sampled

Table 1 Ball mill characteristics and test conditions

Mill	Diameter, D (cm)	20.4		
	Length, L (cm)	16.6		
	Volume, V (cm ³)	5,423		
	Operational speed, N (rpm)	66		
	Critical speed, N_c (rpm)	93.7		
Balls	Diameter, d (mm)	25.4		
	Number	77	38	26
	Weight (g)	5,149	2,540	1,738
	Specific gravity (g/cm ³)	7.85		
	Porosity %	40		
	Ball filling volume, J (%)	20	10	6.7
	Specific gravity (g/cm ³)	2.65		
Material	Powder filling volume, f_c (%)	4		
	Interstitial filling, U	0.5	1	1.5

from several locations to obtain representative samples. The microscopic examination using polished and thin sections showed that the material is compact, homogeneous, and does not show the presence of open cracks, discontinuities or alteration phenomena.

The experiments were performed in a laboratory ball mill that operated at a constant speed of $N = 66$ rpm (1.1 Hz) corresponding to 70 % of its critical speed (Table 1). The mill charge consisted of 25.4 mm (1 inch) stainless steel balls with density $\rho_b = 7.85$ g/cm³.

Three series of tests were performed at J 6.7 %, 10 % and 20 %, while f_c that remains constant at 4 %, corresponds to 345 g of quartz.

The sample was homogenized by the cone and quarter method and 6 kg of the material was used for the tests. This quantity was crushed at a size of -4 mm using a jaw crusher. The product of the crusher was wet screened at 150 μm , while the $+150$ μm fraction was dried and screened using a series of screens with an aperture ratio $\sqrt{2}$ to obtain the feed fractions. As a result, five mono-sized fractions of quartz ($-3.35+2.36$ mm, $-1.7+1.18$ mm, $-0.850+0.600$ mm, $-0.425+0.300$ mm and $-0.212+0.150$ mm) were prepared. The grinding tests were performed at various grinding times t (0.5, 1, 2 and 4 or 8 min). The products obtained from each test were wet sieved using a series of screens with a ratio of $\sqrt{2}$ for the determination of particle size distribution. All tests were carried out in duplicate and average values are given in the results section.

The mill power is calculated by the following formula (Stamboliadis E. et al., 2011):

$$P = 9.9 \cdot M \cdot N \cdot D \quad (16)$$

where M is the total mass (kg) of the feed material and balls, N is the rotational speed (Hz) and D is the internal diameter of the mill (m).

It should be also noted that the following issues were taken into consideration:

- i. A fresh feed charge was used in each test.
- ii. Following the recommendation of Gupta V.K. and Sharma S. (2014), the crushed material was pre-ground in the mill for 2 min in order to avoid abnormal breakage behaviour.
- iii. The feed charge was sampled and screen analyzed in the same way as the mill product.
- iv. The mill was layer loaded with balls and feed charge, following the standard practice (Gupta V.K. et al., 1985).

The energy consumed by the mill is proportional to the time t and is given by Eqn. (17):

$$E = P \cdot t \quad (17)$$

where P is the power of the mill (W), t is the grinding time (s) and E is the net energy consumed (J). If m is the mass of the feed material (kg) then the specific energy for grinding ε' (J/kg) is given by Eqn. (18):

$$\varepsilon' = \frac{E}{m} = \frac{P \cdot t}{m} \quad (18)$$

The specific energy in kWh/t is calculated by dividing Eqn. (18) by 3,600.

Two software packages were used, namely Moly-Cop ToolsTM version 1.0 and MODSIMTM academic version 3.6.25 (King, 2001), to identify breakage parameters and model the process.

Moly-Cop ToolsTM includes a set of easy-to-use excel spreadsheets, that can be used to characterize and evaluate the operating efficiency of any given mineral ore grinding circuit, following standardized methodologies and widely accepted evaluation criteria. More specifically, the spreadsheet (BALLPARAM_BACH) uses all the differential equations of a population balance model for the calculation of S_i and $B_{i,j}$ parameters. The software identifies the best combination of parameters that minimize the residual error between experimental and reproduced size distributions, while the objective function SSE is expressed by the following formula:

$$SSE = \sum_{i=1}^4 \sum_{j=1}^n \frac{w_i}{W} \left(\frac{R_{i(\text{exp})} - R_{i(\text{mod})}}{R_{i(\text{mod})}} \right)^2 \cdot 100\% \quad (19)$$

where $R_{i(\text{exp})}$ represents the particle size distribution of the mill product (as % retained on screen x_i), $R_{i(\text{mod})}$ represents the response of each corresponding $R_{i(\text{exp})}$ for a given set of model parameters, n is the number of screen intervals used, w_i is the weight factor for each screen that quantifies the relative quality and reliability of each particular

screen size value with respect to the other values (high values indicate more reliable measurements) and W is the total sum of the weight factors. The software input requires a minimum of four size distributions obtained at four grinding times t_1 , t_2 , t_3 and t_4 .

For the back calculation of the breakage parameters, the experimentally calculated parameters (α_T , α , μ , A , Φ_j , γ and β) are used as initial input parameters in the Moly-Cop ToolsTM software. As a rule of thumb, the parameters which are generally regarded as characteristics of the material should be kept constant and only those associated with mill conditions should be changed. In this study, the input parameters are α , μ , A , Φ_j , γ and β and the initial value of α_T is the one calculated to give the best fit between experimental and reproduced size distributions. After this, the fit is improved by adjusting the parameters μ , A , Φ_j , and γ , while the parameters that depend on the material, i.e., α and β are kept constant.

MODSIMTM is a software that uses simulation models for the design of mineral processing circuits. The main unit operations include size reduction, crushing and grinding, classification and concentration based on particle mineralogical composition and solid-liquid separations. Furthermore, MODSIMTM which can up-scale laboratory mill results to full-scale mill, provides standard grinding mill units, e.g. MILL and GMSU based on population balance modeling, and thus the calculated experimental breakage parameters can be used as input.

The back calculated breakage parameters from the Moly-Cop ToolsTM software are used as input in the unit model MILL of the MODSIMTM software and the distributions of the products are compared. MILL is the ball milling model that is based on standard Austin's models (Eqns. (14) and (15)) and takes into consideration the breakage parameters as does the Moly-Cop. It is mentioned that the MILL model does not take into consideration the operating conditions (e.g. mill diameter, ball filling volume and mill speed) and a different unit model should be used to elucidate the ball filling effect on the grinding process. For this purpose, the Austin's scaled-up unit model GMSU of MODSIMTM was used in this study. The back calculated breakage and other parameters, e.g. $D = 0.204$ m, $N = 66$ rpm, $d = 25.4$ mm were used as input in the GMSU model. Size distributions varied in relation with J . A total of six J values were examined and each of the obtained distributions was used as input in the Moly-Cop ToolsTM software. Then, the optimum value of α_T (1/min) that minimizes the least-squares objective function (Eqn. (19)) was determined by keeping all other parameters constant.

4. Results and discussion

4.1 Determination of the specific rate of breakage

Fig. 3 shows the relationship between the remaining mass fraction of feed size and grinding time for $J = 20\%$ using a normal-log plot. The feed size is the upper size of the tested size class. The results indicate that breakage follows a first order law (i.e. the specific rate of breakage S_i is independent of time) and the specific rate of breakage can be determined from the slope of the straight lines. Each line corresponds to a different feed size tested. This figure also shows an increase of S_i values when the feed size fraction is increased, except for the largest tested size ($-3.35+2.36$ mm), which exhibits lower breakage rate compared to the smaller fraction ($-1.7+1.18$ mm). This reveals that there is an increase in the rate of breakage up to a certain particle size and that grinding media cannot break coarser material efficiently. The same trend is obtained for $J = 10\%$ and $J = 6.7\%$.

Regarding the effect of J on breakage rate S_i , Fig. 4 shows that the value of S_i increases with increasing J suggesting that breakage is more effective at higher J values.

Variations of specific rates of breakage S_i for different feed size fractions are shown in Fig. 5 on a log-log scale.

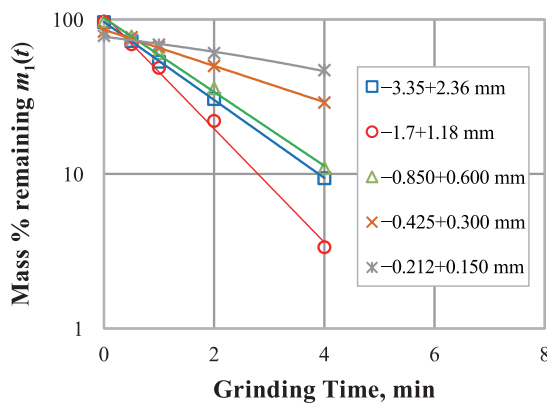


Fig. 3 First order plots for $J = 20\%$.

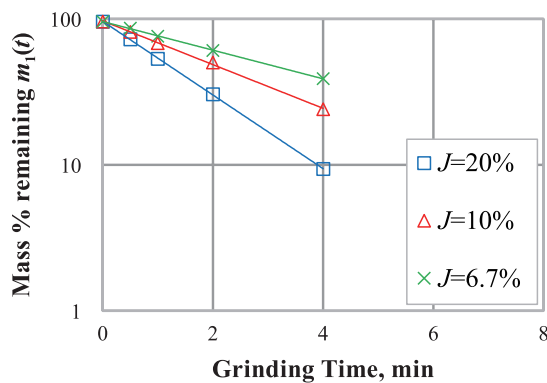


Fig. 4 First order plots for feed size ($-3.35+2.36$) mm.

It is shown that S_i increases up to 1.7 mm (upper size class), but above this size breakage rates decrease sharply for all J values, since the particles are too large to be nipped and fractured by the grinding media used. It appears that the increase of S_i is almost linear up to the optimum size of 1.7 mm and the slope of this linear part remains constant. In addition, it is also seen that the optimum feed size to obtain a maximum S_i is independent of the ball filling volume J . It is believed that this size depends on the material type, the size of the balls and the type of the mill used.

The determined S_i values for each feed size were used in Eqns. (11) and (12) and the parameters α_T , α , μ , and λ were calculated by using a non-linear regression technique. The calculated values are shown in Table 2.

4.2 Determination of the cumulative breakage function parameters

Fig. 6 shows the experimental values of $B_{i,j}$ versus size on log-log scale. The specific graphical representation corresponds to the $(-0.850+0.600$ mm) feed size for three different ball filling volumes. The feed sizes presented are

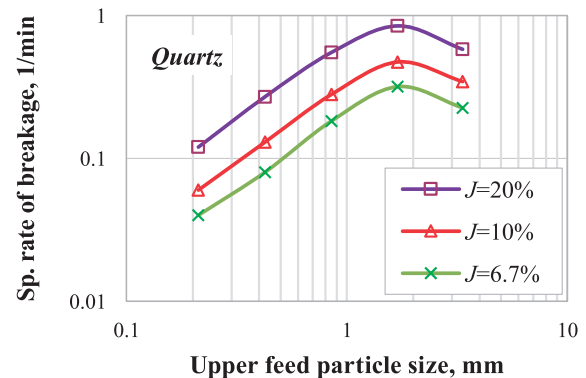


Fig. 5 Variation of specific rate of breakage versus feed size, for various J volumes.

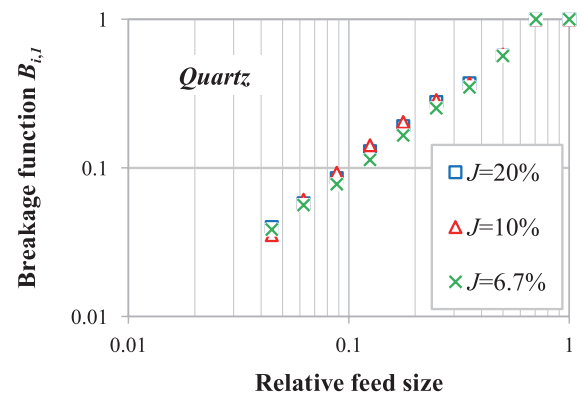


Fig. 6 Cumulative breakage function versus relative feed size for various J volumes.

Table 2 Breakage parameter values for different ball mill filling.

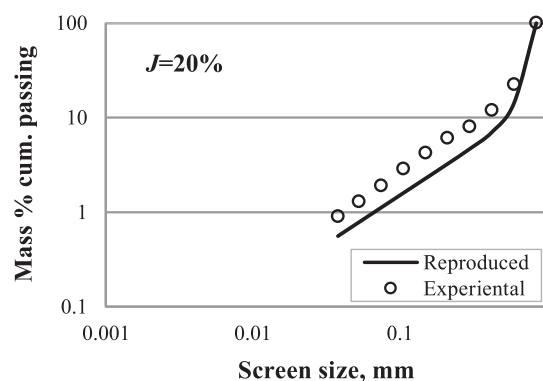
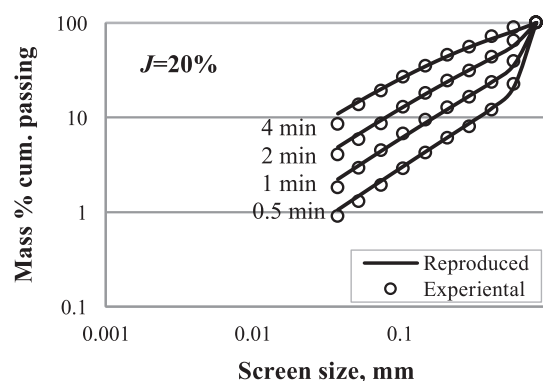
	S_i					$B_{i,j}$		
$J\%$	S_i	α_T	α	μ	Λ	Φ_j	γ	β
	1/min			mm				
20	0.55	0.71	1.13	2.11	2.90	0.76	1.02	5.80
10	0.28	0.35	1.15	2.34	3.15	0.77	1.00	5.80
6.7	0.18	0.23	1.17	2.38	3.33	0.77	1.11	5.80

finer than the optimum size (1.7 mm), while as described previously breakage takes place at the normal region. By definition, the values of $B_{i,j}$ are determined from the size distributions obtained at short grinding times, by fitting the experimental data to Eqn. (14). The Φ_j , γ and β parameters were determined using Eqn. (15) and are shown in **Table 2**. Since β is generally accepted as characteristic constant of the material, it was decided to keep it constant at the value of 5.80, as indicated by Austin L.G. et al. (1984). This was considered necessary in order to reduce the number of parameters used and thus to investigate the sensitivity of only two parameters (Φ_j and γ). From the results obtained it is observed that changes in ball filling volume do not entail any significant changes in the values of parameters Φ_j and γ . This observation is in accordance with earlier studies (Fuerstenau D.W. et al., 2004; Ozkan A. et al., 2009; Chimwani N. et al., 2013), which also state that the $B_{i,j}$ parameters are independent of the mill operating conditions.

4.3 Back-calculation of the breakage parameters

From the calculated breakage parameters S_i and $B_{i,j}$ (**Table 2**) the size distribution of the grinding products can be reproduced using the spreadsheet BALLPARAM_BACH of Moly-Cop ToolsTM.

Fig. 7 presents the reproduced values of cumulative mass passing for the (−0.850+0.600 mm) feed size after 0.5 min grinding time. The reproduction provides a coarser size distribution compared to the experimental values and this is also observed at longer grinding times. It is believed that the deviation between experimental and reproduced values in **Fig. 7** is due to the value of α , which is a characteristic parameter of the material. In order to overcome this shortcoming, a readjustment of the grinding parameters is required. For quartz, the value of α proposed in literature is 0.80 (e.g. Austin L.G. et al., 1984), which is quite different from the calculated values (about 1.15) shown in **Table 2**. On the contrary, α_T is a parameter depending on mill operating conditions and characterizes the grinding process. Thus, the variability of this parameter and the magnitude of its effect on the balling filling

**Fig. 7** Comparison between experimental and reproduced size distributions at 0.5 min grinding time.**Fig. 8** Comparison between experimental and reproduced size distributions at different grinding times, using the back calculated breakage parameters.**Table 3** Back calculated breakage parameters for $J = 20\%$.

α	μ	Λ	Φ_j	γ	β
	mm				
0.80	2.11	2.90	0.73	1.05	5.80

should be investigated.

In this study, the input parameters are $\alpha = 0.80$, $\mu = 2.11$, $\Lambda = 2.90$, $\Phi_j = 0.76$, $\gamma = 1.02$ and $\beta = 5.80$ and the initial value of α_T is the one calculated to enable the best fit between the experimental and the reproduced size distributions. The fit can be improved by readjusting the values of the parameters μ , Λ , Φ_j and γ , while the parameters that depend on the material, i.e., α and β are kept constant. **Table 3** summarizes the best combination of the back calculated parameters. These values are closer to those established in literature by other researchers (Yekeler M. et al. 2001) who obtained an average value of $\gamma = 1.20$ during wet grinding of quartz.

Fig. 8 compares experimental and reproduced size distributions obtained at different grinding times for the (−0.850+0.600 mm) feed size. In this figure a very good

agreement between experimental and predicted values, within the limits of experimental error, can be observed, when the back calculated breakage parameters derived by the Moly-Cop Tools™ (Table 3) were used.

4.4 Simulation of the grinding process and validation of results

It was shown earlier that the value of S_i increases with increasing J and this suggests that breakage is more effective as the ball mill filling volume increases. This conclusion is supported by three series of tests carried out with different J values 6.7 %, 10 % and 20 %.

In order to predict the effect of ball filling volume both the MODSIM™ and the Moly-Cop Tools™ software packages were used. According to this procedure, the back calculated breakage parameters given in Table 3 and other parameters shown in Table 1, i.e., $D = 0.204$ m, $N = 66$ rpm, $d = 25.4$ mm were used as initial input in the unit model GMSU of MODSIM™. Fig. 9 shows the particle size distributions obtained from the model GMSU. The results indicate an agreement between the experimental and the simulated particle size distributions for the

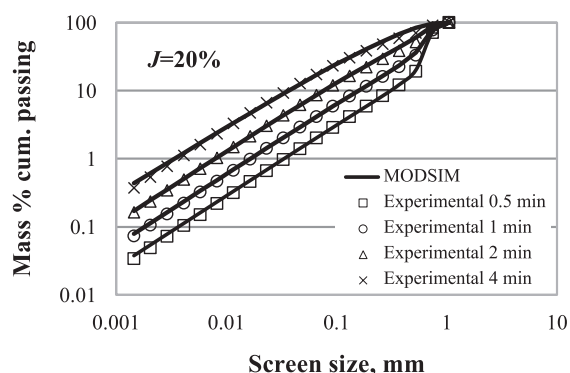


Fig. 9 Comparison between experimental and simulated by MODSIM™ size distributions using the back calculated parameters.

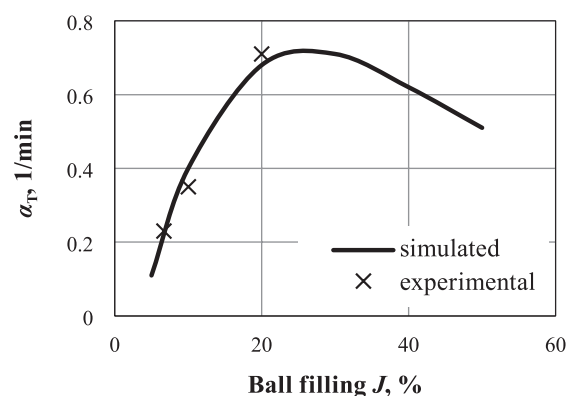


Fig. 10 Comparison between experimental and simulated α_T values

tested ball filling volume $J = 20$ %, since both software packages use the standard Austin's kinetic models.

In order to simulate the grinding process, six J values (5 %, 10 %, 20 %, 30 %, 40 % and 50 %) were used and each of the obtained, from the unit model GMSU, size distributions was used as input in Moly-Cop Tools™. Then, the optimum value of α_T (1/min) that minimizes the least-squares objective function (Eqn. (19)) was obtained, by keeping all other parameters constant.

Fig. 10 shows very good agreement between the experimental and the simulated α_T values in relation to the ball filling volume J . However, the simulation indicated that there is an optimum ball filling volume ($J = 30$ %), for which the specific breakage rate obtains a maximum value. The predicted α_T values were validated by additional experiments for $J = 40$ % and the results are given in Fig. 11. It can be seen from this figure that even above the optimum ball filling volume there is perfect match between experimental and simulated results, indicating that the approach used was able to predict accurately the variation between the α_T values and the ball filling J .

Having successfully validated the simulated results, we attempted to compare them with those obtained from other earlier studies (Eqns. (4)–(8)). Fig. 12 presents the

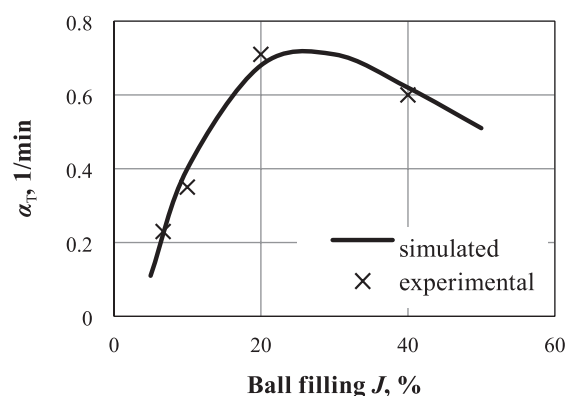


Fig. 11 Validation of predicted α_T values.

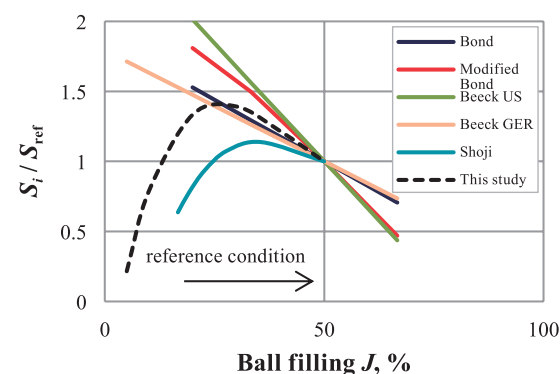


Fig. 12 Normalized breakage rates predicted by different studies.

predicted specific rates of breakage in relation to the ball filling volume J . In order to effectively compare the specific rates of breakage, as predicted from different models, the results are expressed as the ratio between S_i value and a reference value S_{ref} , taken as 50 % of the ball filling volume J . The approach proposed in the present study is indicated with the dashed line. It is clearly shown that Eqns. (4), (5), (6) and (8) are inversely proportional to the ball filling volume J and this is valid also for J values higher than the optimum value of about $J = 30$ %, as predicted in the present study. Eqn. (7) has also an optimum value $J = 40$ %, although the specific values of predicted breakage rates are lower than the ones proposed in this study. However, it can be said that Eqns. (4), (5), (6) and (8) are applicable for higher values of J (in the range of 30 % to 40 %), while the results derived by Shoji K. et al. (1982) (Eqn. (7)) and the present study are applicable over a wider range of ball filling volume J . The minor difference between the latter two studies may be due to different milling conditions and the material type.

5. Conclusions

In this study the grinding of quartz was simulated with the use of population balance modeling. The specific rate of breakage and the cumulative breakage parameters were determined from mono-size, short grinding time batch tests using a non-linear regression approach. The experimentally determined parameters (α_T , α , μ , A , Φ_j , γ and β) were compared for three J values (6.7 %, 10 % and 20 %). It is observed that the breakage rate increases with increasing J , suggesting that grinding in this case becomes more efficient. Grinding of different feed sizes shows that the specific rate of breakage increases up to the size of 1.7 mm, while for coarser sizes it decreases sharply. In addition, the change of J has minor effect on the parameters of the breakage function $B_{i,j}$. The Moly-Cop Tools™ software was used to identify the best combination of the breakage parameters (α_T , α , μ , A , Φ_j , γ and β), for which the reproduced size distributions compare well with the experimentally determined ones. It was revealed that the experimental breakage parameters did not predict very well the size distributions and in order to improve the results a readjustment of the value of α , which is a characteristic parameter of the material, was required. The results of this study propose that for the more accurate prediction of the size distributions during grinding, the parameters which characterize the material (i.e. α and β) should be kept constant and only those associated with mill conditions should be modified accordingly.

The simulation of grinding of quartz was enabled by combining MODSIM™ and Moly-Cop Tools™ software packages. Using the back-calculated breakage parameters,

a good match was observed between the experimental and the simulated α_T values, in relation to J . The simulated results indicated that efficient grinding occurs at $J = 30$ %, for which the specific rate S_i is maximized. Validation of the results was also done for a higher J value, 40 %.

The approach proposed provides more accurate information for the reliable description of the grinding process and enables the scale-up of laboratory results to larger scale mills. Future work will focus on the evaluation and exploration of other important mill operating parameters, e.g. ball size and mill speed.

Nomenclature

$b_{i,j}$	breakage function (–)
$B_{i,j}$	cumulative breakage function (–)
D	internal diameter of the mill (m)
d	ball diameter (mm)
E	grinding consumption energy (J)
ε	bed porosity (%)
ε'	specific grinding consumption energy (J/kg)
f_c	powder filling volume (%)
J	ball filling volume (%)
i	size class index
M	mass of the feed material and balls (kg)
m	mass of the feed material (kg)
$m_i(0)$	mass fraction of size class i at time 0
$m_i(t)$	mass fraction of size class i at time t
N	rotational speed (rpm), (Hz)
P	mill power (W)
$P_i(0)$	mass fraction less than size x_i at time 0
$P_i(t)$	mass fraction less than size x_i at time t
Q_i	correction factor (–)
$R_{i(\text{exp})}$	mass retained on screen x_i (%)
$R_{i(\text{mod})}$	predicted mass retained on screen x_i (%)
S_{ref}	specific rate of breakage at $J = 50$ % (1/min)
S_i	specific rate of breakage (1/min)
t	grinding time (min), (s)
U	interstitial filling (–)
w_i	weight factor (–)
W	total sum of the weight factors (–)
x_0	standard size 1 mm
x_i	the upper size of size class i (mm)
α	parameter depending on the material properties (–)

α_T	parameter depending on milling conditions (–)
β	breakage parameter (–)
γ	breakage parameter (–)
Λ	parameter depending on the material properties (–)
μ	parameter depending on milling conditions (–)
ρ_b	specific gravity of the balls (g/cm^3)
Φ_j	breakage parameter (–)

References

- Austin L.G., Bhatia V.K., Experimental methods for grinding studies in laboratory mills, *Powder Technol.*, 5 (1972) 261–266.
- Austin L.G., Luckie P.T., Methods for determination of breakage distribution parameters, *Powder Technol.*, 5 (1972) 215–222.
- Austin L.G., Bagga P., An analysis of fine dry grinding in ball mills, *Powder Technol.*, 28 (1981) 83–90.
- Austin L.G., Klimpel R.R., Luckie P.T., *Process Engineering of Size Reduction: Ball Milling*, SME–AIME, New York, 1984.
- Austin L.G., Julianelli K., Sampaio de Souza A., Schneider C.L., Simulation wet ball milling of iron ore at Carajas, Brazil, *Int. J. Miner. Process.*, 84 (2007) 157–171.
- Beeck R., Bestimmung der Antriebsleistung von Rohrmühlen auf Grund von Betriebswerten., *Zement-Kalk-Gips*, 23 (1970) 413–416.
- Bilgili E., Scarlett B., Population balance modeling of non-linear effects in milling processes, *Powder Technol.*, 153 (2005) 59–71.
- Bond F.C., The third theory of comminution, *Trans. AIME*, 193 (1952) 484–494.
- Bond F.C., Crushing and grinding calculations, *British Chem. Eng.*, 6 (1960) 378–391.
- Bozkurt V., Özgür I., Dry grinding kinetics of colemanite, *Powder Technol.*, 176 (2007) 88–92.
- Celik M.S., Acceleration of breakage rates of anthracite during grinding in a ball mill, *Powder Technol.*, 54 (1988) 227–233.
- Charles R.J., Energy–size reduction relationships in comminution, *Trans. AIME*, 208 (1957) 80–88.
- Chimwani N., Glasser D., Hildebrandt D., Metzger M.J., Mulenga F.K., Determination of the milling parameters of a platinum group minerals ore to optimize product size distribution for flotation purposes, *Miner. Eng.*, 43–44 (2013) 67–78.
- Deniz V., Onur T., Investigation of the breakage kinetics of pumice samples as dependent on powder filling in a ball mill, *Int. J. Miner. Process.*, 67 (2002) 71–78.
- Deniz V., Comparisons of dry grinding kinetics of lignite, bituminous coal and petroleum coke, *Energ. Source, Part A*, 35 (2013) 913–920.
- Fortsch D.S., Ball charge loading—Impact of specific power consumption and capacity, in: *Cement Industry Technical Conference*, Phoenix, Arizona, USA, Conference Record. IEEE, April 9–14, 2006, pp. 62–72.
- Fuerstenau D.W., Kapur P.C., De A., *Modelling Breakage Kinetics in Various Dry Comminution Systems*, KONA Powder and Particle Journal, 21 (2003) 121–132.
- Fuerstenau D.W., De A., Kapur P.C., Linear and nonlinear particle breakage processes in comminution systems, *Int. J. Miner. Process.*, 74S (2004) 317–327.
- Gupta V.K., Zouit H., Hodouin D., The effect of ball and mill diameters on grinding rate parameters in dry grinding operation, *Powder Technol.*, 42 (1985) 199–208.
- Gupta V.K. and Sharma S., Analysis of ball mill grinding operation using mill power specific kinetic parameters, *Adv. Powder Technol.*, 25 (2014) 625–634.
- Herbst J.A., Fuerstenau D.W., Mathematical simulation of dry ball milling using specific power information, *Trans. AIME*, 254 (1973) 343–348.
- Herbst J.A., Fuerstenau D.W., Scale-up procedure for continuous grinding mill design using population balance models, *Int. J. Miner. Process.*, 7 (1980) 1–31.
- Ipek H., Göktepe F., Determination of grindability characteristics of zeolite, *Physicochem. Probl. Miner. Process.*, 47 (2011) 183–192.
- Kick F., *Das Gesetz der proportionalen Widerstände und seine Anwendungen*, Felix, Leipzig (1885).
- King R.P., *Modeling and simulation of mineral processing systems*, Oxford: Butterworth-Heinemann, p. 147, 2001.
- Klimpel R.R., Austin L.G., The back-calculation of specific rates of breakage and non-normalized breakage distribution parameters from batch grinding data, *Int. J. Miner. Process.*, 4 (1977) 7–32.
- Metzger M.J., Glasser D., Hausberger B., Hildebrandt D., Glasser B.J., Use of the attainable region analysis to optimize particle breakage in a ball mill, *Chem. Eng. Sci.*, 64 (2009) 3766–3777.
- Nomura S., Hosoda K., Tanaka T., An analysis of the selection function for mills using balls as grinding media, *Powder Technol.*, 68 (1991) 1–12.
- Nomura, S., Tanaka T., Callcott T.G., The effect of mill power on the selection function for tumbling and vibration ball mills, *Powder Technol.*, 81 (1994) 101–109.
- Ozkan A., Yekeler M., Calkaya M., Kinetics of fine wet grinding of zeolite in a steel ball mill in comparison to dry grinding, *Int. J. Miner. Process.*, 90 (2009) 67–73.
- Rajamani R.K., Guo D., Acceleration and deceleration of breakage rates in wet ball mills, *Int. J. Miner. Process.*, 34 (1992) 103–118.
- Rittinger P.R., *Lehrbuch der Aufbereitungskunde*, Ernst and Korn, Berlin (1867).
- Shoji K., Austin L.G., Smalia F., Brame K., Luckie P.T., Further studies of ball and powder filling effects in ball mills, *Powder Technol.*, 31 (1982) 121–126.
- Stamboliadis E., A contribution to the relationship of energy and particle size in the comminution of brittle particulate materials, *Miner. Eng.*, 15 (2002) 707–713.
- Stamboliadis E., Emmanouilidis S., Petrakis E., A New Approach to the Calculation of Work Index and the Potential Energy of a Particulate Material, *Geomater.*, 1 (2011) 28–32.
- Umucu Y., Deniz V., Bozkurt V., Çağlar M. F., The evaluation of grinding process using artificial neural network, *Int. J.*

Miner. Process., 146 (2016) 46–53.

Wang X., Gui W., Yang C., Wang Y., Wet grindability of an industrial ore and its breakage parameters estimation using population balances, Inter. J. Miner. Process., 98 (2011) 113–117.

Yahyaie M., Powell M.S., Toor P., Tuxford A., Limpus A.,

Relining efficiency and liner design for improved plant performance, Miner. Eng., 83 (2015) 64–77.

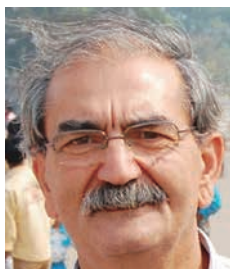
Yekeler M., Ozkan A., Austin L.G., Kinetics of fine wet grinding in a laboratory ball mill, Powder Technol., 114 (2001) 224–228.

Author's short biography



Evangelos Petrakis

Evangelos Petrakis is a member of the Laboratory teaching staff at the Laboratory of Mineral Processing of the Mineral Resources Engineering Department of Technical University of Crete (TUC). He received his diploma degree in 2001 and his M.Sc. in the field of Geotechnology and the Environment in 2004 from the same Department. He is now a third-year Ph.D. candidate and his research interests are in the field of simulation and optimization of grinding systems.



Elias Stamboliadis

Elias Stamboliadis graduated from the Department of Mining and Metallurgical Engineering of National Technical University of Athens (NTUA) in 1971. His Master Degree was in Mineral Process Design from the Royal School of Mines, Imperial College, London (1973) and he received his PhD from McGill University in Montreal (1977). He was a professor at the Department of Mineral Resources Engineering of Technical University of Crete, Greece, until 2014. Now he is Professor Emeritus in the same Department. His research interests are in mineral processing and include grinding, liberation, physical separation of minerals, surface chemistry of minerals and environmental applications.



Konstantinos Komnitsas

Prof. Konstantinos Komnitsas, 1961, holds a PhD degree in Hydrometallurgy and is the director of the Laboratories (i) Waste Management and Soil Decontamination, (ii) Ceramics and Glass Technology and (iii) Ore Beneficiation of the School of Mineral Resources Engineering of Technical University Crete. He is expert in the fields of metallurgy, hydro- and bio-hydrometallurgy, waste management and valorization, new materials, soil decontamination, environmental risk assessment and LCA studies.

Changes in Pore Structures of Porous Beds When Subjected to Vertical Vibration[†]

Rong Yue and Qiang Zhang*

[†] Department of Biosystems Engineering, University of Manitoba, Canada

Abstract

The objective of this study was to investigate the effect of vibration on critical pore structure parameters related to flow in porous beds. The discrete element method was used to simulate particle packing in porous beds of soybean subjected to vibration. The porous bed was simulated as an assembly of spherical particles with diameters randomly distributed between 5.5 mm and 7.5 mm. The simulated porous bed was subjected to vertical vibration at a fixed frequency of 15 Hz and multiple amplitudes from 0.5 to 4.0 mm, resulting in vibration intensities from 0.45g to 3.62g (g = gravitational acceleration). The location (coordinates) of each particle was tracked during vibration. Based on the simulated spatial arrangement of particles, critical flow-related parameters of the porous bed, including porosity, tortuosity, and pore throat width were calculated. It was found that vibration intensity of 1.81g resulted in the lowest porosity, whereas lower vibration intensity did not have enough energy to densify the bed and higher intensity produced less dense packing due to over-excitement. Local porosity fluctuated markedly during vibration, with a general trend of decrease as vibration progressed. Vibration noticeably affected the shape (tortuousness) of flow path. Tortuosity of the porous bed before vibration was higher (2 % to 9 %) than that after vibration. Vibration reduced the pore throat width by 18 % on average (from 3.3 mm before vibration to an average of 2.7 mm after vibration).

Keywords: porous media, porosity, tortuosity, pore throat, vibration, discrete element method

1. Introduction

The knowledge of pore structure of porous beds (media) is critical in understanding fluid flow through porous beds. A number of 2D (Lao H.W. et al., 2004; Ljung A.L. et al., 2012; Xiao Z.F. et al., 2008; Yiotis A.G. et al., 2010) and 3D models (Balhoff M.T. et al., 2007; Sobieski W. et al., 2012; Thompson K.E., 2002; Thompson K.E. and Fogler H.S., 1997) have been developed to describe pore structures of porous media. Those models generally deal with porous beds with fixed pore structures. However, porous beds are often subject to such mechanical disturbances as vibration during operation. When a porous bed consisting of randomly packed particles is vibrated, the pore structure is altered due to re-arrangement of particles. The mechanisms by which the pore structure is affected by vibration are extremely complex. An X.Z. et al. (2005) used the discrete element method to study the densification of porous beds (sphere packing) when subjected

to vertical vibration. They showed that the degree of densification was significantly affected by both vibration frequency and amplitude, and identified two densification mechanisms: pushing filling and jumping filling. Pushing filling generally occurred at low vibration intensity in which the contact between spheres was maintained, while jumping filling at high intensity in which the contact between particles was periodically broken. An X.Z. et al. (2009) conducted experiments to study the effect of vibration on packing density and observed that there existed optimum values of vibration frequency and amplitude to achieve the maximum packing density. Frequency and amplitude should be considered separately in terms of their effect on packing density. Liu C. et al. (2010) used a high speed camera to study the behavior of particles in a bin subjected to vertical vibration. They reported that all particles in a porous bed vibrated as a whole (a continuum) when the bed was subjected to low intensity vibration, whereas individual particles vibrated in their own modes (as a discrete system) when subjected to high intensity vibration.

The effect of vibration on pore structures is complex. Most studies on vibration of porous beds have been focused on particle packing, and few have explored how changes in particle packing caused by vibration would

[†] Received 19 February 2016; Accepted 8 April 2016
J-STAGE Advance Publication online 20 May 2016

[†] Winnipeg, MB R3T 5V6, Canada

* Corresponding author: Qiang Zhang;
E-mail: Qiang.Zhang@umanitoba.ca
TEL: +1-204-474-9819 FAX: +1-204-474-7512

impact such properties as porosity and tortuosity which are related to flow through the porous bed. Traditionally, the studies of particle packing are pursued in the realm of particulate mechanics, while flow through porous media has established itself as a sub-discipline in fluid mechanics. This study attempted to establish a connection between flow in porous media and particulate mechanics. A powerful tool used in particulate mechanics—the discrete element method, was employed to study pore structures from the angle of flow in porous media. The objective of this paper was to investigate the effect of vibration on pore structures of porous beds with an emphasis on parameters that are related to flow through the porous beds. Specifically, a discrete element model (DEM) was used to simulate the formation of porous beds and changes in pore structure during vibration; and an algorithm was developed to use the DEM simulation data to quantify the flow-related characteristics of the porous bed, including porosity, flow path (length and shape), tortuosity, and pore throat diameter.

2. Materials and methodology

2.1 Discrete element simulations of porous bed subjected to vibration

The discrete element method was originally proposed by Cundall P.A. and Strack O.D.L. (1979) to solve problems in rock mechanics. The method has been widely used to analyze granular and discontinuous materials. A commercial discrete element software package PFC^{3D} (Version 4.0 EV, Itasca Consulting Group Inc., Minneapolis, USA) was used to build a simulation model in this study. The PFC^{3D} model first simulated the formation of a porous bed, during which the trajectory and rotation of each particle were tracked to evaluate its position and orientation in a time stepping simulation. Once the porous bed was formed, a vibration excitation was applied. Simulations were conducted for a model bin 0.28 m in height and 0.15 m in diameter, filled with soybean to a depth of 0.25 m (**Fig. 1**). This model bin was used by Liu C. et al. (2010) to study the vibration of soybean in storage. The same mechanical property parameters for the PFC^{3D} model (including the stored soybean) used by Liu C. et al. (2010) were adopted in this study (**Table 1**). Based on the measured sizes of bin and soybean kernels, the model bin was simulated as a cylindrical container filled with spherical particles. It should be noted that soybean kernels are not spherical, but they resemble a sphere with high average sphericity values (above 0.8), and therefore, most researchers have used spheres to approximate soybean kernels when simulating bulk soybean characteristics in DEM models to reduce computation times (Boac J.M. et

al., 2014). Based on the measurements of 24 randomly selected kernels, the average long, intermediate, and short axis dimensions for soybean used in this study were 7.6, 6.7, and 5.7 mm, respectively. The corresponding geometric mean diameter was 6.6 mm, and sphericity 0.87. Considering variations in measured soybean kernel size, a range of particle sizes from 5.5 and 7.5 mm recommended by Liu C. et al. (2010) for DEM simulations was adopted in this study. A coordinate system was set up with x and y representing the horizontal directions, z the vertical direction, and the origin at the bottom-center (**Fig. 1**).

A simple harmonic excitation was used to vibrate the bin. Vibration excitation was applied to the bin floor (bottom) in the vertical direction with prescribed frequencies and amplitudes as follows:

$$D_z(t) = A \sin(\omega t) \quad (1)$$

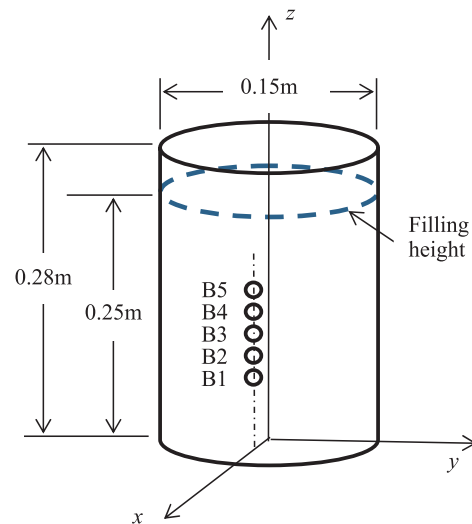


Fig. 1 A Schematic of simulated bin showing the locations (B1–B5) where local porosity was calculated.

Table 1 PFC simulation parameters adopted from Liu C. et al. (2010)

Parameters	Value
Wall normal stiffness (k_n), N/m	1.8×10^7
Wall shear stiffness (k_s), N/m	0.9×10^7
Particle normal stiffness (k_{pn}), N/m	4.0×10^6
Particle shear stiffness (k_{ps}), N/m	2.0×10^6
Friction coefficient between particles (μ_p)	0.47
Friction coefficient between particle and wall (Plexiglas) (μ_w)	0.3
Particle density (ρ_p), kg/m ³	1285
Particle diameter (d_p), mm	5.5–7.5

A frequency of 15 Hz and amplitudes of 0.5, 1.0, 2.0, 3.0, and 4.0 mm were used in simulations. These frequency and amplitude combinations were selected to achieve the maximum densification. According to the experimental results reported by An X.Z. et al. (2009), the dense packing was achieved with vibration intensity between 1.5g and 4.0g (the peak density occurred at 2.0g–2.5g). The vibration intensity levels, determined as $A(2\pi f)^2$, were 0.45g, 0.91g, 1.81g, 2.72g, and 3.62g for amplitudes of 0.5, 1.0, 2.0, 3.0, and 4.0 mm at 15 Hz, respectively.

Vibration was simulated in time steps of 3.3 μ s. This time step (Δt) was determined from the mass (m) and the stiffness (k_{pn}) of particles ($\Delta t = \sqrt{m/k_{pn}}$) (Itasca, 2005). Preliminary simulations were conducted to determine the total length of vibration time required to reach the maximum density and it was found the 16 s was sufficient for all vibration intensities. At each time step, the position (x , y and z coordinates) of each particle was saved in a data file for late use in calculating flow parameters.

One of the most important parameters affecting flow through a porous bed is porosity. In this study, both global (overall) and local porosity values were calculated based on DEM simulation data. The global porosity was calculated as the ratio of the total volume occupied by the particles to the total volume of porous bed as follows:

$$\Phi = 1 - V_p / V \quad (2)$$

$$V_p = \sum \frac{4}{3} \pi r^3 \quad (3)$$

In a porous bed consisting of randomly packed particles, the pore distribution would not be uniform. Therefore, local porosity was also determined using the built-in function in PFC^{3D} at five locations, which were denoted as B1(0.06, 0, 0.119), B2(0.06, 0, 0.129), B3(0.06, 0, 0.130), B4(0.06, 0, 0.136), and B5(0.06, 0, 0.146) (three numbers in parenthesis are x -, y - and z - coordinates, respectively) (Fig. 1). Because the bin was relatively small, these five locations were selected near the bin center to avoid the boundary effects. The instantaneous local porosity values at these locations were calculated at every time step (3.3 μ s) during vibration simulation.

2.2 Airflow path

The airflow path was calculated using the methodology proposed by Yue R. and Zhang Q. (2013). The porous bed was treated as a collection of tetrahedron units, and each tetrahedron contained a pore surrounded by four particles (Fig. 2a). Air (fluid) was assumed to enter the tetrahedron unit from the base (inlet) triangle (ΔABC) and exit from the other three (exit) triangles. The lines connecting the

centroid of the base triangle to the centroids of the three exit triangles represented three local airflow paths. The length of each local path was calculated and the shortest and longest paths were identified. To compare the width of each airflow path, the open area (pore throat) between the three particles that form a triangular face in the tetrahedron unit was calculated for all four face triangles (Fig. 2b). The open area was calculated as the area of face triangle less the projected area of three particles on the triangle face (Dudda W. and Sobieski W., 2014). The equivalent pore throat width was considered as the diameter of a circle which had the same area as the open projected area.

$$d_f = 2\sqrt{\frac{S_f}{\pi}} \quad (4)$$

Based on the calculated pore throat width, the widest and the narrowest local flow paths were identified. To construct a specific type of global flow path (running from the bottom to the top of the porous bed), say the widest path, one of the three exit triangles that had the widest pore throat was selected as the base (inlet) triangle for the next tetrahedron unit. This process was repeated from the bottom to the top surface of the porous bed and a global flow path was obtained by connecting the local paths in all associated tetrahedron units (Fig. 3). It should be noted that simply connecting a series of straight lines (local paths) to form a global path resulted in sharp turn angles between local paths (Fig. 3). However, flowing air cannot make sharp turns. Therefore, a procedure proposed by Sobieski W. et al. (2012) was used to replace each sharp turn angle with an arc (Fig. 3).

2.3 Tortuosity

Different definitions of tortuosity can be found in the literature (Bear J., 2013). The geometric tortuosity was used in this study, which was defined as the ratio of the actual flow path length to the depth of porous bed:

$$\tau = \frac{L_e}{L_0} \quad (5)$$

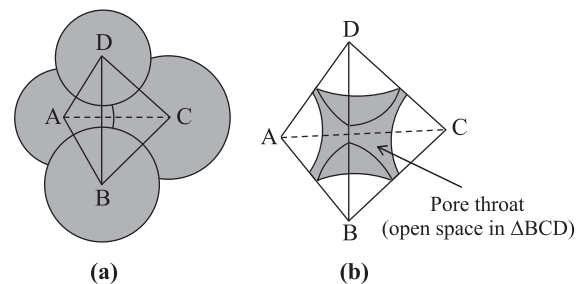


Fig. 2 A tetrahedron as the basic building block in a porous bed. (a) four particles associated with a tetrahedron unit, (b) open space (a pore throat) in a tetrahedron unit.

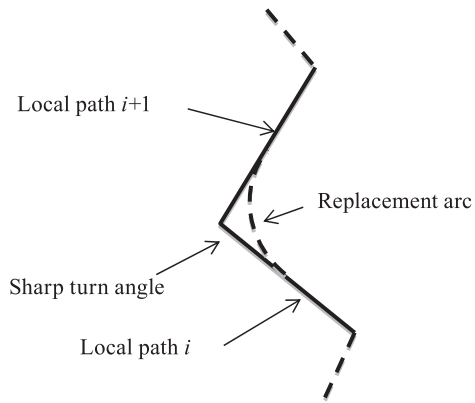


Fig. 3 Replacement of sharp turn angle between two local flow paths with arc.

The actual length of a (global) flow path was determined as the sum of all local path lengths. The depth of porous bed was determined from the positions of particles in the top layer of bed simulated by the DEM model as follows (Sobieski W. et al., 2012):

$$L_0 = (Z_h - Z_l) + d_{ave} \quad (6)$$

2.4 Experiment

A cylindrical model bin of 0.28 m height and 0.15 m diameter was used to conduct tests to verify the DEM simulations (**Fig. 4**). The bin was made of Plexiglas and placed on a vibration table (Model 307-97056, Cougar Industries Inc., Peru, IL, USA). The table was supported by three piston-spring assemblies to permit only vertical displacement. The vibration table was driven by a pneumatic piston with compressed air and controlled by a pressure regulator to achieve different vibration intensities. A portable vibration analyzer (Model 654 CS, Vitec Inc., Cleveland, OH, USA) was used to measure the vibration amplitude and frequency and the signal was displayed on an oscilloscope (Model 190 B/C ScopeMeter, Fluke Industrial B. V., the Netherlands).

For each test, measured amount (mass) of soybean was placed into the bin through a funnel located 350 mm above the bin, and the top surface was levelled manually after filling. The total volume of the porous bed was calculated from the filling depth and the bin diameter, and the packing density (ρ_b) was then calculated from the total volume and the mass of soybean in the bin. All linear dimensions were measured by using a ruler with a resolution of 1 mm, and mass measured by an electronic scale with a resolution of 0.1g.

The liquid displacement method was used to measure the particle density (ρ_p) of soybean kernels. The specific

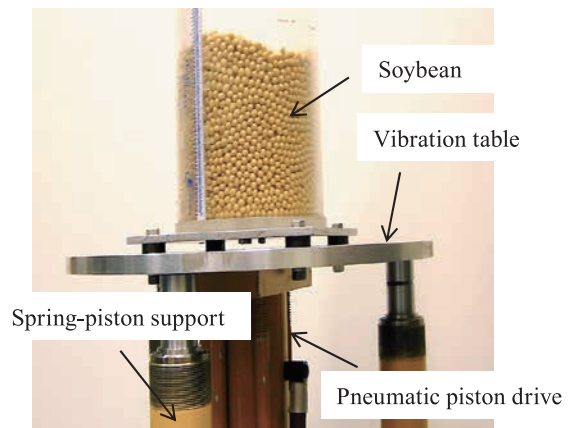


Fig. 4 Model bin test system (the bin was 0.28 m in height and filled to a depth of 0.25 m).

steps were as follows: (1) 100 kernels were weighed and placed into a 50-mL flask filled with toluene, (2) the volume of 100 kernels was determined from the displaced volume of toluene, and (3) the particle density was calculated from the measured kernel mass and volume. A steel calibration ball of 8580 mm³ (25.4 mm in diameter) was used to calibrate the toluene volume displacement before running the test. The (global) porosity was calculated from the measured bulk and particle densities as follows:

$$\Phi = 1 - \frac{\rho_b}{\rho_p} \quad (7)$$

3. Results and discussion

3.1 Properties of simulated porous bed and comparison with experimental data

The DEM model generated a porous bed consisting of 18,188 particles with sizes randomly distributed between 5.5 mm and 7.5 mm (**Fig. 5**). Based on the measured mass and volume of the porous bed, as well as the particle density and size, the total number of particles in the test bin was estimated 18,498. In other words, the total number of particles in the simulation was 1.7 % less than the measured value. It should be noted that estimation of the total number of particles in the bin was based on the assumption that all kernels were spherical and had an average diameter of 6.5 mm (the average of 5.5 and 7.5 mm used in simulations). However, the measured geometric mean diameter of particles was 6.6 mm (as discussed in section 2.1). Using the measured diameter of 6.6 mm, the total number of particles in the bin was estimated to be 17,670, which was 2.9 % less than the simulated value.

The simulated global (overall) porosity before vibration was 0.401, while the measured value was 0.398 ± 0.006

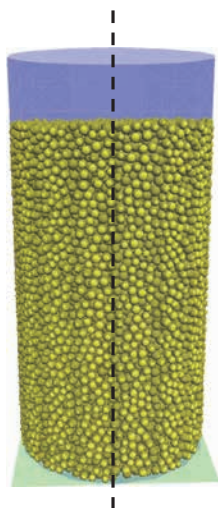


Fig. 5 Simulated porous bed with 18,188 particles.

(\pm standard deviation, $n = 6$). The simulated porosity was within the 95 % CI (Confidence Interval) of the measured porosity (0.391 to 0.404). The simulated minimum porosity was 0.379, whereas the measured value was 0.366 ± 0.001 after vibration (at 1.0g intensity). The relative change (decrease) in porosity after vibration was 5.5 % in simulations, which was lower than that in measurements (8.0 %). Liu C. (2008) reported relative changes between 0.7 % to 6.1 % in porosity of soybean in a model bin after vibration.

The simulated local porosity, calculated from the PFC^{3D} built-in function in a small region within the porous bed, varied with the location. Specifically, the local porosity before vibration was 0.402, 0.395, 0.395, 0.393, and 0.389 at the five selected locations (B1–B5), respectively. The average of the five locations was close to the measured value (0.395 vs. 0.398). Local porosity also varied with both vibration duration and intensity, which is discussed in the next sections.

3.2 Variation of porosity during vibration

Fig. 6 shows typical curves of simulated local porosity during vibration. The minimum porosity was reached at about 9 s for all locations. The local fluctuations in porosity were apparent, and they were attributed to the cyclic nature of vibration which compressed and relaxed the porous material during each vibration cycle (An X.Z. et al., 2005). The magnitudes of these local fluctuations could be as high as 0.018 (e.g., from 0.378 to 0.396 in porosity). The overall trend was that local porosity decreased as vibration progressed, but not monotonically (large global fluctuations were apparent). Taking location B2 as an example, the porosity increased quickly from the initial level of 0.395 to 0.430 in 0.04 s, and then dropped to 0.370 at about 0.3 s (**Fig. 6**). This observed pattern was similar

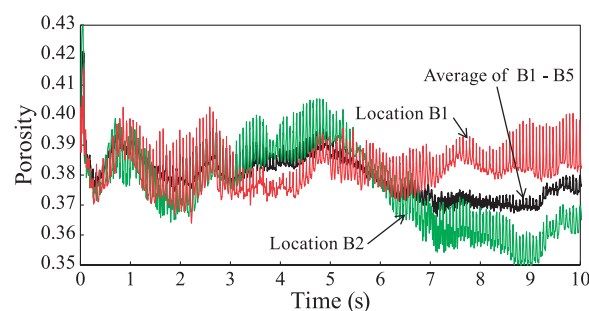


Fig. 6 Simulated local porosity during vibration at locations B1 and B2, and the average porosity of all five locations for vibration intensity of 1.8g.

to the experimental observations by Nowak E.R. et al. (1998), but did not fully agree with the DEM simulation result reported by An X.Z. et al. (2005). They reported that packing fraction (opposite to porosity) increased monotonically with time of vibration (local fluctuations also existed). It should be noted that it was not clear if the porosity reported by An X.Z. et al. (2005) was the local or global porosity. Given that the pore structure in a porous bed varies from location to location, one would expect that local porosity varies with location. An X.Z. et al. (2005) observed that macro-pores (pores large enough to accommodate a particle) existed in loosely packed sphere assemblies. Therefore, high porosity could exist locally where a macro-pore exists. During vibration, particles re-arrange themselves and macro-pores would be destroyed (An X.Z. et al., 2005). However, it was also possible that some macro-pores were created at an instant through particle re-arrangement during vibration, resulting in high local porosity. These instant macro-pores might not be stable and would be destroyed quickly by vibration. During vibration, destruction and creation of macro-pores might occur repeatedly, resulting in fluctuations in local porosity; however, more macro-pores would be destroyed than created, leading to a general trend of decrease in local porosity, as well as gradual decrease in the global porosity. A similar pattern of fluctuations in local porosity were observed by Liu C. (2008) in his experiments to investigate the vibration effect on porosity of soybean. He used a high speed camera to record movements of soybean kernels in a transparent bin made of Plexiglas. Based on the recorded video images, he tracked three particles that formed a triangle and calculated the area of this triangle at different times during vibration. He considered that changes in the triangle area reflected changes in local porosity (i.e., increasing triangle area reflected increasing in porosity, and vice versa). The relative change in local porosity was then estimated as S/S_0 , where S_0 was the initial area of triangle and S the triangle area at a given time. It was apparent that the relative change in local porosity fluctuated during vibration, with an overall

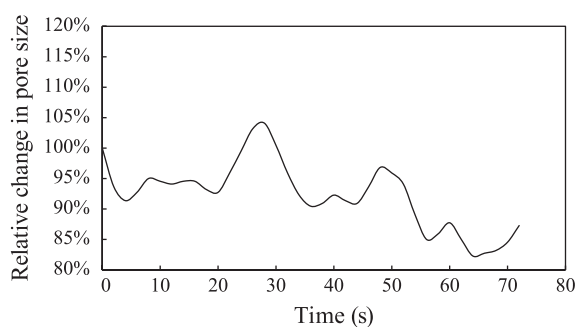


Fig. 7 Relative change in area of triangle formed by three particles during vibration at 25 Hz frequency and 0.45 mm amplitude (based on data reported by (Liu C., 2008).

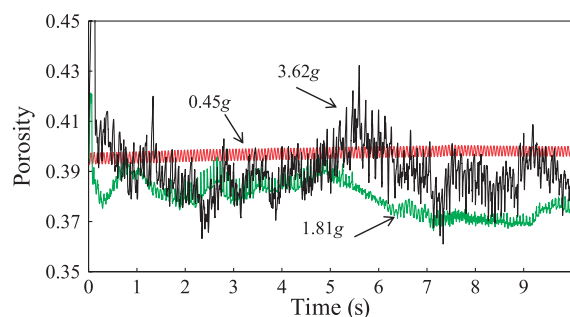


Fig. 8 Simulated average local porosity during vibration at intensities of 0.45g, 1.81g, and 3.62g.

trend of decrease, similar to what was observed in his study (Fig. 7).

3.3 Effects of vibration intensity on porosity

Vibration intensity had noticeable effect on porosity during vibration (Fig. 8). The higher the intensity, the greater the fluctuations. Among the five intensity levels simulated (0.45g, 0.91g, 1.81g, 2.72g, and 3.62g), 1.81g resulted in the lowest porosity (Fig. 9). In other words, there was a “critical” vibration intensity (1.81g) that resulted in a maximum reduction in porosity, and lower or higher vibration intensities generated less dense porous structure. A similar observation was reported by An X.Z. et al. (2009). They measured changes in packing density of an assembly of spheres with diameter of 5.02 mm in a 229.70-mm diameter container when subjected to vibration between 0.25g and 5.0g, and observed that the highest packing density occurred in the mid-range vibration intensities between 2.0g to 2.5g. Theoretically speaking, if the acceleration of particles in a porous bed is greater than 1g in the vertical direction, the particles could become “afloat” once in every vibration cycle, which could result in a high probability of creating a large void into which another particle can slide, thus providing the best opportunity to form a dense structure. Therefore, lower vibration intensity (< 1g) would produce less reduction in

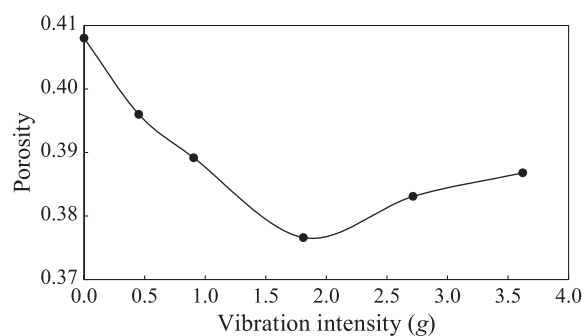


Fig. 9 Effect of vibration intensity on porosity.

porosity. However, it should be noted that a porous bed is a discrete system and not all particles vibrate at the same frequency and amplitude as the excitation applied on the containing structures (the bin bottom in this study). Energy transfer in the porous bed when subjected to vibration is extremely complicated, however it is a reasonable assumption that not all vibration energy from the vibration source applied at the bin bottom would be transferred to the particles in the porous bed because of energy dissipation by collision and friction among particles and between particle and the containing structures. Energy dissipation in granular materials during vibration has been shown to be significant in many studies in the area of particle impact damping (Friend R.D. and Kinra V.K., 2000). Energy dissipation offers a plausible conjecture for the reason why the maximum reduction in porosity occurred at 1.8g instead of 1g. This also means that the critical vibration intensity that produces the maximum reduction in porosity would vary with many factors that influence energy transfer in porous beds, including particle size and shape, particle density, friction between particles, friction between particles and containing structures, restitution coefficient, and even porosity itself, which dictates the distances (clearances) between particles and between particles and containing structure.

An X.Z. et al. (2009) explained that too high energy input would over-excite particles in porous beds, which would lead to less dense structures. While low amplitude vibration induces subtle changes in the microstructure of a granular material, resulting in higher bulk density, strong vibration leads to fluid-like behavior of the granular material, resulting in lower bulk density (Rosato A.D. et al., 2002). Hunt M.L. et al. (1994) conducted experiments to study the behavior of a granular material subjected to vertical vibration at acceleration levels from 1g to 5.5g. They observed that the volume of the granular material began to expand at acceleration of 2g.

At high vibration intensity (3.62g), porosity fluctuated markedly both locally and globally (details are discussed in Section 3.2). In contrast, at low vibration intensity of 0.45g, porosity only fluctuated slightly around its average (Fig. 8).

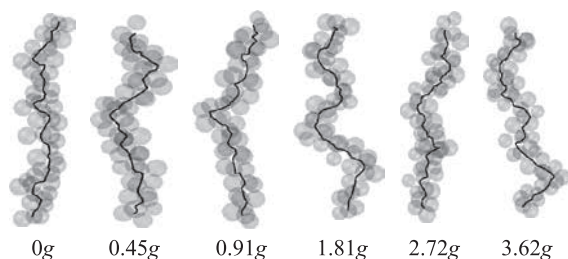


Fig. 10 Typical simulated airflow paths (as a series of associated tetrahedron units) for different vibration intensities.

This meant that vibration energy at low intensity was not sufficient to cause significant particle re-arrangement, resulting in little change in porosity. Liu C. et al. (2010) used a high speed camera to study vibration of individual particles in a bin subjected to vertical vibration and observed that all particles in the bin vibrated as a continuum with the same frequency and amplitude as the excitation at low intensities ($< 1g$), whereas individual particles vibrated “irregularly” (not following the harmonic excitation) when the vibration intensities were high ($> 1g$).

3.4 Effect of vibration on airflow path

Vibration changed the shape and length of airflow path (Fig. 10). Qualitatively speaking, the deviation of flow path (the exit point) from the entry point was less before vibration than after vibration. This was probably because higher flow resistance in more dense porous beds after vibration made it more difficult for flow to go upwards directly. Nwaizu C. and Zhang Q. (2015) used imaging techniques (with smokes) to study airflow through grain bulks subjected to vibration and observed that reduction in porosity after vibration caused more lateral “branching” of flow when air entered the grain bulks vertically. In other words, more air was forced to flow in non-vertical directions after vibration. It was interesting to note that while there was less degree of deviation of flow path from the entry point before vibration, but more sharp local turns was observed. This became apparent when comparing the flow paths between 0g and 1.81g vibration intensities. Specifically, many small sharp local turns could be seen in the 0g path, whereas long sections of relatively smooth line existed in the 1.81g path (Fig. 10).

Both the deviation of flow path from the entry point and the local turns would result in longer flow paths (higher tortuosity). To quantify the differences in airflow path among different vibration intensities, the simulated tortuosity values were compared (Fig. 11). The tortuosity decreased after vibration generally, but no clear pattern could be identified. A maximum reduction of 9 % was observed for vibration intensity of 1.81g and a minimum

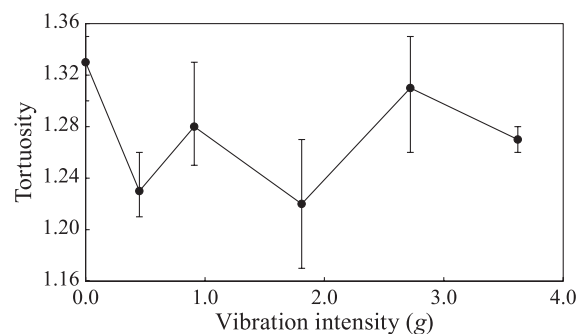


Fig. 11 Variation of simulated tortuosity with vibration intensities (each data point represents the average of three simulated paths and the error bar indicates the minimum and maximum values).

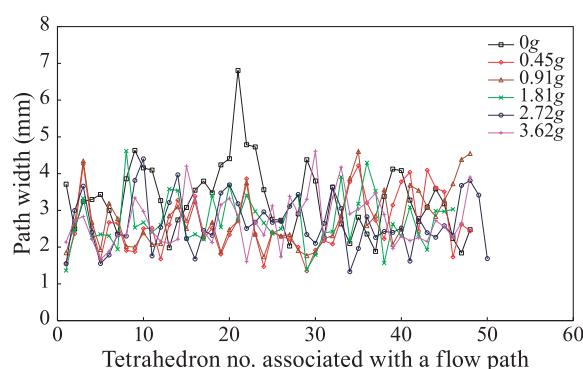


Fig. 12 Pore throat width of local flow paths from the bin bottom (tetrahedron no. 1) to the top under different vibration conditions.

2 % for 2.72g. Many studies have shown that tortuosity of flow through porous media decreases with porosity (Pisani L., 2011). As discussed earlier, the lowest porosity occurred at 1.81g. Therefore, it was expected that flow path for 1.81g vibration would be less tortuous. This also meant that sharp local turns (dominant before vibration) had more effect on the tortuosity of flow path than did the deviation (dominant after vibration) from the entry point. Although the maximum reduction in tortuosity corresponded to the minimum porosity at 1.81g, the pattern of variation in tortuosity with vibration intensity did not quite follow that for porosity shown in Fig. 9.

The pore throat width (the equivalent diameter) of the widest local flow path was calculated for each tetrahedron unit associated with a global flow path (Fig. 12). It was observed that the throat width varied randomly between 1.3 and 4.6 mm, with one exception before vibration—a high value of 6.8 mm was observed. A pore throat of 6.8 mm was apparently greater than the average particle diameter. This meant that a macro-pore, defined as a pore large enough to accommodate a particle (An X.Z. et al., 2005), existed in the porous bed before vibration, but no macro-pores were observed after vibration at any of the

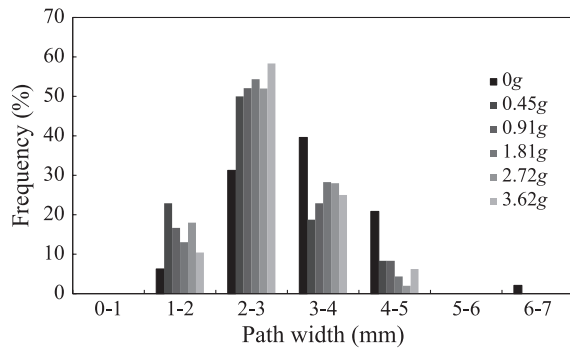


Fig. 13 Distribution of pore throat width under different vibration intensities.

five vibration intensities studied.

To further examine the effect of vibration intensity on pore throat, the distributions of throat width were plotted (**Fig. 13**). The highest percentage of pore throats was in the 3–4 mm range before vibration, while the highest percentage after vibration was in the 2–3 mm range. The percentage of pore throats in the ranges of 1–2 mm and 2–3 mm before vibration was much lower than that after vibration, whereas the percentage in 4–5 mm before vibration was much higher than that after vibration. These observations indicated that vibration reduced the pore throat width. On average, the pore throat width was 3.3, 2.6, 2.8, 2.7, 2.7, and 2.7 mm for 0g (before vibration), 0.45g, 0.91g, 1.81g, 2.72g, and 3.62g, respectively. While the average pore throat before vibration was greater (22 %) than those after vibration, the differences in pore throat width among the five different vibration intensities were negligible (< 0.2 mm).

4. Conclusions

- (1) The discrete element model was capable of predicting some critical pore structure parameters for flow through porous beds, including porosity, tortuosity, pore throat width, and flow path geometry (length and shape).
- (2) The influence of vibration on porosity was clearly demonstrated. A vibration intensity of 1.81g resulted in the lowest porosity (6 % lower than that before vibration). Lower vibration intensity did not have enough energy to cause much change in porosity, while higher intensity over-excited particles, producing less dense packing than did 1.81g.
- (3) Local porosity fluctuated markedly during vibration, probably due to repeated formation and destruction of instant (unstable) macro-pores (defined as pores large enough to accommodate a particle).
- (4) Tortuosity of flow path was noticeably affected by vibration. Tortuosity of the porous bed before vibra-

tion was higher (2 %–9 %) than that after vibration.

- (5) Pore throats larger than the average particle diameter (due to macro-pores) existed in the porous bed before vibration, but were not observed after vibration.
- (6) Vibration reduced the pore throat width. The highest percentage of pore throats was in the range of 3–4 mm before vibration, and reduced to 2–3 mm after vibration. The reduction in average pore throat width was 22 % after vibration.

Nomenclature

A	vibration amplitude (m)
d_{ave}	average particle diameter (m)
d_f	equivalent pore throat width of local path (m)
d_p	particle diameter (mm)
D_z	displacement in the vertical direction (m)
f	vibration frequency (Hz)
g	acceleration due to gravity (m/s ²)
k_n	wall normal stiffness (N/m)
k_{pn}	particle normal stiffness (N/m)
k_{ps}	particle shear stiffness (N/m)
k_s	wall shear stiffness (N/m)
L_0	depth of porous bed (m)
L_e	actual length of flow path (m)
m	particle mass (kg)
r	particle radius (m)
S	the triangle area formed by three particles at a given time (m ²)
S_0	the initial area of triangle formed by three particles (m ²)
S_f	open projected area between three particles in a triangular face of tetrahedron (m ²)
t	time (s)
V	total volume of porous bed (m ³)
V_p	total volume occupied by particles (m ³)
x	x -coordinate (m)
y	y -coordinate (m)
z	z -coordinate (m)
Z_h	z -coordinate of the highest sphere centroid in the porous bed (m)
Z_l	z -coordinate of the lowest sphere centroid in the porous bed (m)
Σ	summation
Δt	simulation time step (s)
τ	tortuosity

ω	angular velocity (rad/s)
Φ	simulated average global porosity (decimal fraction)
ρ_b	packing density (kg/m ³)
ρ_p	particle density (kg/m ³)
μ_p	friction coefficient between particles
μ_w	friction coefficient between particle and wall

References

- An X.Z., Li C.X., Yang R.Y., Zou R.P., Yu A.B., Experimental study of the packing of mono-sized spheres subjected to one-dimensional vibration, *Powder Technology*, 196 (2009) 50–55.
- An X.Z., Yang R.Y., Dong K.J., Zou R.P., Yu A.B., Micromechanical simulation and analysis of one-dimensional vibratory sphere packing, *Physical Review Letters*, 95 (2005) 205502.
- Balhoff M.T., Thompson K.E., Hjortsø M., Coupling pore-scale networks to continuum-scale models of porous media, *Computers & Geosciences*, 33 (2007) 393–410.
- Bear J., *Dynamics of fluids in porous media*, Dover Publications, 2013.
- Boac J.M., Ambrose R.P.K., Casada M.E., Maghirang R.G., Maier D.E., Applications of discrete element method in modeling of grain postharvest operations, *Food Engineering Reviews*, 6 (2014) 128–149.
- Cundall P.A., Strack O.D.L., A discrete numerical model for granular assemblies, *Géotechnique*, 29 (1979) 47–65.
- Dudda W., Sobieski W., Modification of the pathfinder algorithm for calculating granular beds with various particle size distributions, *Technical Sciences*, 17 (2014) 135–148.
- Friend R.D., Kinra V.K., Particle impact damping, *Journal of Sound and Vibration*, 233 (2000) 93–118.
- Hunt M.L., Hsiau S.S., Hong K.T., Particle mixing and volumetric expansion in a vibrated granular bed, *Journal of Fluids Engineering*, 116 (1994) 785–791.
- Itasca, User's guide pfc3d particle flow code in 3 dimensions, Itasca Consulting Group, Inc., Minneapolis, Minnesota, USA, (2005).
- Lao H.W., Neeman H.J., Papavassiliou D.V., A pore network model for the calculation of non-darcy flow coefficients in fluid flow through porous media, *Chemical Engineering Communications*, 191 (2004) 1285–1322.
- Liu C., Study on bulk solid movement and forces in bins, Ph.D., China Agricultural University, 2008.
- Liu C., Zhang Q., Chen Y., Discrete element simulations of vibration characteristics of bulk grain in storage bins, *Transactions of the ASABE*, 53 (2010) 1653–1659.
- Ljung A.L., Frishfelds V., Lundstrom T.S., Marjavaara B.D., Discrete and continuous modeling of heat and mass transport in drying of a bed of iron ore pellets, *Drying Technology*, 30 (2012) 760–773.
- Nowak E.R., Knight J.B., Ben-Naim E., Jaeger H.M., Nagel S.R., Density fluctuations in vibrated granular materials, *Physical Review E*, 57 (1998) 1971–1982.
- Nwaizu C., Zhang Q., Characterizing tortuous airflow paths in a grain bulk by using smoke visualization, *Canadian Biosystems Engineering*, 57 (2015) 3.13–13.22.
- Pisani L., Simple expression for the tortuosity of porous media, *Transport in Porous Media*, 88 (2011) 193–203.
- Rosato A.D., Blackmore D.L., Zhang N., Lan Y., A perspective on vibration-induced size segregation of granular materials, *Chemical Engineering Science*, 57 (2002) 265–275.
- Sobieski W., Zhang Q., Liu C., Predicting tortuosity for airflow through porous beds consisting of randomly packed spherical particles, *Transport in Porous Media*, 93 (2012) 431–451.
- Thompson K.E., Pore-scale modeling of fluid transport in disordered fibrous materials, *AIChE Journal*, 48 (2002) 1369–1389.
- Thompson K.E., Fogler H.S., Modeling flow in disordered packed beds from pore-scale fluid mechanics, *AIChE Journal*, 43 (1997) 1377–1389.
- Xiao Z.F., Yang D.Y., Yuan Y.J., Yang B.B., Liu X.D., Fractal pore network simulation on the drying of porous media, *Drying Technology*, 26 (2008) 651–665.
- Yiotis A.G., Tsimpanogiannis I.N., Stubos A.K., Fractal characteristics and scaling of the drying front in porous media: A pore network study, *Drying Technology*, 28 (2010) 981–990.
- Yue R., Zhang Q., Modeling airflow path through grain bulks using the discrete element method, Annual Meeting of Canadian Society for Bioengineering (CSBE), Canadian Society for Bioengineering, Saskatoon, Saskatchewan, Canada, Paper No. CSBE13-031 (2013).

Author's short biography



Rong Yue

Rong Yue is a PhD student in the Department of Biosystems Engineering, University of Manitoba, Canada. She received her M.S. and B.S. degrees from Northwest A&F University in China. Her current research focuses on modeling airflow through porous beds using the discrete element method and pore-scale models. She presented several conference papers on airflow paths through grain bulks and resistance to airflow in grain bulks.



Qiang Zhang

Dr. Qiang Zhang is a Professor in the Department of Biosystems Engineering, University of Manitoba, Canada, and a Registered Professional Engineer (P.Eng.) in the Province of Manitoba. He received his Ph.D. and M.S. degrees in Agricultural Engineering from Pennsylvania State University and B.S. degree in Mechanical Engineering from Hefei University of Technology, China. Dr. Zhang's research interests include constitutive behavior of granular materials, loads in bulk solids storage structures, and finite and discrete element modeling of bulk solids systems.

Visible Light Photocatalytic Bacterial Inactivation on Titanium Dioxide Coatings[†]

Vignesh Nandakumar¹, Zhao Han¹, Zachary Fritz²,
Vijay Krishna⁴, Ben Koopman³ and Brij Moudgil^{1*}

¹ Department of Materials Science and Engineering, University of Florida, USA

² Department of Chemical Engineering, University of Florida, USA

³ Department of Environmental Engineering, University of Florida, USA

⁴ Department of Biomedical Engineering, Cleveland Clinic, USA

Abstract

The increasing number of touch surface mediated infections has steered research to look for alternative strategies that can prevent infection transmission via pathogen inactivation on surfaces. Anatase, a crystalline form of titanium dioxide, shows strong UV induced photocatalytic properties. However, nanoparticles of anatase have been found to inactivate organic contaminants in the visible spectrum. Degradation of mordant orange and inactivation of *S. aureus* was evaluated on anatase surfaces under visible light band pass filters across the visible light region. Inactivation shows a strong co-relation to the absorption spectrum of the dye/microbe on the surface of the anatase coating. The phenomenon is similar to dye sensitized solar cells and was not found to exist in coatings with a higher bandgap such as amorphous silica. Photocatalytic nano-crystalline anatase coatings hold potential as a visible light active disinfectant to inactivate microbes on touch surfaces over long periods of time.

Keywords: TiO₂, visible light photocatalysis, antibacterial coatings

1. Introduction

Decontamination of organic and biological pollutants has gained significant attention owing to the increase in the number of infectious diseases. The increase in the number of hospital acquired infections in the last decade has led to significant research in developing alternate strategies for microbial inactivation and prevention of the transfer of such pathogens.

Hospital acquired infections or nosocomial infections are defined as infections that emanate from a stay in medical facilities and are caused by strains of microbes that have gained resistance to several bactericidal agents (Lobdell et al., 2012). These infections are extremely difficult to treat and have dramatically increased direct costs ranging from \$28 billion to \$45 billion in the United States of America (Scott II, 2009). The number of deaths caused by Methicillin Resistant *Staphylococcus aureus* (MRSA) account to 99,000 annually in the United States

alone (Klein et al., 2007). The transfer of such pathogens causing nosocomial infections is primarily touch surface mediated (Otter et al., 2013; Weber et al., 2013). Thus there is a clear need for inactivation of microbes on these surfaces to reduce the number of nosocomial infections.

Photocatalytic coatings have shown tremendous potential for inactivating organic contaminants and bacteria (Erkan et al., 2006; Lilja et al., 2012; Wei et al., 2014). The principle of photocatalysis for microbial inactivation has been discussed in many reviews and primarily involves the generation of reactive oxygen species (ROS) including hydroxyl free radicals and superoxide free radicals (Fujishima et al., 2008; Henderson, 2011; Linsebigler et al., 1995). Titanium dioxide is one such heterogeneous photocatalyst that is an extremely efficient generator of ROS in the presence of UV light (Ishibashi et al., 2000; Konaka et al., 1999). Inactivation of various bacteria, fungi and oxidative stresses on mammalian cells has been shown due to the ROS generated on UV photo-excited TiO₂ surfaces (Chen et al., 2009; Sunada et al., 2003; Tucci et al., 2013). In addition, complete degradation of organics on TiO₂ surfaces ensures that there is no residue on the surface thereby reducing ‘masking effects’ which often reduce the efficacy of active coatings. Although TiO₂ surfaces show very high potential for photocatalysis, they have only been used for surfaces that can receive a

[†] Received 22 July 2015; Accepted 12 May 2016
J-STAGE Advance Publication online 9 July 2016

^{1,2,3} Gainesville, Florida 32611, USA

⁴ Cleveland, Ohio 44195, USA

* Corresponding author: Brij Moudgil;

E-mail: bmoudgil@perc.ufl.edu

TEL: +1-253-846-1194 FAX: +1-352-846-1196

significant amount of UV light. Anatase, which is a crystalline form of TiO_2 , has very good photocatalytic properties but absorbs only in the near UV and UV region and has been largely ignored for use in indoor applications. This has led to extensive research into the area of visible light activated photocatalysis on modified titanium dioxide surfaces (Mitoraj et al., 2007; Yu et al., 2003). Doping of TiO_2 with nitrogen and carbon has been shown to reduce the bandgap and thus enhance visible light photocatalysis. Asahi and co-workers have modified titanium dioxide with nitrogen doping to show significant increase in the photocatalytic activity under visible light (Asahi et al., 2001). Shen and group have also shown visible light photocatalysis on anatase surfaces when doped with carbon (Shen et al., 2006). The evaluation of the antibacterial performance of unmodified titanium dioxide in the presence of visible light however has largely been ignored primarily owing to a very small contribution of visible light in anatase induced photocatalysis.

However TiO_2 -based dye sensitized solar cell applications were based on the premise that light-absorbing organic molecules can insert electrons into the TiO_2 conduction band, generate free electrons on TiO_2 and activate photocatalysis (Bach et al., 1998; Krasovec et al., 2009; Oregan and Gratzel, 1991; Yu et al., 2003). We extended this concept using contaminant dyes and microbes to sensitize an otherwise inactive anatase photocatalyst to become active in the visible spectrum (Krishna et al., 2015). This property of anatase can be exploited for coating indoor surfaces which over a long period of time can lead to significant inactivation of microbes and thus reduction in the number of touch surface mediated infections.

2. Experimental section

2.1 Chemical reagents

Most Chemicals were purchased from Fisher Scientific. Mordant Orange was acquired from Sigma-Aldrich Inc. (St. Louis, MO) and anatase and silica were obtained from MKnano (M K Impex Corp. Mississauga, TO).

2.2 Microbial culture and enumeration

Staphylococcus aureus (ATCC 25923) was cultured in Tryptic Soy Agar (Becton, Dickinson and Company, Sparks, MD) and grown for 48 hours in the incubator at 37 °C. An individual colony from the streak plate was recovered and inoculated in Tryptic Soy broth (TSB) and grown to an OD_{600} of 0.6 at 37 °C in a shaker incubator at 150 RPM. The culture was washed thrice and harvested by centrifugation at 4800 RCF and 4 °C. The final concentration for use on the tiles was set to 2×10^6 cells per

ml. Enumeration of bacteria were performed using the pour plate method. 0.1 ml of bacterial suspension was transferred to a petri dish and covered with melted TSA and mixed well. After the agar solidifies at room temperature the plates were incubated at 37 °C for 24 hours.

2.3 Coating preparation

Coatings were made of anatase (7 nm crystallite size) and silica (15 nm crystallite size). The coatings were prepared in accordance with a protocol suggested by Bai et al (Bai et al., 2012). 10 mg of anatase was added to 10 ml of water to have a final concentration of 0.1 wt% and sonicated (Misonix Sonicator 3000, Farmingdale, NY) for 30 minutes at 90 W with NaOH as the electrostatic stabilizer at a pH of around 9.5. The dispersions were then applied as uniform coatings on ceramic tiles of dimensions 2.5 cm \times 2.5 cm, with a total volume of 0.4 ml of coating spread over the surface of the tile. A second coat of anatase was applied after the tiles were dried overnight to ensure complete coverage on the surface of the tile. Coatings of silica were prepared the same way and all coatings were stored in a dark cabinet until use.

2.4 Estimation of bacterial inactivation

Tiles coated with anatase and silica were inoculated with 0.1 ml of bacteria at a starting concentration of $1-2 \times 10^6$ cells per ml. The tiles were then exposed to a light intensity of 1.8 W/m² under fluorescent lamps (General Electric model T8 Ultramax F28T8-SPX41) for 18 h at 23 °C and 40 % RH. A dark control with anatase double coat was also included for the experiments. Microbial recovery from tiles was performed by the sonication of the inoculated tiles at 90 W in 20 ml DI water for 1 minute. 0.1 ml of the bacteria suspension after sonication was enumerated as mentioned before. A zero hour reading taken immediately after initial bacteria inoculation on selected tiles was acquired to estimate the number of bacterial cells that can be recovered from the tile. The tiles were then exposed to visible light under various filters to assess the performance of the coatings at the limits of the absorption spectrum of the contaminant. The recovered microbes were then cultivated in TSA and enumerated using a colony counter. Effect of sonication on bacterial viability was also assessed to eliminate possible inactivation due to sonication

$$\% \text{ Bacterial Inactivation} = \frac{C_0 - C_t}{C_t} * 100 \quad (1)$$

Where C_0 is the concentration of bacteria in CFU at time $t = 0$ and C_t is the concentration of the bacteria at an exposure of time ' t '.

2.5 Estimation of dye degradation

Tiles coated with anatase were inoculated with 0.002 ml of mordant orange at a concentration of 100 ppm. The tiles were then exposed to a light intensity of about $\sim 1.8 \text{ W/m}^2$ for 24, 48, 72 and 96 h at 23 °C and 40 % RH. Reflectance of coated and uncoated tiles were measured with a spectrometer. Absorbance was calculated as the negative \log_{10} of reflectance expressed as a fraction. Dye degradation was calculated by comparing the reflectance measurements of coated tiles at 0 hour exposure to the groups exposed to light.

$$\% \text{ dye degradation} = \frac{A_0 - A_t}{A_t} * 100 \quad (2)$$

Where A_0 is the absorption of dye at time $t = 0$ and A_t is the absorption of the dye at an exposure of time ' t '.

2.6 Effect of optical cut-off filters on the inactivation experiments

Optical filters with cut-off wavelengths were chosen in accordance with the absorption spectrum of the dye and the bacteria. Anatase tiles inoculated with bacteria or dye and were placed under 400, 495 and 550 nm filters. Bacterial and dye degradation was calculated for an exposure of 18 and 24 hours respectively at 23 °C and 40 % RH. The results were then plotted comparing the photocatalytic performance under different cut off filters.

3. Results and discussion

3.1 Absorbance spectrum of mordant orange, anatase and *S. aureus*

The absorbance spectrum of mordant orange, *S. aureus* and anatase on a ceramic tile substrate was acquired using the spectrometer. **Fig. 1** illustrates an absorption cut off for anatase at 380 nm. The absorption of staphylococcus aureus and mordant orange extends well into the visible spectrum with a cut off at around 550 nm.

The spectrum indicates that any absorption in the visible region is accounted for by the dye or the bacterium on the surface of anatase.

3.2 Photocatalytic inactivation of *Staphylococcus aureus*

Photocatalytic inactivation of *S. aureus* was estimated on coatings of anatase and silica. Anatase coating, kept in the dark, was included as a negative control. Test coatings were exposed to a light intensity of about 2 W/m^2 , 32 °C, 40 % RH and an exposure time of 18 h. The spectral dis-

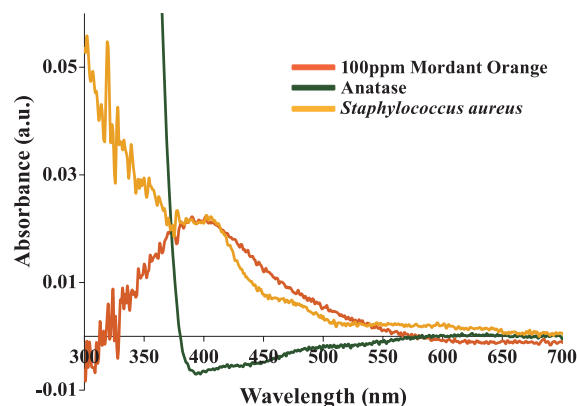


Fig. 1 Absorption spectrum of anatase (green), *S. aureus* (yellow) and Mordant Orange (Orange) across UV and visible spectrum obtained from reflectance measurements on ceramic tiles.

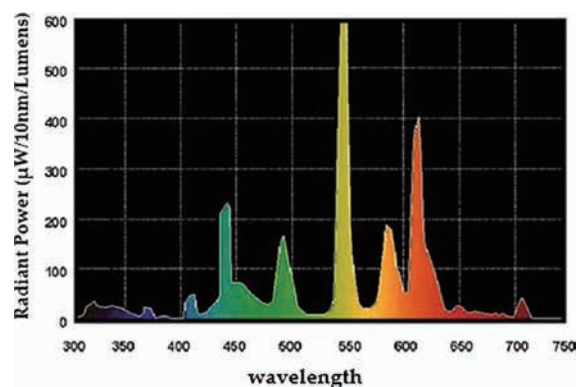


Fig. 2 Spectral distribution of the fluorescent lamp used for bacterial inactivation on tile surfaces. Image courtesy of General Electric Company (General Electric, 2016). Copyright: (2016) G.E.

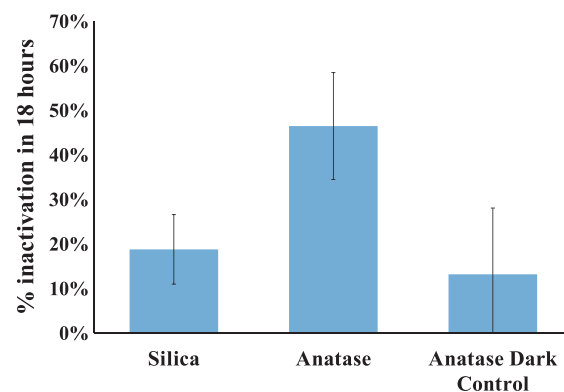


Fig. 3 Inactivation of *S. aureus* on anatase, silica and in the dark over 18 hours at 23 °C and 40 % RH.

tribution of the fluorescent lamp used for the experiment is shown in **Fig. 2** (GeneralElectric). A 400 nm filter was used for all visible light photocatalysis to eliminate the small amount of UV present in the luminescent bulb spectra. **Fig. 3** shows about 45 % photocatalytic inactivation of *S. aureus* on unmodified anatase surfaces. The in-

activation on silica and dark control are significantly lower and are attributed to desiccation of microbes over the period of 18 h. The experiment indicates a synergy between the bacteria and the anatase surface introducing photocatalysis on anatase surfaces.

The lower inactivation on the silica and dark surfaces also eliminates the contribution of photolysis or oxidative degradation of dye under experimental conditions.

3.3 Contribution of bacteria and dye (contaminant) to the process of visible light photocatalysis

The contribution of contaminants to the process of visible light induced photocatalysis was studied by measuring the inactivation of *S. aureus* as the model bacterium and 5-(4-Nitrophenylazo) salicylic acid, (mordant orange) as a model dye. The kinetics of degradation for mordant orange on unmodified anatase surface were studied as a model for the bacteria. The dye was placed under long pass filters with exposure for 24, 48, 72 and 96 hours. The absorption spectrum of mordant orange exhibits a peak at 410 nm and gradually decreases with a cut off at 550 nm as shown in Fig. 1. Long pass filters cut off wavelengths at 400 nm, 495 nm and 550 nm filters were chosen to ensure non-interference of UV light (400 nm filter), reduced absorbance of dye (495 nm) and cut off of dye absorption (550 nm).

Dye degradation data was analyzed by comparing the reflectance data of dye at the start of the experiment to the tiles at different time points of the experiment. Results in Fig. 4 illustrate a reduction in photocatalytic activity of anatase surfaces with increasing wavelength cut off filters. A sharp decrease in the photocatalytic activity at the 495 filter is seen due to significantly decreased participation of the dye in the process. The photocatalytic degradation under a 550 nm is comparable to the dark control

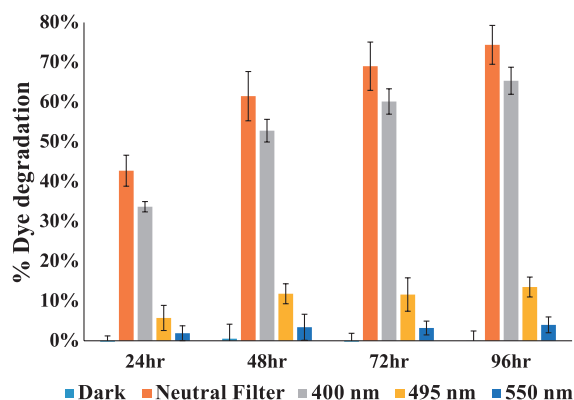


Fig. 4 Degradation of dye on anatase coatings over a period of 24 h, 48 h, 72 h and 96 h under various optical filters. The absorption of the dye clearly sensitizes the visible light photocatalysis of anatase.

indicating no participation of dye in the process. The reduction in light intensities under various filters were recorded and show a maximum reduction of 5 % at the 495 nm cut off and 16 % at the 550 nm cutoff wavelengths. Subsequently, inactivation of *S. aureus* on anatase surfaces was carried out under similar spectral conditions to validate the mechanism of photocatalytic inactivation with biological contaminants. The results plotted in Fig. 5 show that *S. aureus* inactivation under visible light gradually decreased with increasing cut off limits up to 550 nm in accordance with dye degradation results. It is also noted from the absorption spectrum in Fig. 1 that the only component absorbing in the visible spectrum is the bacteria. Additionally, the trend of bacterial inactivation on anatase in visible light follows the trend in absorption intensity of bacteria. This indicates the antibacterial potential of unmodified anatase with visible light.

From the data obtained we hypothesize that the mechanism of microbial inactivation on unmodified anatase surfaces is similar to that of TiO_2 dye sensitized solar cells (DSSC). In TiO_2 based DSSC's irradiation with visible light leads to (i) excitation of the dye molecule, (ii) subsequent oxidation of dye molecule, and (iii) transfer of electrons from the dye molecule to the TiO_2 conduction band. The electrons then diffuse through the circuit to the counter electrode. The electrolyte is reduced from I_3^- to I^- which diffuses and combines with the oxidized dye molecule to complete the circuit. Similarly in a contaminant activated photocatalyst, the dye or microbe acts as the electron source when irradiated with visible light. Fig. 6 is a schematic of the hypothesized mechanism of action on unmodified anatase surfaces when in contact with or-

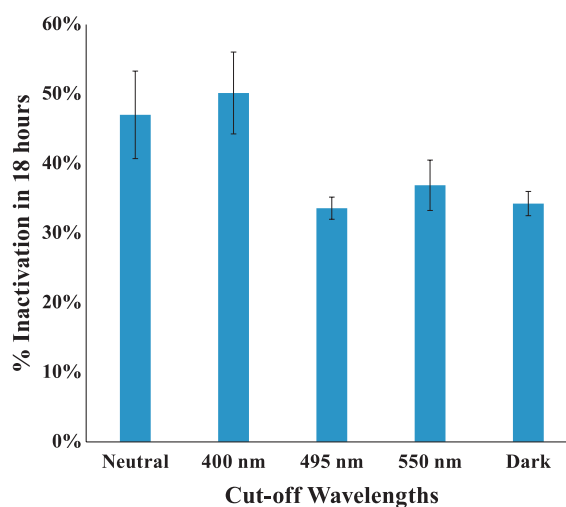


Fig. 5 Inactivation of *S. aureus* on anatase under different optical filters over 18 hours at 23 °C and 40 % RH. The inactivation of bacteria decreases with the increase in cut off wavelengths of the long pass filters from 400 to 550 nm.

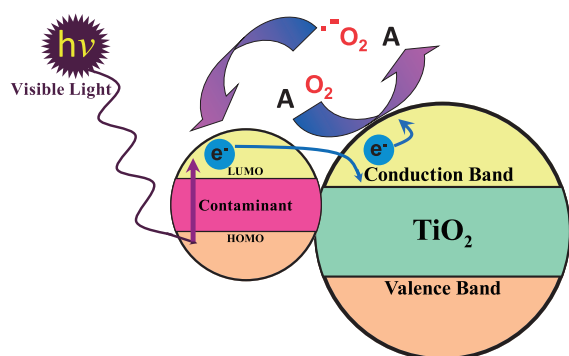


Fig. 6 Schematic for possible mechanism of inactivation on unmodified TiO₂ surfaces (Krishna et al., 2016).

ganic contaminants such as microbes (Krishna et al., 2015). Electrons inserted in the conduction band of TiO₂ catalyze the small molecules like oxygen and water into super oxide free radicals. These reactive radicals in turn oxidize most organic molecules to CO₂ and water. The generation of free radicals in the photocatalyst with availability of microbial contaminants leads to their continued inactivation.

4. Conclusions

The present study illustrates the potential of unmodified nano-crystalline anatase as a photocatalytic disinfectant in visible light when in contact with microbes. While the kinetics of inactivation of bacteria on such unmodified surfaces is not as fast as in the case of conventional disinfectants, photocatalytic coatings can last much longer and have a very high cumulative contribution towards surface disinfection. Masking by inactivated microbes often hampers the performance of active coatings by forming a barrier between the active species and the microbes. However, the complete degradation of microbes (organic contaminants) on anatase surfaces ensures no ‘masking effect’ unlike on other potent antimicrobial surfaces like copper and silver. Thus, anatase surfaces in comparison can function for long inactivation periods. We would also like to further indicate that these coatings can be applied to surfaces and complemented with additional disinfection treatments to have increased efficacies of surface disinfection. A combination of disinfection approaches can be used for surfaces that do not receive large amounts of UV light and kill pathogens that are transferred through touch mediation.

Acknowledgements

The authors would like to acknowledge the National Science Foundation Grant No. 1127830 for their financial support and the industry members of the Centre for Particulate and Surfactant Systems (CPaSS) for their help

and contribution to this project. Experimental work was carried out the University of Florida Water Reclamation and Reuse laboratory and at the Particle Science and Technology Laboratory. We would like to thank Dr. Wei Bai for the SEM micrographs.

Nomenclatures

CFU/ml	Colony forming units per ml
A_0	Absorbance at time 0
A_t	Absorbance at time t
C_0	Concentration at time 0 (CFU/ml)
C_t	Concentration at time t (CFU/ml)
RCF	Relative Centrifugal Force
RH	Relative Humidity (%)
RPM	Rotations per minute
W/m ²	Watt/ Square meter

References

- Asahi R., Morikawa T., Ohwaki T., Aoki K., Taga Y., Visible-light photocatalysis in nitrogen-doped titanium oxides, *Science*, 293 (2001) 269–271.
- Bach U., Lupo D., Comte P., Moser J.E., Weissortel F., Salbeck J., Spreitzer H., Gratzel M., Solid-state dye-sensitized mesoporous TiO₂ solar cells with high photon-to-electron conversion efficiencies, *Nature*, 395 (1998) 583–585.
- Bai W., Krishna V., Wang J., Moudgil B., Koopman B., Enhancement of nano titanium dioxide photocatalysis in transparent coatings by polyhydroxy fullerene, *Appl. Catal. B-Environ.*, 125 (2012) 128–135.
- Chen F.N., Yang X.D., Wu Q., Antifungal capability of TiO₂ coated film on moist wood, *Build. Environ.*, 44 (2009) 1088–1093.
- Erkan A., Bakir U., Karakas G., Photocatalytic microbial inactivation over Pd doped SnO₂ and TiO₂ thin films, *J. Photoch. Photobio. A*, 184 (2006) 313–321.
- Fujishima A., Zhang X.T., Tryk D.A., TiO₂ photocatalysis and related surface phenomena, *Surf. Sci. Rep.*, 63 (2008) 515–582.
- GeneralElectric, Spectral Power Distribution Curves: Tri-Phosphor Fluorescent Colors, SPX41. *Commercial Products and Solutions*. http://www.gelighting.com/LightingWeb/na/resources/tools/lamp-and-ballast/pop_curves.jsp?15, accessed 06.06.2016.
- Henderson M.A., A surface science perspective on TiO₂ photocatalysis, *Surf. Sci. Rep.*, 66 (2011) 185–297.
- Ishibashi K., Fujishima A., Watanabe T., Hashimoto K., Quantum yields of active oxidative species formed on TiO₂ photocatalyst, *J. Photoch. Photobio. A*, 134 (2000) 139–142.
- Klein E., Smith D.L., Laxminarayan R., Hospitalizations and deaths caused by methicillin-resistant *Staphylococcus aureus*, United States, 1999–2005, *Emerg. Infect. Dis.*, 13 (2007) 1840–1846.
- Konaka R., Kasahara E., Dunlap W.C., Yamamoto Y., Chien

- K.C., Inoue M., Irradiation of titanium dioxide generates both singlet oxygen and superoxide anion, *Free Radical Bio. Med.*, 27 (1999) 294–300.
- Krasovec U.O., Berginc M., Hocevar M., Topic M., Unique TiO₂ paste for high efficiency dye-sensitized solar cells, *Sol. Energ. Mat. Sol. C*, 93 (2009) 379–381.
- Krishna V., Bai W., Han Z., Thakur A., Koopman B., Moudgil B., Contaminant-Activated Visible Light Photocatalysis for Reducing Healthcare-Acquired Infections, In review, *Nature* (2016).
- Lilja M., Forsgren J., Welch K., Astrand M., Engqvist H., Stromme M., Photocatalytic and antimicrobial properties of surgical implant coatings of titanium dioxide deposited through cathodic arc evaporation, *Biotechnol. Lett.*, 34 (2012) 2299–2305.
- Linsebigler A.L., Lu G.Q., Yates J.T., Photocatalysis on TiO₂ Surfaces—Principles, Mechanisms, and Selected Results, *Chem. Rev.*, 95 (1995) 735–758.
- Lobdell K.W., Stamou S., Sanchez J.A., Hospital-Acquired Infections, *Surg. Clin. N. Am.*, 92 (2012) 65–77.
- Mitoraj D., Janczyk A., Strus M., Kisch H., Stochel G., Heczko P.B., Macyk W., Visible light inactivation of bacteria and fungi by modified titanium dioxide, *Photoch. Photobio. Sci.*, 6 (2007) 642–648.
- Oregan B., Gratzel M., A Low-Cost, High-Efficiency Solar-Cell Based on Dye-Sensitized Colloidal TiO₂ Films, *Nature*, 353 (1991) 737–740.
- Otter J.A., Yezli S., Perl T.M., Barbut F., French G.L., The role of ‘no-touch’ automated room disinfection systems in infection prevention and control, *J. Hosp. Infect.*, 83 (2013) 1–13.
- Scott II R.D., The Direct medical costs of healthcare-associated infections in U.S. hospitals and the benefits of prevention, Centers for Disease Control and Prevention (2009). <http://stacks.cdc.gov/view/cdc/11550/>, accessed 06.06.2016.
- Shen M., Wu Z.Y., Huang H., Du Y.K., Zou Z.G., Yang P., Carbon-doped anatase TiO₂ obtained from TiC for photocatalysis under visible light irradiation, *Mater. Lett.*, 60 (2006) 693–697.
- Sunada K., Watanabe T., Hashimoto K., Studies on photokilling of bacteria on TiO₂ thin film, *J. Photoch. Photobio. A*, 156 (2003) 227–233.
- Tucci P., Porta G., Agostini M., Dinsdale D., Iavicoli I., Cain K., Finazzi-Agro A., Melino G., Willis A., Metabolic effects of TiO₂ nanoparticles, a common component of sunscreens and cosmetics, on human keratinocytes, *Cell Death Dis.*, 4 (2013).
- Weber D.J., Anderson D., Rutala W.A., The role of the surface environment in healthcare-associated infections, *Curr. Opin. Infect. Dis.*, 26 (2013) 338–344.
- Wei X.J., Yang Z.D., Tay S.L., Gao W., Photocatalytic TiO₂ nanoparticles enhanced polymer antimicrobial coating, *Appl. Surf. Sci.*, 290 (2014) 274–279.
- Yu J.C., Xie Y.D., Tang H.Y., Zhang L.Z., Chan H.C., Zhao J.C., Visible light-assisted bactericidal effect of metalphthalocyanine-sensitized titanium dioxide films, *J. Photoch. Photobio. A*, 156 (2003) 235–241.

Author's short biography



Vignesh Nandakumar

Vignesh Nandakumar is a third year graduate student in the Materials Science and Engineering at the University of Florida. His Scientific activities and research interests focus on understanding cell materials interactions, and designing systems that can manipulate surface properties of cells to remove, kill or enhance adhesion onto surfaces. Vignesh received his Bachelors from SASTRA University, Tanjore, India and his M.S. in Material Science and Engineering from the University of Florida, Gainesville, Florida.



Zhao Han

Zhao Han is an Analytical Chemist/Material Scientist of Western Digital (WD) located in San Jose, California. Zhao is a graduate of University of Florida, where he received a M.S. in Materials Science and Engineering (MSE) 2013. He also received his B.S. in MSE from Beijing University of Technology 2011 with expertise in Metal Processing. During his graduate study, Zhao researched on visible light activated TiO₂ antimicrobial coating and developed the mechanism of contaminant activation by using optical cut-off filters and organic dye. After graduation, Zhao started his professional career at WD and focuses on hard disk drive development.

Author's short biography



Zachary Fritz

Zachary Fritz is a research scientist at a food-testing biotech company and will be pursuing graduate studies in Biomedical Engineering at Rutgers University (New Brunswick, New Jersey). His research interests include immunological engineering and tissue engineering. He received his B.S.'s in Chemical Engineering and Microbiology from the University of Florida (Gainesville, Florida).



Vijay Krishna

Vijay Krishna, Ph.D., was a Postdoctoral Fellow with the Particles Engineering Research Center at the University of Florida. Dr. Krishna has been awarded 6 patents and is primary inventor on 12 current patent applications. He has authored 16 journal publications and presented at more than 30 technical conferences. Dr. Krishna earned a Ph.D. in Materials Science and Engineering at the University of Florida. He is currently a Project Scientist at the Lerner Research Institute, Cleveland Clinic. His research interests include carbon nanostructures, bio-nano interactions, surface and colloid science.



Ben Koopman

Ben L. Koopman, Ph.D., is a Professor and Undergraduate Coordinator in the Department of Environmental Engineering Sciences at the University of Florida. He earned a B.S. in Civil Engineering from Oregon State University before pursuing a Ph.D. in the same field at the University of California, Berkeley. His research interests include removal of microorganisms by surface-modified filter media and bio films, photocatalytic antimicrobial coatings, water treatment, one-dimensional modelling of activated sludge secondary settling tanks, and biological nutrient removal.



Brij M. Moudgil

Dr. Brij M. Moudgil is a Distinguished Professor of Materials Science and Engineering at the University of Florida. His current research interests are in particulate materials based systems for enhanced performance in bioimaging, nanomedicine, photocatalytic degradation of hazardous microbes, polymer and surfactant adsorption, dispersion and aggregation of fine particles and nanotoxicity. Dr. Moudgil received his B.E from the Indian Institute of Science, Bangalore, India and his M.S and Eng.Sc.D degrees from Columbia University, New York. He has published more than 400 technical papers and has been awarded 14 patents. He is a member of the U.S National Academy of Engineering.

Eddy Current Separation of Nonferrous Metals Using a Variable-Frequency Electromagnet[†]

Nakul Dholu, James R. Nagel, Dave Cohrs and Raj K. Rajamani*

[†] Department of Metallurgical Engineering, University of Utah, USA

Abstract

We present a novel technique for sorting nonferrous metal scrap by using eddy current separation. However, rather than vary the magnetic field with a spinning rotary drum, our system utilizes a fixed electromagnet excited by an alternating electric current. The technique requires no moving parts other than a feeding mechanism and has the capacity to operate at excitation frequencies up to 50 kHz and beyond. Sorting results are demonstrated using various combinations of metal spheres, which resulted in nearly perfect performance in terms of grade and recovery. We also demonstrate sorting of aluminum alloys from other aluminum alloys, with consistent grade and recovery between 85–95 %.

Keywords: eddy-current separator, electromagnet, nonferrous, metals, alloys

1. Introduction

Metal recycling is a multibillion dollar industry with tremendous economic opportunities and positive environmental impact. In 2015 alone, global aluminum production from mined ore reached well over 58 million metric tons, selling at an average price of \$0.88 per pound (USGS, 2016). Global copper production likewise reached over 18 million tons with an average price of \$2.77 per pound. Nearly all of this material eventually ends up in municipal waste streams wherein local scrap recyclers generate significant wealth by collecting and selling the valuable metals. In 2013, for example, 55 % of all aluminum produced in the United States came from recycled scrap (USGS, 2015). Copper, in comparison, was produced from 33 % recycled material. In principle, these values could reach much higher if not for the great difficulty in sorting various materials into more pure streams. Consequently, there is a strong economic pressure to find new ways to efficiently sort municipal waste streams into their basic, elemental components.

To meet this challenge, many industrial machines and processes have been engineered specifically to sort valuable materials from a mixed stream of waste (Gaustad et al., 2012). For example, separation of ferrous metals, such as iron and steel, is readily accomplished through large,

permanent magnets mounted into specialized conveyors and collectors (Weiss, 1985). This typically leaves behind a stream of nonferrous metals like copper, aluminum and brass, mixed with other nonmetallic fluff like rubber, textiles, and plastic. Recovery of nonferrous metals then typically occurs through the use of standard eddy current separators, which consist of a spinning drum of permanent magnets placed under a moving conveyor belt (Schloemann, 1975; Lungu and Rem, 2003; Lungu, 2005). As metallic particles pass over the magnets, electrical eddy currents are induced by the alternating magnetic field, which in turn produces a net magnetic force that alters their trajectories.

Once the nonferrous metals have been separated from the fluff, it is desirable to further separate the base metals into purified streams. For example, aluminum and copper are two common metals that might exist in relative mass concentrations of 90 % Al to 10 % Cu. Since copper is a distinctly red metal that contrasts against the gray of aluminum, one common sorting method might utilize computerized optical sorting via basic color recognition (Kutilla et al., 2005). Alternatively, one could exploit the fact that copper is nearly three times more dense than aluminum, thereby utilizing the popular technique of dense medium separation (Weiss, 1985). In many developing countries, the cost of human labor is so low that metals are simply sorted directly by hand (Spencer, 2005). All of these methods have various costs, capabilities, and throughputs associated with them, and individual recycling firms must generally weigh the pros and cons within their own economic niche.

In this paper, we will introduce a new method for sepa-

[†] Received 3 May 2016; Accepted 14 June 2016
J-STAGE Advance Publication online 9 July 2016

[†] Salt Lake City, UT 84112, USA

* Corresponding author: Raj k. Rajamani
E-mail: raj.rajamani@utah.edu
TEL: +1-801-581-3107

rating nonferrous metals from other nonferrous metals, including nonferrous alloys. Dubbed *electrodynamic sorting* (EDX), our system utilizes a time-varying magnetic field generated by an alternating electric current within a fixed electromagnet. The principle was originally pioneered by Saveliev to extract gold particles from rocky ore (Saveliev, 1998) but has since remained relatively unnoticed and unrefined. The process is very similar to traditional eddy current separators mentioned earlier, but without the need for mechanically intense spinning of any heavy, rotary magnets. Another distinct advantage to our approach is the ability to tune the frequency of excitation to as high as 50 kHz and beyond. This allows for much more active recovery of smaller particles in the realm of 1.0 cm and below, which can be especially difficult for rotary-based separators and human separators to work with. Our system also has the distinct advantage of being completely dry, thus avoiding the wet slurry contamination commonly used in many flotation-based separators.

Beginning in Section 2, we discuss the basic physical mechanism of eddy current separation as a derived principle of Maxwell's equations. Section 3 then follows with a high-level description of the EDX system, including a mechanical diagram and electrical circuit model. Sorting data is then presented in Section 4, wherein metal spheres of various sizes and conductivities are separated by our system. Section 5 finally concludes with a discussion of further applications and research goals for EDX.

2. Theory of eddy current separation

Eddy current separation is a highly mature technology with many practical applications in the recycling industry. The basic principle is derived from the fact that when a permanent magnet passes over a conductive metal object, electric charges within the metal tend to experience a net magnetic force (Rem et al., 1997). This causes the charges to flow around in distinct swirling patterns, commonly referred to as eddy currents or Foucault currents. If the magnetic field is strong enough and the relative motion quick enough, this force can significantly accelerate the entire metal particle. Thus, a common design theme with modern eddy current separators is a large, rotary drum implanted with a series of permanent magnets. When the drum is mechanically rotated at a very high velocity, nearby metal particles tend to deflect along distinct kinematic trajectories away from other nonmetallic fluff. A physical barrier is then placed somewhere between the two trajectories, thus separating material into two distinct streams.

For the case of electrodynamic sorting, we completely do away with the spinning permanent magnets, replacing them instead with a single fixed electromagnet excited by

an alternating electric current. This significantly changes the mathematical nature of the physics involved as now the relative velocity between the magnet and particle is no longer a significant factor. We may therefore begin with Faraday's law of electromagnetic induction, which states that a time-varying magnetic field \mathbf{B} will give rise to an electric field \mathbf{E} in accordance with (Jackson, 1999)

$$\nabla \times \mathbf{E} = -\frac{\partial \mathbf{B}}{\partial t} . \quad (1)$$

If we next assume sinusoidal steady-state operation at angular frequency ω , all time derivatives can be replaced with $\partial/\partial t = -j\omega$. The phasor form of Faraday's law is therefore written as

$$\nabla \times \mathbf{E} = j\omega \mathbf{B} . \quad (2)$$

Now let us consider a metal particle placed somewhere in the magnetic field \mathbf{B} . Because of the induced electric field \mathbf{E} , electric charges within the metal are accelerated accordingly, thus giving rise to an eddy current density \mathbf{J} . The relation between \mathbf{E} and \mathbf{J} is then given by the point form of Ohm's law, written as

$$\mathbf{J} = \sigma \mathbf{E} , \quad (3)$$

where σ is the electrical conductivity of the metal. Changing magnetic fields therefore give rise to electric fields, which in turn give rise to eddy currents in metallic objects.

Next, we note that electrical currents also give rise to magnetic fields of their own in accordance with Ampere's law,

$$\nabla \times \mathbf{B}_e = \mu_0 \mathbf{J} , \quad (4)$$

where \mathbf{B}_e indicates the magnetic fields produced just by the eddy current density \mathbf{J} . This implies more changing magnetic fields that must be accounted for in Eqn. (1), which in turn cause changes in the resultant eddy current \mathbf{J} . Thus, a complete solution for \mathbf{J} , \mathbf{E} , and \mathbf{B} requires us to solve Eqns. (1)–(4) simultaneously. While such a process extends well beyond the scope of this article, we can at least note that once a solution for \mathbf{J} is finally obtained, it becomes possible to calculate the net Lorentz force \mathbf{F} acting on the metal particle. This is given by the magnetic force law,

$$\mathbf{F} = \iiint \mathbf{J} \times \mathbf{B} dV , \quad (5)$$

where the integral is carried out over the volume defined by the space within the particle. Thus, if the excitation field \mathbf{B} is strong enough and the frequency ω great enough, the net force \mathbf{F} will be great enough to significantly deflect arbitrarily large particles of metal.

3. Description of electrodynamic sorting

The basic configuration of our EDX system is depicted in **Fig. 1**. The core of the system is a wire-wound ferrite toroid, excited by an alternating electric current. A specialized gap is then cut out from the toroid and serves as the concentration point of time-varying magnetic fields. As particles enter the gap, eddy currents are induced in accordance with various factors, like conductivity, geometry, B -field variation, and frequency of excitation. In particular, particles with very high conductivity will tend to experience very strong forces, thus pushing them away from their natural kinematic trajectories. Dense particles, however, have greater inertia and will therefore resist being accelerated. Where exactly the particles land will therefore depend on a combination of both factors, which are fortunately varied enough to produce highly distinct trajectories among most materials of interest. Thus, a simple mechanical splitter is all that is required to finally separate materials into their corresponding bins.

Fig. 2 shows an electrical circuit diagram for the EDX drive electronics. A small-signal voltage V_s is produced by a standard signal generator, which determines the frequency and amplitude of the excitation signal. This signal is then fed to the high-power amplifier U_1 , which is needed in order to drive the core with enough current to saturate the magnet. For this particular system, we used the AE Techron model 7796, which is rated to deliver upwards of 5 kW of continuous power. In practice, however,

our system usually only requires about 350 W to operate.

At the output of the power amplifier, we employ a series RLC circuit to drive the core. Because the primary electromagnet is comprised of a wire-wound ferrite, it naturally manifests as a lumped inductance L with values typically ranging between 1–10 mH. In series with the inductor is an equivalent resistance R , representing the internal thermal loading of the magnet that occurs during operation. Typical values may reach as high as 20 Ω , but can vary strongly with the size of the magnet, the magnetic material, and the frequency of operation. However, this value is usually dwarfed by the reactive impedance of the inductor, which can easily reach many hundreds of Ohms when excited to several kilohertz. We therefore placed a lumped capacitance C in series with L , thus creating a resonant RLC circuit. When excited at the resonant frequency $f_0 = 1/(2\pi\sqrt{LC})$ the capacitive reactance perfectly negates the inductive reactance, thus leaving only the series resistance R to impede current.

Fig. 3 shows an isometric view of the magnetic core itself, which has been shaped into a square toroid. The dimensions are given by an outer radius of 440 mm, inner radius of 240 mm, and height of 30 mm. The gap is a specialized double-cut, which is used to funnel flux into a tight volume of space and serves as the feeding point for small metal particles. At the point of inner radius, the gap separation starts at 10 mm with a flare angle of 10°. The flare then extends radially outward for 30 mm before opening up to a widened flare of 40°.

Considering that the core must channel strong magnetic fields at high frequency, the specific choice of material is very important. In particular, electrical conductivity must be very low, or else eddy currents induced within the core, itself tend to result in heavy thermal dissipation. It is also important that the material be magnetically soft, meaning that hysteresis effects must be small as well. NiZn ferrite is well-known for satisfying both of these properties (Leary et al., 2012) and was therefore used to construct our EDX magnet.

Finally, the core must be wound with electrical wiring and excited by an alternating current. The exact number of turns in the windings is somewhat arbitrary, though many practical issues must be carefully weighed. In principle, if the drive current I is held constant, then a doubling of the number of turns N will subsequently double

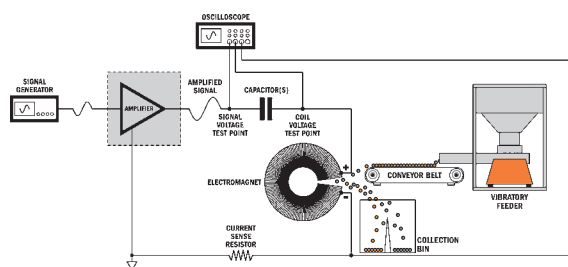


Fig. 1 Schematic diagram of the electrodynamic sorting system.

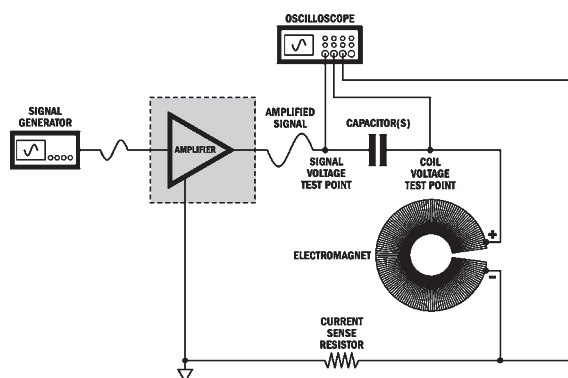


Fig. 2 Equivalent circuit model for EDX drive electronics.

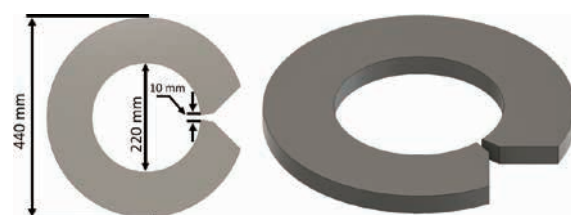


Fig. 3 Ferrite core geometry.

the magnetic field intensity B within the gap. However, this also increases the inductance of the coil by a factor of four, thus quadrupling the corresponding voltage at a given frequency. If this voltage gets too large, then the insulation around the wiring itself can potentially break down and halt the system. Likewise, we can reduce the value of N to maintain a reasonable voltage, but only by reducing the current density around the core. This causes B to fall accordingly, which can only be compensated for by increasing I . After careful trial-and-error, we eventually settled on a value of $N = 300$ turns, which was enough to saturate the magnet at a peak current of roughly $I = 4.5$ A.

4. Sort demo and results

In order to quantify our sorting data, it is first necessary to define the quality metrics for a given sorting process. We begin by considering two initial masses, m_0 and M_0 , of differing materials mixed together at the input of the sorter. At the output are two bins, labeled bin A and bin B. The goal of the sort process is for all of mass m_0 to collect in bin A and for all of mass M_0 to collect in bin B, with no errors either way. We therefore define m_A as the total mass from material m_0 that falls into bin A, with m_B as the total mass falling into bin B. Likewise, we can define M_A and M_B as the total masses from M_0 that fall into their respective bins.

Let us now define the *recovery* of bin A as the fraction of initial material that collects in its proper bin:

$$R_A = \frac{m_A}{m_0} \quad (6)$$

Likewise, the recovery of bin B is defined as

$$R_B = \frac{m_B}{M_0} \quad (7)$$

Next, we define the *grade* of bin A as the fraction of total mass in bin A comprised of its target material. This is written as

$$G_A = \frac{m_A}{m_A + M_A} \quad (8)$$

with the grade of bin B likewise following

$$G_B = \frac{m_B}{m_B + M_B} \quad (9)$$

Thus, in a perfectly ideal world, both R and G would approach 100 % for each bin.

Fig. 4 shows a photograph of our experimental test bed with the feeder, magnet, and sort bins all visible. The divider is fixed at a distance of 60 cm below the magnet but could be translated horizontally to an optimal position for

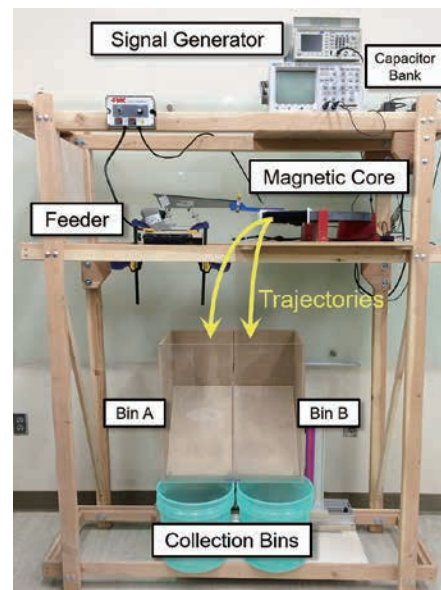


Fig. 4 Primary EDX components (power amplifier not shown).

Table 1 Electrical conductivity and mass density for various metals and alloys under consideration

Material	Conductivity [MS/m]	Density [g/cm ³]
Copper	58.5	9.0
Brass	15.9	8.5
Al-1100	34.4	2.7
Al-6061	24.6	2.7
Al-2024	17.3	2.8

each sort. To demonstrate the EDX system, we mixed together various batches of metal spheres with contrasting material properties and then sorted them accordingly. In all cases, the number of spheres was at least 100 for each material being sorted.

Table 1 lists the materials under consideration for this study as well as their relevant physical properties. In particular, we were interested in two distinct groups of trials. The first case focused solely on the dissimilar metals Al/Cu, Cu/Brass, and Al/Brass, using uniform spheres with 6.0 mm diameter. In this case, the magnet was excited to a frequency of 6.5 kHz and driven to a peak current of 4.5 A. The second case then focused on sorting metal alloys, including Al-1100, Al-6061, and Al-2024. In this case, the sphere diameters were slightly larger at 12.5 mm and the frequency was lowered down to 1.9 kHz.

Table 2 shows a summary of our sorting trials. For the case of dissimilar metals, the disparity in trajectories was somewhat dramatic and highly consistent. For example, upon reaching the separator, the disparity between aluminum spheres and copper spheres was well over 6 cm (10 diameters), with random variations of only 1–2 cm. As a

consequence, both recovery and grade were consistently 100 % over multiple runs. Similar results were also manifest with Cu/Brass and Al/Brass, likewise giving perfect outcomes. **Figs. 5a** and **5b** show samples of typical sorting results both before and after the sort.

Only when we attempted to sort aluminum alloys from other alloys did separation errors begin to emerge. In this case, the mass density of the particles is virtually identical, leaving only small variations in conductivity by which to sort. Thus, the separation distances were typically in the range of only 3–4 cm (3 diameters), with almost as much variance causing errors. Even so, the results were still consistently very good, leading to both grade and recovery of well over 85 %. A typical sorting out-

come is further depicted in **Fig. 5c**, which shows the alloy mixtures before and after the sort.

5. Discussion and conclusion

As the results in **Table 2** show, the principle of electrodynamic sorting exhibits a powerful capacity for sorting nonferrous metals from other nonferrous metals. This capacity was also extended to metal alloy separation, being demonstrated with various combinations of aluminum alloys. While we only limited ourselves to particles on the order of 0.5–1.0 cm, the basic principle could easily be re-designed for both larger and smaller geometries. The system utilizes no moving parts other than those needed to physically feed material into the magnet and requires no special chemical treatment or slurry in order to process material.

While such results are initially very impressive, it is important to remember that our particles were perfectly uniform spheres. This provided a tremendous level of consistency that would likely not exist under real-world conditions. It also has the added advantage of being mathematically symmetric, thus lending itself to closed-form analytic solutions to the resulting force equations (Lohofer, 1989). This is invaluable in identifying the primary fac-

Table 2 Grade and recovery results under various sorting conditions

Materials (A/B)	R_A [%]	R_B [%]	G_A [%]	G_B [%]
Al/Cu	100	100	100	100
Al/Brass	100	100	100	100
Cu/Brass	100	100	100	100
Al-1100/Al-2024	100	100	100	100
Al-1100/Al-6061	99	91	92	99
Al-6061/Al-2024	91	86	87	91

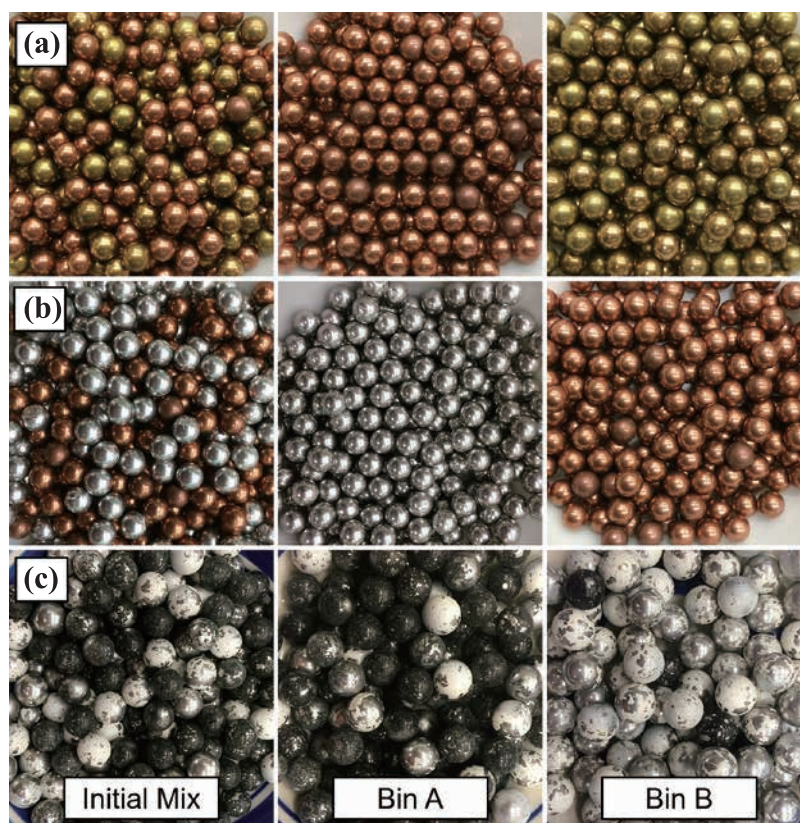


Fig. 5 (a) Sorting results between 6.0 mm copper and brass spheres. (b) 6.0 mm aluminum and copper spheres. (c) 12.5 mm aluminium alloys. Al-6061 spheres are painted black with Al-2014 spheres painted white.

tors which contribute to particle forces as well as their varying significance when compared to each other. In practice, however, real-world scrap is highly variable in size, geometry, and even composition, and will naturally exhibit much greater variance in trajectories during the sorting process. We are therefore currently in the process of collecting real-world scrap material and testing our system's performance accordingly. The results of these investigations, as well as the challenges we overcome, will be the subject of future publications.

One particular feature that requires further research is the problem of throughput. In practice, it will be necessary to process many hundreds of kilograms per hour in order to gain any interest from industrial recyclers. However, due to the bottleneck inherent to the magnetic gap, our current system can only process perhaps 50–100 kg per hour when pushed to its limits. Increasing throughput also tends to add greater chaotic variation to the feed process, thereby reducing grade and recovery in the outcome. Further design iterations must therefore increase throughput by at least a factor of 10 while also maintaining reasonable values in both grade and recovery. For example, the use of a conveyor belt will greatly improve consistency when feeding material to the magnet while simultaneously increasing throughput. Such challenges are also currently being investigated by our research team, and the results will likewise be presented in future publications.

Acknowledgements

This work was funded by the United States Advanced Research Project Agency-Energy (ARPA-E) METALS Program under cooperative agreement grant DE-AR0000411.

Nomenclature

B	magnetic field intensity (T)
C	capacitance (F)
E	electric field intensity (V/m)
EDX	electrodynamic sorting
F	force (N)
f_0	resonant frequency (Hz)
G_A	grade of sort bin A (%)
G_B	grade of sort bin B (%)
I	electric current (A)
j	imaginary unit
J	electric current density (A/m)
L	inductance (H)
m_0	initial mass of material 1 (kg)

M_0	initial mass of material 2 (kg)
m_A	mass of material 1 in bin A (kg)
M_A	mass of material 2 in bin A (kg)
m_B	mass of material 1 in bin B (kg)
M_B	mass of material 2 in bin B (kg)
N	wire turn number
R	electrical resistance (Ω)
R_A	recovery of sort bin A (%)
R_B	recovery of sort bin B (%)
RLC	resistor, inductor, capacitor
V	volume (m^3)
σ	electrical conductivity (S/m)
μ_0	permeability of free space (H/m)
ω	angular frequency (rad/s)

References

- Gaustad G., Olivetti E., Kirchain R., Improving aluminum recycling: A survey of sorting and impurity removal technologies, Resources, Conservation, and Recycling, 50 (2012) 79–87.
- Jackson J.D., Classical Electrodynamics, Wiley, New York (1999).
- Kuttila M., Viitanen J., Vattulainen A., Scrap metal sorting with colour vision and inductive sensor array, International Conference on Computational Intelligence for Modeling, Control and Automation, and International Conference on Intelligent Agents, Web Technologies and Internet Commerce (CIMCA-IAWTIC'06) 2 (2005) 725–729.
- Leary A.M., Ohodnicki P.R., McHenry M.E., Soft magnetic materials in high-frequency, high-power conversion applications, Journal of Minerals, Metals & Materials Society, 64 (2012) 772–781.
- Lohof G., Theory of an electromagnetically levitated metal sphere I: absorbed power, SIAM Journal of Applied Mathematics, 49 (1989) 567–581.
- Lungu M., Rem P., Eddy-current separation of small nonferrous particles by a single-disk separator with permanent magnets, IEEE Transactions on Magnetics, 39 (2003) 2062–2067.
- Lungu M., Separation of small nonferrous particles using an angular rotary drum eddy-current separator with permanent magnets, International Journal of Minerals Processing, 78 (2005) 22–30.
- Rem P.C., Leest P.A., van den Akker A.J., A model for eddy current separation, International Journal of Minerals Processing, 49 (1997) 193–200.
- Saveliev V., System and method for separating electrically conductive particles, US Patent, (1998) 5772043A.
- Schloemann E., Separation of nonmagnetic metals from solid waste by permanent magnets. I. Theory, Journal of Applied Physics, 46 (1975) 5012–5021.

Schloemann E., Separation of nonmagnetic metals from solid waste by permanent magnets. II. Experiments on circular disks, *Journal of Applied Physics*, 46 (1975) 5022–5029.

Spencer D.B., The high-speed identification and sorting of non-ferrous scrap, *Journal of Materials*, 57 (2005) 46–51.

USGS (United States Geological Survey), 2015, minerals yearbook <<http://minerals.usgs.gov/minerals/pubs/commodity/>

[aluminum/myb1-2013-alumi.pdf](http://minerals.usgs.gov/minerals/pubs/commodity/aluminum/myb1-2013-alumi.pdf)> accessed 16.06.2016.

USGS (United States Geological Survey), 2016, Mineral Commodity summaries 2016 <<http://minerals.usgs.gov/minerals/pubs/mcs/2016/mcs2016.pdf>> accessed 16.06.2016.

Weiss N.L., SE Mineral Processing Handbook, Volume 2, Society of Mining Engineers of the American Institute of Mining, Metallurgical, and Petroleum Engineers (1985).

Author's short biography



Nakul Dholu

Nakul Dholu completed his undergraduate degree in Metallurgical Engineering from Gujarat Technological University, Gandhinagar, India, in 2013. He graduated with MS degree in Metallurgical Engineering as well from the University of Utah, USA, in 2016 under the supervision of his Professor Dr. Raj Rajamani. Currently he is working as a Metallurgist-I at the Freeport-McMoRan Inc. in Arizona, USA. His research interests are in the field of light metal scrap recycling techniques and developing energy efficient mineral processing operations.



James Nagel

Dr. James Nagel completed his undergraduate degree in 2004 and MS degree in 2006, both in Electrical Engineering, from Brigham Young University in Provo, Utah. He then completed his PhD in 2011, also in Electrical Engineering, from the University of Utah in Salt Lake City, Utah and was awarded the Stockham Medal of Excellence for Conspicuously Effective Teaching. He now works as a research associate for the University of Utah, where his research focuses on applied electromagnetics with a specialty in numerical methods.



Dave Cohrs

Dave studied Environmental Science with emphasis on Analytical Chemistry at University of Maryland, Baltimore County in Maryland. He managed water quality laboratories at public aquariums for 16 years and has consulted for aquariums, zoos, and academia on water chemistry and life support topics. He now works for the University of Utah as a research associate.



Raj K. Rajamani

Raj Rajamani has been on the faculty of the Metallurgical Engineering Department of the University of Utah, Salt Lake City, Utah, USA since 1980. Currently he holds the position of professor. His research interests include population balance modeling of tumbling mills, computational fluid dynamics of hydrocyclones, discrete element modeling of semi-autogenous grinding mills, eddy current sorting of metallic particles and modeling of high pressure grinding rolls. He received the Antoine M. Gaudin Award, presented by the Society of Mining, Metallurgy and Exploration Engineers Inc. in the year 2009.

Impact Dispersion Using 2D and 3D Composite Granular Packing[†]

Surajit Sen^{1*}, T. R. Krishna Mohan² and Mukesh Tiwari³

¹ Department of Physics, State University of New York, USA

² CSIR Centre for Mathematical Modelling and Computer Simulation (C-MMACS), India

³ Group in Computational Science and High Performance Computing, DA-IICT, India

Abstract

We present a study of efficient dispersion of an impact onto structured and potentially scalable granular beds. We use discrete element method based dynamical simulations of shock wave propagation and dispersion in 2D and 3D arrangements of granular spheres. The spheres are geometrically packed in a nested columnar structure, which leads to the severe attenuation and spreading of the incident energy within the structure. We further show that by incorporating inhomogeneity in material properties, or by introducing layers of a dissimilar material in the middle of the arrangement, impact mitigation can be enhanced significantly. Such an arrangement can therefore be useful in the design of effective impact decimation systems. Using a 2D arrangement we first show the basic idea behind impact dispersion in such an arrangement. With this understanding the system is scaled to 3D. The influence of the system size and material properties on the wave propagation within the packing is also presented.

Keywords: elastic grains, mass mismatch, impact dispersion, granular chain, solitary waves

Introduction

Impact dispersion is an important area of research with wide ranging combat related applications, applications in the study of earthquake resistant structures and so on. Impulse propagation in granular systems has been an important area of research for more than 30 years due to the unique properties observed as a result of the highly non-linear contact law between the grains (Nesterenko V.F., 2001; Jaeger H.M. et al., 1996; Katsuragi H., 2016).

Starting with the pioneering work of Nesterenko (Nesterenko V.F., 1983), who showed the existence of solitary waves in a 1-dimensional arrangement of equal radius spheres, extensive work based on experiments (Coste C. et al., 1997), numerical simulations (Sinkovits R.S. and Sen S., 1995; Sen S. and Manciu M., 2001) and analytical methods (Mackay R.S., 1999; Lindenberg K. et al., 2011) have been performed for one dimensional chains (see e.g., Sen S. et al., 2008 for an exhaustive review). These stud-

ies have been instrumental in the design of novel granular materials with widespread applications. It is now well understood that introducing a mass mismatch in these one dimensional granular systems, either by changing the size of the spheres such as in tapered (Doney R. and Sen S., 2005; Nakagawa M. et al., 2003; Melo F. et al., 2006) and decorated chains (see e.g., Doney R. and Sen S., 2006; Machado L.P. et al., 2014), or by changing of the material properties by introducing spheres of different materials (Hong J. and Xu A., 2002; Hong J., 2005; Nesterenko V.F. et al., 2005; Daraio C. et al., 2006; Wang P.J. et al., 2007; Fraternali F. et al., 2010) leads to the rapid disintegration of the moving solitary wave, which would be of importance in designing materials for impact decimation.

Impact response of 2-dimensional granular systems has been studied extensively through experiments and numerical simulations of photoelastic disks by Shukla et al. (Rossmann H.P. and Shukla A., 1982; Zhu Y. et al., 1996; Sadd M.H. et al., 1993). More recently, Nishida et al. have studied projectile impact and wave propagation in two dimensional granular arrangement, including the effect of dissimilar materials (Nishida M. et al., 2001; Tanaka K. et al., 2002; Nishida M. and Tanaka Y., 2010). Leonard et al. through a series of works have systematically studied the role of the intruders and disorder on two dimensional square and hexagonal arrangements of granular systems (Leonard A. and Daraio C., 2012; Leonard A.

[†] Received 18 April 2016; Accepted 18 June 2016
J-STAGE Advance Publication online 30 July 2016

¹ Buffalo, New York 14260-1500, USA

² Bangalore, Karnataka 560037, India

³ Gandhinagar, Gujarat 382007, India

* Corresponding author: Surajit Sen;

E-mail: sen@buffalo.edu

TEL: +1-716-907-4961 FAX: +1-716-645-2507

et al., 2012, 2013, 2014). The role of the intruders and the different modes of propagation have been studied numerically by Awasthi et al. (Awasthi A.P. et al., 2012; Awasthi A.P. et al., 2015). The force propagation speed and effects of dissipation has also been analyzed (Abd-Elhady M.S. et al., 2010; Pal R.K. et al., 2013; Burgoyne H.A. and Daraio C., 2015). The 3-dimensional studies on monodispersed sphere arrangements have explored wave propagation (Manjunath M. et al., 2014), effect of impact conditions on the rebound velocity of the incident projectile (Nishida M. et al., 2004) and the impact response of heterogeneous granular systems (Burgoyne H.A. et al., 2015).

2. Model and numerical method

2.1 Quasi-2D bed

Fig. 1 shows the schematic of a recently proposed two dimensional granular arrangement (Tiwari M. et al., 2016) for impact decimation, wherein, spherical granular particles are assembled in a block-type arrangement. The spheres in a block are of equal masses and have the same material properties. The radius of the spheres in any block is, however, twice that of spheres in the block immediately below it. It should be emphasized that the geometries of the systems discussed here all require a factor of two reduction in sphere radius at each interface. Within each block we have rectangular arrangement of monodispersed spheres, and the blocks are placed in such a way that at the interface the sphere with larger radius is placed symmetrically above the two smaller spheres in the block below. This is also shown in the enlarged view in **Fig. 1**.

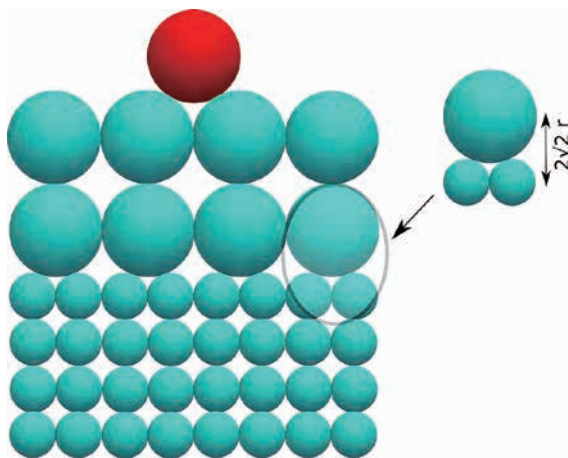


Fig. 1 Schematic of a part of the two dimensional granular arrangement with two blocks. The side walls are to be regarded as infinitely far away. The lower block is made up of spheres of radius r and the top block has spheres of radius $2r$.

The spheres are initially assumed to be in contact with no precompression, and interact elastically upon compression. The normal and tangential components of the force depend on the overlap and can be written as,

$$F_n = k_n \delta_n, \quad (1)$$

$$F_t = k_t \delta_t, \quad (2)$$

δ_n and δ_t are the normal and tangential overlap, respectively. For two spheres with separation r and radii R_1 and R_2 the normal overlap $\delta_n = R_1 + R_2 - r$ and the contact force is nonzero only when $\delta_n > 0$. The tangential overlap δ_t is the relative tangential displacement between the two spheres for the entire contact duration and the tangential force is limited by the coulomb criterion $F_t = \min(F_t, \mu F_n)$. We use the nonlinear Hertz contact interaction for describing the normal force in our simulations (Hertz H., 1881). The spring constants k_n and k_t therefore depend on the normal overlap in addition to the material parameters, $k_n = \frac{4}{3} Y^* \sqrt{R^* \delta_n}$ and $k_t = 8 G^* \sqrt{R^* \delta_n}$. For spheres with

the same Young's modulus Y and Poisson's ratio ν the effective Young's modulus $Y^* = \frac{Y}{2(1-\nu^2)}$ and the effective

shear modulus $G^* = \frac{Y}{4(1-2\nu)(1+\nu)}$. R^* is the effective

radius and equals $\frac{R_1 R_2}{R_1 + R_2}$. For numerical simulation

of the system we use the open source DEM package LIGGGHTS (Cundall P.A. and Strack O.D.L., 1979; Kloss C. et al., 2012; Plimpton S.J., 1995). We do not include gravity in our numerical simulations. The effect due to gravity would become significant for a large number of particles and weak impulse. For strong impulse the disturbance would still travel as solitary waves (Hong J. and Xu A., 2001). No dissipation of any form is taken into account, however, we do consider the effect of static friction on the distribution of energy. Incorporating dissipation would undoubtedly improve the impact decimation capabilities of the systems we study. However, ignoring dissipation in the following calculations help us set an upper bound on how much energy can be dispersed by the systems we examine.

Since the spheres interact only if they are in contact, the energy due to the impact by the striker travels along

Table 1 Densities, Young's moduli and Poisson's ratio of different materials used in numerical simulations.

	ρ (kg/m ³)	Y (Pa)	ν
Steel	7833	193×10^9	0.3
Teflon	2170	1.46×10^9	0.46

the chains of spheres in line with the contact point of the striker. We assume that the striker impact is in between two of the spheres in the upper most layer. For simplicity, we also assume that the striker is of the same mass and material as the spheres in the top block. The energy in the top block therefore travels sideways in the top layers, and downwards along two vertical chains. For a single block system with a square arrangement of purely elastic spheres it has been observed that around 71.5 % of the energy propagates downwards whereas the sideward propagation is around 24.5 % (Leonard A. et al., 2013). Our numerical simulations were consistent with these observations. The sideward propagation was observed to be significantly suppressed if static friction was included in our numerical simulations. We therefore, focus only on the downward propagating part. We will briefly comment in the following on what happens when the mass of the striker is increased or decreased.

2.2 Impact decimation by a quasi 2D bed

The system in the absence of multiple blocks is only one dimensional. Presence of multiple blocks makes it quasi two dimensional, since due to the proposed arrangement of spheres at the interface of two blocks, the energy from any excited larger spheres gets transmitted to two smaller spheres that are in contact with it in the block below. The spatial extent, however, remains the same due to

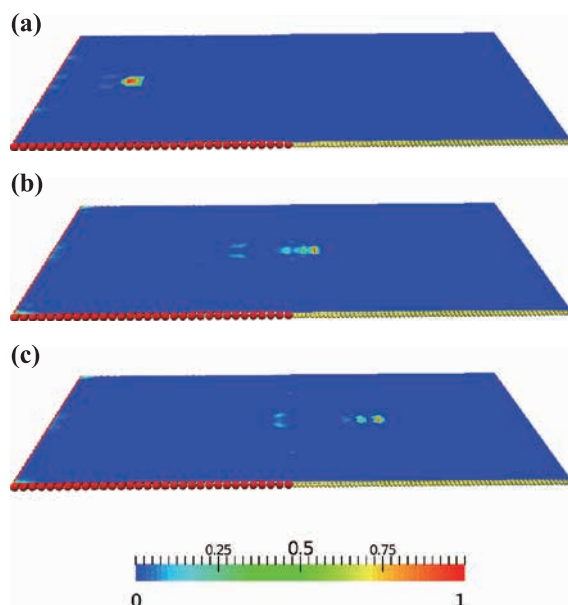


Fig. 2 Surface plots of the kinetic energy propagation in a two block system for three different time instants: (a) the energy is in the upper block (b) at the interface and (c) the energy is in the lower block. The kinetic energy is normalized to its maximum value for that time instant. The spheres in upper and lower blocks are shown in red and yellow respectively.

the smaller radii of the spheres across the interface.

In **Fig. 2** we show the propagation of kinetic energy in a two block system at different time instants for particles made from steel in both the blocks. The energy as expected propagates in a localized manner in the top block (**Fig. 2(a)**) along two chains. As this energy crosses the interface and moves to the block with lighter spheres it tends to spread out in its direction of propagation (see **Fig. 2(b)**), and after this transient phase it is seen to move as well separated discrete packets or solitary wave trains with much smaller energies in each pulse. The energy in each pulse of the wave train depends on the difference of the masses of the two spheres (Job S. et al., 2007). It is worth noting that impact of a striker which is more massive than the masses of the grains in the bed leads to the formation of solitary wave trains in the first block itself. No such trains form when a striker of lighter mass impacts on to the bed.

Presence of more blocks would lead to further frag-

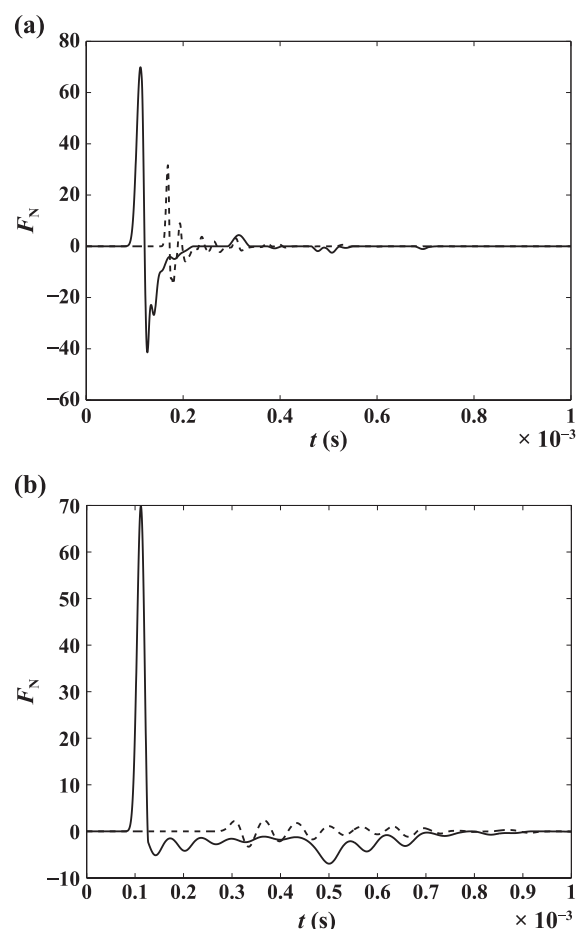


Fig. 3 Normal force experienced by the larger sphere at the interface of a 3 block system made of (a) steel grains and (b) block made from Teflon spheres sandwiched between two blocks made of steel spheres. The solid line is for a sphere at the top interface while dashed line is for the bottom interface.

mentation of these pulses at each interface. An effective impact decimation system can be constructed by having a multiple block arrangement. We consider two such arrangements each consisting of three blocks. In the first arrangement all the blocks are made from steel spheres, whereas, in the second arrangement a block made from lighter material such as teflon is sandwiched between two blocks made from steel spheres. The masses differ by a factor of 8 at each interface in the first arrangement whereas in the second arrangement they differ by a factor of 29.5 and 2.2 at the steel-teflon and teflon-steel interface respectively. Even though the numbers of interfaces are the same the difference in mass mismatch is seen to affect the impact decimation ability significantly. The normal force experienced by the larger sphere at the interface for the two arrangements are shown in **Figs. 3(a) and (b)** respectively. At the first interface (solid line in **Fig. 3**) sustained small amplitude oscillations are observed in the second arrangement. For larger mass mismatch values the solitary wave in the top block splits into more number of pulses with smaller amplitude when it moves to the second block. Each of these pulses split further at the second interface since they still move from a heavier side to a lighter side. This results in the further decimation of each pulse. This is shown through the dashed line in **Fig. 3**.

2.3 Hard sphere collision approximation (energy transmission in a multi-block system)

In the previous section we observed that a multi-block system results in significant decimation of the impact energy. Using a hard sphere approximation we provide an estimate of the output kinetic energy of the system. We consider a simplified picture in which we first estimate the transmitted energy in a general three sphere collision

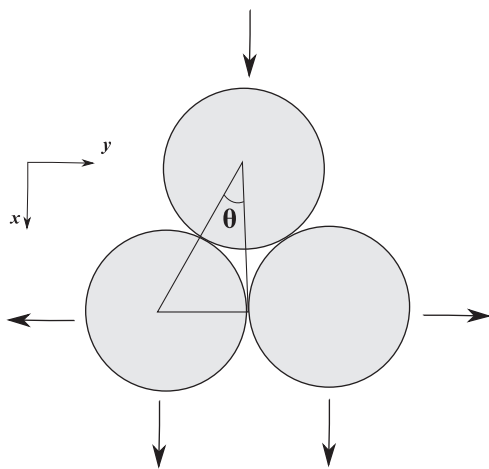


Fig. 4 Schematic for the sphere arrangement at the interface. The vertical downward direction is the x -direction and horizontal direction is the y -direction.

with the arrangement shown in **Fig. 4**. This is similar to the arrangement of the spheres at the interface of $i-1^{\text{th}}$ and i^{th} block. We ignore any horizontal momentum transfer to these spheres from the adjacent spheres. Using conservation of energy and momentum we can write for the momentum of the spheres

$$\begin{aligned} p_{i,1}^y &= p_{i,2}^y, \\ p_{i-1}^x(0) &= p_{i-1}^x(f) + 2p_{i,1}\cos\theta, \\ p_{i-1}^2(0) &= p_{i-1}^2(f) + 2\epsilon p_{i,1}^2 \end{aligned} \quad (3)$$

where $p_i^{x,y}$ represents the x, y component of the momentum of the spheres in the i^{th} block, $\epsilon = \frac{m_{i-1}}{m_i}$ is the ratio of the masses of the sphere in the two blocks, and for the arrangement considered at the interface, $\cos\theta = \frac{2\sqrt{2}}{3}$. Due to the symmetry in the collision, the two smaller spheres move with equal momentum ($p_{i,1}^x = p_{i,2}^x$) after impact. The final momentum of the spheres from **Eq. (3)** is

$$\frac{p_{i,1}^x}{p_{i-1}^x(0)} = \frac{2\cos^2\theta}{\epsilon + 2\cos^2\theta}, \quad (4)$$

$$\frac{p_{i-1}}{p_{i-1}(0)} = \frac{\epsilon - 2\cos^2\theta}{\epsilon + 2\cos^2\theta}. \quad (5)$$

If $\epsilon - 2\cos^2\theta > 0$ ($\epsilon > 16/9$) from **Eq. (5)**, the top sphere would continue to move in its original direction. This leads to multiple collisions at the interface in the proposed system. Each collision leads to the generation of a solitary wave. From **Eq. (4)**, the momentum transfer is inversely related to the mass ratio. Therefore larger mass mismatch would result in a smaller momentum or energy transmission at each collision. It has been shown that the total energy carried by the solitary wave is $E = P^2/2m_{\text{eff}}$ where the effective mass of the solitary wave is $m_{\text{eff}} \approx \Omega m$. The value of Ω is approximately 1.4 (Job S. et al., 2007; Tichler A.M., et al., 2013). We further assume that the energy and momentum transfer between subsequent blocks is through the collision between solitary waves, and that the individual pulses in the solitary wave train are separated significantly. To calculate the output energy of the system we therefore only need to consider the leading solitary wave pulse in each block. Under these assumptions the complete energy transfer can be thought to occur as discrete events. At the initial time, the impact by the striker results in the generation of a solitary wave in the top block. Therefore, the collision process here is between a particle and solitary wave treated as a quasiparticle. At the second interface, the collision is between the two leading solitary waves on either side of the interface. Finally, in the lowest block the solitary wave transfers its

complete energy to the last particle which is taken to be the output energy of the system. The ratio of the momentum of the last particle in an n block system and the striker can then be written as:

$$\frac{p_{n,L}}{p_{st}(0)} = \left(\frac{p_{n,L}}{p_{sw,n}} \right) \left(\frac{p_{sw,n}}{p_{sw,n-1}} \right) \left(\frac{p_{sw,n-1}}{p_{sw,n-2}} \right) \dots \left(\frac{p_{2,L}}{p_{sw,1}} \right) \left(\frac{p_{sw,1}}{p_{st}(0)} \right). \quad (6)$$

$p_{n,L}$ is the momentum of the last particle in the n^{th} block, $p_{sw,i}$ is the momentum of the leading solitary wave pulse in the i^{th} block and $p_{st}(0)$ is the initial momentum of the striker, $\frac{p_{n,L}}{p_{sw,n}} = \frac{2}{\Omega + 1}$, and, $\frac{p_{sw,1}}{p_{st}(0)} = \frac{2\Omega \cos^2 \theta_1}{1 + 2\Omega \cos^2 \theta_1}$. θ_1 is the angle that the striker makes with the two spheres ($\cos \theta_1 = 1/\sqrt{3}$). If the spheres are made from the same material Eq. (6) can be simplified and written as:

$$\frac{p_{n,L}}{p_{st}(0)} = \left(\frac{p_{n,L}}{p_{sw,n}} \right) \left(\frac{2 \cos^2 \theta}{\epsilon + 2 \cos^2 \theta} \right)^{n-1} \left(\frac{p_{sw,1}}{p_{st}(0)} \right). \quad (7)$$

For alternating blocks of hard and soft material, such as steel-teflon-steel-teflon we can obtain a similar expression,

$$\frac{p_{n,L}}{p_{st}(0)} = \left(\frac{p_{n,L}}{p_{sw,n}} \right) \left(\frac{2 \cos^2 \theta}{\epsilon_{st,tf} + 2 \cos^2 \theta} \right)^p \left(\frac{2 \cos^2 \theta}{\epsilon_{tf,st} + 2 \cos^2 \theta} \right)^q \left(\frac{p_{sw,1}}{p_{st}(0)} \right), \quad (8)$$

where, $\epsilon_{st,tf} = \frac{m_{st}}{m_{tf}}$. The powers p and q equals, respectively, $n/2$ and $\frac{n}{2} - 1$ if n is even, while, if n is odd they

are both equal to $(n-1)/2$. A better approximation to the energy transmission is obtained if we assume that within each block the solitary wave transfers its momentum and energy to the last particle of the block. Each collision of this last particle with the top particle in the next block leads to the generation of a solitary wave. Therefore at each interface the collision is between the particle on one side and the leading edge of the solitary wave treated as a quasiparticle on the other side. Under this assumption we obtain for spheres of the same material

$$\frac{p_{n,L}}{p_{st}(0)} = \left(\frac{p_{n,L}}{p_{sw,n}} \right) \left(\frac{2}{\Omega + 1} \right)^{n-1} \left(\frac{2\Omega \cos^2 \theta}{\epsilon + 2\Omega \cos^2 \theta} \right)^{n-1} \left(\frac{p_{sw,1}}{p_{st}(0)} \right), \quad (9)$$

and, for alternate blocks of steel and teflon

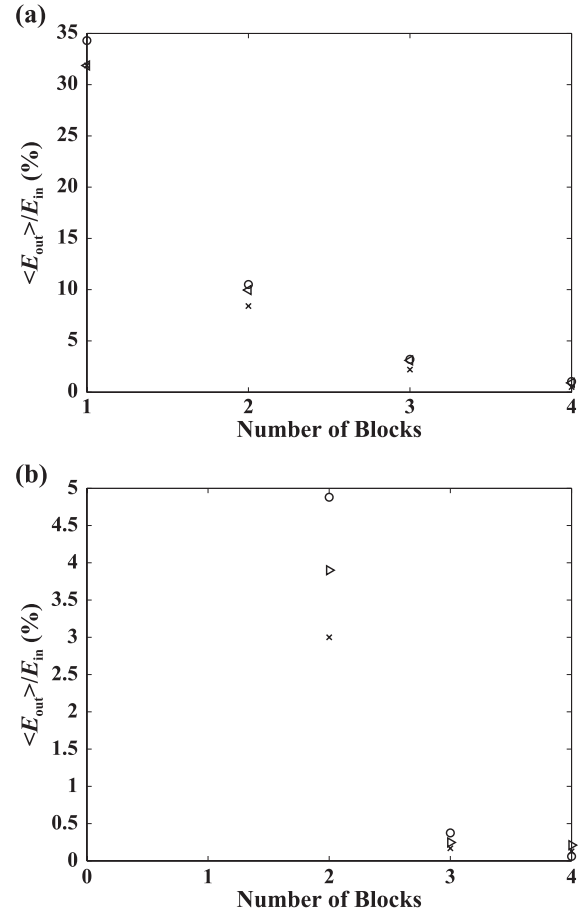


Fig. 5 Average Kinetic energy for 1–4 block system with (a) each block made of steel spheres and (b) alternate blocks with steel and Teflon spheres. The circles are obtained through numerical simulation whereas (×) is obtained from Eqs. (7) and (8), and, (△) is obtained from Eqs. (9) and (10).

$$\frac{p_{n,L}}{p_{st}(0)} = \left(\frac{p_{n,L}}{p_{sw,n}} \right) \left(\frac{2}{\Omega + 1} \right)^{n-1} \left(\frac{2\Omega \cos^2 \theta}{\epsilon_{st,tf} + 2\Omega \cos^2 \theta} \right)^p \left(\frac{2\Omega \cos^2 \theta}{\epsilon_{tf,st} + 2\Omega \cos^2 \theta} \right)^q \left(\frac{p_{sw,1}}{p_{st}(0)} \right). \quad (10)$$

The average kinetic energy transmitted $\left(\frac{m_{st}}{m_n} \right) \left(\frac{\langle p_{n,L}^2 \rangle}{p_{st}^2(0)} \right)$ is shown in **Fig. 5** for multiple blocks (1–4 block system), m_n is the mass of the sphere in the n^{th} block. The average here is over the energies of all the excited spheres in the bottom layer of the last block. For comparison, in **Fig. 5** we only show the kinetic energy when the leading pulse reaches the last layer. In both the cases, Eqs. (9) and (10) are able to provide a better estimate, however, for dissimilar materials the fit is only qualitative. In **Fig. 5**, the energy shown is the leading energy of the pulse reaching the last sphere. The energy with which the last particle ejects is slightly larger than this value. Nevertheless, this difference is insignificant. More importantly, even with three blocks the average output energy is only around 0.4 % of

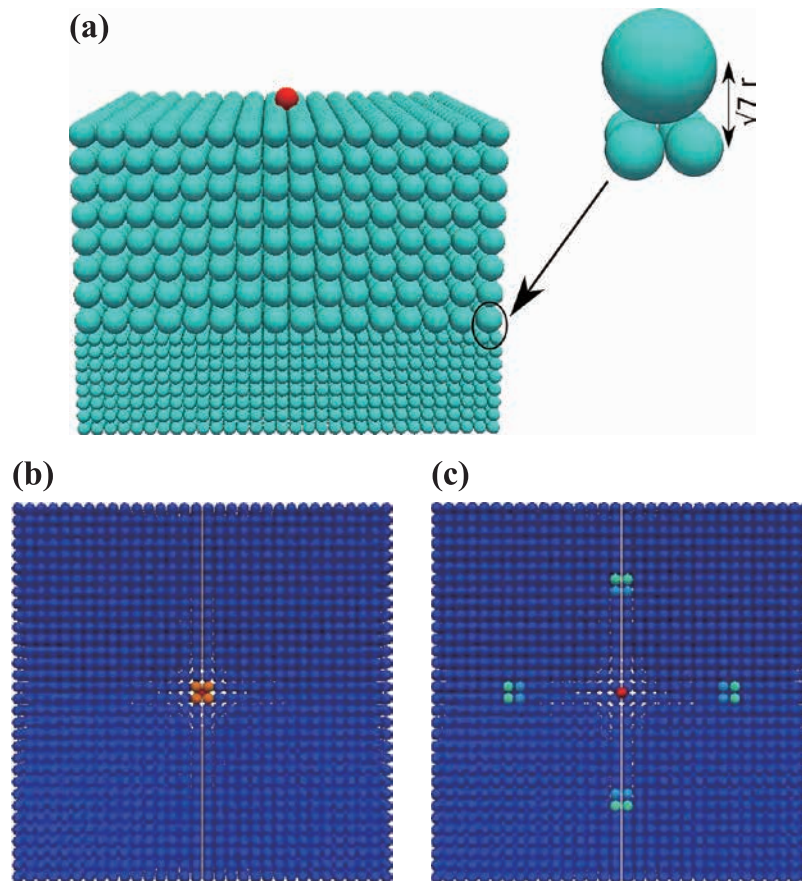


Fig. 6 (Top) Schematic of the 3-dimensional system with two blocks. (Bottom) Propagation of energy in a single block system (Left) vertically downward and (Right) sideward.

the impact energy. This energy does not show any significant dependence on the size of the system.

3. Impact decimation by a 3D bed

The advantage of the proposed system in two dimensions is that it can be easily extended to three dimensions. In **Fig. 6** (top) we show a typical three dimensional system with two blocks. As is evident from the enlarged view of the sphere arrangement at the interface, the larger sphere is in contact with four spheres in the layer below. The centers of the spheres form a pyramid like structure, with the base made from the plane connecting the centers of the four small spheres and the larger sphere is centered at the top of the pyramid at a vertical distance of $\sqrt{7}$ from the base. This pyramid structure forms the basis of energy partitioning at each interface. Each excited sphere transmits its energy to four spheres in the downward direction. The energy propagation for a single excited sphere is therefore through four chains vertically downward and eight chains in the lateral direction (see **Fig. 6** (bottom)). The process gets repeated at each interface and the energy is transferred to four times the number of ex-

cited spheres in the upper block. We show this energy partitioning for a completely elastic 1-block system in **Fig. 7**. What is notable is that the net energy transmission in the horizontal and vertical directions is almost the same. The rebound energy of the striker is higher (approx 12.5 %) than that of the two dimensional system (approx 4 %). Before energy exits from the system the distribution between potential and kinetic energy follows the virial theorem. Since the energy partitioning along the two directions are the same we also look at the effect of static friction on the distribution of energy. As shown in the bottom plot in **Fig. 7(b)** static friction does have the effect of reducing the sideward energy propagation. For higher values of static friction and when the boundaries are sufficiently far away or the side walls are made to be energy absorptive, these multi-block systems may be useful in many impact dispersion applications. The system properties would not change if the grain sizes were smaller as long as the elastic properties of the spheres were unaffected. Realistically this means the systems envisioned here could well be realized possibly even in the micron scale. In a regularly arranged closed packing we do not expect much rotational motion to occur, and therefore it is possible that energy propagation in the sideward direction

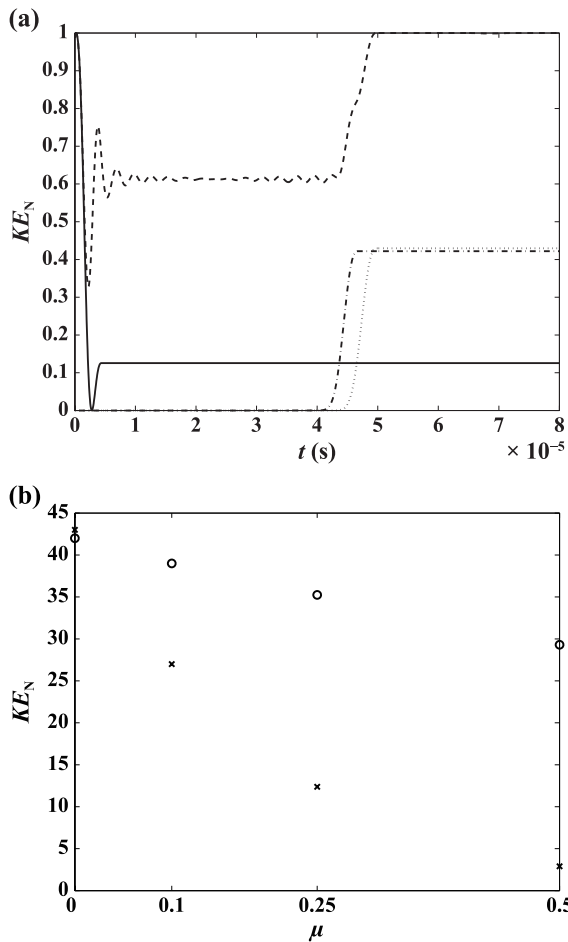


Fig. 7 (a) Partitioning of the normalized energy in a 1 block system, between the striker (solid line), four particles in the bottom layer (dashed-dotted line), and eight particles in the top layer (dashed-line). The dashed line shows the overall kinetic energy of the entire system (bed and striker). (b) Variation of normal (\circ) and side-ward (\times) transmission of total kinetic energy propagation with static friction μ .

would be significant. At this moment we concentrate only on the downward propagation of energy.

In **Fig. 8** we show the vertical force propagation in a three block system. Two different systems are considered. In the first, all the blocks are made of steel spheres, while in the second, a block made from lighter mass Teflon spheres is sandwiched between blocks made from heavier steel spheres. In both the systems within the top block the force propagates as a single hump. At the top interface the transmission of force is significantly different. In the first case when the mass mismatch is comparatively smaller the force gets transmitted almost entirely and over a shorter time interval. As mass mismatch increases, the force propagates slowly inside the Teflon block and is more uniformly distributed over the overall length of the block. There is also a sharp reduction of the maximum force on the sphere at the interface in the second arrangement.

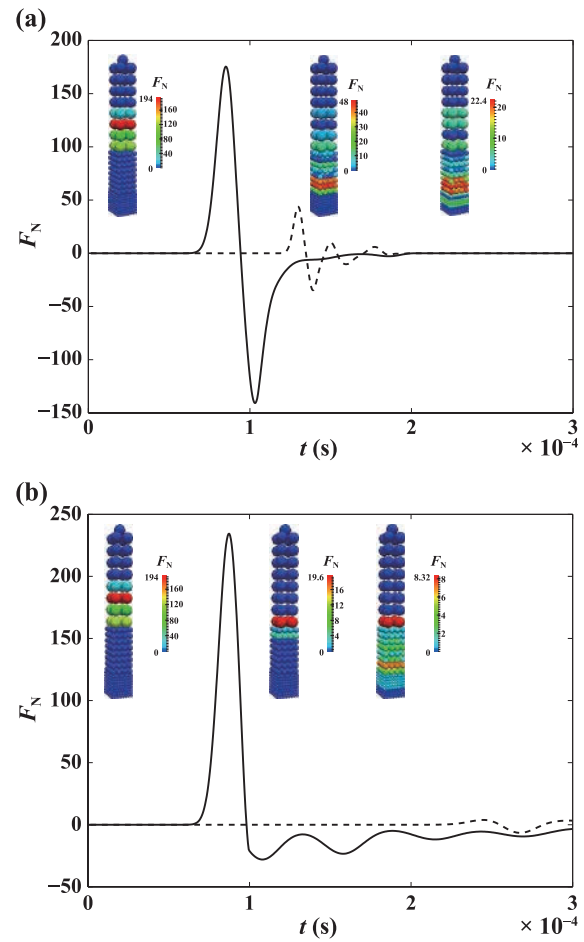


Fig. 8 Force at an interface sphere in a 3-block system for (a) all blocks made from steel sphere and (b) block with teflon spheres sandwiched between blocks made from steel sphere. The solid line shows the force on interfacial sphere in the top block while the dashed line shows the force on the interfacial sphere in the second block. The inset shows the vertical cross sectional view of the overall force distribution at different time instants. The color bar shows the absolute value of the normal force acting on a sphere.

4. Conclusions

The wave propagation in the presence of mass mismatch was investigated numerically for an impact decimation system. Our numerical simulations show that such a system is capable of suppressing incident impact significantly. The setup presented here takes advantage of the fact that when a solitary wave crosses from a denser to a lighter medium, a series of solitary waves with smaller energies are generated. This splitting is also borne out of the approximate hard sphere collision theory for the system under consideration. A larger mass difference at the interface results in more splitting and thereby lesser energy in each pulse. A block with smaller mass spheres sandwiched between blocks with heavier mass spheres on both sides shows better impact decimation capability. The

arrangement of spheres at the interface (triangular in 2D and pyramid in 3D) leads to energy being partitioned between more spheres at the interface. The proposed three dimensional system is therefore seen to demonstrate superior impact dispersion capabilities. The sideward propagation is however significantly larger in three dimensions. While we have not considered this situation in the current work, in actual design of systems this would be quite important. Since the impact dispersion and decimation is due to the geometry of the packing at the interface, the qualitative features should not be affected by varying the size or the angle of impact of the striker.

Nomenclature

F_n	normal force (N)
F_t	tangential force (N)
k_n	normal spring constant (N/m)
k_t	tangential spring constant (N/m)
δ_n	normal overlap (m)
δ_t	tangential overlap (m)
μ	static friction
Y	Young's modulus (Pa)
ν	Poisson's ratio
R	radius of the sphere (m)
ρ	density of the sphere (kg/m^3)
R^*	effective radius of two particles in contact
Y^*	effective Young's modulus
G	Shear modulus (Pa)

References

- Abd-Elhady M.S., Abd-Elhady S., Rindt C.C.M., Van Steenhoven A.A., Force propagation speed in a bed of particles due to an incident particle impact, *Adv. Powder Technol.*, 21 (2010) 150–164.
- Awasthi A.P., Smith K.J., Geubelle P.H., Lambros J., Propagation of solitary waves in 2D granular media, *Mechanics of Materials*, 54 (2012) 100–112.
- Awasthi A.P., Wang Z., Broadhurst N., Geubelle P., Impact response of granular layers, *Granular Matter*, 17 (2015) 27–31.
- Burgoyne H.A., Daraio C., Elastic–plastic wave Propagation in uniform and periodic granular chains, *Journal of Applied Mechanics*, 82(8) (2015) 081002.
- Burgoyne H.A., Newman J.A., Jackson W.C., Daraio C., Guided impact mitigation in 2D and 3D granular crystals, *Procedia Engineering*, 103 (2015) 52–59.
- Coste C., Falcon E., Fauve S., Solitary waves in a chain of beads under Hertz contact, *Phys. Rev. E*, 56 (1997) 6104–6117.
- Cundall P.A., Strack O.D.L., A discrete numerical model for granular assemblies, *Géotechnique*, 29(1) (1979) 47–65.
- Daraio C., Nesterenko V.F., Herbold E.B., Jin S., Energy trapping and shock disintegration in composite granular medium, *Phys. Rev. Lett.*, 96 (2006) 058002.
- Doney R., Sen S., Impulse absorption by tapered horizontal alignment of elastic spheres, *Phys. Rev. E*, 72 (2005) 041304.
- Doney R., Sen S., Decorated, tapered and highly nonlinear granular chain, *Phys. Rev. Lett.*, 97 (2006) 155502.
- Fraternali F., Porter M.A., Daraio C., Optimal design of composite granular protectors, *Mech. Adv. Mat. Struct.*, 17 (2010) 1–19.
- Hertz H., Über die Berührung fester elastischer Körper, *Journal für die reine und angewandte, Mathematik*, 92 (1881) 156–171.
- Hong J., Xu A., Effects of gravity and nonlinearity on the waves in the granular chain, *Phys. Rev. E*, 63 (2001) 061301.
- Hong J., Xu A., Nondestructive identification of impurities in granular medium, *Appl. Phys. Lett.*, 81 (2002) 4868–4870.
- Hong J., Universal power-law decay of the impulse energy in granular protectors, *Phys. Rev. Lett.*, 97 (2005) 108001.
- Jaeger H.M., Nagel S.R., Behringer R.P., Granular solids, liquids, and gases, *Rev. Mod. Phys.*, 68 (1996) 1259.
- Job S., Melo F., Sokolow A., Sen S., Solitary wave trains in granular chains: experiments, theory and simulations, *Granular Matter*, 10 (2007) 13–20.
- Katsuragi H., *Physics of soft impact and cratering*, Springer, Tokyo (2016). ISBN 978-4-431-55648-0.
- Kloss C., Goniva C., Hager A., Amberger S., Pirker S., Models, algorithms and validation of opensource DEM and CFD-DEM, *Progr.Computat. Fluid Dyn.*, 12 (2012) 140–152.
- Leonard A., Daraio C., Stress wave anisotropy in centered square highly nonlinear granular systems, *Phys. Rev. Lett.*, 108 (2012) 21430.
- Leonard A., Fraternali F., Daraio C., Directional wave propagation in a highly nonlinear square packing of spheres, *Exp. Mech.*, 57 (2013) 327–337.
- Leonard A., Daraio C., Awasthi A., Geubelle P., Effects of weak disorder on stress-wave anisotropy in centered square nonlinear granular crystals, *Phys. Rev. E*, 86(3) (2012) 031305.
- Leonard A., Chong C., Kevrekidis P.G., Daraio C., Traveling waves in 2D hexagonal granular crystal lattices, *Granular Matter*, 16 (2014) 531–542.
- Lindenberg K., Harbola U., Romero H., Rosas A., Pulse propagation in granular chains, *Am. Inst. Phys. Conf. Ser.*, 1339 (2011) 97–110.
- Machado L.P., Rosas A., Lindenberg K., A quasi-unidimensional granular chain to attenuate impact, *Eur. Phys. J. E*, 37(11) (2014) 1–7.
- Mackay R.S., Solitary waves in a chain of beads under Hertz contact, *Phys. Lett. A*, 251 (1999) 191–192.
- Manjunath M., Awasthi A.P., Geubelle P.H., Plane wave propagation in 2D and 3D monodisperse periodic granular media, *Granular Matter*, 16 (2014) 141–150.
- Melo F., Job S., Santibanez F., Tapia F., Experimental evidence

- of shock mitigation in a Hertzian tapered chain, *Phys. Rev. E*, 73 (2006) 041305.
- Nakagawa M., Agui J.H., Wu D.T., Extramiana D., Impulse dispersion in a tapered granular chain, *Granular Matter*, 4 (2003) 167–174.
- Nesterenko V.F., Propagation of nonlinear compression pulses in granular media, *J. Appl. Mech. Tech. Phys.*, 24 (1983) 733–743.
- Nesterenko V.F., *Dynamics of heterogeneous materials*, Springer, New York, 2001.
- Nesterenko V.F., Daraio C., Herbold E.B., Jin S., Anomalous wave reflection at the interface of two strongly nonlinear granular media, *Phys. Rev. Lett.*, 95 (2005) 158702.
- Nishida M., Tanaka K., Kunimochi T., Takagi T., Discrete element simulation in projectile impacts on granular materials, *Proc. 23rd Int. Symp. Shock Waves*, (2001) 655–661.
- Nishida M., Tanaka K., Matsumoto Y., Discrete element method simulation of the restitutive characteristics of a steel spherical projectile from a particulate aggregation, *JSME international journal, Series A, Solid mechanics and material engineering*, 47(3) (2004) 438–447.
- Nishida M., Tanaka Y., DEM simulations and experiments for projectile impacting two-dimensional particle packings including dissimilar material layers, *Granular Matter*, 12 (2010) 357–368.
- Pal R.K., Awasthi A.P., Geubelle P.H., Wave propagation in elasto-plastic granular systems, *Granular Matter*, 15 (2013) 747–758.
- Plimpton S.J., Fast parallel algorithms for short-range molecular dynamics, *J. Comput. Phys.*, 117(1) (1995) 1–19.
- Rossmann H.P., Shukla A., Photoelastic investigation of dynamic load transfer in granular media, *Acta Mech.*, 42 (1982) 211–225.
- Sadd M.H., Tai Q., Shukla A., Contact law effects on wave propagation in particulate materials using distinct element modelling, *Int. J. Non-linear Mech.*, 28 (1993) 251–265.
- Sen S., Manciu M., Solitary wave dynamics in Generalized Hertz chains: An improved solution to the equation of motion, *Phys. Rev. E*, 64 (2001) 056605.
- Sen S., Hong J., Bang J., Avalos E., Doney R., Solitary waves in the granular chain, *Phys. Rept.*, 462 (2008) 21–66.
- Sinkovits R.S., Sen S., Nonlinear dynamics in granular columns, *Phys. Rev. Lett.*, 74 (1995), 2686.
- Tanaka K., Nishida M., Kunimochi T., Takagi T., Discrete element simulation and experiment for dynamic response of two-dimensional granular matter to impact of a spherical projectile, *Powder Technol.*, 124 (2002) 160–173.
- Tichler A.M., Go'mez L.R., Upadhyaya N., Campman X., Nesterenko V.F., Vitelli V., Transmission and reflection of strongly nonlinear solitary waves at granular interfaces, *Phys. Rev. Lett.*, 111 (2013) 048001.
- Tiwari M., Krishna Mohan T.R., Sen S., Decorated granular layers for impact decimation, *Granular Matter*, 18 (2016) 1–5.
- Wang P.J., Xia J.H., Li Y.D., Liu C.S., Crossover in the power-law behavior of confined energy in a composite granular chain, *Phys. Rev. E*, 74 (2007) 041305.
- Zhu Y., Shukla A., Sadd M., The effect of microstructural fabric on dynamic load transfer in two dimensional assemblies of elliptical particles, *J. Mech. Phys. Solids*, 44 (1996) 1283–1303.

Author's short biography



Surajit Sen

Surajit Sen is a Professor of Physics at the State University of New York at Buffalo. His research interests are focused on understanding the dynamics of strongly nonlinear systems. He has worked on impulse propagation in granular systems since 1995. He received his PhD in Physics from the University of Georgia in 1990 and is a Fellow of the American Physical Society and the American Association for the Advancement of Science and serves as an editor of International Journal of Modern Physics B and Modern Physics Letters B.



T. R. Krishna Mohan

Krishna Mohan, T. R. is currently working as a Scientist at CSIR Fourth Paradigm Institute in Bangalore, India where he has been working since 1991. In between, he worked at State University of New York at Buffalo for around four years at the Department of Physics and Department of Pharmaceutics. He received his PhD. from Jawaharlal Nehru University, New Delhi, India in 1988 working on nonlinear dynamics. His current interests include, apart from impulse absorption in granular systems, modelling of CNS, earthquake dynamics and nonlinear dynamics of FPU-like systems.



Mukesh Tiwari

Mukesh Tiwari is currently an Associate Professor at the Dhirubhai Ambani Institute of Information and Communication Technology (DA-IICT) where he has been working since 2009. He received his M.Sc degree in Physics from Indian Institute of Technology, Delhi in 2003 and PhD in Optical Science and Engineering from the University of New Mexico, USA in 2008. His research interests are mainly focused on statistical physics and nonlinear systems.

Flow of Bi-modal Slurry through Horizontal Bend[†]

Deo Raj Kaushal^{1*}, Arvind Kumar², Yuji Tomita³,
Shigeru Kuchii⁴ and Hiroshi Tsukamoto⁴

¹ Department of Civil Engineering, IIT Delhi, India

² Department of Mechanical Engineering, YMCA UST, India

³ Kyushu Institute of Technology, Japan

⁴ Kitakyushu National College of Technology, Japan

Abstract

Extensive experimental investigations were carried out for pressure drop and concentration profile in the flow of bi-modal slurry comprising silica sand and fly ash with mean diameter of 450 and 75 μm , respectively, at six silica sand:flyash ratios (namely, 100:0, 90:10, 80:20, 70:30, 60:40 and 0:100) in a 53 mm diameter horizontal bend. Flow velocity was varied up to 3.56 m/s (namely, 1.78, 2.67 and 3.56 m/s) at two efflux concentrations of 8.82 % and 16.28 % for each silica sand:flyash ratio. The experimental data were compared with the CFD modelling results using an Eulerian two-phase model available in the FLUENT software. Eulerian model predicted almost all the experimental data collected in the present study for pressure drop and concentration profile with fair accuracy. The bend loss coefficient k_t was found to decrease with increase in percentage of flyash for silica sand:flyash ratio up to 70:30. Further increase in flyash did not show any significant change in the value of k_t .

Keywords: Eulerian model, CFD modelling, Bi-modal slurry, pipe bend, pressure drop, concentration profile

1. Introduction

Transportation of granular solids in slurry form through pipeline is widely applied in industries due to its several inherent advantages, such as, continuous delivery, flexible routing, ease in automation and long distance transport capability. Slurry pipelines are used for transportation of mineral ore, coal, flyash and tailings materials. In dredging operations, sand dredged from rivers is often pumped with water through a pipeline to a construction site. The flow mechanism of slurry transport through pipeline is of vital importance to the designers of slurry transport system. Pipeline bends normally incur relatively higher pressure drop and are prone to excessive erosion compared to the straight equivalent length of pipe. Flow in bends is quite complex and complexity is further increased for two-phase mixtures. Studies available in literature have shown that the flow in bends for solid-liquid mixture system is much more complicated than in gas-

solid system (Kumar, 2010). Reported literature for solid-liquid flow in bends is limited which may be due to complexities involved. It is already well established that bends in general are prone to excessive erosion wear and hence need frequent replacements resulting in shut-downs of plants leading to loss of man hours. In order to increase the longevity of the pipe bends and to minimise the pressure loss through bends, a detailed knowledge of the flow properties in the pipe bends and downstream of the bend is essential. Most of the experimental and computational work related to the effect of bends in slurry pipeline system concern the erosion, concentration profiles and pressure drops for the flow of mono-dispersed particles (Kaushal et al., 2013). However, there is only few studies available on flow of bi-modal and multi-sized particles through pipe bends.

Nasr-El-Din and Shook (1987) have measured the concentration profile and velocity distribution for flow of bi-modal slurry in a vertical pipe with short and long radius bends. They observed axi-symmetric flow for short radius bend whereas the coarser and finer particles migrate towards the outer and inner wall, respectively, for the long radius bend. Ahmed et al. (1994) have measured the pressure drop in a 90° horizontal bend using two multi-sized particulate slurries namely iron ore and zinc tailings slurries. From their studies they concluded that the presence of the finer particles reduces the additional pressure drop in the flow of multi-sized particulate slurries across the

[†] Received 18 January 2016; Accepted 20 July 2016
J-STAGE Advance Publication online 30 August 2016

¹ Hauz Khas, New Delhi-110016, India

² Faridabad, Haryana, India

³ 1-1 Sensui cho, Tobata, Kitakyushu 804-8550, Japan

⁴ 5-20-1 Shii, Kokura-minami, Kitakyushu 802-0985, Japan

* Corresponding author: Deo Raj Kaushal;

E-mail: kaushal@civil.iitd.ac.in

TEL: +91-98-1828-0867 FAX: +91-11-2658-1117

bends. They found from bi-modal viewpoint that particles re-distribute more in the bend as compared to the straight pipe but could not identify the plane of movement. The extent of re-distribution reduces as the flow velocity and concentration increases. Gupta et al. (1997) confirmed the findings of Ahmed et al. (1994) for multi-sized particulate slurries. They observed the maximum concentration to be at the bottom of the bend along the vertical plane even at higher concentration also. They however observed that largest size particles moved outward and its concentration was higher in outer bottom periphery. The finer particles were observed to be uniformly distributed. Literature on studies of pressure drop by Kazanskij and Hinsch (1974), Boothroyde et al. (1979), Hayashi et al. (1980) and Verkerk (1982) reveals that mixing of fine particles in small percentage up to 20–30 % in coarse slurry helps to reduce the pressure drop and makes the distribution of particles homogeneous.

Advent of highly sophisticated computers with advanced numerical techniques involved in computational fluid dynamics (CFD) analysis made it possible to analyse the operation of slurry transport systems using numerical simulations but the literature review clearly reveals that the application of CFD for such systems is few (Thinglas and Kaushal, 2008a, 2008b). Kaushal et al. (2012) numerically simulated using mixture and granular-Eulerian two-phase models for mono-dispersed high concentrate slurry flow in Pipeline. Standard $k-\epsilon$ model per phase and the standard wall function with no slip were used. They concluded that mixture model failed to predict but granular-Eulerian model per phase gave better predictions for pressure drop at all efflux concentrations and flow velocities. However, this model failed to predict solid concentration distribution, more dominantly at higher concentrations and flow velocities, for few experimental data near the pipe bottom. Kaushal et al. (2013) made use of Eulerian model in FLUENT software to calculate the pressure drop and concentration profile in mono-dispersed silica sand slurry flow through pipe bend. Eulerian model was found reasonably effective with the slurry pipe bend on the basis of good agreement between their experimental and computational results. Messa and Malavasi (2014) simulated the fully-suspended slurry flow in horizontal pipe based on the standard $k-\epsilon$ model. Phase diffusion fluxes are introduced in all conservation equations to reproduce the effect of the turbulent dispersion of particles. The mixture viscosity approach is employed to model the effect of the presence of multiple particles on interfacial momentum transfer. Equilibrium wall function for smooth walls is applied to both phases and no slip is assumed between the phases at the inlet section. In comparison with similar models, the authors revealed that the used model showed better performance in terms of numerical efficiency, quality of the solution and range of applicability. Gopaliya and

Kaushal (2015) investigated the effects of particle size on slurry flow parameters using CFD by implementing granular RNG $k-\epsilon$ turbulence model with standard wall function and no-slip at the wall. It is reported that high deviations in the values between simulated and experimental data of local solid concentration values are observed in the lower half of the cross-section just near the wall for coarser grain sizes. Gopaliya and Kaushal (2016) analysed the effects of particle size on various slurry flow parameters such as pressure drop, solid phase velocity distribution, friction factor, granular pressure, turbulent viscosity, turbulent kinetic energy and its dissipation. However, there is no study available in literature for modelling the flow of bi-modal or multi-sized particulate slurries through pipeline using three-dimensional CFD based Eulerian two-phase model. The present research work delves deep into the transport mechanism of bi-modal slurries through pipe bend by conducting experiments and numerical simulations.

In the present study, measurements of concentration and particle size distribution are made at downstream of the bend at different locations to understand the phenomena of re-distribution of particles belonging to two size fractions of the bi-modal slurry. Concentration profiles and pressure drops are modelled using Eulerian model in a pipe bend for the flow of bi-modal silica sand and fly ash slurries at six silica sand:flyash ratios. The CFD based modelling results are compared with the experimental data.

2. Experimental setup

In the present study, pilot plant test loop having inside diameter of 53 mm and length of 30 m is used. Pipe bend is laid horizontally in the loop. **Fig. 1** shows the schematic layout of the pilot plant test loop. The loop is described in detail by Kumar (2010) Kaushal et al. (2013).

We measured concentration profiles by sampling tube in the mid-vertical plane in the downstream of bend exit as shown in **Fig. 2** Sampling tube was having a 4 mm x 6mm rectangular slot 2 mm above the end to collect representative samples in the pipe line. Samples are collected from different heights from bottom of the pipe in the vertical plane of the cross-section to measure the concentration profile under near isokinetic conditions. As the flow is under pressure, slurry comes out from the sampling tube with the same velocity and volumetric concentration as it is flowing in the pipeline at the location of measurement. During the collection of samples it is ensured that the flow of the slurry through the sampling tube outlet is nonstop and uniform. At the end of the pipe loop a sampling point is provided in the vertical portions to collect an average efflux sample. The size of rectangular opening

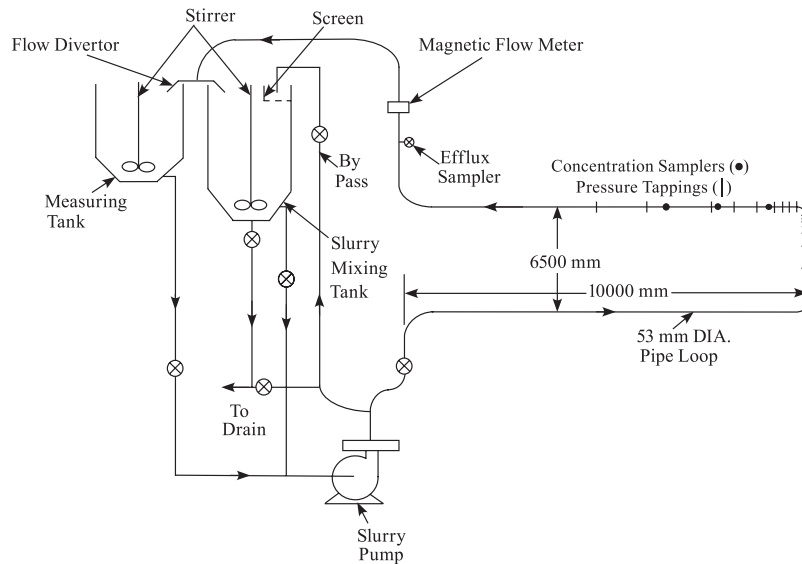


Fig. 1 Schematic diagram of pilot plant test loop.

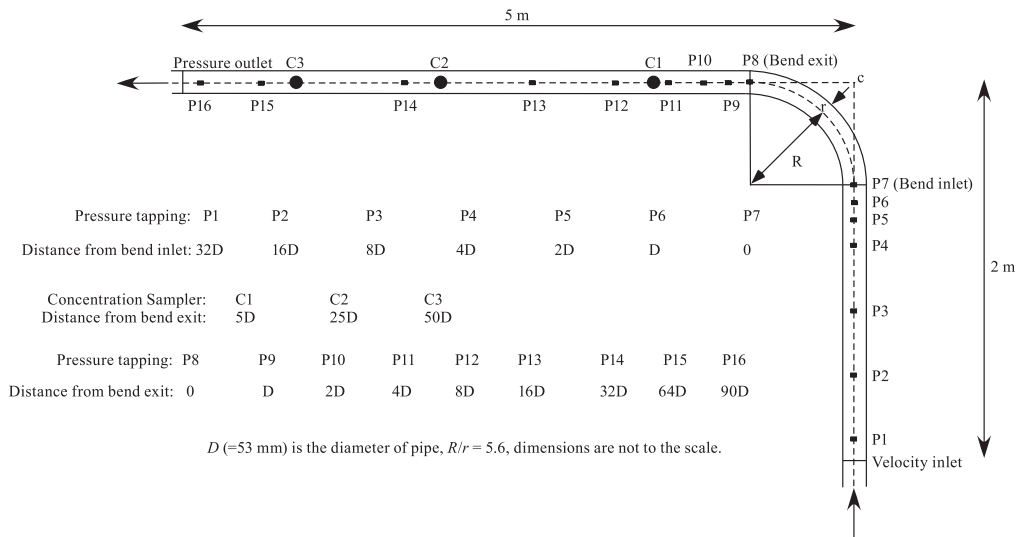


Fig. 2 Locations of pressure tapings and concentration samplers

was optimized after extensive trials to ensure smooth flow of slurry. The accuracy of the sampling tube is checked by integrating the measured concentration profile to obtain overall concentration and comparing it with the measured efflux concentration. An error included in the measurement was found to be $\pm 1\%$. This error may be attributed to the slip velocity between primary water phase and secondary silica sand or fly ash phase. The bend geometry used in the simulations was identical to that of bend used in experiments. The bend was horizontally laid in (x, y) plane. In the present study, concentration samples are collected from six different locations for each experimental run by traversing the sampling probe in the mid-vertical plane of pipe cross-section located at $z' = 0.094, 0.189, 0.377, 0.566, 0.755$ and 0.943 , where

$z' = z/D$. Three sampling probes located at $5D, 25D$ and $50D$ from bend exit are used for collecting such concentration samples (**Fig. 2**). Overall volumetric concentrations α_s are experimentally measured for each run, where subscript “s” represents the slurry. The slurry samples are dried in oven and sieved to determine the concentrations of silica sand (α_{ss}) and flyash (α_f) considering $\alpha_s = \alpha_{ss} + \alpha_f$. A sieve of aperture diameter of 150 micron is used to separate out silica sand and flyash particles from each dried sample.

Two methods were applied for the flow rate measurement (measuring tank and electro-magnetic flow meter) in this study as shown in **Fig. 1**. Magnetic flow meter was also used in adjusting the flow velocity to the desired value. The accuracy of flow rate measurement by electro-

Table 1 Details of pipe bend used in the present study.

(a) R/r and length of bend		
Radius of curvature (R)	Radius ratio (R/r)	Length of pipe bend
148.4 mm	5.6	4.40 D
(b) Inside radius of pipe bend: $r = 26.5$ mm		
(c) D = Pipe diameter = 53 mm		
(d) $k_s = 0.15$ mm and $k_s/D = 0.0003$		

magnetic flow meters is of the order of $\pm 0.5\%$. The calibration of the meters was periodically checked for slurry flows at various concentrations using measuring tank.

Efflux sampler is used to monitor the efflux concentration as shown in **Fig. 1**. If we consider the concentration profile in vertical section of pipeline as uniform across the pipe cross-section and $V_{ss} = V_f = V_w = V_{sl} = V_m$, the efflux concentration (C_{vf}) of slurry may be defined as $C_{vf} = C_{ss} + C_f$, where C_{ss} and C_f is the efflux concentration of silica sand and flyash, respectively. C_{ss} and C_f may be mathematically defined as follows:

$$C_{ss} = \frac{1}{A} \int \alpha_{ss} dA \quad (1)$$

$$C_f = \frac{1}{A} \int \alpha_f dA \quad (2)$$

Experiments are carried out on rough bend of which geometric details are tabulated in **Table 1**. Specific gravity of silica sand and flyash is measured experimentally as 2.65 and 2.1, respectively. Silica sand and fly ash particles are having median diameter of 450 μm and 75 μm with geometric standard deviation of 1.15 and 1.10, critical deposition velocity of 1.5 m/s and 1.1 m/s, respectively. Mixtures having different silica sand:flyash ratios at a particular efflux concentration are prepared by mixing the silica sand and flyash in that ratio by volume.

3. Mathematical model

The ranges of Stokes number of particles and Dean number for the pipeline slurry flows carried out in the present study are 0.02 to 2.0 and 33385 to 59152, respectively. The mathematical model implemented is described in Kaushal et al. (2013) and given in Appendix A. Water, silica sand and fly ash are considered as three phases having different properties in the calculations. Water is considered as fluid and primary phase. Silica sand and fly ash are considered as granular and secondary phases with different concentration, particle size and mass densities. Momentum equations have been solved for each phase

separately. Other steps in computations are similar to that described in earlier work by Kaushal et al. (2013).

4. Modeling results

4.1 Pressure drop

The normalized pressure drops at different locations [$\Delta h/(V_m^2/2g)$, where, $\Delta h = \Delta p/(\rho_m g)$] are presented in **Fig. 3** and **4** for $C_{vf} = 8.82$ and 16.28 % for 70:30 silica sand:flyash ratio at $V_m = 1.78, 2.67$ and 3.56 m/s.

From **Fig. 3** and **4**, it is clear that the flow is slightly disturbed before and after the bend. The permanent pressure loss reduces with increase in V_m . This reduction is interpreted from the slope of the pressure drop line, upstream and downstream of the bend.

It is observed from **Fig. 3** and **4** that the pressure drop reduces as the amount of flyash increases. However, the decrease in pressure drop is negligible for amount of

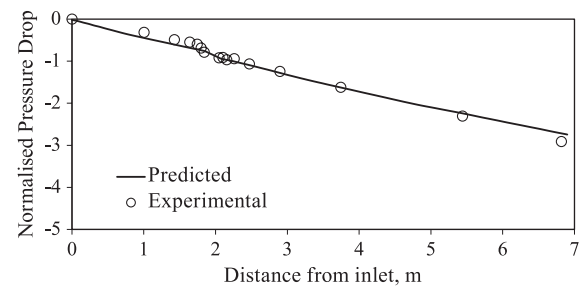
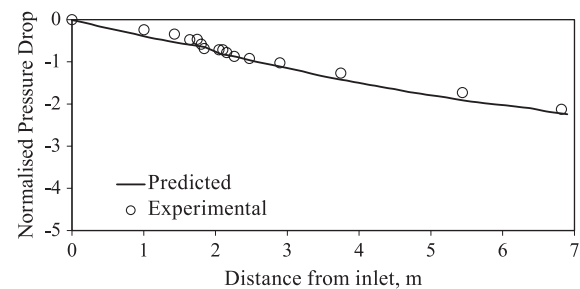
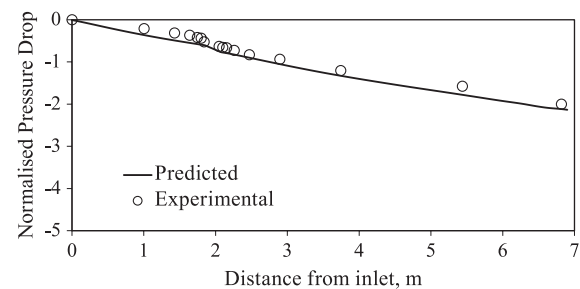
(a) $V_m = 1.78$ m/s(b) $V_m = 2.67$ m/s(c) $V_m = 3.56$ m/s

Fig. 3 Normalised Pressure drop [$\Delta p/(\rho_m V_m^2/2)$] distributions at different flow velocities at $C_{vf} = 8.82\%$ (sand:fly-ash = 70:30).

flyash more than 30 %.

Ito (1960) has shown that to establish permanent pressure loss across a bend, considerable lengths of the pipe on both sides of the bend have to be included and this is shown schematically in **Fig. 5** as described below:

- A-B-C-D-E shows the actual hydraulic gradient.
- A-B'-C'-D'-E' shows hydraulic gradient in a corresponding straight pipe.

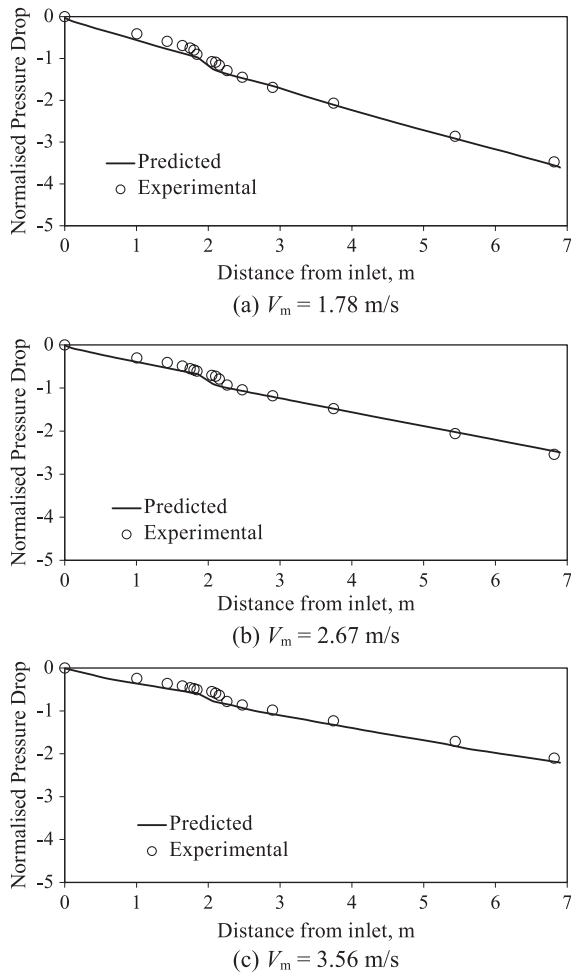


Fig. 4 Normalised Pressure drop $[\Delta p/(\rho_m V_m^2/2)]$ distributions at different flow velocities at $C_{vf} = 16.28\%$ (sand:flyash = 70:30).

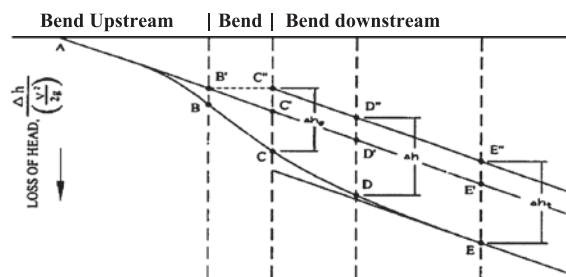


Fig. 5 Typical hydraulic gradient in pipe flow in the presence of bend.

iii. A-B'-C''-D''-E'' shows hydraulic gradient without pipe bend or when the pipe bend is removed. It is clear from these hydraulic grade lines that total head loss across the pipe bend is Δh_t .

iv. The total bend loss coefficient (k_t) is defined as

$$k_t = \frac{\Delta h_t}{\left(\frac{V_m^2}{2g}\right)} \quad (3)$$

The measured and simulated bend loss coefficients (k_t) are evaluated for each run as and are shown graphically in **Fig. 6** and **7** for $C_{vf} = 8.82\%$ and 16.28% as a function

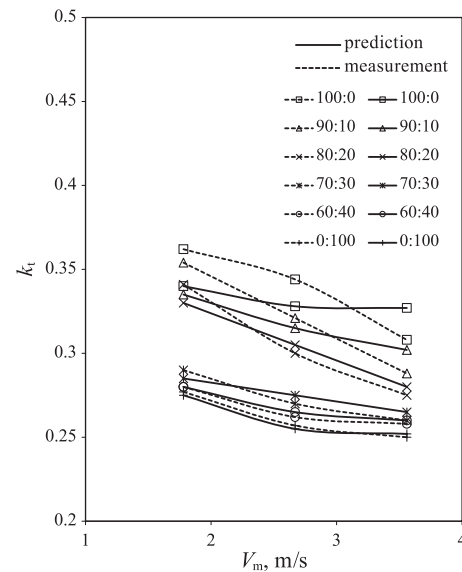


Fig. 6 Measured and predicted bend loss coefficient (k_t) at $C_{vf} = 8.82\%$ for various sand:flyash ratios.

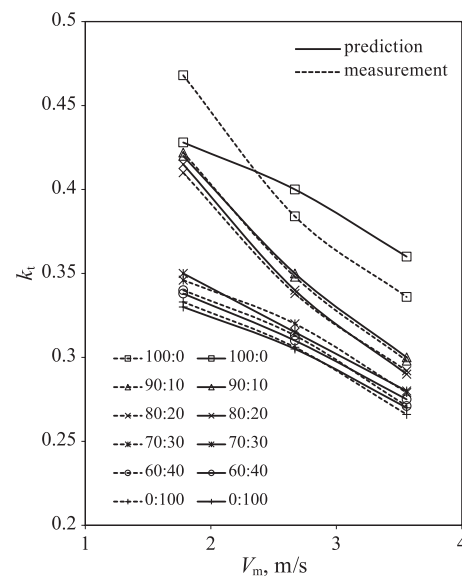


Fig. 7 Bend loss coefficient (k_t) at $C_{vf} = 16.28\%$ for various sand:flyash ratios.

of V_m at different mix proportions. It is observed that value of k_t increases as C_{vf} increases. Value of k_t reduces as flow velocity increases for all sand:flyash ratios and efflux concentrations. However, the rate of this reduction decreases with increase in amount of flyash. A reduction in total bend loss coefficient is seen with increase in the flyash mixed in the bi-modal slurry up to 70:30. However, further increase in flyash do not show any significant change in the value of k_t . The uniform distribution of fine

particles, that is flyash, across the pipe for the bi-modal slurry provides a uniform suspension of increased viscosity for the coarse particles. This uniform suspension of finer particles provides better suspension to coarse particles resulting into the reduced pressure drop. At the lowest velocity, appreciably high value of k_t is obtained for all the mix proportions when compared to that obtained at lower concentration. **Fig. 6** and **7** also show that the CFD modeling gives good predictions with error of $\pm 10\%$.

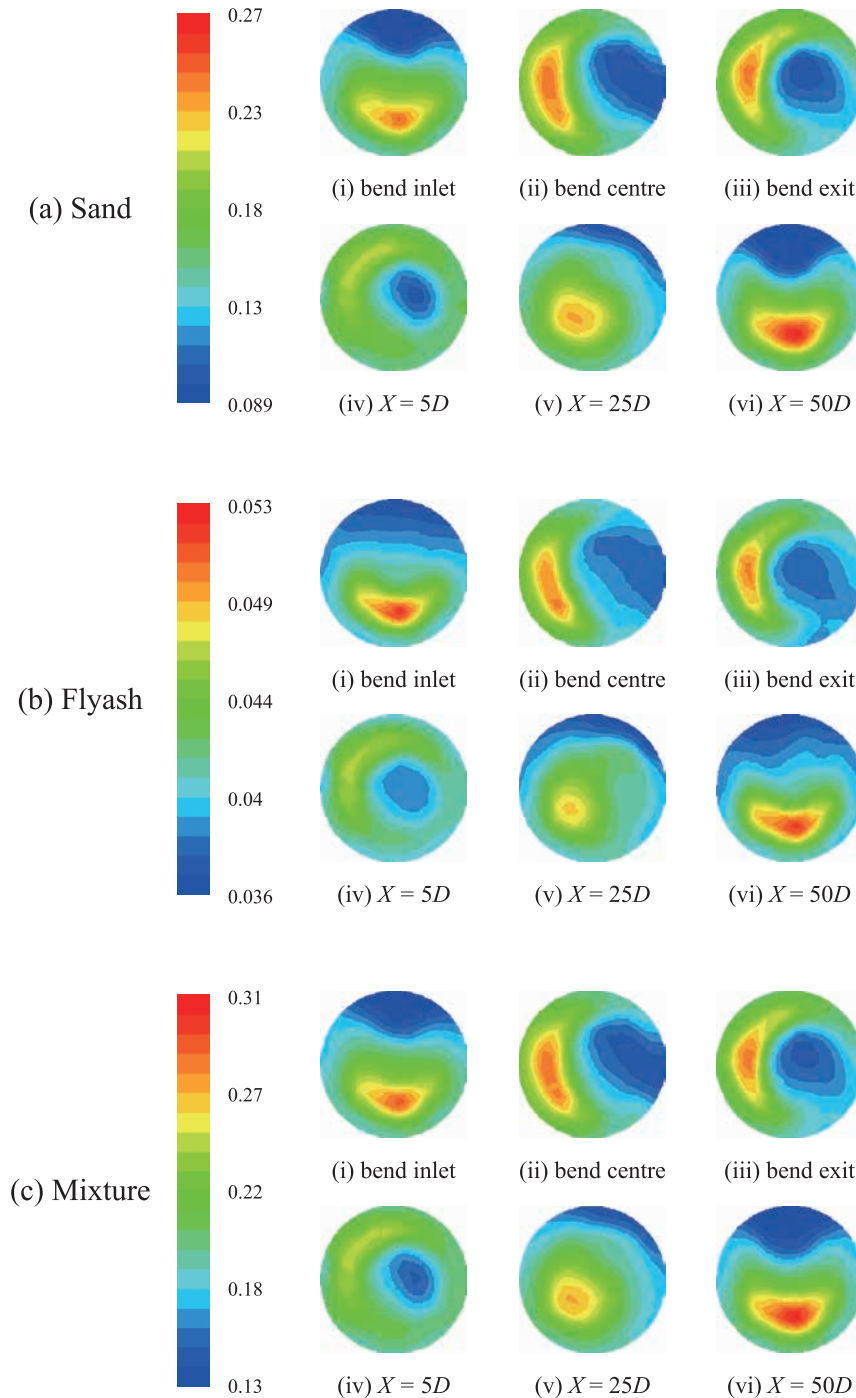


Fig. 8 Cross-sectional concentration distributions of (a) α_{ss} , (b) α_f and (c) α_s in fraction at different locations for sand:flyash = 70:30 at $V_m = 3.56$ m/s and $C_{vf} = 16.28\%$.

In the present study, the turbulent viscosity at bend outlet is 0.151, 0.268 and 0.305 kg/m-s for $C_{vf} = 16.28\%$ at $V_m = 1.78, 2.67$ and 3.56 m/s, respectively. Turbulent viscosity at bend outlet is 0.056, 0.230 and 0.307 kg/m-s for $C_{vf} = 8.82\%$ at $V_m = 1.78, 2.67$ and 3.56 m/s, respectively.

4.2. Concentration distribution

Cross-sectional concentration distributions of silica sand (α_{ss}), flyash (α_f) and mixture (α_s) for different silica sand:flyash ratios are calculated using CFD based FLUENT (2006) software. One of such concentration distributions α_{ss} , α_f and α_s for silica sand:flyash ratio of 70:30 at $C_{vf} = 16.28\%$ and $V_m = 3.56$ m/s is shown in **Fig. 8(a)**, **(b)** and **(c)** for silica sand, fly ash and mixture, respectively. The particles are forced outwards in the vicinity of bend due to the interaction of centrifugal force and pressure driven secondary flows. In a curved flow, there appears a centrifugal force and in order to balance this force pressure increases outward. However, near the wall, fluid velocity is negligibly small and there appears pressure driven flow near the wall inward, thus, secondary flow appears.

Flyash particles are forced outwards along with the silica sand particles (**Fig. 8**). However, Nasr-El-Din and Shook (1987) observed experimentally that coarser particles (0.45 mm diameter) moving towards the outer and finer particles moving towards the inner edge for long radius bend.

The concentration profiles at bend inlet, $X = 25D$ and $50D$ shows maximum concentration away from bottom of

the pipeline at lower velocities for lower concentration and at all velocities for higher concentration. In **Fig. 9**, distributions of v_{fz} , v_{sz} and v_{ssz} in m/s at $C_{vf} = 16.28\%$ and $V_m = 3.56$ m/s are shown. The effect of bend on velocity profiles is more prominent at $X = 5D$. The observations made previously in **Fig. 8** are reaffirmed in **Fig. 10** showing the z-component of velocity for sand, flyash and water. In this figure, very low values of $v_{fz}(x, y)$, $v_{sz}(x, y)$ and $v_{ssz}(x, y)$ at $X = 50D$ indicate vanishing of the secondary flows.

Fig. 11 depicts the direction and magnitude of velocity component in the perpendicular plane for $C_{vf} = 16.28\%$ and $V_m = 3.56$ m/s at $X = 5D, 25D$ and $50D$. This figure reaffirms the observations in earlier figures.

Figs. 12 to 17 present concentration profiles at $X = 5D, 25D$ and $50D$ from bend outlet at $V_m = 1.78, 2.67$ and 3.56 m/s and $C_{vf} = 8.82\%$ and 16.28% . Normalized concentration is defined as $\frac{\alpha_{ss}(z')}{C_{ss}}$ for silica sand, $\frac{\alpha_f(z')}{C_f}$ for flyash and $\frac{\alpha_s(z')}{C_{vf}}$ for overall slurry. **Figs. 12 to 17** shows good resemblance in experimental and CFD values.

Concentration profiles of sand in bimodal (sand:flyash = 70:30) slurry at $C_{vf} = 8.82\%$ and 16.28% are shown in **Fig. 18 to 21**. It is observed that spread in the solids concentration profiles is the least at $X = 5D$ and the particles are occupied in the entire cross-section of the pipeline. However, the spread in solids concentration profile increases with increasing X to the extent that solids concentration becomes zero at topmost zone in the pipeline at $X = 25D$ and $50D$. Furthermore, this area of occupancy by

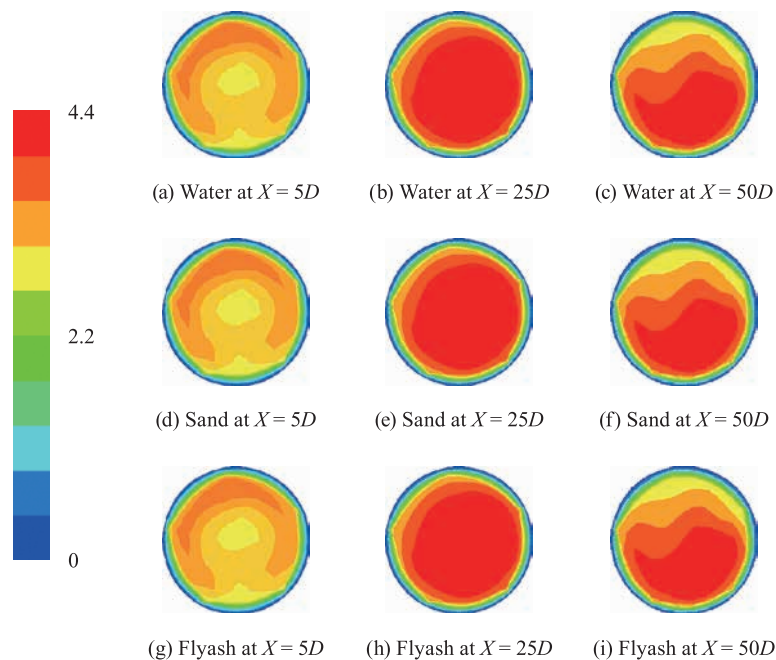


Fig. 9 Distributions of v_{fz} , v_{sz} and v_{ssz} in m/s at $C_{vf} = 16.28\%$ and $V_m = 3.56$ m/s.

particles increases with increase in velocity of flow.

Fig. 19 shows predicted mid-vertical concentration profiles of sand, in monodispersed (sand:flyash = 100:0) slurry measured by Kaushal et al. (2013) and in bimodal slurry (sand:flyash = 70:30) at different X and V_m at $C_{vf} = 8.82\%$. Asymmetry in the concentration profiles for bi-modal slurry is less. Such a reduction in asymmetry may be attributed to the uniform distribution of flyash across the pipe in the bi-modal slurry, which provides a uniform suspension of increased viscosity and less asymmetric mid-vertical solids concentration profile for the coarse particles. **Figs. 20** and **21** reaffirms the fact that re-distribution of solid particles takes place downstream of the bend. This effect decays with increase in distance from bend.

5. Conclusions

Following conclusions are drawn the present study:

- Pressure drop for bi-modal mixture of silica sand and flyash having particle diameter $450\ \mu\text{m}$ and $75\ \mu\text{m}$, respectively, is found to be less than that of mono-dispersed (silica sand) slurry flow. In bi-modal slurry flow, the bend loss coefficient (k_t) decreases with increase in percentage of flyash up to silica sand:flyash ratio of 70:30. Further increase in flyash does not show any significant change in the value of k_t .
- CFD based Eulerian two-phase model predicts pressure drops with fair accuracy (within percentage error of $\pm 10\%$) for the flow of bi-modal slurry in the efflux concentration upto 16.28% at flow velocities ranging from 1.78 to $3.56\ \text{m/s}$.

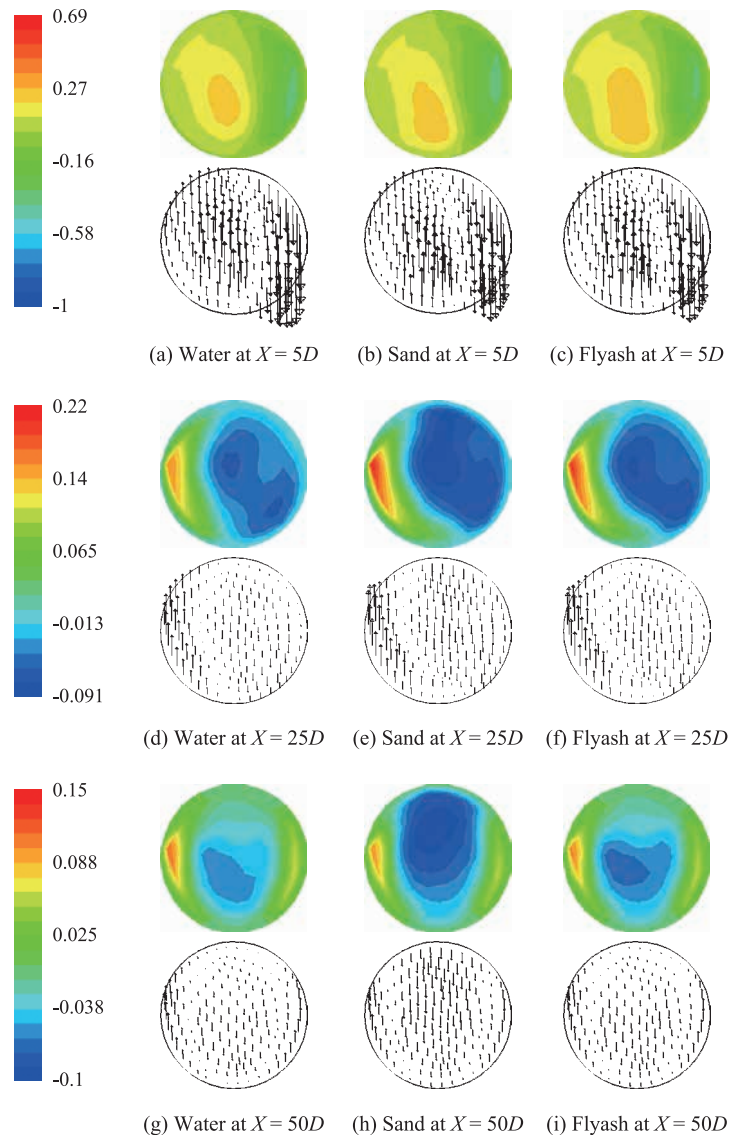


Fig. 10 Vertical velocity $v_{fz}(x, y)$, $v_{sz}(x, y)$ and $v_{ssz}(x, y)$ at different locations for sand:flyash = 70:30 in m/s for $C_{vf} = 16.28\%$ and $V_m = 3.56\ \text{m/s}$.

- c. Concentration profiles become uniform in the downstream of bend near the bend exit.
- d. The uniform distribution of fine particles across the pipe for the bi-modal slurry provides a uniform suspension of increased viscosity for the coarse particles. This uniform suspension of finer particles provides better suspension to coarse particles, which in turn make the re-distribution of particles after the bend exit at a much faster rate.
- e. Redistribution of particles take place in the downstream of the bend. The effect of bend is seen in the downstream of bend near the exit, and this effect decays with increase in distance.
- f. Asymmetry in the mid-vertical solids concentration profiles for bi-modal (sand:flyash = 70:30) is less than the mono-dispersed (sand:flyash = 100:0) particulate slurry.
- g. More work needs to be performed to expand the CFD based Eulerian two-phase model for more complex slurries containing particles with broad or multimodal size distributions. Also work should be done to determine how best to deal with slurries containing different species of particles with multiple densities.

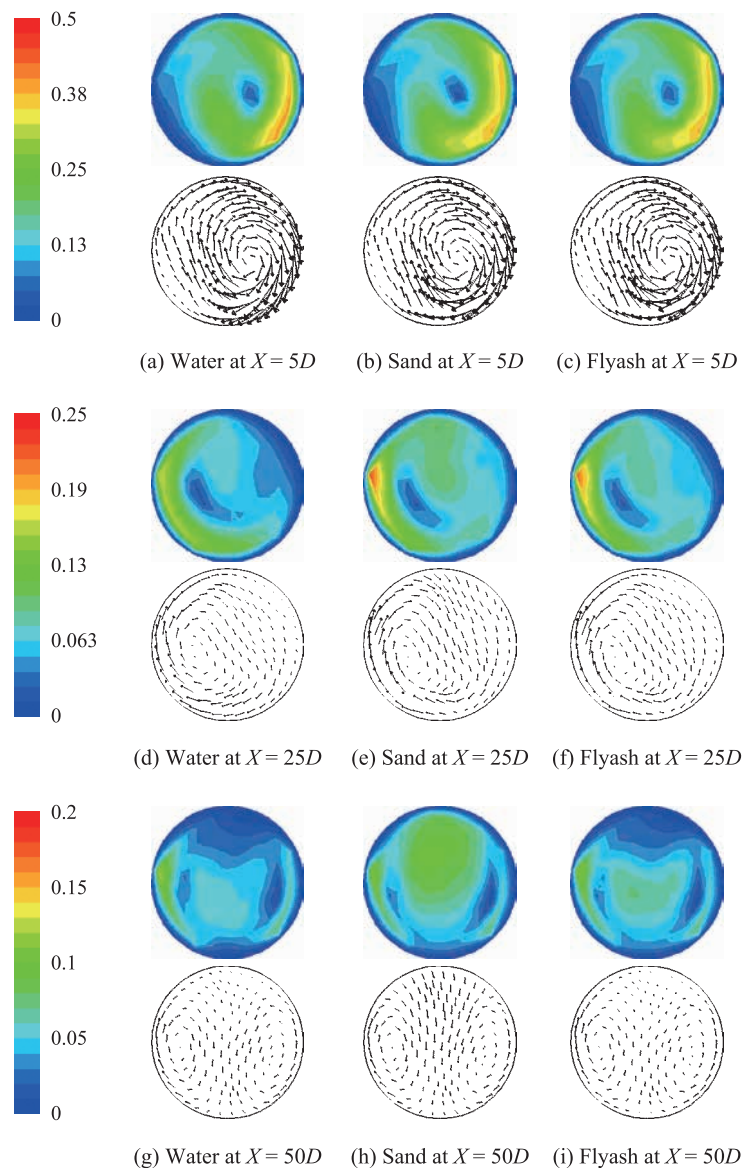


Fig. 11 Perpendicular velocity component at different locations for sand:flyash = 70:30 in m/s for $C_{vf} = 16.28\%$ and $V_m = 3.56$ m/s.

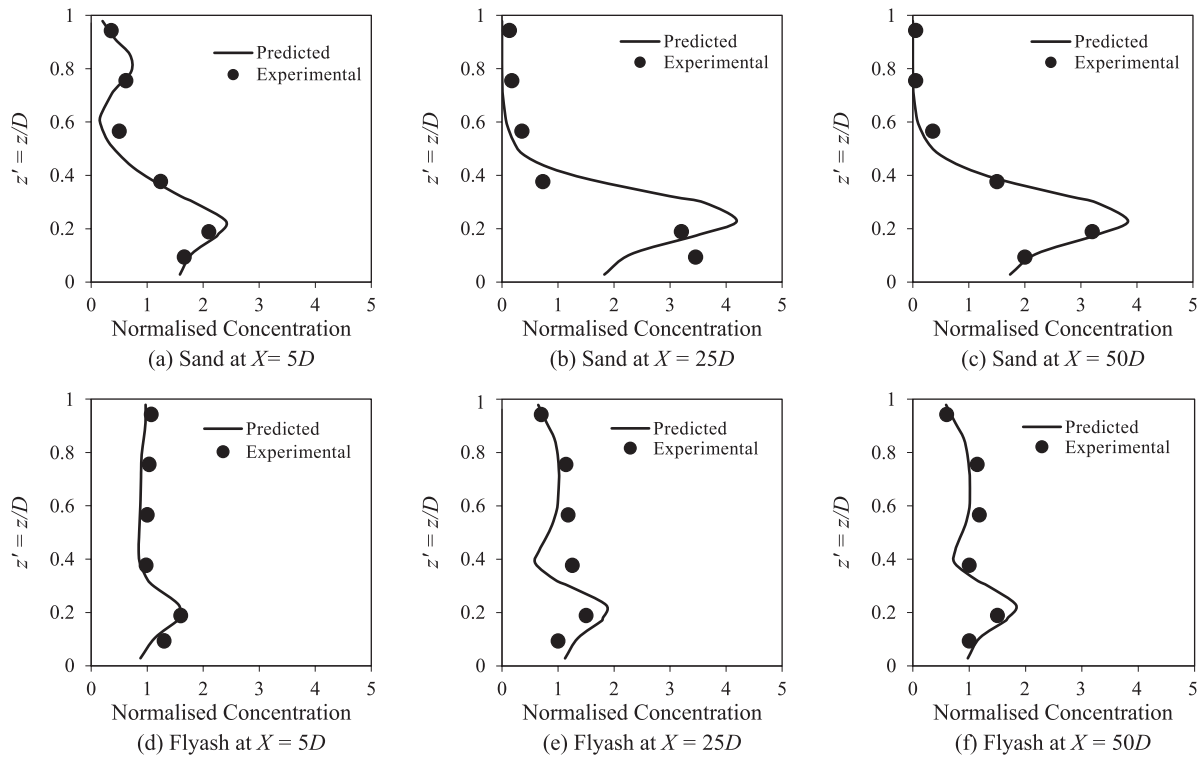


Fig. 12 Concentration distributions at $C_{vf} = 8.82\%$ (sand:flyash = 70:30) and $V_m = 1.78$ m/s (Normalised Concentration for sand = $\alpha_s(z')/C_{ss}$) and Normalised Concentration for fly ash = $\alpha_f(z')/C_f$).

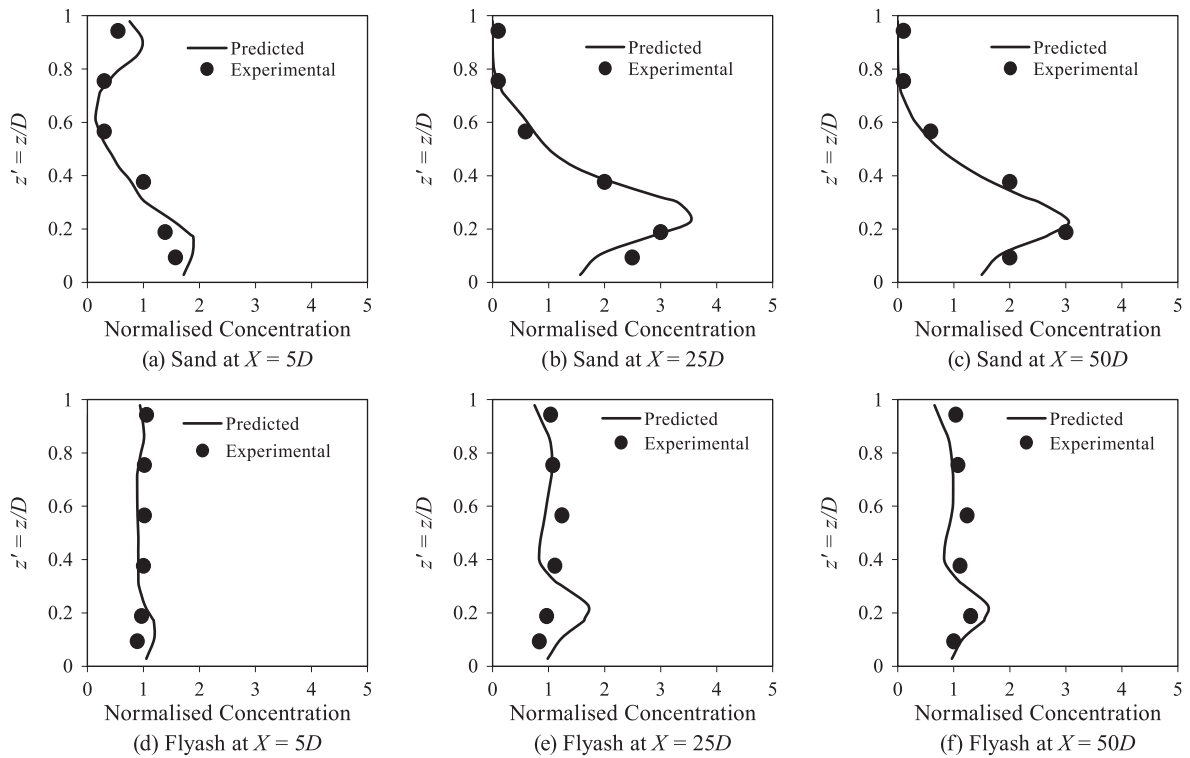


Fig. 13 Concentration distributions at $C_{vf} = 8.82\%$ (sand:flyash = 70:30) and $V_m = 2.67$ m/s (Normalised Concentration for sand = $\alpha_s(z')/C_{ss}$) and Normalised Concentration for fly ash = $\alpha_f(z')/C_f$).

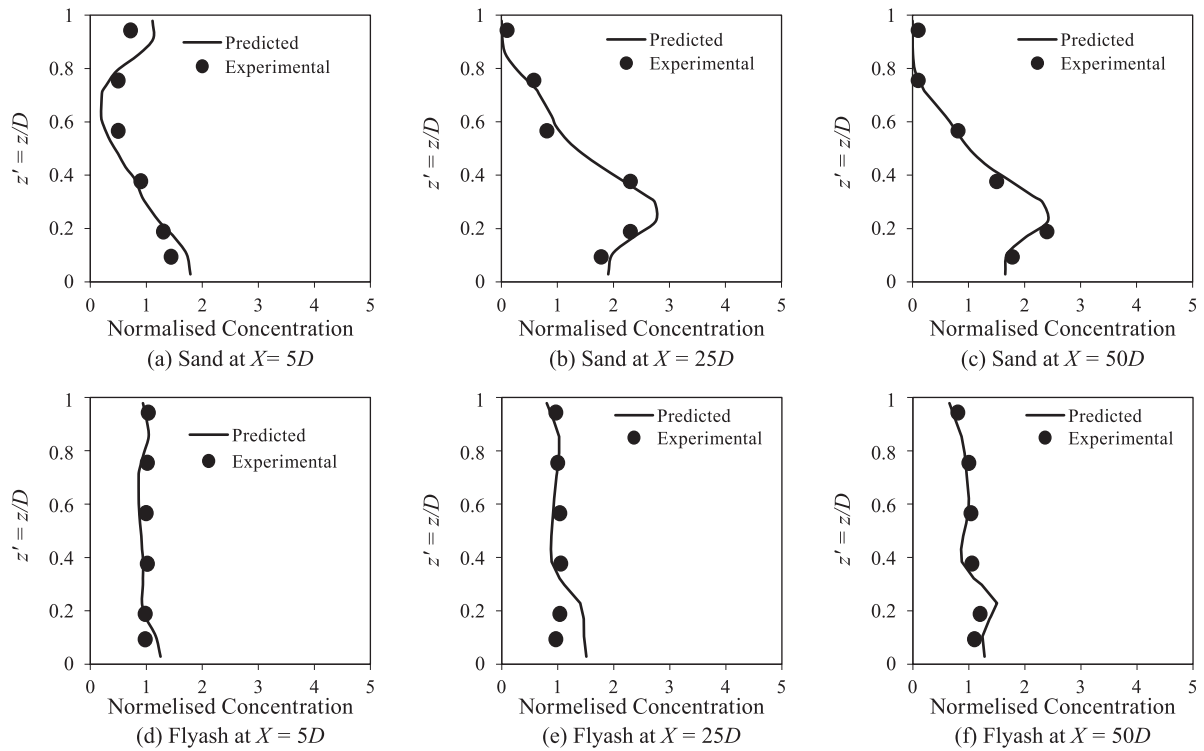


Fig. 14 Concentration distributions at $C_{vf} = 8.82\%$ (sand:flyash = 70:30) and $V_m = 3.56$ m/s (Normalised Concentration for sand = $\alpha_s(z')/C_{ss}$ and Normalised Concentration for fly ash = $\alpha_f(z')/C_f$).

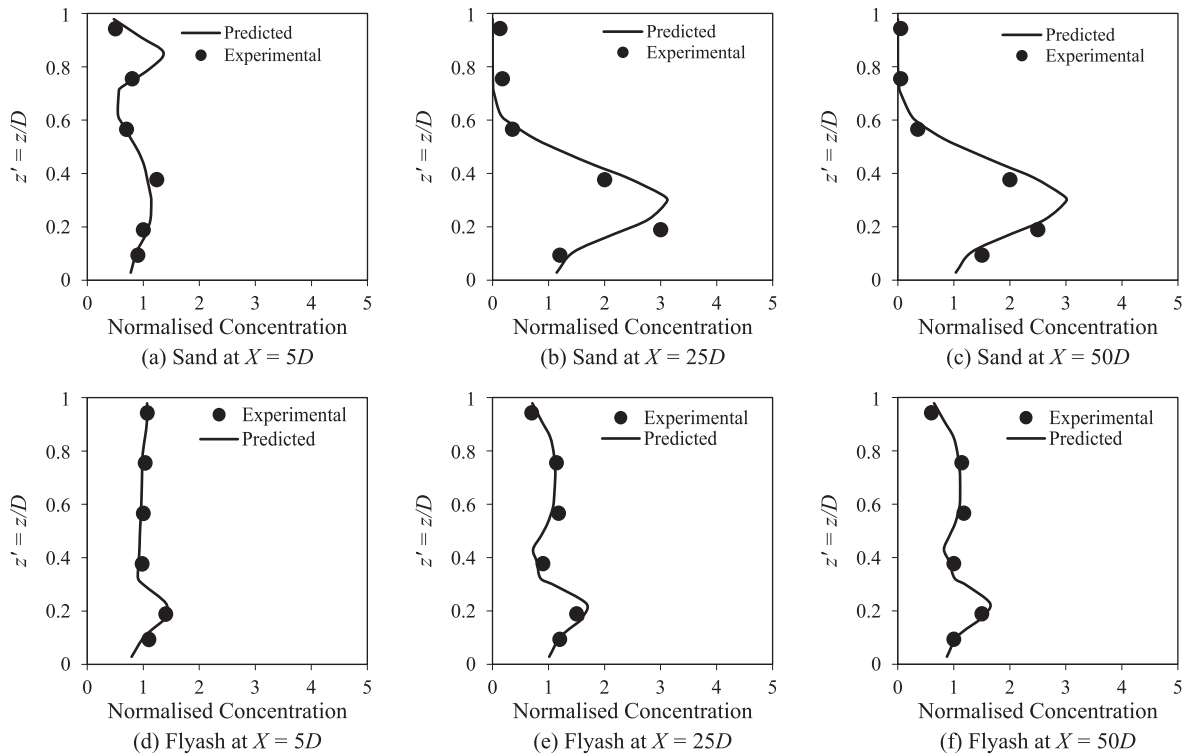


Fig. 15 Concentration distributions at $C_{vf} = 16.28\%$ (sand:flyash = 70:30) and $V_m = 1.78$ m/s (Normalised Concentration for sand = $\alpha_s(z')/C_{ss}$ and Normalised Concentration for fly ash = $\alpha_f(z')/C_f$).

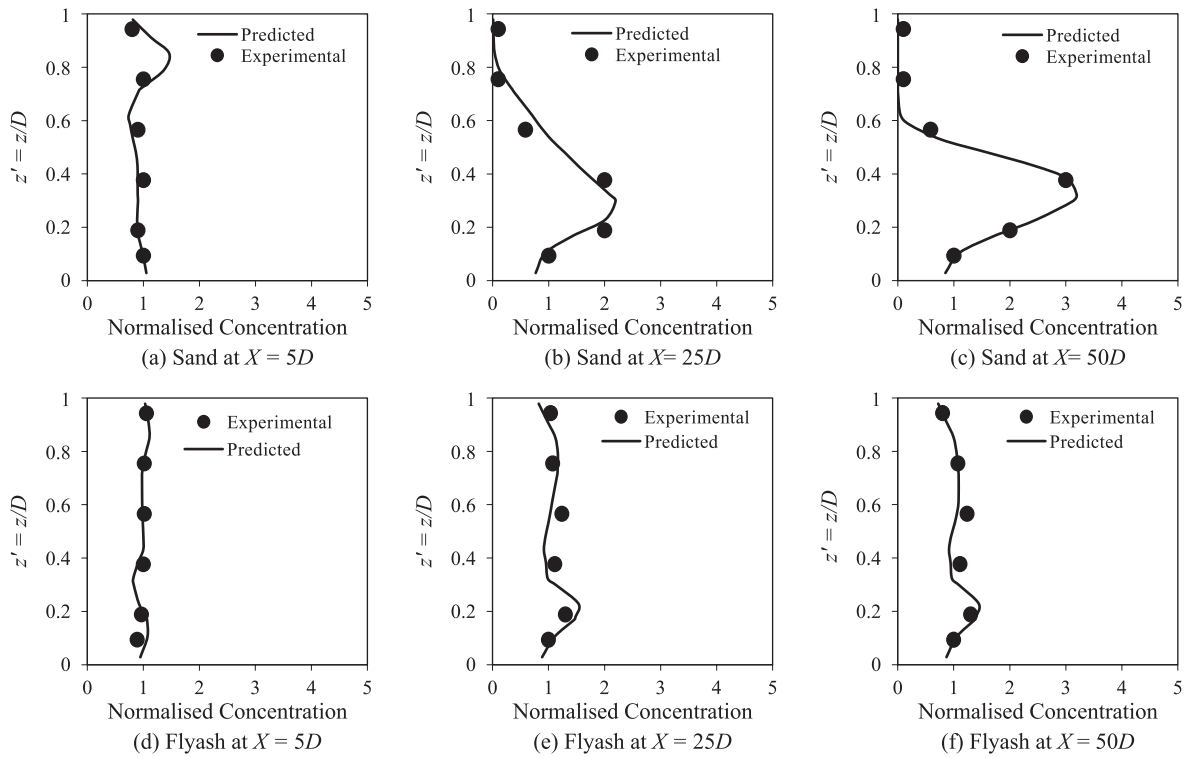


Fig. 16 Concentration distributions at $C_{vf} = 16.28\%$ (sand:flyash = 70:30) and $V_m = 2.67$ m/s (Normalised Concentration for sand = $\alpha_s(z')/C_{ss}$) and Normalised Concentration for fly ash = $\alpha_f(z')/C_f$).

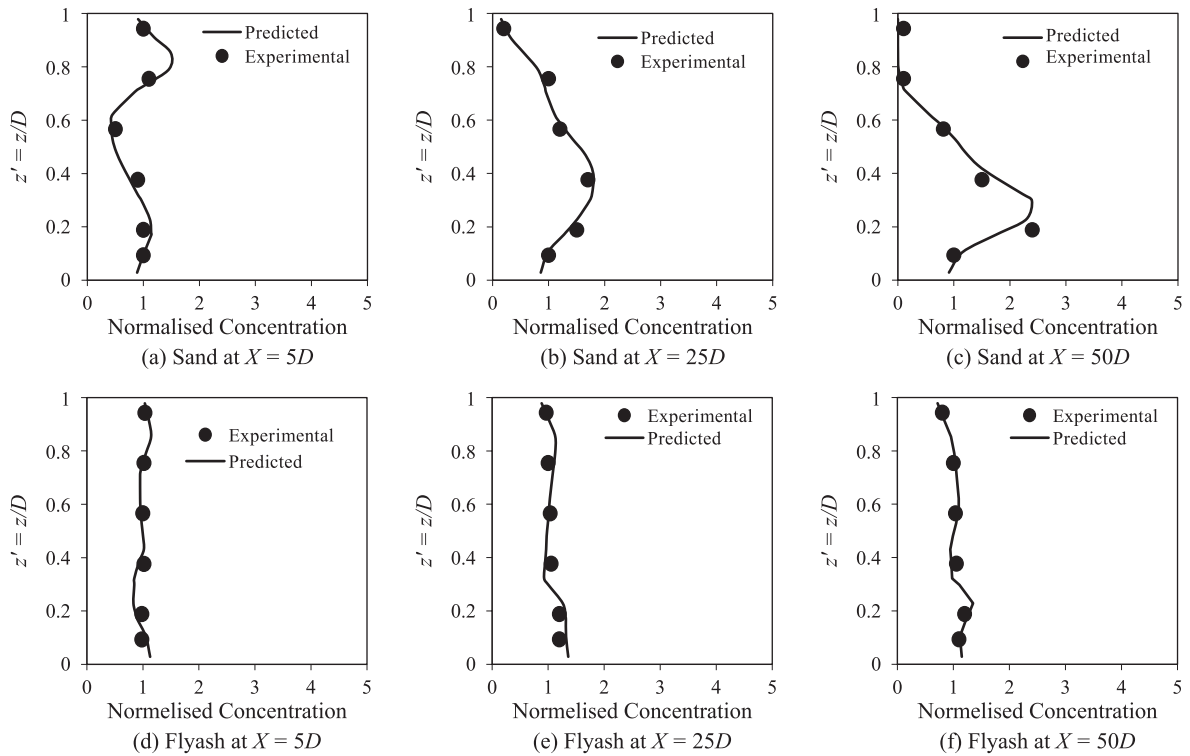


Fig. 17 Concentration distributions at $C_{vf} = 16.28\%$ (sand:flyash = 70:30) and $V_m = 3.56$ m/s (Normalised Concentration for sand = $\alpha_s(z')/C_{ss}$) and Normalised Concentration for fly ash = $\alpha_f(z')/C_f$).

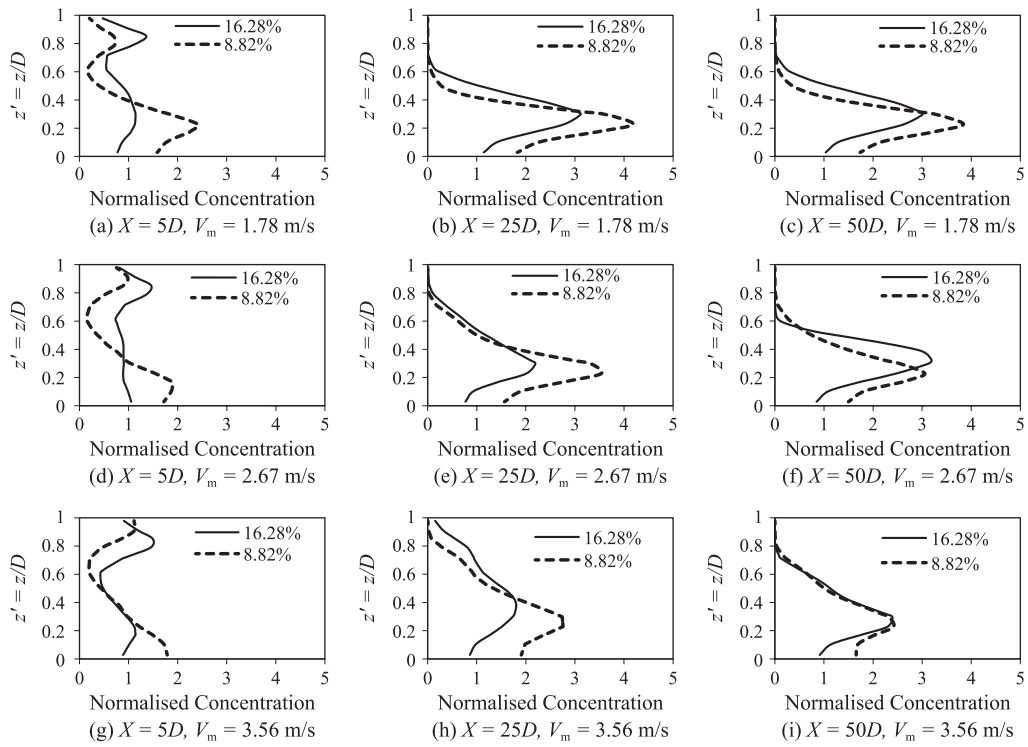


Fig. 18 Predicted mid-vertical concentration profiles of sand at different X and V_m for sand:flyash = 70:30 at $C_{vf} = 8.82\%$ and 16.28% (Normalised Concentration = $\alpha_s(z')/C_{ss}$).

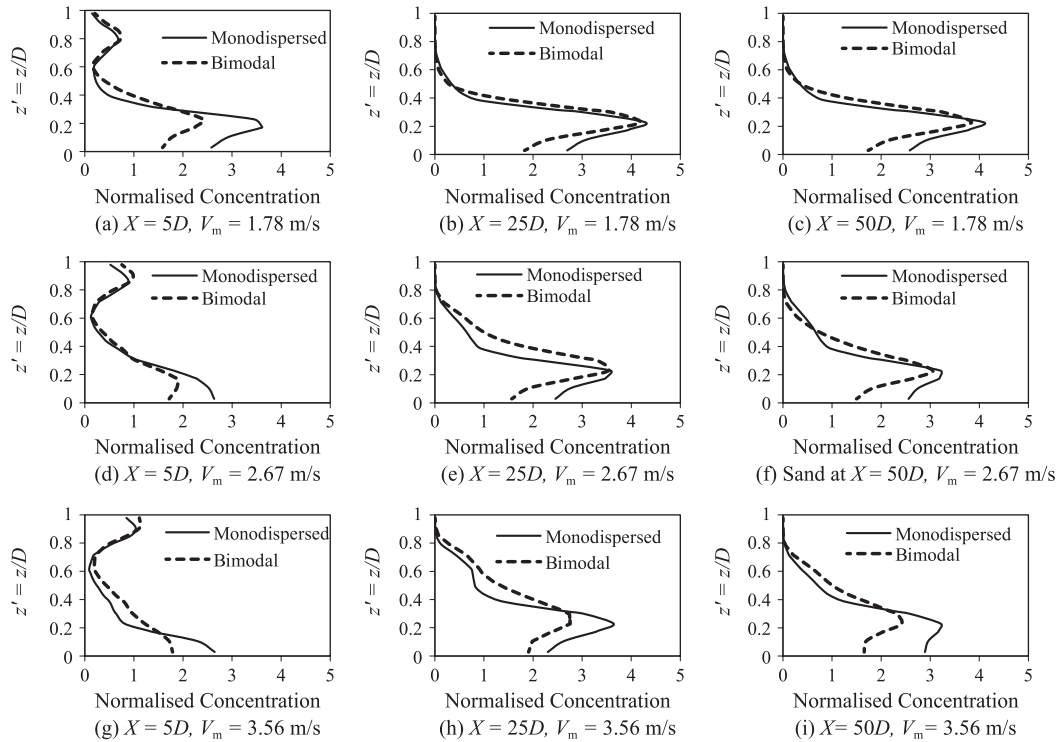


Fig. 19 Predicted mid-vertical concentration profiles of sand in monodispersed and bimodal (sand:fly-ash = 70:30) slurry at different X and V_m at $C_{vf} = 8.82\%$ (Normalised Concentration = $\alpha_s(z')/C_{ss}$).

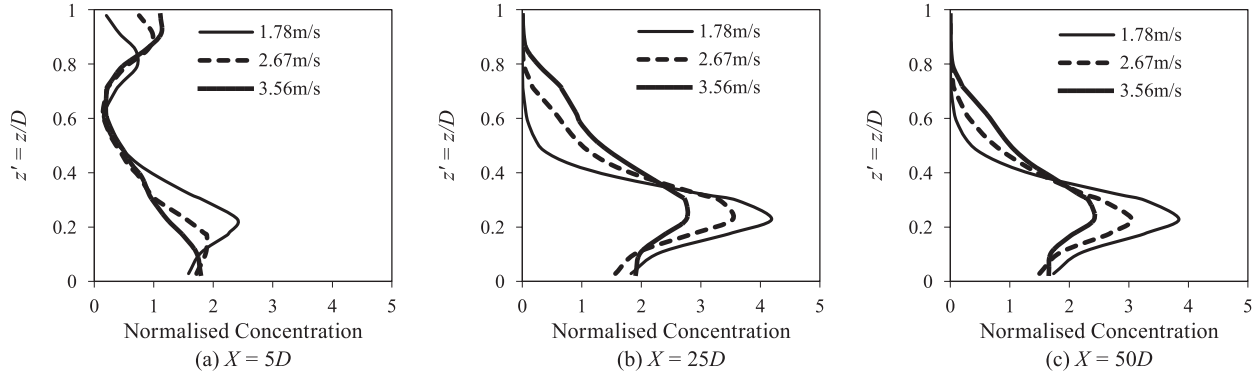


Fig. 20 Concentration profile of sand for sand:flyash = 70:30 at $C_{vf} = 8.82\%$ (Normalised Concentration = $\alpha_s(z')/C_{ss}$).

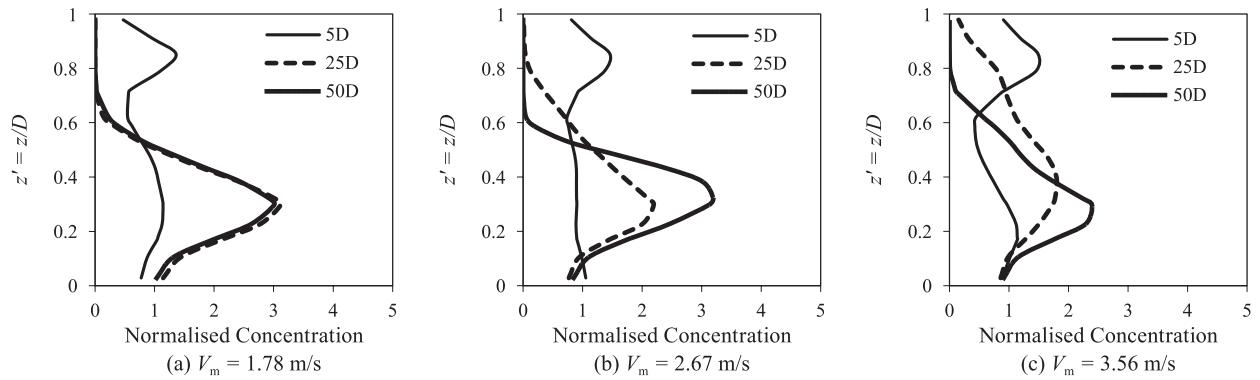


Fig. 21 Concentration profiles of sand for sand:flyash = 70:30 at $C_{vf} = 16.28\%$ (Normalised Concentration = $\alpha_s(z')/C_{ss}$).

Nomenclature

D	internal diameter of pipeline (mm)
d_{mean}	mean diameter of particles (μm)
z	distance from bottom of the pipe (mm)
α_s	overall concentration of slurry (–)
α_{ss}	concentration of silica sand (–)
α_f	concentration of flyash (–)
V_{ss}	velocity of silica sand (m/s)
V_f	velocity of flyash (m/s)
V_w	velocity of water (m/s)
V_{sl}	velocity of slurry (m/s)
V_m	mean flow velocity (m/s)
C_{vf}	efflux concentration of slurry (–)
C_{ss}	efflux concentration of silica sand (–)
C_f	efflux concentration of flyash (–)
A	pipe cross-sectional area (m^2)
Δp	pressure drop with reference to the velocity inlet (Pa)
ρ_m	density of the flowing fluid (Kg/m^3)
g	acceleration due to gravity (m/s^2)
Δh_t	total head loss across the pipe bend (m)

k_t	bend loss coefficients (–)
k	turbulent kinetic energy (m^2/s^2)
ε	turbulent dissipation rate (m^2/s^3)
K_{sf}	inter-phase drag coefficient (–)
\bar{v}_s	velocity of solid phase (m/s)
\bar{v}_f	velocity of fluid phase (m/s)
C_L	lift coefficient taken as 0.5 in the present study (–)
∇P_s	solid pressure gradient (Pa)
∇P	static pressure gradient (Pa)
C_{vm}	coefficient of virtual mass force taken as 0.5 in the present study (–)
τ_f	stress tensor for fluid (Pa)
τ_s	stress tensors for solid (Pa)
λ_s	bulk viscosity of the solids (Pa.s)
d_s	particle diameter put as $440\ \mu\text{m}$ for silica sand and $75\ \mu\text{m}$ for flyash (μm)
$g_{o,ss}$	radial distribution function (–)
$\alpha_{s,\text{max}}$	static settled concentration measured as 0.52 and 0.50 for sand and flyash particles, respectively (–)
Θ_s	granular temperature (Pa)
e_{ss}	restitution coefficient (–)

μ_f	shear viscosity of fluid (Pa.s)
μ_s	shear viscosity of solids (Pa.s)
R	radius of curvature of pipe bend (mm)
r	internal radius of pipeline (mm)
k_s	pipe roughness (mm)

References

- Ahmed M., Singh S.N., Seshadri V., Pressure drop in a long radius 90° horizontal bend for the flow of multi-sized heterogeneous slurries, *International Journal of Multiphase Flow*, 1994 (21) 329–334.
- Boothroyde J., Jacobs B.E.A., Jenkins P., Coarse particle hydraulic transport, *Proceedings Hydrotransport, BHRA Fluid Engineering, Cranfield, Bedford, England*, 6 (1979), 405–428.
- FLUENT 6.3.26 User's Guide, Chapter 23: Modelling Multiphase Flows, Fluent Incorporation, USA, 2006.
- Gidaspow D., Bezburuah R., Ding J., Hydrodynamics of circulating fluidized beds, kinetic theory approach in fluidization VII, *Proc. 7th Engineering Foundation Conference on Fluidization*, 1992.
- Gopaliya M.K., Kaushal D.R., Analysis of Effect of Grain Size on Various Parameters of Slurry Flow through Pipeline Using CFD, *Particulate Science and Technology: An International Journal*, 33 (2015) 369–384.
- Gopaliya M.K., Kaushal D.R., Modeling of sand-water slurry flow through horizontal pipe using CFD, *J. Hydrol. Hydromech.*, 64 (2016) 261–272.
- Gupta R., Singh S.N., Seshadri V., Migration of solid particles in the heterogeneous slurry flow through a 90° bend, *Indian Journal of Engineering and Material Science*, 4 (1997) 10–20.
- Hayashi H., Sampei T., Oda S., Ohtomo S., Some Experimental Studies on Iron Concentrate Slurry Transportation in Pilot Plant, *Proceedings of Hydrotransport, BHRA Fluid Engineering, Cranfield, Bedford, England*, 7 (1980) D2.
- Ito H., Pressure losses in smooth pipe bends, *Journal of Basic Engineering, ASME*, 82 (1960) 131–140.
- Kaushal D.R., Thinglas T., Tomita Y., Kuchii S., Tsukamoto H., CFD Modeling for Pipeline Flow of Fine Particles at High Concentration, *Int. J. of Multiphase Flow*, 43 (2012) 85–100.
- Kaushal D.R., Kumar A., Tomita Y., Kuchii S., Tsukamoto H., Flow of mono-dispersed particles through horizontal bend, *Int. J. of Multiphase Flow*, 52 (2013) 71–91.
- Kazanskij B.H., Hinsch J., Influence of added fine particles on the flow structure and the pressure losses in sand-water mixture, *Proceedings of Hydrotransport, BHRA Fluid Engineering, Colorado, USA*, 3 (1974) 11–21.
- Kumar A., Kaushal D.R., Kumar U., Bend Pressure Drop Experiments compared with FLUENT, *Institution of Civil Engineers journal of Engineering and Computational Mechanics*, Thomas Telford Publication London, 161 (2008) 35–42.
- Kumar A., Experimental and CFD modeling of hydraulic and pneumatic conveying through pipeline, Ph.D. Thesis, Indian Institute of Technology Delhi, 2010.
- Lun C.K.K., Savage S.B., Jeffrey D.J., Chepurniy N., Kinetic theories for granular flow: inelastic particles in couette flow and slightly inelastic particles in a general flow field, *Journal of Fluid Mechanics*, 140 (1984) 223–256.
- Messa G.V., Malavasi S., Numerical Prediction of Particle Distribution of Solid-Liquid Slurries in Straight Pipes and Bends, *Engineering Applications of Computational Fluid Mechanics*, 8 (2014) 356–372.
- Nasr-El-Din H., Shook C.A., Effects of 90° bend on slurry velocity and concentration distribution, *Journal of Pipelines*, 6 (1987) 239–252.
- Thinglas T., Kaushal D.R., Comparison of two dimensional and three Dimensional CFD Modeling of Invert Trap Configuration to be used in Sewer Solid Management, *Particology*, 6 (2008a) 176–184.
- Thinglas T., Kaushal D.R., Three Dimensional CFD Modeling for Optimization of Invert Trap Configuration to be used in Sewer Solid Management, *Particulate Science and Technology*, 26 (2008b) 507–519.
- Verkerk C.G., Transport of Fly Ash Slurries. *Proceedings of Hydrotransport, BHRA Fluid Engineering, Johannesburg, South Africa*, 8 (1982) 307–316.

Appendix A: Mathematical model

Two-phase Eulerian model adopted in present research assumes that the slurry comprises solid “so” and fluid “fl”. These phases are considered as separated but continuous and interpenetrating in such a way that $\alpha_{so} + \alpha_{fl} = 100\%$. These phases are made to satisfy continuity and momentum equations separately. Equations of fluid and solid phases were coupled using inter-phasic exchange coefficients and pressure. Different forces existing in the slurry flow are listed below.

1. Body forces, $\rho \vec{g}$
2. Drag force, $K_{sf}(\vec{v}_s - \vec{v}_f)$
3. Lift force, $C_L \alpha_s \rho_f (\vec{v}_f - \vec{v}_s) \times (\nabla \times \vec{v}_f)$
4. Pressure gradient for solid phase, ∇P_s
5. Static pressure gradient, ∇P
6. Virtual mass force: $C_{vm} \alpha_s \rho_f (\vec{v}_f \cdot \nabla \vec{v}_f - \vec{v}_s \cdot \nabla \vec{v}_s)$
7. Viscous forces, $\nabla \cdot \tau_f$

The continuity equation (equation A1) and momentum equations (equations A2 and A3) need to be satisfied by each phase separately. These equations are coupled using exchange coefficients and pressure (equations A4 and A5).

Continuity equation:

$$\nabla \cdot (\alpha_f \rho_f \vec{v}_f) = 0 \quad (A1)$$

Momentum equation for fluid phase:

$$\begin{aligned} \nabla \cdot \left(\alpha_f \rho_f \vec{v}_f \vec{v}_f \right) = & -\alpha_f \nabla P + \nabla \cdot \tau_f + \\ & \alpha_f \rho_f \vec{g} + K_{sf} \left(\vec{v}_s - \vec{v}_f \right) + \\ & C_{vm} \alpha_f \rho_f (\vec{v}_s \cdot \nabla \vec{v}_s - \vec{v}_f \cdot \nabla \vec{v}_f) \\ & + C_L \alpha_s \rho_f (\vec{v}_f - \vec{v}_s) \times (\nabla \times \vec{v}_f) \end{aligned} \quad (A2)$$

Momentum equation for solid phase:

$$\nabla \cdot \left(\alpha_s \rho_s \vec{v}_s \vec{v}_s \right) = -\alpha_s \nabla P - \nabla P_s + \nabla \cdot \boldsymbol{\tau}_s + \alpha_s \rho_f \vec{g} + K_{fs} \left(\vec{v}_f - \vec{v}_s \right) +$$

$$C_{vm} \alpha_s \rho_f (\vec{v}_f \cdot \nabla \vec{v}_f - \vec{v}_s \cdot \nabla \vec{v}_s) + C_L \alpha_s \rho_f (\vec{v}_s - \vec{v}_f) \times (\nabla \times \vec{v}_f)$$

$$\boldsymbol{\tau}_s = \alpha_s \mu_s \left(\nabla \vec{v}_s + \nabla \vec{v}_s^T \right) + \alpha_s \left(\lambda_s - \frac{2}{3} \mu_s \right) \nabla \cdot \vec{v}_s \boldsymbol{I} \quad (A4)$$

and

$$\boldsymbol{\tau}_f = \alpha_f \mu_f \left(\nabla \vec{v}_f + \nabla \vec{v}_f^T \right), \quad (A5)$$

Bulk viscosity of solids λ_s is proposed by Lun et al. (1984) as:

$$\lambda_s = \frac{4}{3} \alpha_s \rho_s d_s g_{o,ss} (1 + e_{ss}) \left(\frac{\Theta_s}{\pi} \right)^{\frac{1}{2}} \quad (A6)$$

Radial distribution function $g_{o,ss}$ is proposed by Gidaspow et al. (1992) as:

$$g_{o,ss} = \left[1 - \left(\frac{\alpha_s}{\alpha_{s,max}} \right)^{\frac{1}{3}} \right]^{-1} \quad (A7)$$

Granular temperature Θ_s is taken into account in the mathematical model by using transport equations as described by Kaushal et al. (2013).

Turbulence closure for the fluid and solid phase:

Turbulent quantities for the fluid and solid phase are calculated using RNG k - ε model and Tchen's theory, respectively, supplemented by additional terms accounting interfacial turbulent momentum transfer as described by Kaushal et al. (2013).

Wall function:

The region very near to the walls needs special attention. In this region, the flow parameters have very high gradients. This region is dealt with a very fine boundary layer meshing. Standard wall functions along with RNG k - ε model is used. Wall functions are semi-empirical formulas used for reducing the difficulty in calculation and better results close to the wall.

Boundary Conditions

There are three boundaries available in the given flow domain namely the inlet boundary, the wall boundary and the outlet boundary. Constant concentration and flow velocity were considered at the inlet boundary. A 0.15 mm of pipe wall roughness is adopted during simulation. Wall boundary conditions are adopted phase-wise: no slip for liquid phase and specularly co-efficient of 0.5 for solid phase. Pressure outlet boundary condition is adopted at the outlet boundary where mixture pressure is mentioned.

Solution Process and Convergence Criteria

The convergence criteria is decided on the basis of proper residual values for different parameters at the end of computation for better results. In the present study a residual value of 10^{-3} is set as convergence criteria. The solution was converged and computations were stopped in 1475 iterations for slurry flow with sand:flyash = 70:30 at $V_m = 3.56$ m/s and $C_{vf} = 16.28$ % through pipe bend. The actual values of the residuals at convergence for mass, u , v and w components of water, sand and flyash in x , y and z directions, k and ε for water and volume fractions of sand and flyash were 2.9024×10^{-4} , 9.1087×10^{-5} , 5.5728×10^{-6} , 3.0933×10^{-6} , 1.1206×10^{-5} , 3.3552×10^{-6} , 2.4197×10^{-6} , 1.2064×10^{-5} , 4.6818×10^{-6} , 3.1317×10^{-6} , 2.9304×10^{-4} , 9.9960×10^{-4} , 3.5810×10^{-4} and 2.6986×10^{-4} , respectively.

Author's short biography



Deo Raj Kaushal

Dr. D.R. Kaushal was trained to be a slurry pipeline designer during his Ph.D. at IIT Delhi and Post Doctoral Research at KIT Japan. He has been an Associate Professor of Hydraulics in Water Resources Engineering Section of Civil Engineering Department at IIT Delhi since 2004. He has visited KIT Japan and KCT Japan as visiting Professor. During his teaching and postdoctoral research, he has carried out several research and consultancy projects. He has worked with several mining, mineral-processing and production companies, either through direct consultation or through collaboration with other companies or research organizations.

Author's short biography



Arvind Kumar

Dr. A. Kumar is currently Professor in Mechanical Engineering Department at YMCA University of Science and Technology, Faridabad (Haryana) India. He obtained his B.Tech. (Mechanical Engg.) from AMU, Aligarh and M.Tech. and PhD From Indian Institute of Technology Delhi, India. He is having 25 years Teaching, Research and Industrial experience. His areas of specialization include Computational Fluid Dynamics, Multiphase flow, Slurry flow in pipeline system. Energy efficiency and energy management in thermal system, heat transfer, Refrigeration and Air-conditioning.



Yuji Tomita

Prof. Yuji Tomita was born in Dalian, China in 1942. From 1970 to 2006, he has been working at Kyushu Institute of Technology in the mechanical engineering department. He taught fluid mechanics and powder technology. His research topics include fluid drag reduction, pipeline conveying of solids by pneumatic, slurry and capsule method, performance characteristics of blow-tank solids conveyor, rotary and injection feeders, flushing phenomena of fine powder by compression and vibration, and air entrainment by free falling powder jet.



Shigeru Kuchii

Prof. Shigeru Kuchii is a Professor from Department of Creative Engineering, National Institute of Technology (NIT), Kitakyushu College. He received the B.S, M.S and Ph D. degrees all in Mechanical Engineering from Kyushu Institute of Technology, Japan. He is working on research topic in Powder Technology, Mechanical Engineering, Mechatronics and Information Technology.



Hiroshi Tsukamoto

Prof. Hiroshi Tsukamoto is the President of National Institute of Technology, Kitakyushu College. After receiving the Ph.D. degree from the University of Tokyo, Tokyo, Japan, he was a Lecturer in the Department of Mechanical Engineering, University of Tokyo, and an Associate Professor, a Professor in the Department of Mechanical Engineering, and a Professor of biological functions and engineering, Kyushu Institute of Technology, Kitakyushu, Japan, where he has been a Professor Emeritus since 2009. Dr. Tsukamoto is a fellow of The Japan Society of Mechanical Engineers, and a member of The Engineering Academy of Japan.

A Study of the Mixing Index in Solid Particles[†]

Shih-Hao Chou, Yue-Lou Song and Shu-San Hsiau*

[†] Department of Mechanical Engineering, National Central University, Taiwan

Abstract

This study focuses on investigating the mixing state by different mixing indices for different pre-organized particles. We also try to propose a new mixing index and discuss the advantages and disadvantages of different cases.

The results show that the Avg. distance mixing index indicates the degree of mixing more accurately than other mixing indices for a case of complete segregation. In some cases the degree of mixing would be higher with the Lacey mixing index compared with the other indices, with the size of the cells greatly affecting this value. In other words, the use of any single specific mixing index on its own cannot accurately reflect the correct degree of mixing for all different kinds of systems. The only difference between mixing indices is which one can provide more accurate and stable results.

Keywords: mixing index, degree of mixing, granular material, pre-organized condition

1. Background

The mixing of powders is very important in industry as well as in our daily life. Many products or semi-products are made from different ingredients in the form of powders which need to be well mixed to make ensure a high quality end product. For example, for manufacturing pharmaceuticals, avoiding segregation and achieving a well-mixed powder is essential. Thus, the problem of mixing/segregation in powdered or granular materials has been studied by many industrial engineers and academics.

Powders can be mixed by mechanical excitation, gas-flow agitation, gravity-driven free-falling, and many other different complex methods (Masuda H. et al., 2006). Different types of blenders/mixers have been developed for industry. The mechanisms of powder mixing include convective mixing, shear mixing and diffusive mixing (Lacey P.M.C., 1954; Kaye B.H., 1997; Ottino J.M. and Khakhar D.V., 2000). The rate of mixing by diffusive mixing is low compared with convective mixing mechanisms. However, diffusive mixing is essential for microscopic homogenization (Gotoh K. et al., 1997).

What is a so-called “well-mixed” granular material? The mixing status is usually determined based upon one or several samples taken from a batch. The way the sam-

ple is taken, the number of samples, the locations the samples are taken from, the size of the samples, and so on, all influence the evaluation of the mixing status (Weidenbaum S.S., 1958). The statistical method for investigating the samples is also critical. This paper studies determination of the mixing index for particle mixing by sampling.

As mentioned above, the mixing index is an important parameter to indicative of the status of mixing, with a value of 1 indicating that the material is fully mixed; 0 represents fully segregated. However there are many different mixing indices with different ways of determining the status some of which are investigated in this study to determine which one is the best and the most user friendly?

2. Introduction to some mixing indices

Currently, there are a number of suitable mixing indices that can be used to analyze granular mixing behavior. Gayle J.B. et al. (1958) proposed a mathematical method to solve the mixing problem based on the chi square value. Their method can not only be used for a binary mixture system but also to for systems with any finite number of components. Leggatt C.W. (1951) studied the mixing process for weeds and crops, and determined the dispersion of homogeneity in a unit weight. Poux M. et al. (1991) also made a careful review of many different mixing indices.

Most investigations of mixing indices are based on the

[†] Received 23 June 2016; Accepted 1 August 2016
J-STAGE Advance Publication online 30 August 2016

[†] No. 300, Zhongda Rd. Zhongli City, Taoyuan County 32001, Taiwan

* Corresponding author: Shu-San Hsiau;

E-mail: sshsiau@cc.ncu.edu.tw

TEL: +886-3-426-7341 FAX: +886-3-425-4501

statistical method but photometric and kinetic approaches are also employed. However, the conditions for power mixing are defined differently in different mixing indices indicating the uncertainty and complicated nature of the mixing process. In this study, some of the mixing indices commonly used in academic research or in industry are reviewed; only binary mixtures are considered.

(1) Lacey Mixing Index

Lacey P.M.C. (1943) first introduced what is now known as the Lacey mixing index in 1943, by dividing the area of interest into N cells. Assume that ϕ_i is the concentration of the reference component in the “ i th” cell and ϕ_m is the overall concentration of the reference component. The variance of σ^2 for the concentration of a reference component in each cell can be expressed by

$$\sigma^2 = \sum_{i=1}^N \frac{(\phi_i - \phi_m)^2}{N-1}, \quad (1)$$

where N is the total number of cells occupied by the total particles; ϕ_i is the local concentration of tracer particles in each cell; ϕ_m is the average concentration of tracer particles in the whole system. Theoretically, for a binary-mixture solid system, the maximum value of mixture variance, σ_0 , can be expressed by

$$\sigma_0^2 = \phi_m(1 - \phi_m). \quad (2)$$

The possible minimum variance in a cell, σ_r , is defined by

$$\sigma_r^2 = \frac{\phi_m(1 - \phi_m)}{n}, \quad (3)$$

where n denotes the possible number of particles in a cell. Then the Lacey mixing index M can be defined by

$$M = \frac{\sigma_0^2 - \sigma^2}{\sigma_0^2 - \sigma_r^2}. \quad (4)$$

Given the concentrations of the reference component in each cell, the mixing index can be defined and calculated by the statistical method. Lacey pointed out that this index is related to the number of the cells. Although it is not easy to represent the real mixing condition by one single index, the Lacey mixing index is still a good parameter for comparing the mixing status at different times or for different apparatus (Lacey, 1943). However this mixing index may be greater than 1 in some cases which causes some problems. This issue will be discussed further below.

(2) Kramer Mixing Index

Kramer proposed this mixing index (Kramer H.A., 1968) based on the same statistical variances as Lacey as in Eqs. (1–3):

$$M = \frac{\sigma_0 - \sigma}{\sigma_0 - \sigma_r}. \quad (5)$$

(3) Lacey, Weidenbaum and Bonilla Mixing Index (L.W.B. Mixing Index) (Weidenbaum S.S. and Bonilla C.F., 1953)

This index was first proposed for a horizontal cylindrical mixer. The mixing index M can be defined by

$$M = \frac{\sigma_r}{\sigma}, \quad (6)$$

where σ and σ_r are the same as defined in Eqs. (1) and (3).

(4) Mixing index by distance between the volume centers of two species (Avg. distance mixing index)

Two differently colored particles (with the same volumes) are often used to perform mixing/segregation experiments/simulations in academic studies. The distance (width or height, depending on the mixing/segregation direction) between the volume centers of each species is used to denote the mixing status. For example, **Fig. 1(a)** shows pre-organized particles (black on the left and white on the right) in a container. They are in a completely segregated state. The distance between the two volume centers is denoted by Δ_{seg} . **Fig. 1(b)** shows a similar case but the particles are organized so that black is on the bottom and white above. The distance between the volume centers of the two species in the horizontal direction (or in the vertical direction) is denoted as Δx . Thus the mixing index can be defined as follows:

$$M = \frac{\Delta_{\text{seg}} - \Delta x}{\Delta_{\text{seg}} - \Delta_{\text{mix}}}, \quad (7)$$

where Δ_{mix} is the value of Δx in a fully-mixed state which is usually 0 as shown in **Fig. 2**. This index is really based on the idea of the geometric positions of the particles as determined by identifying the volume (weight) center of particles. Calculation for this method would appear to be easy, but failure may occur because Δx could be 0 even when the particles are segregated, for example, if all the black particles were located in the upper-right and lower-left quadrants.

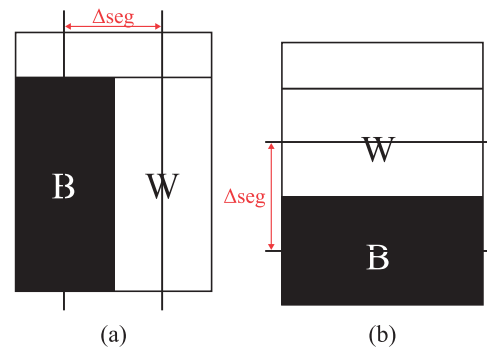


Fig. 1 Pre-organized particles with (a) black on the left and white on the right; (b) black on the bottom and white above in a container.

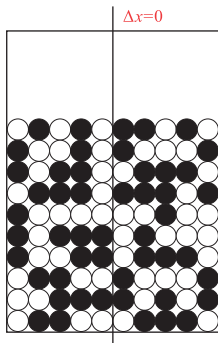


Fig. 2 Schematic representation of the fully-mixed particle state.

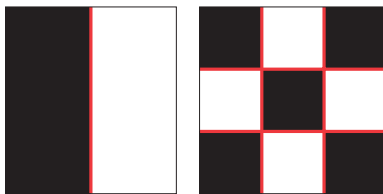


Fig. 3 The relation between the mixing degree and the length of the boundary between two different species.

3. Coordinate mixing index

As can be seen in **Fig. 3**, the mixing status (mixing degree or mixing index) has a strong relation with the length of the boundary between the two different species. The right configuration in **Fig. 3** has a better mixing condition than the left configuration, with the length of the boundary between the black-white areas of the right one being four times that of the left one. Based on the above idea, we try to develop a new mixing index, the coordinate mixing index, in this study.

An examination of **Fig. 4** is useful to explain how the coordinate mixing index is defined. Since the lengths of the contact interface between the black and white particles should be the same, whether counting either the white or the black particles, here we only use the white particles as the target. We can use the (coordinate) number of different-color contacts as the length, therefore the numbers inside each white circle (particle) denote the number of black particle(s) located in the neighboring position of the white particles. For example, in the lower left corner, the white particle has two black particles around it, so the coordinate number is 2. After counting the coordinate number for each white particle, the sum of all white particles is the total coordinate number for this system. The coordinate number for the granular system in **Fig. 4** is 17. A higher coordinate number indicates a better mixing status.

Let Ω denote the coordinate number of the system, and Ω_{ran} denote the coordinate number of the well-mixed (most random) system. Then the mixing index can be defined as

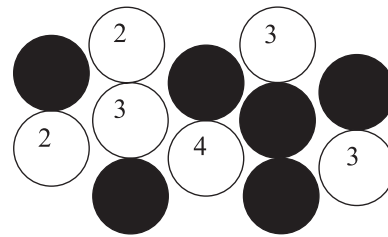


Fig. 4 Schematic representation of the method of calculation of the coordinate mixing index.

$$M = \frac{\Omega}{\Omega_{\text{ran}}} \quad (8)$$

If a cuboid box contains a , b , c particles in three directions (total abc particles), the coordinate number of the well-mixed arrangement would be

$$\Omega_{\text{ran}} = (a-1)bc + (b-1)ca + (c-1)ab \quad (9)$$

It is simpler to test and explain Eq. (9) using a 2D system with a and b particles distributed in the two directions. The right-hand image in **Fig. 3** represents a 3×3 particle system ($a = 3$, $b = 3$) in a well-mixed condition. For each row there are $a - 1 = 2$ coordinate numbers. With $b = 3$ rows, there would be $(a - 1) \times b = 6$ coordinate numbers. Similarly there are $(b - 1) \times a = 6$ coordinate numbers in the column direction. Therefore $\Omega_{\text{ran}} = (a - 1)b + (b - 1)a = 12$ coordinate numbers.

4. Results and discussions

In this study, we analyze the performance of different mixing indices with different examples of pre-organization, as in **Fig. 5**. Three different types of examples are examined: series A includes three different completely segregated initial system configurations; series B is devoted to investigating cases with different percentages of mixing particles; and in series C we investigate mixing starting with different special pre-organized patterns. The Lacey mixing index has been widely used in previous studies. However, the extent of the Lacey mixing index could be more than 1 in some cases. Therefore, we compare the Lacey mixing index and coordinate mixing index in a simulation of the granular mixing process in a vibrating bed.

Fig. 6 shows the degree of mixing obtained using different kinds of mixing indices for three different completely segregated initial configurations. In case I and case II, the degree of mixing with each mixing index is 0 except for the coordinate mixing index. This is because of the existence of a contact interface between the black and white particles in each case, which has to be counted when calculating the coordinate mixing index. In addition, although the Avg. distance mixing index is still indicates zero, the degree of mixing is calculated to be greater

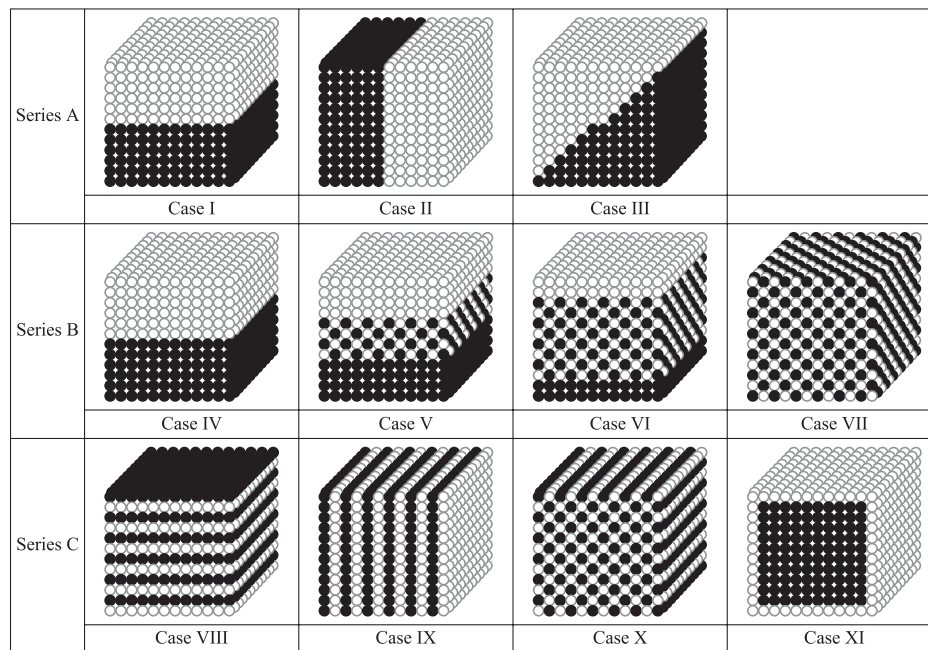


Fig. 5 Schematic representation of the configurations of black-white particles for different pre-arranged cases.

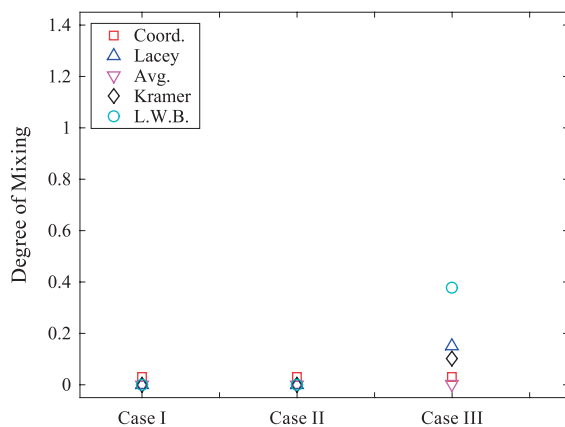


Fig. 6 The relation between the degree of mixing for different kind of mixing indices and different initial configurations of black-white particle systems. Total particle number of system is 1728; cell number N is 216; and number of particles (cell size) is $n = 8$.

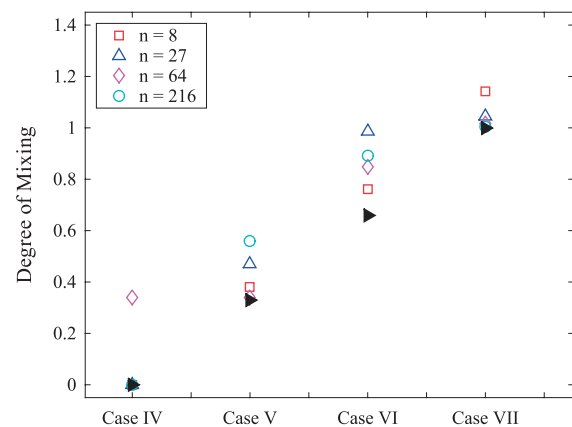


Fig. 7 The degree of mixing with the Lacey mixing index with different sizes of cells for series B. The cell number $N = 216$ for $n = 8$, $N = 64$ for $n = 27$, $N = 27$ for $n = 64$, and $N = 8$ for $n = 216$. Symbol fill: black, exact value.

than 0 in case III. Overall, the degree of mixing obtained with the L.W.B. mixing index is the highest while the Lacey Mixing Index is slightly larger than the Kramer Mixing Index.

Therefore, if a contact interface still exists between the black and white particles even in a well segregated situation, the degree of mixing obtained with the coordinate mixing index would not be zero. Differences in the length (number) of the interface also cause little deviation; the degree of mixing is similar. Meanwhile, the degree of mixing for the Avg. distance mixing index for series A is calculated to be zero. This is because the variances in the initial completely segregated state and the symmetry of the system both affect the calculated value.

The number and size of the cells should be chosen before using the Lacey mixing index to calculate the degree of mixing. If the size of the system is the same, the number of cells is dependent on the number of particles in a cell. For example, observation of series B shows 4 different configurations having 0 %, 33 %, 66 % and 100 % of particle mixing, respectively. The mixing states of the particle system are defined by four different volume ratios with fully mixed particles. For example, a mixing degree of 33 % means that 1/3 of the volume of particles is in a completely mixed condition in the system. **Fig. 7** shows the degree of mixing obtained with the Lacey mixing index for different sizes of cells for cases IV to VII. In case V, the calculated degree of mixing is close to the defined

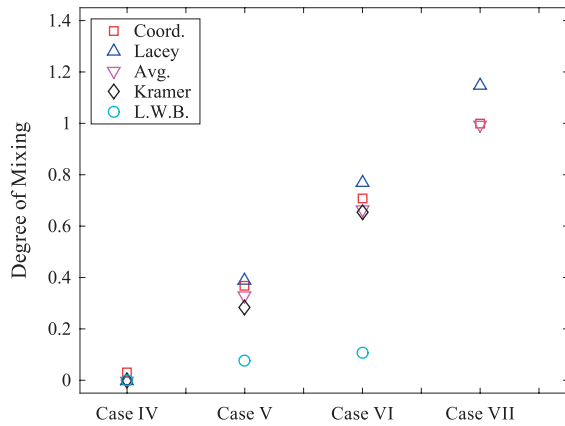


Fig. 8 The degree of mixing for different mixing indices for series B. The size of cell size is $n = 8$.

degree of mixing with $n = 64$. The error becomes larger while the cell size increases. However, this tendency does not occur in case VI. In case VII, the degree of mixing will be close to 1 when the cell size becomes larger. The degree of mixing even exceeds 1 with $n = 8$. In summary, accuracy is higher if we use a suitable cell size. The accuracy is highest for case V where all the white and black particles are well-mixed in each cell. This situation could not be achieved in case VI. Therefore, reducing the size of the cells could lead to variation in the system if we cannot find a suitable size of cell.

According to the results discussed above, $n = 8$ is chosen for all mixing indices, while the cell size varies in the formulation and the ensuing discussion. **Fig. 8** shows the degree of mixing obtained using different mixing indices for series B with a cell size of 8. We found the degree of mixing obtained with the Avg. distance mixing index to be closest to the pre-mixed value for this system. The error for the degree of mixing for the coordinate mixing index was almost 10 %, and for the Lacey mixing index it was 15 % in all cases. The degree of mixing obtained with the Kramer mixing index was either higher or lower than the pre-mixed value for different cases, but the value was abnormally high for case VII. We also found the degree of mixing to be larger than one for mixing indices based on the statistical method.

The degree of mixing obtained with different mixing indices for series C is shown in **Fig. 9**. In this figure, we can see that in addition to the coordinate mixing index, calculation with the other mixing indices shows a relatively high degree of mixing. From case VIII to case X, the degree of mixing calculated from the Lacey Mixing Index and Kramer Mixing Index is the same as for the well-mixed case, but this result is unreasonable. This is because if the number of different species of particle are the same in a cell, the mixing degree is indicated as well-mixed regardless of whether the different species of particle are mixed or not. The Avg. distance mixing index fails

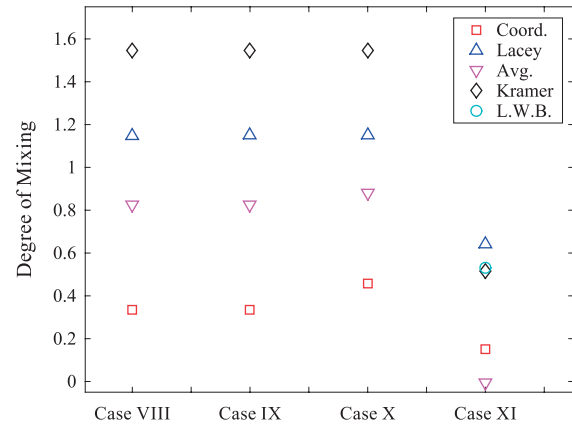


Fig. 9 The degree of mixing for different mixing indices for series C. The cell size is $n = 8$.

for case X and case XI, because the systems are symmetrical. In addition, since $\sigma = 0$ in each case for series C, the degree of mixing obtained with the L.W.B. mixing index is close to infinity. In these cases, this unreasonable situation does not happen when the coordinate mixing index is used. This also indicates that the coordinate mixing index has better accuracy and wider applicability.

From the above discussion, it can be seen that the degree of mixing obtained with the Lacey mixing index will be larger than one in some cases. This situation is contrary to expectations and is well known. The mixing behavior results in a situation between complete segregation and being well-mixed (the degree of mixing is between 0 and 1). Therefore, below we will discuss the mixing behavior of particles under different operating conditions. The dynamic behaviors of the particles were simulated by the discrete element method (DEM) in a vibrated granular bed, and the degrees of mixing were calculated with the Lacey mixing index and coordinate mixing index. The only difference between these two cases are the electrostatic force exist or not. The granular beds are energized by vertical sinusoidal oscillations at different vibrated acceleration and amplitude. The relevant operating conditions and parameters could be referred to the previous study (Lu L.S. and Hsiau S.S., 2005).

The evolution of the degree of mixing over time under different operating conditions is shown in **Figs. 10(a)** and **(b)**. We can see that both the trend and the final mixing degree for the different mixing indices are almost that same, as shown in **Fig. 10(a)**. In **Fig. 10(b)**, we consider the influence of the electrostatic force between the particles. To simplify the electrostatic effect, the two groups of glass beads are given opposite charges and the charge strength is assumed to be constant. In this case, the degree of mixing is greatly increased (Lu L.S. and Hsiau S.S., 2005). We found that the degree of mixing found with the Lacey mixing index would not exceed one, but this is unreasonable. At the same time, the final degree of

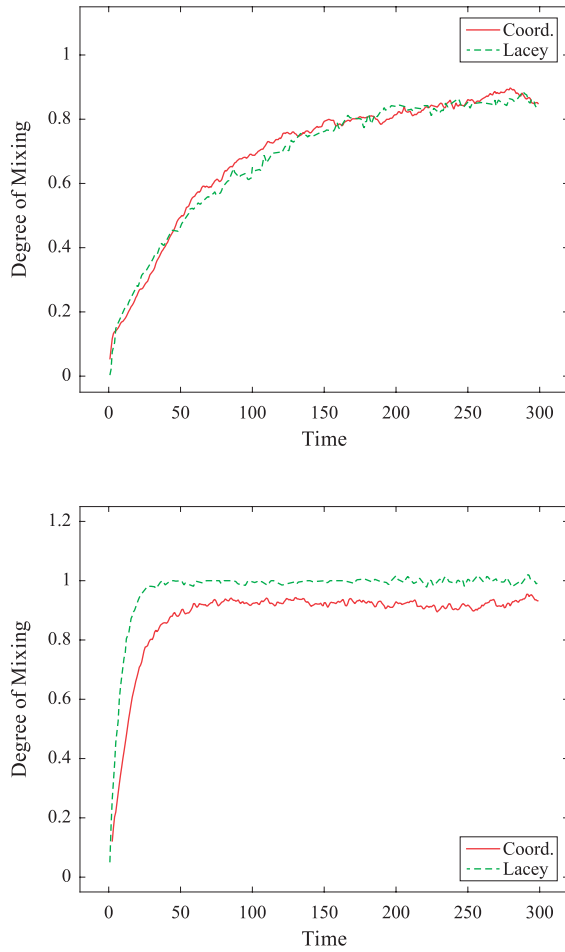


Fig. 10 Comparison of time evolution of mixing degree for the case where (a) $\Gamma = 3$, $f = 20$ Hz and the electrostatic force does not exist; and (b) $\Gamma = 5$, $f = 20$ Hz, but electrostatic force does exist. The dimensionless acceleration amplitude Γ was defined as $\Gamma = a/g$, where a is the acceleration; g was the acceleration due to gravity. The vibrational frequency is f .

mixing for the coordinate mixing index is quite stable. The final average mixing degree is about 0.95. If the overall concentration is about 0.5 in the system, the Lacey mixing index could be rewritten as

$$M = \frac{n}{n-1} \left(1 - \frac{\sigma^2}{0.25} \right), \quad (10)$$

and if the $M > 1$, the root mean square of the deviation σ is given by

$$\sigma^2 = \overline{(\phi_i - \phi_m)^2} < \frac{1}{4n}. \quad (11)$$

From the above equation, it can be seen that the size of the cell will affect the degree of mixing. Meanwhile, the mixing degree for the Lacey mixing index will be larger than one, if the variance σ^2 for the concentration of a reference component in each cell and overall concentration is smaller than a critical value.

5. Conclusions

In the granular mixing process, there are many factors that can affect the state of mixing in the system. The degree of mixing results also differ for different mixing indices. In this study, we discuss the performance obtained with different indices using different pre-organized particle configurations.

The results show that the cell size has a significant effect on the degree of mixing calculation given the criterion of the mixing index about a standard deviation. In some cases the degree of mixing for the Lacey mixing index, L.W.B. mixing index and Kramer mixing index will be larger than 1. Moreover, if the number of different species of particle in a cell is the same, the degree of mixing will be higher than the correct value regardless of how these different species of particle are mixed. In some cases, the Avg. distance mixing index will fail because the variation in the initial state and the symmetry of the system both affect this index.

In this study, we propose a new mixing index, called the coordinate mixing index. This index is relatively simple and widely applicable. According to the results obtained with different examples of pre-organized particles, we found that the degree of mixing obtained with the coordinate mixing index to always be between 0 and 1. Therefore, for now, the coordinate mixing index may be also a suitable index.

Acknowledgements

The authors would like to acknowledge the support from the National Science Council of the R.O.C. for this work through Grants MOST 103-2221-E-008-042-MY3.

Nomenclature

- f The vibrational frequency
- N Total number of cells occupied by the total particles
- n The possible number of particles in a cell
- Δx Distance between the volume centers of the two species in the horizontal direction (or in the vertical direction)
- Γ Dimensionless acceleration amplitude was defined as $\Gamma = a/g$, where a is the acceleration; g was the acceleration due to gravity
- Ω The coordinate number of the system
- ϕ_i Concentration of the reference component in the “ i th” cell
- ϕ_m Overall concentration of the reference component

References

- Gayle J.B., Lacey O.L., Gary J.H., Mixing of Solids. Chi Square as a Criterion, *Journal of Industrial and Engineering Chemistry*, 50 (1958) 1279–1282.
- Gotoh K., Masuda H., Higashitani K., *Powder Technology Handbook*, 2nd ed., Marcel Dekker, New York, 1997.
- Kaye B.H., *Powder Mixing*, Chapman & Hall, UK, 1997.
- Kramer H.A., Effect of grain velocity and flow rate upon the performance of a diverter type sampler, U.S. Department of Agriculture, Agricultural Research Service, (1968) ARS No.51–25.
- Lacey P.M.C., The mixing of solid particles, *Transactions of the Institution of Chemical Engineers*, 21 (1943) 53–59.
- Lacey P.M.C., Developments in the theory of particle mixing, *Journal of Applied Chemistry*, 4 (1954) 257–268.
- Leggatt C.W., Method of making the homogeneity test, *Association of Official Seed Analysts News Letter*, 25 (1951) 3–8.
- Lu L.S. and Hsiao S.S., Mixing in vibrated granular beds with the effect of electrostatic force, *Powder Technology*, 160 (2005) 170–179.
- Masuda H., Higashitani K., Yoshida H., *Powder Technology Handbook*, 3rd ed., CRC Press, Boca Raton, 2006.
- Ottino J.M., Khakhar D.V., Mixing and segregation of granular materials, *Annual Review of Fluid Mechanics*, 32 (2000) 55–91.
- Poux M., Fayolle P., Bertrand J., Bridoux D., Bousquet J., Powder mixing some practical rules applied to agitated systems, *Powder Technology*, 68 (1991) 213–234.
- Weidenbaum S.S., Bonilla C.F., A Fundamental Study of the Mixing of Particulate Solids, Ph.D. Thesis, Columbia University (1953).
- Weidenbaum S.S., Mixing of Solids, in: *Advances in Chemical Engineering II*, Academic Press, New York, 1958, pp. 211–321.

Author's short biography



Shih-Hao Chou

Dr. Shih-Hao Chou received his bachelor and PhD degrees in Department of Mechanical Engineering, National Central University, Taiwan in 2007 and 2013. He is currently a post-doctoral researcher at National Central University, Taiwan. His research interests include powder technology, mixing and segregation, DEM modeling of granular flow.



Yue-Lou Song

Mr. Yue-Lou Song received his bachelor in Department of Mechanical Engineering, National Central University, Taiwan in 2012. He served as an assistant of Department office (2008-2009). His research interests include mixing behavior in a vibrated granular bed.



Shu-San Hsiao

Shu-San Hsiao is an Associate Vice President for Research & Development of National Central University (NCU). He received his MS and PhD degrees from California Institute of Technology. He start his professorship life in NCU and majored in Mechanical Engineering in 1993. He also is a Distinguished Professor of Mechanical Engineering and Institute of Energy Engineering of NCU. His researches including Powder Technology, Clean Coal Technology, Modelling and Design of MOCVD, Energy Technology, Debris Flow and Avalanche, Hot-Gas Cleanup and Thermo-Fluids. He served as the chairman of Mechanical Engineering (2010–2013) and also as the director of Institute of Energy Engineering (2008–2013).

Characterisation of the Wetting Behaviour of Poor Wetting Food Powders and the Influence of Temperature and Film Formation[†]

John J. Fitzpatrick^{1*}, Justine Salmon¹, Junfu Ji² and Song Miao²

¹ Process & Chemical Engineering, School of Engineering, University College Cork, Ireland

² Teagasc Food Research Centre, Moorepark, Ireland

Abstract

Characterisation of the wettability of five poor wetting food powders was performed using static immersion and contact angle measurements. The effect of temperature (20, 50 and 70 °C) on wettability showed varying effects on the powders. Higher temperatures majorly improved the wettability of chocolate and high fat powders but worsened the wettability of sodium caseinate and milk protein isolate. Rate-limiting regime testing was performed by pouring a fixed mass of powder on to the surface of water in an agitated beaker and visually assessing what was rate-limiting rehydration after 1 minute. The rate limiting regime tended to be floating at lower agitation speeds and dispersed clumps of varying sizes at higher speeds. However, there were major differences observed between the powders. Some of the powders formed strong films at powder/water interfaces, that could act as a barrier to water penetration and wettability. Consequently, force displacement testing was performed on a layer of powder on the water surface to assess the strength of any powder film formed. Some of the powders formed strong films that may in-part explain their poor wetting behaviour and their propensity to form strong clumps that were difficult to disrupt.

Keywords: food powders, rehydration, wettability, clumping, film/skin strength

1. Introduction

Ease of rehydration is a very important functional property of food powders (Schubert, 1993), as many food powders eventually end up being rehydrated. Powders that rehydrate easily and are not problematic are essential for industrial users and home consumers. Some food powders rehydrate easily while others are more difficult (Barbosa-Canovas et al., 2005). Consequently, a good understanding of rehydration behaviour is necessary along with a knowledge of the factors that influence poor rehydration behaviour.

Rehydration has a number of steps, but it can be broadly broken down into wetting, where the powder is initially contacted with water to wet the powder particles, followed by solubilisation where the powder particles disperse and dissolve in water. It is desirable that both these steps occur rapidly and completely, however some powders may prove difficult to wet and/or solubilise.

There are many factors that can influence the wettability of a powder. Poor wetting powders tend to float on the surface of still water and sink very slowly into water. Powder particle surface composition will influence powder hydrophobicity, and this will influence wetting behaviour with water. Powder formation, for example by spray drying, may influence powder properties that influence rehydration (Gaiani et al., 2010). Porowska et al. (2015) showed that spray drying parameters and feed composition can be manipulated to influence the surface composition which can influence wetting behaviour.

Powder physical properties, such as particle size, densities, porosity and morphology, can influence wetting behaviour. Powders with higher densities tend to sink more rapidly. Powders with larger particle size tend to have better wetting behaviour because water can penetrate more easily into the larger void spaces between the particles. Consequently, granulation is commonly used to improve the wettability of powders, however slimy skin or film formation at the powder/water interface may impede water penetration into the bulk powder (Ji et al., 2016).

The wetting process can be made more difficult by the formation of powder clumps by some poor wetting powders, as these clumps need to be broken down (Barbosa-Canovas et al., 2005). Clumps may form where skins or

[†] Received 24 June 2016; Accepted 19 August 2016

¹ Western Road, Cork, Ireland

² Teagasc, Fermoy, Co. Cork P61 C996, Ireland

* Corresponding author: John J. Fitzpatrick;

E-mail: j.fitzpatrick@ucc.ie

TEL: +353-21-4903089

films occur at the water/powder interface which can inhibit water penetration into the powder clump. Agitation helps improve sinking, clump disruption and dispersion of powder particles. Many food powders are rehydrated in tanks that are mechanically agitated. The tank configuration, agitator type used and mechanical power intensity coupled with water temperature and its conductivity may all impact on rehydration behaviour (Richard et al., 2013; Jeantet et al., 2010; Schober and Fitzpatrick, 2005; Fitzpatrick and Cuthbert, 2004).

The wettability of powders has been assessed using a variety of techniques, including the International Dairy Federation standard method (IDF, 1979), the Washburn method (Washburn, 1921), dynamic contact angle measurement (Dupas et al., 2013) and the turbidity method (Gaiani et al., 2007, 2009). Food powder rehydration may be complex in nature, and quantitative techniques may not fully capture this complexity. Powders may float on the surface for prolonged periods of time; they may settle and form sediments at the bottom of the vessel; they may disperse as clumps that prove difficult to disrupt. Consequently, Mitchell et al. (2015) described a qualitative approach to help provide further insight into describing and understanding powder rehydration. They describe a rate-limiting regime mapping approach that qualitatively describes the particular aspect or regime that limits the overall rehydration in a stirred vessel at a specific condition of agitation.

The focus of this paper is on poor wetting powders. In particular, it examines factors that influence poor wetting behaviour, investigates the influence of temperature and agitation on the wetting, clumping and dispersion behaviour of poor wetting powders, and investigates clumping and the strength of skins formed at powder water interfaces.

2. Materials and methods

2.1 Powders and their composition

Five poor wetting powders and one easy wetting powder were tested and compared and these are presented in **Table 1**. Skim milk, 73 % high fat milk, milk protein isolate (MPI) and sodium caseinate powders were obtained from dairy powder manufacturers in Ireland, and chocolate and wheat flour powders were purchased in a local supermarket. The composition data provided in **Table 1** were obtained from product packaging or dairy powder manufacturer data, except for the water content which was measured by an oven drying test (102 °C for 24 hours).

Table 1 Powders and their % composition

powder	protein	fat	carbo-hydrate	water	ash
Skim milk	35	1	52	4.8	7
Chocolate	6.3	6	75	2.9	0.9
High fat	9	73	13	2	3
Caseinate	85	1.3	1.3	8.8	4
MPI	86	1.5	0.5	7.4	6
Flour	10	1.3	76	11.8	0.8

Table 2 Powder particle size and densities

powder	particle size (microns)	apparent density	poured BD ¹ (kg m ⁻³)	tapped BD ¹
Skim milk	132	1220	490	548
Chocolate	109	1530	638	722
High fat	76	934	280	433
Caseinate	90	1310	500	620
MPI	50	809	291	387
Flour	85	1490	590	729

¹ bulk density

2.2 Powder particle size and densities

The median (d_{50}) of a volume particle size distribution, particle apparent density, poured and tapped bulk densities were measured, as described by Fitzpatrick et al. (2016), and these data are provided in **Table 2**.

2.3 Wettability

The method used was an extension of the International Dairy Federation (IDF) method (IDF, 1979), and is described by Fitzpatrick et al (2016). The method essentially measures the time for a given mass of powder to sink beneath the water surface, and this time is referred to as the wetting time. Powders having a wetting time less than 1 minute can be considered as easy wetting powders and powders having wetting times greater than 5 minutes can be considered as poor wetting powders. The temperature of the water was maintained at either 20, 50 or 70 °C. Poor wetting powders may take very long time to wet or may not totally wet. To overcome this time limitation, the % wettability was evaluated as defined in equation 1. This consisted of measuring the amount of powder that disappeared from the water surface after 60 minutes, as described by Fitzpatrick et al. (2016).

$$\% \text{ Wettability} = 100 \times \frac{\text{mass of powder disappeared}}{\text{mass of initial powder}} \quad (1)$$

This test was applied to evaluate the wetting time of a powder if less than 60 minutes, and the % wettability at 60 minutes for those powders whose wetting time was greater than 60 minutes. This represents an improved approach for assessing and comparing the wettability of poor wetting powders.

2.4 Rate-limiting regime mapping

This is a similar method to that described by Fitzpatrick et al. (2016) and is based on that reported by Mitchell et al. (2015). A 2 L glass beaker with a diameter of 125 mm was filled with 1600 mL of water, as illustrated in **Fig. 1a**. An agitator with a four-bladed pitch-blade impeller was inserted axially into the water at a fixed location and was operated at speeds between 100 to 750 rpm. Little or no vortex formation occurred at speeds up to 300 rpm. At 400 rpm and higher, a vortex formed and deepened progressively with higher speed, as illustrated in **Fig. 1b**, engaging the impeller at around 750 rpm.

The water was heated to the required temperatures (20, 50 and 70 °C) using a hotplate. 16 grams of powder (1 % w/v) was weighed and emptied into the agitated water. The rehydration was visually observed and a qualitative evaluation of any rate-limitation(s) to achieving complete dispersion or dissolution was made at the end of the first minute. Key words were used to describe any rate-limitations, such as sedimentation (if powder remained on the bottom of the beaker); floating (if powder remained floating on the surface of the water); and clumps in dispersion (if powder formed clumps that were visible in the dispersion). The procedure was carried out in duplicate for each powder.

2.5 Film strength at powder water interface

A force-displacement test was used to measure the strength of films developed at the powder/water interface. 110 g of water was filled into a small glass beaker with internal diameter and height of 65 mm and 40 mm, respectively. Powder was sieved onto the water surface until it filled the beaker giving a powder thickness of 7 mm. Excess powder was removed to produce a smooth surface. A 35 mm plunger was then centered and moved axially through the powder at a constant speed of 0.08 mm/s, as illustrated in **Fig. 2**, and force vs displacement was measured using a TA HD Plus Texture Analyser (Stable Microsystems, UK). With no powder present the force-displacement through water is illustrated in **Fig. 3a**. Powders displaying measurable film strength showed behavior similar to that illustrated in **Fig. 3b** with a noticeable peak. This is the peak force required for the plunger to penetrate through the film and was used as an index of film strength. Powders displaying negligible film strength

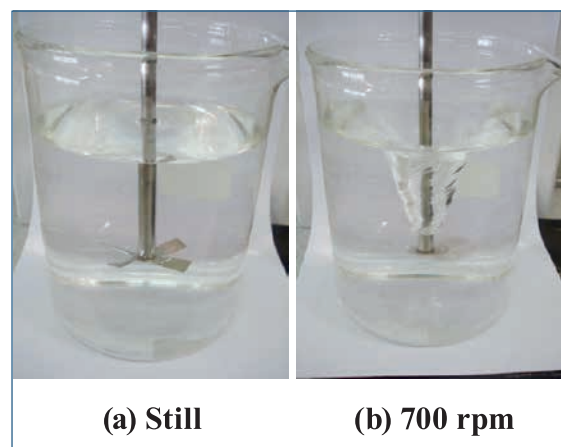


Fig. 1 Rate-limiting regime mapping: (a) beaker and agitator; (b) agitation at 600 rpm, deep vortex.

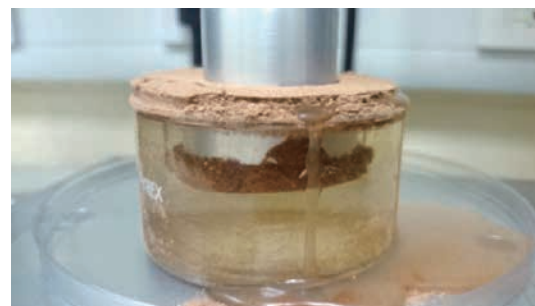


Fig. 2 Plunger moving axially through chocolate powder (1 min, 20 °C).

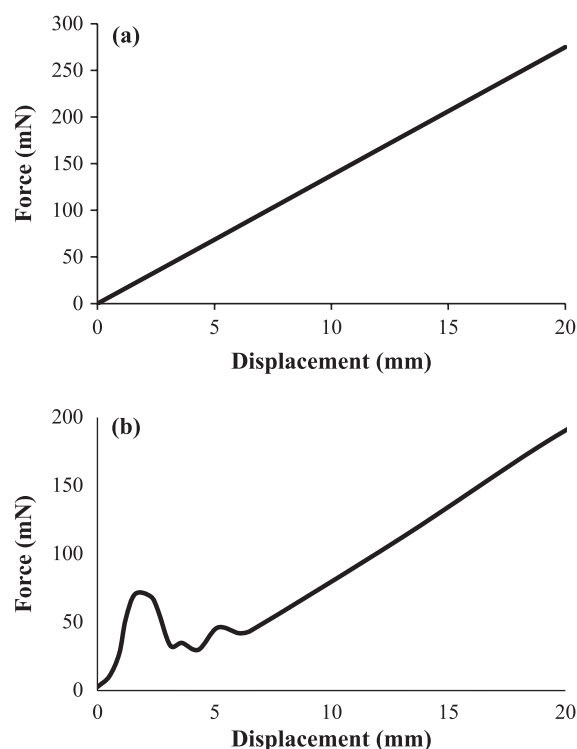


Fig. 3 Force displacement: (a) water; (b) SMP (1 min, 20 °C).

displayed a similar linear behavior to that illustrated in **Fig. 3a**. Measurements were conducted at water temperatures of 20, 50 and 70 °C and powder water contact times of 1 and 20 minutes.

3. Results and discussion

3.1 Wettability and effect of temperature

Results from wettability testing are presented in **Tables 3 and 4**, along with contact angle data presented in **Table 5**. The poor wetting powders, except for the wheat flour, had contact angles greater than 90 degrees. Hydrophobic surfaces tend to be the major determinant of high contact angles, and surface chemistry and composition determine hydrophobicity. Consequently, bulk composition, which influences surface composition, is having a major impact on the wettability of the powders. The wettability results were closely related to the contact angle data, except for the SMP and wheat flour where the flour had a lower contact angle than the SMP even though it had a longer wetting time.

At 20 °C, the high fat powder had very poor wettability at only 5 % after 60 minutes, where it essentially floated on the water surface. This is most likely due to the hydrophobic nature of fat and its low apparent density, which is lower than the density of water. The chocolate powder is poor wetting, displaying 50 % wettability after 60 minutes. Its poor wettability is most likely due to its composition, in particular a significant fat content of 5.9 %, giving rise to a hydrophobic surface, as evidenced by its contact angle data. Its particle size and densities were not unusually low and should not be contributing to its poor wettability. The high milk protein powders, sodium caseinate and MPI, were both poor wetting powders, having poorer wettability than the chocolate powder. Both powders displayed high contact angles, and this is most likely due to their composition. Consequently, their high protein contents, being derived mainly from caseins, were mainly responsible for the poor wettability of these powders. Crowley et al. (2015) showed how composition influenced the contact angle of milk protein concentrate powders, with higher protein (lower lactose) content resulting in higher contact angles. The low apparent density and relatively small particle size of the MPI powder may also contribute to its poor wettability.

The effect of temperature on wettability is presented in **Tables 3 and 4**. For the easy wetting SMP with a wetting time less than 1 minute, wettability improved with increasing temperature. However, temperature displayed differing impacts on the poor wetting powders. Increasing temperature had a very beneficial impact on the chocolate powder. Likewise, for the high fat powder, where at 50

Table 3 Powder wetting times

powder	20 °C	50 °C	70 °C
Skim milk	51 s	16 s	10 s
Chocolate	> 1 h	2 min	1.2 min
High fat	> 1 h	3 min	1 min
Caseinate	> 1 h	> 1 h	> 1 h
MPI	> 1 h	> 1 h	> 1 h
Flour	31 min	13 min	> 1 h

Table 4 % Wettability of poor wetting powders after 60 minutes

powder	20 °C	50 °C	70 °C
Chocolate	50	100	100
High fat	5	100	100
Caseinate	27	15	15
MPI	22	16	18
Flour	100	100	73

and 70 °C the powder sank just below the surface, wetted and formed a layer due to the lower density of fat. The greatly improved wetting behaviour may be related to the fact that milk fats melt in the range of –40 to 37 °C (McCarthy, 2006).

Increasing temperature did not improve the wettability of the caseinate and MPI powders; in fact the wettability disimproved as shown in **Table 4**. Both of these powders are high protein powders containing caseins which are thermally resistant in the experimental range and the caseins appear to be maintaining their surface hydrophobicity and poor wettability. The flour powder displayed a different behavior with an optimum wetting temperature somewhere between 20 and 70 °C. Increasing temperature from 20 to 50 °C showed improved wettability but increasing further to 70 °C showed a wettability that was worse than at 20 °C. The reduced wettability at 70 °C is most likely due to the effect of temperature on the gelatinisation of starch which occurs typically in the range of 53 to 64 °C for wheat flours (Fennema, 1985) and the interaction between starch and wheat proteins which can form films when heated (Potter, 1986).

3.2 Rate-limiting regime mapping

Rate-limiting regime mapping tests were undertaken to visually investigate the effect of agitation and temperature on the wetting, sinking, clumping and dispersion of the powders. For SMP, the rate limiting regime at low agitation (200 rpm and less) was sedimentation at 20 °C. Dispersed clumps were observed at 300 and 400 rpm agi-

tation speeds, however the powder was well dispersed at 500 rpm and higher. Sedimentation was less rate-limiting at higher temperature, but dispersed clumps were still observed up to 400 rpm. Clumping is most likely due to the presence on the particle surface of fat and some types of proteins that make the surface less hydrophilic. Furthermore, fat and proteins often concentrate to the surface in spray dried powders. Kim et al. (2002) showed the surface fat content was much higher than the bulk value in spray dried dairy powders.

The rate-limiting regime map of the chocolate powder is presented in **Table 6**. The dominant rate-limitation at 20 °C was floating, most likely due to the significant fat content. Increasing temperature had a major effect on the chocolate powder with it being well dispersed by 300 rpm at both 50 and 70 °C. The high fat powder essentially floated on the surface of the water up to 300 rpm at 20 °C, as illustrated **Fig. 4a**. This could be expected due to its inherently hydrophobic nature and its low apparent density. At 400 rpm and greater, a stronger and stronger vortex formed and more powder was drawn into dispersion as fine clumps. However, **Fig. 4b** shows many powder clumps still circulating in the vortex, although these became less and less at higher speeds, but some were still

present at 750 rpm along with fine clumps in dispersion. Increased temperature had a major effect by reducing the floating limitation and increasing dispersion, as illustrated by comparing **Fig. 4a & c**.

Floating was the dominant rate-limiting regime for both the MPI and sodium caseinate powders at 20 °C, most likely due to their high casein protein content, as both powders have low fat contents. The MPI powder behaved somewhat similar to the high fat and chocolate powders in the sense that increased dispersion occurred at higher speeds and complete dispersion was only achieved at the highest speed of 750 rpm. Temperature did not appear to significantly influence the regime map of MPI, and the rehydration behaviour appeared similar at all three temperatures.

The rate-limiting regime map of the sodium caseinate powder is presented in **Table 7**. **Fig. 5a** shows that floating was the dominant rate-limiting regime up to 400 rpm at 20 °C. A stronger vortex developed at 500 rpm and more powder submerged into the water but formed many dispersed clumps, thus clumping became the rate-limiting regime. Even at the highest speed of 750 rpm, powder

Table 5 Contact angle formed between deionized water (20 °C) and powder surface over a 10 second period

powder	1 s	2 s	5 s	10 s
Skim milk	82	60	58	58
Chocolate	104	94	91	86
High fat	104	103	102	98
Caseinate	130	130	130	129
MPI	150	145	142	137
Flour	38	30	25	21

Table 6 Rate-limiting regime map for chocolate powder

Speed (rpm)	20 °C	50 °C	70 °C
100	floating (decreased with agitation)	some floating + sedimentation	some floating + sedimentation
200		light sedimentation	light sedimentation
300		well-dispersed	well-dispersed
400			
500			
600			
700			
750	well-dispersed		

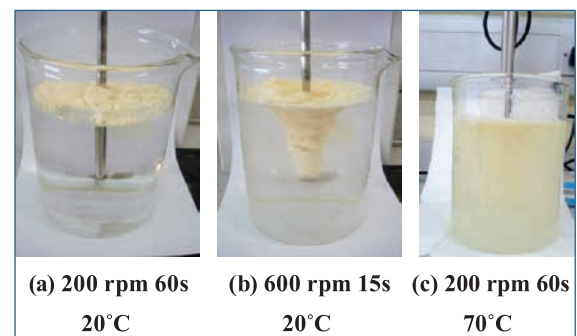


Fig. 4 Pictures from rate limiting regime mapping for high fat powder.

Table 7 Rate-limiting regime map for sodium caseinate powder

Speed (rpm)	20 °C	50 °C	70 °C
100	floating (decreased with agitation)	floating	floating
200			
300			
400	some floating + clumps in dispersion	some floating + smaller clumps in dispersion	
500			
600	big clumps in dispersion	some floating + big clumps in dispersion	floating + clumping
700			big clumps on surface + in dispersion
750			

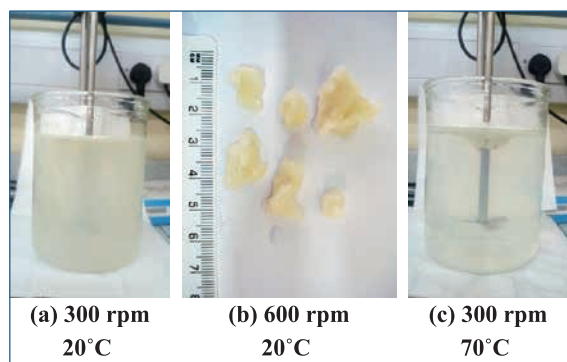


Fig. 5 Pictures from rate limiting regime mapping for sodium caseinate powder at 60 seconds.

clumps remained in dispersion. Many of the powder clumps were large in size (**Fig. 5b**) and the surface had a strong skin or film with dry powder inside that greatly impeded water's ability to penetrate into the bulk. Furthermore, the surface skin of the sodium caseinate was noticeably much stronger than skins developed on other poor wetting powders. Consequently, sodium caseinate powder clumps proved difficult to disrupt by the agitation. At higher temperatures, especially at 70 °C, floating was more persistent and the powder dispersed more slowly, as illustrated by comparing **Fig. 5a & c**. Clumping appeared to become more severe at higher temperatures with larger and stronger clumps being formed.

The most complex behavior was displayed by the flour powder. Both sedimentation and floating were observed up to 300 rpm at all temperatures. Floating was more dominant at lower speed, but even at 100 rpm, some lumps of powder would sink to the bottom and this would increase with higher speed. As the vortex became stronger at 400 and 500 rpm, floating disappeared and the rate-limiting regime was due to clumps either becoming dispersed in the water or sinking to the bottom. Sedimentation ceased at 600 and 700 rpm, and rate-limitation was due to clumps in suspension. The major impact of temperature was on clumping. There was the least amount of clumping at 50 °C while there were more clumping and larger clumps formed at 20 and 70 °C.

Overall, poor wetting powders tend to display floating and clumping behaviours. Many of the reasons for clumping are the same as those for floating, that is, hydrophobic surfaces and slimy skin or film formation. In stirred systems, wettability may be a rate-limiting step whereby powder clumping may occur on the surface and when submerged, and the agitator may have difficulty and take significant amount of time to sink and break up the clumps. Some of the poor wetting powders, most noticeably, sodium caseinate, flour and chocolate, developed noticeable slimy skins/films at the powder/water interface at 20 °C, which would further inhibit water penetration.

The strength of these films could make the clumps more resistant to disruption by the agitation system, and make it more difficult to disperse the powder residing within the clumps. Consequently, the next section of this work examined the film strength developed by the powders tested and how it is influenced by temperature.

3.3 Film strength at powder/water interface

The SMP is an easy wetting powder but did show a measurable film strength of 70 mN at 20 °C at 1 min, as illustrated in **Fig. 3b**. There were no other measurements as SMP had wetted at all the other conditions. The chocolate powder and high fat powders were poor wetting powders at 20 °C, however their film strengths were low with 80 mN at 1 and 20 minutes for chocolate and negligible strength for the high fat at all contact times. Consequently, strong film formation was not a major impediment to the wetting of these powders.

The sodium caseinate, MPI and flour powders all displayed measurable film strengths. These are presented in **Table 8** as a function of time and temperature. They all showed similar film strengths of around 150 to 200 mN

Table 8 Film strength (mN) of sodium caseinate, MPI and flour

powder	20 °C	50 °C	70 °C
<u>Sodium caseinate</u>			
1 min	180	150	170
20 min	200	860	900
<u>MPI</u>			
1 min	0	170	160
20 min	160	380	520
<u>Flour</u>			
1 min	200	150	170
20 min	220	410	490

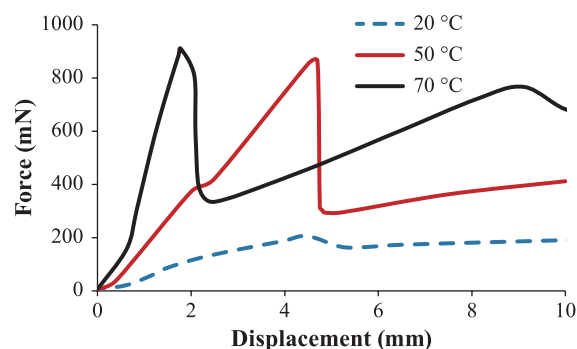


Fig. 6 Effect of temperature on film strength of sodium caseinate at 20 minutes contact time.

after one minute contact time, irrespective of temperature, except for the MPI which showed negligible strength at 20 °C although this did increase to 160 mN after 20 minutes. However, increasing the temperature to 50 and 70 °C had a major impact on film strength at the longer exposure time of 20 minutes, especially for the caseinate as illustrated in **Fig. 6**. The caseinate displayed the strongest film strength, which concurs with that visually observed in the rate-limiting regime mapping. Consequently, these results suggest that the caseinate has a propensity to develop very strong films at these higher temperatures, especially when the powder film is exposed for longer time. The MPI and flour showed similar behaviour to caseinate at higher temperatures but the film strengths were not as strong.

4. Conclusions

In this study, composition was a major cause of poor wettability due to either higher fat or high milk protein contents, making the powder surfaces hydrophobic. Furthermore, the low apparent densities of the high fat and MPI powders may contribute to their poor wettability and their tendency to float. The formation of a slimy skin or film at the powder/water interface may contribute to poor wettability where water penetration into the bulk is greatly impeded. This enhances both floating and clump formation.

Vortexing in a stirred tank greatly improved wetting of even very poor wetting powders by rapidly submerging powder into the water and disruption of clumps by the action of the impeller. However, the formation of strong films by some powders, such as sodium caseinate, may result in the formation of clumps with strong skins that are difficult to disrupt and thus impede powder dispersion. Force-displacement testing can be applied to assess the susceptibility of powders to clumping and strong skin formation by measuring the strength of films formed at powder/water interfaces.

Temperature had a varied impact on the wettability of the poor wetting powders. Increasing temperature greatly improved the wetting and rehydration abilities of the chocolate and high fat powders. On the other hand, it reduced the wettability of the caseinate and MPI powders, which in-part is due to higher temperatures producing stronger films that impede the penetration of water into the bulk.

References

Barbosa-Canovas G.V., Ortega-Rivas E., Juliano P., Yan H., Bulk properties, in: *Food Powders: Physical Properties,*

Processing, and Functionality, Kluwer Academic/Plenum Publishers, New York, 2005.

Crowley S.V., Desautel B., Gazi I., Kelly A.L., Huppertz T., O'Mahony J.A., Rehydration characteristics of milk protein concentrate powders, *J. Food Engineering*, 149 (2015) 105–113.

Dupas J., Verneuil E., Ramaoli M., Forny L., Talini L., Lequeux F., Dynamic wetting on a thin film of soluble polymer: Effects of nonlinearities in the sorption isotherm, *Langmuir*, 29 (2013) 12572–12578.

Fennema O., Ed, *Food Chemistry*, Marcel Dekker, New York, 1985.

Fitzpatrick J.J., Cuthbert R., Effect of temperature on the reconstitution of milk powder to high solids content in a stirred-tank, *Milchwissenschaft*, 59 (2004) 55–58.

Fitzpatrick J.J., van Lauwe A., Coursol M., O'Brien A., Fitzpatrick K.L., Ji J., Miao S., Investigation of the rehydration behaviour of food powders by comparing the behaviour of twelve powders with different properties, *Powder Technology*, 297 (2016) 340–348.

Gaiani C., Schuck P., Scher S., Desobry S., Banon S., Dairy powder rehydration: Influence of protein state, incorporation mode, and agglomeration, *J. Dairy Science*, 90 (2007) 570–581.

Gaiani C., Schuck P., Scher S., Desobry S., Banon S., Use of a turbidity sensor to determine dairy powder rehydration properties, *Powder Technology*, 190 (2009) 2–5.

Gaiani C., Morand M., Sanchez C., Arab Tehrani E., Jacquot M., Schuck P., Jeantet R., Scher S., How surface composition of high milk protein powders is influenced by spray drying temperature, *Colloids and Surfaces B: Biointerfaces*, 75 (2010) 377–384.

IDF, International IDF Standard 87: 1979. International Dairy Federation, Brussels, Belgium, 1979.

Jeantet R., Schuck P., Six T., Andre C., Delaplace G., The influence of stirring speed, temperature and solid concentration on the rehydration time of micellar casein powder, *Dairy Science and Technology*, 90 (2010) 225–236.

Ji J., Fitzpatrick J., Cronin K., Maguire P., Zhang H., Miao S., Rehydration behaviours of high protein dairy powders: The influence of agglomeration on wettability, dispersibility and solubility, *Food Hydrocolloids*, 58 (2016) 194–203.

Kim E.H.J., Chen X.D., Pearce D., Surface characterization of four industrial spray-dried powders in relation to chemical composition, structure and wetting property, *Colloids and Surfaces B: Biointerfaces*, 26 (2002) 197–212.

McCarthy O.J., Physical characteristics of milk fat and milk fat based products, in: Fox P.F., McSweeney P.L.H. (Eds), *Advanced Dairy Chemistry*, vol. 2 Lipids. Springer, New York, 2006, pp. 725–778.

Mitchell W.R., Forny L., Althaus T.O., Niederreiter G., Palzer S., Hounslow M.J., Salman A.D., Mapping the rate-limiting regimes of food powder reconstitution in a standard mixing vessel, *Powder Technology*, 270 (2015) 520–527.

Porowska A., Gianfrancesco A., Fries L., Dosta M., Palzer S., Heinrich S., Influence of feed composition and drying parameters on surface composition of a spray dried multi-component particle, *Drying Technology*, 33 (2015) 1911–

1919.
Potter N.N., Food Science, AVI publishing Company, Connecticut, 1986.
Richard B., Le Page J.F., Schuck P., Andre C., Jeantet R., Delaplace G., Towards a better control of dairy powder rehydration processes. *International Dairy Journal*, 31 (2013) 18–28.
Schober C., Fitzpatrick J.J., Effect of vortex formation on powder sinkability for reconstituting milk powders in water to high solids content in a stirred-tank, *J. Food Engineering*, 71 (2005) 1–8.
Schubert H., Instantization of powdered food products, *International Chemical Engineering*, 33 (1993) 28–44.
Washburn E.W., The dynamics of capillary flow, *Physical Review*, 17 (1921) 273–283.

Author's short biography



John J. Fitzpatrick

Dr. John Fitzpatrick is a senior lecturer in Process & Chemical Engineering. His research interests are in food particle & powder technology and sustainability & environmental protection. He has been involved in research projects in powder flowability and caking; protein precipitation and sugar crystallisation; dry powder mixing and rehydration of food powders.



Justine Salmon

Justine Salmon is a student in food science at the “Agrocampus Ouest” food engineering school in Rennes (France). She undertakes her studies through an apprenticeship and works at Entremont in the production of dairy powders. As part of her studies, she carried out a work placement in University College Cork and participated in a research project on the rehydration behaviour of poor wetting powders.



Junfu Ji

Junfu Ji is currently a Walsh fellow in Teagasc Food Research Centre Moorepark and also a PhD candidate in Process & Chemical Engineering, University College Cork. His research focuses on dairy powder agglomeration processes (fluidised bed and high shear mixer granulation) and the rehydration behaviour, physical & structural properties and flowability of dairy powders and their agglomerates.



Song Miao

Dr. Song Miao is Senior Research Officer in Food Technology at Teagasc Food Research Centre Moorepark. His current research programme focuses on development of novel food structures for functional delivery, water structuring and powder technologies. His research interests cover dehydration and granulation, foods structural and textural design, powder technology, state transition and phase transition in foods, encapsulation of functional food ingredients, stabilization of probiotics and dairy ingredients.



The 50th Symposium on Powder Technology

The 50th Symposium on Powder Technology was held at Tokyo Marriott Hotel, Japan on Tuesday, September 13, 2016. It was organized by Hosokawa Powder Technology Foundation (HPTF) with the sponsorship of Hosokawa Micron Corporation. About 160 people from the industries and universities attended this symposium. The theme of the symposium this year was “Powder Technology to Create a Prosperous Future”. There were six lectures with questions and answers followed by a get-acquainted party for further free discussions.

The first lecture was given by Dr. Makino, who was presented the KONA Award last year, on his lifework research in the field of coal utilization power engineering including the recent trends of CO₂ capture and storage. The lectures were carried out by the professors with the diversity of the fields including the cancer treatment with the inorganic/bio-complex nanoparticle, the new food flours produced by glassy state foods materials, the continuous production of nanoparticles by supercritical hydrothermal synthesis. The other one lecture was from the industrial field introducing the Internet-of-Things (IoT), which has been applied to powder processing systems for several manufacturing industries.

The last lecture was Special Lecture for the 25th Anniversary of the founding of the HPTF, which was given by Prof. Akira Fujishima, Special University Professor Emeritus of the University of Tokyo and President of Tokyo University of Science, who discovered the titanium dioxide photocatalysis. Prof. Fujishima looked back the history of the discovery of the titanium oxide photocatalysis and explained the important applications across the various fields, as well as the preparation method and characteristics of the diamond electrode.

The contents of the symposium are shown in the followings.

The 50th Symposium on Powder Technology

Theme: Powder Technology to Create a Prosperous Future

Opening address Mr. Yoshio Hosokawa (President of Hosokawa Powder Technology Foundation)

Session 1 Chaired by Prof. emeritus Ko Higashitani (Kyoto University)

- Lecture 1
“Coal Utilization Power Engineering and Powder Technology for the Stable Power Supply in Low-Carbon Society”
Dr. Hisao Makino (Central Research Institute of Electric Power Industry, JAPAN)
- Lecture 2
“The Cancer Treatment Strategy with the Inorganic/Bio-Complex Nanoparticle”
Prof. Chiaki Ogino (Kobe University)

Session 2 Chaired by Prof. emeritus Kikuo Okuyama (Hiroshima University)

- Lecture 3
“Glassy State Foods Materials Produce New Food Flour”
Prof. emeritus Rikuo Takai (Tokyo University of Marine Science and Technology)

- Lecture 4
“Continuous Production of Nanoparticles by Supercritical Hydrothermal Synthesis
-Nanoparticles Synthesis, Nanohybrid Materials, and Surface Controlled Nanocatalysts-”
Prof. Tadafumi Adschiri (Tohoku University)
- Lecture 5
“The Internet-of-Things, Opportunities to Improve Manufacturing Processes”
Dr. Iain Crosley (Hosokawa Micron Ltd. (UK))

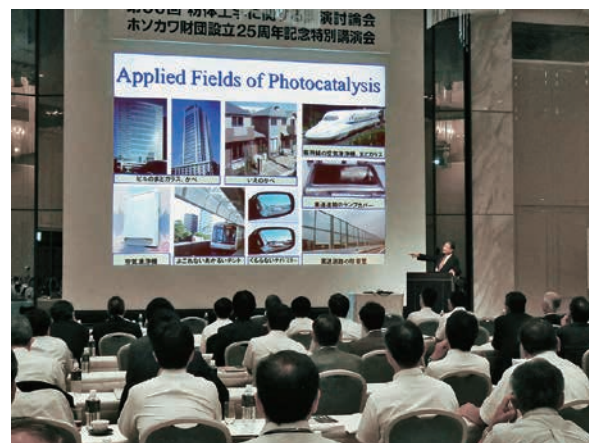
Session 3 Chaired by Prof. emeritus Minoru Takahashi (Nagoya Institute of Technology)

Special Lecture for the 25th Anniversary of the founding of HPTF

- Lecture 6
“Titanium Dioxide Photocatalysis and Diamond Electrode”
Special University Professor Emeritus of the University of Tokyo, Akira Fujishima (President
of Tokyo University of Science)



Symposium on Powder Technology



Special Lecture of 25th Founding Anniversary



Get-acquainted Party

The 23rd KONA Award

Dr. Hisao Makino, Executive Research Scientist of CRIEPI (Central Research Institute of Electric Power Industry), was selected as the winner of the 23rd KONA Award. The KONA Award is sponsored by Hosokawa Powder Technology Foundation and presented to scientists or groups who have achieved distinguished research work in the field of particle science and technology.

After finishing all the required curricula of Kyoto University for B.E. in 1977 and M.E. in 1979 respectively with each degree, Dr. Hisao Makino obtained his Doctoral degree from the same university in 1995. He joined CRIEPI in 1979 and became a Director of Chemical Energy Engineering Department of CRIEPI in 1997. Through the carrier as an Acting Vice President nominated in 2008, he has been serving as an Executive Research Scientist of CRIEPI since 2012. In parallel with his steady works in CRIEPI, he performed his academic contributions as a Visiting Research Fellow of Delft University of Technology in the Netherlands from 1989 to 1990. He has also carried out his educational activities by serving as a Visiting Professor of Gunma University since 2000 as well as Kyushu University since 2009.

His major research subject is the development of clean coal technologies for stable electric power supply. One of his distinguishing accomplishments is the development of new type high performance burners such as an advanced low NO_x burner and an advanced high turn down burner. He also investigated the estimation methods of the performance of electrostatic precipitator in pulverized coal combustion power stations and the control methods of degradation of the denitrification catalyst. Recently, he is developing a new type power generation system using oxygen and carbon dioxide blown gasification technology for the system of high efficiency power generation and high performance removal of carbon dioxide.

He has published over 100 research papers and more than 100 reviewed articles in journals and academic magazines. He has a great deal of experiences invited as an lecturer in about 100 conferences including about 20 international conferences. His research field covers the major subjects of powder technology, they are, (1) high temperature reaction of pulverized hydrocarbon resources, (2) dust collection technology in flue gas, (3) analysis of flow behavior in gas-solid phase flow, (4) measurement technology of fine particles, and (5) analysis of particle characteristics of coal ash.

He served Vice President of the Society of Powder Technology, Japan from 2003 to 2015 and President of this Society 2011–2015. And he has been serving the Vice president of Association of Powder Process Industry and Engineering, Japan since 2014 and the Vice President of The Japan Institute of Energy since 2008.

In summary, his contributions to academics and societies are outstanding as we can realize that the products of his research works are promoting the construction of high efficiency and clean power generation system for fossil fuel utilization.

On March 22, 2016, Mr. Yoshio Hosokawa, President of Hosokawa Foundation, presented the 23rd KONA Award to Dr. Hisao Makino at the presentation ceremony held at Hosokawa Micron Corporation in Hirakata.



General Information

History of the Journal

In the history of KONA Powder and Particle Journal, two organizations have been playing an important role. The one is the Council of Powder Technology, Japan (CPT) and the other is the Hosokawa Powder Technology Foundation (Hosokawa Foundation). The CPT was established in 1969 by Hosokawa Micron Corporation as a nonprofit organization to enhance the activities of research and development on powder science and technology. The Hosokawa Foundation was established in 1991 as a public-service corporation approved by the Ministry of Education, Culture, Sport, Science and Technology of Japan. The issues from No.1 (1983) to No.12 (1994) of KONA were published by CPT and the issues from No.13 (1995) by the Hosokawa Foundation.

The aim of KONA in the early days was to introduce excellent Japanese papers to the world and thus KONA consisted of papers recommended by some Japanese academic societies and translated from Japanese to English. From the issue of No.8, the CPT changed its editorial policy to internationalize the KONA and to incorporate papers by authors throughout the world in addition to translated papers. In response to this change, three editorial blocks have been organized in the world; Asian-Oceanian, American and European. The policy and system have not changed even after the Hosokawa Foundation has taken over from the CPT. From the issue of No.27 (2009), publication of translated papers has been terminated and only original papers have been published. The CPT is active still today and collaborates with the Hosokawa Foundation.

Aims and Scope

KONA publishes papers in a broad field of powder science and technology, ranging from fundamental principles to practical applications. The papers describing technological experiences and critical reviews of existing knowledge in special areas are also welcome.

The submitted papers are published only when they are judged by the Editor to contribute to the progress of powder science and technology, and approved by any of the three Editorial Committees.

The paper submitted to the Editorial Secretariat should not have been previously published.

Category of Papers

- Invited articles
Review papers and special articles invited by the KONA Editorial Committees.
- Contributed papers
Original research and review papers submitted to the KONA Editorial Committees, and refereed by the reviewers and editors.

Submission of Contributed Papers

"Inquiry Letter" for submission on the KONA website (<http://www.kona.or.jp>) needs to be sent to the Editor-in-Chief (mail to: contact_zasubmit@hmc.hosokawa.com) prior to the submission of the manuscript. After then, papers will be guided to each KONA Editorial Secretariat as follows.

- Asian/Oceanian Editorial Secretariat
Dr. T. Yokoyama or Dr. L. Cui
Hosokawa Powder Technology Foundation
1-9, Shodaitajika, Hirakata-shi, Osaka, 573-1132 Japan
- European / African Editorial Secretariat
Dr. S. Sander or Ms. L. Kneisl
Hosokawa Alpine AG
Peter-Dörfler-Straße 13-25, D - 86199 Augsburg, Germany
- American Editorial Secretariat
Dr. C. C. Huang
Hosokawa Micron Powder Systems
10 Chatham Road, Summit NJ 07901 USA

Publication in KONA is free of charge.

Please visit KONA's website for the most current Submission Information at <http://www.kona.or.jp>

Publication Schedule

KONA is published annually. The publication date is around January 10th.

Subscription

KONA is distributed free of charge to senior researchers at universities and laboratories as well as to institutions and libraries in the field throughout the world. The publisher is always glad to consider the addition of names of those, who want to obtain this journal regularly, to the mailing list.

Free electronic publication of KONA is available at <http://www.kona.or.jp>

Instructions to Authors

(1) Manuscript format

- Electric files should be submitted to the Editorial Secretariat by online. Authors' short biography with less than 100 words per person and color photographs of all the authors should be attached to the final version.
- The structure of manuscripts should follow the following order; title, authors, affiliations, abstract, graphical abstract, keywords, main text, (acknowledgement), (appendix), (nomenclature), references. The items with parentheses are not mandatory.
- Full postal addresses must be given for all the authors. Indicate the corresponding author by the mark "*" after the name. Telephone and fax numbers and e-mail address should be provided for the corresponding author.
- Abstract should not exceed 200 words.
- Graphical abstract should be a concise, visual summary of the article which will be displayed in the contents list both online and print.
- The appropriate number of keywords is 5 or 6.
- The maximum pages printed in KONA are supposed to be: 15 for an original paper and 25 for a review paper.
- Symbols and units should be listed in alphabetical order with their definition and dimensions in SI units.
- The color figures will appear in color both on the KONA Website (<http://www.kona.or.jp>) and also in the paper version.
- Concerning references, the alphabetical system should be adopted. Please use reference management software such as Endnote to manage references as far as possible.

List: References should be arranged first alphabetically and then further sorted chronologically if necessary. More than one reference from the same author(s) in the same year must be identified by the letters "a", "b", "c", etc., placed after the year of publication.

Examples:

- Reference to a book:

Strunk Jr. W., White E.B., The Elements of Style, fourth ed., Longman, New York, 2000.

- Reference to a chapter in an edited book:

Mettam G.R., Adams L.B., How to prepare an electronic version of your article, in: Jones B.S., Smith R.Z. (Eds.), Introduction to the Electronic Age, E-Publishing Inc., New York, 2009, pp.281-304.

- Reference to a journal publication:

Tsuji Y., Tanaka T., Ishida T., Lagrangian numerical simulation of plug flow of cohesionless particles in a horizontal pipe, Powder Technology, 71 (1992) 239-250.

Text: All citations in the text should refer to:

1. Single author: the author's name (without initials, unless there is ambiguity) and the year of publication;
2. Two authors: both authors' names and the year of publication;
3. Three or more authors: first author's name followed by "et al." and the year of publication.

Citations may be made directly (or parenthetically). Groups of references should be listed first alphabetically, then chronologically.

Examples: "as demonstrated (Hidaka J. et al., 1995; Tsuji Y., 1992a, 1992b, 1993). Mori Y. and Fukumoto Y. (2002) have recently shown"

(2) Copyright and permission

- The original paper to be submitted to KONA has not been published before in any language or in any journal or media; it is not submitted and not under consideration for publication in whole or in part elsewhere.
- Authors are responsible for obtaining permission from the copyright holders to reproduce any figures, tables and photos for which copyright exists.
- The KONA Journal applies the **Creative Commons Attribution License** to all works published by the Journal. Copyright stays with the agreed copyright owner, and the Hosokawa Powder Technology Foundation is granted the exclusive right to publish and distribute the work, and to provide the work in all forms and media.
- Users of the journal will be able to reuse the contents in any way they like, provided they are accurately attributed. No permission is required from either the authors or the publisher.

Start out small and hit it really big.

The picoline® series includes 10 function modules for fine milling, classifying or mixing powders and suspensions and for wet milling and for dispersing suspensions. These modules are derived from the established product lines. You can rest assured that there will be no problems in scaling up a process developed with a picoline® machine to a production scale.

HOSOKAWA ALPINE Aktiengesellschaft
Peter-Dörfler-Straße 13 – 25
86199 Augsburg, Germany
Tel.: +49 821 5906-0 · Fax: +49 821 5906-101
E-Mail: mail@alpine.hosokawa.com
www.hosokawa-alpine.com



HOSOKAWA ALPINE

Mixing, Drying & Agglomeration Solutions



Briquetting Drying Milling Extrusion
Containment Nano-Technology
Toll processing Agglomeration
Classifying Micronisation Filling & Weighing Pelletising
Mixing De-Agglomeration
Compaction

Hosokawa Micron B.V. is expert in the design, manufacture and supply of powder processing systems and equipment for the mechanical and thermal processing of dry and wet powders, specifically mixing, drying and agglomeration.

The company's strong emphasis on system design capability is backed up by extensive test centre and toll processing facilities to support you in finding optimal solutions for your applications.

Hosokawa Micron B.V. is a member of the Hosokawa Micron Group, responding to global needs through emphasis on materials science and engineering.



HOSOKAWA MICRON B.V.

Gildenstraat 26 - PO Box 98 - 7000 AB Doetinchem, NL
Phone: +31 (0)314 37 33 33 - Fax: +31 (0)314 37 34 56
E-mail: info@hmbv.hosokawa.com - Internet: www.hosokawam micron.nl

MIKRO AIR JET SIEVE® MAJS_x

Particle Size Analyzer



- Analyzes the particle size of dry powders from 20 µm to 4,750 µm (#635 to #4 mesh)
- Touch screen controls, built in analysis computer & easy-to-follow instructions
- Suitable for Chemical, Pharmaceutical, Food, Mineral, Plastic & Cosmetic applications
- Aerodynamic sieving continuously disperses the sample and cleans test sieve
- Economical, Fast, Accurate & Easy to Use

Watch a short demo at www.MikroAirJetSieve.com



HOSOKAWA MICRON POWDER SYSTEMS

Summit, New Jersey, USA • (973) 273 - 6360 • www.MikroAirJetSieve.com • help@hmps.hosokawa.com

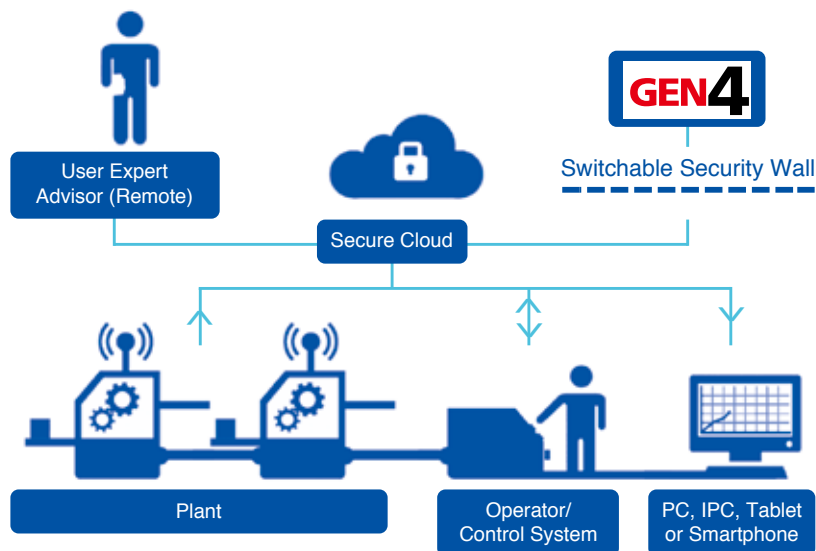


HOSOKAWA GEN4

Data Driven Manufacturing

Addressing your manufacturing challenges

Gen4 converts data mining and machine learning into measurable manufacturing improvements.



With modular solutions we work at a pace that meets your specific business needs.

- remote data collection
- analysis and interrogation
- online advisory systems
- intelligent monitoring solutions
- closed loop control systems

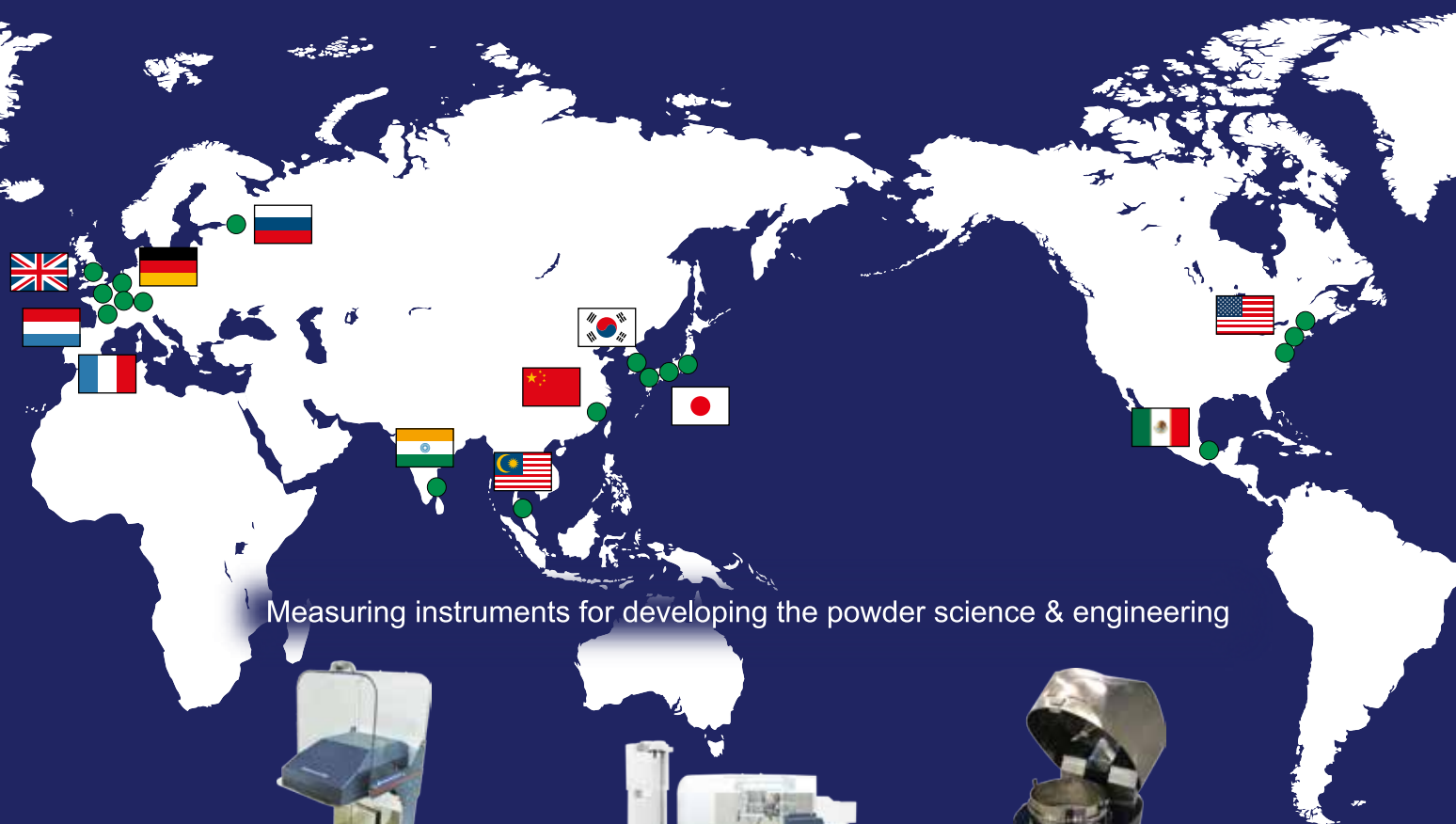
Understand • Monitor • Control



T: +44 (0)1928 755100 • info@hosokawagen4.com • hosokawagen4.com

HOSOKAWA MICRON GROUP

The Hosokawa Micron Group will always be the leading global company covering the mountain range of Powder Technologies. The Group has been a pioneer in the field of powder and particle processing, blown film processing, and confectionary and bakery technologies. We provide R&D, engineering, manufacturing and services in various fields of the world's major industrial markets.



Measuring instruments for developing the powder science & engineering



Penetration speed
Peneto Analyzer, PNT-N



Carr's indices
Powder characteristics tester, PT-X



Wet sieving
Viblette, VBL



Process Technologies for Tomorrow

HOSOKAWA MICRON

Headquarters Location :

HOSOKAWA MICRON CORPORATION

<http://www.hosokawamicron.com/>